1

AD-A213 358

PORT DOCUMENTATION PAGE

1b RESTRICTIVE MARKINGS

2b DECLASSIFICATION DOWNGRADING SCHEDULE	3 DISTRIBUTION/AVAILABILITY OF REPORT Approved for public release; distribution unlimited

4. PERFORMING ORGANIZATION REPORT NUMBER(S) —	5 MONITORING ORGANIZATION REPORT NUMBER(S) 5553-MS-01

6a NAME OF PERFORMING ORGANIZATION Imperial College of Science, Technology and Medicine	6b OFFICE SYMBOL (If applicable)	7a NAME OF MONITORING ORGANIZATION USARDSG-UK

6c ADDRESS (City, State, and ZIP Code) Department of Mechanical Engineering Exhibision Road London SW7 2BX	7b ADDRESS (City, State, and ZIP Code) Box 65 FPO New York 09150-1500

8a NAME OF FUNDING/SPONSORING ORGANIZATION European Research Office, USARDSG-UK	8b OFFICE SYMBOL (If applicable) AMXSN-UK-RM	9 PROCUREMENT INSTRUMENT IDENTIFICATION NUMBER DAJA45-86-C-0037

8c ADDRESS (City, State, and ZIP Code) Box 65 FPO New York 09150-1500	10 SOURCE OF FUNDING NUMBERS			
	PROGRAM ELEMENT NO 61102A	PROJECT NO. 1L161102BH5	TASK NO 7 0	WORK UNIT ACCESSION NO

11 TITLE (Include Security Classification)
(U) ADHESIVE BONDING OF THERMOPLASTIC COMPOSITES

12 PERSONAL AUTHOR(S)
Professor A. J. Kinloch

13a TYPE OF REPORT Final	13b TIME COVERED FROM 23 Jul 86 TO 23 Sep 89	14 DATE OF REPORT (Year, Month, Day) 1989/9/19	15 PAGE COUNT 335

16 SUPPLEMENTARY NOTATION
—

17	COSATI CODES		18 SUBJECT TERMS (Continue on reverse if necessary and identify by block number)
FIELD	GROUP	SUB-GROUP	Adhesives Composites Fracture Energy, Thermoplastic Composites

19 ABSTRACT (Continue on reverse if necessary and identify by block number)

See Overleaf

DTIC
ELECTE
OCT 11 1989
S B D

20 DISTRIBUTION/AVAILABILITY OF ABSTRACT ☒ UNCLASSIFIED/UNLIMITED ☒ SAME AS RPT ☐ DTIC USERS	21 ABSTRACT SECURITY CLASSIFICATION Unclassified
22a NAME OF RESPONSIBLE INDIVIDUAL Dr. Wilbur C. Simmons	22b TELEPHONE (Include Area Code) 01-409-4423	22c OFFICE SYMBOL AMXSN-UK-RM

DD FORM 1473, 84 MAR

83 APR edition may be used until exhausted
All other editions are obsolete.

SECURITY CLASSIFICATION OF THIS PAGE

Unclassified

ABSTRACT

This thesis first discusses the problems that occur when thermoplastic-based fibre-composite materials are bonded using structural engineering adhesives, such as epoxy and acrylic adhesives. A double-cantilever beam joint has been employed and it is shown that the value of the adhesive fracture energy, G_C, is very low when a simple abrasion/solvent-wipe surface pretreatment is used for the thermoplastic fibre-composites. This arises from crack growth occurring along the adhesive/composite interface, which is relatively weak when such a pretreatment is employed.

Secondly, the surfaces of the corona-discharge treated composites have been characterised using X-ray photoelectron spectroscopy, contact angle analysis and scanning electron microscopy. These studies were undertaken to identify the detailed mechanisms whereby corona-discharge treatment may so effectively modify the surfaces of the thermoplastic fibre-composites. These studies revealed that the strong adhesion associated with corona pretreatment is via increasing the wettability and intrinsic adhesion of the thermoplastic fibre-composite materials.

Thirdly, it is demonstrated how very effective a corona-discharge surface pretreatment may be for these materials. Indeed, when such a pretreatment is used, interfacial crack growth is no longer observed but the crack now propagates either cohesively in the adhesive or through the composite substrate; both failure modes lead to relatively high values of G_C, with the former resulting in the highest values of G_C being recorded. From measuring the fracture properties of the composites, and combining these data with a detailed analysis of the stresses in the DCB joint, calculated using a finite element analysis, the reasons for these different loci of failure have been understood and predicted.

Finally, having identified techniques for obtaining good interfacial adhesion, the thesis concludes by describing a study on designing efficient lap joints. A comparison is drawn between the experimentally obtained values and the theoretical predictions from finite element analysis.

THE ADHESIVE BONDING OF THERMOPLASTIC COMPOSITES

Final Technical Report

by

A.J. Kinloch and G.K.A. Kodokian

September 1989

United States Army

EUROPEAN RESEARCH OFFICE OF THE U.S. ARMY

London, England

CONTRACT NUMBER DAJA-45-86-C-0037

Imperial College of Science, Technology and Medicine

London, England

Approved for Public Release; distribution unlimited
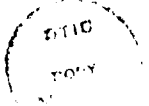
ACKNOWLEDGEMENTS

My sincerest thanks go to my supervisor Dr. A. J. Kinloch for his guidance and advice.

I am indebted to my colleagues, friends and family for their useful discussions and encouragement, to the technicians who prepared many of my samples and for their technical advice, and to the many companies who took direct interest in my project by providing novel materials. Of those companies I would like particularly to mention: Du Pont (U.S.A.), I.C.I. (U.K.), Phillips Petroleum (U.S.A.), American Cyanamid (U.S.A.), Cyanamid Aerospace (U.K.), Ciba Geigy (Switzerland), Westland Helicopters (U.K.) and Hysol Dexter (Switzerland).

I am also indebted to Dr. J. F. Watts and the University of Surrey for their kind support with the surface chemistry analyses.

I wish to express my gratitude to the the U.K. Government for considering me as a home student for fee purposes through its committee of Vice-Chancellors and Principals of the Universities of the United Kingdom (O.R.S. Award).

Finally, I would like to thank the U.S. Government who supported and financed this project through its European Research Office of the U.S. Army. In this respect, I would like to thank Dr. S. E. Wentworth for his many contributions.

CONTENTS

NOMENCLATURE

a	:	Crack length
a_0	:	Length of crack-starter
A	:	Area
A_i	:	Constant coefficient
b	:	Ligament size
B	:	Width
c	:	Rate
C_A	:	Acid constant from acid-base interaction
C_B	:	Base constant from acid-base interaction
C_{ij}	:	Stiffness
d	:	Depth
E and E_{ii}	:	Young's moduli
E_A	:	Acid constant from acid-base interaction
E_B	:	Base constant from acid-base interaction
E_{co}	:	Corona energy
G and G_{ij}	:	Shear moduli
G_c	:	Adhesive fracture energy
$G_c(il)$	:	Interlaminar fracture energy
G_{Ic}	:	Critical energy release rate in Mode I
$G_c(plateau)$	:	Adhesive fracture energy in the plateau region
G_0	:	Purely interfacial fracture energy
h	:	Height
I	:	Second moment of inertia
J	:	Rate of change of energy with crack area
J_{Ic}	:	J-integral in Mode I
k	:	Bending moment factor
K	:	Stress intensity factor
K_I	:	Stress intensity factor in Mode I
K_{Ic}	:	Critical fracture toughness in Mode I

l and L	:	Lengths
L_e	:	Length of electrode
M	:	Bending moment
n^{ab}	:	Number of acid-base pairs per unit area
N	:	Number of cycles
P	:	Load
P_c	:	Critical load
P_{co}	:	Power of corona-discharge treater
r	:	Polar coordinate
r_c	:	Surface roughness correction factor
R	:	Radius
R	:	Chemical ring
R_g	:	Gas constant
S and S_{ij}	:	Compliances
S_c	:	Spreading coefficient
S_{xx}, S_{yy} and S_{zz}	:	Compliances in x, y and z-directions respectively
S_{xy}, S_{yz} and S_{zx}	:	Compliances in the xy, yz and zx planes respectively
SH_{xy}, SH_{xz} and SH_{yz}	:	Shear compliances in the xy, xz and yz planes respectively
t	:	Thickness
T	:	Temperature
T_g	:	Glass transition temperature
T_m	:	Crystalline melting temperature
T_{tm}	:	Torsional moment
u, v and w	:	Displacements in the x, y and z directions respectively
U	:	Elastic energy
V	:	Velocity
V_{mv}	:	Molar volume
W	:	Strain energy per unit volume
W_A	:	Thermodynamic work of adhesion
W_A^{ab}	:	Thermodynamic work of adhesion arising from acid-base interactions
W_{AL}	:	Thermodynamic work of adhesion in the pesence of a liquid

W^d	:	Thermodynamic work of adhesion arising from dispersion interactions
W^p	:	Thermodynamic work of adhesion arising from polar interactions
W_J	:	Depth of J-integral test specimen
Z	:	Work

GREEK SYMBOLS

α	:	Adhesive fillet angle
∞	:	Infinity
	:	Composite taper angle
δ_s	:	Solubility parameter
Δ	:	Deflection
ΔH^{ab}	:	Enthalpy due to acid-base interaction
ΔH_v	:	Molar heat vaporization
$\bar{\varepsilon}^p$	:	Equivalent plastic strain
ε_i	:	Strain
$\varepsilon_x, \varepsilon_y$ and ε_z	:	Strains in the x,y and z directions respectively
γ	:	Surface free energy
γ_a	:	Adhesive surface free energy
γ_{as}	:	Adhesive/substrate interfacial free energy
γ_a^d	:	Dispersion surface energy of adhesive
γ_a^p	:	Polar surface energy of adhesive
γ_C	:	Critical surface tension

γ^d	:	Dispersion energy
γ^h	:	Hydrogen bonding energy
γ_{LV}	:	Surface tension of a liquid on a solid
γ_{LV}^d	:	Dispersion energy of a liquid
γ_{LV}^p	:	Polar energy of a liquid
γ^p	:	Polar energy
γ_s	:	Total surface free energy of a solid
γ_s^d	:	Dispersion surface energy of the substrate
γ_s^p	:	Polar surface energy of the substrate
γ_{SL}	:	Solid/liquid interfacial tension
γ_{SV}	:	Soild/vapour interfacial tension
γ_{ss}	:	Shear strain
$\%\gamma^p$	:	Percent polar surface energy
γ_{xy}, γ_{xz} and γ_{yz}	:	Shear strains in the xy, xz and yz planes respectively
γ_1 and γ_2	:	Surface energy due to phase 1 and 2 respectively
γ_{12}	:	Surface energy due to phases 1 and 2
λ	:	Inelastic mean free path
μ	:	Dipole moment
π_e	:	Equilibrium spreading pressure
θ	:	Polar angle
θ_a	:	Apparent contact angle
θ_t	:	Intrinsic contact angle

σ_c	:	Compressive stress
σ_{ij}	:	Components of the stress tensor
σ_t	:	Tensile stress
σ_x, σ_y and σ_z	:	Stresses in the x, y and z directions respectively
σ_{ys}	:	Yield stress
σ_{yy}	:	Predicted transverse tensile stress
σ_{yyc}	:	Transverse tensile fracture stress
σ	:	Equivalent stress
σ_0	:	Applied stress
τ	:	Shear stress
τ_{xy}, τ_{xz} and τ_{yz}	:	Shear stresses in the xy, xz and yz planes respectively.
υ and υ_{ij}	:	Poisson's ratios
Φ_{SL}	:	Solid-liquid interaction parameter
Φ_{12}	:	Interaction parameter

ABBREVIATIONS

ABS	:	Acrylonitrile-butadiene-styrene
AES	:	Auger electron spectroscopy
AR	:	Aromatic ring
ASTM	:	American Society for Testing and Materials
ATR	:	Attenuated total reflectance
CAA	:	Contact angle analysis
Coh	:	Cohesive
CPU	:	Computer time
DCB	:	Double-cantilever beam
DLJ	:	Double-lap joint

ESCA	:	Electron spectroscopy for chemical analysis
FEA	:	Finite element analysis
FRP	:	Fibre-reinforced plastic
hµ	:	Electron binding energy
HF	:	High-frequency
HP	:	High-power
HSA	:	Hemispherical sector analyser
Il	:	Interlaminar
IMFP	:	Inelastic mean free path
ISS	:	Ion scattering spectroscopy
LEFM	:	Linear elastic fracture mechanics
LDPE	:	Low-density polyethylene
L o F	:	Locus of failure
LVDT	:	Linear-variable displacement-transducer
MEK	:	Methyl-ethyl ketone
PA	:	Polyamide
PE	:	Polyethylene
PEEK	:	Poly(ether-ether ketone)
PEI	:	Poly(ether imide)
PI	:	Polyimide
PPS	:	Poly(phenylene sulphide)
Pre-preg	:	Pre-impregnated
PWHM	:	Peak width at half the maximum
R.H.	:	Relative humidity
SEM	:	Scanning electron microscopy
SIMS	:	Secondary ion mass spectroscopy
SLJ	:	Single-lap joint
TAT	:	Thick-adherend-test
TPFC	:	Thermoplastic fibre-composite
TSFC	:	Thermoset fibre-composite
U/C	:	Unidirectional-carbon-fibre
UHV	:	Ultra high vacuum
U/K	:	Unidirectional-"Kevlar"-fibre
W/C	:	Woven-carbon-fibre
WDM	:	Weighted percent dipole moment
W/K	:	Woven-"Kevlar"-fibre
XPS	:	X-ray photoelectron spectroscopy
XRF	:	X-ray flourescence

CHAPTER ONE

INTRODUCTION

1.1. GENERAL

The aerospace, automotive and military equipment industries have shown great interest in bonding the structures of aeroplanes, vehicles and helicopters using engineering adhesives. This interest arises because polymeric adhesives offer many advantages when compared with other more conventional methods such as welding, riveting, bolting, brazing etc. The following points characterise the use of adhesives in engineering applications:

1. Their ability to join dissimilar materials.
2. Their ability to join thin sheets of materials.
3. An improved stress distribution is obtained.
4. An increase in design flexibility and an improved strength to weight ratio is often introduced.
5. A reduction in manufacturing costs may be obtained, since adhesives can easily be coupled with automation for mass production.

Polymeric adhesives are a particularly good method for joining fibre-reinforced plastics (FRPs) and these type of materials are being increasingly used in engineering structures. Indeed, there has been a rapid growth in the use of FRPs in engineering applications in the last few years. The rapid growth has been achieved mainly by the replacement of traditional materials, primarily metals. The following points characterise the use of FRPs in engineering applications:

1. A higher modulus per unit weight (specific modulus).
2. A higher strength per unit weight (specific strength).
3. Directional properties permit further weight reductions and allow the possibility of introducing stiffness and strength into a structure where it is really required.

Therefore, coupling the advantages of adhesives with those of FRP materials would be a significant advantage in many engineering structures. However, although these advantages are well recognized by engineering industries, there is still a reluctance to employ structural adhesives. This largely stems from a lack of basic engineering data of the properties of the adhesives under service environments. Thus, as emphasized in a Cabinet Office report [1]:

"There is a need for research into techniques to demonstrate the quality of adhesive joints and to predict their in-service behaviour and life". This reluctance is further aggravated by the fact that adhesive bonding of thermoplastic resins is hampered by the poor adhesion associated with these materials. A good example being, the adhesive bonding of polyethylene. Hence, thermoplastic fibre-composites (TPFCs) might also be expected to represent "difficult-to-bond" materials.

1.2. THE AIMS OF THE PROJECT

The present work examines the adhesive bonding of fibre-composites based upon thermoplastic matrices which offer several advantages compared to those based upon thermosetting resins. Such advantages include the ability to readily form the fibre-composite materials into complex shapes and a greater resistance to damage due to thermoplastic matrices usually being tougher than thermosetting matrices. However, many technical and economic problems have to be resolved before TPFC materials may be widely used by industry. One such problem is that of bonding TPFC materials using conventional structural adhesives technology [2]. Therefore, the main aims of the present project were:

1. To investigate the extent of the problem associated with the adhesive bonding of thermoplastic fibre-composite (TPFC) materials and, if necessary, to develop suitable bonding methods.

2. To identify the mechanisms of adhesion between typical engineering adhesives and TPFC materials.

3. To use the above information to investigate whether the superior material properties of TPFC materials, as compared to thermosetting fibre-composite (TSFC) materials, can be used to obtain stronger overlap joints; such joint designs being typically used in industrial applications. Also, to develop a finite element analysis (FEA) approach to predict theoretically the experimental results.

1.3. THESIS LAYOUT

The thesis is divided into several main chapters, each dealing with a specific topic and each containing a literature survey, experimental details, results, discussions and conclusions. Chapter Two describes the materials employed and the development of a suitable surface pretreatment technique for the TPFC substrates which was found necessary to attain good adhesion and high joint strenghts. To characterise the surfaces of the fibre-composite materials

prior to bonding, techniques such as contact angle analysis (CAA), scanning electron microscopy (SEM) and X-ray photoelectron spectroscopy (XPS) were employed, and the use of these methods are discussed in Chapter Three. The following chapter considers the measurement of the adhesive fracture energy, G_c, which was undertaken to study the bonding of TPFC materials using the various engineering adhesives. To assist in establishing the mechanisms of adhesion the locus of failure in these joints was of particular interest. The results of the SEM, XPS and FEA analyses which were employed to identify and predict the locus of failure are presented in Chapter Five. Next, in Chapter Six, the mechanisms of adhesion are considered, and conclusions are established by drawing together results presented in the earlier chapters. Chapter Seven is concerned with an attempt to employ the superior material properties of the TPFC materials in order to obtain higher joint strengths and efficiencies, as compared to thermosetting-fibre-composite joints. Chapter Eight states the main conclusions and the recommendations for future work.

CHAPTER TWO

MATERIALS AND PRETREATMENT TECHNIQUES

2.1. INTRODUCTION

In this chapter the characteristics of thermoplastic and thermoset fibre-composite materials will first be outlined and the work reported in the literature concerning the surface pretreatment of thermoplastic fibre-composite (TPFC) materials will be presented. The materials used in the present research work will then be described. Finally, the surface pretreatment techniques which were developed and employed for the TPFC materials will be discussed.

2.2. LITERATURE SURVEY

2.2.1. Introduction

First it is essential to consider some of the terminologies used in fibre-composite materials.

1. Fibre orientation: as will be discussed later, all the composites used were prepared using continuous fibres and in this case a conventional approach to identify the fibre orientations is that the angle is taken positive when read clockwise from the vertical, which is taken as 0^0, and negative when read anticlockwise.

2. Stacking sequence: the stacking sequence in fibre-composite materials is also important since the many mechanical properties of composite materials frequently depend upon the stacking sequence. The terminology used is shown in Figure 2.1(a) which is a $[0^0]_4$ composite, where 0^0 represents the fibre orientation and 4 represents the number of plies. In the same way the four plies in Figure 2.1(b) are represented by $[90^0, 0^0]_2$ where 2 is the repetition sequence. Composite sheets can also be manufactured using woven-fibres, as shown in Figure 2.2.
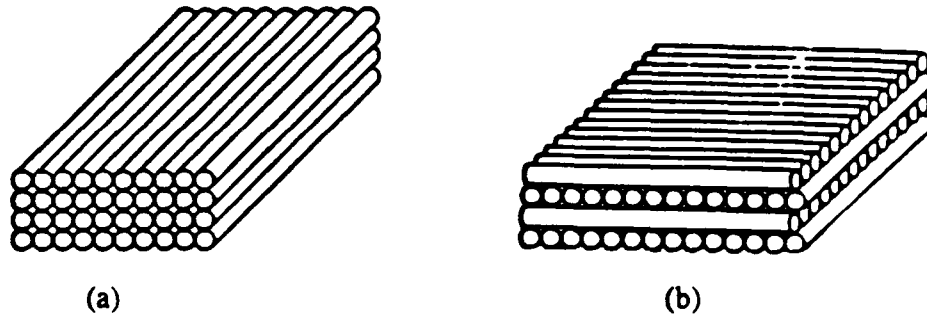
Fig. 2.1. Lay-up of reinforced plastics: (a) unidirectional-fibres and (b) crossed-fibres.
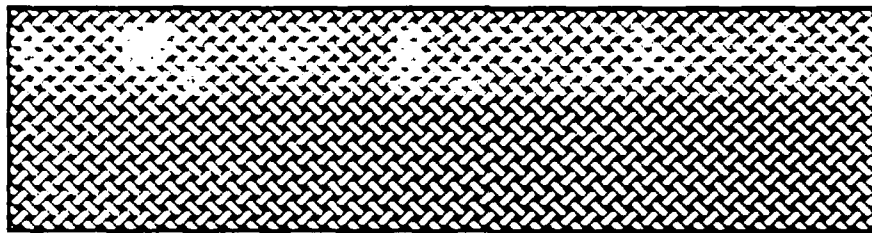
Fig. 2.2. Schematic presentation of woven-fibres.

2.2.2. Characteristics of Thermoplastic and Thermoset Fibre-Composites

Th.rmoplastic polymers have linear or branched polymer chains which can melt again when the temperature is raised above their consolidation temperature, see Figure 2.3(a) and (b). The molecular chains are able to slide with respect to each other when the temperature is raised above their melting temperature. There are two types of thermoplastic polymers; crystalline and amorphous. These materials derive their strength and stiffness from the inherent properties of the monomer units and the very high molecular weight. This ensures that in amorphous thermoplastics there is a high concentration of molecular entanglements, which act like cross-links. In crystalline thermoplastics there is a high degree of molecular order and alignment. Examples of semi-crystalline thermoplastics are polyethylenes, poly(ether-ether ketone) and polyamides. Such polymers contain both crystalline and amorphous regions and are usually relatively tough.

In simple terminology, thermosetting polymers are those polymers which char when the temperature is raised above their curing temperature. They have highly cross-linked three-dimensional molecular networks, see Figure 2.3(c). The mechanical properties depend on the molecular units making up the network of chains and on the length and density of

crosslinking. These polymers are usually brittle. Example of thermosetting polymers include phenol-formaldehyde resins and high-performance resins and adhesives which are based upon epoxy resins.

| (a) Linear | (b) Branched | (c) Network |
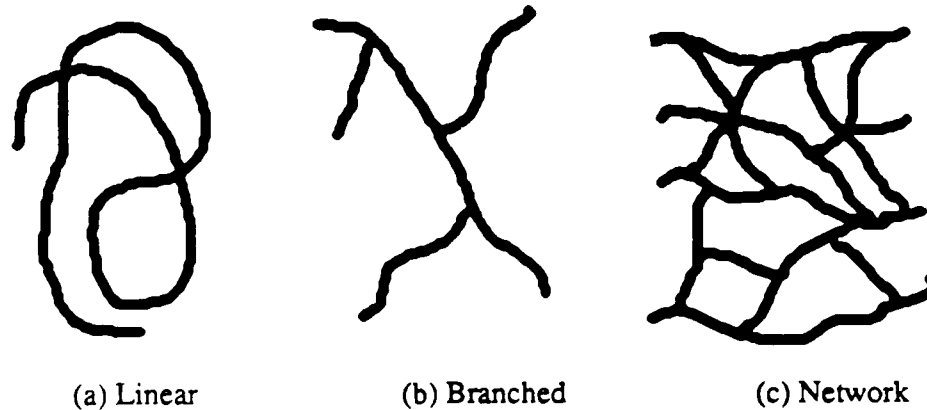
Fig. 2.3. Schematic representation of different types of polymer molecules.

The advantages of employing thermoplastic fibre-composite (TPFC) over thermosetting fibre-composite (TSFC) materials are:

1. The melting property of the thermoplastic resin means an element of flexibility in the bonding techniques that can be employed, example resistance welding. The melting property also adds an element of flexibility, which is desired by industry, in repairing TPFC components this is specially true when a big TPFC component has a minor structural damage, example the wing of an aircraft.

2. Better resin properties such as higher T_g and higher fracture energy means better performance and mechanical properties for the TPFC materials. Obviously, future materials will be required not only to be lighter but also to have better performance properties.

2.2.3. Adhesive Bonding of Thermoplastic Fibre-Composites

The joining of thermoplastic-composite structural components will be essential in industrial fabrication processes. This may be accomplished by either welding, a fusion bonding process, or bonding with adhesives. Joining thermoplastic composites by means of fusion bonding has been attempted by several researchers [3, 4]. Techniques, such as resistance welding, induction welding, laser welding, hot plate welding and ultrasonic welding have been investigated. However, the high carbon-fibre content in the thermoplastic matrix, and the high thermal and electrical conductivity of the fibres, make the fusion bonding processing difficult. For example, problems such as uneven heating through the bonded area, delamination and distortion of the composite materials, have to be overcome before this technique can be readily

employed. Further, the above problems become more acute when bonding large composite parts such as aircraft components. Therefore, the adhesive bonding of TPFC materials is a very attractive alternative method to a welding process.

Before reviewing the work which has been reported on the pretreatment of TPFC materials it is of interest to describe the pretreatments required for the adhesive bonding of thermosetting based fibre-composites. Such methods will obviously act as a starting point for the pretreatment of TPFC substrates.

The work reported [5-8] in the literature suggests that thermosetting-based fibre-composites (TSFC) require only a simple abrasion and solvent-wipe pretreatment prior to adhesive bonding. This technique ensures that any weak boundary layers and/or releasing agents, transferred to the surface whilst processing, are reduced substantially. In fact, a McDonnel Douglas report [9] suggests that grit blasting with aluminium oxide is the best surface preparation known.

There is little information available in the literature regarding pretreatment of TPFC materials. This largely stems from the fact that these materials are relatively new and indeed most of the TPFC materials employed in this project are still categorised as "developing" materials as opposed to being widely used in industrial production. Initial work by Kinloch and Taig [10] on the adhesive bonding of carbon-fibre/poly(ether-ether ketone) (PEEK) thermoplastic composite, termed "PEEK composite", found that if this material was bonded using structural epoxy adhesives then the typical surface pretreatment used for clean and dry thermosetting-based fibre-composites, namely a light-abrasion/solvent-wipe pretreatment, was clearly inadequate. The resulting lap shear joints were very weak, yielding failure loads per unit width of about 0.45MN/m when a cold-cured epoxy-paste adhesive was employed. They also observed a large variation of about 15 to 35% in the joint strength values. However, if this same pretreatment is employed for a thermosetting-based fibre-composite then employing the same adhesive a value of 1.85MN/m may be obtained with a coefficient of variation less than 11%, as will be shown in Chapter Seven. Finally, Kinloch and Taig employed scanning electron microscopy and observed that the locus of joint failure was apparently at the adhesive/thermoplastic-composite interface. Therefore, they concluded that future work should focus upon increasing the level of intrinsic adhesion at the adhesive/composite interface.

It was precisely for the above reason that the current research work was undertaken. In the last year or two there has been some research work reported [11-13] on the adhesive bonding of thermoplastic composites. However, it should be noted that several of these reports appeared after the current research work was well underway. (The first publication of the

current research work appeared in the Journal of Materials Science in 1988 [14]).

Wu et al. [12] attempted to improve the intrinsic adhesion of a PEEK carbon-fibre composite. They employed eight different types of pretreatment techniques which were: methyl-ethyl ketone (MEK) wipe, abrasion, abrasion plus water rinse, chromic-sulphuric acid etch, plasma treatment with oxygen, etching in a solution of naphtalene and tetrahyrofuran, silane coupling agent treatment and employing a primer ("De Soto 823-707"). They employed lap shear experiments bonded to epoxy-based adhesives, similar to those employed by Kinloch and Taig [10]. Wu et al. reported that the loads at failure could be increased from about 0.75MN/m from employing abraded specimens to about 3MN/m from chromic-sulfuric acid etch and oxygen plasma etch pretreated specimens. From their lap shear experiments Wu et al. deduced that the chromic-sulfuric acid etch and oxygen plasma pretreatments were the best techniques for adhesive bonding of the PEEK composite. They employed X-ray photoelectron spectroscopy to analyse the surfaces after treatment. They concluded that the improved bonding was due to the increased concentration of surface oxygen groups, which was highest for the two aforementioned pretreatments. Furthermore, they employed scanning electron microscopy to analyse the fractured surfaces. They concluded that the higher loads to failure were associated with failures initiating in the adhesive. Their analyses imply that, once the right functional groups are present on the surface of the PEEK composite then the problem of premature interfacial failure occurring at low applied loads is prevented.

From the above discussions it may be concluded that the PEEK composite requires a surface pretreatment to improve its intrinsic adhesion. However, the above studies do not indicate the fundamental mechanisms involved in the adhesion process and the work is confined to one type of thermoplastic composite and two types of epoxy adhesives. Obviously, one can raise the question of whether the poor adhesion is confined only to this particular type of thermoplastic composite bonded using the epoxy adhesives. In this thesis, a number of TPFC materials and a number of different types of adhesives will be employed. These materials will be presented next.

2.3. MATERIALS USED

2.3.1. Fibre-Composites

The fibre-composites studied consisted of nine different thermoplastic-based materials and one thermosetting-based composite, included for comparative purposes. The materials employed are listed in Table 2.1 below.

Table 2.1. The thermoplastic and thermoset fibre-composites employed.

Material	Manufacturer	Commercial name	Shortened name

Thermoplastic Fibre-Composites (TPFC)

(a) Unidirectional-carbon-fibre based on poly(ether-ether ketone)	I.C.I. plc.	"APC-2"	U/C-PEEK
(b) Unidirectional-carbon-fibre based on polyamide copolymer	Du Pont	"Carbon/J2"	U/C-PA
(c) Woven-carbon-fibre based on polyamide copolymer	Du Pont	"Carbon/J2"	W/C-PA
(d) Unidirectional-"Kevlar"-fibre based on polyamide copolymer	Du Pont	"Kevlar/J2"	U/K-PA
(e) Woven-"Kevlar"-fibre based on polyamide copolymer	Du Pont	"Kevlar/J2"	W/K-PA
(f) Woven-carbon-fibre based on poly(ether imide)	American Cyanamid	"CYPAC X7005"	W/C-PEI
(g) Unidirectional-carbon-fibre based on polyimide	British Petroleum plc	"JD861"	U/C-PI
(h) Woven-carbon-fibre based on polyimide	British Petroleum plc.	"JD861"	W/C-PI
(i) Unidirectional-carbon-fibre based on poly(phenylene sulphide)	Phillips Petroleum	"AC40-60"	U/C-PPS

Thermosetting Fibre-Composite (TSFC)

(g) Unidirectional-carbon-fibre based on modified epoxy	Ciba Geigy Ltd.	"913C-XAS-5-34%"	U/C-epoxy

Notes: U: unidirectional; W: woven; C: carbon; K: "Kevlar"; PEEK: poly(ether-ether ketone); PA: polyamide; PEI: poly(ether imide); PI: polyimide and PPS: poly(phenylene sulphide).

The details of these materials are:

(a) U/C-PEEK: a continuous carbon-fibre composite containing a nominal volume fraction of fibres of about 61% based upon a matrix of the thermoplastic resin poly(ether-ether ketone)

(PEEK). The composite substrate was prepared by laying the desired number of the pre-preg tapes (125μm thick) into a stack. The moulding was carried out in a heated press at 380°C for 10 minutes at a pressure of 0.7MPa and afterwards it was consolidated for 5 minutes under a pressure of 1.4MPa. Post consolidation cooling was carried out by cooling down the press quickly to room temperature, by allowing water into the hot platens, under a pressure of 2MPa.
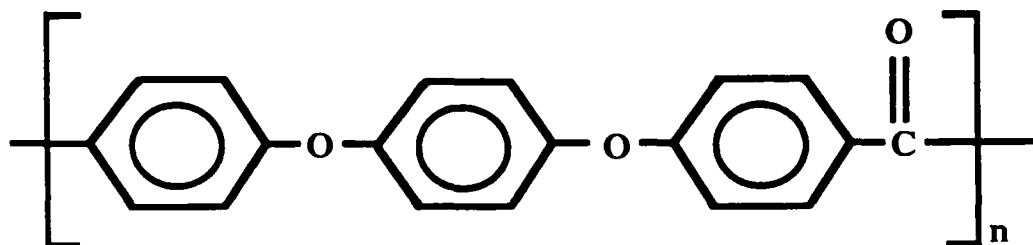
Fig. 2.4. Chemical structure of poly(ether-ether ketone) (PEEK).

(b) U/C-PA: a continuous carbon-fibre composite containing a nominal volume fraction of fibres of 55% based upon a matrix of the thermoplastic resin of an amorphous polyamide coploymer which is based on bis(para-amino cyclohexyl methane). The composite substrate was prepared by laying a desired number of the pre-preg tapes (125μm thick) into a stack. The moulding was carried out in a heated press at 300°C for 25 minutes under a pressure of 2MPa. After consolidation the press was cooled down quickly to 150°C, by allowing water to the hot platens, under a pressure of 2MPa.

(c) W/C-PA: same as in (b) above except that the fibres were woven and the thickness of each layer was 140μm.

(d) U/K-PA: a continuous "Kevlar"-fibre composite containing a nominal volume fraction of fibres of 60% based upon a thermoplastic resin of an amorphous polyamide coploymer which is based on bis(para-amino cyclohexyl methane). The composite substrate was prepared by laying a desired number of the pre-preg tapes (90μm thick) into a stack. The processing cycle was the same as that of the unidirectional-carbon/PA.

(e) W/K-PA: same as in (d) above except that the fibres were woven and the thickness of each layer was 165μm.
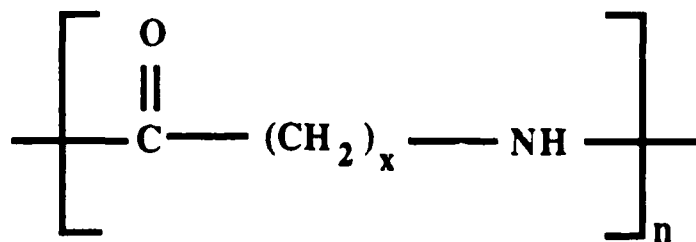
Fig. 2.5. Chemical structure of a polyamide (PA).

(f) W/C-PEI: a woven carbon-fibre composite containing a nominal fibre volume fraction of 62% based upon a thermoplastic matrix of a poly(ether imide). The composite substrate was prepared by laying the desired number of the pre-preg tapes (200µm thick) into a stack. The moulding was carried out in a heated press at 315°C for 30 minutes under a pressure of 0.7MPa. After consolidation the press was cooled down slowly to 150°C, by allowing pressurized air into the hot platens, not exceeding a cooling rate of 3°C/minute.
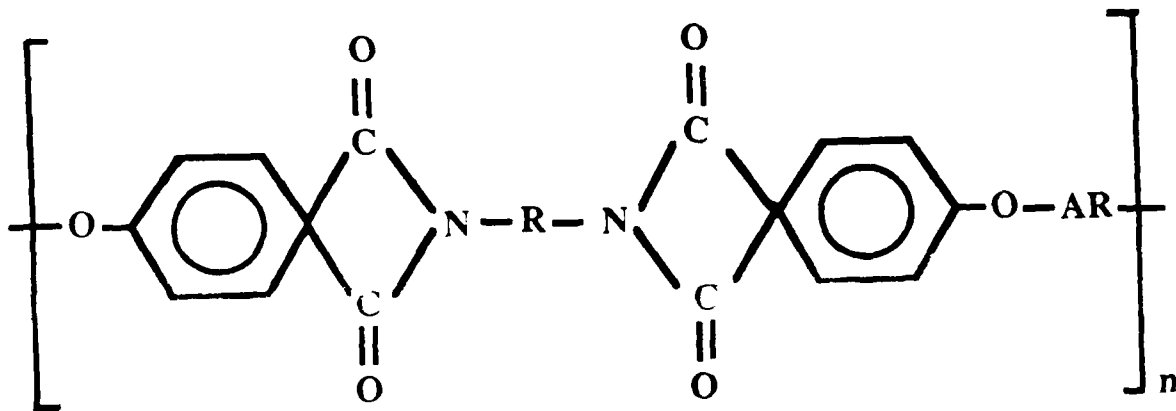
Fig. 2.6. Chemical structure of a poly(ether imide) (PEI).

(g) U/C-PPS: a continuous carbon-fibre composite containing a nominal volume fraction of fibres of 53% based upon a thermoplastic matrix of poly(phenylene sulphide). The composite substrate was prepared by laying the desired number of the pre-preg tapes (165µm thick) into a stack. The moulding was carried out at 360°C for 5 minutes under a pressure of 2MPa. After consolidation the press was cooled down to room temperature and under pressure by allowing water into the hot platens.
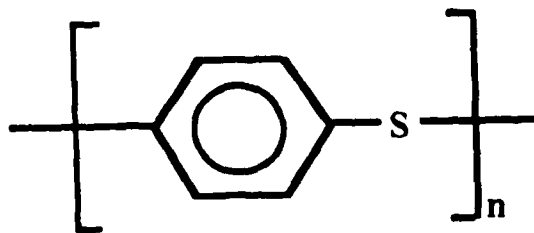
Fig. 2.7. Chemical structure of the poly(phenylene sulphide) (PPS).

(h) U/C-PI: a continuous carbon-fibre composite containing a nominal volume fraction of fibres of 60% based upon a thermoplastic matrix of polyimide. The composite substrate was prepared by laying the desired number of the pre-preg tapes (175µm thick) into a stack. The moulding was carried out with the following procedure:

- the mould was heated from room temperature to 250°C at a rate of 5°C/minute,

- followed by 15 minutes dwell at 250°C,

- then a pressure of 3.5MPa was applied,

- followed by further heating from 250°C to 300°C at a rate of 5°C/minute,

- followed by 15 minutes dwell at 300°C, and

- then the mould was cooled down from 300°C to 150°C, by allowing pressurized air into the hot platens, not exceeding a cooling rate of 3°C/minute.

(i) W/C-PI: same as in (h) above except that the fibres were woven and the thickness of each layer was 350μm.
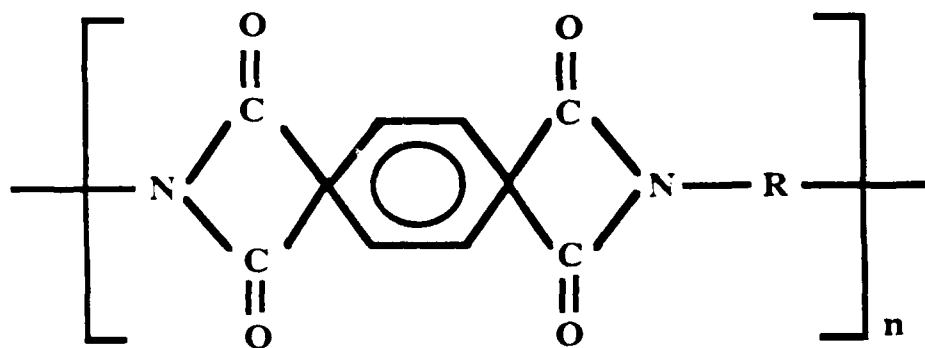
Fig. 2.8. Chemical structure of a typical polyimide (PI).

(j) U/C-epoxy: a thermoset composite based upon a modified-epoxy supplied by Ciba-Geigy. It was a continuous carbon-fibre composite containing a nominal resin weight of about 34%. The composite substrate was made by laying unidirectional tape (125μm thick) into a stack. The curing was carried out at 150°C for 20 minutes under a pressure of 2MPa. The press was cooled down quickly to 100°C, by allowing water into the hot platens. This thermoset composite was employed for comparative purposes.

The glass transition temperatures and the melting temperatures of the above composites are given in Table 2.2. These composites were chosen for their different resin and fibre properties. It was hoped that the wide variety of composites would enable the mechanisms of adhesion to be identified, since it would be expected that different resins may have different intrinsic adhesion characteristics. The thermosetting composite was employed for comparative purposes. The thermoplastic composites most widely employed in the present research work were the U/C-PEEK and U/C-PA, since they possess the best mechanical properties.

Table 2.2. Glass transition and melting temperatures of the composites employed.

Material	Glass transition temperature T_g (^{0}C)	Crystalline melting temperature T_m (^{0}C)
Thermoplastics		
PEEK	140	345
PA	160	285
PEI	158	315
PI	266	Not applicable
PPS	97	290
Thermoset		
Epoxy	131	Not applicable

The composites were prepared according to the curing cycles stated above but it should noted that a custom-made press was employed, which gave accurate control of temperature and pressure as well as maintaining uniform temperature across the platens. The dimensions of the mould used are shown in Figure 2.9. The most important feature of the mould is its brass platens. Brass has a higher thermal conductivity than steel therefore, for fast heating and cooling, this design constitutes an important feature. For a smooth finish of the surfaces of the composites, graphite sheets (1mm thick) were used in between the release-coated brass surface and the releasing-coated aluminium foils. The releasing agent used was "Frekote 44" supplied by Hysol Dexter. This particular type of releasing agent was used because it remains stable at the high processing temperatures required for thermoplastic composites and this minimizes the transfer of releasing agent from the mould to the surfaces of the fibre-composites. The stacking sequence of the mould is shown in Figure 2.9. Note that the brass platens, mould frame, graphite sheets and the aluminium foils were sprayed with the releasing agent and allowed to dry prior to making the composite sheets.

300mm

Top brass platen		8mm
Graphite sheet		1mm
Aluminium foil		0.2mm
Composite		
Mould frame		15mm
Aluminium foil		
Graphite sheet		
Bottom brass platen		

300mm

150mm

170mm

320mm
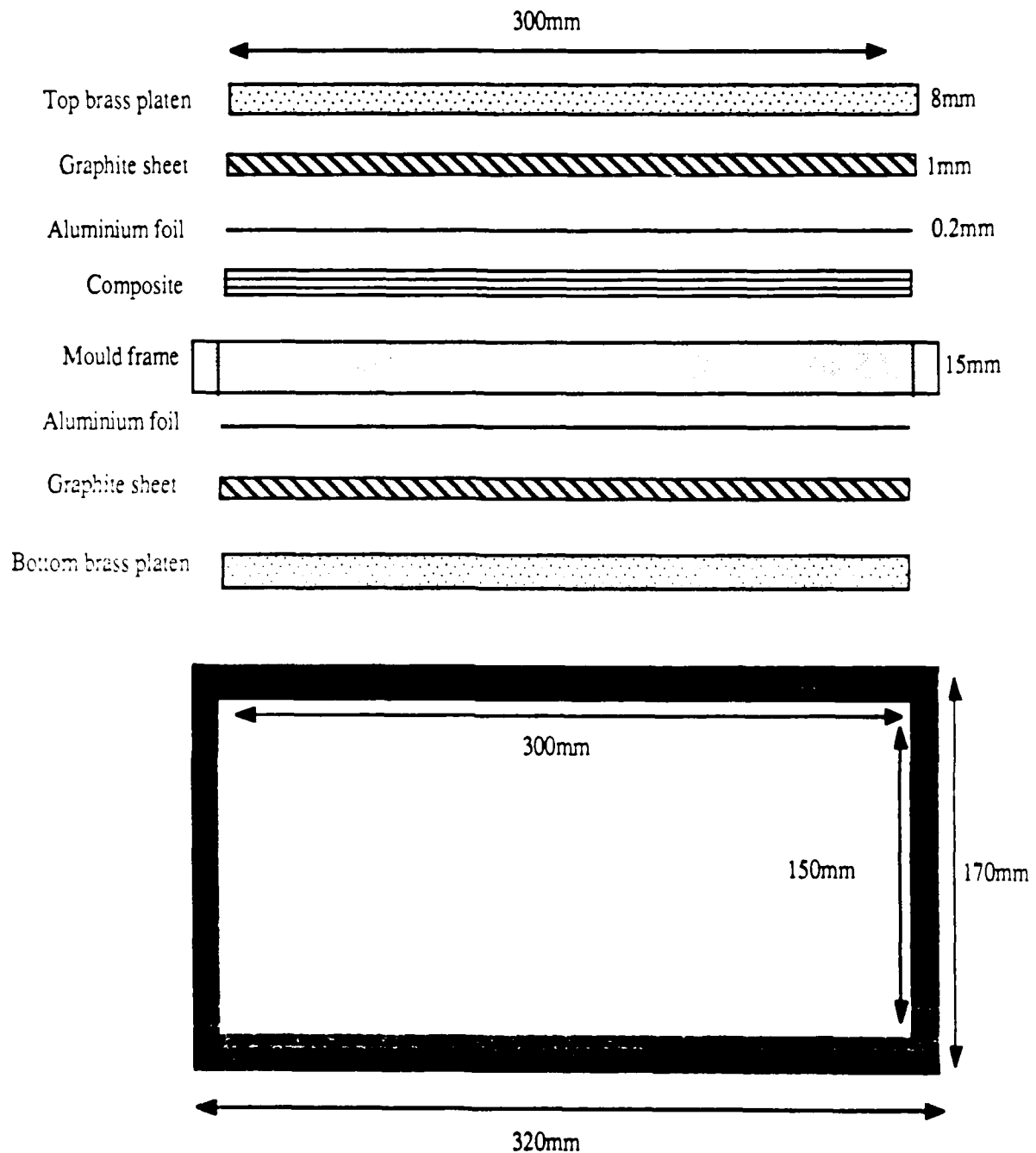
Fig. 2.9. Order of stacking and dimensions of the mould.

2.3.2. Adhesives

2.3.2.1. Introduction

Epoxy, acrylic and thermoplastic adhesives were employed in the present project. The epoxy adhesives were the main adhesives employed whereas the thermoplastic adhesives were employed as "hot-melt" adhesives and the acrylic adhesives were employed for their fast curing

cycles.

2.3.2.2. Types and Cure Cycles

As mentioned above, epoxy, acrylic and thermoplastic adhesives were investigated. The details of the first two types of adhesives are given in Table 2.3. As may be seen, two aerospace "state-of-the-art" rubber-toughened epoxy adhesives were employed. One was room temperature curing and the other cured at $120^{0}C$. These type of adhesives are usually employed in engineering structures where structural integrity is important, such as in the aircraft industry.

Table 2.3. The epoxy and acrylic adhesives employed.

Adhesive	Manufacturer	Commercial name	Short name
Two-part rubber-toughened epoxy-paste	Hysol Dexter Corp.	"EA 9309.3NA"	Epoxy-paste
Rubber-toughened epoxy-film	American Cyanamid	"FM73M"	Epoxy-film
Two-part acrylic-paste	Permabond Ltd.	"F241"	*
Two-part acrylic-paste	Permabond Ltd.	"F245"	*
Two-part acrylic-paste	Permabond Ltd.	"F246"	*
Two-part acrylic-paste	Permabond Ltd.	"V501"	*
Two-part acrylic-paste	Bostik	"M890"	*
Two-part acrylic-paste	Bostik	"M896"	*

Note: (*): No short name employed.

The curing cycles employed for the adhesives were:

(a) Epoxy-paste: cured at room temperature for 5 days under a pressure of 69kPa.

(b) Epoxy-film: cured at a temperature of $120^{0}C$ for 1 hour under a pressure of 275kPa.

(c) Two-part acrylic-paste adhesives ("F241", "F245" and "F246"): cured at room temperature for 5 minutes under a pressure of 30kPa.

(d) A two-part acrylic-paste adhesive ("V501"): cured at room temperature for 2 hours under a pressure of 30kPa.

(e) Two part acrylic-paste adhesives ("M890" and "M896"): cured at room temperature for 5 minutes under a pressure of 30kPa.

To enable a comparison to the more common types of structural adhesives listed above the use of a hot-melt adhesive film, of the same chemical type as employed for the matrix of the thermoplastic composite, was also studied. The adhesive hot-melt films were:

(a) Poly(ether-ether ketone) (PEEK) - the PEEK hot-melt adhesive was applied to the corresponding composite substrate and the joints were prepared by subjecting the joint assembly to a temperature of 380^0C for 5 minutes under a pressure of 0.5MPa.

(b) Polyamide (PA) - the PA hot-melt adhesive was applied to the corresponding composite substrate and the joints were prepared by subjecting the joint assembly to a temperature of 300^0C for 5 minutes under a pressure of 1MPa.

(c) Poly(phenylene sulphide) (PPS) - the PPS hot-melt adhesive was applied to the corresponding substrate and the joints were prepared by subjecting the joint assembly to a temperature of 360^0C for 2 minutes under a pressure of 1MPa.

2.4. PRETREATMENT TECHNIQUES

2.4.1. Introduction

The conclusion from the literature review, Section 2.2.3, that TPFC materials do not readily bond with conventional structural adhesives when a simple abrasion/solvent-wipe pretreatment is employed was confirmed in the present studies, as will be discussed in Chapter Four. Hence, different types of pretreatment techniques were considered and, in particular, a corona-discharge technique developed for treating the TPFC materials prior to bonding. The different pretreatments employed are described below.

2.4.2. Abrasion

The composite sheets were lightly abraded at a pressure of 30kPa, using 180/220 mesh alumina. The relative angle between the nozzle and the composite sheet was about 45^0 to minimize the effect of forcing releasing agents present on the surface further into the composite sheet. The composite sheets were then wiped with methyl-ethyl ketone (MEK) and allowed to dry.

2.4.3. Aluminium/Etch

To ensure that no releasing agent was on the surface of the thermoplastic composite, sheets were moulded against clean aluminium foil. The aluminium foil had previously been etched in a bath of chromic-acid solution to ensure that the surfaces were free from releasing agents. The

acidic solution was made up of 1.44 litres of Analar quality sulphuric acid (specific gravity 1.84), 8 litres of distilled water, 264g of sodium dichromate and optimised by the addition of 12g of aluminium and 8g of copper. The solution was contained within a 5mm thick stainless steel tank. The temperature of the solution was maintained at 68^0C using a heater which also supplied the mechanical agitation of the solution. The aluminium foils were then immersed in the heated acidic bath for 20 minutes and afterwards were thoroughly rinsed in tap water. The aluminium foils were then used to cover the surfaces of the composite stacks, and composite sheets were prepared using the techniques discussed previously. After the moulding operation the aluminium foils were dissolved away using a two molar sodium hydroxide solution.

2.4.4. Acid-Etch

Thermoplastic composite specimens were etched in an acidic solution [15] based upon 1% solution of potassium permanganate in a 5.2.2 solution of sulphuric acid (98% minimum purity), orthophosphoric acid (85% minimum purity) and distilled water. The etch was carried out in a stainless steel tank of 5mm thick. This tank was immersed in a larger tank containing an ice bath. This etching process was conducted for different immersion times between 2 to 10 minutes. After the etching process the samples were immersed in a 7:2 solution of distilled water and sulphuric acid. Finally, the samples were washed in a 30% hydrogen peroxide solution before being washed in distilled water. This pretreatment technique was employed since it has been previously employed in improving the resin/fibre interface of the U/C-PEEK composite [15].

2.4.5. Corona-Discharge

This technique was developed for the TPFC materials since it is known that it improves the adhesion of difficult-to-bond thermoplastic polymers such as polyethylene [16].

The major components of the corona-discharge equipment are the generator producing high-frequency (HF) (15-20kHz) power (0.1-0.9kW), the high-power (HP) transformer giving the high voltage (15-20kV) and the HP-cables carrying the high voltage to the electrodes and the treater-station, see Figure 2.10. This equipment was designed to include two noteworthy features:

i) Conventional corona-discharge equipments can treat non-conducting materials but the transformer of this equipment was redesigned to give good impedance and capacitance matching between the electrode and the somewhat conductive carbon-fibre-reinforced plastics. For electrically conductive materials a modified electrode was designed with rubber silicone covering the surface. For non-conducting materials a metallic conventional knife-edged

electrode was used.

ii) The power output from the electrode was current controlled and not voltage controlled. Hence the power output from the electrode could be read directly from the power gauge of the generator.
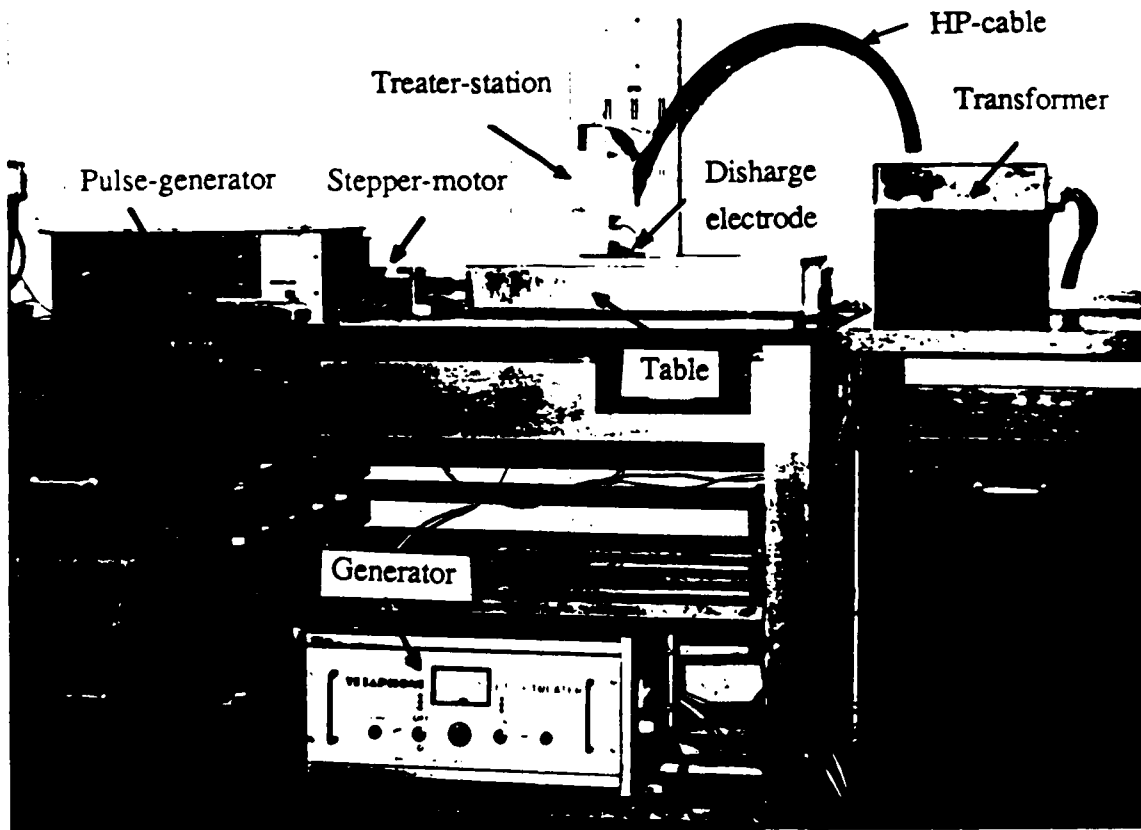
Fig. 2.10. The corona-discharge equipment.

After a light abrasion and a solvent-wipe treatment, as described above, the TPFC substrates were placed on an automatically controlled table which travelled horizontally backwards and forwards under the discharge electrode, see Figure 2.11. The velocity of the table could be selected to be between 14.5 to 62mm/s and the velocity was controlled accurately by a stepper motor and a pulse generator (0.1-4.8kHz). Therefore, the energy output per unit area from the electrode onto the composites may be determined from:

$$E_{co} = \frac{P_{co}N}{L_e V}$$

(2.1)

where E_{co} is the energy output per unit area, P_{co} is the power of the high-frequency generator, N is the number of cycles of the table, L_e is the length of the treater and V is the velocity of the

table.

Fig. 2.11. A thermoplastic composite during treatment. Note that the
right-hand side of the silicone rubber was made 1mm thicker to give
a constant air gap between the electrode and the substrates.

2.5. CONCLUDING REMARKS

In this chapter the adhesives and composites employed in the present studies have been
described and a review of the pretreatment techniques to be employed has been presented.

The following chapter will be concerned with surface characterisation of the
fibre-composite materials when subjected to these various pretreatment techniques, such
studies should greatly assist in identifying the mechanisms of adhesion.

CHAPTER THREE

SURFACE CHARACTERISATION

3.1. INTRODUCTION

This chapter discusses the characterisation of the surfaces of the fibre-composite substrates. The surface characterisation was undertaken using three techniques: contact angle analysis (CAA), scanning electron microscopy (SEM) and X-ray photoelectron spectroscopy (XPS). The aim of this chapter is to provide a basic understanding of the surface physical and chemical properties of the fibre-composites before and after being subjected to the treatment techniques. The effects from corona pretreatment will be examined in some detail due to firstly, the novelty of such an application to TPFC materials and secondly, due to the ease with which it can be adopted to an industrial environment. Further, this chapter will also consider the effects of ageing on corona-pretreated TPFC substrates prior to adhesive bonding.

3.2. CONTACT ANGLE STUDIES

3.2.1. Introduction

In this technique, the contact angle of a sessile drop of a test-liquid of known properties is measured on the solid surface under examination. Such measured contact angles may give an indication of the surface wettability and enable the surface free energy of the solid to be determined.

3.2.2. Literature Survey

3.2.2.1. Surface Tension

The surface tension of a given solid [17] is a direct measurement of intermolecular forces. The most important type of physical attractive forces are the van der Waals forces of attraction and they are due to two effects namely:

a) dispersion or London forces of attraction arising from internal electron motions which are independent of the dipole moments and

b) polar or Keesom forces of attraction arising from the dipole moments.

The dispersion forces, unlike polar forces, are present in all materials. Another type of attractive force that might operate on a surface is that due to the hydrogen bond.

3.2.2.2. Wetting

Wetting may be quantitatively defined to be the relative angle between a drop on a solid liquid and the solid surface as shown in Figure 3.1.
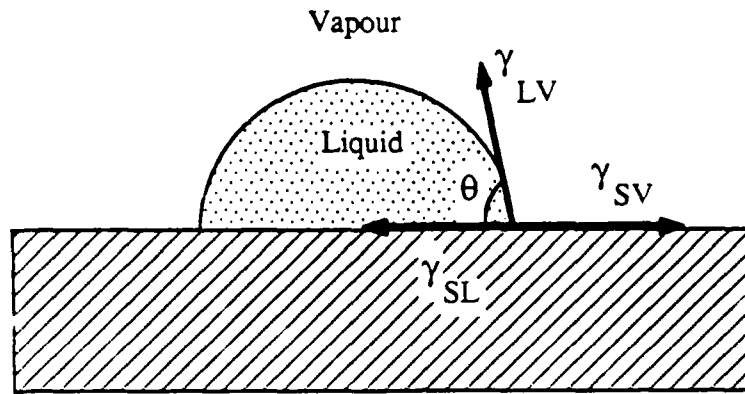
Fig. 3.1. A liquid drop resting on a solid surface.

Now, if the liquid has a surface tension γ_{LV} at rest on a solid whose surface energy in vacuum is γ_s then the equilibrium situation is governed by Young's equation [18, 19] where:

$$\gamma_{SV} = \gamma_{SL} + \gamma_{LV}\cos\theta \qquad (3.1)$$

where: $\gamma_{SV} = \gamma_s + \pi_e$

γ_{SV} being the interfacial tension at the solid-vapour interface in a saturated vapour of the wetting liquid and π_e being the equilibrium spreading pressure of the saturated vapour on the solid surface. γ_{SL} is the solid-liquid interfacial tension and θ is the equilibrium contact angle. Ideally, the solid should be smooth, undeformable, homogeneous and planar. When $\theta > 0^0$ the liquid is nonspreading, but when $\theta = 0^0$ the liquid wets the surface.

In many analyses where γ_s is low the value of π_e has been considered to be near zero and has therefore been neglected. This approximation is applicable for composites and plastics, which have low surface free energy [20]. Therefore:

$$\gamma_s \approx \gamma_{SL} + \gamma_{LV}\cos\theta \qquad (3.2)$$

3.2.2.3. Zisman's Concept of Critical Surface Tension

Zisman and his colleagues [21-25] undertook some of early work on determining the surface free energies of polymers. They showed that if the values of $\cos\theta$ for a series of liquids are plotted against γ_{LV} then the points either fall on a straight line or within a rectilinear band. When the line is extrapolated to $\cos\theta = 1$ the corresponding value of γ_{LV} Zisman called the critical surface tension, γ_C. This value, γ_C, corresponds to the surface tension of a liquid which will just spread on the surface.

In a more recent work Dann [26] has re-examined Zisman's studies. He noted many important points as to why Zisman observed linear relationships between γ_{LV} and $\cos\theta$. Firstly, Zisman had frequently used hydrocarbon liquids which possess a narrow range of surface tensions. Secondly, these type of liquids will measure only the dispersion force component of the solid. Thirdly, the liquids used by Zisman had the unusual characteristic that the dispersion force component decreased as the total surface free energy increased. Dann [26] also demonstrated correctly that whilst using liquids possessing only dispersion forces, then the critical surface tension equals only the dispersion force component of the surface free energy of the solid.

3.2.2.4. Estimation of the Surface Free Energy of Solids

A number of researchers have attempted to modify and extend Zisman's work to calculate the surface free energy of a solid. These developments are summarized below.

Good and Girifalco [27, 28] derived an expression for the interfacial free energy, γ_{12}, between phases 1 and 2:

$$\gamma_{12} = \gamma_1 + \gamma_2 - 2\Phi_{12}(\gamma_1\gamma_2)^{0.5} \tag{3.3}$$

where Φ_{12} is an interaction parameter which can be estimated from the molecular properties of both phases. Combining this equation with Equation (3.2) then:

$$\cos\theta = -1 + 2\Phi_{SL}(\gamma_s/\gamma_{LV})^{0.5} \tag{3.4}$$

where for most systems $0.5 < \Phi_{SL} < 1$. Hence, for a series of liquids on a solid surface a plot of $\cos\theta$ versus square root of γ_{LV} produces a linear relationship from which γ_s may be estimated from the intercept at $\cos\theta = 1$ provided Φ_{SL} is known at $\cos\theta = 1$. However, Equation (3.4) is at best approximate because of the difficulty in estimating Φ_{SL}.

More recently Fowkes [29] suggested that the total surface free energy of a solid or liquid can be described as the sum of components which arise from the different intermolecular forces, example dispersion (d), polar (p) and hydrogen bonding (h):

$$\gamma = \gamma^d + \gamma^p + \gamma^h \tag{3.5}$$

but Schultz et al. [30] have suggested that the surface free energy may be generally expressed by only the first two terms of Equation (3.5).

Fowkes [29, 31] also proposed that for interactions involving only dispersion forces then:

$$\gamma_{12} = \gamma_1 + \gamma_2 - 2(\gamma_1^d \gamma_2^d)^{0.5} \tag{3.6}$$

He confirmed the validity of Equation (3.6) and extended this concept to solid/liquid systems by combining Young's equation with Equation (3.6) to give:

$$\gamma_{LV}\cos\theta = -\gamma_{LV} + 2(\gamma_s^d \gamma_{LV}^d)^{0.5} \tag{3.7}$$

where γ_s^d and γ_{LV}^d are the dispersion force components to the solid and liquid surface energies, respectively.

Dann [32] and Tamai et al. [33] introduced an energy term into Equation (3.7) to account for the polar forces. Kaelble and Uy [34] and Owens and Wendt [35] by analogy with the work presented by Fowkes, proposed this energy term to be expressed by $2(\gamma_s^p \gamma_{LV}^p)^{0.5}$. Introducing this expression into Equation (3.7) then:

$$\gamma_{LV}\cos\theta = -\gamma_{LV} + 2(\gamma_s^d \gamma_{LV}^d)^{0.5} + 2(\gamma_s^p \gamma_{LV}^p)^{0.5} \tag{3.8}$$

γ_{LV}, γ_{LV}^d and γ_{LV}^p for many liquids of interest have been determined by several workers, see Table 3.1. From measurements of the contact angle of at least two such liquids on a solid surface, γ_s^d and γ_s^p can be evaluated from two simultaneous equations constructed using Equation (3.8). The sum of these values then provides an estimate of the surface free energy of the solid. Kaelble [34] recommended the use of as many different liquids as possible to provide values with least errors for the surface free energy components.

Table 3.1. Surface free energy of various liquids.

Liquid	γ_{LV} (mJ/m^2)	γ_{LV}^d (mJ/m^2)	γ_{LV}^p (mJ/m^2)	Reference
Double-distilled water	72.6	24.9	47.7	[36]
Glycerol	63.4	37.0	26.4	[29]
Formamide	58.2	39.5	18.7	[29]
Methylene Iodide	48.6	48.6	0.0	[36]
1-Bromonaphtalene	44.6	44.6	0.0	[37]
Polyglycol E200	43.5	28.2	15.3	[37]
Dimethyl Sulphoxide	43.3	29.6	13.7	[36]
Iodoethanol	44.9	41.1	3.8	[36]

3.2.2.5. Surface Roughness Factor

The fibre-composites were subjected to different pretreatment techniques and some of these techniques may greatly increase the surface roughness of the composites. This leads to an increase in the surface area. However, surface roughness may also affect the contact angle measurements. To account for the surface roughness effect, Wenzel [38] has proposed the following equation:

$$r_c = \cos\theta_t / \cos\theta_a \tag{3.9}$$

where θ_a is the apparent contact angle of the drop to the horizontal surface and θ_t is the intrinsic contact angle, i.e. that which would be obtained on an ideally smooth surface. Therefore, the roughness factor, r_c, of a surface is the ratio of the true area of a surface to its apparent area considered as a planar surface. More recently, Carre and Schultz [39] proposed a novel method for calculating this surface roughness factor, r_c. They measured the contact angle of a liquid on a rough surface coated with a thin layer of gold-film and the contact angle of the same liquid on a perfectly smooth surface prepared by depositing a thin layer of gold on a smooth glass plate. The surface roughness factor, r_c, was then estimated from Equation (3.9).

3.2.2.6. Advancing and Receding Contact Angles and Hysteresis

As mentioned above, surfaces are seldom ideally smooth or chemically homogeneous. As a result different contact angles may be obtained depending on whether a liquid drop is advanced or withdrawn across the surface. By definition, the contact angle which the three phase contact line makes with the surface when brought to rest after being slowly advanced or withdrawn across the surface are the advancing and receding contact angles respectively. The sessile drop can be advanced or withdrawn across the surface by increasing or decreasing the volume of the test-liquid, which is dispensed by the syringe needle. The needle remains in the liquid drop to avoid distortion or vibration of the sessile drop.

Hysteresis is the difference between the advancing and receding contact angles as defined above. Zisman [40] has argued that from a thermodynamic viewpoint, contact angle hysteresis should not exist if the surface being studied is smooth and of a homogeneous nature. (Also provided that the contact angle measurements are carried out under conditions where the three phase contact line moves sufficiently slowly).

3.2.3. Experimental Technique

Equilibrium contact angles were measured from the profile of liquid drops resting on a planar surface. This method is known as the sessile drop method. The contact angle was measured directly using a microscope fitted with a goniometer eyepiece. The volume of the sessile drop was kept constant throughout the experiments at 0.002ml. The flat stage, for mounting the specimens, under the syringe was covered with a special chamber open only at the top (through a small hole) to allow for the needle from the syringe. At least six contact angle measurements were recorded from each liquid/composite combination. The test-liquids that were used are listed in Table 3.1. To create the test-liquid vapour necessary for reliable

contact angle measurements a small amount of the test-liquid was poured into a small container and allowed into the closed chamber. The fibre-composite specimen, having typical dimensions of 5X6X0.15cm, was then inserted into the chamber. Then, the syringe was carefully lowered to the surface and a sessile drop dispensed onto the fibre-composite surface. Before recording the contact angle, time was allowed for the sessile drop to reach equilibrium condition.

To calculate the surface roughness factor, fibre-composites after being subjected to different pretreatment techniques were coated with a thin layer of gold. Laboratory slides were also coated with gold for comparative purposes, see Figure 3.2. The coating of gold was carried out in a thermal evaporation unit. The source of the gold was from an alumina coated molybdenum boat. The vacuum chamber had a 6MHz quartz crystal to monitor the thickness of the gold being deposited. The evaporation rate was 5Å per second. The thickness of gold deposited was also confirmed by using a "talysurf". The average thickness of gold deposited on the specimens was about 700Å ± 50Å. The very thin layer of gold deposited on the surfaces of the specimens ensured that very little of the detailed surface morphology was lost by gold

depositing. Finally it should be noted that the typical reproducibility of the contact angle, θ, measurements was within ±3^0.
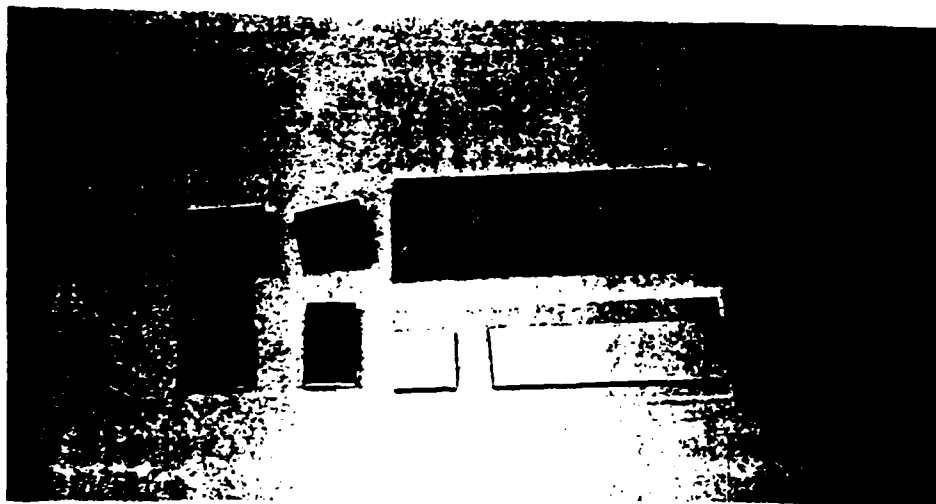
Fig. 3.2. Gold-coated slide and composites; top from an evaporation unit used
in scanning electron microscopy; bottom from a thermal evaporation unit
used in the electronics industry giving a relatively better coating.

3.2.4. Results and Discussion

In this section, the results from pretreatment techniques on contact angle measurements will be presented. However, before definitive measurements could be made several preliminary experiments had to be conducted. These were (i) time-dependent effects on the contact angles,

(ii) advancing and receding contact angles to determine the hysteresis and (iii) surface roughness effects on the contact angles measured. The preliminary general studies were largely conducted using the unidirectional-carbon/poly(ether-ether ketone) (U/C-PEEK) thermoplastic composite.

3.2.4.1. Time-Dependent Effects

As mentioned above, some preliminary experiments had to be first conducted before embarking on a detailed surface characterisation of the fibre-composites employed. One such experiment was to assess the time required for a particular test-liquid sessile drop to reach an equilibrium condition.

Two test-liquids, glycerol (having a relatively high viscosity of 14.9 poise) and double-distilled water (having a relatively low viscosity of 0.01 poise), were employed to determine the time required for the contact angles to reach equilibrium condition. The substrates employed for this analysis were U/C-PEEK thermoplastic composites which had been abraded, see Section 2.4.2. To reach equilibrium condition, the glycerol test-liquid required about 5 minutes, see Figure 3.3, whereas the double-distilled water required about 30 seconds, see Figure 3.4.
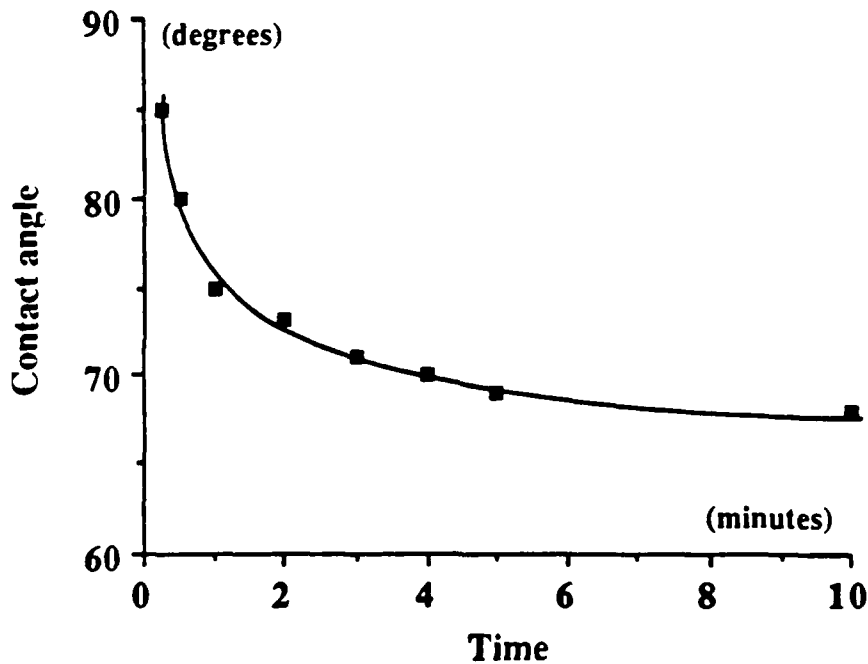
Fig. 3.3. Contact angle measurements of glycerol versus time on U/C-PEEK composite subjected to abrasion/solvent-wipe pretreatment.
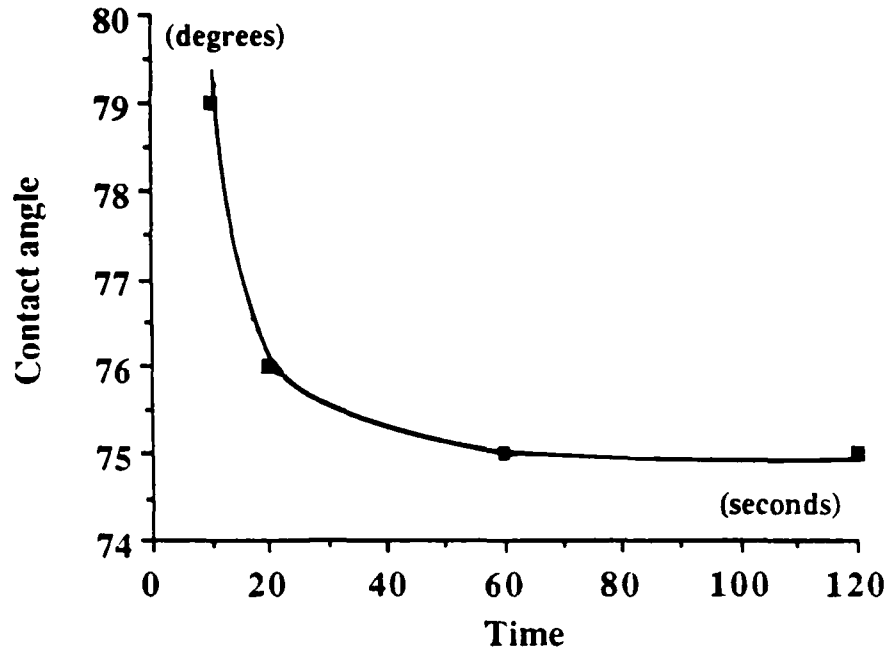
Fig. 3.4. Contact angle measurements of double-distilled water versus time on
U/C-PEEK composite subjected to abrasion/solvent-wipe pretreatment.

The time required to reach equilibrium condition, from these two experiments, were used as a guide in the ensuing experiments. Therefore, before reading the contact angle values, about 5 minutes was allowed for the viscous liquids; i.e. glycerol, methylene iodide, formamide and polyglycol E-200 and about 60 seconds for the low viscosity liquids employed; i.e. double-distilled water, iodo-ethanol, dimethyl sulphoxide and 1-bromonaphtalene.

3.2.4.2. Advancing and Receding Contact Angle Analysis

Advancing and receding contact angle analysis (CAA) was conducted on several types of pretreatment techniques notably, on U/C-PEEK thermoplastic composite subjected to different levels of corona pretreatment energies. The experimental technique employed was described in the literature survey: whereby the liquid is advanced or receded by increasing or decreasing its volume. Table 3.2 summarizes results from such experiments. It can be seen from this table that there is no apparent difference between the advancing and receding contact angles and therefore, the hysteresis is small and can be ignored. So far the contact angle results presented have not been corrected for the surface roughness of the fibre-composites and this will be discussed in the next section.

Table 3.2. The mean and maximum/minimum results from advancing and receding contact
angle analysis obtained from six experiments; the test-liquid
is double-distilled water; fibre-composite is U/C-PEEK.

Treatment	Advancing contact angle (^{0})	Receding contact angle (^{0})
Abrasion	75±3; 74±3; 77±4; 73±3	73±3; 72±3; 74±4; 75±3
Corona treatment energy: 1J/mm^2	22±2; 21±3; 20±2; 21±2	21±2, 20±2; 19±3; 20±2
Corona treatment energy: 5J/mm^2	17±1; 16±2; 18±2; 16±2	16±2; 17±2; 16±1; 16±2
Corona treatment energy: 10J/mm^2	12±1; 14±2; 13±1; 10±1	10±1; 11±2; 11±1; 12±2

3.2.4.3. Effect of Surface Roughness on CAA

Two test-liquids, methylene iodide and formamide, were employed to assess the surface roughness. The procedure for calculating the surface roughness factor was presented earlier in this chapter (see page 42). It should be noted that only one type from each resin/fibre composite was chosen i.e., fibre-composites which had the same resin with either unidirectional or woven fibres then only one of these two types was employed. For all the ensuing CAA and XPS analyses the same material selection was retained.

(i) Surface Roughness Correction Factors for Untreated Fibre-Composites

Obviously, the starting point to calculate the surface roughness correction factors was to assess the correction factors for the untreated fibre-composite materials. Table 3.3 summarizes results from such calculations. These results show that the surfaces of untreated fibre-composites are not perfectly smooth, as might have been assumed initially. This is especially true for the woven-fibre composites, where the surface area of such composites is about 10% greater than a perfectly smooth surface. The most likely reason for this surface roughness is the effect of the woven-fibres and/or resin on the overall surface morphology during the consolidation process.

Table 3.3. The mean and standard deviation results of the surface roughness correction factors for gold-coated untreated composites; reference is gold-coated smooth glass slide (r_c=1.0).

Material	Contact angle (^{0})		Surface roughness correction factor (r_c)
	Methylene iodide	Formamide	
U/C-PEEK	45±1	51±1	1.04±3
U/C-PA	45±1	51±1	1.04±3
U/K-PA	46±1	51±1	1.03±3
W/C-PEI	42±2	48±1	1.10±5
W/C-PI	43±2	48±1	1.09±4
U/C-PPS	45±2	51±1	1.04±4
U/C-epoxy	46±1	51±1	1.03±3

Note: The contact angles for the gold-coated slide were 48±1 and 52±1 for the methylene iodide and the formamide test-liquids respectively.

(ii) Surface Roughness Correction Factors for Fibre-Composites Subjected to Abrasion

The surfaces of the fibre-composites were abraded and solvent-wiped with methyl-ethyl ketone (MEK) and the surface roughness correction factors, r_c, determined, see Table 3.4.

Table 3.4. The mean and standard deviation results of the surface roughness correction factors for gold-coated composites subjected to abrasion/solvent-wipe pretreatment; reference is gold-coated smooth glass slide (r_c=1.0).

Material	Contact angle (^{0})		Surface roughness correction factor (r_c)
	Methylene iodide	Formadide	
U/C-PEEK	43±2	48±1	1.09±4
U/C-PA	42±2	48±2	1.10±5
U/K-PA	42±2	48±2	1.10±5
W/C-PEI	40±2	44±1	1.15±3
W/C-PI	40±2	45±1	1.14±4
U/C-PPS	42±2	48±2	1.10±5
U/C-epoxy	43±2	48±1	1.09±4

As expected, the results in the above table show that the surface roughness of all fibre-composites increases when abraded.

(iii) Surface Roughness Correction Factors for U/C-PEEK Composite Subjected to Aluminium/Etch and Acid-Etch Pretreatment Techniques

Next, the surface roughness correction factors for the U/C-PEEK, thermoplastic composite were assessed which was subjected to aluminium/etch (aluminium-foil/sodium-hydroxide) and acid-etch pretreatment techniques, see Table 3.5. These results show that the surface roughness correction factor is dependent on the type and duration of pretreatment employed. For example, the surface area of the 10 minute acid-etched U/C-PEEK specimen is about 14% greater than a smooth surface.

Table 3.5. The mean and standard deviation results of the surface roughness correction factors for gold-coated U/C-PEEK composite; subjected to aluminium/etch and acid-etch pretreatment techniques; reference is gold-coated smooth glass slide ($r_c=1.0$).

Treatment	Contact angle (^{0})		Surface roughness correction factor (r_c)
	Methylene iodide	Formadide	
Aluminium/etch	45±1	51±1	1.04±3
Acid-etch: 2 minutes	42±2	48±2	1.10±5
Acid-etch: 5 minutes	41±2	47±1	1.12±4
Acid-etch: 10 minutes	40±2	45±1	1.14±4

(iv) Surface Roughness Correction Factors for TPFC Materials Subjected to Corona-Discharge Pretreatment Technique

It was mentioned earlier in this chapter that the results from corona pretreatment will be examined in detail. The surface roughness correction factors have been obtained for the selected TPFC materials. It should be noted that prior to corona pretreatment the fibre-composites were subjected to abrasion/solvent-wipe pretreatment to ensure the removal of contaminants from the surfaces of the TPFC materials employed. Afterwards, these materials were subjected to various levels of corona pretreatment.

Figures 3.5 and 3.6 show typical results obtained for the surface roughness correction factors from U/C-PEEK and unidirectional-"Kevlar"/Polyamide (U/K-PA) composites

subjected to corona pretreatment. The results from the rest of the TPFC materials follow a similar pattern to that of the U/C-PEEK composite. The reason that the pretreatment levels employed vary from one composite to another is that these pretreatment energies represent levels at which no more interfacial failure is observed in the double-cantilever beam specimens, as will be discussed in Chapter Four. These results in Figures 3.5 and 3.6 show that as the level of corona treatment is increased then the surface roughness also increases. However, Figure 3.6 shows that the surface roughness is also a function of the type of fibre employed. The surface roughness of the U/K-PA composite is lower than the U/C-PEEK composite for a similar pretreatment level. This can be understood by considering the fact that the electrical sparks would try to reach the carbon-fibres due to their electrical conductivity and hence leave a rougher texture on the surfaces of the carbon-fibre reinforced thermoplastic composites. It should be mentioned that the standard deviation in these results did not exceed ±6%.

Finally, all the results reported in this section were used to correct the subsequent contact angle measurements employing Equation (3.9) (page 42).
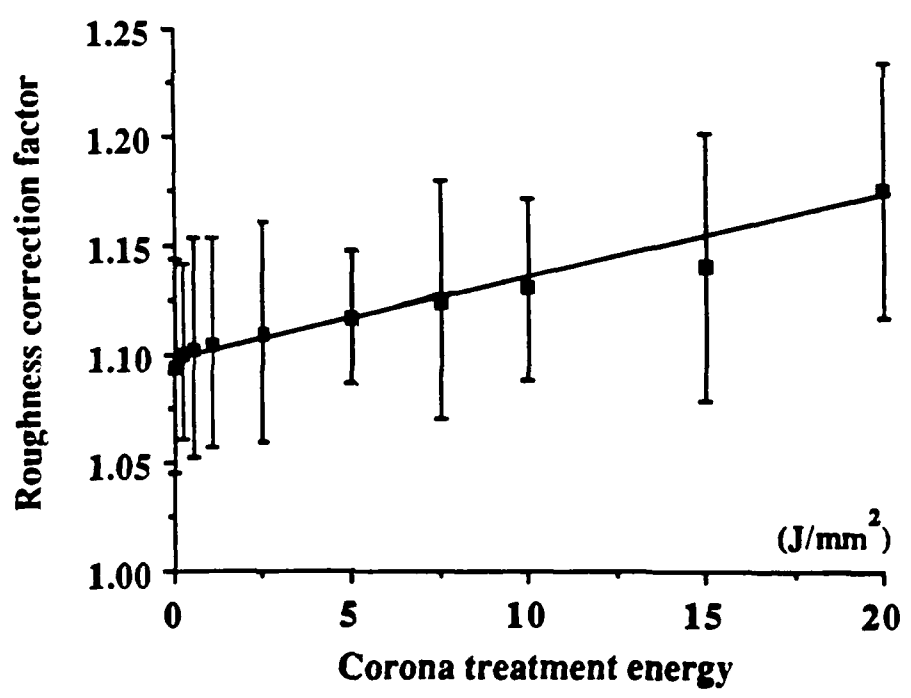
Fig. 3.5. Roughness correction factor versus corona treatment
energy for the U/C-PEEK composite.
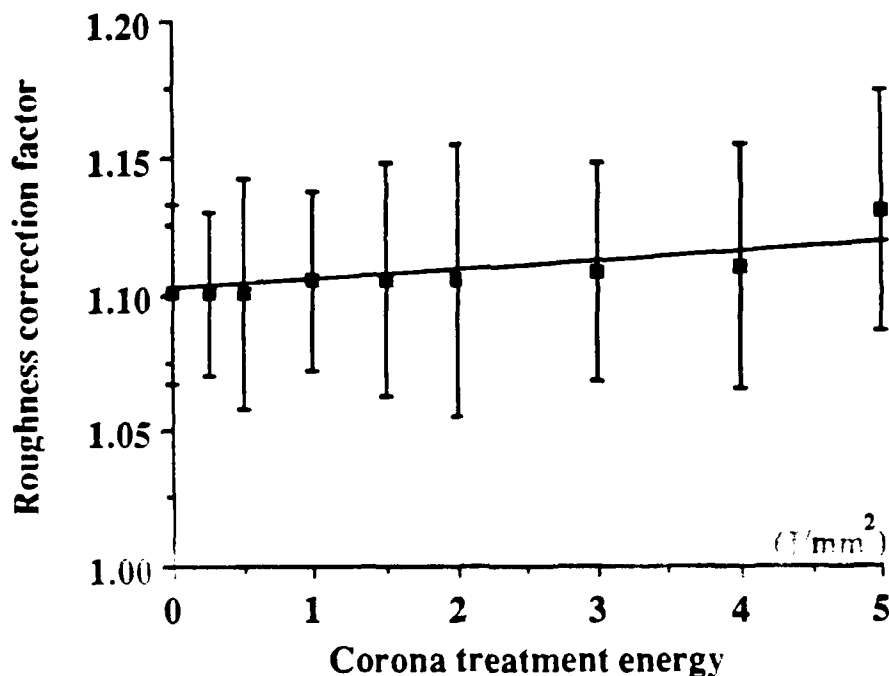
Fig. 3.6. Roughness correction factor versus corona
treatment energy for the U/K-PA composite.

3.2.4.4. A New Mathematical Technique for CAA

Researchers in adhesion, wettability and surface analysis who have used CAA have resorted to mathematical techniques to solve Equation (3.8), which may be rearranged to give:

$$2\frac{(\gamma_s^d \gamma_{LV}^d)^{0.5}}{\gamma_{LV}} + 2\frac{(\gamma_s^p \gamma_{LV}^p)^{0.5}}{\gamma_{LV}} = 1 + \cos\theta \qquad (3.10)$$

This equation involves two unknowns to be solved, namely γ_s^d and γ_s^p which are the dispersion and polar energy components of a solid respectively. Therefore, at least two different liquids must be used to solve two equations for the two unknowns. To reduce the error in calculating the surface free energy Kaelble [34] recommended the use of as many liquids as possible. For this reason, he and subsequent researchers [37], have used mathematical techniques to solve more than two equations for the two unknowns. Consider Figure 3.7, where if the four energy lines (from four liquids) are plotted then previous reported work has solved for the two unknowns in one of the two following techniques:

(1) solving for each individual pair of lines and then averaging the results, or

(2) as above but ignoring results which are negative, point A, and values which are not close to the majority of intersections such as point B. Kaelble [34] defined the boundaries of the rectangle shown in Figure 3.7 and suggested that the pairs of energy lines which have a value of $D>10mJ/m^2$ be ignored. D is an arbitrary value and the surface energy components (determined from a pair of liquids) can be compared with D by:

$$D = \left[(\gamma_{LV}^d)_i \, (\gamma_{LV}^p)_j \right]^{0.5} - \left[(\gamma_{LV}^d)_j \, (\gamma_{LV}^p)_i \right]^{0.5} \qquad (3.11)$$
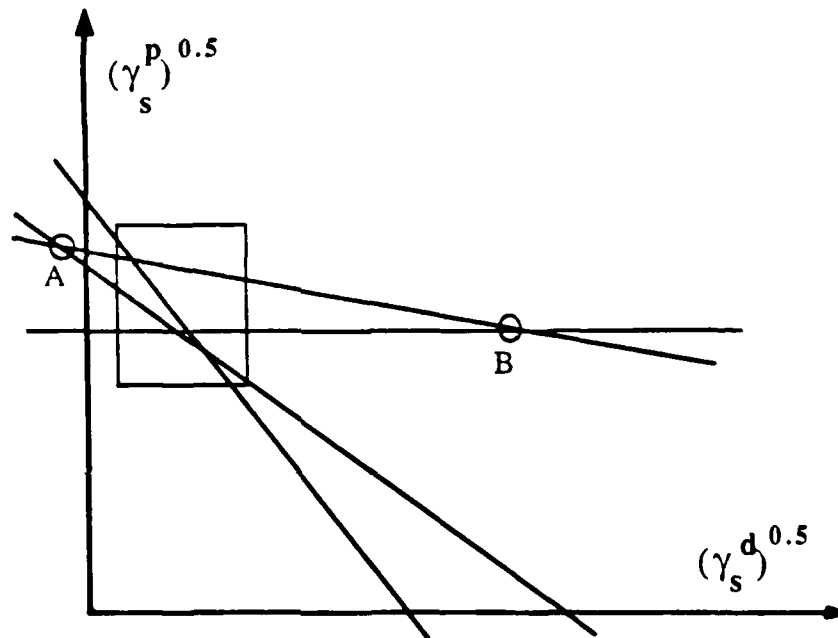
Fig. 3.7. Individual energy lines drawn to assess the surface energy values, point A is ignored because it has a negative energy value, point B is ignored because it is far away from the core of intersections which are included in the rectangle.

Obviously, using the above schemes would induce an element of approximation and therefore, the results for the surface energy values can be seriously questionable, as will be shown later in this section. However, it is still possible to assess the surface energy values by not only accepting all the data but also obtaining the least error in doing so. This technique, least squares, does not depend on the individual intersections but on the slopes of the straight lines. Now consider m equations with two unknowns in matrix form:

$$[A]_{mx2} \, [X]_{2x1} = [B]_{mx1} + [e]_{mx1} \qquad (3.12)$$

where matrix A represents the constant coefficients of the two unknowns in matrix X, matrix B is the contstant values of the equations and matrix e is the error involved in balancing the

individual equations. Now, if matrix B is taken to the left-hand side then:

$$\{[A]_{mx2} [X]_{2x1} - [B]_{mx1}\} = [e]_{mx1} \tag{3.13}$$

Multiplying both sides of the equality with the transpose of the left-hand side then:

$$\{[A]_{mx2} [X]_{2x1} - [B]_{mx1}\}^T \{[A]_{mx2} [X]_{2x1} - [B]_{mx1}\} = [E]_{1x1} \tag{3.14}$$

expanding the above equation gives:

$$\{[X]^T[A]^T[A][X]\}_{1x1} - \{[X]^T[A]^T[B]\}_{1x1} - \{[B]^T[A][X]\}_{1x1} +$$
$$\{[B]^T[B]\}_{1x1} = [E]_{1x1} \tag{3.15}$$

When the partial derivative of matrix E is taken with respect to the two unknowns (X_1 and X_2) and equated to zero to minimize the error then:

$$\partial[E]/\partial X_1 = [A]^T[A][X] + [X]^T[A]^T[A] - [A]^T[B] - [B]^T[A] = 0$$

and $\qquad\qquad\qquad\qquad\qquad\qquad\qquad\qquad\qquad\qquad\qquad\qquad$ (3.16)

$$\partial[E]/\partial X_2 = [A]^T[A][X] + [X]^T[A]^T[A] - [A]^T[B] - [B]^T[A] = 0$$

Since the above two equations are the same then rearranging one of them gives:

$$\{[A]^T[A][X] - [A]^T[B]\}_{2x1} + \{[X]^T[A]^T[A] - [B]^T[A]\}_{1x2} = 0 \tag{3.17}$$

but the above equation is in the form of: $[Z] + [Z]^T = 0$. Therefore, to satisfy the equality to zero then both matrix $[Z]_{2x1}$ and its transpose $[Z]^T_{1x2}$ should be individually equal to zero, therefore:

$$\{[A]^T[A][X]\}_{2x1} = \{[A]^T[B]\}_{2x1} \tag{3.18}$$

and

$$\{[X]^T[A]^T[A]\}_{1x2} = \{[B]^T[A]\}_{1x2} \tag{3.19}$$

Equation (3.18) is the transpose of Equation (3.19) therefore, only one of these two equations is required for CAA analysis, where (i) all the constant coefficients are known, (ii) will give the minimum error, (iii) will accept all the data and (iv) is very simple to employ.

Table 3.6 shows the results obtained by the "old" methods employed in the literature and the results obtained from employing Equation (3.18). The contact angle data employed for the surface energy calculations are from published work by Andrews and Kinloch [37]. They used a fluorinated ethylene-propylene copolymer (FEPA) which had been chemically etched in a proprietary organic dispersion of sodium naphthalene for varying periods of time. Obviously, solving the energy equations with the "old" methods leads into considerable error and scatter, as is obvious from the higher treatment times. Therefore, all the subsequent contact angle analyses have been carried out implementing the new mathematical approach presented above.

Table 3.6. Comparison of the various methods employed for calculating the surface energy components; the results shown are the mean and the standard deviation; contact angle values employed for these calculations were obtained from work by Andrews and Kinloch [37].

| Treatment | "Old methods" | | | | New method | |
| | Method 1 | | Method 2 | | Method 3 | |
	γ_s^d	γ_s^p	γ_s^d	γ_s^p	γ_s^d	γ_s^p
FEPA etched: 10 s	38.0±16.8	5.9±6.5	35.4±8.4	5.3±4.3	40.0±2.6	3.2±0.7
FEPA etched: 60s	39.8±46.0	14.3±22.0	33.8±13.7	13.4±10.2	39.7±4.6	6.1±4.6
FEPA etched: 120s	34.9±37.7	24.8±27.5	34.4±13.3	15.9±13.4	37.8±5.4	9.7±2.9
FEPA etched: 1000s	29.2±17.6	28.0±26.1	35.4±12.7	15.1±12.3	38.5±5.2	9.4±2.8

Notes: (1) All units are in mJ/m^2.

(2) Results from method 1 were obtained by solving all energy equations (21 pairs).

(3) Results from method 2 were obtained by Andrews and Kinloch [37] employing Kaelble's approach [34] where $D=10mJ/m^2$, see Equation (3.11).

(4) Results from method 3 were obtained by employing Equation (3.18).

3.2.4.5. CAA of Fibre-Composites

In this section the surface free energy results from untreated (as prepared) and pretreated fibre-composites will be presented and discussed. The values of the surface energy values, γ_s^d, γ_s^p and γ_s, were obtained by firstly, correcting for the surface roughness. This was necessary to distinguish the effects of surface chemistry from those of surface roughness on the measured contact angles. This will enable the effects of changes in the surface chemistry and surface roughness on the measured adhesive fracture energy, G_c, to be identified. Secondly, by implementing the new mathematical approach, Equation (3.18).

(i) CAA Results from Untreated Fibre-Composites

The results from untreated fibre-composites are shown in Table 3.7. These results reveal that each fibre-composite has a different surface energy value, this is especially true when the individual polar, γ_s^P, energy components are compared. This suggests that although the surfaces of the fibre-composites may be contaminated by releasing agents used in the moulding process, as will be discussed later in this chapter, the polar energy value is still a function of the base material. Further, the γ_s^P values are much lower than the γ_s^d values which may suggest that the composite materials lack a high concentration of polar groups.

Table 3.7. The mean and maximum minimum surface
energies from untreated fibre-composites.

Material	Dispersion energy γ_s^d (mJ/m^2)	Polar energy γ_s^P (mJ/m^2)	Total surface free energy γ_s (mJ/m^2)
U/C-/PEEK	39.0±1.4	2.0±0.7	41.0±2.1
U/C-PA	35.5±5.8	5.5±2.5	41.0±8.3
U/K-PA	35.4±4.6	6.3±2.0	41.7±6.6
W/C-PEI	33.5±6.4	2.0±1.6	35.5±8.0
W/C-/PI	33.5±5.2	3.8±1.8	37.3±7.0
U/C-PPS	31.4±1.8	1.4±0.7	32.8±2.5
U/C-epoxy	31.3±3.8	7.2±2.9	38.5±6.7

(ii) CAA Results from Fibre-Composites Subjected to Abrasion

The results from employing abrasion/solvent-wipe pretreatment are given in Table 3.8. These results show several noteworthy features. Firstly, the polar energies of all fibre-composites employed are higher than those from the untreated fibre-composites, see Table 3.7. Perhaps indicating the removal of surface contaminants which have a very low polar energy component to their total surface free energy. Secondly, and perhaps the most important result from this table is indeed the relatively high polar energy component of the U/C-epoxy

composite when compared with all the TPFC materials employed. A consequence of this high polar energy component is the better wettability and higher intrinsic adhesion with respect to the epoxy and acrylic adhesives, as will be shown in Chapter Four.

Table 3.8. The mean and maximum/minimum surface energies of fibre-composites subjected to an abrasion/solvent-wipe pretreatment.

Material	Dispersion energy γ_s^d (mJ/m^2)	Polar energy γ_s^p (mJ/m^2)	Total surface free energy γ_s (mJ/m^2)
U/C-PEEK	39.5±2.2	2.9±0.8	42.4±3.0
U/C-PA	35.2±2.3	6.8±1.8	42.0±4.1
U/K-PA	34.8±3.2	7.5±1.9	42.3±5.1
W/C-PEI	35.7±2.9	5.0±1.4	40.7±4.3
W/C-PI	35.8±3.8	6.1±1.9	41.9±5.7
U/C-PPS	34.7±1.9	3.1±0.7	37.8±2.6
U/C-epoxy	34.2±4.3	14.6±3.5	48.8±7.8

(iii) CAA Results from U/C-PEEK Composite Subjected to Aluminium/Etch and Acid-Etch Pretreatment Techniques

The results from pretreatment techniques excluding abrasion and corona-discharge pretreatment from U/C-PEEK thermoplastic composite are presented in Table 3.9. These results show that the dispersion energy component is relatively constant and independent of the type and duration of pretreatment employed. The polar energy component seems to be a strong function of not only of the type of pretreatment employed but also of the duration of the pretreatment. The polar energy components from abraded (Table 3.8) and aluminium/etch pretreatment techniques seem to be very much the same, suggesting that the surface active polar groups are not affected, i.e. are of the same level, and perhaps suggesting that the contamination level from these two pretreatment techniques are indeed very low. Further, for the acid-etch pretreatment, the polar energy increases as the time of pretreatment is increased. This type of behaviour suggests that the surface polar species have increased. Finally, the greater value of γ_s^p increases the total surface free energy.

Table 3.9. The mean and maximum/minimum surface energies of U/C-PEEK thermoplastic composite subjected to aluminium/etch and acid-etch pretreatment techniques.

Pretreatment	Dispersion energy γ_s^d (mJ/m^2)	Polar energy γ_s^p (mJ/m^2)	Total surface free energy γ_s (mJ/m^2)
Aluminium/etch	37.2±3.8	3.1±0.8	40.3±4.6
Acid-etch: 2 minutes	39.4±3.3	4.2±1.0	43.6±4.3
Acid-etch: 5 minutes	38.8±3.8	7.5±2.3	46.3±6.1
Acid-etch: 10 minutes	40.4±5.0	13.2±2.9	53.6±7.9

(iv) CAA Results from TPFC Materials Subjected to Corona-Discharge Pretreatment Technique

Figures 3.8 and 3.9 show typical results from CAA on two corona-treated TPFC materials. The results from the other TPFC materials follow similar patterns to the above and are presented in Appendix A.1. Figures 3.8 and 3.9 show several common features. Firstly, the dispersion energy component remains constant in value, independent of the level of corona treatment energy. This feature suggests that species which are polar only are being added to the surfaces of corona-treated composites. Secondly, and perhaps more important, is that in all the

types of fibre-composites examined, the value of γ_s^p increases dramatically as the corona

energy level is increased to a certain level. This increased level γ_s^p indicates that corona-discharge pretreatment increases the concentration of the active polar species on the

surfaces of the fibre-composites. Thirdly, the rate of increase in γ_s^p decreases as the level of corona treatment is further increased past a certain point, and finally reaches a plateau value. This indicates that the thermoplastic composites subjected to corona-discharge pretreatment reach a saturation level and therefore cannot accommodate further active polar groups.
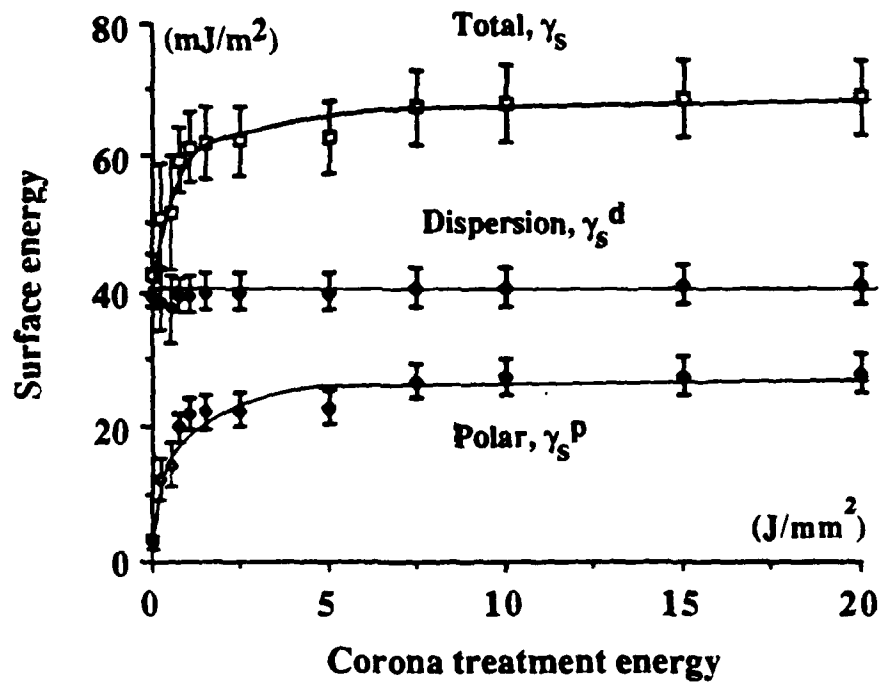
Fig. 3.8. Surface energy versus corona pretreatment energy of U/C-PEEK composite.
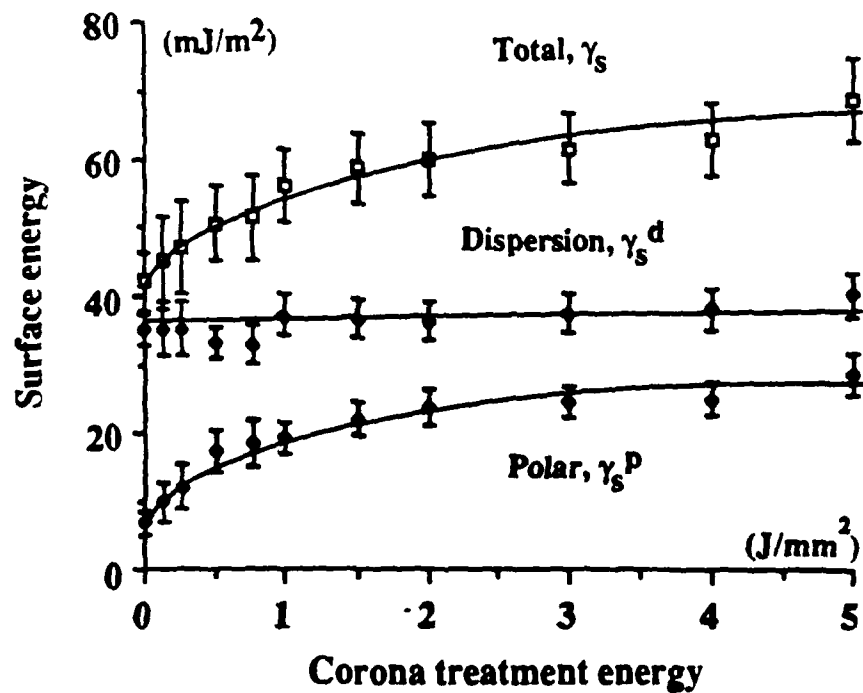
Fig. 3.9. Surface energy versus corona pretreatment energy of U/C-PA composite.

(v) Effect of Surface Roughness on the Surface Free Energy

The results presented so far have been corrected for any changes in surface roughness which accompany the chemical changes. As explained earlier, this will enable the effect on the adhesive fracture energy, G_c, due to changes in the surface chemistry alone to be identified. However, when considering the mechanisms of adhesion it is important to understand also the effect of surface roughness on the surface free energy. Therefore, in this section results from uncorrected contact angle measurements will first be presented followed by results from the effect of surface roughness on the measured surface free energy. Figure 3.10 shows the results from uncorrected contact angle measurements on the U/C-PA composite; the results from the other TPFC materials follow a similar pattern (except, of course, the U/K-PA composite). The surface energies in this figure are due to the surface chemical changes plus the effect of changes in the surface roughness. The effect of surface chemistry change on the surface free energy was presented in the previous section and it may be seen that the uncorrected values are higher than those in Figure 3.9. The effect of surface roughness on the surface energy values may be calculated by subtracting the results from Figure 3.9 from those in Figure 3.10. Such results are shown in Figure 3.11. Surface roughness increases with corona treatment level, see Figures 3.5 (page 50), and therefore, an increase in the calculated surface energy components as depicted in Figure 3.11 is observed.
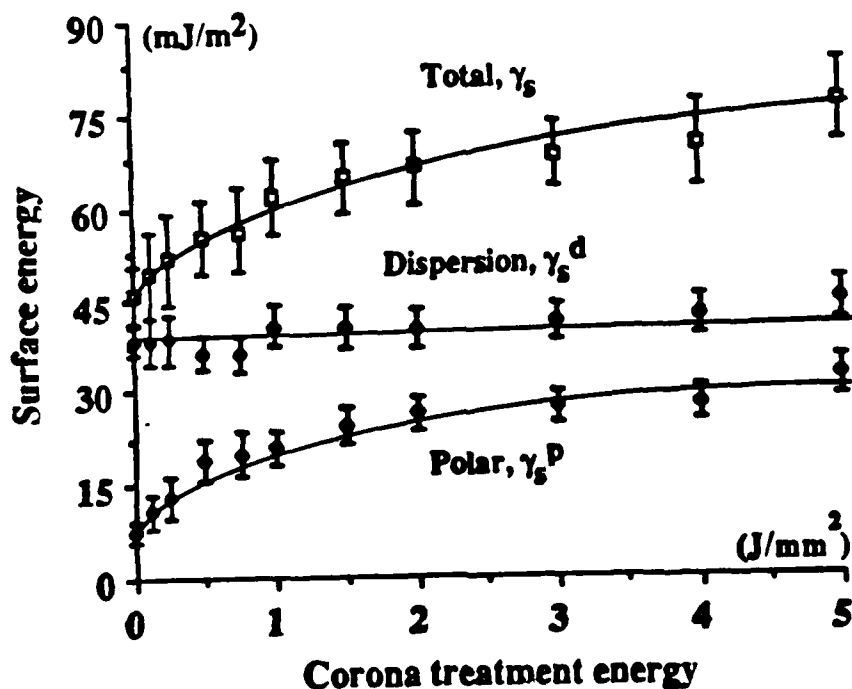
Fig. 3.10. Surface energy versus corona treatment energy
for U/C-PA composite from uncorrected CAA.
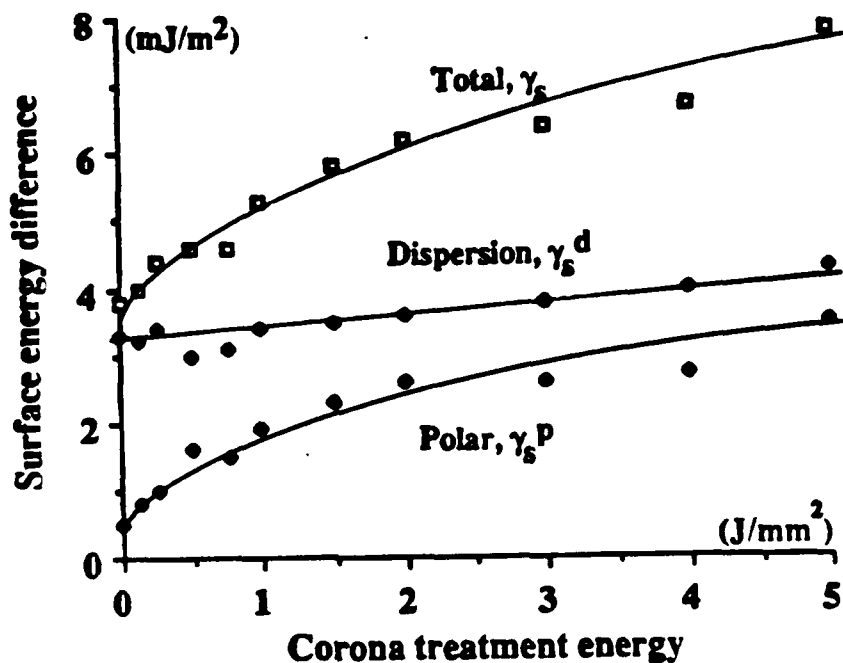
Fig. 3.11. Effect of surface roughness on surface energy for U/C-PA composite.

3.2.4.6. CAA of Corona-Pretreated Thermoplastic Fibre-Composites After Ageing

The results presented in the above section were from freshly pretreated fibre-composites. In this section the U/C-PEEK and PA thermoplastic composites were pretreated using corona-discharge and then allowed to age, for up to six months, in a laboratory environment (temperature $(T)=20\pm2^{0}C$ and relative humidity $(R. H.)=60\%$). Contact angle measurements were then carried out on these fibre-composites. Information from such analyses should indicate the time-period for which the corona treatment remains effective.

The U/C-PEEK and PA thermoplastic composites were corona-treated to energy levels of $20J/mm^2$ and $5J/mm^2$ respectively. These levels were selected because at these energy levels cohesive failures were recorded from the double-cantilever beam joint specimens, see Chapter Four. The fibre-composites were corona-treated and were placed in a closed chamber which had two small 45^0 holes to allow the laboratory atmospheric conditions to age the TPFC materials without accumulating dust on the surfaces.

The results from Figures 3.12 and 3.13 show several noteworthy features. Firstly, the dispersion energy component is constant in value. Secondly, in the first few weeks there is a

rather rapid drop in the polar energy, and this is accompanied by a similar drop in the total surface free energy. These values, γ_s^P and γ_s, seem to reach constant minimum values. The drop in the γ_s^P and consequently γ_s values can be due to several factors such as accumulation of hydrocarbons from the atmosphere on the surfaces of the freshly treated TPFC materials and/or chemical degradation of the very active polar species. These problems will be further understood by using XPS which will act not only as a complimentary technique to CAA, but will also enable a better understanding of the type of chemical modifications accompanying corona treatment.
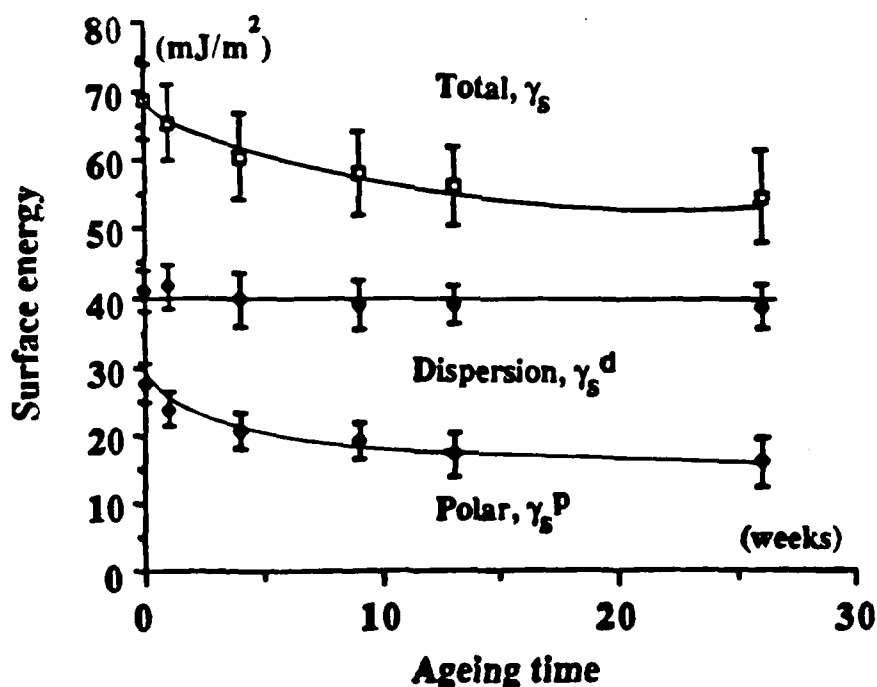
Fig. 3.12. Surface energy of aged U/C-PEEK composite treated to a corona energy level of 20J/mm^2.
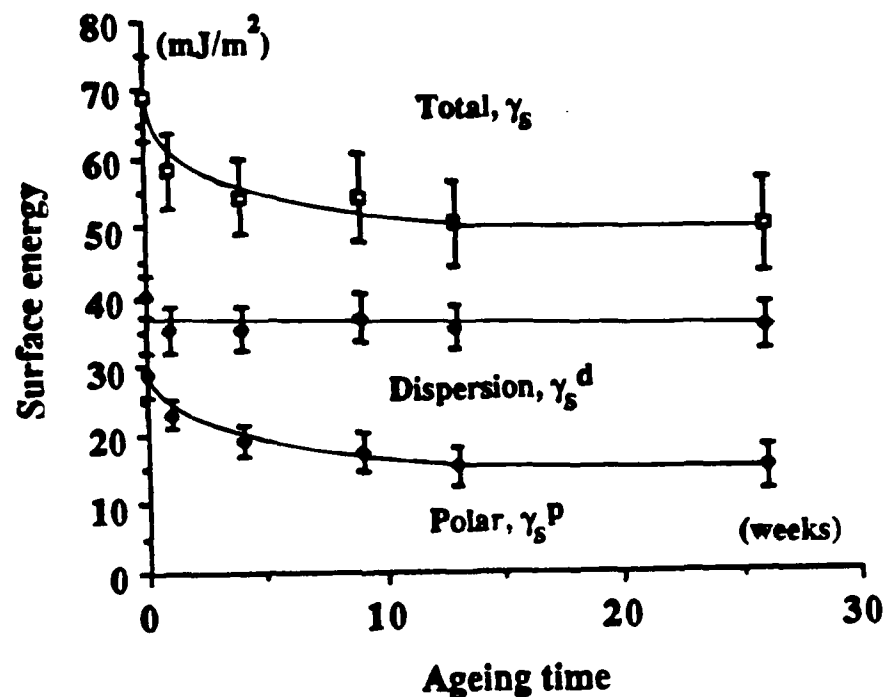
Fig. 3.13. Surface energy of aged U/C-PA composite
treated to a corona energy level of $5J/mm^2$.

3.2.4.7. Conclusions

The conclusions from the CAA studies are.

1. The surface roughness of all the fibre-composites materials is dependent on the type and duration of the treatment employed, and this affects the measured contact angles. The values of the contact angles were corrected using Wenzel's approach and the effects of surface roughness on the surface energy values were analysed.

2. The improved mathematical approach provides a far sounder method for calculating the surface energy components than previously used methods. This technique overcomes some of the approximations in calculating these values.

3. The polar energy components of all fibre-composites subjected to abrasion/solvent-wipe pretreatment are higher than those from untreated (as prepared) specimens. One very important result from the abrasion/solvent-wipe pretreatment of the fibre-composites was that of the U/C-epoxy thermoset composite. This composite possesses a relatively high polar energy component compared to the TPFC materials.

4. The polar energy component of U/C-PEEK is the same from the abrasion/solvent-wipe and aluminium/etch pretreatments, which indicates that the active polar species are not affected with these pretreatment techniques and that contaminants, if present, are relatively low. Further, the polar energy component is a strong function of the duration of the acid-etch pretreatment.

5. The polar energy component increases dramatically after corona treatment whilst the dispersion energy component remained constant. This observation suggests that the concentration of active polar species on the surfaces of the treated fibre-composites have increased. The increased level of the polar energy component led to a similar increase in the total surface free energy.

6. The polar energy component seems to be a function of the ageing time and drops to a minimum constant value. However, this minimum value is still higher than the polar energy value obtained from abrasion/solvent-wipe pretreatment. Which suggests that, even after ageing there are still more active polar species on the surfaces of corona-pretreated fibre-composites compared to the untreated materials.

3.3. SCANNING ELECTRON MICROSCOPY STUDIES

3.3.1. Introduction

The surface topographies of fibre-composite may be examined in detail by scanning electron microscopy (SEM) and are important since they reflect the physical changes caused by the pretreatment techniques. The surface topography may also influence the intrinsic wetting and adhesion [5, 9, 12, 15, 41, 42]. Therefore, a study of the fibre-composite surfaces was undertaken.

3.3.2. Experimental Technique

A JEOL JSM-T200 scanning electron microscope (SEM) was used and an Edwards S150A sputter coater was employed for coating the specimens with a thin layer of gold prior to examination in the electron microscope. The surfaces to be examined were cut out from fibre-composite laminates to 2X2cm in size suitable for mounting on the SEM specimen holder. The specimens were gold-coated in the Edwards S150A sputter coater for about 4.5 minutes at a deposition rate of 150Å per minute. After sputtering, a small amount of silver paint was applied between the specimen and an aluminium stub to improve the conductivity and to hold the specimen on the stub. This was necessary to prevent charging when the specimen was

examined in the SEM. The surfaces of the fibre-composites were then examined using the secondary electron image at an acceleration voltage of 15kV, and a working distance of 20mm.

3.3.3. Results and Discussion

3.3.3.1. Untreated Fibre-Composites

Typical SEM micrographs from untreated fibre-composite materials are shown in Figure 3.14. These two micrographs show that the U/C-PA composite has a smoother surface than the W/C-PEI composite. This physical observation is in agreement with the CAA observations where the surface roughness factor, r_c, for the woven composites was higher (see Table 3.3 page 48).

(a)   (b)
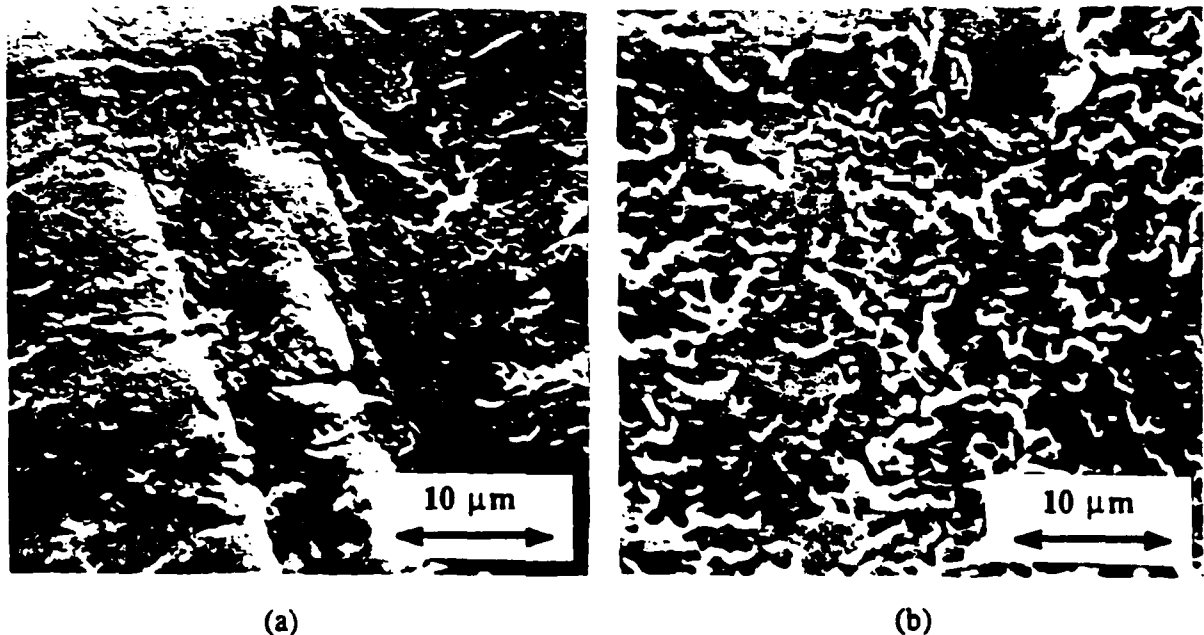
Fig. 3.14. Scanning electron micrographs of (a) untreated, unidirectional-carbon/polyamide (U/C-PA) and (b) untreated woven-carbon/poly(ether imide) (W/C-PEI) composites.

3.3.3.2. Fibre-Composites Subjected to Abrasion/Solvent-Wipe Pretreatment

Figure 3.15 shows typical micrographs from fibre-composites subjected to an abrasion/solvent-wipe pretreatment. When these micrographs are compared with the micrographs in Figure 3.14 they reveal that abrasion introduces a rougher texture. This observation agrees with the surface roughness correction factors, r_c, deduced from the contact angle measurements where it was demonstrated that the surface roughness factor increases after

the fibre-composites are subjected to an abrasion/solvent-wipe pretreatment (see Table 3.4 page 48).

(a)   (b)
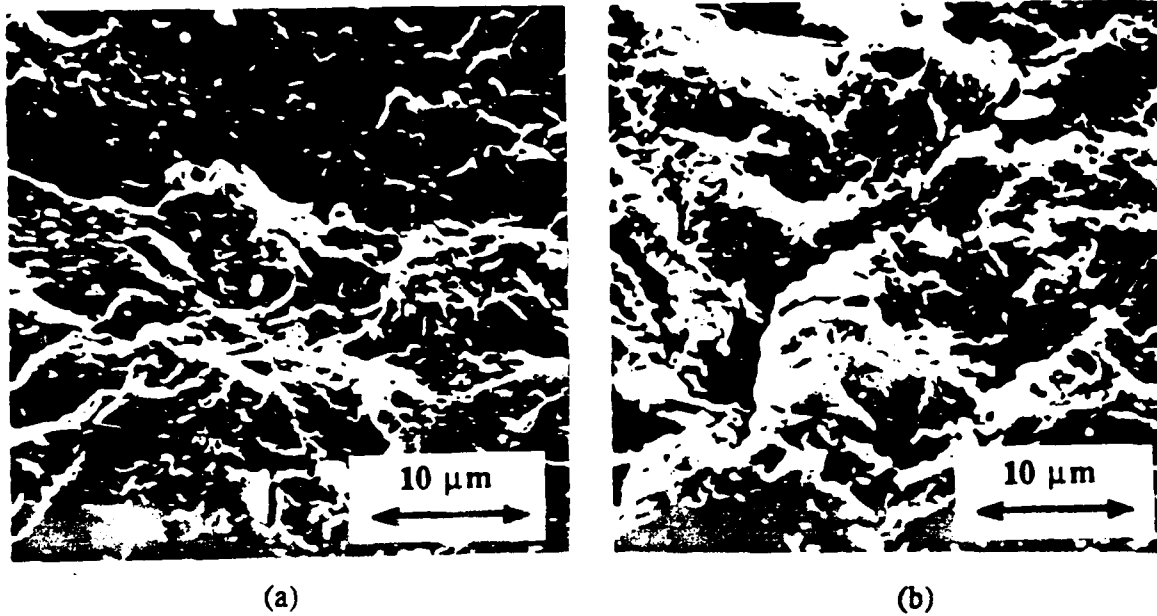
Fig. 3.15. Scanning electron micrographs from an abrasion/solvent-wipe
surfaces of (a) U/C-PA and (b) W/C-PEI composites.

3.3.3.3. U/C-PEEK Composite Subjected to Aluminium/Etch and Acid-Etch Pretreatments

Figures 3.16 and 3.17 show typical micrographs from aluminium-foil/sodium-hydroxide (aluminium/etch) and acid-etch pretreatments respectively.
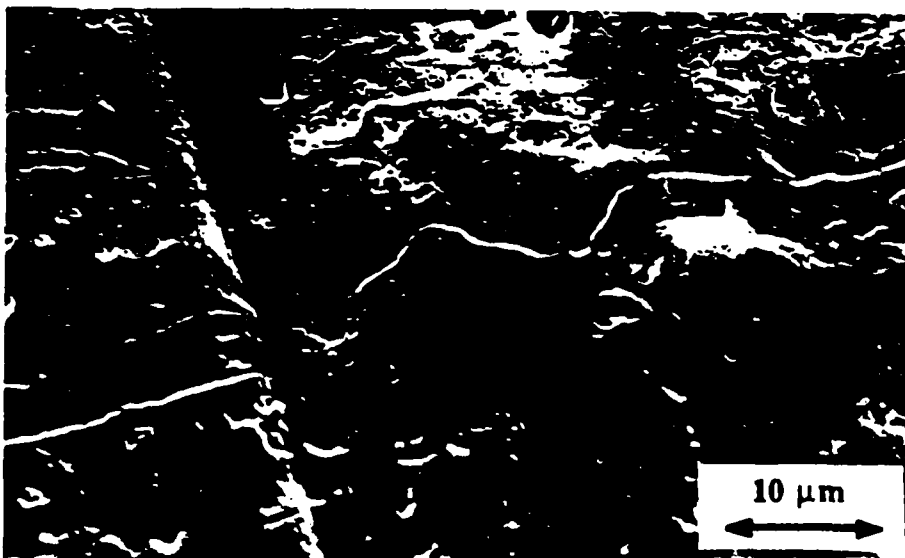
Fig. 3.16. Scanning electron micrograph of U/C-PEEK composite
subjected to an aluminium/etch pretreatment.

(a)   (b)
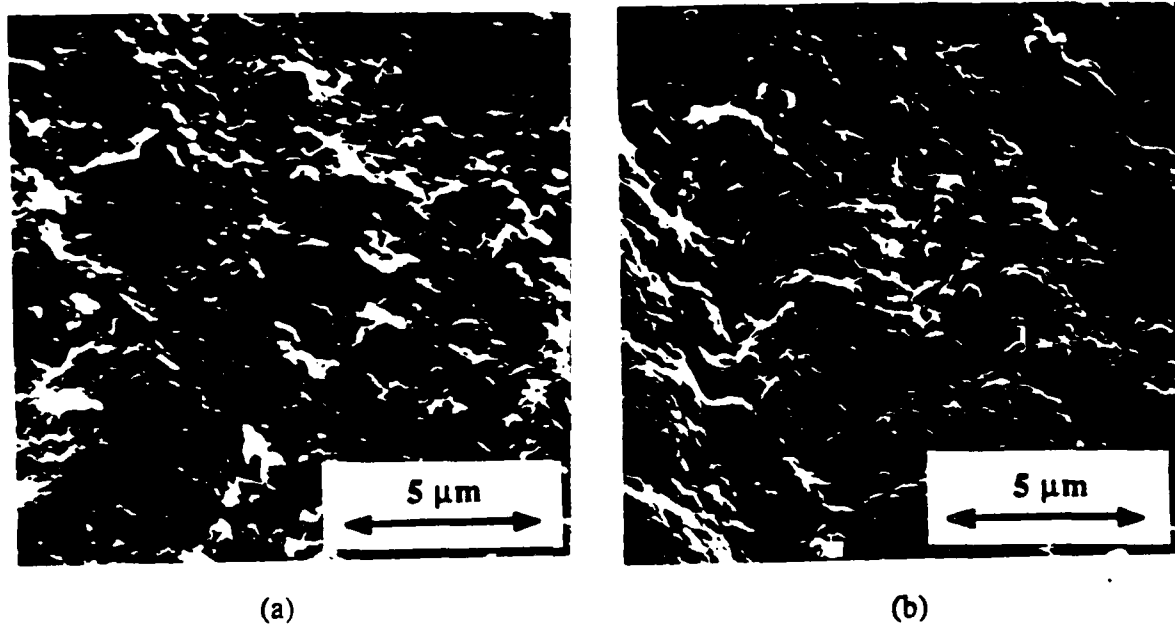
Fig. 3.17. Scanning electron micrographs of U/C-PEEK composite subjected to
acid-etch pretreatment (a) for 2 minutes and (b) for 10 minutes.

The above micrographs show several noteworthy features. Firstly, that the aluminium/etch pretreatment leaves behind a smoother surface than the abrasion pretreatment. Secondly, that acid-etching is accompanied by an increase in the surface roughness which is also dependent on the duration of the etching. Finally, all these observations are in agreement with the calculations of the surface roughness correction factors presented in Table 3.5 (page 49).

3.3.3.4. TPFC Materials Subjected to Corona-Discharge Pretreatment Technique

In this section results from corona-treated TPFC materials will be presented. In Section 3.2.4.3 it was mentioned that the surface roughness correction factor increases with the increased level of corona pretreatment. Considering the typical micrographs in Figure 3.18 it is evident that corona-discharge treatment does indeed increase the level of surface roughness for the U/C-PEEK thermoplastic composite. It is evident that as the corona energy level is increased then some carbon-fibres may get exposed. This may be understood from the fact that the carbon-fibres are electrically conductive. The electrical sparks (from the treater) would ablate some of the resin covering the carbon-fibres. This leaves behind not only a rough texture but also exposes the carbon-fibres at treatment levels of $20J/mm^2$ and beyond.

The typical micrograph in Figure 3.19(a) shows that the corona-treated "Kevlar"-PA

thermoplastic composite does not possess as rough a surface as that of the carbon-fibre PA composite, see Figure 3.19(b). This can be understood with a similar argument presented above i.e., that "Kevlar"-fibres are non conductive and hence the electrical sparks do not ablate the thermoplastic resin. Hence, the surfaces of the "Kevlar"-fibre reinforced PA materials are smoother than the carbon-fibre reinforced thermoplastic composites.

(a)   (b)

(c)   (d)
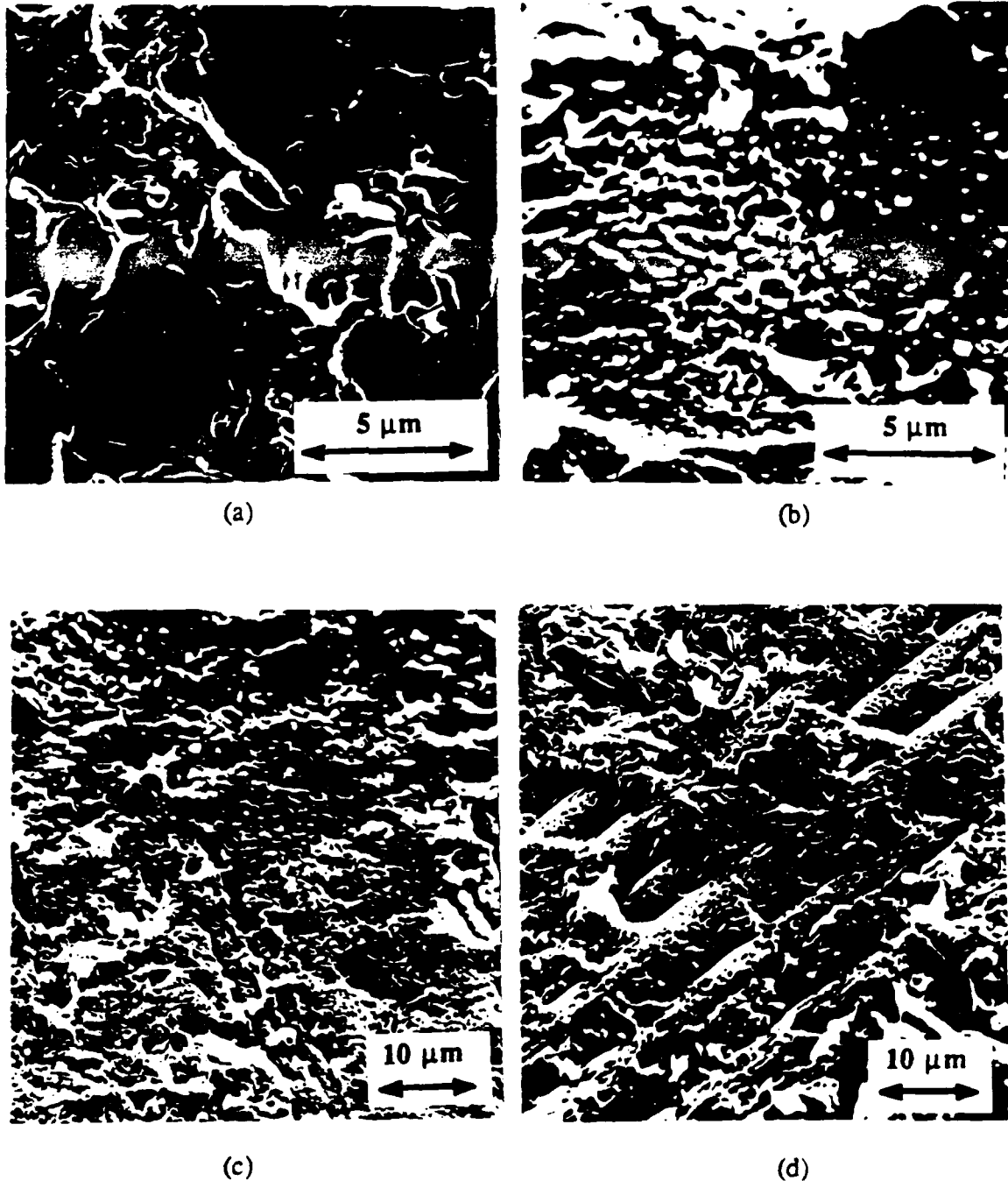
Fig. 3.18. Scanning electron micrographs of U/C-PEEK composite subjected to: (a) abrasion; and corona treatments at: (b) 10J/mm^2, (c) 20J/mm^2 and (d) 40J/mm^2.

<center>(a)</center> <center>(b)</center>
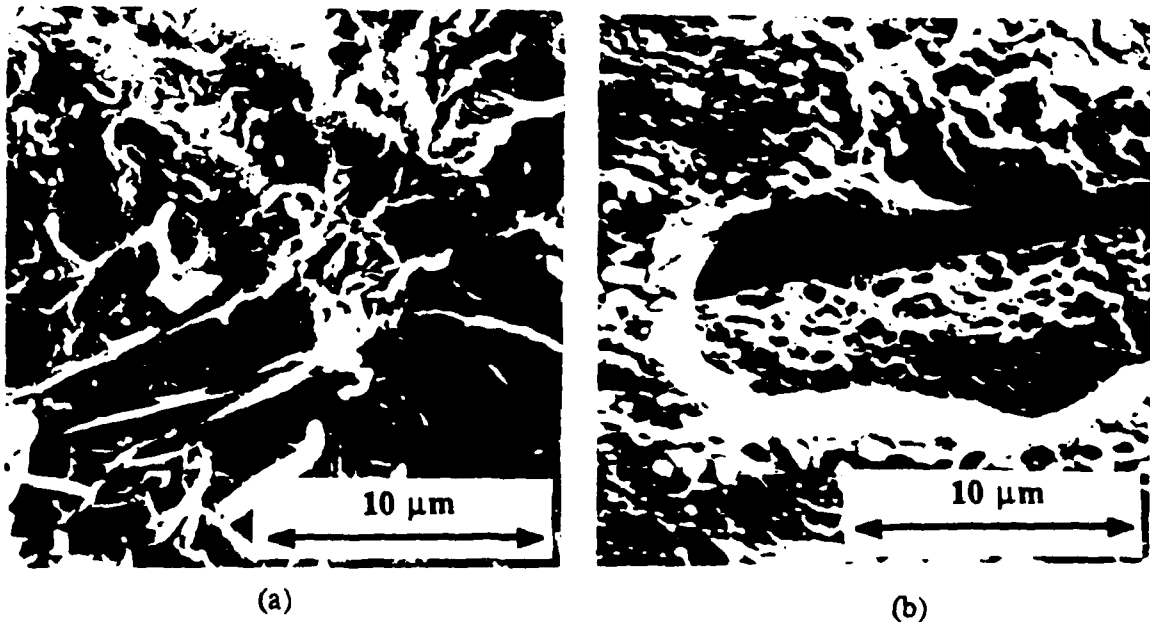
Fig. 3.19. Scanning electron micrographs of (a) U/K-PA composite and (b) U/C-PA composite; both specimens subjected to a corona treatment level of $20J/mm^2$.

3.3.4. Conclusions

SEM reveals that the surface roughness is a function of the type and duration of pretreatment employed. The micrographs show that corona treatment exposes the carbon-fibres on the surfaces of carbon-fibre reinforced thermoplastic composites if treated at energy levels of $20J/mm^2$ and beyond. The observations from the SEM studies confirm the results from calculating the surface roughness correction factors from CAA.

3.4. X-RAY PHOTOELECTRON SPECTROSCOPY STUDIES

3.4.1. Introduction

Obviously, any assessment of the surface characteristics would be incomplete without a thorough understanding of the surface chemical changes accompanying the treatment employed. For this reason X-ray photoelectron spectroscopy (XPS) was employed to provide a detailed chemical analysis of the surfaces.

3.4.2. Literature Survey

3.4.2.1. Introduction

The literature survey will outline the basic principles of XPS and present relevant work on

the use of XPS in characterising changes in the surface chemistry arising from using different pretreatment methods to increase the adhesion performance of polymers.

3.4.2.2. Surface Chemistry Characterisation Techniques

There are several types of surface chemistry characterisation techniques available. Choosing the one which is suitable requires a knowledge of the capabilities and limitations of these surface analytical techniques. Table 3.10 summarizes some of the important features of the surface chemistry analysis techniques available. Several requirements were set for the surface chemical characterisation of fibre-composites. These were:

1. the analysis of the very top surface regions, between 2 to 6nm,

2. the use of the X-ray incident beam technique for low energy ionization rather than the electron beam technique, the former being less disruptive of the surface,

3. the quantification of the elements present on the surface, and

4. the quantification of the species which make up the relevant individual elements.

The technique which is most suitable in satisfying the above rather stringent requirements was found to be XPS. However, this does not mean that XPS does not have its limitations. The principles of XPS, its advantages, limitations and a literature survey will be presented in the following section.

Table 3.10. Types and features of surface chemistry analysis techniques.

Technical name	Incident beam	Detected beam	Depth of analysis
1) Attenuated total reflectance (ATR)	Infrared beam	Attenuated beam	Few microns
2) X-ray flourescence (XRF)	Electron beam	X-ray	Few microns
3) Auger elctron spectroscopy (AES)	Electron beam	Ejected auger electron	Few nanometers
4) X-ray photoelectron spectroscopy (XPS)	X-ray	Ejected photo electron	Few nanometers
5) Ion scattering spectroscopy (ISS)	Inert gas ions	Backscattered ions	Fraction of monolayer
6) Secondary ion mass spectroscopy (SIMS)	Inert gas ions	Target ions sputtered from surface	Fraction of monolayer

3.4.2.3. Principles of XPS

(i) The Photoemission Process

XPS is concerned with a special form of photoemission, i.e. the ejection of an electron from a core level by X-ray photons. The energy of the emitted photoelectrons is analysed by an electron spectrometer. The data is presented as a graph of intensity (counts per second) versus electron energy (eV). The kinetic energy of an ejected photoelectron is not an intrinsic material property since it depends on the energy of the X-ray source. However, the binding energy is a material characteristic parameter and is related to the kinetic energy. The process of photoemission is shown schematically in Figure 3.20.

(ii) Chemical Shift

The binding energy of a photoelectron peak defines not only the energy level within the atom from which it emerged but also the chemical environment (valence state) of the atom. The Swedish Nobel Prize winner responsible for the development of this technique, Siegbahn, described it as electron spectroscopy for chemical analysis (ESCA) [43]. Both terms XPS and ESCA describe the same type of analysis and only the former term will be used here. The chemical shift phenomenon can be especially useful in characterising thin oxide films, on for example metals, as it is possible to distinguish the metal ion of the oxide from that of the parent metal. Calculations of this type have been described by Castle [44].
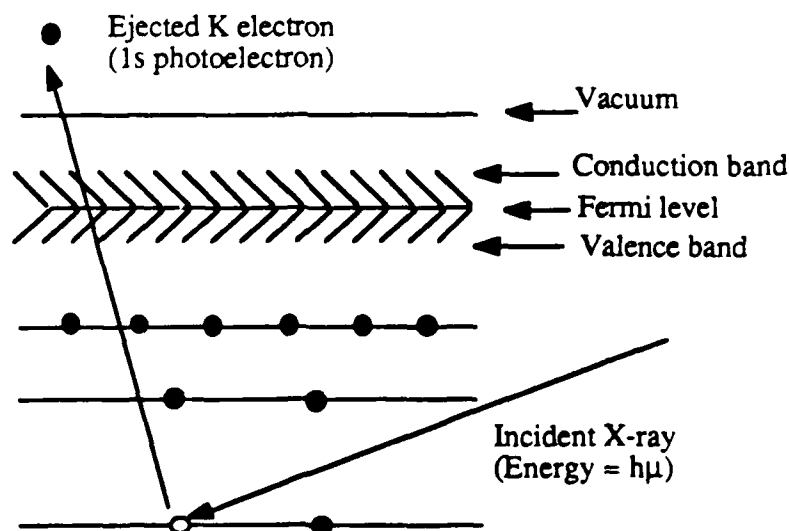
Fig. 3.20. The schematic presentation of the photoemission process.

(iii) Depth of Analysis

Although X-rays will penetrate deep into the material, the inelastic mean free path (IMFP), of an electron in a solid is very small compared with that of the X-ray. Therefore, it is the kinetic energy of the outgoing electrons which determines the analysis depth of the XPS experiment. The IMFP of electrons in the energy range of interest in XPS (30 to 1400eV) varies from 0.3nm to 3.0nm whereas the analysis depth is between 2 to 7nm. It is possible in XPS to achieve a compositional depth profile by using photoelectrons of different kinetic energies. This can be easily achieved by changing the X-ray source. The anlysis depths for the

C1s photoelectron in MgKα and AlKα (X-rays) are approximately 6.0 and 7.0nm respectively. The analysis depth is given by:

$$d = 3\lambda.\sin\theta \qquad (3.20)$$

where d is the depth of analysis, λ is the inelatic mean free path and θ is the angle subtended by sample surface and analyser optics, (take-off angle). However, a simpler method of depth profiling can be achieved by changing the take-off angle. The depth of analysis achieved with grazing emission and normal emission are shown schematically for the C1s electron in Figure 3.21.

$$\theta = 35° \quad d = 1.7\lambda \qquad\qquad \theta = 90° \quad d = 3\lambda$$
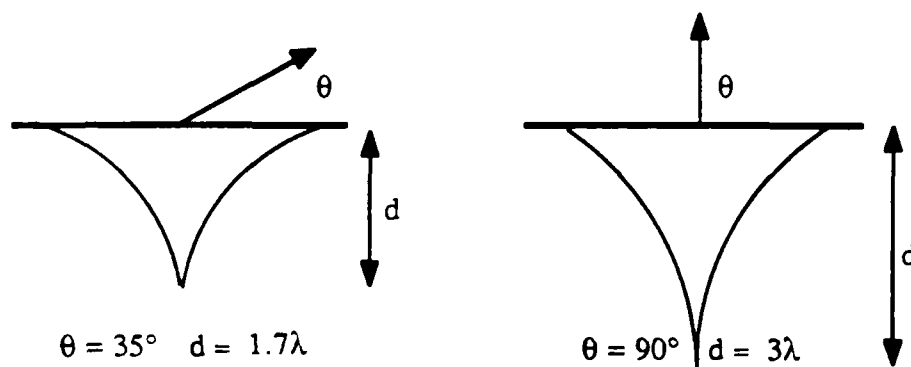
Fig. 3.21. Schematic presentation of the depth profiling of the C1s electron as a function of the take-off angle.

(iv) Quantification of XPS Data

For a quantitative analysis of XPS data it is better to employ, peak areas rather than peak intensities. This allows for the fact that sometimes peak broadening is observed if the element is present in a mixture of chemical states. Not all elements have the same photoemissivity in the XPS experiment and care has to taken to employ the proper "sensitivity" factors.

(v) Disadvantages of XPS

Perhaps the most important disadvantage in employing XPS is its spatial resolution, for XPS is an area averaging technique with a typical analysis area of about $6mm^2$. The analysis area can be decreased by inserting an aperture plate between the specimen and the analyser. However, this technique would lead to a substantial reduction in the total count rate, therefore requiring the acquisition time to be increased, which in turn leads to the degradation of the surfaces being analysed.

(vi) Useful Electron Binding Energies

Table 3.11 shows the electron binding energies of the elements and species that were most frequently encountered in the current research work.

Table 3.11. Electron binding energies of elements and their corresponding important

species from line positions of $AlK\alpha$ or $MgK\alpha$ (X-rays).

Element/electron type	Electron binding energy (eV)
Aluminium (Al2p)	75
Silicon (Si2p)	99
Sulphur (S2p)	164
Chlorine (Cl2p)	200
Carbon (C1s)	
C-C, C-H	285.0
-N(CH3)$_2$, -NH$_2$	285.2
C-O	286.5-286.7
O-C-O, >C=O	288.0-288.4
O-C=O	289.5-290.1
Calcium (Ca2p)	347
Nitrogen (N1s)	
-CN, -NH$_2$	399-401
-ONO$_2$, -NO$_2$, -NO	405-408
Oxygen (O1s)	532-534
Fluorine (F1s)	685
Sodium (Na1s)	1072

3.4.2.4. Previous Work

Corona-discharge treatment of the thermoplastic polymer, low-density polyethylene (LDPE), has been studied by many workers, particularly with reference to the autoadhesion of the polymer (adhesion of a polymer to an identical polymer). LDPE autoadheres when two surfaces are contacted under pressure at temperatures above 90^0C. However, after fairly low levels of corona treatment the surfaces will autoadhere at lower temperatures $\approx 70^0C$. Two theories had been proposed to account for this effect. The first by Stradal and Goring [45], who suggested that electret formation was involved. The evidence for this was that corona treatment in both active (air, oxygen) and inert (nitrogen, argon, helium) gases gave the same effect. The second by Owens [46], who suggested that hydrogen bonding between polar groups was responsible. However, he studied only LDPE treated in air. Therefore, until the advent of XPS there was no conclusive evidence of the type of surface chemical changes accompanying corona-treated thermoplastics.

The original work in employing XPS to study the adhesion of LDPE was reported by Briggs et al. [16, 47-49]. Brewis and Briggs [47] employed corona-discharge on LDPE to promote the adhesion of this material. They showed how successfully one can employ XPS to probe the chemical changes accompanying corona treatment. They showed that as the treatment level was increased then:

1. The level of the oxygen element increased from undetectable levels to very high levels.
2. The high binding energy shoulder of the carbon element became more active and also increased.
3. The peel strength of the joints increased.

They reported that the oxidation of the surfaces of LDPE was independent of the type of gas they employed, which were, air, nitrogen and argon. They attributed the increase in the peel strength to the increase in the oxidation level. Thus, giving Owens theory [46] a firmer foundation. However, they did not provide any details of how a polymer based on the ethylene monomer, $CH_2=CH_2$, could attain oxygen-rich species when treated in an inert gas such as argon. Obviously, this observation cannnot be true from a theoretical point of view. But, may be explained if traces of oxygen in the apparatus, or very small amounts of absorbed and adsorbed oxygen in the LDPE, are present.

3.4.3. Experimental Approach and Spectrometer Description

The fibre-composite materials under investigation were freshly prepared and stored in a desiccator before conducting the XPS analyses. The specimens 1X1cm in size were mounted

using double-sided adhesive tape onto stubs. Six specimens were loaded onto a special carousel which was then mounted onto the spectrometer driving rails. The spectrometer used was a VG MKIII model which had three seperate chambers. The first was a loading and unloading chamber, which also acted as a low vacuum chamber. The second was an ultra high vacuum (UHV) chamber where the pressure was allowed to drop down to 10^{-9}mbar before allowing the specimen into the third chamber which was the analysis compartment. The X-ray source used was AlKα (hμ=1486.6eV). The spectrometer had a hemispherical sector analyser (HSA) for electron energy analysis which offered relatively high sensitivity with high resolution, which is important to obtain the benefits of the chemical shift phenomenon. The HSA was combined with an electron preretardation unit to achieve adequate resolution. The HSA was operated at a fixed analyser transmission mode. In this mode a constant voltage was applied across the hemispheres of the analyser allowing only electrons of a particular energy to pass through. Thus, the resolution of the spectral peaks of interest was constant across the entire energy range of the spectrum. The photoelectrons emitted from the sample were transferred to the focal point of the analyser by a lens assembly. These electrons with an energy matching the pass energy were transmitted to the analyser and counted by the channel electron multiplier. The emerging signal was then amplified and processed as a series of pulses. Thus the acquisition of a spectrum was achieved by ramping the potential of the returning field analyser and plotting the graph of counts per second (cps) versus electron energy (eV). The step sizes used were 2eV and 0.2eV for the wide and narrow scans respectively and the analyser energies were 50eV and 20eV for the former and the latter respectively. Finally, the take-off angle was kept constant at 45^0 except where indicated otherwise.

3.4.4. Results and Discussion

In this section results from the XPS analyses will be presented. First, the results from freshly-prepared or treated fibre-composites will be reported followed by the results from corona-pretreated TPFC materials which had been aged in the laboratory atmosphere. The quantitative results reported in this section represent the average of at least two similar specimens and elements which may be present but are less than 0.5% in value will not be reported. Also, all values are in percentages of the elements present on a given surface.

3.4.4.1. Analysis of Untreated Fibre-Composites

Figure 3.22 shows a typical spectrum which reveals very high levels of contaminants. The results from untreated fibre-composites are summarized in Table 3.12. Perhaps, the most important feature of these results is the relative high concentration of contaminants such as releasing agents (from silicon and fluorine) present on the surfaces of the untreated

fibre-composite laminates. The presence of such high concentrations of releasing agents indicates the relative ease with which these releasing agents can get transferred from the surfaces of the mould to the laminates whilst the composite sheet is being prepared. Furthermore, the presence of releasing agents in these concentrations may hinder the adhesion of the composites, as will be discussed in Chapter Four.
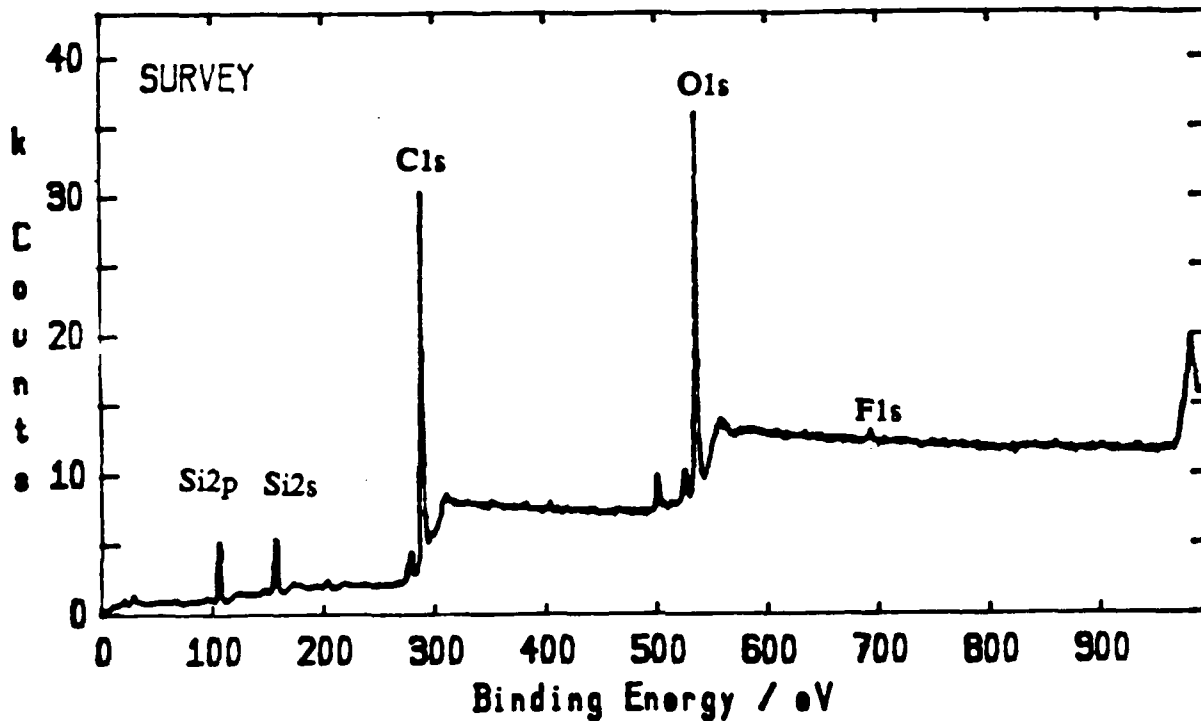
Fig. 3.22. Wide scan XPS spectrum of untreated U/C-PEEK composite.

Table 3.12. The mean and maximum/minimum of the atomic % concentrations of elements present on the surfaces of untreated fibre-composite materials.

Material	C1s	O1s	N1s	Si2p+F1s	S2p	Na1s
U/C-PEEK	64.6±2.3	28.4±1.6	1.7±0.3	4.2±0.8	*	*
U/C-PA	74.6±2.4	15.8±1.2	4.7±0.7	3.1±0.5	*	1.2±0.3
U-K/PA	79.5±2.1	13.2±1.1	3.7±0.5	2.7±0.4	*	*
W/C-PI	68.8±3.7	19.7±2.1	3.4±0.9	4.9±1.6	*	2.2±1.2
W/C-PEI	65.1±1.8	27.0±1.9	3.7±0.2	2.9±0.4	*	1.1±0.2
U/C-PPS	83.9±2.9	6.6±1.0	1.6±0.4	3.0±0.4	4.9±1.2	*
U/C-epoxy	65.6±3.2	23.2±1.4	3.4±0.6	4.4±1.1	*	1.9±0.5

Note: (*): Not detected.

3.4.4.2. Analysis of Fibre-Composites Subjected to Abrasion/Solvent-Wipe Pretreatment

Results from XPS analysis on fibre-composites subjected to abrasion/solvent-wipe pretreatment are presented in Table 3.13 with a wide scan XPS spectrum for the U/C-PEEK composite shown in Figure 3.23. These results should be compared to the results presented from the untreated fibre-composite laminates, see Table 3.12 and Figure 3.22. Now, it can be seen that the abrasion/solvent-wipe pretreatment leads to a substantial reduction in the concentration of the releasing agents for all the fibre-composite materials employed. Since abrasion can so effectively reduce the concentration of silicon and fluorine based releasing agents then this indicates that these type of elements are from the releasing agents employed in the processing of the laminates. However, some silicon and fluorine are still left on the surfaces of the composites even after abrasion. Although a relative angle of about 45^0 was used between the grit nozzle and the composite surfaces, some of the releasing agents may get pushed further into the composites and this may account for detecting rather low concentrations of elements from releasing agents.

Table 3.13. The mean and maximum/minimum of the atomic % concentrations
of elements present on the surfaces of fibre-composites subjected
to abrasion/solvent-wipe pretreatment.

Material	C1s	O1s	N1s	Si2p+F1s	S2p	Na1s
U/C-PEEK	77.6±1.5	18.1±1.1	0.4±0.4	2.2±0.5	*	*
U/C-PA	75.9±1.8	18.1±0.9	3.8±0.8	1.2±0.4	*	1.1±0.5
U/K-PA	73.1±1.7	18.3±1.0	4.0±0.8	1.6±0.3	*	*
W/C-PI	71.8±2.1	22.7±0.8	3.7±0.9	1.0±0.4	*	0.7±0.5
W/C-PEI	69.8±1.9	23.5±1.3	3.4±0.9	1.3±0.4	*	1.3±0.4
U/C-PPS	82.3±1.7	7.3±0.7	1.2±0.3	1.7±0.5	7.2±0.7	*
U/C-epoxy	81.0±2.2	15.7±0.9	1.7±0.45	1.1±0.3	*	*

Note: (*): Not detected.
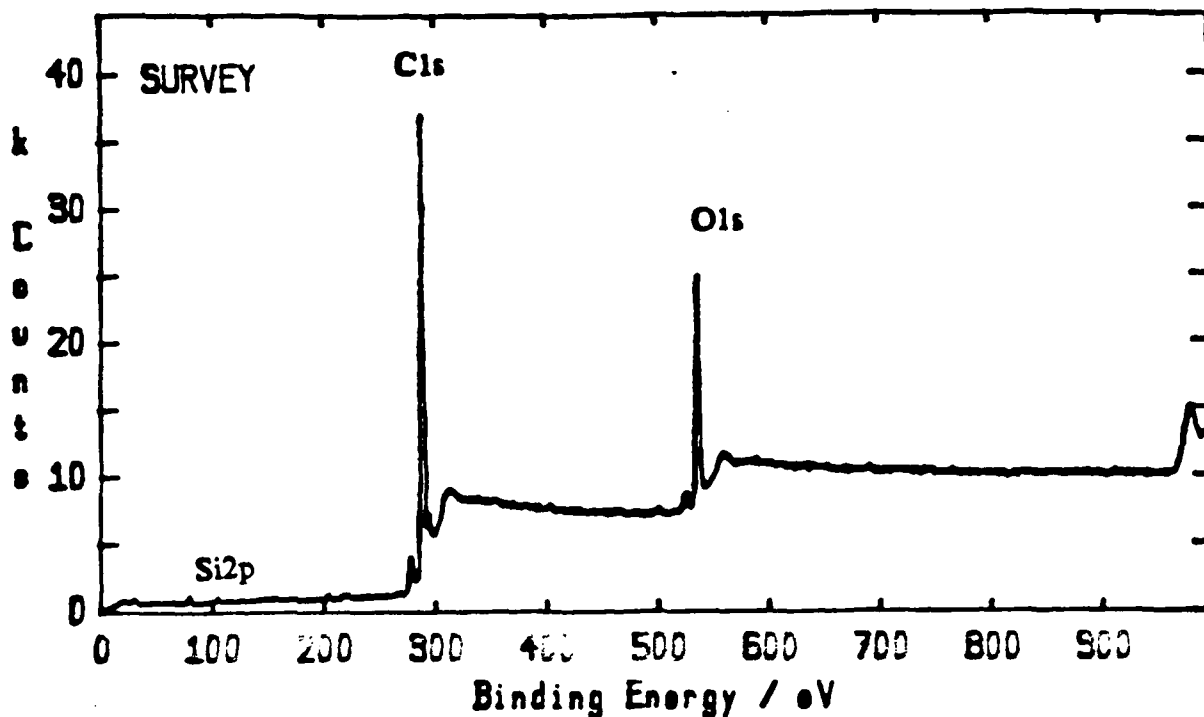
Fig. 3.23. Wide scan XPS spectrum of the U/C-PEEK composite
subjected to abrasion/solvent-wipe pretreatment.

3.4.4.3. Analysis of U/C-PEEK Composite Subjected to Aluminium/Etch and Acid-Etch Pretreatments

The U/C-PEEK composite was subjected to an aluminium-foil/sodium-hydroxide (aluminium/etch) and an acid-etch pretreatments and the results are presented in Table 3.14.

These results show that firstly, as expected for the aluminium/etch pretreatment technique, there is now some aluminium on the surfaces of the U/C-PEEK composite, which obviously has not completely dissolved away. Secondly, as expected, results from this pretreatment technique do not show any level of releasing agents. Thirdly, the aluminium/etch pretreatment technique has increased the concentration of the oxygen element.

For the acid-etch pretreatment technique, there is an increase in the oxygen element concentration whereas, the carbon element concentration drops as the treatment time is increased. This indicates the oxidising nature of the acidic solution employed. Finally, due to the contact of the laminates with water, there is now a trace of calcium, most probably in the form of calcium carbonate ($CaCO_3$).

If the concentrations of releasing agents from different pretreatments are compared then an interesting feature emerges, see Table 3.15. The concentration of such elements is highest for

the untreated U/C-PEEK composite and lowest (undetectable) for the 10 minute acid-etch and aluminium/etch pretreatments. The absence or very low concentrations of releasing agents is desirable for adhesive bonding of materials especially, for difficult-to-bond TPFC materials.

Table 3.14. XPS results of U/C-PEEK thermoplastic composite subjected to aluminium/etch and acid-etch pretreatment techniques.

Treatment	C1s	O1s	N1s	Si2p+F1s	AL2p	Ca2p
Aluminium/etch	69.0±2.9	25.7±1.9	1.3±0.7	*	0.8±0.4	1.7±0.5
Acid-etch: 2 minutes	76.6±1.8	18.4±1.2	1.3±0.6	1.2±0.4	*	0.8±0.4
Acid-etch: 5 minutes	71.2±2.2	24.5±1.3	0.8±0.4	0.8±0.4	*	1.1±0.3
Acid-etch: 10 minutes	67.6±2.0	29.6±1.3	1.5±0.4	*	*	0.7±0.2

Note: (*): Not detected.

Table 3.15. The ratio of the concentrations of the releasing agents over the carbon element for the U/C-PEEK composite subjected to different pretreatment techniques.

Treatment	(Si2p + F1s)/C1s
Untreated	0.065
Abrasion/solvent-wipe	0.028
Acid-etch: 2 minutes	0.016
Acid-etch: 5 minutes	0.011
Acid-etch: 10 minutes	*
Aluminium/etch	*

Note: (*): No elements from releasing agents detected.

3.4.4.4. Analysis of TPFC Materials Subjected to Corona-Discharge Treatment

(i) Wide Scans

The wide scans revealed that as the corona pretreatment level is increased then the relative intensities of the carbon to oxygen concentrations changed, see Figure 3.24(a) and (b). This change is accompanied by an increased concentration of the element nitrogen. These

observations were true for all the TPFC materials employed. Therefore, to probe these changes further a detailed analysis of the narrow scans of the TPFC materials was undertaken.
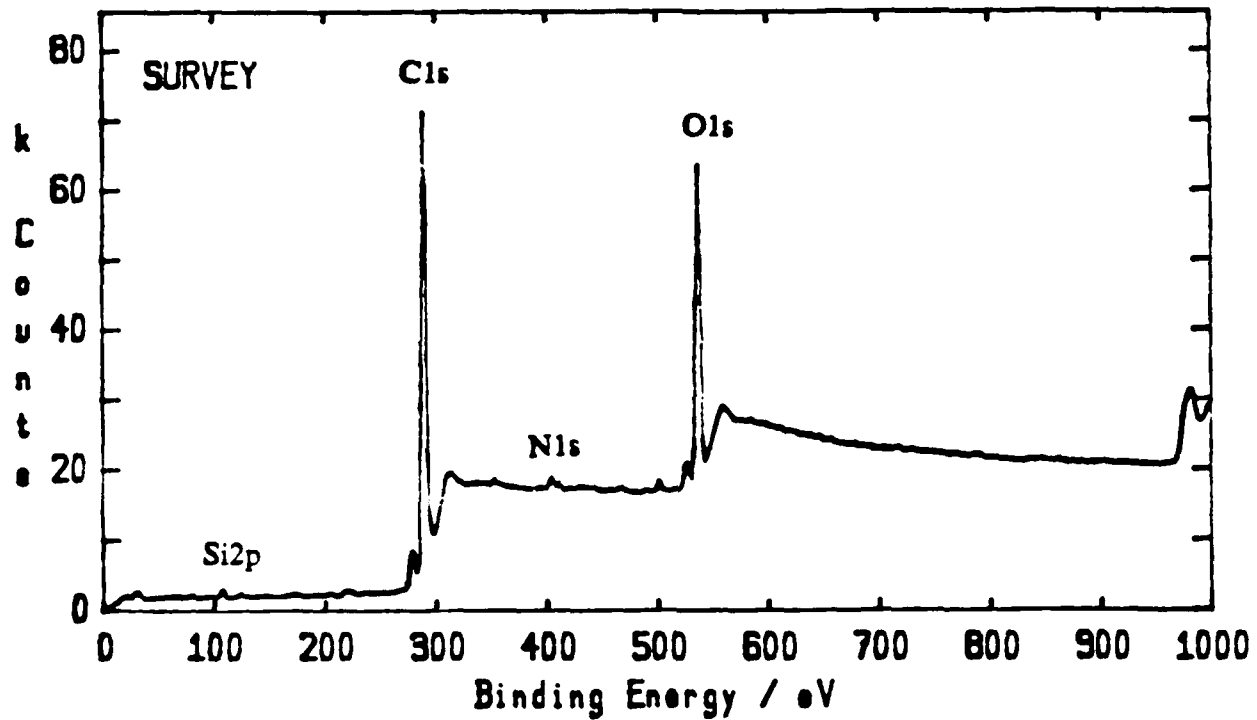
(a)
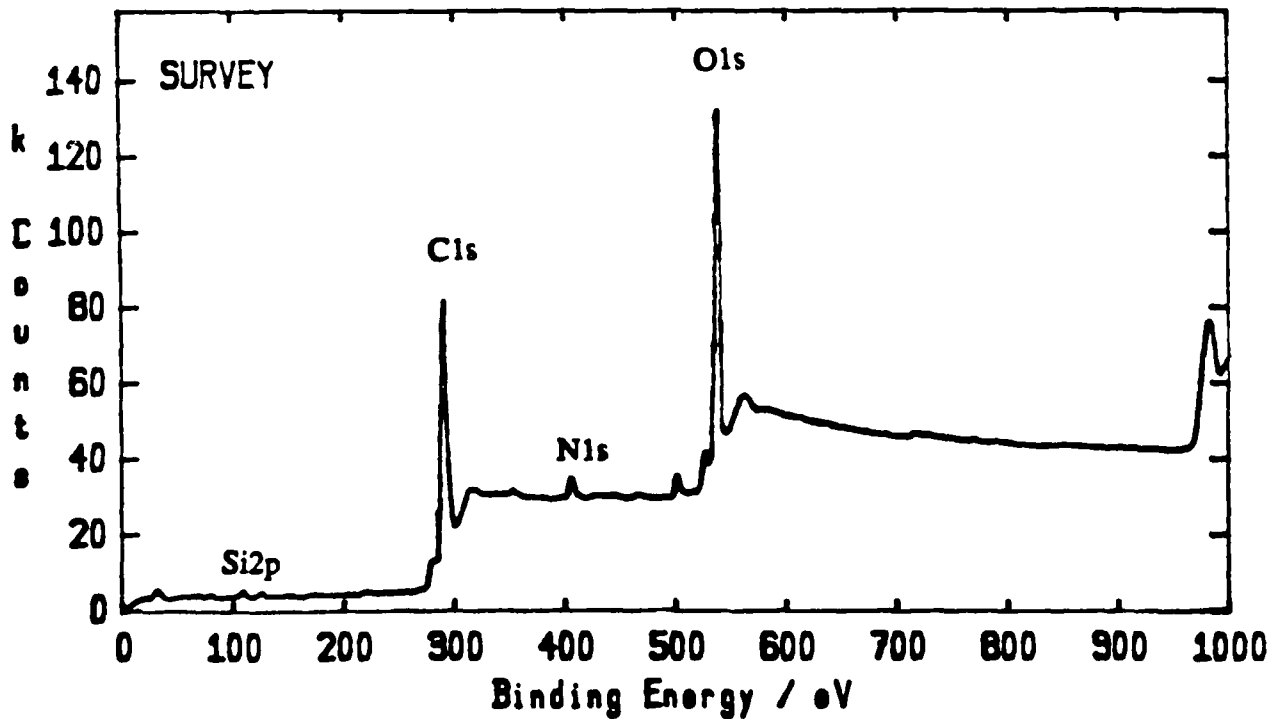
(b)

Fig. 3.24. Wide scans of U/C-PEEK composite subjected to corona pretreatment energy of (a) 0.5 J/mm^2 and (b) 20J/mm^2.

(ii) Narrow Scans

The individual elements present on the surfaces of the TPFC materials were analysed and Figures 3.25 and 3.26 show the effects of corona pretreatment on the carbon and oxygen elements of the U/C-PEEK composite. From these figures several features emerge. Firstly, the intensity of the carbon peak increases and the area under the high binding energy shoulder of the carbon peak increases, see Figure 3.25. This suggests that species such as ether (C-O) and ketone (C=O) have increased, as will be demonstrated in Chapter Six where the individual peaks have been deconvoluted. Therefore, corona treatment leads to an increase of the oxygenated carbon species. Secondly, as shown in Figure 3.26, the intensity of the oxygen peak increases as the level of treatment is increased. Therefore, this is positive evidence that corona treatment is truly an oxidising technique.
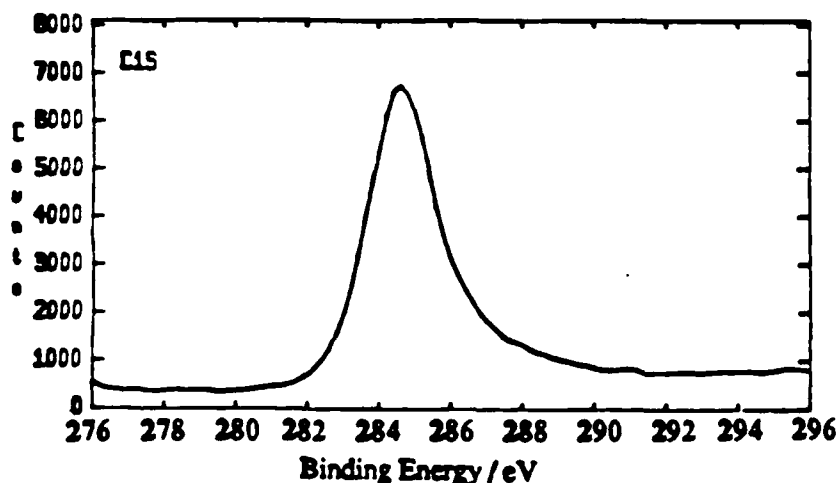
(a)
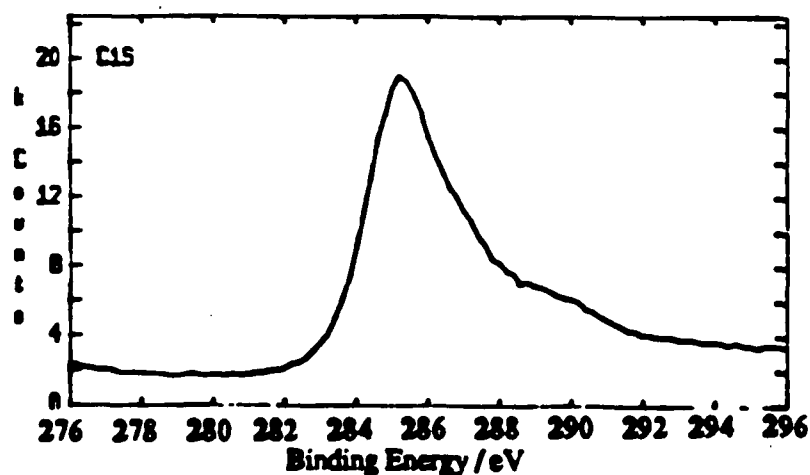
(b)

Fig. 3.25. Narrow scans of the carbon element of the U/C-PEEK composite subjected to corona treatment; (a) $0.5J/mm^2$ and (b) $20J/mm^2$.
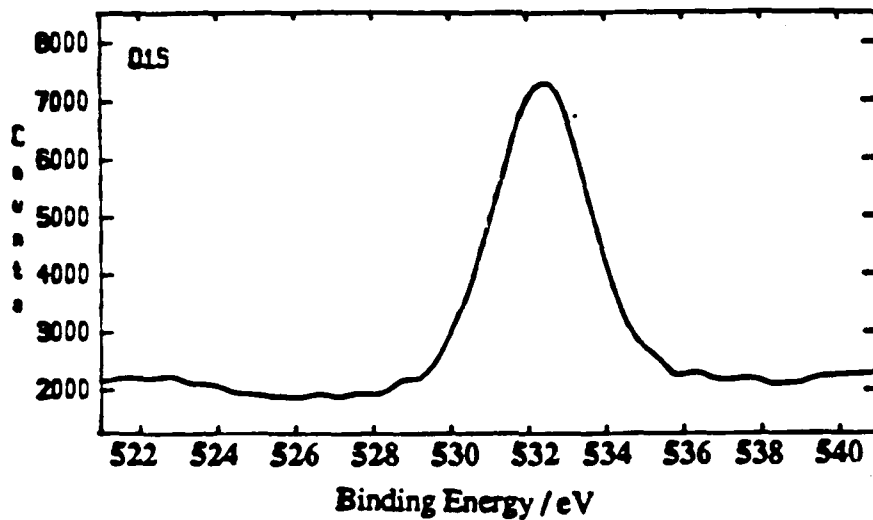
(a)
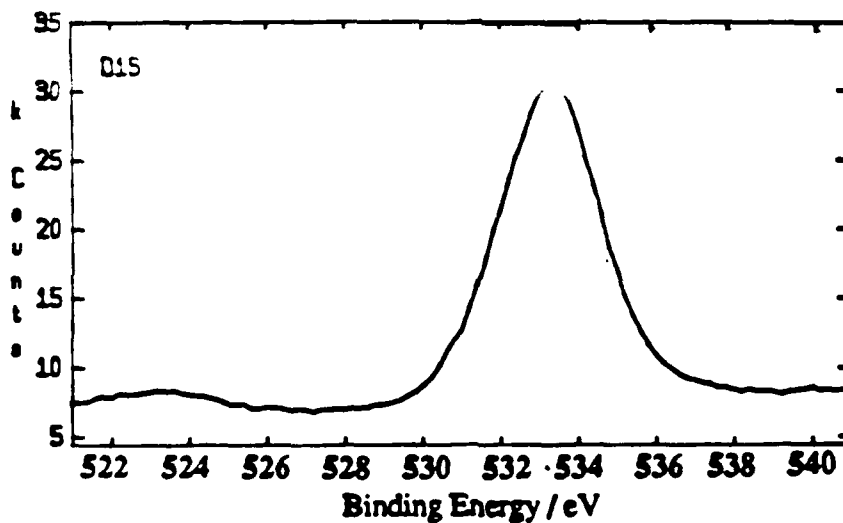
(b)

Fig. 3.26. Narrow scans of the oxygen element of the U/C-PEEK composite subjected to corona treatment; (a) $0.5J/mm^2$ and (b) $20J/mm^2$.

(iii) Quantification of the Elements

To understand fully the surface chemical modifications accompanying the corotreatment a detailed quantitative analysis of all the important elements will be presented. The important elements are carbon (C1s), oxygen (O1s), nitrogen (N1s) and silicon (Si2p). For the U/C-PPS composite the sulphur (S2p) concentration will also be considered. It should be noted that the silicon element mentioned above, if present, will include the element fluorine (F1s) since the concentrations of these elements are very low. The detailed quantitative results from several TPFC materials are shown in Figures 3.27 to 3.36, results from other TPFC materials follow similar patterns to the results presented here and are given in Appendix A.2.

Several noteworthy features emerge from the data shown in Figures 3.27 to 3.36.

Firstly, the concentration of the element carbon decreases as the corona treatment level is increased, see Figures 3.27 and 3.28. This drop in the concentration of the carbon element has to be relative because (i) as discussed above the carbon peak intensity increases and (ii) the carbon peak gets wider especially in its high energy binding shoulder suggesting in effect an increase in the absolute value of the carbon element. However, this increased area under the carbon peak does not lead to a relative increase in the concentration of the carbon element with respect to the increase of oxygen and therefore a drop is recorded.

Secondly, the concentration of the oxygen peak increases as the treatment level is increased, see Figures 3.27 and 3.28. This increase arises from the dramatic increase in the intensity of the oxygen peak. The increased intensity in the oxygen element can be understood if it is considered that corona treatment generates an air plasma. Further, Figures 3.29 and 3.30 show that as the level of treatment is increased then the ratio of the oxygen to carbon element increases. This rate of increase decreases as the corona treatment level is increased. Indicating that the surfaces of the fibre-composites reach saturation level where it becomes more difficult to further increase the oxygen element.

Thirdly, the level of the nitrogen peak increases as the level of treatment is increased, see Figures 3.31, 3.32 and 3.33. To understand the dramatic increase in the level of the nitrogen element the narrow scans of the nitrogen peak were analysed, see Figure 3.37. It is apparent from this figure that the increase cannot be due to increased level of oxygenated nitrogen species since, if nitrogen was bonded to oxygen then the nitrogen peak should have had a broader high energy binding shoulder, see Table 3.11 (page 72). Therefore, if this increase is not due to oxygen, then the most other likely mechanism for this increase should be due to nitrogen from the atmosphere combining with the element carbon. In fact, the binding energy in Figure 3.37(b) suggests that nitrogen has indeed combined with carbon.

Fourthly, the concentration of the silicon element drops, see Figures 3.31, 3.32 and 3.33. This can be understood if one considers the following arguments. Firstly, the surface is being constantly etched by the electrical sparks which ablate the material embedding the carbon-fibres. It should be noted that the results from the other TPFC materials follow similar patterns to that of the U/C-PA composite, Figure 3.32. Secondly, due to the dramatic increase of the oxygen element then a drop in the silicon value may be recorded. The results in Figures 3.34 and 3.35 show that the silicon/carbon ratios for carbon-fibre composites drops initially and then reaches a minimum constant value. Further, the silicon/carbon ratio, see Figure 3.36, remains constant in value for the U/K-PA composite indicating that the surface does not get

ablated. These results indicate that corona treatment may ablate some of the material embedding the carbon-fibres resulting in lower concentrations of releasing agents being recorded.

Further, for the U/C-PA composite, see Figure 3.35, even at relatively low corona treatment levels the silicon to carbon ratio drops to undetectable levels. However, for the U/C-PEEK composite even at levels of $20J/mm^2$ releasing agents can still be detected, see Figure 3.34. This can be understood if one considers the initial levels of contamination, see Table 3.13 (page 76). The U/C-PEEK composite possesses the highest contamination level. Therefore, the above observations show that the drop in the recorded silicon levels depends on the type of fibres, initial contamination level and duration of treatment.

Fifthly, the concentration of sulphur for the U/C-PPS composite drops, see Figure 3.33. This drop can only be relative since Figure 3.38(b) shows that the sulphur peak has now combined with oxygen giving two peaks instead of one as from the untreated specimen, see Figure 3.38(a).
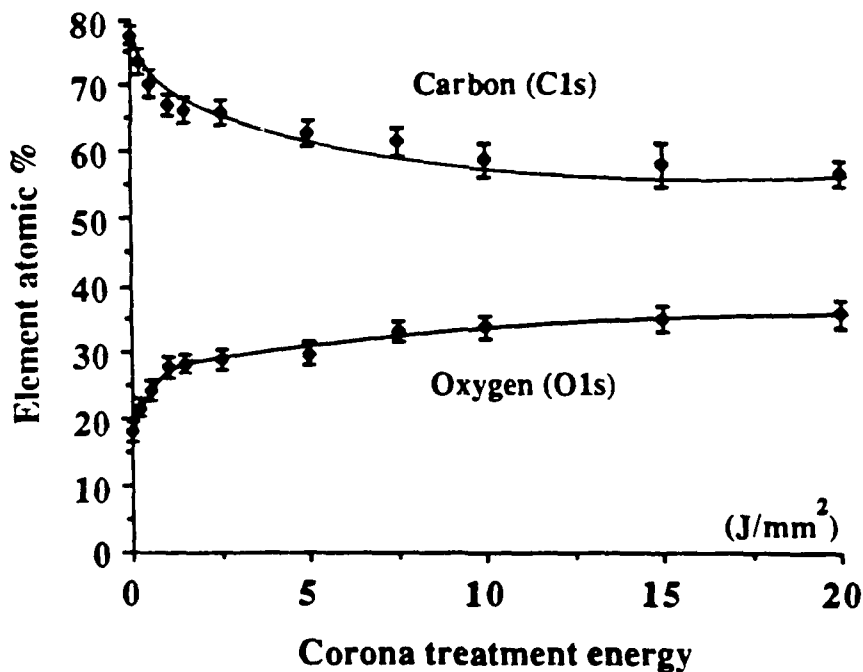
Fig. 3.27. Concentrations of the carbon and oxygen
elements for the U/C-PEEK composite.
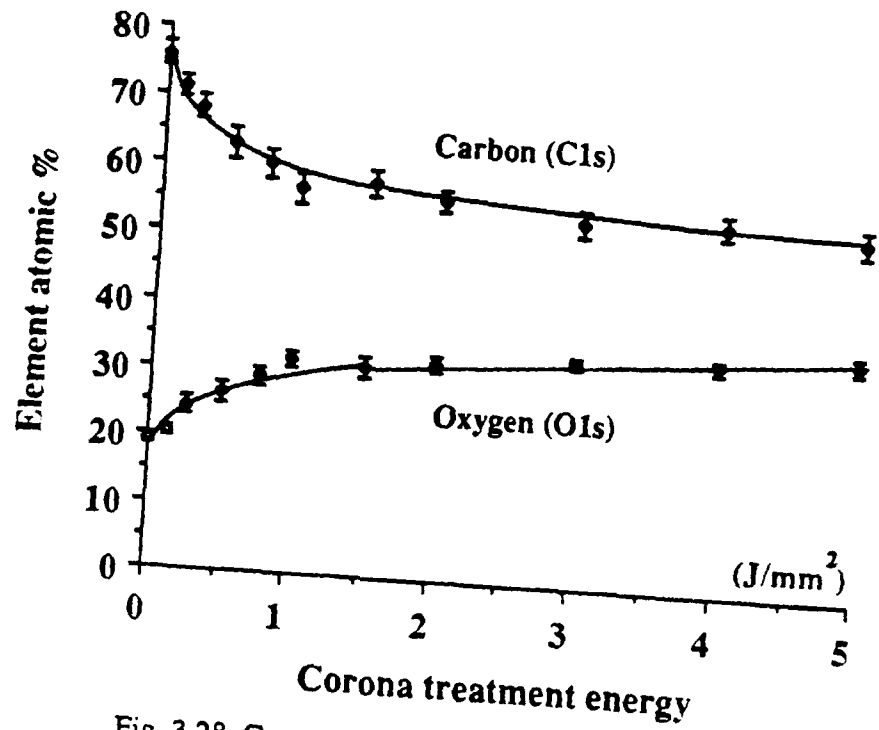
Fig. 3.28. Concentration of the carbon and oxygen
elements for the U/C-PA composite.
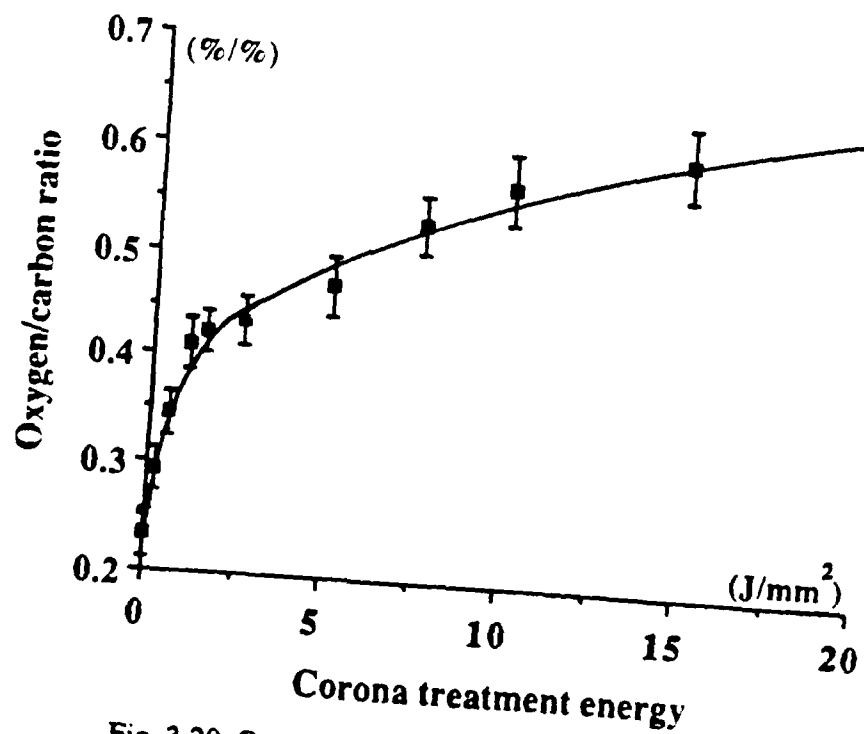
Fig. 3.29. Oxygen over carbon ratio of U/C-PEEK
composite subjected to corona treatment.
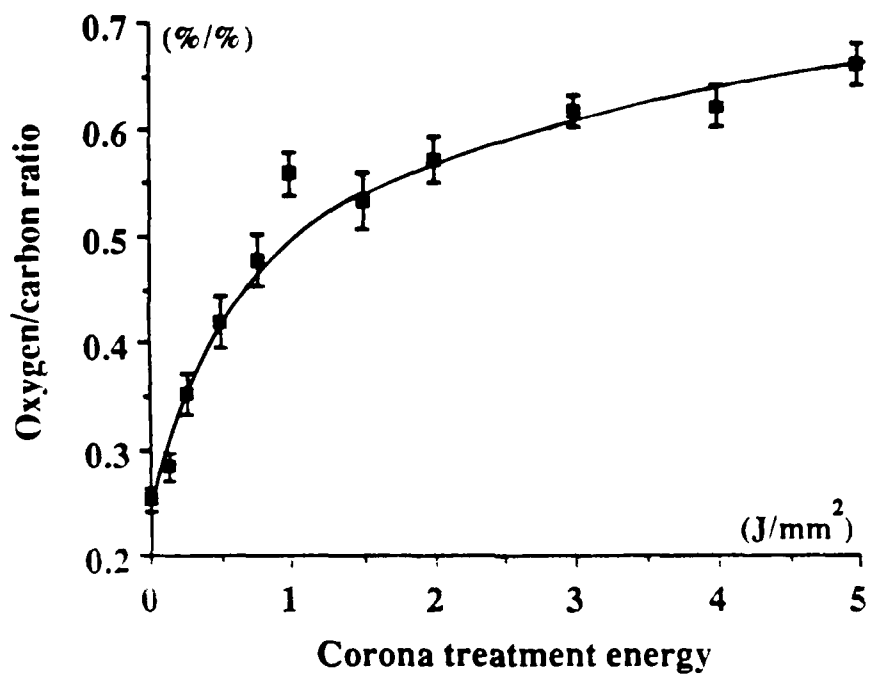
Fig. 3.30. Oxygen over carbon ratio of U/C-PA
composite subjected to corona treatment.
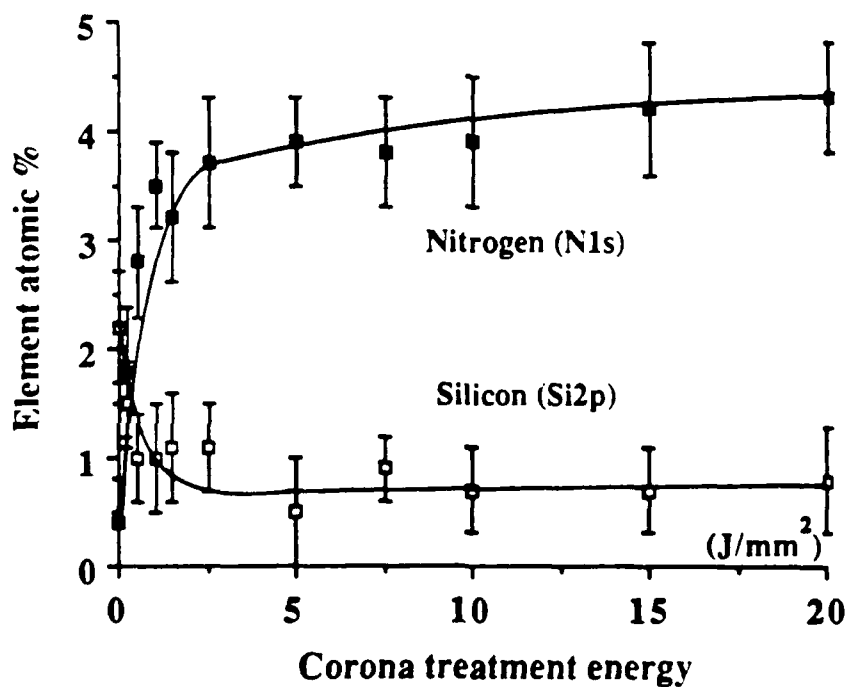
Fig. 3.31. Concentration of the nitrogen and silicon elements for the
U/C-PEEK composite subjected to corona treatment.
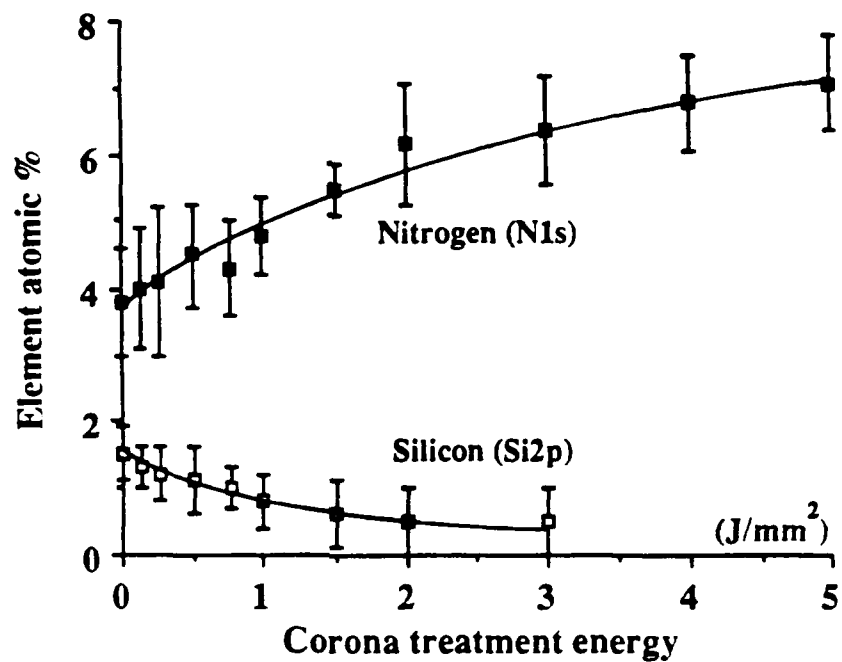
Fig. 3.32. Concentrations of the nitrogen and silicon elements for the
U/C-PA composite subjected to corona treatment.
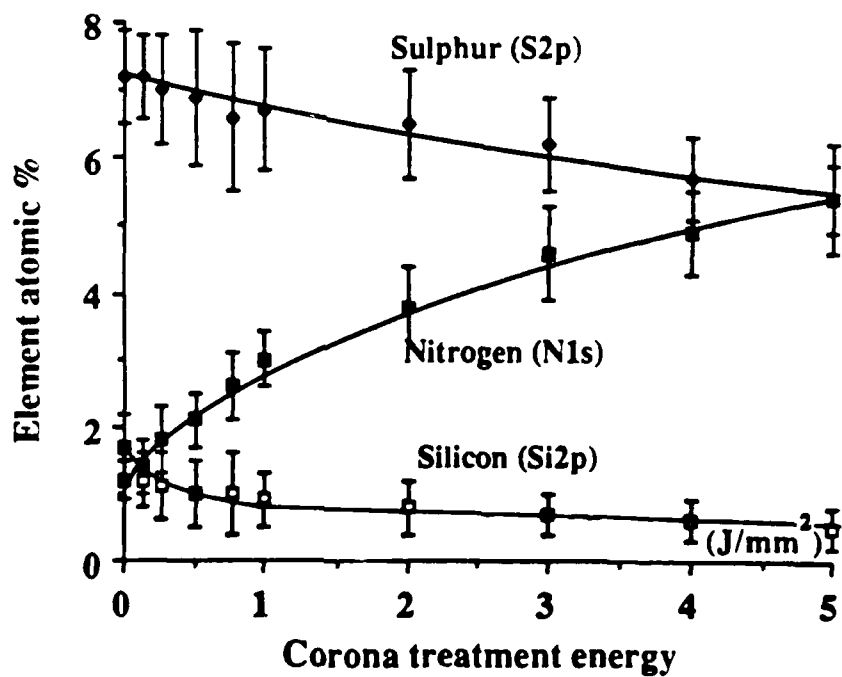
Fig. 3.33. Concentrations of the sulphur, nitrogen and silicon elements for the
U/C-PPS composite subjected to corona treatment.
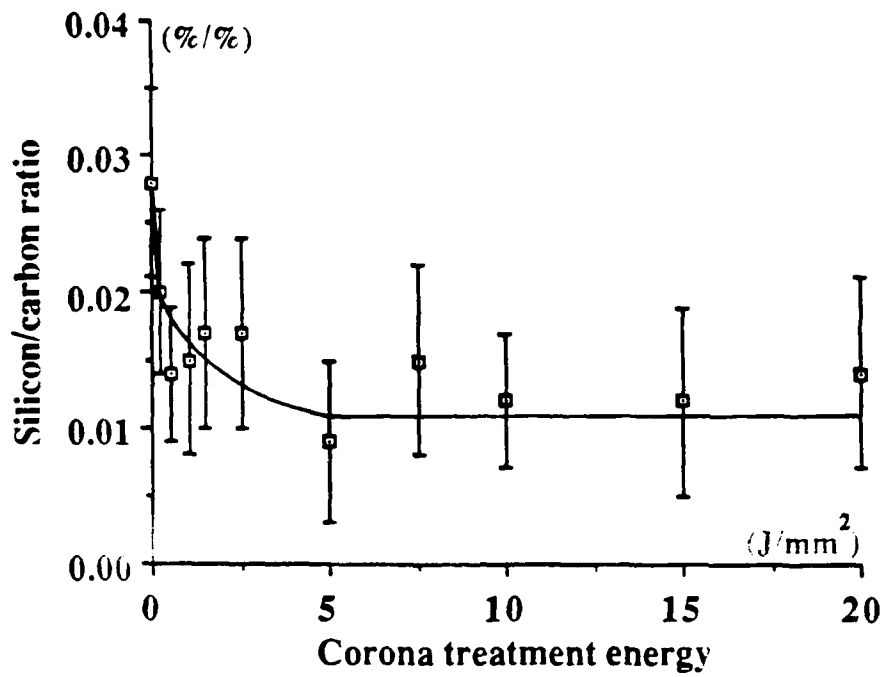
Fig. 3.34. Silicon/carbon ratio versus corona treatment of U/C-PEEK composite.
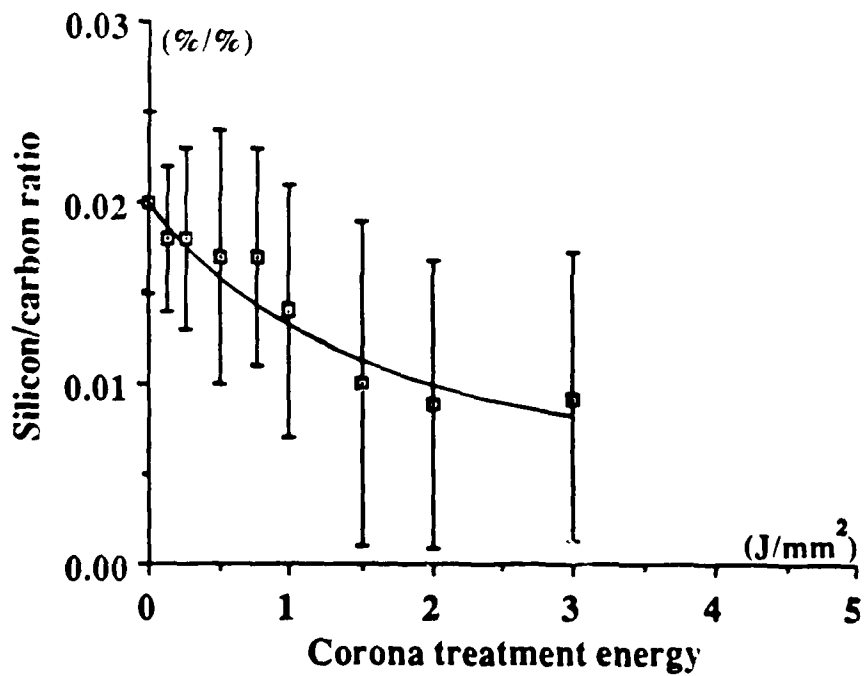
Fig. 3.35. Silicon/carbon ratio versus corona treatment of U/C-PA composite.
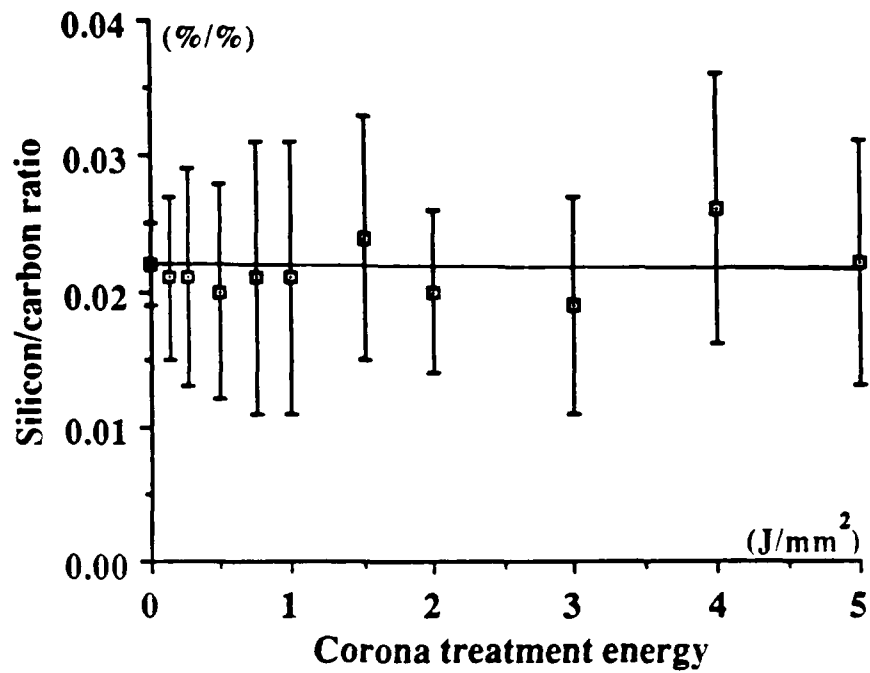
Fig. 3.36. Silicon/carbon ratio versus corona treatment of U/K-PA composite.

(a)   (b)
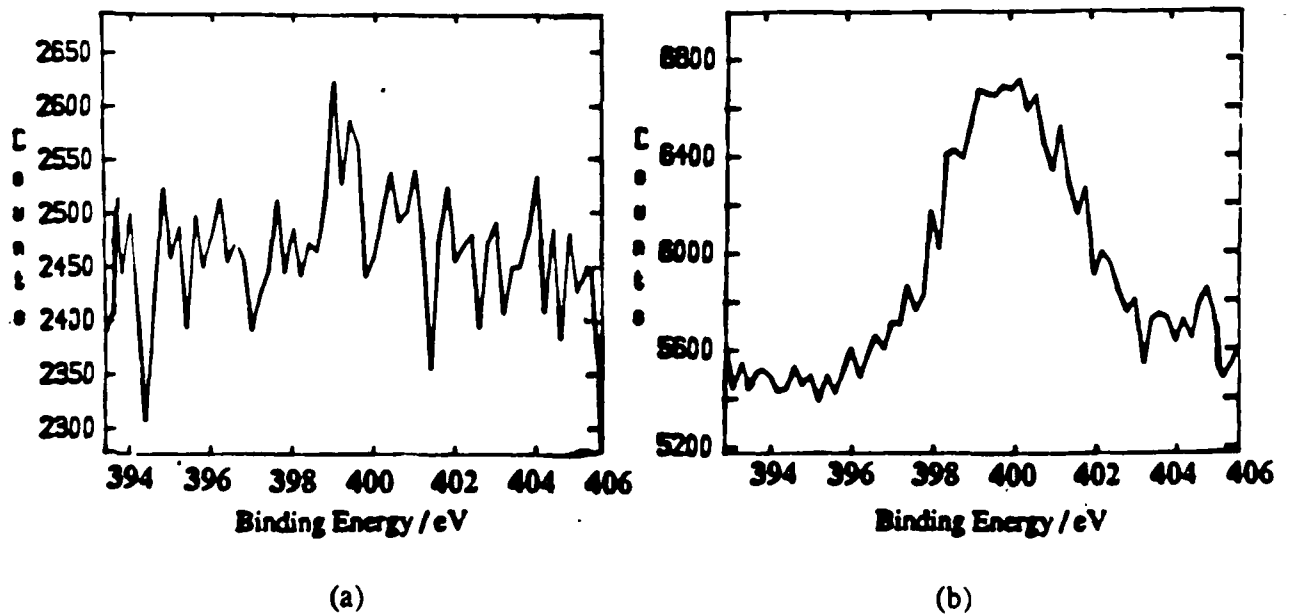
Fig. ...37. XPS spectra of the nitrogen peak of U/C-PEEK composite subjected to: (a) abrasion/solvent-wipe pretreatment and (b) corona pretreatment at $20J/mm^2$.
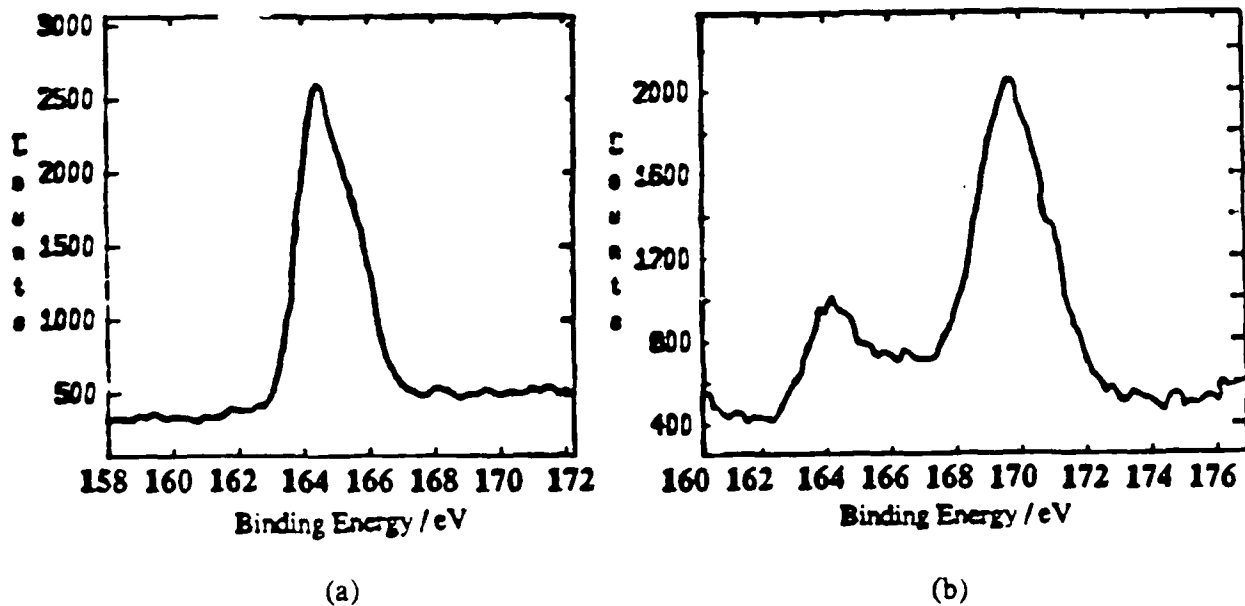
Fig. 3.38. XPS spectra of the sulphur peak of the U/C-PPS composite subjected to:
(a) abrasion/solvent-wipe pretreatment and (b) corona pretreatment at $5J/mm^2$.

3.4.4.5. Depth Profiling Analysis of TPFC Materials Subjected to Corona-Discharge Treatment

Fakes et al. [50] have shown that for a oxygen-plasma treated contact lens alkyl-acrylate/polysiloxane co-polymer the concentration of oxygen-rich species increased with increased treatment time. They used different sources of radiation to estimate the depth of the modified zone and showed that the concentrations of the oxygenated carbon species decreased as the depth of analysis was increased and that the depth of the modified zone was about 20nm. Further, Watts [51] has shown that the high binding energy shoulder of the carbon peak is indeed very sensitive to depth profiling.

The XPS results reported so far were for a take-off angle of 45^0. In this section the effects from different take-off angles will be considered. The inelastic mean free path (IMFP),

λ, for C1s will be considered to be 23Å [52]. The take-off angles considered were 15^0, 30^0, 45^0, 60^0, 90^0 giving analysis depths approximately 18Å, 35Å, 49Å, 60Å and 69Å respectively for the carbon, C1s, element calculated via Equation (3.20) (page 71).

The results from such experiments showed no significant relative change in the concentrations of the elements from the results shown in the previous section. Furthermore, the angular variation on the carbon element showed no significant change in the profile of the high

energy binding shoulder of the corona-treated carbon peak, see for example Figure 3.39. These results show that the surfaces are uniformly oxidised in at least the first 7nm. This observation suggests that corona treatment may have affected a far deeper section of the surfaces under consideration.
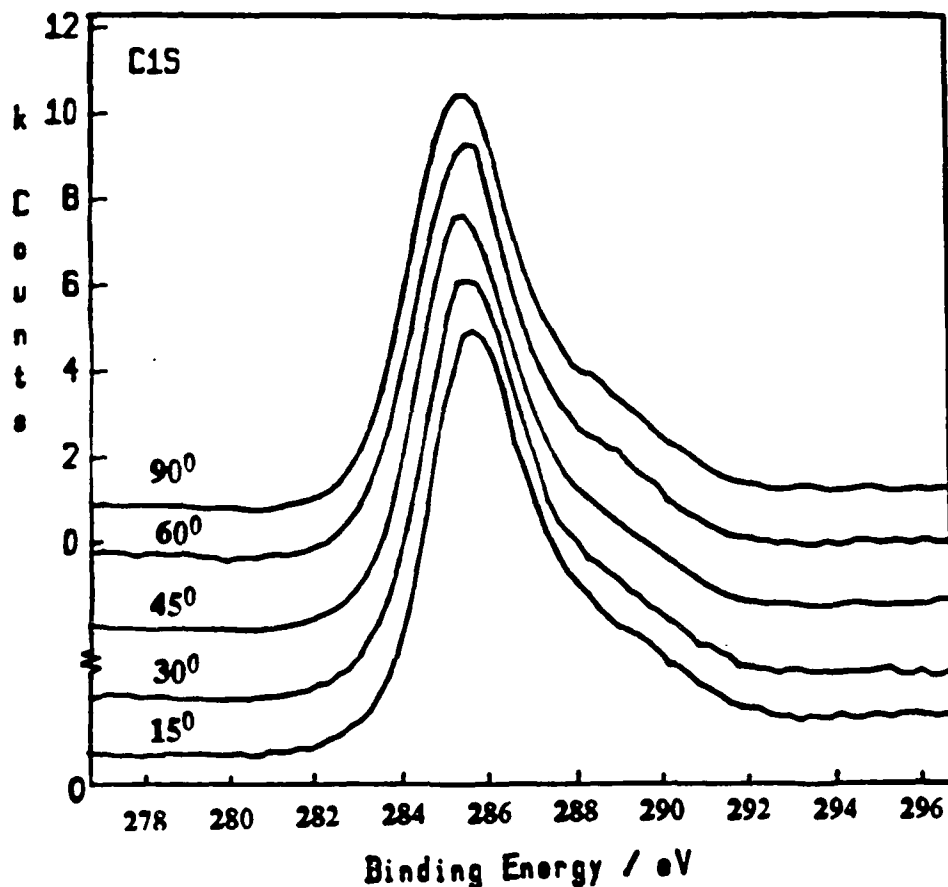
Fig. 3.39. Depth profiling of the U/C-PA composite subjected to corona treatment level of $5J/mm^2$; take-off angles are: 15^0, 30^0, 45^0, 60^0 and 90^0.

3.4.4.6. Analysis of Aged Corona-Pretreated TPFC Materials

U/C-PEEK and PA thermoplastic composites were subjected to corona pretreatment and allowed to age under a controlled laboratory condition ($T=20\pm2^0C$ and R.H.=60%). The results from such experiments are shown in Figures 3.40 to 3.45, several features emerge from these figures.

Firstly, for both materials, the concentration of the carbon element increases to a plateau value and at the same time the level of oxygen element decreases to a minimum constant level, see Figures 3.40 and 3.41. To understand these observations certain analyses and comparisons had to be made:

(a) The analysis of the carbon peak revealed that the intensity remained the same but the profile of the high energy binding shoulder showed some change (decreased) with ageing time, see Figure 3.46. This observation suggests that some of the oxygen-rich carbon species are unstable.

(b) Depth profiling showed no difference in the carbon peak and its profile remained the same, see for example Figure 3.47, indicating that the surfaces remain uniformly oxidised.

(c) The intensity of the oxygen peak decreased as the ageing time increased and indeed the oxygen to carbon ratio shows a dramatic drop, see Figure 3.42. Therefore, it can be argued that freshly prepared TPFC materials attain certain oxygenated species which are not stable and dissolve back to the atmosphere. However, it can be argued that the surfaces of the thermoplastic composites are now covered with hydrocarbons from the atmosphere and this accounts to the relative increase in the carbon element. But the latter argument is unlikely since the intensity of carbon element remained constant and results from angular profiling did not show any apparent change. Finally, it is important to remember that the polar surface energy component also decreased to a minimum value as the ageing time was increased. Such a decrease in the value of the polar energy and the oxygen-rich species may lead to somewhat weaker joints as will be discussed in Chapter Four.

Secondly, the concentration of nitrogen and silicon elements show very modest gains for longer ageing times, see Figures 3.43 and 3.44. These observations can be understood by the above arguments. That is, the nitrogen and silicon elements do not increase in absolute terms but owing to the relative decrease of the oxygen peak the relative concentrations of these elements now show an increase. Further, Figure 3.45 shows that indeed the silicon/carbon ratio remains constant confirming the above conclusion.
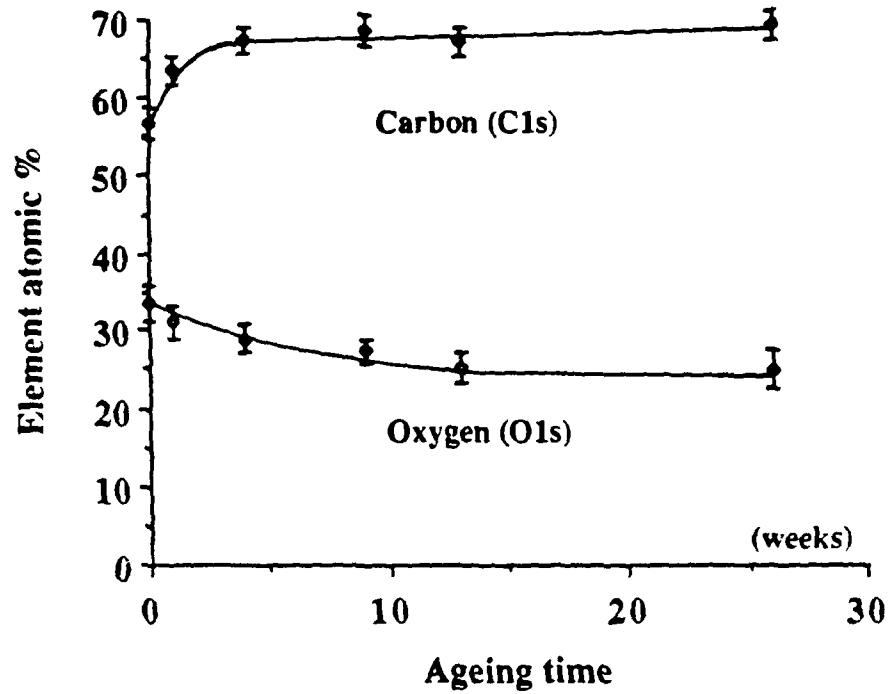
Fig. 3.40. Concentrations of the oxygen and carbon elements of aged corona-pretreated U/C-PEEK composite.
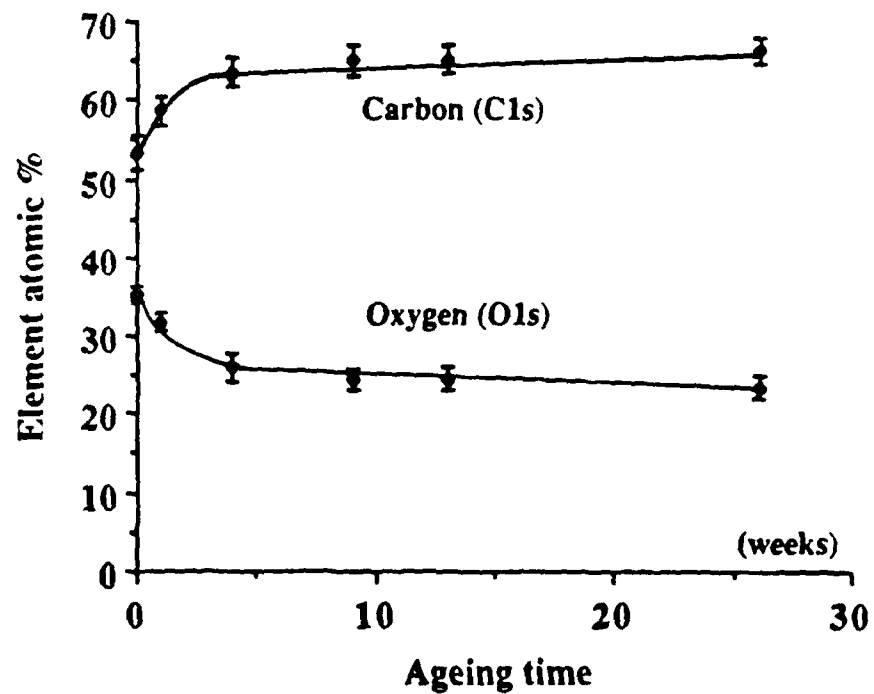
Fig. 3.41. Concentrations of the carbon and oxygen elements of aged corona-pretreated U/C-PA composite.
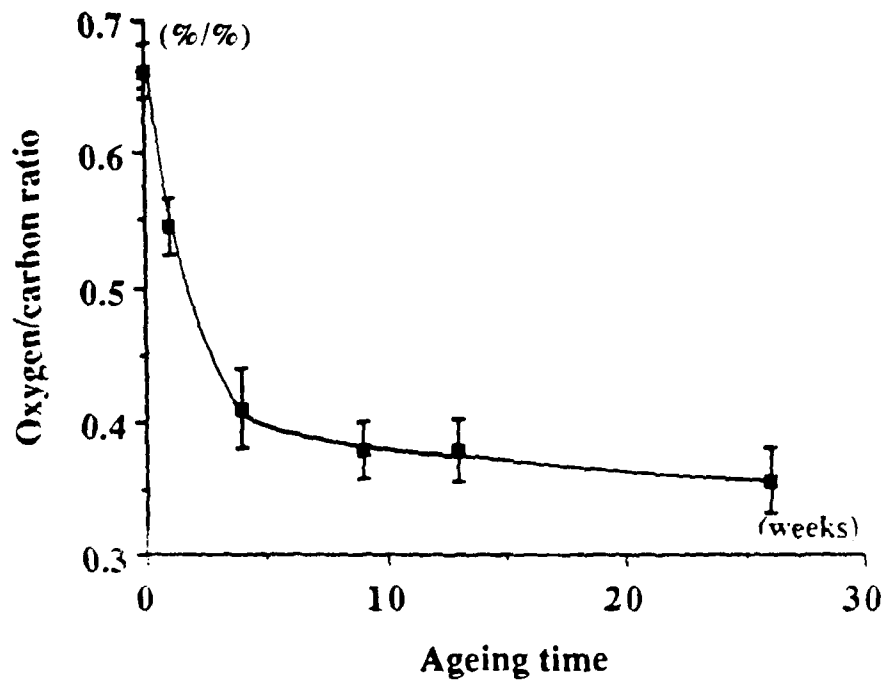
Fig. 3.42. Oxygen to carbon ratio versus ageing time
for corona-pretreated U/C-PA composite.
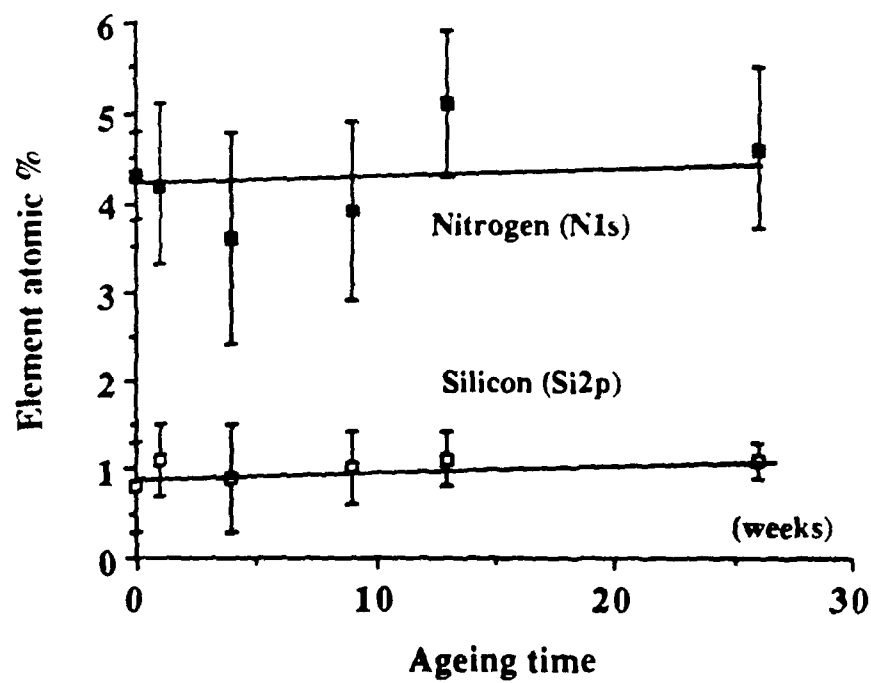
Fig. 3.43. Concentrations of the nitrogen and silicon elements of aged
corona-pretreated U/C-PEEK composite.
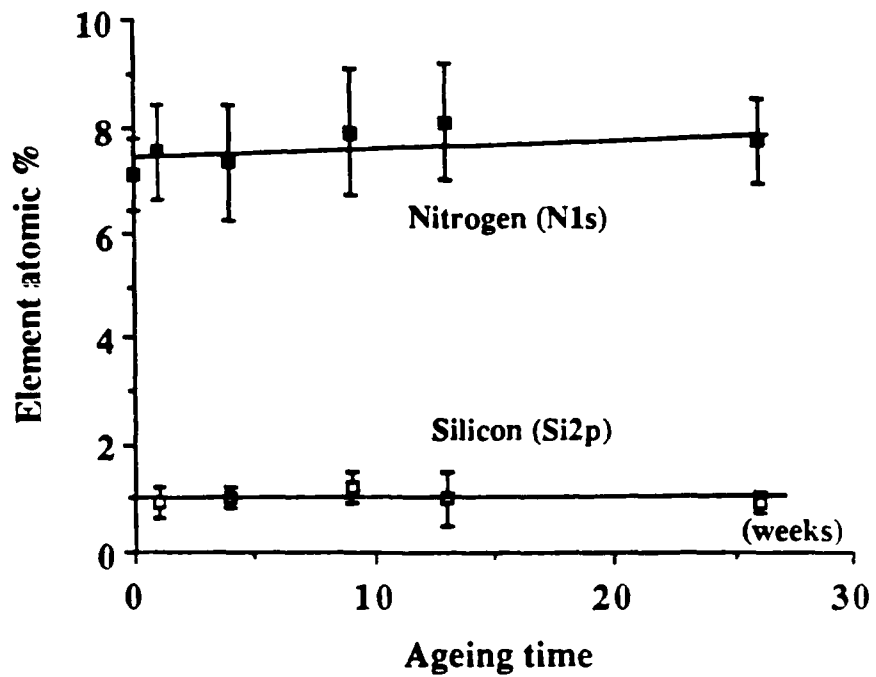
Fig. 3.44. Concentrations of the nitrogen and silicon elements of aged
corona-pretreated U/C-PA composite.
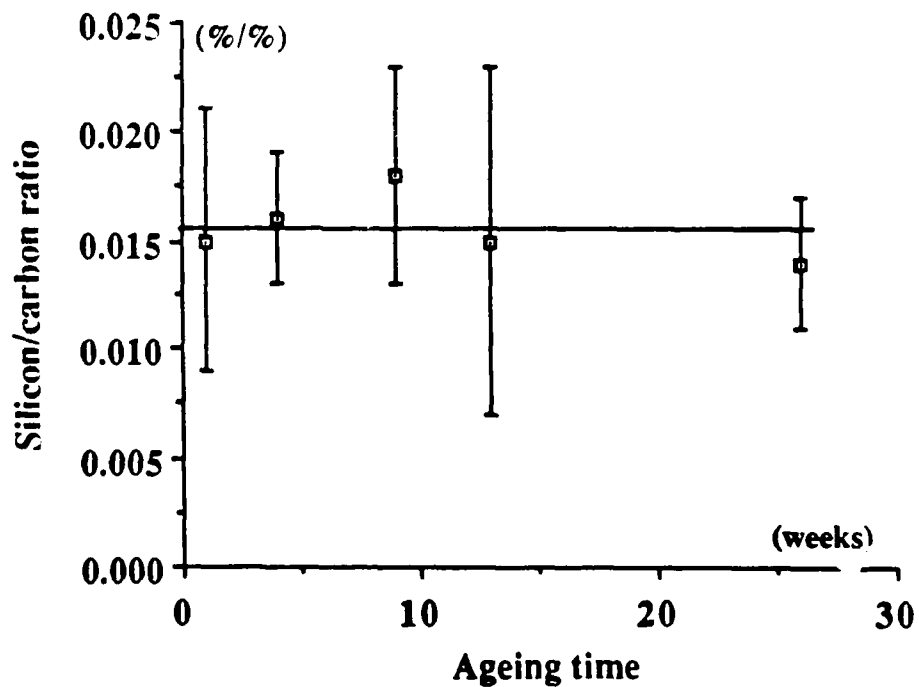
Fig. 3.45. Silicon to carbon ratio of aged
corona-pretreated U/C-PA composite.
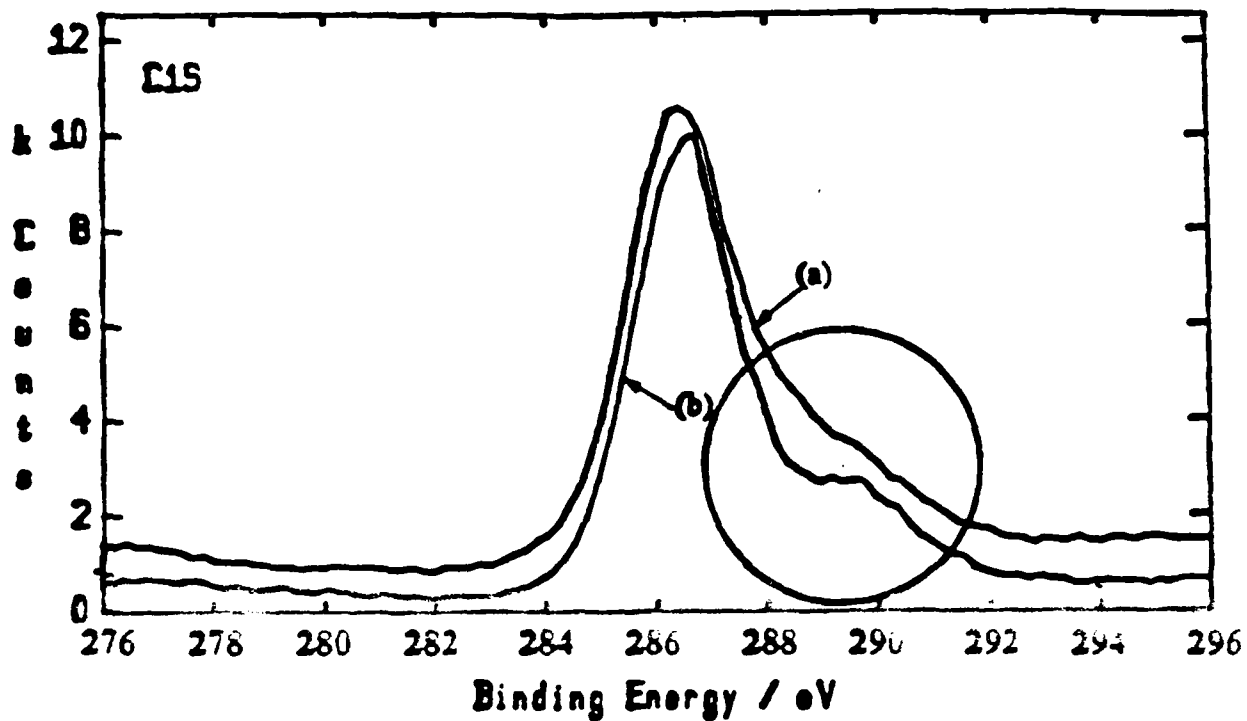
Fig. 3.46. Carbon peak of the U/C-PA composite (a) for freshly treated and (b) aged
for six months. Curves (a) and (b) differ in the high energy binding shoulder.
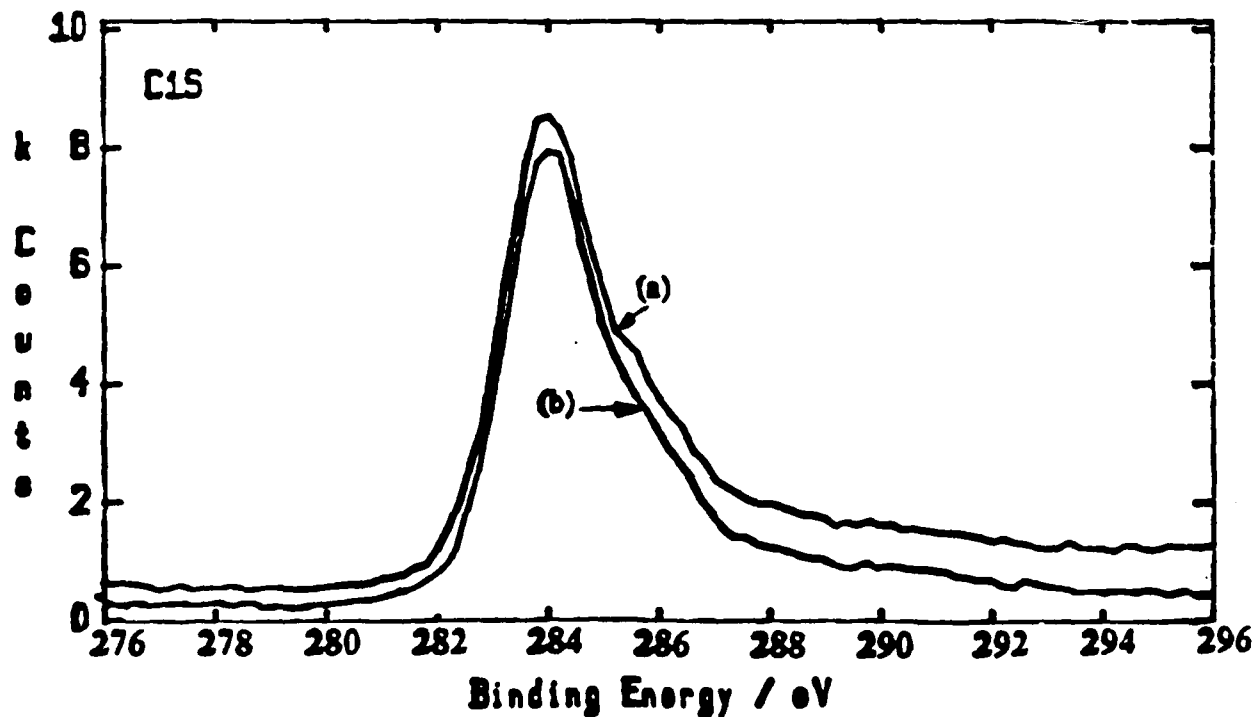
Fig. 3.47. Carbon peak of aged U/C-PEEK composite from take-off
angles of (a) 15^0 and (b) 90^0. Curves (a) and (b) very similar.

3.4.5. Conclusions

The conclusions from the XPS analyses are:

1. Untreated fibre-composites have relatively high concentration of releasing agents and this is due to releasing agents being transferred from the mould onto the surfaces of the laminates during the moulding operation.

2. It was demonstrated how effectively abrasion/solvent-wipe pretreatment reduces the concentrations of these releasing agents. The aluminium/etch pretreatment technique leaves a releasing-free surface whereas the acid-etch technique increases the relative concentration of the oxygen peak due to oxidising the surfaces of the laminates.

3. It was demonstrated that the corona treatment leads to changes in the chemical nature of the surfaces of the TPFC materials. These changes were due to increasing the concentration of the oxygen peak which led to a relative decrease of the concentration of the carbon peak. However, it was demonstrated that the carbon peak exhibits oxygen-rich species in its high energy binding shoulder. Furthermore, it was demonstrated that the nitrogen peak increases but this increase is not due to nitrogen-oxygen species being formed but nitrogen from the atmosphere combining with the element carbon in the materials employed.

4. Corona treatment leads to a decrease in the concentrations of releasing agents. It was shown that this drop is due to constantly ablating the surfaces of carbon-fibre composites and that for composites reinforced with "Kevlar" fibres the concentrations from releasing agents remained constant in value.

5. Depth profiling was successfully employed to demonstrate surface chemical changes accompanying corona treatment. It was demonstrated that the carbon peak does not alter as the take-off angle is varied which led to the conclusion that the surface modifications are uniform through at least the first 7nm of the surfaces examined.

6. Ageing of the corona-pretreated TPFC materials revealed that the concentration of carbon peak increases and that of the oxygen peak decreases. The relative decline in the oxygen peak leads to a modest increase in the concentration of the releasing agents. Some increase in the nitrogen concentration was also recorded. Finally, it was demonstrated that the oxygen-rich carbon species are not stable since there is a difference in the high binding energy shoulder of the carbon element.

3.5. SUMMARY

In this chapter surface characterisation of the fibre-composites employed was undertaken. It was shown that all types of pretreatment techniques lead to an increased surface roughness. This was demonstrated via a quantitative technique using CAA and a qualitative technique using SEM analyses. It was demonstrated that to obtain reliable results from CAA the contact angles not only had to be corrected, for the surface roughness, but also an improved mathematical approach had to be adopted to minimize the error in such calculations.

The above techniques were employed to calculate the components of the surface free energy. It was shown that the abraded surfaces of the thermosetting composite have a relatively high surface free energy due to a high value of the polar component when compared to the TPFC materials employed. However, when corona treatment is employed then the polar component of the surface of the TPFC materials increases dramatically and surpasses that of the thermosetting composite. In contrast, the dispersion component, for the TPFC materials, remains constant in value independent of the treatment level.

Finally, XPS was successfully employed to characterise the surfaces of the fibre-composites. It was demonstrated that the abrasion/solvent-wipe pretreatment leads to a substantial reduction of the releasing agents. Analysis of specimens from aluminium/etch pretreatment revealed that the surfaces were free of elements from releasing agents. The acid-etch and corona treatment techniques lead to a reduction of the relative concentrations of the releasing agents and lead to an increase in the concentrations of the oxygen and nitrogen peaks. It was successfully demonstrated that the modified surfaces are uniform through the first 7nm and that the oxygenated carbon species decrease as the ageing time is increased.

CHAPTER FOUR

MECHANICS OF FRACTURE

4.1. INTRODUCTION

In the present chapter, a fracture mechanics approach will be described in order to evaluate the adhesive fracture energy of the bonded composite joints, where the composite substrates have been subjected to the treatment techniques discussed in the previous chapters. First, the basic principles of fracture mechanics, and their extension to cover adhesive joints and composite materials will be presented, followed by a description of the experimental techniques employed and finally the experimental results will be presented and discussed.

4.2. LITERATURE SURVEY

4.2.1. Introduction

Only sufficient details on the principles of fracture mechanics will be presented in the thesis to enable the reader to follow the ensuing discussions. More detailed reviews may be found in several excellent articles [53-55] and books [56-59]. The basic tenet of fracture mechanics is that the strength of most solids is governed by the presence of flaws. There are various fracture mechanics approaches and all are concerned with analysing mathematically the way in which cracks propagate.

4.2.2. Basic Principles

Two main inter-relatable, conditions for fracture are proposed. Firstly, the energy criterion arising from Griffith's [60] and later Orowan's [61] work which supposes that fracture occurs when sufficient energy is released - from the stress field - by growth of the crack to supply the requirements of fracture surfaces. The energy comes from the stored elastic or potential energy of the loading system and can be calculated for any type of test piece. This approach, therefore provides a measure of the energy required to extend a crack over a unit area, and this is termed the energy release rate, G_{Ic} (in Mode I, which is the tensile-opening mode). Secondly Irwin [53] found that, the stress field around a crack could be uniquely defined by a parameter, named the stress intensity factor, K, and stated that fracture occurs

when the value of K exceeds some critical value, K_{Ic}. It is important to note that the stress intensity factor, K, is a stress field parameter and is independent of the material, whereas K_{Ic}, often referred to as the fracture toughness, is a measure of material property.

4.2.2.1. The Stress-Intensity Factor Approach

Figure 4.1 shows a sharp crack in a uniformly stressed, infinite lamina, and assuming Hookean behaviour and infinitesimal strain, Westergaard [62] has developed certain stress
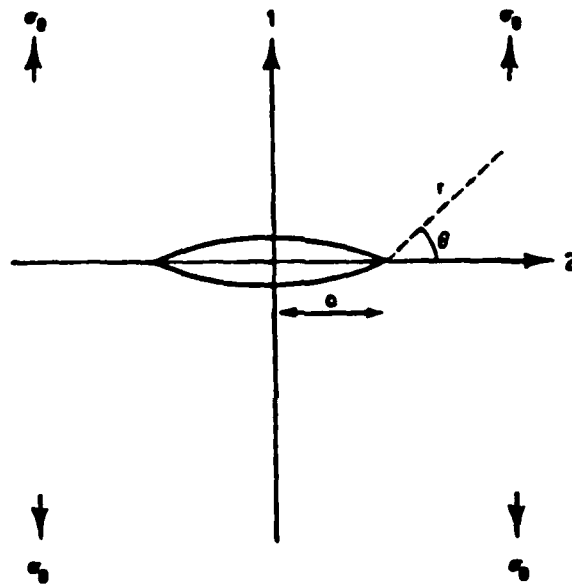
Fig. 4.1. A sharp crack in a uniformly stressed infinite lamina.

function solutions which relate local concentration of the stresses at the crack tip to the applied stress, σ_0. For regions close to the crack tip they take the form:

$$\sigma_{ij} = \sigma_0 \left[\frac{a}{2r} \right] f_{ij}(\theta) \tag{4.1}$$

where σ_{ij} are the components of the stress tensor at a point, r and θ are the polar coordinates of the point, taking the crack tip as the origin, and 2a is the length of the crack. Irwin [53] employed this solution to give:

$$\sigma_{ij} = \left[\frac{K}{\sqrt{2\pi r}} \right] f_{ij}(\theta) \tag{4.2}$$

The parameter K is the "stress intensity factor" and relates the magnitude of the stress-intensity local to the crack in terms of the applied loadings and geometry of the structure in which the crack is located.
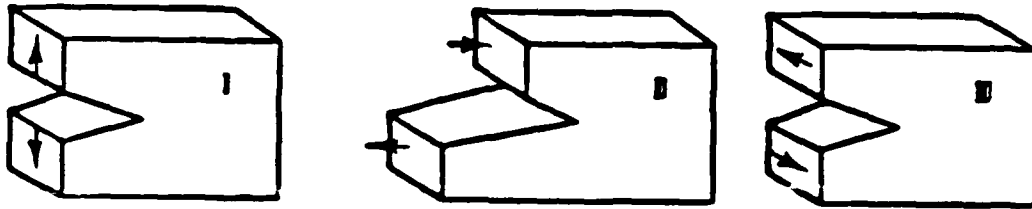
Fig. 4.2. Modes of loading. I, tensile-opening mode; II, in-plane-shear mode; III, antiplane-shear mode.

Now a crack in a solid may be stressed in three different modes, denoted I, II and III as shown in Figure 4.2, and superposition of the three modes constitutes the general case of crack loading. The cleavage or the tensile-opening mode, Mode I, is technically the most important since it is the most commonly encountered and usually the one which most readily results in failure. Since Mode I is the mode employed in this project, the ensuing discussions will be confined to this situation, although analogous arguments may be developed for the other two modes [63]. For Mode I, the crack tip stresses may be developed from Equation (4.2) as:

$$
\begin{bmatrix} \sigma_{11} \\ \\ \sigma_{12} \\ \\ \sigma_{22} \end{bmatrix} = \frac{K_I}{(2\pi r)^{0.5}} \cos\left[\frac{\theta}{2}\right] \begin{bmatrix} 1 + \sin\left[\frac{\theta}{2}\right]\sin\left[\frac{3\theta}{2}\right] \\ \\ \sin\left[\frac{\theta}{2}\right]\cos\left[\frac{3\theta}{2}\right] \\ \\ 1 - \sin\left[\frac{\theta}{2}\right]\sin\left[\frac{3\theta}{2}\right] \end{bmatrix} \tag{4.3}
$$

and $\quad \sigma_{33} = 0 \qquad$ (plane-stress)

$$\tag{4.4}$$

or $\quad \sigma_{33} = \upsilon\,(\sigma_{11} + \sigma_{22}) \qquad$ (plane-strain)

and $\quad \sigma_{23} = \sigma_{13} = 0 \qquad\qquad\qquad\qquad\qquad\qquad$ (4.5)

where υ is Poisson's ratio. From Equation (4.3) it may be seen that as $r \Rightarrow 0$ then the stress σ_{ij} $\Rightarrow \infty$ and hence stress alone does not make a reasonable local fracture criterion. Therefore, since the level of K_I uniquely defines the stress field around the crack, Irwin postulated that the condition:

$$K_I \geq K_{Ic} \qquad (4.6)$$

represented a fracture criterion; where K_{Ic} is a critical value for crack growth in the material and, as such. is a material property and termed the fracture toughness.

4.2.2.2. The Energy Approach

The energy criterion [64] for fracture is simply an extension of Griffith's hypothesis which describes quasi-static crack propagation as the conversion of the work, Z, done by the external force and the elastic energy, U, stored in the bulk of the sample into surface free energy, γ. It may be written:

$$\frac{\partial(Z - U)}{\partial a} \geq \frac{\gamma \partial A}{\partial a} \qquad (4.7)$$

where γ is the surface free energy per unit area, A is the interfacial area of the crack and a is the crack length. If the differentiation is carried out at a constant overall length, l, of the test-piece then for a crack propagation in a lamina of width, B, the criterion becomes:

$$-\left[\frac{\partial U}{\partial a}\right]_l \frac{1}{B} \geq 2\gamma \qquad (4.8)$$

Orowan [61] and Rivlin and Thomas [65] examined this criterion with respect to metals and cross-linked elastomers, respectively, and commented that greater energy is usually required to cause crack growth than the surface free energy. This is because, in most materials inelastic deformation mechanisms are present. Example of such mechanisms include plastic, viscoelastic, etc., energy dissipative processes and are magnified by the relative high strains experienced at, and close to, the crack tip. The above authors assumed that such energy was dissipated in the immediate vicinity of the crack tip in a manner independent of the test

arrangement and the manner in which forces were applied to it. Thus, 2γ may be replaced in Equation (4.8) by the symbol G_{Ic} which encompasses all the energy losses incurred around the crack tip and is the energy required to increase the crack by unit length in a test-piece of unit width, hence:

$$-\left[\frac{\partial U}{\partial a}\right]_1 \frac{1}{B} \geq G_{Ic} \qquad (4.9)$$
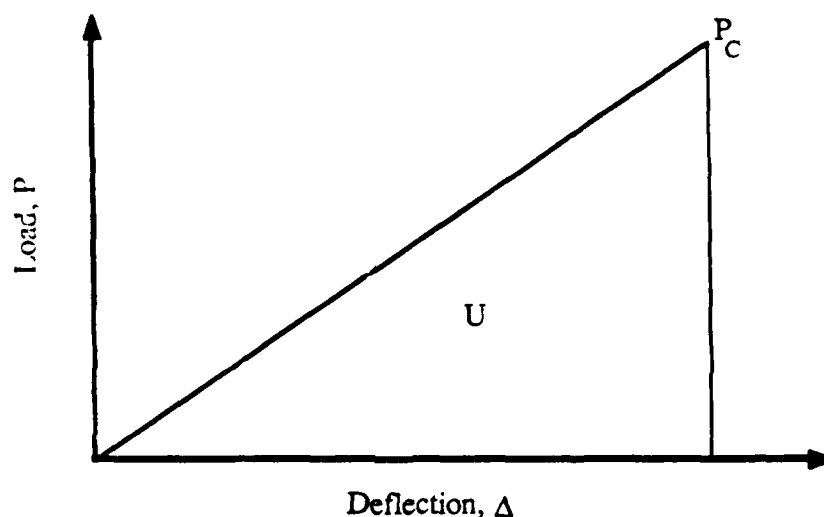
Fig.4.3. Load versus deflection diagram.

For structures exhibiting bulk linear elastic behaviour, in other terms, structures which obey Hooke's Law away from the crack tip, Equation (4.9) becomes:

$$G_{Ic} = \frac{P_c^2}{2B} \frac{\partial S}{\partial a} \qquad (4.10)$$

where P_c is the load required for crack propagation and S is the compliance of the structure and is given by:

$$S = \frac{\Delta}{P} \qquad (4.11)$$

where Δ is the deflection or displacement and P is the load, see Figure 4.3.

4.2.3. Application of Fracture Mechanics to Interlaminar Failure of Fibre-Composites

Several approaches have been developed to apply linear elastic fracture mechanics to interlaminar testing of composites. These approaches being the, load, displacement, energy and compliance calibration [66-68]. Basically, all the equations developed in these approaches are in fact inter-relatable and are extensions of the fundamental equation for G_{Ic} (Equation (4.10)) which is the compliance calibration approach. Further, some of the above mentioned approaches require correction factors, due to large deflections and/or end rotations (see [68, 69]), which may correct the G_{Ic} results by as much as 20% [69]. Here, in the current research work only the compliance calibration technique is employed which does not require any correction factors.

The standard approach [70-75] for Mode I interlaminar testing of composites is using double-cantilever beam (DCB) specimens as shown in Figure 4.4(a). The DCB specimen can be tapered or be of constant width B. An analysis for predicting the behaviour of tapered cantilever beam can be complex. The complexity is due to two main factors. Firstly, the width of the specimen (in the slender region) must be chosen such that plane-strain condition is satisfied; secondly, with the toughened thermoplastic composites large non-linear bending may occur in the slender region which will be a source of error in the analyses. Hence, the constant width specimen was adopted in this research work. Figure 4.4(b) shows a typical load versus deflection diagram with the monitored crack lengths marked on the plot.

The Mode I interlaminar fracture energy release rate of DCB specimens of composite materials have been determined by different forms of compliance calibration [76-79] techniques. The relationship:

$$S = f(a) \tag{4.12}$$

can be generated from experimental data by adopting a suitable curve-fitting procedure, see Figure 4.5. This allows the calculation of the fracture energy release rate G_{Ic} to be calculated via Equation (4.10).
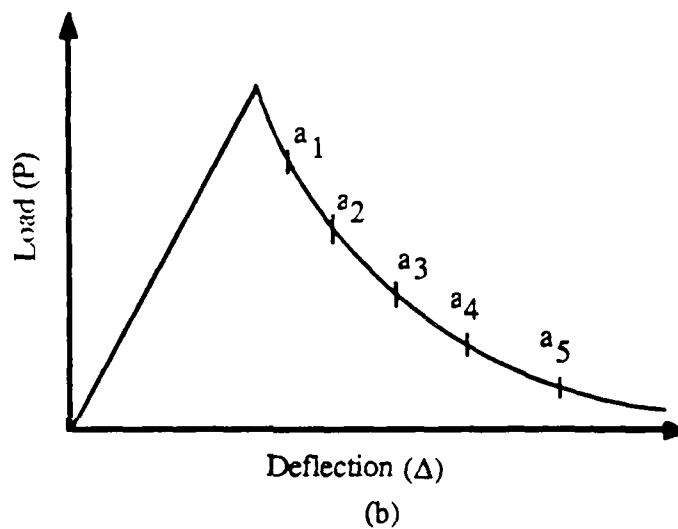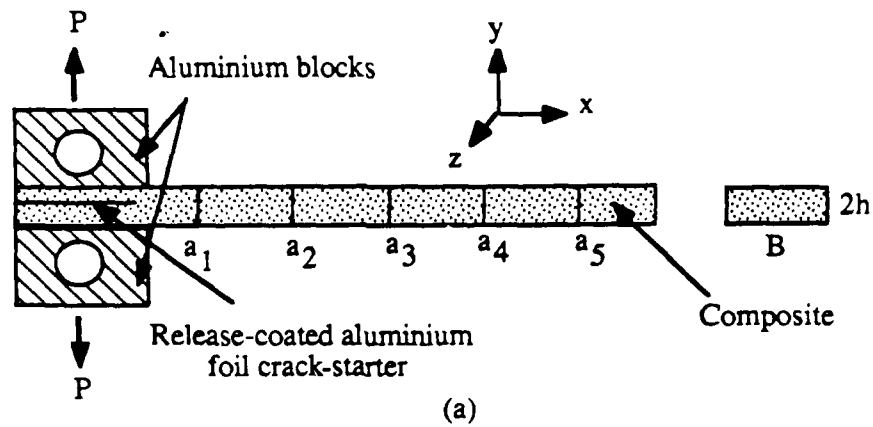
Fig. 4.4. (a) A precracked DCB specimen and (b) typical load deflection diagram (note that the fibres are in the x-z plane and that the unidirectional-fibres are in the x-direction).
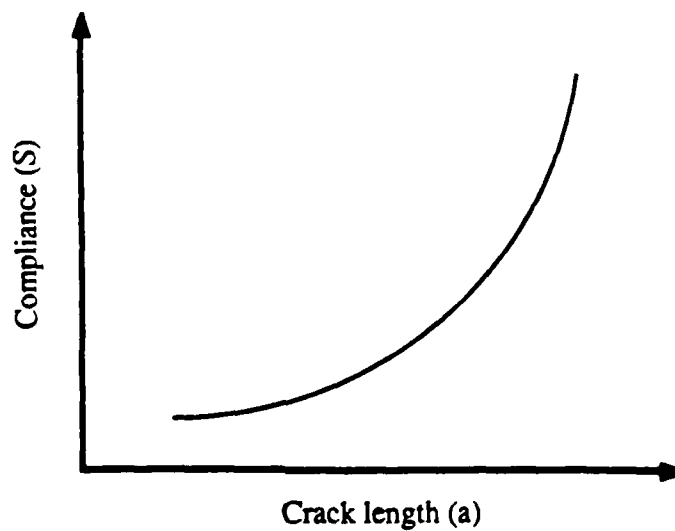
Fig. 4.5. A typical compliance versus crack length curve.

4.2.4. Application of Fracture Mechanics to Adhesive Joints

4.2.4.1. Previous Work and Unresolved Problems

There is very little published work on adhesively bonded composite joints from a fracture mechanics approach. Some of the work [80-84] on adhesively bonded composite joints consists of *ad hoc* tests seeking to demonstrate the better performance of adhesive joints without providing any real engineering data. Further, some of the above mentioned research works may mislead the reader as will be discussed below.

Jemian and Ventrice [80] use Equation (4.10) to calculate the adhesive fracture energy, G_c, from DCB joints and defined the compliance to be of the form:

$$S = A_0 - A_1 a + A_2 a^2 + A_3 a^3 + A_4 a^4$$

therefore: as $a \Rightarrow 0$ then $\partial S / \partial a = A_1$ which cannot be true since $\partial S / \partial a$ should tend to zero as crack length, a, tends to zero. In the current research work, a computer program was developed to curve fit the experimental data to take into account the theoretical requirement that as $a \Rightarrow 0$ then $\partial S / \partial a \Rightarrow 0$, see Appendix A.3 for the listing of the computer program.

Mangalgiri et al. [83] and Mall and Johnson [84] evaluated Mode I and mixed Mode I/II adhesive fracture energy by using symmetrical and unsymmetrical (one arm of the specimen thicker than the other) DCB joint specimens. They argued the presence of 15% of Mode II contibution in the measured fracture energy values for unsymmetrical type specimens. However, their argument is doubtful due to the equal and opposite bending moments being applied to the specimen. Therefore, from bending moment theory it can be argued that the unsymmetrical DCB specimen should yield only Mode I type fracture. This conclusion is important in the current research work since many of the DCB joint specimens failed in an interfacial or interlaminar manner thus yielding unsymmetrical type specimens.

4.2.4.2. Effect of Adhesive and Composite Thickness on G_c

Several workers [85-89] have shown that as the thickness of the adhesive layer is decreased than the measured fracture energy increases initially until it reaches a critical value and then drops, see Figure 4.6. This behaviour is explained by the following reasoning:
The toughness of a material is derived from the energy dissipated in forming the plastic zone, the adhesive fracture energy will steadily decrease as the adhesive layer thickness is reduced

past the critical value, see Figure 4.6. Wang et al. [90], employing finite element analysis (FEA), reported that the constraint imposed on the adhesive layer by rigid substrates may increase the level of the local tensile stresses ahead of the crack tip (when the adhesive layer thickness is around the critical value). They argued that this effect will increase the length of the plastic zone ahead of the crack tip and hence yield higher fracture energy values. Kinloch and Shaw [86] suggested that the critical thickness of the adhesive layer at which the maximum fracture energy can be obtained is double the bulk material's plane-stress plastic zone size. There is experimental evidence in the literature to support their argument. However, they did not explain why the critical adhesive thickness should be equal to the plane-stress plastic zone size. Further, Chai [87, 89] also reported a similar effect on G_c when the adhesive thickness was varied. However, he claimed to have obtained adhesive thicknesses of the order of 2.5μm. Undoubtedly, such claims should be considered cautiously since surface roughness of the substrates can indeed be of that order.
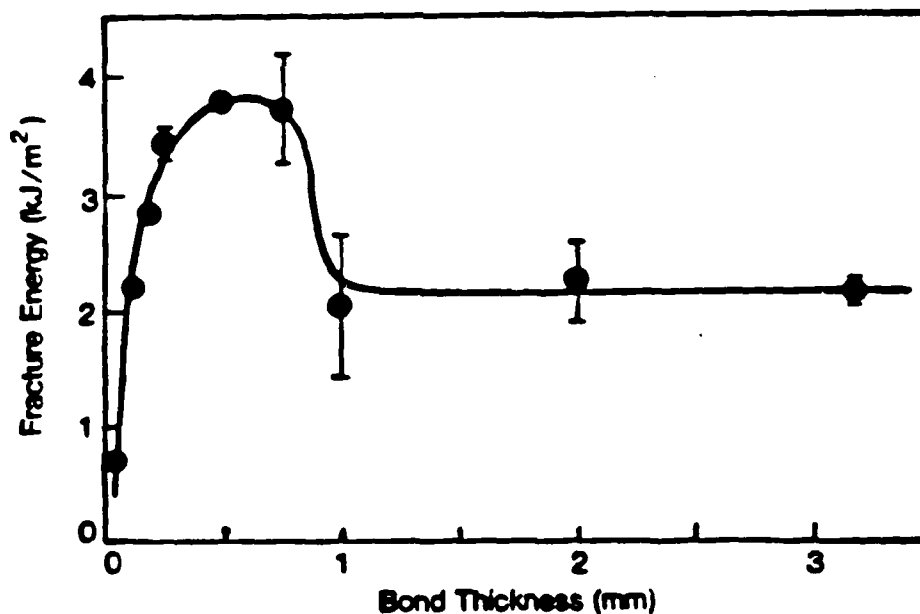
Fig.4.6. Effect of adhesive thickness on the measured fracture
energy of a rubber-toughened epoxy adhesive [86].

Crews et al. [91] used FEA to predict the stresses in front of the crack tip for adhesively bonded composite joints. From analysis of the stresses they constructed a curve similar to the one depicted in Figure 4.6, thus confirming the earlier experimental observations by Kinloch and Shaw [86]. Further, they showed that substrate thickness had no effect on the stress distribution in front of the crack. This observation by Crews et al. confirms the earlier

experir .ntal results obtained by Devitt et al. [92] who observed constant G_c values from employing specimens with different composite thicknesses. In the current work, the adhesive and composite thicknesses will be varied in attempt to choose suitable thicknesses as will be discussed in Section 4.4.3.2.

4.3. EXPERIMENTAL TECHNIQUES

4.3.1. Specimen Preparation

Double-cantilever beam (DCB) specimens were used with an appropriate adhesive and they were cured according to the manufacturers' curing cycles as mentioned in Chapter Two. After applying the adhesive a two-layer releasing-coated aluminium foil was inserted into the ....e to act as a c.../ starter. The typical specimen details are:

Length	L	= 140mm
Width	B	= 20mm
Thickness or height of each substrate	h	= 1.5 mm
Length of crack-starter	a_0	= 20 mm

After the adhesive bonding of the substrates, aluminium blocks were bonded to the end of the composite which had the crack-starter. The adhesive used for bonding on the aluminium blocks was room-temperature curing epoxy-paste adhesive ("E38" from Permabond Ltd.). Then the edges of the beams were painted white using a typewriter correction fluid and were marked-off typically at 0.5cm intervals along the complete length of the beam by taking the load line to be the start of the crack length.

4.3.2. Specimen Testing

The specimens were mounted on a screw driven tensile-testing machine and tested in tension at a crosshead speed of 2mm/minute. The experimental arrangement is shown in Figure 4.7. The tensile-testing machine was connected to a computer which gave a plot of load versus deflection. The crack was monitored through a microscope mounted in front (i.e. to give a side-view) of the specimen. As the crack length increased and crossed the marked crack lengths a chart-pipper was used to mark the crack lengths on the load-deflection diagram.
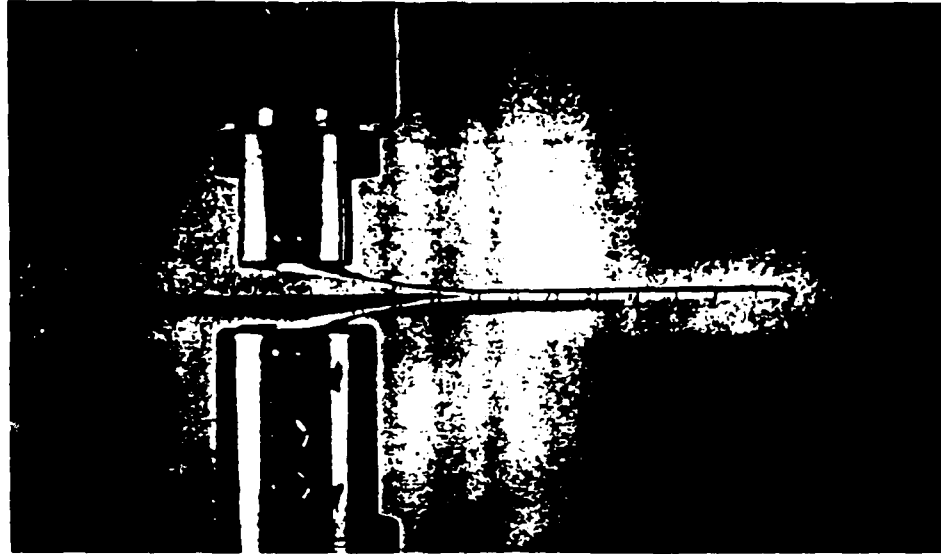
Fig. 4.7. The DCB adhesively bonded composite joint (side-view) under slow-rate
testing in a screw driven Instron 1185 computer linked machine.

4.4. RESULTS AND DISCUSSION

4.4.1. Introduction

The load, deflection and crack lengths were obtained by the technique described above
and Equation (4.10) was used to evaluate the fracture energy. A special computer program was
developed to evaluate the compliance as a function of crack length. The most noteworthy
feature of this computer program (see Appendix A.3 for the listing of the computer program) is
the fact that the coefficient of the first power of the crack length can be forced to be zero so that

the condition $\partial S/\partial a=0$ as $a \Rightarrow 0$ is satisfied. In the following sections the results from using
the composites and adhesives mentioned in Chapter Two will be presented. Each point in the
graphs, and each value in the tables, represents the average value obtained from at least three
specimens.

4.4.2. Interlaminar Failure of the Composite Materials

In this section results from the tests to evaluate the interlaminar fracture energy, G_c(il) of
the composites will be presented. Figure 4.8 shows a typical plot of a load-deflection diagram
from an interlaminar test. The special computer program developed to curve fit the compliance
and the crack lengths was used together with Equation (4.10) to calculate the interlaminar
fracture energy, G_c(il).
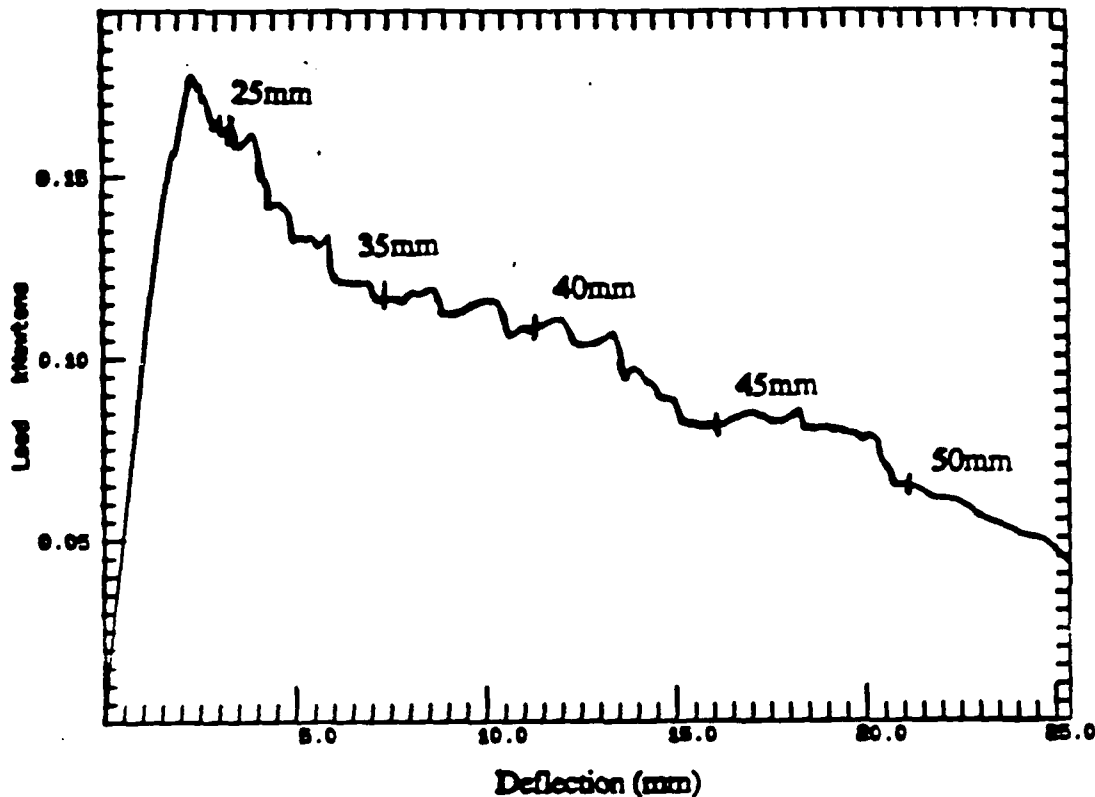
Fig. 4.8. A typical load-deflection plot from interlaminar fracture test of U/C-PA composite.

Table 4.1 shows the results from interlaminar tests of the fibre-composite materials employed. Several interesting features emerge from these results. Firstly, the interlaminar fracture energy values appear to be independent of the fibre orientation; for example the $G_c(il)$ values of the U/C-PA and W/C-PA composites are within 5%. Secondly, the interlaminar fracture energy value is a function of the type of fibre employed. For example, the interlaminar fracture energy values of U/C-PA and U/K-PA composites differ by about 70%. This difference may arise from the quality of the fibre/resin bond. (A qualitative assessment of the fracture surfaces will be made in the following chapter). Thirdly, the results show that the thermoset composite i.e., U/C-epoxy, has a very low interlaminar fracture energy value when compared to the thermoplastic fibre-composites especially when compared to the U/C-PEEK composite which has the highest interlaminar fracture energy value. Fourthly, there was no evidence of an "R-curve", i.e., $G_c(il)$ increasing with crack length, in most of the composites except a slight effect in the U/C-PEEK and the "Kevlar"/PA composites (in these cases $G_c(il)$ increased by about 10% as the crack length increased, in the latter composites mainly due to "fibre-bridging" i.e., fibres extending from one lamina to another in front of the crack). Fifthly, the $G_c(il)$ values reported here are in agreement with the results available in the literature [93, 94]. For example, Hashemi et al. [93] reported a value of about $2.4kJ/m^2$ for the

U/C-PEEK composite. However, most $G_c(il)$ values could not be compared due to the materials being relatively new.

Table 4.1. Interlaminar test results.

Composite	Interlaminar fracture Energy, $G_c(il)$, (kJ/m^2)
U/C-PEEK	2.30±0.25
U/C-PA	1.10±0.10
W/C-PA	1.15±0.15
U/K-PA	0.65±0.10
W/K-PA	0.68±0.11
W/C-PEI	1.60±0.14
U/C-PI	1.46±0.16
W/C-PI	1.68±0.16
U/C-PPS	1.45±0.16
U/C-epoxy	0.25±0.03

4.4.3. Failure of Bonded Fibre-Composite Joints

4.4.3.1. Load-Deflection Diagrams

The DCB composite joints visually appeared to fail in one of three modes and these were: (i) interfacial at the adhesive/composite interface, (ii) cohesive through the adhesive and (iii) interlaminar through the composite. The plots in Figures 4.9, 4.10 and 4.11 show typical load-deflection diagrams from such failures. Several interesting features may be seen from these plots. Firstly, as expected for the case of interfacial failure, Figure 4.9, a very low load is required for the crack to propagate through the weak interface. Secondly, for the case of cohesive failure, Figure 4.10, the load required for the crack to propagate through the adhesive is higher when compared to the interfacial failure mode. Thirdly, in the case of interlaminar failure, Figure 4.11, then the sequence of events is that when the crack in the adhesive attempts to propagate through the adhesive then the load increases to a critical value whereby before the adhesive fails the composite delaminates, above and/or below the tip of the crack-starter, and from that point onwards the crack propagates through the composite in an interlaminar manner. Further analysis on this final mode of failure will be made in Chapter Five in an attempt to understand the mechanics behind the occurrence of such a failure.
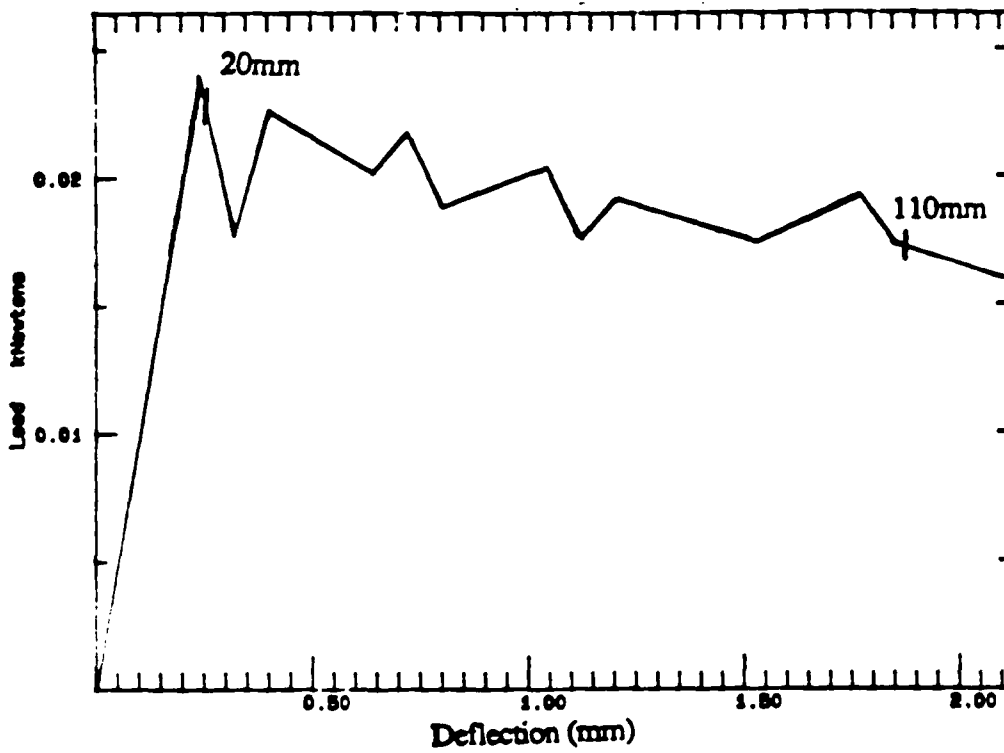
Fig. 4.9. Load-deflection diagram from untreated U/C-PEEK composite bonded to the epoxy-paste adhesive; failure is interfacial at the adhesive/composite interface.
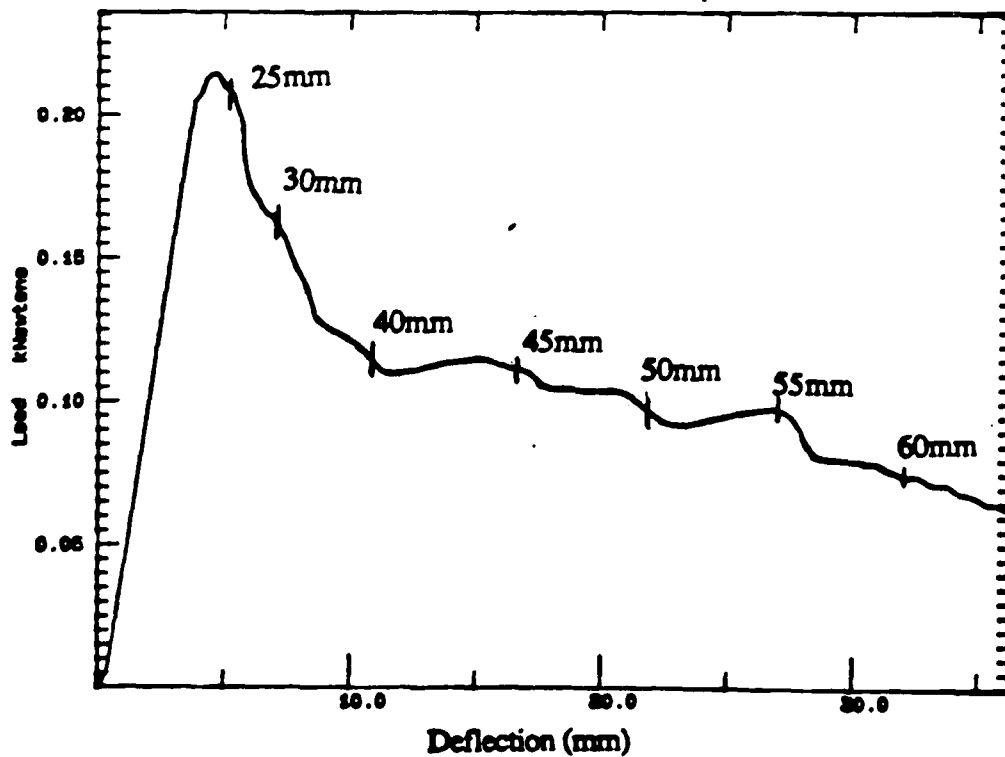
Fig. 4.10. Load-deflection diagram from corona-treated U/C-PA composite bonded to the epoxy-film adhesive; failure is cohesive through the adhesive.
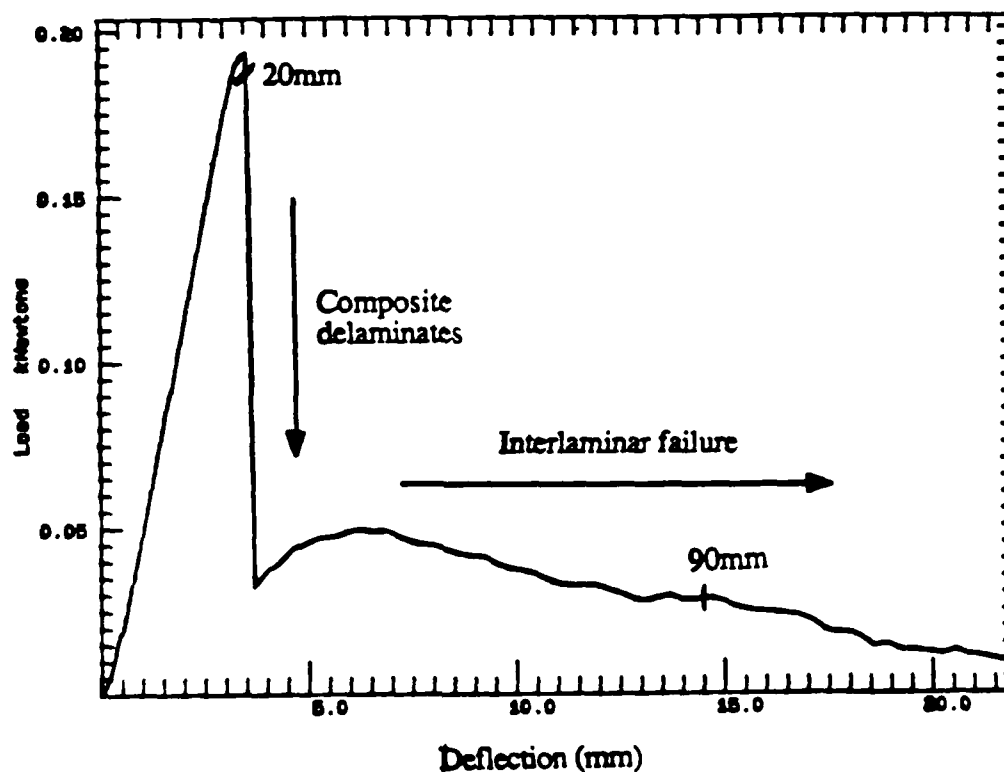
Fig. 4.11. Load-deflection diagram from abraded U/C-epoxy composite bonded to the epoxy-paste adhesive; failure is interlaminar through the composite.

4.4.3.2. Validity of Linear Elastic Fracture Mechanics (LEFM) to Adhesively Bonded Composite Joints

Before discussing the values of adhesive fracture energy determined for the various bonded fibre-composite joints the validity of LEFM to adhesively bonded joints will be investigated. Further, the thicknesses of the adhesives and the composites will be chosen. As mentioned earlier three modes of failure were observed for the DCB joints.

(i) Interfacial manner: In this mode the initial crack jumps from within the adhesive to the interface and the crack propagates along the weak adhesive/composite interface. This results in an unsymmetrical specimen whereby one side of the specimen will have the adhesive layer. Several researchers [95-101] have shown that it is still possible to apply Equation (4.10) for bimaterial systems. Further, as discussed in the literature survey the unsymmetrical specimen should still yield Mode I fracture since the applied bending moments to the arms of the substrate are equal and opposite.

(ii) Cohesive failure: In this mode the crack runs through the adhesive yielding a symmetrical specimen. Thus in this case Equation (4.10) can be confidently applied. Figure 4.12 shows a

typical plot of compliance versus crack length. The special computer program was employed to the data shown in Figure 4.12 to obtain the relationship between the compliance and the crack length from which the partial derivative was calculated and is given here:

$$\partial S/\partial a = 0.0604a + 1.291a^2 + 18.04a^3 + 199.45a^4$$
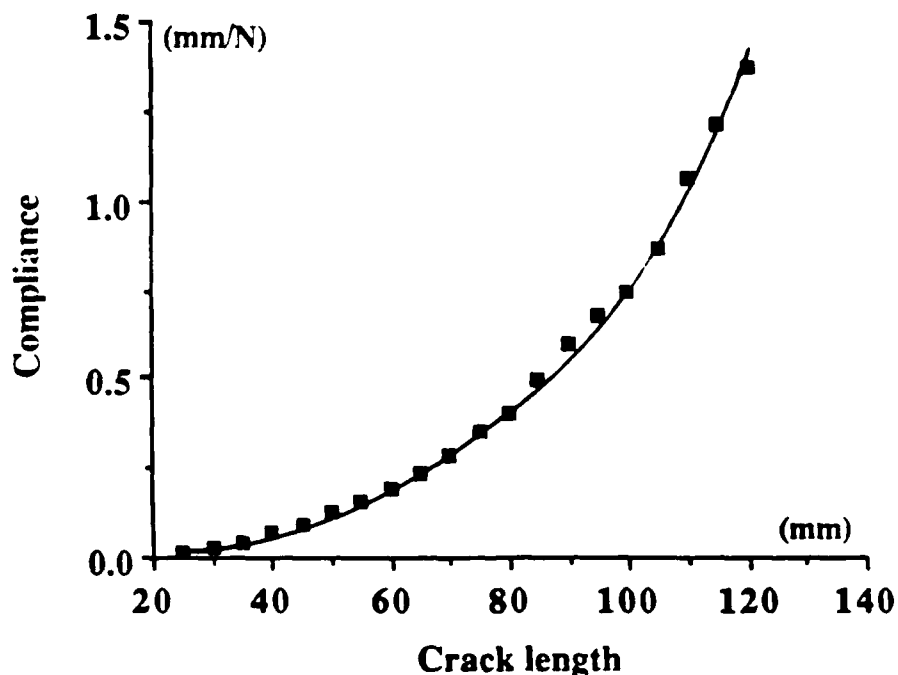
Fig. 4.12. Compliance versus crack length of U/C-PA composite bonded to the epoxy-film adhesive; composite is subjected to corona treatment level of $5J/mm^2$.

(iii) Interlaminar manner: In this mode, as was demonstrated earlier, the crack jumps from within the adhesive to the composite and the composite fails in an interlaminar manner. Thus yielding an unsymmetrical specimen. However, this type of specimen would still yield Mode I fracture for the reasons discussed above.

As discussed in the literature survey, several approaches exist for calculating the fracture energy. In the current research work only the compliance calibration technique was adopted since this approach does not assume that the composites behave as perfect "built in" beams, as the other approaches do. Furthermore, the superiority of this technique, in this project, stems from the fact that one equation yields the fracture energy for all kinds of crack propagation. But as discussed earlier, this approach has to be used with the correct mathematical curve fit.

The adhesive thicknesses in the composite joints were estimated employing a travelling

microscope. Composite joints were prepared from the epoxy-paste and the epoxy-film adhesives. The adhesive thicknesses were varied between 0.2mm and 0.6mm by employing spacers at the ends of the joints, and the results are shown in Table 4.2. It should be noted that for the adhesive thicknesses considered the crack propagated in a cohesive manner when the U/C-PEEK thermoplastic composite was subjected to corona pretreatment level of 20J/mm^2. The thickness of the adhesive layer was not increased further due to (i) the difficulty in ensuring uniform adhesive thickness along the length of the specimens and (ii) to avoid very large deflections of the arms especially from the epoxy-paste DCB joints (large deflections of the arms can introduce error in the calculated G$_c$ values, see [68]). The results in this table show a similar pattern to that of Figure 4.6 (page 106). Further, the bulk adhesive fracture energy of the epoxy-paste adhesive was 3.9kJ/m^2 which was determined from J-integral tests, see Appendix A.4. The above observations suggest that the maximum fracture energy may not have been obtained yet. In the subsequent sections an adhesive thickness of 0.5mm for the epoxy-film adhesive was chosen due to the ease of attaining this particular thickness by applying four layers of the adhesive film with the adequate pressure, see Chapter Two. For the epoxy-paste adhesive an adhesive thickness of 0.4mm was employed to investigate the behaviour of the loci of failure from pretreatment techniques at higher adhesive fracture energy values.

Table 4.2. Effect of the adhesive thickness on the measured fracture energy of DCB U/C-PEEK composite joints; nominal thickness of each substrate is 1.5mm.

Thickness t (mm)	Epoxy-paste adhesive G_c (kJ/m^2)	Epoxy-film adhesive G_c(kJ/m^2)
0.20	2.52±0.28	1.44±0.11
0.30	3.41±0.32	1.58±0.13
0.40	3.82±0.33	1.74±0.15
0.50	5.12±0.62	1.84±0.17
0.60	5.85±0.74	2.54±0.24

Note: U/C-PEEK composites subjected to corona treatment level of 20J/mm^2.

The composite thickness was varied but for the present experiments the adhesives' thicknesses were kept constant. From the data shown in Table 4.3 it can be seen that the composite thickness had very little effect on the measured adhesive fracture energy, G$_c$ (a "t-test" statistical analysis revealed that the variation in the data is insignificant). This

observation is in agreeement with previous reported work by Crews et al. [91] and Devitt et al. [92]. Therefore, since the amount of composite material was limited then the thickness of the composites was kept as thin as possible (i.e. before very large deflections of the composite arms was observed).

Table 4.3. Effect of U/C-PEEK composite thickness on the adhesive fracture energy; nominal adhesive thicknesses are 0.4mm and 0.5mm for the epoxy-paste and epoxy-film adhesives respectively.

Thickness t (mm)	Epoxy-paste adhesive G_c (kJ/m^2)	Epoxy-film adhesive G_c(kJ/m^2)
1.00	3.9± ±0.48	2.04±0.20
1.50	3.82±0.33	1.84±0.17
2.00	3.75±0.36	1.88±0.15
3.00	3.88±0.42	1.74±0.18
4.00	3.64±0.40	1.73±0.24

Note: U/C-PEEK composites subjected to corona treatment level of 20J/mm^2.

4.4.3.3. G_c Values from Untreated Composite Joints

The adhesive fracture energy values measured from these experiments were very low for all composite/adhesive combinations employed, except for the U/C-epoxy composite. The results from these experiments varied from not being able to test a joint i.e., the joint would fail prior to the test, to resulting in very low fracture energy values with very high coefficient of variation typically ±65%, see Table 4.4. The reason for these very low fracture energy values was due to the crack propagating along the interface between the composite and the adhesive. The detailed reasons for these observations will be discussed in Chapter Six but it is interesting to recall that XPS revealed low levels of oxidised species for the TPFC materials and the presence of relatively high concentrations of releasing agents on the surfaces may further hinder the adhesion of untreated fibre-laminates, see Table 3.12 (page 75). Indeed it is interesting that the untreated U/C-epoxy composite possesses the highest polar energy value, see Table 3.7 (page 55), which may be the reason for its better adhesion performance here.

Table 4.4. Adhesive fracture energy, G_c, and locus of failure
data for untreated fibre-composites.

Composite	Epoxy-paste adhesive		Epoxy-film adhesive	
	G_c (kJ/m^2)	Locus of failure	G_c (kJ/m^2)	Locus of failure
U/C-PEEK	*	Interfacial	*	Interfacial
U/C-PA	0.08±0.05	Interfacial	0.13±0.07	Interfacial
W/C-PA	0.09±0.06	Interfacial	0.12±0.08	Interfacial
U/K-PA	0.05±0.03	Interfacial	0.15±0.10	Interfacial
W/K-PA	0.07±0.05	Interfacial	0.09±0.06	Interfacial
W/C-PEI	0.12±0.08	Interfacial	0.17±0.10	Interfacial
U/C-PI	0.22±0.14	Interfacial	0.30±0.18	Interfacial
W/C-PI	0.18±0.11	Interfacial	0.23±0.15	Interfacial
U/C-PPS	0.05±0.04	Interfacial	0.08±0.05	Interfacial
U/C-epoxy	0.42±0.27	Interfacial	0.92±0.51	Interfacial

Note: (*): Failed prior to testing.

4.4.3.4. G_c Values from Abraded Composite Joints

Before discussing the results from the thermoplastic composite joints it is of interest to consider the values of the adhesive fracture energy, G_c, which were obtained for the U/C-epoxy composite joints, which was a unidirectional carbon-fibre/epoxy composite. Such results obviously act as a starting point when considering later the adhesive bonding of the thermoplastic composites. Following a simple light abrasion and solvent-wipe pretreatment, the values of G_c and locus of failure which were recorded are shown in Table 4.5.

As may be seen from the data shown in Table 4.5, the simple abrasion/solvent-wipe pretreatment employed for the epoxy-based composite has been sufficient to ensure good wetting and adhesion of the adhesive to the composite substrates to that extent that the joints typically fail by the crack-starter, which was inserted in the adhesive layer, propagating cohesively through the adhesive layer or, in one instance by, a new crack initiating and growing in the composite substrate to give an interlaminar locus of failure. Indeed, the observation that, for a freshly-prepared thermosetting composite, a simple abrasion/solvent-wipe pretreatment is sufficient to avoid any indications of failure at the adhesive/composite interface is in accord with previously published results [102].

Table 4.5. Fracture energy and locus of failure data for U/C-epoxy
composite subjected to abrasion/solvent-wipe pretreatment.

Adhesive	G_c (kJ/m^2)	Locus of Failure
Epoxy-paste	0.25±0.02	Interlaminar
Epoxy-film	1.90±0.11	Cohesive
Two-part acrylic-paste "F241"	1.30±0.15	Cohesive
Two-part acrylic-paste "F245"	1.50±0.20	Cohesive
Two-part acrylic-paste "F246"	1.45±0.15	Cohesive
Two-part acrylic-paste "V501"	0.90±0.23	Cohesive
Two-part acrylic-paste "M890"	0.70±0.20	Cohesive
Two-part acrylic-paste "M896"	0.75±0.23	Cohesive

The same adhesives used in bonding the U/C-epoxy were also used for bonding the U/C-PEEK composite. The results from these experiments are shown in Table 4.6. The conclusion that can be drawn from the data in Table 4.6 is that a simple abrasion/solvent-wipe pretreatment is clearly inadequate for the U/C-PEEK composite when either the epoxy or acrylic adhesives are employed.

Table 4.6. Fracture energy and locus of failure data for U/C-PEEK
composite subjected to abrasion/solvent-wipe pretreatment.

Adhesive	G_c (kJ/m^2)	Locus of Failure
Epoxy-paste	0.02±0.01	Interfacial
Epoxy-film	0.03±0.02	Interfacial
Two-part acrylic-paste "F241"	0.02±0.01	Interfacial
Two-part acrylic-paste "F245"	0.03±0.02	Interfacial
Two-part acrylic-paste "F246"	0.03±0.02	Interfacial
Two-part acrylic-paste "V501"	0.05±0.03	Interfacial
Two-part acrylic-paste "M890"	0.05±0.03	Interfacial
Two-part acrylic-paste "M896"	0.05±0.03	Interfacial

For the rest of the thermoplastic composites, not all the adhesives employed in Tables 4.5 and 4.6 will be used, instead only the two epoxy adhesives were employed and the results are summarized in Table 4.7.

Table 4.7. Fracture energy and locus of failure data of the other thermoplastic composites subjected to abrasion/solvent-wipe pretreatment.

Composite	Epoxy-paste adhesive		Epoxy-film adhesive	
	G_c (kJ/m^2)	Locus of failure	G_c (kJ/m^2)	Locus of failure
U/C-PA	0.12±0.07	Interfacial	0.30±0.15	Interfacial
W/C-PA	0.11±0.07	Interfacial	0.27±0.14	Interfacial
U/K-PA	0.10±0.06	Interfacial	0.30±0.17	Interfacial
W/K-PA	0.12±0.07	Interfacial	0.25±0.13	Interfacial
W/C-PEI	0.28±0.18	Interfacial	0.37±0.19	Interfacial
U/C-PI	0.44±0.18	Interfacial	0.61±0.21	Interfacial
W/C-PI	0.47±0.21	Interfacial	0.61±0.21	Interfacial
U/C-PPS	0.11±0.04	Interfacial	0.20±0.09	Interfacial

The conclusion that can be drawn so far from Tables 4.6 and 4.7 is that, all the TPFC materials employed seem to have a common fundamental problem in adhesive bonding when compared to the thermoset composite. They all fail in an interfacial manner resulting in low G_c values with very high coefficients of variation.

4.4.3.5. G_c Values from Aluminium/Etch Composite Joints

To ensure no releasing agent was present on the surfaces of the thermoplastic composites, sheets were moulded against clean aluminium foil which was etched in a bath of chromic-acid solution. After the moulding process, the aluminium foil was dissolved away in two molar sodium hydroxide solution leaving releasing-free composite sheets. The U/C-PEEK composite obtained from aluminium/etch pretreatment was bonded to the epoxy-paste and epoxy-film adhesives and the adhesive fracture energy, G_c, were 0.12 and 0.40kJ/m^2 respectively. Although there is an improvement in the measured G_c values, the apparent failure was still interfacial between the composite and the adhesive. Such results suggest that for thermoplastic composites the problem in attaining good adhesion is not due to weak boundary layers of residual releasing agents being present on the TPFC substrates.

4.4.3.6. G_c Values from Acid-Etch Composite Joints

Composite samples were acid-etched as described in Section 2.4.4. A summary of the results from this pretreatment technique for the U/C-PEEK composite material etched for different immersion times is shown in Table 4.8. From the data presented in Table 4.8 it can be seen that this technique gives higher G_c values, especially for the epoxy-film adhesive. However, this technique was not pursued further due to the exothermic reactions involved which made the experiments very hazardous. It is also an impractical approach if it is to be employed in bonding, say, large structures of TPFC materials. Although impractical, this pretreatment technique did lead to an increase in oxidised species, see Table 3.14 (page 78), increased the surface free energy, see Table 3.9 (page 57), and increased the measured G_c values, see Table 4.8. Therefore, this work led to the idea of employing a controlled oxidation technique and for this purpose, the corona-discharge pretreatment technique was developed.

Table 4.8. Adhesive fracture energy and locus of failure data of the U/C-PEEK composite subjected to acid-etch pretreatment technique.

Etch time (min.)	Adhesive	G_c (kJ/m^2)	Locus of failure
2	Epoxy-paste	0.07±0.04	Interfacial
5	Epoxy-paste	0.30±0.15	Interfacial
10	Epoxy-paste	0.90±0.41	Interfacial
2	Epoxy-film	0.50±0.23	Interfacial
5	Epoxy-film	1.30±0.52	Mainly interfacial
10	Epoxy-film	1.65±0.33	Mainly cohesive

4.4.3.7. G_c Values from Corona-Treated Composite Joints

The aim of employing corona treatment for the TPFC substrates prior to adhesive bonding was to increase the oxygen-rich species and hence increase the surface wettability and adhesion of these materials. The results obtained for various treatment energies per unit area are given in the following tables and figures. In these figures open points represent interfacial failure, star points represent interlaminar failure and closed points represent cohesive failure through the adhesive. It should be noted that all specimens were abraded and wiped with methyl-ethyl ketone (MEK) prior to corona-discharge pretreatment. However, as will be discussed in Chapter Six, provided the surfaces are not heavily contaminated with releasing agents, then

abrasion/solvent-wipe pretreatment is not required prior to corona treatment and subsequently in obtaining high G_c values.

The results for the bonded U/C-PEEK thermoplastic composite are shown in Figures 4.13 and 4.14. There are several interesting points to note in these figures. Firstly, for both adhesives the value of G_c increases steadily as the treatment level is increased until a plateau value of G_c is reached. Once the maximum, plateau value of G_c is reached then it appears that an increased level of corona pretreatment offers no further advantages to the performance of the joint. The plateau values of the adhesive fracture energy, G_c, are about 2 and 4 kJ/m^2 for the joints bonded using the epoxy-film and the epoxy-paste adhesives respectively. Secondly, as might be expected, it is only when the treatment level is sufficient to give an intrinsically strong interface that cohesive failure through the adhesive is observed, as opposed to the interfacial locus of failure which is observed at low pretreatment levels. Thirdly, again as expected, the treatment level needed for the joint to attain the maximum value of G_c is dependent upon the adhesive being employed: a tougher adhesive, having the potential to give a higher value of the adhesive fracture energy, G_c, requires a higher level of corona treatment to be applied to the U/C-PEEK thermoplastic composite in order to achieve the maximum crack resistance for the joint than a less tough adhesive.

Fig. 4.13. The adhesive fracture energy of U/C-PEEK composite bonded to the epoxy-paste adhesive; open points interfacial failure; closed points cohesive failure.

Fig. 4.14. The adhesive fracture energy of U/C-PEEK composite bonded to the epoxy-film adhesive; open points interfacial failure; closed points cohesive failure.

The results for the U/C-PEEK composite bonded using the acrylic adhesives are shown in Table 4.9. It can be seen from the data presented in this table that the adhesive fracture energy values are far higher than the values from the abrasion/solvent-wipe pretreatment reported in Table 4.6 (page 117). The reason for the fracture energy value being higher is due to the crack propagating now through the adhesive in a cohesive manner, rather than in an interfacial manner between the composite and the adhesive. Furthermore, these results compare well with the results obtained from the thermosetting composite bonded to the acrylic adhesives, see Table 4.5 (page 117).

Table 4.9. Effects of a corona-discharge pretreatment on the values of G_c
and the observed locus of failure for the U/C-PEEK composite bonded
with the acrylic-based adhesives; treatment level is $20J/mm^2$.

Adhesive	G_c (kJ/m^2)	Locus of failure
Two-part acrylic-paste "F241"	1.25±0.18	Cohesive
Two-part acrylic-paste "F245"	1.55±0.12	Cohesive
Two part acrylic-paste "F246"	1.38±0.15	Cohesive
Two-part acrylic-paste "V501"	0.97±0.23	Cohesive
Two-part acrylic-paste "M890"	0.67±0.18	Cohesive
Two-part acrylic-paste "M896"	0.81±0.24	Cohesive

The adhesive fracture energy, G_c, for the rest of the TPFC materials employed are shown in Figures 4.15 to 4.30. It should be noted for all these TPFC materials only the two epoxy adhesives were employed. Several noteworthy features emerge from these figures:

(i) The results shown in Figures 4.15 to 4.18 for the U/C- and W/C-PA thermoplastic composites are very similar in form to those shown in Figures 4.13 and 4.14 for the U/C-PEEK composite. Namely, the value of G_c rises to a maximum, plateau value as the level of corona pretreatment used prior to bonding is increased, and this effect is accompanied by a change in the locus of joint failure from interfacial to cohesive in the adhesive or in few cases interlaminar in the composite. However, note that the level of corona treatment needed to attain the plateau value of G_c is significantly less than that required for the U/C-PEEK composite, reflecting the higher initial polarity of the amorphous polyamide copolymer, which is based on bis(para-amino cyclohexyl methane), compared to the poly(ether-ether ketone)matrix. For the U/C- and W/C-PA composites bonded with the epoxy-film adhesive the failure mode always changed from interfacial at the adhesive/composite interface to cohesive in the adhesive, as the corona energy level is increased. However, for these composites bonded to the epoxy-paste adhesive the locus of joint failure was more complex. As the level of corona treatment was increased, in about 75% of the specimens tested, the locus of failure changed from being interfacial to cohesive in the adhesive whereas in about 25% of the specimens tested, the locus of failure changed from being interfacial to interlaminar in the composite. The latter locus of failure resulted in the plateau region of a relatively lower value of G_c of about $1.15kJ/m^2$. The premature delamination of the composite substrate obviously preventing the far higher values of G_c associated with the cohesive failure through the tough epoxy-paste adhesive from being observed.

(ii) Figures 4.19 to 4.22 show the values of G_c versus the level of corona-discharge treatment employed for the U/K and W/K-PA composites respectively. Note in both cases that corona treatment is effective in increasing the adhesive fracture energy but with both composites, and using either the epoxy-paste or the epoxy-film adhesives, the plateau value of G_c is relatively low; well below the values observed in Figures 4.17 and 4.18 for example. Thus, the plateau values of G_c obtained for the "Kevlar"-fibre/PA composites are significantly lower than the carbon-fibre/PA composites. The reason for this may be readily understood by observing that the locus of joint failure for the "Kevlar"-fibre/PA composites bonded using the epoxy-paste and the epoxy-film adhesives is by an interlaminar fracture through the composite, i.e. the composite substrate delaminates by a new crack initiating and propagating between the laminae forming the composite. The premature interlaminar failure of the composite substrate prevents the far higher values of G_c associated with cohesive fracture through the tough adhesives from being obtained. Thus, again whilst the corona pretreatment has been effective in preventing interfacial failure along the adhesive/composite interface, the weak link in the joint is now the premature delamination of the substrate itself.

(iii) The data for the unidirectional-carbon-fibre/thermoplastic polyimide (U/C-PI), woven-carbon-fibre/polyimide (W/C-PI), woven-carbon-fibre/poly(ether imide) (W/C-PEI) and unidirectional-carbon-fibre/poly(phenylene sulphide) (U/C-PPS) thermoplastic composites are shown in Figures 4.23 to 4.30 respectively, and a similar picture to that described in the preceeding paragraphs emerges.

Therefore, corona-discharge pretreatment is very effective in enhancing the adhesive bonding of all the thermoplastic composites, as the corona treatment level is increased the locus of failure changed from that of interfacial at the adhesive/composite interface to one of cohesive in the adhesive or interlaminar through the composite.
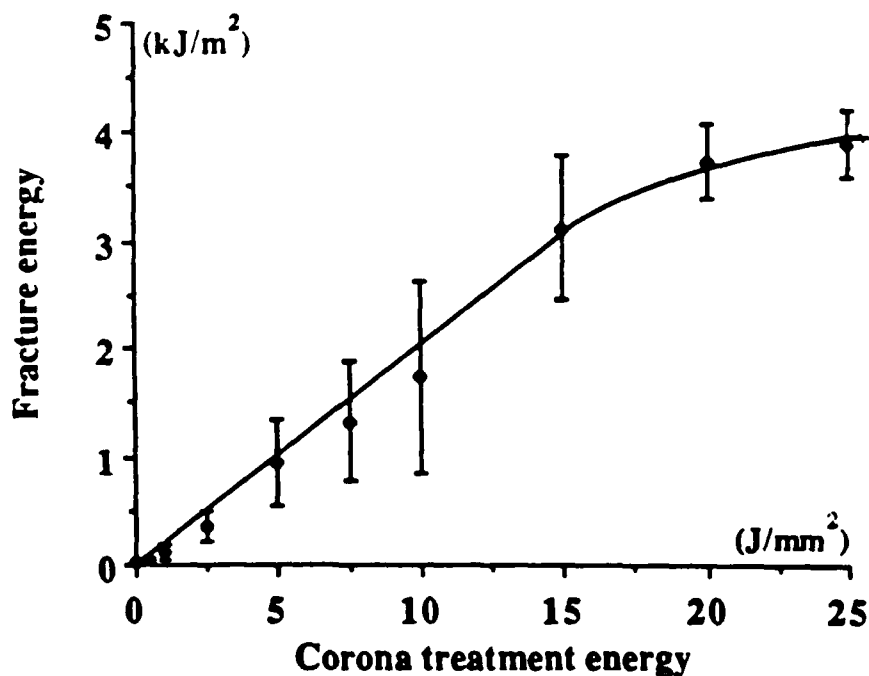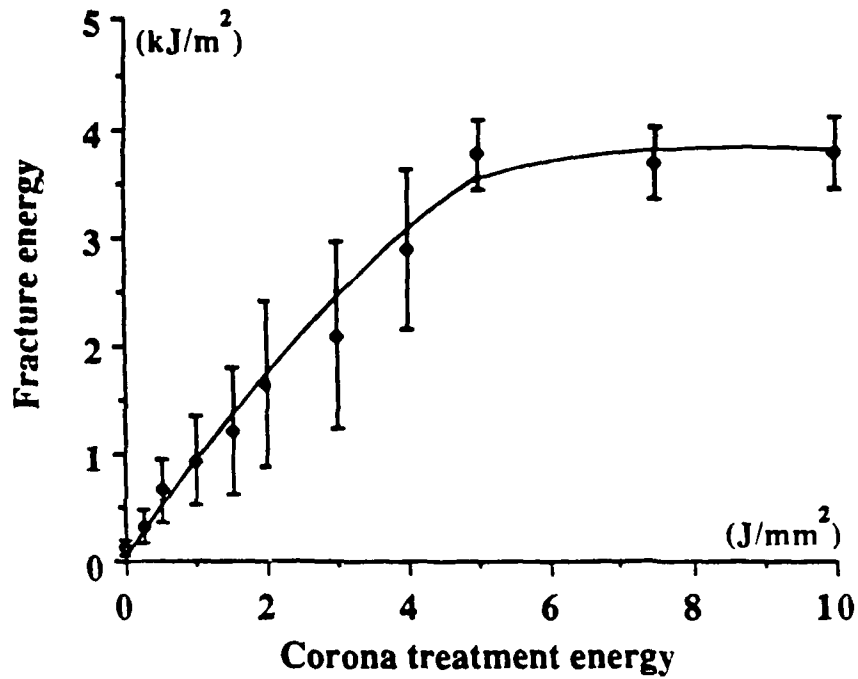
Fig. 4.15. The adhesive fracture energy of U/C-PA composite bonded to the epoxy-paste adhesive; open points interfacial failure; closed points cohesive failure.
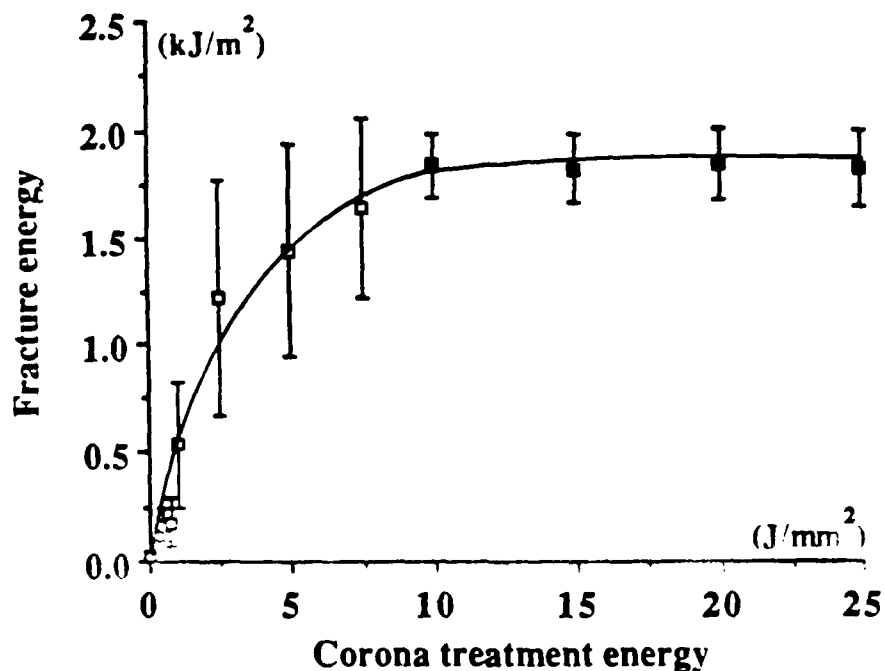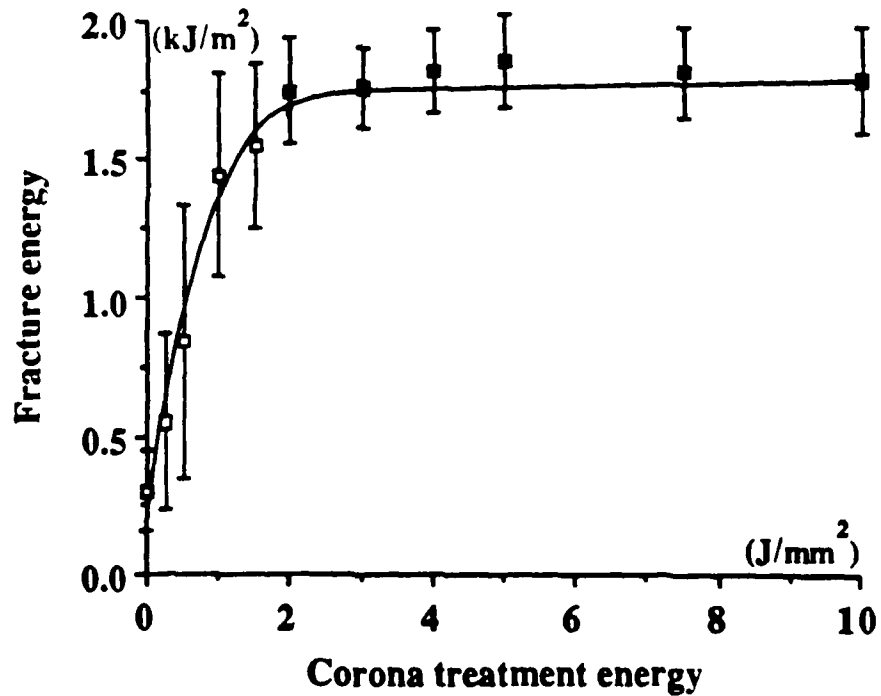

Fig. 4.16. The adhesive fracture energy of U/C-PA composite bonded to the epoxy-film adhesive; open points interfacial failure; closed points cohesive failure.
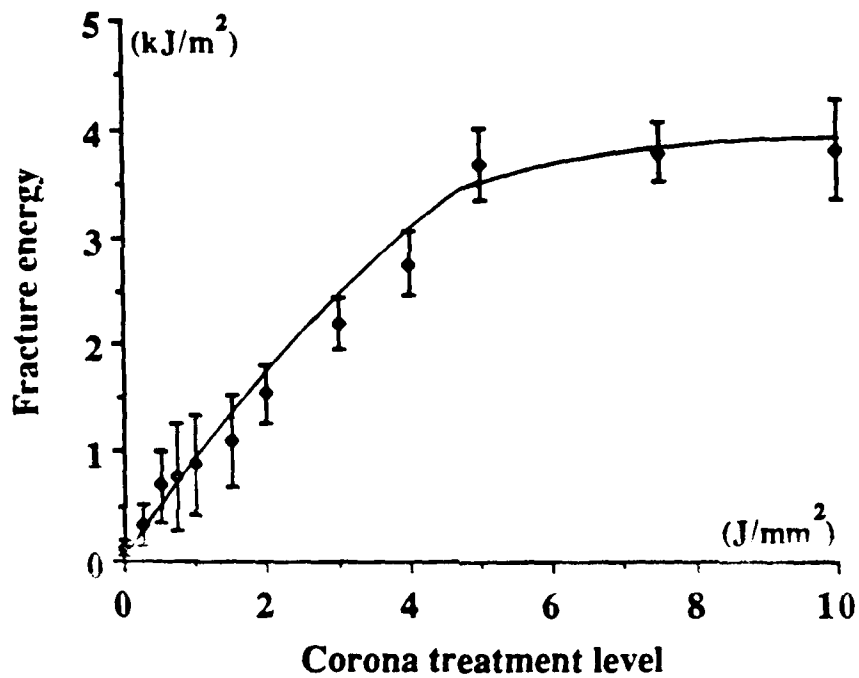
Fig. 4.17. The adhesive fracture energy of W/C-PA composite bonded to the epoxy-paste adhesive; open points interfacial failure; closed points cohesive failure.
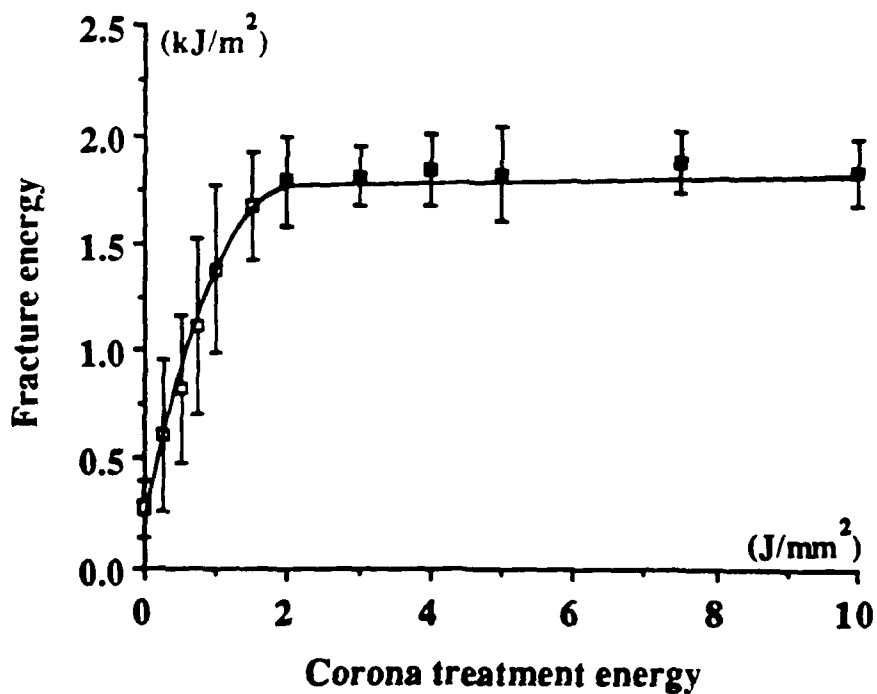
Fig. 4.18. The adhesive fracture energy of W/C-PA composite bonded to the epoxy-film adhesive; open points interfacial failure; closed points cohesive failure.
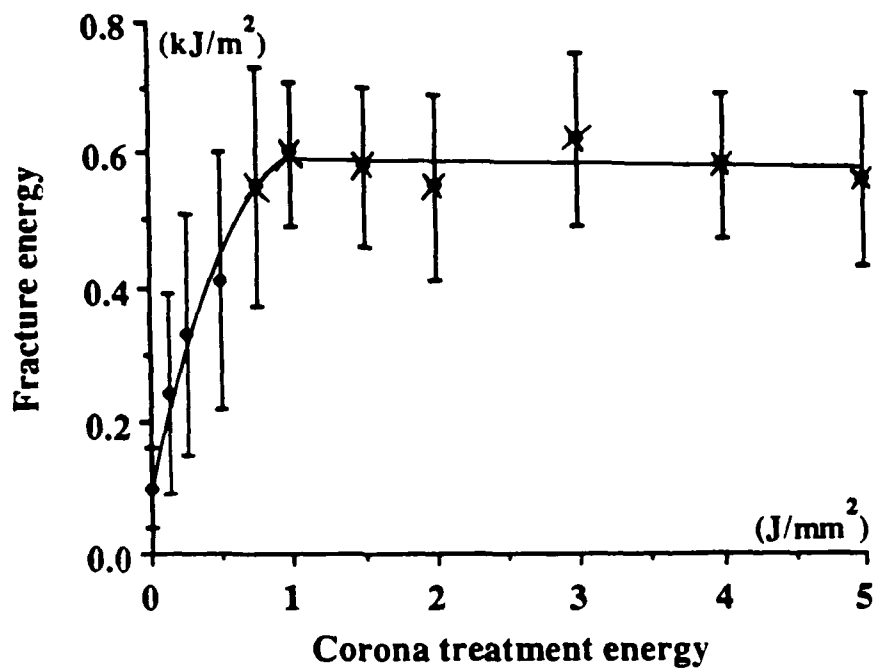
Fig. 4.19. The adhesive fracture energy of U/K-PA composite bonded to the epoxy-paste adhesive; open points interfacial failure; star points interlaminar failure.
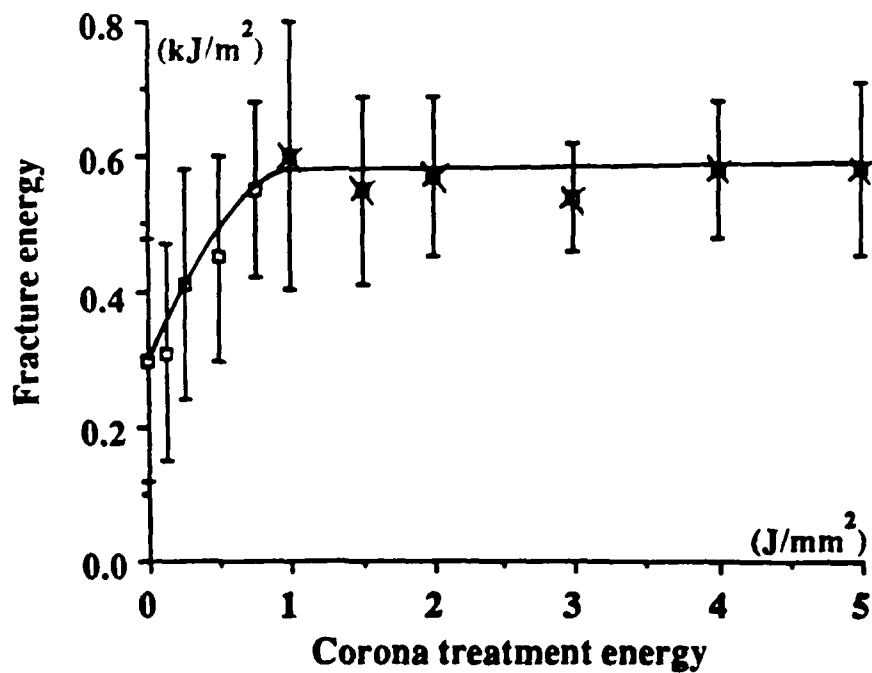
Fig. 4.20. The adhesive fracture energy of U/K-PA composite bonded to the epoxy-film adhesive; open points interfacial failure; star points interlaminar failure.
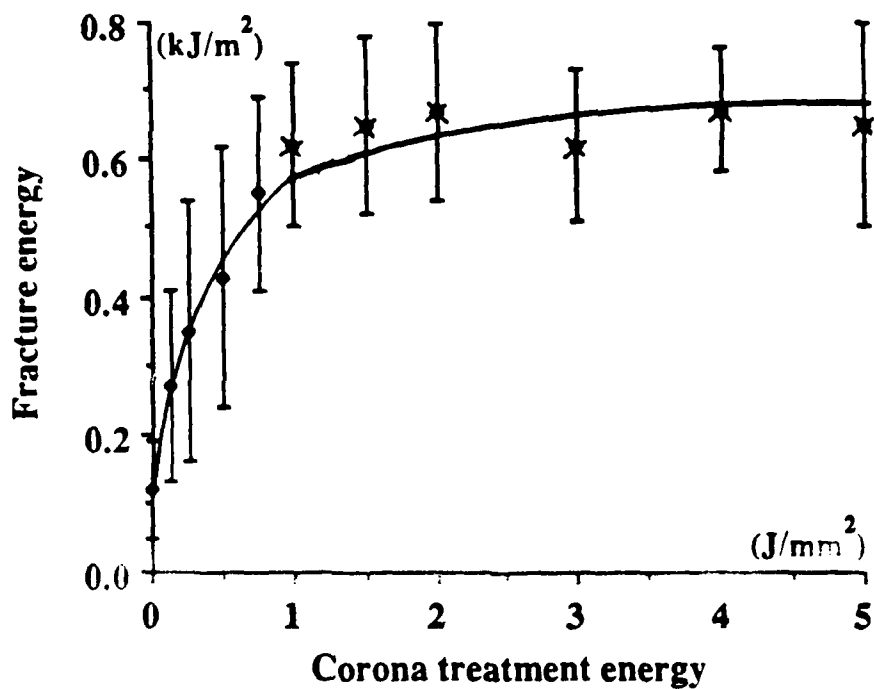
Fig. 4.21. The adhesive fracture energy of W/K-PA composite bonded to the epoxy-paste adhesive; open points interfacial failure; star points interlaminar failure.
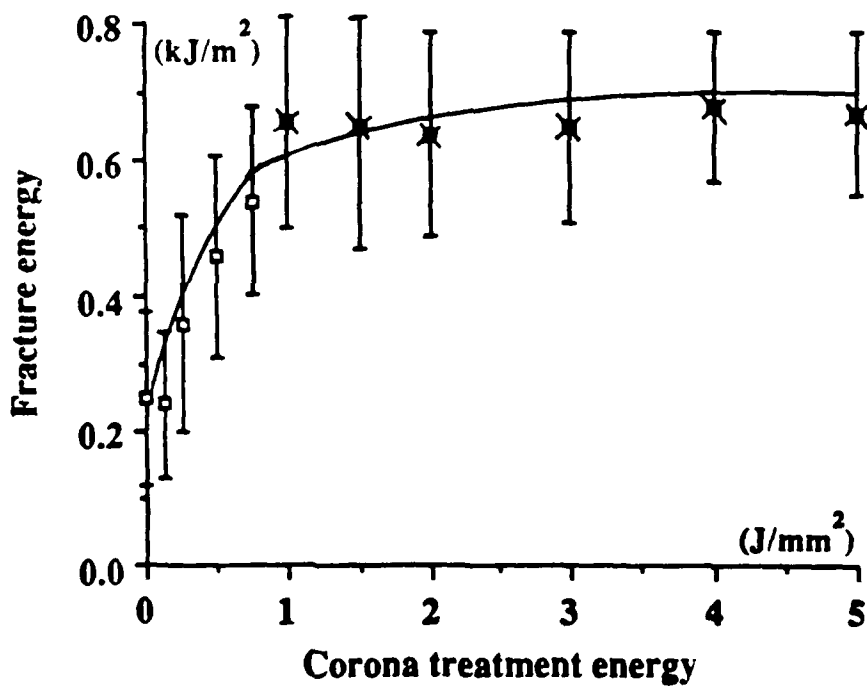
Fig. 4.22. The adhesive fracture energy of W/K-PA composite bonded to the epoxy-film adhesive; open points interfacial failure; star points interlaminar failure.
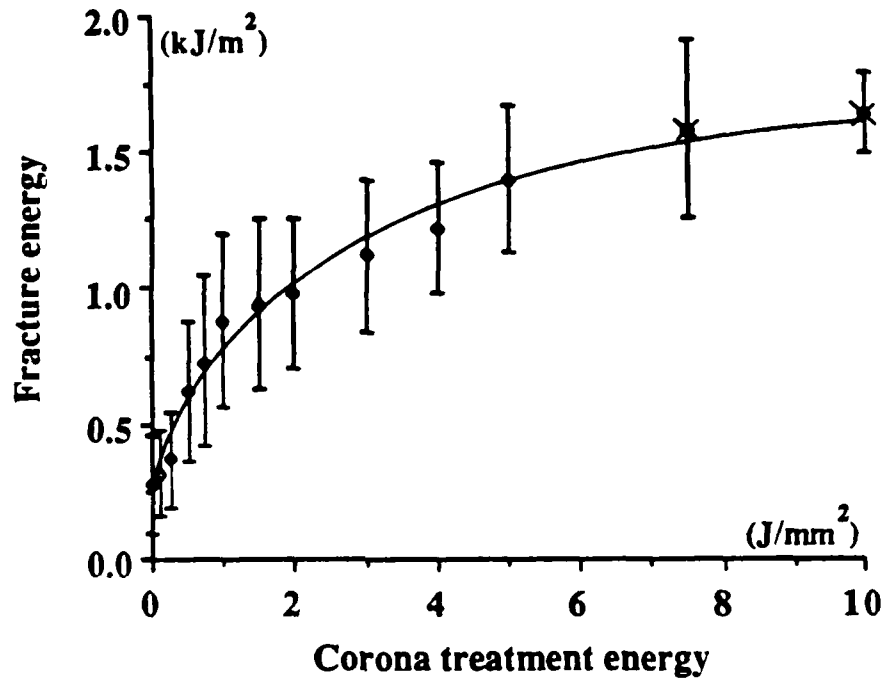
Fig. 4.23. The adhesive fracture energy of W/C-PEI composite bonded to the epoxy-paste adhesive; open points interfacial failure; star points interlaminar failure.
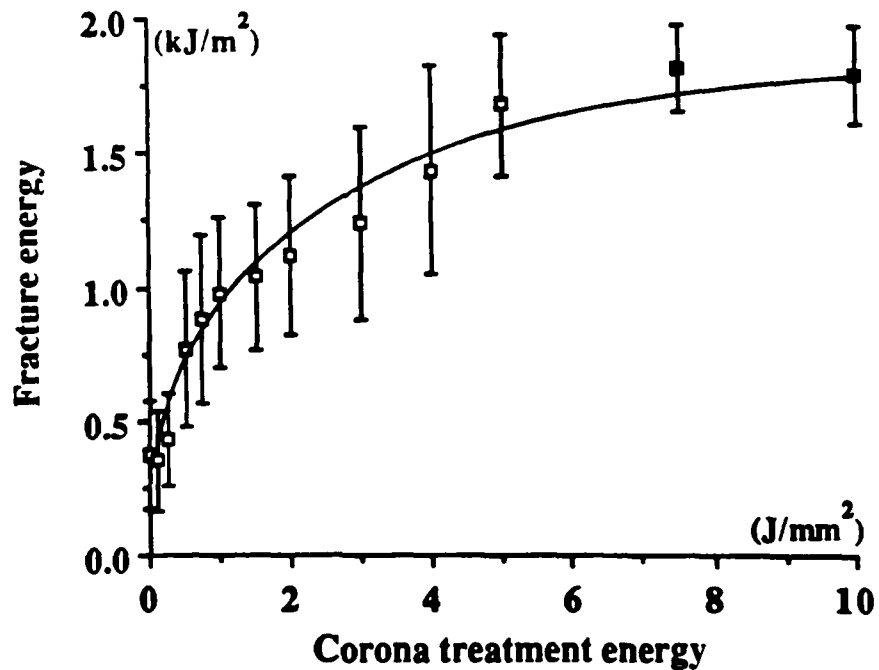
Fig. 4.24. The adhesive fracture energy of W/C-PEI composite bonded to the epoxy-film adhesive; open points interfacial failure; closed points cohesive failure.
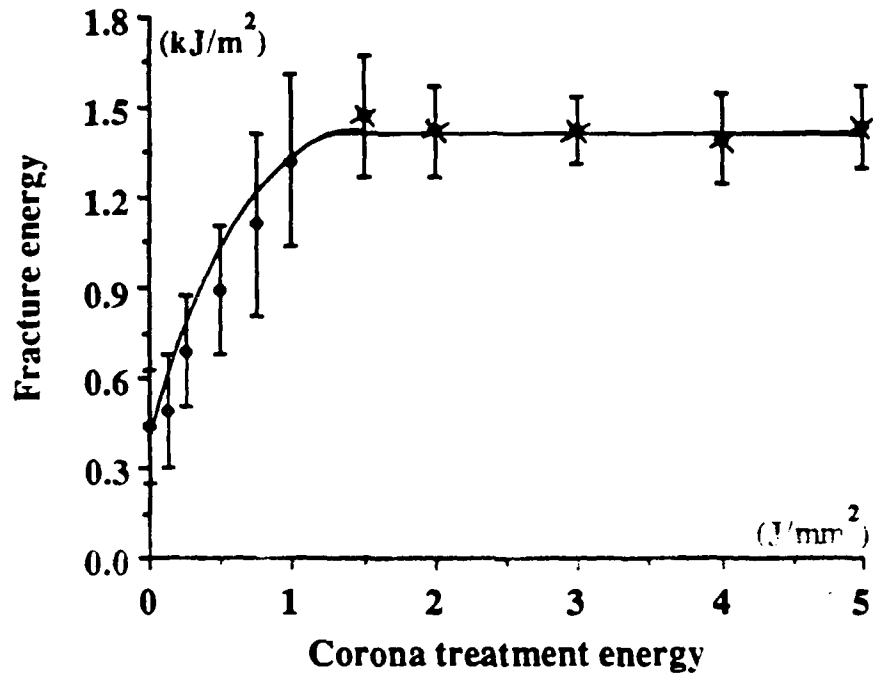
Fig. 4.25. The adhesive fracture energy of U/C-PI composite bonded to the epoxy-paste adhesive; open points interfacial failure; star points interlaminar failure.
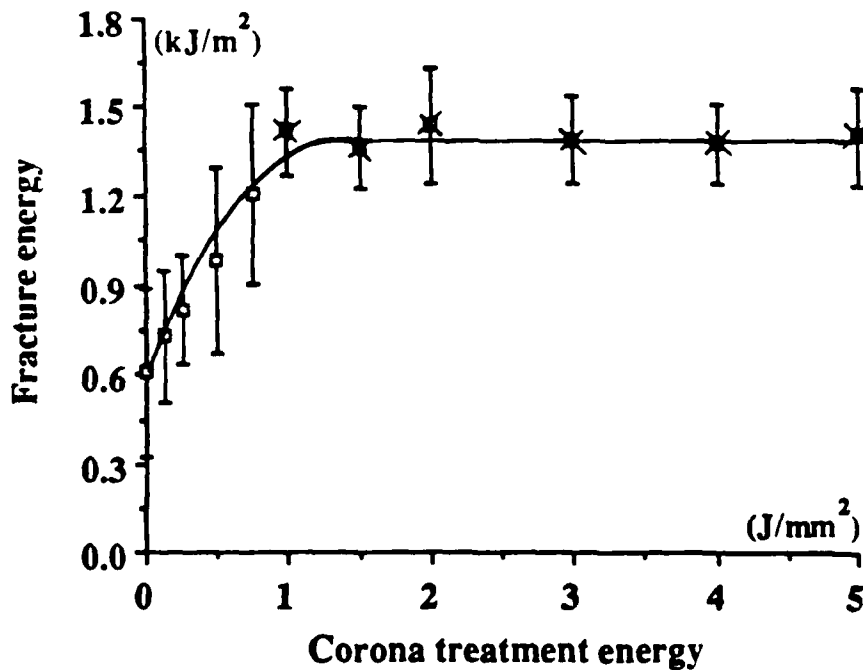
Fig. 4.26. The adhesive fracture energy of U/C-PI composite bonded to the epoxy-film adhesive; open points interfacial failure; star points interlaminar failure.
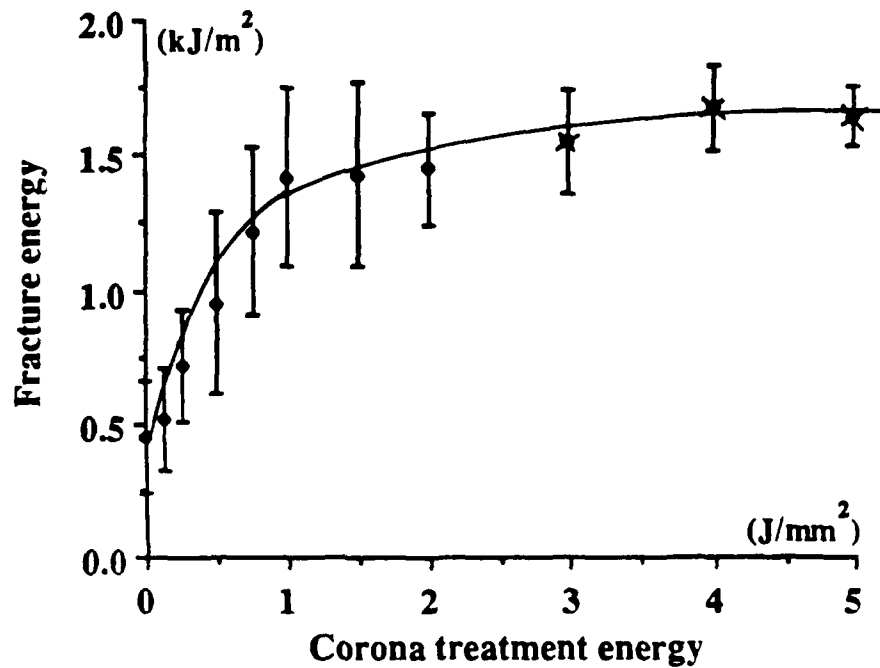
Fig. 4.27. The adhesive fracture energy of W/C-PI composite bonded to the epoxy-paste adhesive; open points interfacial failure; star points interlaminar failure.
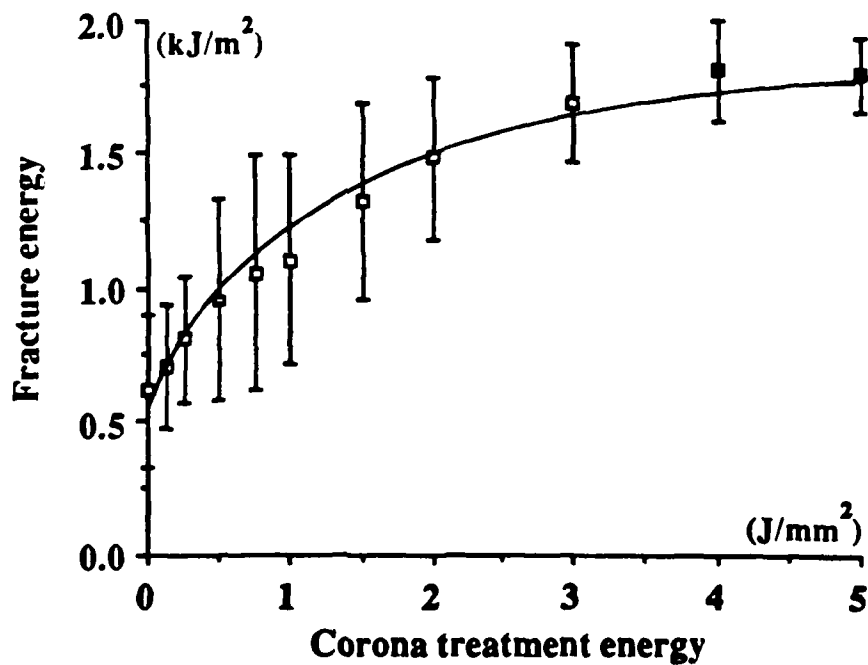
Fig. 4.28. The adhesive fracture energy of W/C-PI composite bonded to the epoxy-film adhesive; open points interfacial failure; closed points cohesive failure.
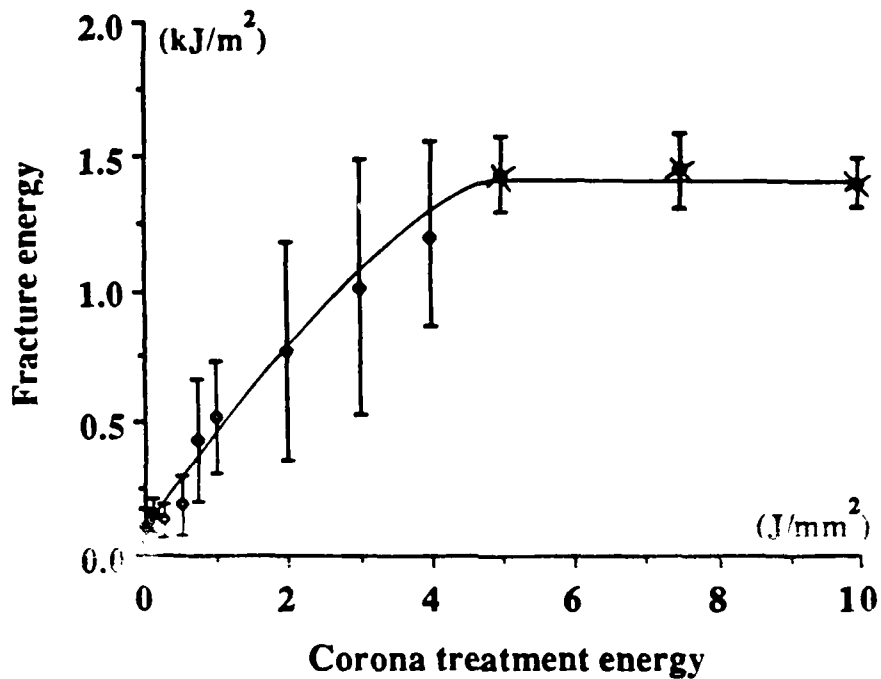
Fig. 4.29. The adhesive fracture energy of U/C-PPS composite bonded to the epoxy-paste adhesive; open points interfacial failure; star points interlaminar failure.
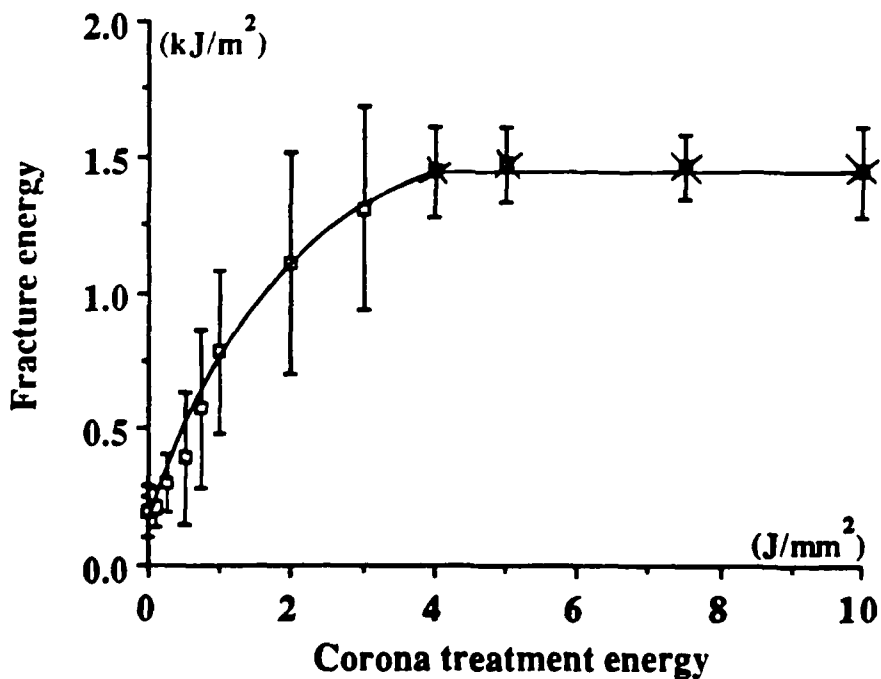
Fig. 4.30. The adhesive fracture energy of U/C-PPS composite bonded to the epoxy-film adhesive; open points interfacial failure; star points interlaminar failure.

4.4.3.8. Use of Thermoplastic Adhesives

The TPFC substrates were bonded using their corresponding resin films (note that some of the resins were not available) as "hot-melt" adhesives. These substrates were first subjected to abrasion/solvent-wipe pretreatment. The results from these experiments are shown in Table 4.10.

Comparing the results presented in Table 4.1 (page 110) with those of Table 4.10 it can be concluded that thermoplastic composite specimens can readily bond to their corresponding resins and give the same fracture energy values as from interlaminar tests. Hence, it can be deduced that the "hot-melt" adhesives do not encounter weak boundary layers, of either releasing agents or low molecular weight matrix material, on the surfaces of the TPFC materials.

Table 4.10. Test results of thermoplastic composites bonded to their resins.

Composite	Interlayer	Fracture Energy, G_c, (kJ/m^2)
U/C-PEEK	PEEK	2.25±0.25
U/C-PA	PA	1.05±0.10
W/C-PA	PA	1.15±0.12
U/K-PA	PA	0.60±0.10
W/K-PA	PA	0.60±0.11
U/C-PPS	PPS	1.45±0.13

In a further experiment, the thermoplastic resin PA was used as a "cross-hot-melt" adhesive for bonding U/C-PEEK thermoplastic substrates. These substrates were first abraded and then bonded with the PA thermoplastic resin. Such samples could not be tested due to the failure of the DCB joints prior to mounting onto the tensile-testing machine. This can be explained by the results presented in the previous chapter, Table 3.8 (page 56), whereby the U/C-PEEK composite had a similar total surface free energy when compared with the U/C-PA thermoplastic composite thus indicating that the PA resin will not wet on the U/C-PEEK composite. However, when the U/C-PEEK thermoplastic composite was treated with corona-discharge to 20J/mm^2 the observed locus of failure was now cohesive through the PA hot-melt thermoplastic resin, yielding an adhesive fracture energy value of 0.45kJ/m^2 for an adhesive thickness of 0.1mm. Therefore, when the surface free energy of the U/C-PEEK composite is increased then it would readily bond with epoxy, acrylic and another

thermoplastic resin.

4.4.4. Aspects of the Corona Pretreatment Process

4.4.4.1. Ageing of Corona-Pretreated TPFC Materials Prior to Bonding

Having successfully achieved the adhesive bonding of the TPFC materials, then the U/C-PEEK and PA thermoplastic composites were treated with corona-discharge and allowed to age in a laboratory condition (T=20^{0}C and R.H.=60%) in the chamber described in Chapter Three (Section 3.2.4.6). The level of pretreatments for these thermoplastic composites was 20J/mm^2 and 5J/mm^2 respectively. After a given ageing time, the thermoplastic samples were bonded to the two epoxy adhesives and the fracture test results from such experiments are presented in Figures 4.31 and 4.32. Several noteworthy features emerge from these two figures.

For the epoxy-film adhesive bonded to any of the two thermoplastic composites the loci of failure was cohesive through the adhesive for the entire six months ageing process. Resulting in adhesive fracture energy values of about 2kJ/m^2. Secondly, for the tougher epoxy-paste adhesive the fracture energy began to fall after several weeks of ageing the pretreated TPFC substrates from values of about 4kJ/m^2 to values under 3kJ/m^2. These G$_c$ values reflect a change in the loci of failure. For freshly-treated substrates the locus of failure was cohesive through the adhesive but after several weeks of ageing the locus of failure reverted to mixed interfacial/cohesive failure along the adhesive/composite interface. Therefore, the fracture results from the epoxy-paste adhesive indicate a fundamental change in the surface properties of the treated composites i.e., the corona-treated surfaces lose some of their adhesion characteristics with ageing time, and more interfacial failure is observed in the joints prepared from the TPFC materials which had been aged for a relatively longer times. This observation correlates with the earlier observations made in Chapter Three where the polar component of the surface energy dropped (see Figure 3.12 page 61) and XPS revealed a drop in the concentration of the oxygen element (see Figure 3.40 page 92). These points will be discussed in more detail in Chapter Six.
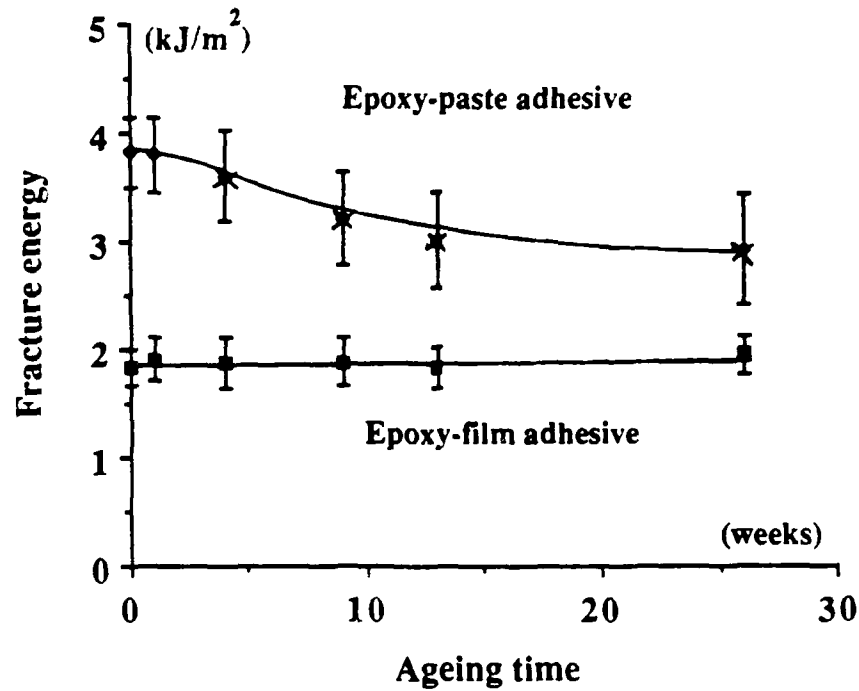
Fig. 4.31. The adhesive fracture energy of aged U/C-PEEK composite; closed points cohesive failure; star points mixed interfacial/cohesive failure.
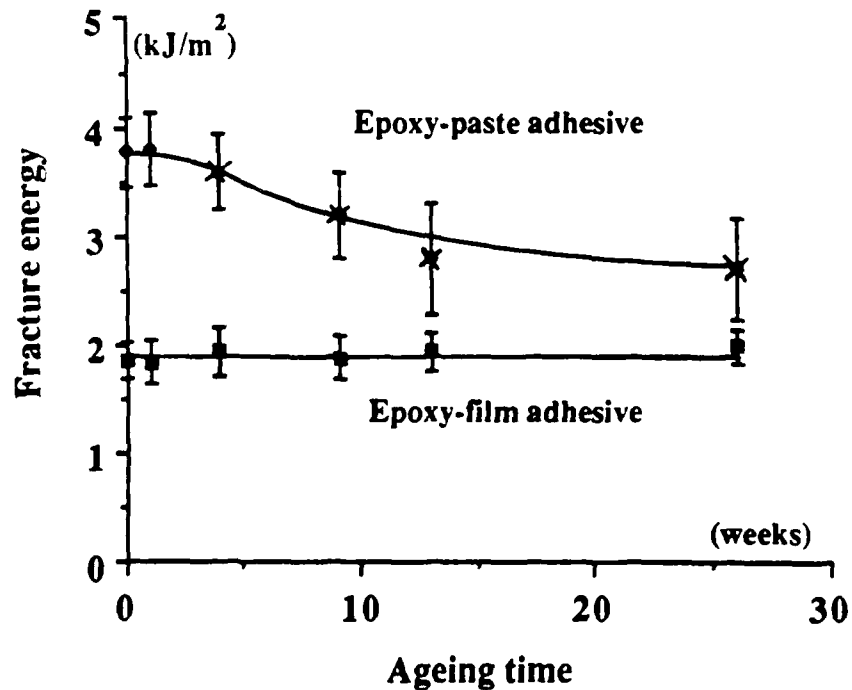
Fig. 4.32. The adhesive fracture energy of aged U/C-PA composite; closed points cohesive failure; star points mixed interfacial/cohesive failure.

4.4.4.2. Environmental Ageing of Bonded Corona-Pretreated TPFC Materials

The effects of environmental attack on the bonded composite joints was undertaken since such analyses could indicate the behaviour of the corona-treated and bonded composites from water ingress. U/C-PEEK composite substrates were treated with corona-discharge to $20J/mm^2$ and $10J/mm^2$ and bonded with the epoxy-paste and to the epoxy-film adhesives respectively. The joints were then immersed in a bath of water heated to 50^0C by a thermal agitator.

Figure 4.33 shows the results obtained from the fracture experiments. The conclusions and the observations that emerge are several. Firstly, and perhaps most importantly, is that the loci of failure for both types of adhesives employed was cohesive through the adhesive. This demonstrates that the interface between the adhesive and the corona-treated U/C-PEEK composite remains stable, at least up to two months of environmental exposure. Secondly, for both types of adhesives employed the G_c values drop.

The decrease in the G_c values could be the result of one, or a combination, of the following three mechanisms:
(a) For low ageing times, water plasticises the crack tip resulting in crack tip blunting. Hence, the somewhat higher than usual fracture energy values observed for the epoxy-film adhesive.
(b) The adhesive properties deteriorate by water diffusion and the engineering properties of polymers (such as modulus, fracture toughness, yield stress etc.) are known to be susceptible to water absorption.
(c) The water at 50^0C post cures the cold-cured epoxy-paste adhesive resulting in a more crosslinked adhesive, and hence a more brittle material.

To assess the extent of water attack on the adhesive properties and the extent of post curing, composite joints were made and allowed to age in a heated oven at 50^0C. The fracture results from such experiments are shown in Figure 4.34. It can be seen that the adhesive fracture energy for the epoxy-paste adhesive drops and that of the epoxy-film adhesive remains constant in value. Further, the measured fracture energy values reported in this figure are higher than the ones shown at similar ageing times but immersed in the bath of heated water, see Figure 4.33. Therefore, the heated water does affect the properties of the cold-cured epoxy-paste adhesive by making it more brittle and it also alters the material properties of the epoxy-film adhesive (by water ingress) resulting in both cases a somewhat lower adhesive fracture energy values being recorded.
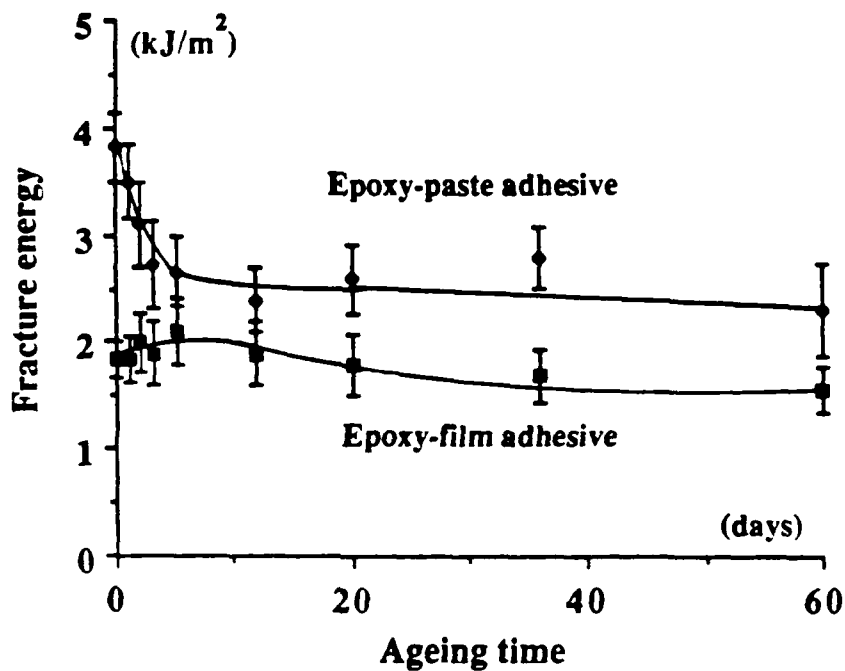
Fig. 4.33. The adhesive fracture energy of the U/C-PEEK composite pretreated to corona energy level of 20J/mm^2 and immersed in a heated bath of water at 50^{0}C.
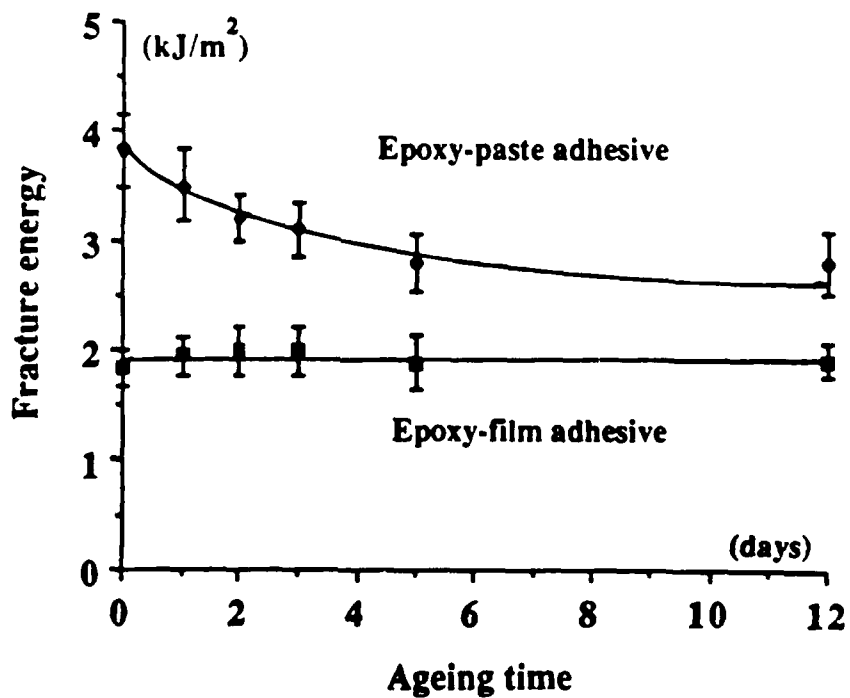
Fig. 4.34. The adhesive fracture energy of the U/C-PEEK composite subjected to corona treatment energy of 20J/mm^2 and aged in heated oven at 50^{0}C.

4.5. CONCLUSIONS

The main conclusions from this chapter are:

1. Fracture mechanics was successfully employed to measure the fracture energies of different combinations of composites and adhesives. The compliance calibration approach was adopted to give the adhesive fracture energy values. For this reason a computer program was developed to curve-fit the compliance versus the crack length in which the coefficient of the first power of the crack length was forced to be zero.

2. For freshly-prepared thermosetting composites there was generally no problem in attaining adequate adhesion using epoxy- and acrylic-based structural adhesives; a simple abrasion solvent-wipe pretreatment was sufficient.

3. For the wide range of thermoplastic-based composites which have been examined it was possible to use a hot-melt film adhesive, of the same chemical composition as the matrix, to attain relatively high values of the adhesive fracture energy, G_c; using a simple abrasion/solvent-wipe pretreatment. The values of G_c obtained were very similar to those measured for the interlaminar failure of the composites. However, the use of these films as hot-melt adhesives does, of course, require high temperatures to be reached in the bonding operation.

4. If the epoxy- and acrylic-based structural adhesives were to be employed, then a simple abrasion/solvent-wipe pretreatment was insufficient to ensure adequate bonding. This surface pretreatment resulted in the composite joints possessing very low values of G_c with the locus of joint failure being by crack growth along the weak adhesive/composite interface.

5. It was shown that as the adhesive thickness was increased to 0.6mm the measured adhesive fracture energy values increased. The effects of the composite thickness on the measured fracture energy were also analysed and it was found that the thickness of the substrates had little effect on the measured G_c values provided the adhesive thicknesses were kept constant in value. Therefore, the thicknesses employed were 1.5mm for the composites and, 0.5 and 0.4mm for the epoxy-film and epoxy-paste adhesives respectively.

6. The corona-discharge technique was successfully developed and was extremely effective in increasing the intrinsic adhesion of the adhesives to the thermoplastic composite,

provided the composite substrates were not heavily contaminated with releasing agents. For the corona-pretreated thermoplastic composite joints the values of G_c increased steadily with the level of corona treatment employed until a maximum, plateau value of G_c was reached.

7. The highest plateau values of the adhesive fracture energy, G_c(plateau), were recorded when the joint failed by crack growth through the adhesive layer. It is of interest to note that under such conditions the value of G_c(plateau) may be far higher than the interlaminar fracture energy, G_c(il), of the composite. However, for some of the joints, before failure via crack growth through the adhesive can occur, the thermoplastic composite substrate delaminated. Thus, the composite was now the "weakest link" in the joint and the measured value of G_c(plateau) was now approximately equal in value to the interlaminar fracture energy, G_c(il), of the composite.

8. The ageing effects of corona pretreated surfaces were analysed. Such experiments revealed that the measured G_c values decreased reflecting the change in the locus of failure whereby more interfacial failure is observed for the longer aged substrates.

9. Finally, analysis of environmental attack on corona-treated composite joints revealed that water attacks the adhesive and the G_c values change. However, the locus of failure remained cohesive through the adhesive.

Having successfully achieved the adhesive bonding of TPFC materials, novel ideas will be put forward in Chapter Six in an attempt to correlate the results from contact angle analysis, X-ray photoelectron spectroscopy and fracture mechanics. But before presenting the mechanisms of adhesion, the locus of failure studies from fracture mechanics will be presented in Chapter Five.

CHAPTER FIVE

LOCUS OF JOINT FAILURE

5.1. INTRODUCTION

In the previous chapter results from the fracture tests were presented and the locus of failure was visually assessed to be either, or a combination of:

   (a) Interfacial; i.e. the crack propagated along the adhesive/composite interface.

   (b) Interlaminar; i.e. the crack propagated in the composite substrate.

   (c) Cohesive in the adhesive; i.e. the crack propagated in the adhesive layer.

In this chapter these type of failures will be first visually described, followed by scanning electron microscopy (SEM) studies. Next, the locus of failure will be studied by X-ray photoelectron spectroscopy (XPS). Finally, an attempt will be made to predict the locus of failure in the adhesively-bonded double-cantilever beam (DCB) composite joints by comparing the stresses generated in the composite substrates (analysed using finite element analysis (FEA)) to the measured transverse (delamination) strength of the composites.

5.2. LITERATURE SURVEY

5.2.1. Introduction

Surface characterisation using XPS has already been presented in some detail in Chapter Three. Therefore, in the present literature survey, the use of XPS to predict the locus of failure in adhesive joints will be briefly reviewed. Further, a literature survey will be presented on the subject of stresses in anisotropic materials, since these stresses may lead to the premature (delamination) failure of the composite substrates in the DCB joint specimens.

5.2.2. Weak Boundary Layers

If a region of low strength exists in an adhesive joint, the failure load will be low. When a region of low strength exists in the surface regions of the substrate (or adhesive) adjacent to the interface, it is termed a "weak boundary layer". Bikerman [103] has discussed the various sources of weak boundary layers. Potential weak boundary layers include dust, grease and oxides of relatively low strengths. There is no doubt that weak boundary layers do exist in some circumstances; for example Bullett and Prosser [104] show how such layers can lead to

poor adhesion between metals and paints. Further, in a recent work Kinloch and Yuen [105] bonded a polyimide-copper laminate to an acrylic adhesive. They employed in situ peel tests conducted in a scanning electron microscope and demonstrated the occurrence of a weak boundary layer in the polyimide film. However, the importance of weak boundary layers has probably been exaggerated. For example, Bikerman [106] first suggested that adhesion problems associated with polyethylene (PE) were due to weak boundary layers. Since then there has been considerable controversy over whether this is the case or whether lack of chemical functionality is the basic cause. Several publications by Briggs et al. [16, 47-49] have demonstrated that weak boundary layers are not the essence of the problem in the weak adhesion of PE. For example, Briggs et al. [48] treated PE in a bath of chromic acid solution and then bonded treated and untreated PE substrates to aluminium specimens employing an epoxy adhesive. They tested lap joints and conducted XPS analyses on the fractured surfaces. They concluded from their analyses that their was no evidence of transfer of PE from untreated weak specimens, which failed interfacially, to the adhesive surfaces; as would be expected if a region of low strength existed in the PE surface. Indeed, they concluded that the improved lap-shear strengths from treated PE specimens was due to the increase of the oxidation level of the treated polyethylene.

5.2.3. Previous Work on the Prediction of Stresses in DCB Joints

In the literature, there is a considerable amount of research work reported on the application of FEA to adhesively bonded composite joints. Most of these research work either deal with stresses in lap joints, as will be discussed later in Chapter Seven, or with the stress distribution in front of a crack tip in joints [90, 91]. Perhaps the most relevant works in the application of FEA in DCB joints are by Wang et al. [90] and more recently by Crews et al. [91].

Wang et al. [90] analysed a DCB joint specimen under elastic conditions. The substrates were aluminium and, therefore, their analysis was isotropic. They predicted the stress distribution in front of the crack tip in the x- and y-directions. Their aims were to explain the effects of substrate to adhesive moduli and that of adhesive thickness on the stress distribtion in a DCB joint design. Their research work provides little information about actual stress distribution in a DCB joint specimen since:
(i) The stress distributions were obtained from the application of unit loads and therefore could not provide information on the stress distribution from an actual experiment. However, it does provide a comparative technique.
(ii) They did not take into consideration the fact that the stress distribution in front of a crack tip in a DCB specimen is independent of the crack length by virtue of the bending moments being

constant along the entire length of the specimen, as will be shown in Section 5.4.4.2.

More recently, Crews et al. have [91] repeated Wang et al.'s [90] work by applying, in some cases, actual loads (i.e. loads obtained from experiments) and in other cases unit loads to DCB joint specimens of either isotropic or orthotropic substrates. They were also concerned with the stresses in front of the crack tip, in the horizontal direction and their aims were, to understand the effects of adhesive thickness and substrate stiffness on these stress distributions. They reported in their research work that, although the stresses along the interface are important, but that these stresses were beyond the scope of their study.

Therefore, for the first time, the stresses in the regions of the adhesive/composite interface in DCB joints will be predicted and will be compared to the measured transverse strength of the composites. Such a comparison may give an indication of the mode of failure in DCB composite joir...

5.3. EXPERIMENTAL ASSESSMENT OF THE LOCUS OF JOINT FAILURE

The different modes of failure of the DCB composite joints were first analysed by a detailed visual assessment, secondly by using scanning electron microscopy (SEM) and finally by employing X-ray photoelectron spectroscopy (XPS).

5.3.1. Visual Assessment

It was shown in Chapter Four that the adhesion of untreated TPFC materials to the epoxy and acrylic adhesives was very poor. Figure 5.1(a) shows one such case where the adhesion between the epoxy-paste adhesive and the U/C-PA thermoplastic composite is so poor that the epoxy adhesive was peeled free from the substrate using "finger nail" pressure. It was also shown that when the TPFC materials were abraded then a very low adhesive fracture energy value was again obtained. The failure mode still being interfacial at the adhesive/composite interface, see Figure 5.1(b). If this pretreatment was followed by a moderate level of corona-discharge pretreatment then the failure mode was either interfacial plus interlaminar or interfacial plus cohesive, depending on the type of composite employed. For example, at a corona treatment level of $0.5J/mm^2$ the "Kevlar"-fibre/PA composites failed in mixed interfacial plus interlaminar manner whereas for a treatment level of $3J/mm^2$ the carbon-fibre/PA composites failed in a mixed interfacial plus cohesive manner, see Figure 5.1(c).
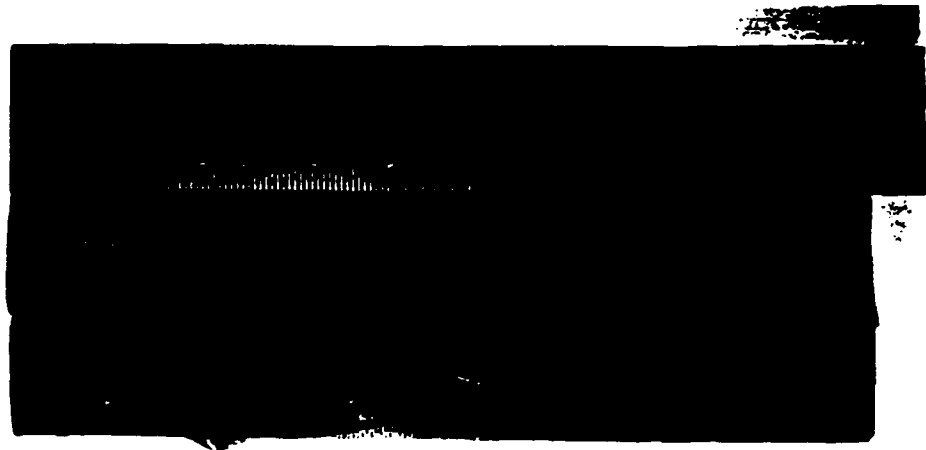
(a)
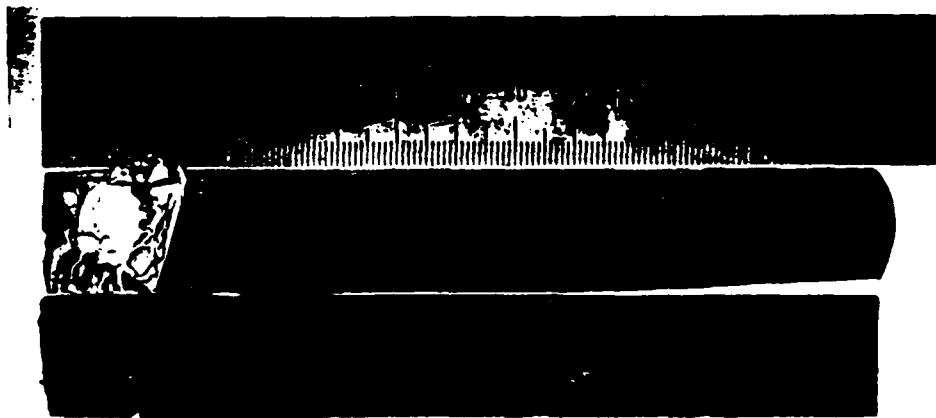
(b)
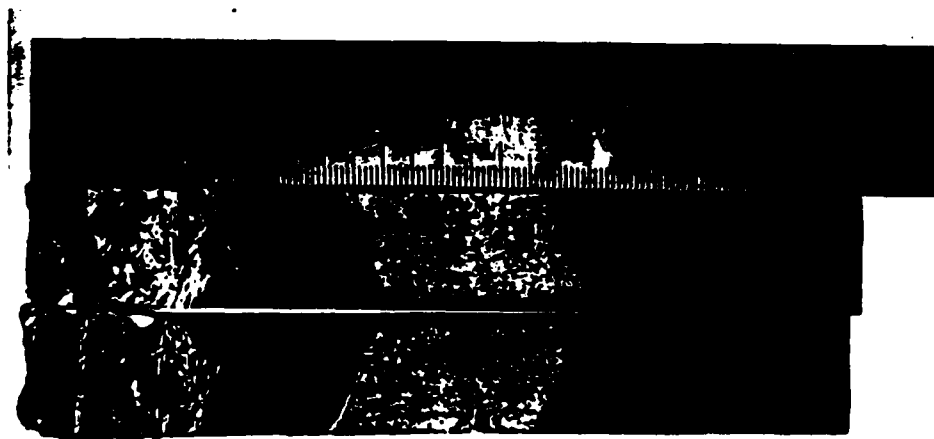
(c)

Fig. 5.1. Fracture surfaces of U/C-PA composite bonded to the epoxy-paste adhesive; (a) untreated, failure is apparently interfacial at the adhesive/composite interface; (b) composite subjected to abrasion/solvent-wipe pretreatment, failure is interfacial; and (c) corona pretreatment level of $3J/mm^2$, failure is interfacial plus cohesive.

Further, if the TPFC materials were sufficiently treated then the observed locus of failure was shown to be either cohesive through the adhesive, see Figure 5.2(a), or interlaminar through the composite substrate, see Figure 5.2(b). In the latter case, where the composites delaminated, it was interesting to observe how a secondary crack developed in the U/C-PPS composite beyond the adhesive layer and above or below the precracked region, see for example Figure 5.3. Once this second crack developed in the composite substrate then the locus of failure was interlaminar through the composite as shown in Figure 5.2(b). This observation will be discussed in some detail later in this chapter and finite element analysis (FEA) will be employed in an attempt to predict the locus of failure.

(a)
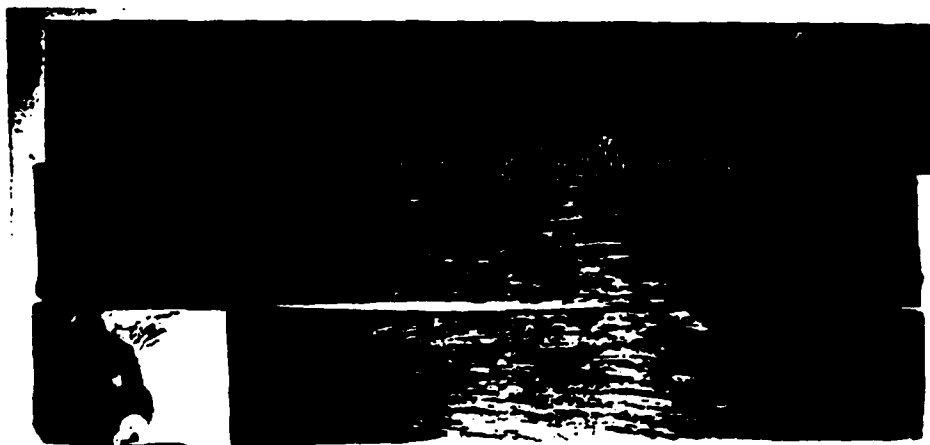
(b)

Fig. 5.2. U/C-PA thermoplastic composite bonded to the epoxy-paste adhesive; composite subjected to corona pretreatment level of $5J/mm^2$; failure is cohesive through the adhesive; and (b) U/C-PPS composite bonded to the epoxy-paste adhesive; the composite was subjected to corona-discharge pretreatment level of $5J/mm^2$; the locus of failure is apparently interlaminar through the composite.
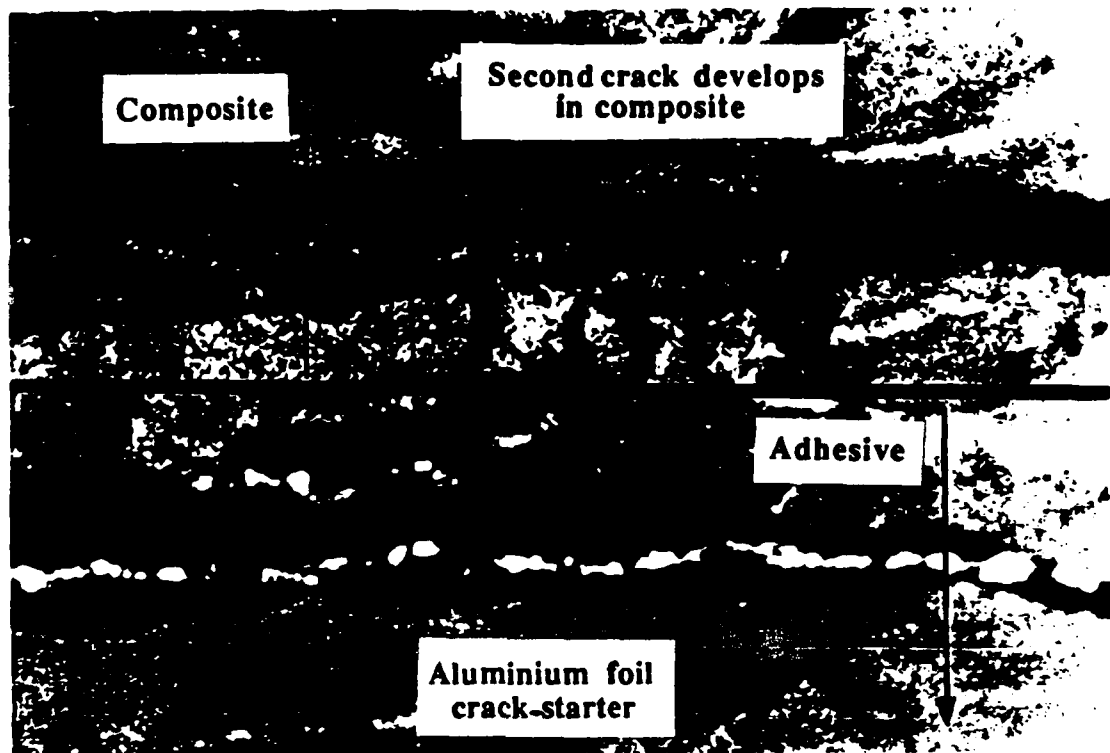
Fig. 5.3. A second crack develops in the substrate above the adhesive layer in the U/C-PPS composite bonded to the epoxy-paste adhesive; the composite was subjected to corona pretreatment level of $5J/mm^2$; horizontal line indicates adhesive/composite interface.

5.3.2. Scanning Electron Microscopy Studies

Scanning electron microscopy (SEM) was also employed to study the modes of failure. Figures 5.4 and 5.5 show typical micrographs of the U/C-PEEK composite bonded to the epoxy adhesives. Several features emerge from these micrographs. Firstly, micrograph 5.4(a) is very similar to the micrograph shown in Figure 3.18(a) (page 67). Indicating interfacial failure along the adhesive/composite interface. Secondly, micrograph 5.4(b) shows a somewhat rougher surface than micrograph (a), indicating surfaces due to interfacial failure which have been subjected to corona-discharge pretreatment. Thirdly, in micrograph 5.5(a) microvoiding in the rubbery particles is clearly visible which indicates cohesive failure through the rubber-toughened epoxy-paste adhesive. Fourthly, in micrograph 5.5(b) some fibres are clearly visible which belong to the carrier-mat of the epoxy-film adhesive. Therefore, indicating again cohesive failure through the epoxy-film adhesive. Micrographs from interlaminar tests will be presented in Section 5.4.2.2. Such micrographs will give a qualitative assessment of the fibre/resin bond and so will serve as a guide to understanding the modes of failure in the composite DCB joint specimens.
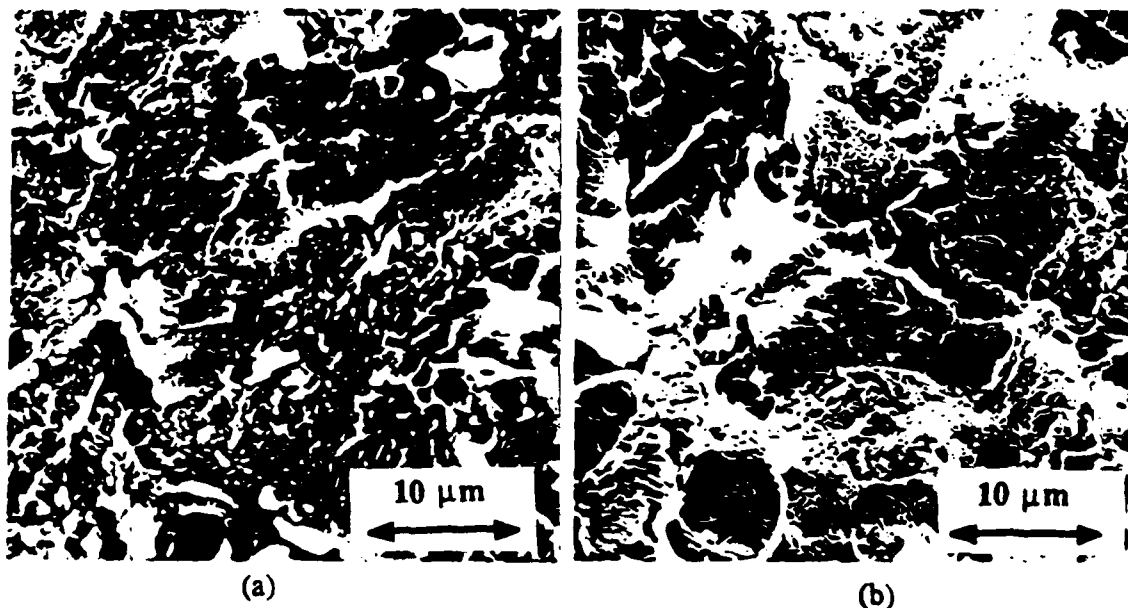
Fig 5.4. U/C-PEEK composite bonded to the epoxy-paste adhesive and subjected to (a) abrasion/solvent-wipe pretreatment, and (b) corona pretreatment level of $5J/mm^2$; locus of failure in both cases is interfacial along the adhesive/composite interface.
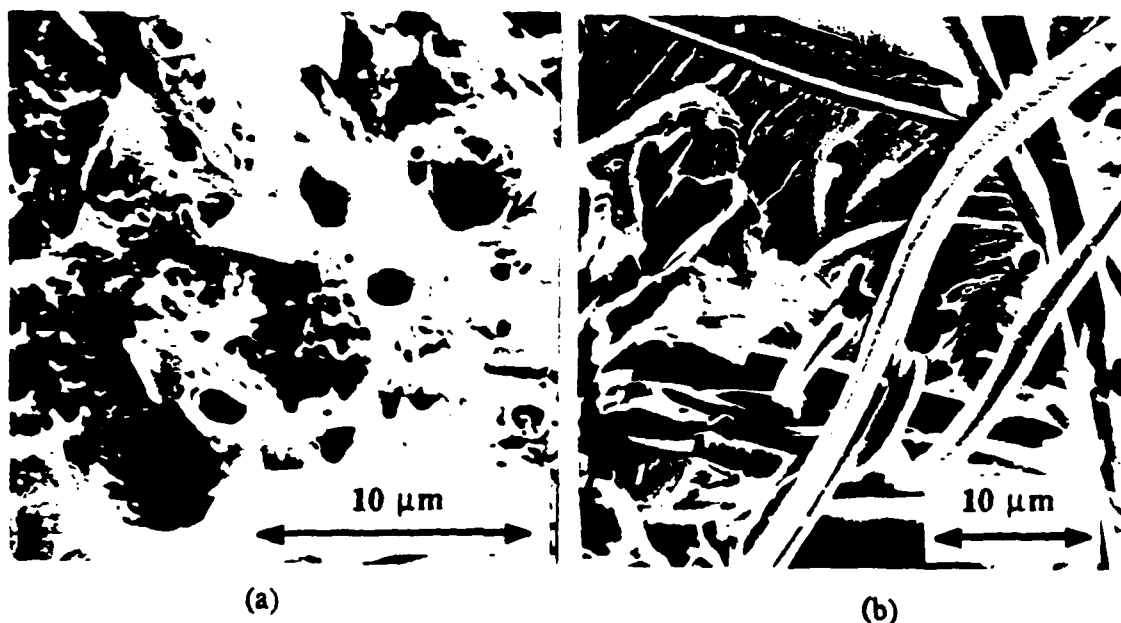
Fig. 5.5. U/C-PEEK composite subjected to (a) corona pretreatment level of $20J/mm^2$ and bonded to the epoxy-paste adhesive, and (b) corona pretreatment level of $10J/mm^2$ and bonded to the epoxy-film adhesive; locus of failure in both cases is cohesive through the adhesive.

5.3.3. X-Ray Photoelectron Spectroscopy Studies

The results from using XPS to study the locus of joint failure are summarized in Table 5.1 and the loci of failure in this table are from the SEM studies. Several noteworthy features

emerge from this table. Firstly, the surfaces of the joints which failed in a cohesive manner through the epoxy-paste adhesive have a lower concentration of oxygen to carbon ratio than from composite specimens which were abraded and solvent-wiped but not employed in adhesive bonding (control). Secondly, where the locus of failure was a mix of cohesive plus interfacial, then the XPS results reveal that the concentrations from elements, such as carbon and oxygen, have values between those from cohesive failures and those from "control" specimens. (It should be noted that the surfaces which had failed in a cohesive manner from using the epoxy-film adhesive had elements of similar concentrations as that of the "control" U/C-PEEK composite and therefore, distinctive comparisons could not be made). Thirdly, the surfaces of composites which had failed in an interfacial manner have similar concentrations of all the elements as the ones from "control" specimens. Fourthly, the surfaces of the adhesives from joints which had failed in an interfacial manner have similar concentrations of all the elements as the ones which had failed in a cohesive manner. Further, the electron binding energies from such specimens were equal. Therefore, these observations clearly show that weak boundary layers in the composite substrates or in the adhesive are not the essence of the poor adhesive bonding of the TPFC materials.

Table 5.1. X-ray photoelectron spectroscopy analysis of the modes of failure from U/C-PEEK composite DCB joints bonded to the epoxy-paste adhesive.

SEM observations	% concentration of elements			
(XPS analysis surfaces)	C1s	O1s	Si2p+F1s	O1s/C1s
Cohesive failure				
(analysis of the adhesive surfaces)	88.4±1.7	7.8±0.8	0.9±0.2	0.09
Cohesive + interfacial failure				
(analysis of the mixed adhesive/composite surfaces)	83.0±1.5	12.3±0.8	1.1±0.4	0.15
Interfacial failure				
(analysis of the composite surfaces)	78.6±1.6	17.1±0.7	2.3±0.4	0.22
Interfacial failure				
(analysis of the adhesive surfaces)	87.6±1.8	8.0±0.7	1.1±0.3	0.09
Not bonded "control"				
(analysis of the composite surfaces)	77.6±1.5	18.1±1.1	2.2±0.5	0.23

5.4. PREDICTION OF THE LOCUS OF JOINT FAILURE

5.4.1. Introduction

The studies reported in the previous chapter have clearly shown that for the thermosetting epoxy fibre-composite a simple abrasion/solvent-wipe pretreatment was all that was required to ensure a good interfacial strength with the bonded joints failing either by a cohesive fracture through the adhesive layer at high values of the adhesive fracture energy, G_c, or by interlaminar fracture through the composite substrate. In the case of the thermoplastic composites, a corona pretreatment was necessary to prevent the structural adhesive/composite interface failing at a very low value of G_c. Also, after the thermoplastic composites had been subjected to a certain level of corona treatment the value of G_c reached a maximum, plateau value. However, whilst in some cases this did correspond to a cohesive fracture through the adhesive layer at a high value of G_c, in other cases the "weak link" appeared to be the composite substrate itself. In those instances the bonded DCB joints failed by a new crack initiating between the laminae in the composite, very close to the adhesive/composite interface, and just above and/or below the crack-starter placed in the adhesive layer. This interlaminar crack then propagated through the composite substrate resulting in joint fracture. The important practical consideration is that such an interlaminar crack propagates at an applied load, and hence an adhesive fracture energy, G_c, below that associated with cohesive failure through the adhesive layer, see for example Figure 4.11 (page 112).

The above points may be clearly seen from the data shown in Table 5.2. Firstly, note that when the bonded joint fails by interlaminar fracture of the composite substrate the associated value of the maximum adhesive fracture energy, G_c(plateau), attained is significantly lower than when the locus of joint failure is via cohesive fracture through the adhesive layer. Indeed, when the joints fail by interlaminar fracture of the composite the measured value of G_c is very similar to that of G_c(il), as would be expected. Hence, using the present tough adhesives, this leads to the measured value of G_c plateau being sometimes only about 15 to 20% of what would be attainable if interlaminar fracture of the thermoplastic composite did not intervene as the operative failure mechanism. Secondly, as might be expected there is a greater tendency for the joints employing the epoxy-paste adhesive to exhibit an interlaminar failure of the composite substrate. This is because the epoxy-paste adhesive is the tougher of the two epoxy adhesives used and, hence, higher loads need to be applied to the joint to cause crack growth through the adhesive layer. These higher loads will give rise to higher stresses in the composite

substrate. Therefore, the composite may be able to withstand delamination when bonded with the less tough epoxy-film adhesive but will delaminate when subjected to the higher loads and stresses which can be imposed when the tougher epoxy-paste adhesive is employed. Thirdly, there appears to be little correlation between the interlaminar fracture energy, $G_c(il)$, of the composite and the propensity of the adhesive joint to fail by interlaminar failure of the composite substrate. For example, the epoxy-based composite has by far the lowest $G_c(il)$ value, but when bonded using the epoxy-film adhesive the joints show no signs of any interlaminar failure. Also, the unidirectional or the woven-carbon-fibre/PA thermoplastic composites possess only a moderate value of $G_c(il)$, but again DCB joints using these composites show no signs of any interlaminar fracture. Thus, it appears that some other property of the composite must control its tendency to delaminate when bonded and tested as a DCB joint.

Table 5.2. Joint and composite failure properties.

Composite	Epoxy-paste adhesive		Epoxy-film adhesive		Composite
	G_c(plateau)	Locus of failure	G_c(plateau)	Locus of failure	$G_c(il)$
U/C-PEEK	3.82	Cohesive	1.84	Cohesive	2.30
U/C-PA	3.77	Cohesive	1.86	Cohesive	1.10
W/C-PA	3.69	Cohesive	1.82	Cohesive	1.15
U/K-PA	0.60	Interlaminar	0.60	Interlaminar	0.65
W/K-PA	0.62	Interlaminar	0.66	Interlaminar	0.68
W/C-PEI	1.58	Interlaminar	1.82	Cohesive	1.60
U/C-PI	1.47	Interlaminar	1.42	Interlaminar	1.46
W/C-PI	1.43	Interlaminar	1.81	Cohesive	1.68
U/C-PPS	1.44	Interlaminar	1.48	Interlaminar	1.45
U/C-epoxy	0.25	Interlaminar	1.90	Cohesive	0.25

Notes:(i) "G_c(plateau)" is the plateau value of the adhesive fracture energy which for, the thermoplastic composites, occurs after a given corona pretreatment level; obviously this is the uniform constant value for the carbon-fibre/epoxy composite since no corona treatment is needed for this composite to ensure high G_c values and cohesive fracture.

(ii) "$G_c(il)$" is the interlaminar fracture energy for the composite.

(iii) All G_c values are in kJ/m^2.

5.4.2. Out-of-Plane Transverse Tensile Fracture Stress, σ_{yyc}, of the Composite Materials

5.4.2.1. σ_{yyc} Measurements

Since a new crack must form in the composite substrates by a transverse tensile fracture between the laminae the obvious property to investigate is the out-of-plane transverse tensile fracture stress, σ_{yyc}, of the composite materials. The recommendations of ASTM Standard D3039 were followed and specimens of 125X25X1.5mm were tested with the fibre direction being 90^0 with respect to the loading direction. Five such specimens were tested for each type of composite. It should be noted in these studies two assumptions have been made. Firstly, that the transverse tensile strengths of a unidirectional composite are equal in the directions perpendicular to the reinforced direction, and secondly that the transverse tensile strength is the same for both woven and unidirectional composites, provided the fibre type and the matrix resin are the same. The mean values of σ_{yyc} for the various composites are shown in Table 5.3 and, as may be seen, there is a good qualitative agreement between the values of σ_{yyc} and the propensity of the bonded DCB joint to exhibit an interlaminar failure mode: low values of σ_{yyc} are invariably associated with an interlaminar failure mode for the DCB joint, whilst high values of σ_{yyc} are associated with a cohesive failure through the adhesive layer.

Table 5.3. Correlation between the out-of-plane transverse tensile, σ_{yyc}, stresses to

failure for different cor:posites, SEM observations of the quality of

the fibre/resin bond and the locus of joint failure studies.

Composite	Transverse tensile stress σ_{yyc} (MPa)	Quality of fibre/resin bond	Locus of failure:	
			Epoxy-paste	Epoxy-film
U/C-PEEK	84.3±4.1	Good	Cohesive	Cohesive
U/C-PA	83.7±4.2	Good	Cohesive	Cohesive
W/C-PA	83.7±4.2	Good	Cohesive	Cohesive
U/K-PA	21.5±2.9	Poor	Interlaminar	Interlaminar
W/K-PA	21.5±2.9	Poor	Interlaminar	Interlaminar
W/C-PEI	42.8±2.5	Somewhat poor	Interlaminar	Cohesive
U/C-PI	46.7±3.1	Somewhat poor	Interlaminar	Interlaminar
W/C-PI	46.7±3.1	Somewhat poor	Interlaminar	Cohesive
U/C-PPS	29.4±3.6	Poor	Interlaminar	Interlaminar
U/C-epoxy	58.9±3.3	Good	Interlaminar	Cohesive

5.4.2.2. Fractographic Studies

Micrographs in Figures 5.6, 5.7 and 5.8 show the fractured surfaces from interlaminar tests of fibre-composites. There are distinctive features in these micrographs which reflect the quality of the fibre/resin bond and give some indication of the material's property. The property which is relevant in this chapter is the transverse tensile stress, σ_{yyc}. When the value of σ_{yyc} for the composite was low the fracture surface from the interlaminar tests revealed bare fibres ("poor" fibre/resin bond), see for example Figure 5.7(a). In this micrograph for the unidirectional-"Kevlar"-fibre/PA composite the "Kevlar" fibres are clearly visible and appear to have completely debonded from the polyamide copolymer matrix; the value of σ_{yyc} for this composite was found only to be about 21.5 MPa. In the case of the unidirectional-carbon/PI composite, see Figure 5.7(c) for example, the fibres do not seem to be completely exposed ("somewhat poor" fibre/resin bond) from the polyimide matrix, reflecting its higher σ_{yyc} value when compared to the U/K-PA composite. In the case of the unidirectional-carbon-fibre/PA

composite, see Figure 5.6(b) and the unidirectional-carbon-fibre/epoxy composite, see Figure 5.8 for example, the fibres appear to be relatively well embedded in the matrix polymer (i.e. "good" fibre/resin bond). Hence, the adhesion across the fibre/matrix interface appears to be higher, which leads to higher values of the transverse tensile fracture stress, σ_{yyc}, and so to less likelihood of the composite substrate delaminating during testing of the bonded DCB joint. Therefore, assuming that the intrinsic adhesion forces across the composite/adhesive interface are sufficiently strong, (assured by using a corona pretreatment in the case of the thermoplastic composites), then high values of σ_{yyc} lead to the crack being forced to remain in the adhesive layer and to a relatively high value of the adhesive fracture energy, G_c, being measured. It should be noted that the qualitative assessment of the adhesive at the fibre/resin interface is summarized in Table 5.3.

(a)   (b)
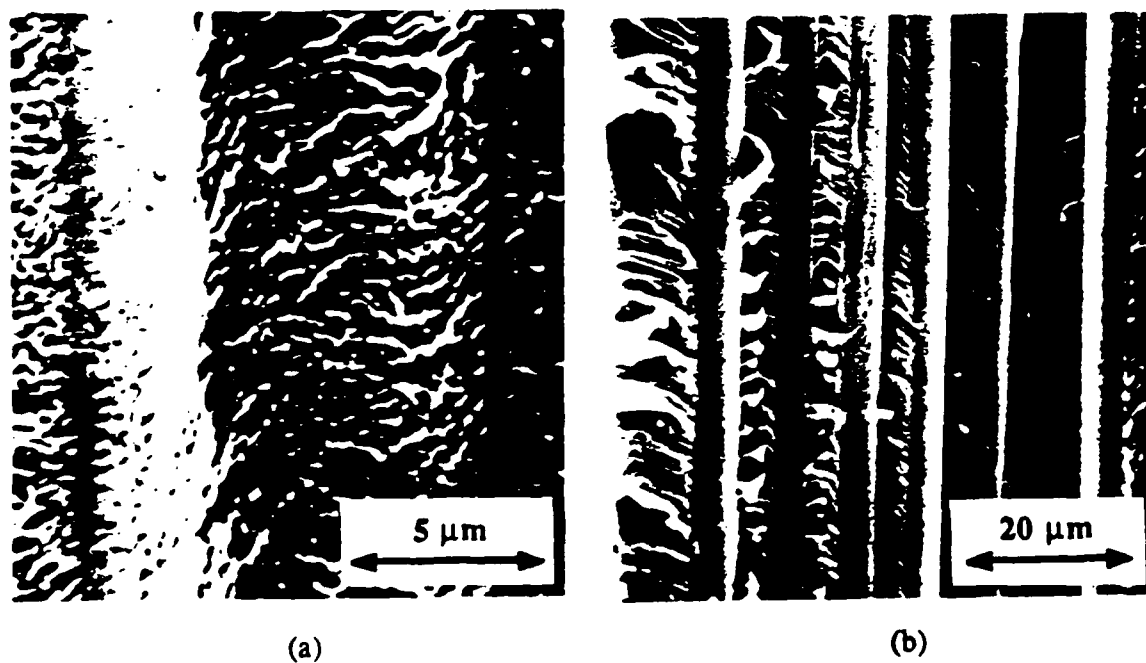
Fig. 5.6. SEM micrographs from interlaminar tests of the;
(a) U/C-PEEK and U/C-PA composites.
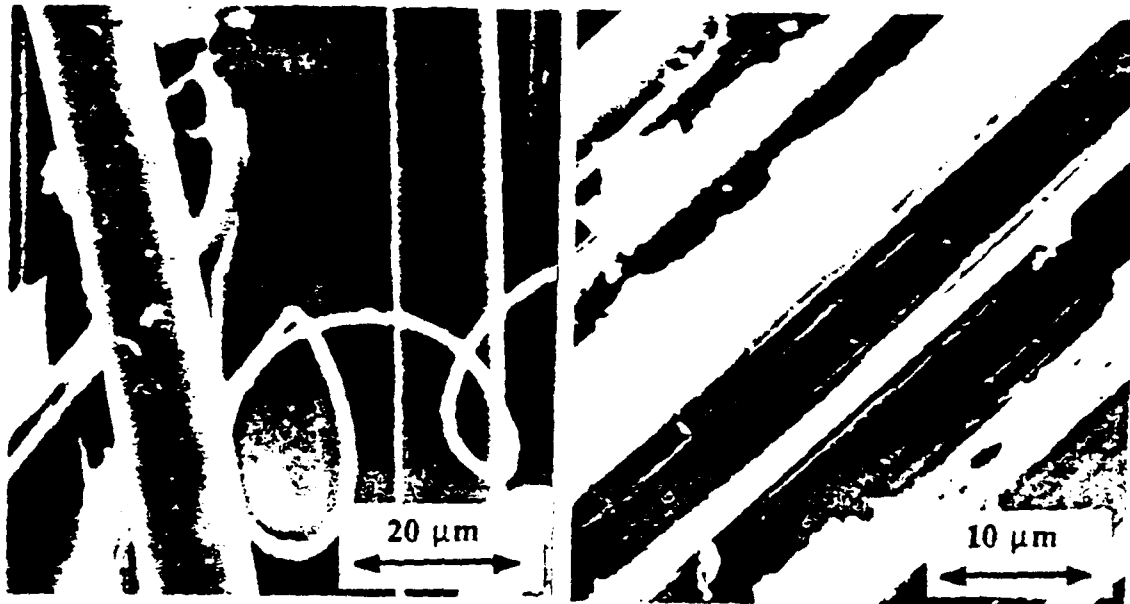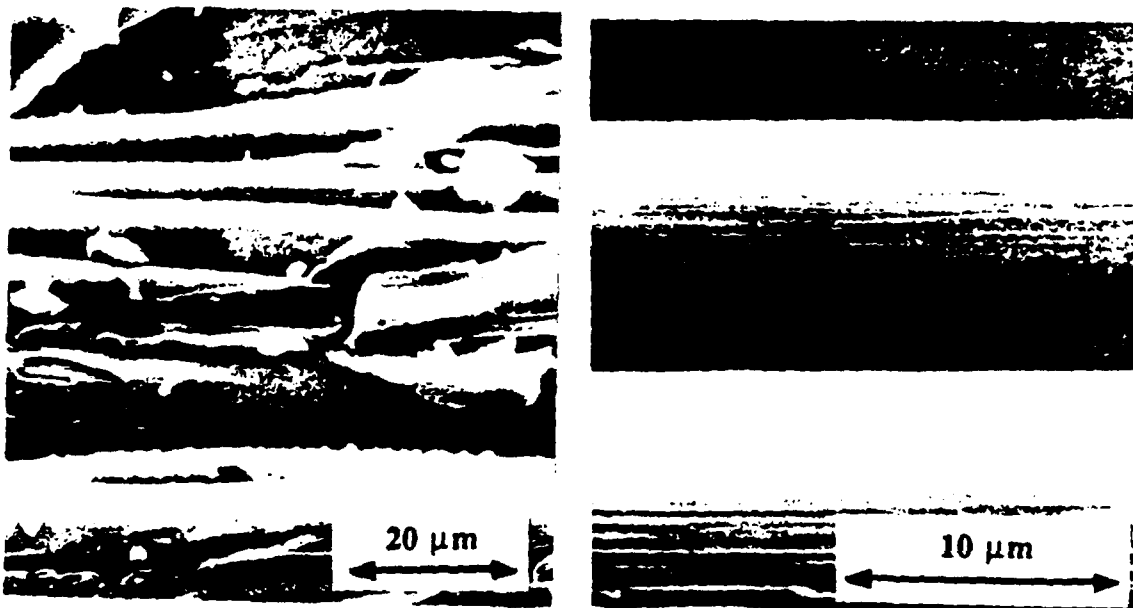
Fig. 5.7. SEM micrographs from interlaminar tests of the; (a) U/K-PA, (b) W/C-PEI, (c) U/C-PI, and (d)U/C-PPS composites.
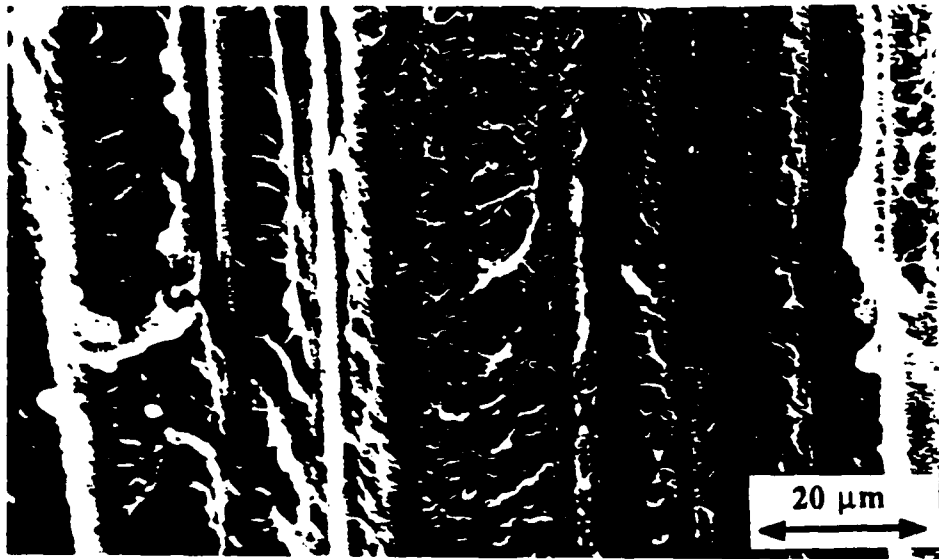
Fig. 5.8. SEM micrograph from interlaminar test of the U/C-epoxy composite.

5.4.3. Finite Element Analysis (FEA) Studies

To extend the above argument to a quantitative description it is necessary to ascertain the stress field surrounding the initial crack tip in the adhesive layer in the DCB joint. This stress field will extend into those regions of the composite substrates above and below the crack tip in the adhesive layer and will give rise to out-of-plane tensile stresses, σ_{yy}, acting to delaminate the composite. If the values of these σ_{yy} stresses can be estimated and compared to the values of σ_{yyc} (i.e. the measured out-of-plane transverse tensile fracture stress of the composite) then the tendency of the composite substrate to delaminate may be quantitatively assessed. To ascertain the values of the out-of-plane transverse tensile stresses, σ_{yy}, a numerical finite element analysis (FEA) approach was adopted. Before embarking on a detailed FEA studies of stresses in DCB composite joints some equations have to be derived and terminologies defined which are relevant to orthotropic materials.

5.4.3.1. Orthotropic Materials

The stress-strain relationships for anisotropic materials have been derived and are presented in Appendix A.5. Here, only special cases of anisotropy will be considered which are relevant to the unidirectional- and woven-fibre composites.

(i) Generally Orthotropic Materials

If there are two orthogonal planes of mechanical-property-symmetry for a material, then symmetry will exist relative to a third mutually orthogonal plane. Therefore, the compliance matrix, [S] will have nine independent constants and this type of material is defined as a generally orthotropic material [107].

$$[S] = \begin{bmatrix} S_{11} & S_{12} & S_{13} & 0 & 0 & 0 \\ S_{12} & S_{22} & S_{23} & 0 & 0 & 0 \\ S_{13} & S_{23} & S_{33} & 0 & 0 & 0 \\ 0 & 0 & 0 & S_{44} & 0 & 0 \\ 0 & 0 & 0 & 0 & S_{55} & 0 \\ 0 & 0 & 0 & 0 & 0 & S_{66} \end{bmatrix} \tag{5.1}$$

where $\quad S_{11}=S_{xx}=1/E_{11} \qquad S_{22}=S_{yy}=1/E_{22} \qquad S_{33}=S_{zz}=1/E_{33}$

$$S_{12}=S_{xy}=-\upsilon_{12}/E_{11} \quad S_{23}=S_{yz}=-\upsilon_{23}/E_{22} \qquad S_{31}=S_{zx}=-\upsilon_{31}/E_{33} \tag{5.2}$$

$$S_{44}=SH_{yz}=1/G_{23} \quad S_{55}=SH_{xz}=1/G_{13} \qquad S_{66}=SH_{xy}=1/G_{12}$$

and where E is the Young's modulus, G is the shear modulus, SH is shear compliance, υ is Poisson's ratio and S_{ij} are the compliances.

(ii) Transversely Isotropic Materials

A transversely isotropic material is an orthotropic material which is isotropic about one axis, for example, a unidirectional composite material. Therefore, for materials exhibiting transversely isotropic properties then the compliance matrix has only five independent constants. Now, if the material is isotropic around the x-axis, see Figure 5.9 then [108]:

$$S_{33} = S_{22} \qquad S_{66} = S_{55}$$

$$S_{13} = S_{12} \qquad S_{44} = 2(S_{22} - S_{23}) \tag{5.3}$$
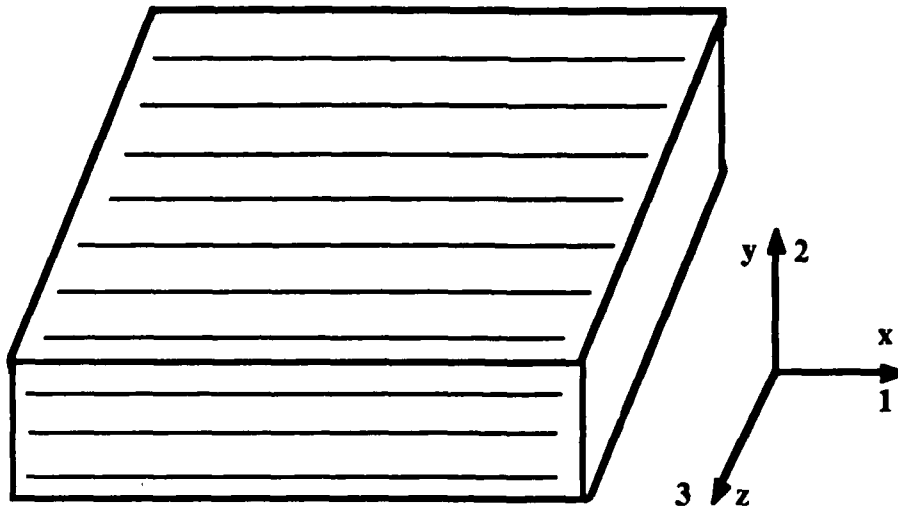
Fig. 5.9. A schematic drawing of an anisotropic material with its corresponding set of axes.

(iii) Square Symmetric Materials

A square symmetric material is one in which there are equal amounts of reinforcements in one plane, in two mutually perpendicular directions. An example is a bi-directional tape laminate, such as a woven-fibre composite. Now, in this case the compliance matrix has six independent constants [108] and if these reinforcements are in the x-z plane, see Figure 5.9, then:

$$S_{33} = S_{11} \qquad S_{23} = S_{12} \qquad S_{66} = S_{44} \qquad (5.4)$$

5.4.3.2. Application of Orthotropic Theory to 2-Dimensional Isotropic Finite Element Analysis in Plane-Strain Condition

To apply FEA to an orthotropic material, then commercially available packages make use of the relationships and equations set to solve for an isotropic material. The only difference encountered in these set equations is the stiffness matrix, [C], due to the anisotropy of the material. To set up this matrix for an orthotropic material, the elements of the compliance matrix, [S] are calculated since these are easily defined in terms of the material moduli and the respective Poisson's ratios, see Equation (5.2). Once the compliance matrix, [S], is calculated it is inverted to give the stiffness matrix, [C], corresponding to the stiffness matrix for an isotropic case.

For a 2-dimensional FEA in plane-strain condition then:

$$\varepsilon_{zz}=\gamma_{yz}=\gamma_{xz}=0 \quad \text{and} \quad \tau_{yz}=\tau_{xz}=0 \qquad (5.5)$$

Hence, the compliance matrix is given by:

$$[S] \quad \cdot \cdot \quad \begin{bmatrix} S_{11} & S_{12} & S_{13} & 0 \\ S_{12} & S_{22} & S_{23} & 0 \\ S_{13} & S_{23} & S_{33} & 0 \\ 0 & 0 & 0 & S_{66} \end{bmatrix} \qquad (5.6)$$

Therefore, to obtain the stiffness matrix, [C], then the terms of the compliance matrix, [S], in Equation (5.6) should be known which will be given in the following section.

5.4.3.3. Mesh Generation, Convergence and Material Properties

The numerical finite element analysis (FEA) adopted consisted of using the "PAFEC" FEA package [109]. For the FEA studies a DCB joint specimen was directly drawn on a "Sigmax 6164" terminal using the "PIGS" [110] multicolour 2-dimensional package. The terminal was connected to a "VAX 8600" computer on which the "PAFEC" FEA input files were run.

Because of the mid-plane symmetry, only the upper half of the DCB specimen was modelled in the finite element analysis. The experimental situation was simulated on the computer such that the top left hand node of the specimen was loaded. This same node was also constrained from moving in the x-direction. The nodes between the crack tip (point A) and the bottom right-hand node (point B) were constrained from moving in the y direction, see Figure 5.10. Eight-noded isoparametric-curvilinear-quadrilateral elements were used throughout the specimen, except at the crack tip where four six-noded quarter-point triangular elements were used to account for the singularity of the stresses at the crack tip. The elements were refined near the crack tip region where high stress variations and concentrations were expected. The crack-starter length was 20mm.

Loading node

Composite

1.5mm

Crack tip

Adhesive

0.2mm *

A

B

Crack length 20mm

Composite

Adhesive*

*) Four and five layers of elements employed
for the cold-cured (0.2mm) and the hot-cured
(0.25mm) adhesives respectively.

Crack tip

Z₀ X Y
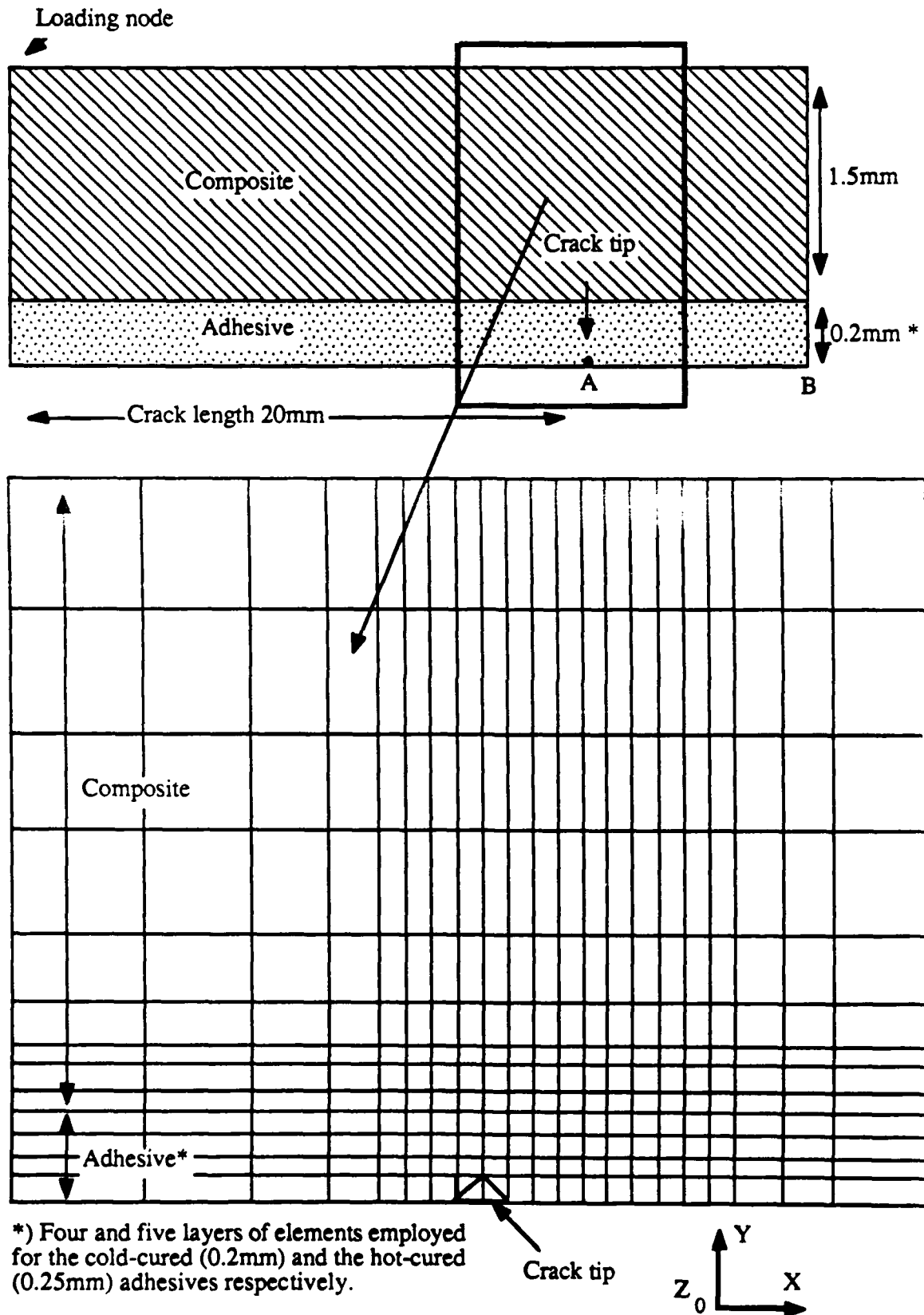
Fig. 5.10. Mesh distribution around the crack tip.

Prior to predicting the stresses, several conditions had to be satisfied. Some of these conditions were particular to the type of the FEA package employed. For example, the ratio of the longest side to the shortest side, in a quadrilateral element, had to be less than 15. Perhaps of greater importance was to satisfy a condition of convergence to ensure that the predicted stresses were accurate. For this purpose several meshes were generated and the predicted loads from the applied deflections were compared with the theoretical results from Equations (5.7) and (5.8):

$$G_c = \frac{P^2 a^2}{B^2 E h^3} \tag{5.7}$$

$$G_c = \frac{3P\Delta}{2Ba} \tag{5.8}$$

where P is load, a is crack length, B is width, E is Young's modulus, h is the height of one arm of the substrate, Δ is deflection of the substrate and G_c is the adhesive fracture energy. (The derivation of these equations from the compliance calibration, Equation (4.10), can be found in Appendix A.6).

The results from convergence analysis are shown in Figure 5.11. By employing 964 elements it was found that the error in the predicted load was about 1%. A further check was also conducted by comparing the stresses from adjacent elements which shared the same nodes in the region of the crack tip, which obviously is the critical area. It was found that these stresses from such nodes differed by a maximum value of 2.43%.
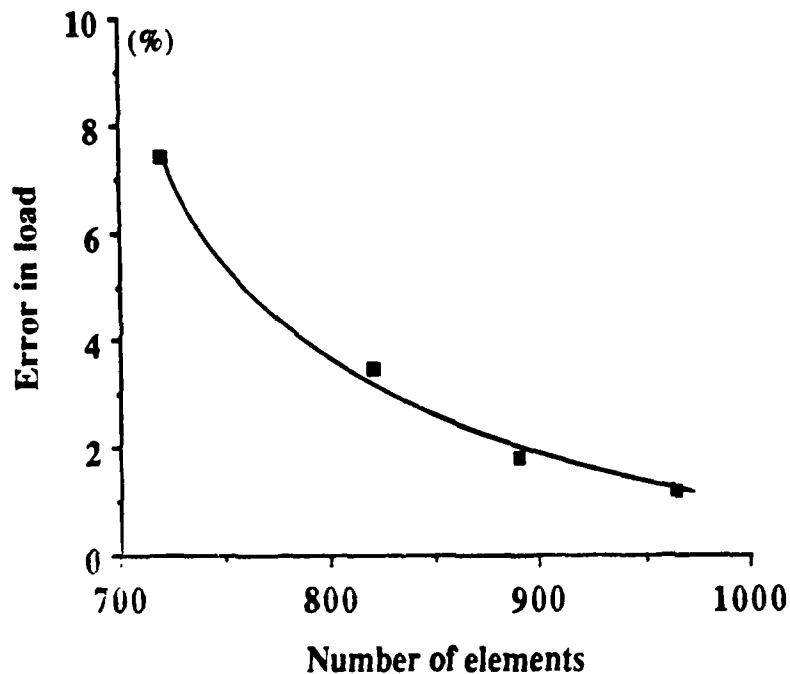
Fig. 5.11. Convergence test on the meshes generated.

Having obtained a satisfactory mesh then throughout the analysis 964 elements and 3070 nodes and 1038 elements and 3296 nodes were used for the DCB specimens bonded with the cold-cured epoxy-paste (EA9309.3) (total adhesive thickness 0.4mm) and the hot-cured epoxy-film (FM73M) (total adhesive thickness 0.5mm) respectively. The type of elements used were orthotropic for the substrates and isotropic for the adhesives. All the FEA studies were carried out assuming a plane-strain condition. Several assumptions were made for the FEA studies. Firstly, it was assumed that the adhesives and composites behaved in an elastic manner. Secondly, the deflections used in the FEA studies were calculated via Equation (5.8), assuming that the crack was going to run in a cohesive manner in the adhesive. For generally orthotropic material analysis "PAFEC" requires the seven directional compliances mentioned earlier in this chapter. The material properties used in the FEA studies for the adhesives and the composites are given in Table 5.4. Finally, it should be noted that the fibre reinforcement in the FEA studies is always in the x-z plane, as shown in Figure 5.9.

Table 5.4. Material property values used in the FEA studies.

(a) Adhesive properties

Adhesive	Tensile modulus (GPa)	Poisson's ratio
Epoxy-paste	1.85	0.36
Epoxy-film	2.45	0.36

(b) Composite compliance properties

Composite	S_{xx}	S_{yy}	S_{zz}	S_{xy}	S_{yz}	S_{zx}	SH_{xy}
				(m^2/N x 10^{-12})			
U/C-PEEK	7.41	97.1	97.1	-2.15	-29.1	-2.15	208
U/C-PA	8.0	105	105	-2.32	-31.6	-2.32	200
W/C-PA	13.7	105	13.7	-3.97	-3.97	-0.82	200
U/K-PA	13.1	178	178	-4.41	-53.6	-4.41	476
W/K-PA	26.7	178	26.7	-8.0	-8.0	-2.94	145
W/C-PEI	17.8	105	17.8	-5.36	-5.36	-1.43	200
U/C-PI	9.1	105	105	-2.7	-31.5	-2.7	200
W/C-PI	17.5	105	17.5	-5.26	-5.26	-1.4	200
U/C-PPS	8.13	105	105	-2.44	-31.5	-2.44	200
U/C-epoxy	6.67	105	105	-1.73	-31.5	-1.73	200

Notes: (a) Data for adhesives measured using tensile "dog-bone" specimens; at 20^0C and at a crosshead displacement-rate of 1mm/min.

(b) Data for composites from manufacturer.

5.4.4. Stress Analysis

In this section the details of the FEA stress studies will be presented in an attempt to analyse the effects of the composite's transverse tensile stress, crack length, composite and adhesive thickness on the locus of failure. The applied deflections, Δ, to the joints correspond to cohesive failure through the adhesive. Δ was calculated by solving for the load, P, in Equation (5.7) (where B=20mm, h=1.5mm, a=20mm and E=1/S_{xx} (see Table 5.4)) and then substituting P in Equation (5.8).

5.4.4.1. Prediction of Transverse Tensile Stresses from FEA

Figures 5.12 to 5.14 show the transverse tensile stress in the vicinity of the crack. These figures reveal several interesting features. Firstly, as expected for the tougher adhesive i.e., the epoxy-paste adhesive, the predicted transverse tensile stresses are higher than from employing the epoxy-film adhesive, compare Figures 5.12 and 5.13. This can be readily understood if it is considered that a larger deflection has to be applied for the crack to run in a cohesive manner in the tougher adhesive. Secondly, the directional moduli and Poisson's ratios of a particular composite affect the stress distribution in the substrate, for example the σ_{yy} stress distributions are different from employing the same epoxy-paste adhesive but different composite substrates, such as U/C-PA and W/K-PA, see Figures 5.12 and 5.14. Therefore, the choice of the adhesive and the composite will affect the σ_{yy} stress in the composite substrates, influencing the locus of joint failure.

It was shown earlier in this chapter that, for the composite joints which exhibited interlaminar failure then the fractured surfaces revealed that there was always a thin layer (approximately one lamina thick) of the composite on the adhesive side of the fractured surface. For this purpose not only the transverse tensile stress along the adhesive/composite interface will be presented but the values of the σ_{yy} stress in the composite substrate about one lamina thickness from the interface will also be considered. These stresses have been plotted from a position on the y-axis passing through the crack tip to a distance of 0.5mm along a line parallel to the x-axis, see Figures 5.15 to 5.18. Note that (i) the centre of the x-y axes is the crack tip and (ii) the stress predictions from the other composites are given in Appendix A.7.

Fig. 5.12. Transverse tensile stress distribution in the vicinity of the crack
tip for the U/C-PA composite bonded to the epoxy-paste adhesive.

Fig. 5.13. Transverse tensile stress distribution in the vicinity of the crack
tip for the U/C-PA composite bonded to the epoxy-film adhesive.

Fig. 5.14. Transverse tensile stress distribution in vicinity of the crack tip for the W/K-PA composite bonded to the epoxy-paste adhesive.

The numerical predictions in Figures 5.15 to 5.18 confirm the earlier observations that the moduli, Poisson's ratios and the adhesive type affect the transverse tensile stress distribution.

Furthermore, these figures reveal that for composites with thicker laminae then σ_{yy} at a lamina distance is lower than from those where the laminae are thinner. This feature may explain why for example the U/C-PI composite (thickness of one lamina 175μm) fails in an interlaminar manner whereas the W/C-PI composite (thickness of one lamina 350μm) fails in a cohesive manner through the adhesive when the epoxy-film adhesive is applied. The maximum values occurring in these figures are presented in Table 5.5, which are at the interface and at a distance of about a lamina in the composite. The distances at which these maximum values occur are around 0.1mm along a line parallel to the x-axis. Also, given in this table are the

measured out-of-plane transverse tensile fracture stresses, σ_{yyc}, for the composites.
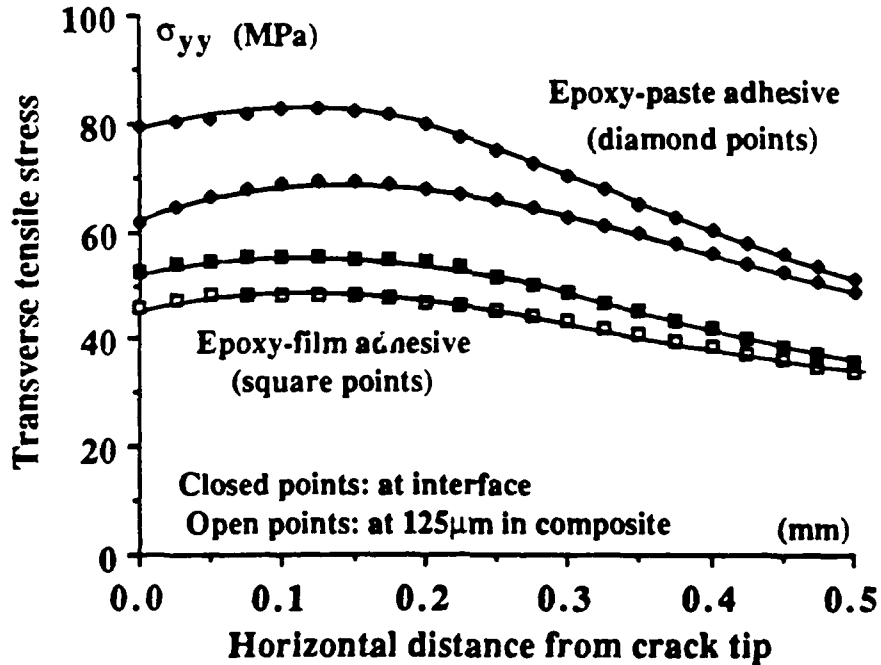
Fig. 5.15. Transverse tensile stress distribution in the
crack tip regions for the U/C-PA composite joint.
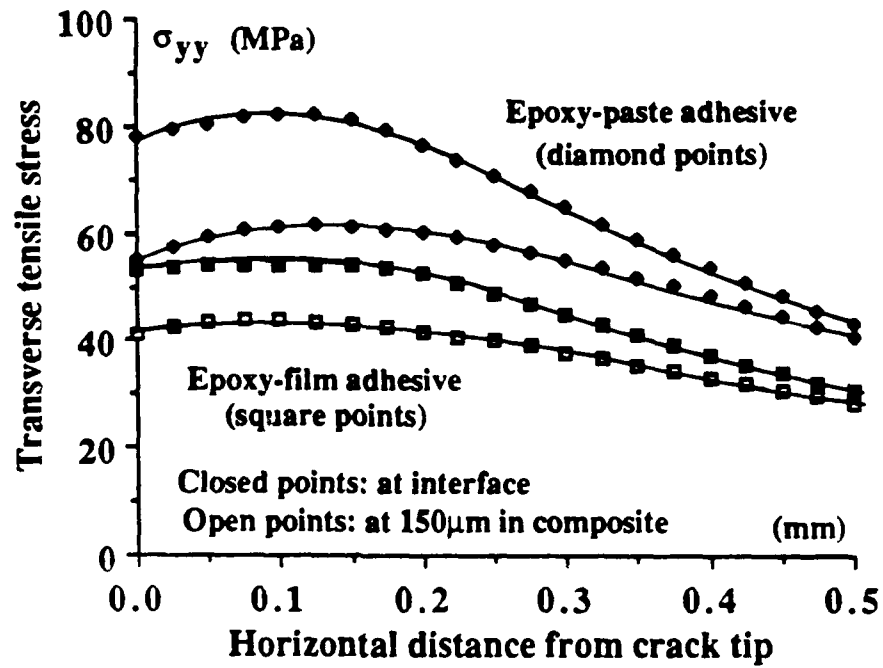
Fig. 5.16. Transverse tensile stress distribution around the crack tip regions for the W/K-PA composite joint.
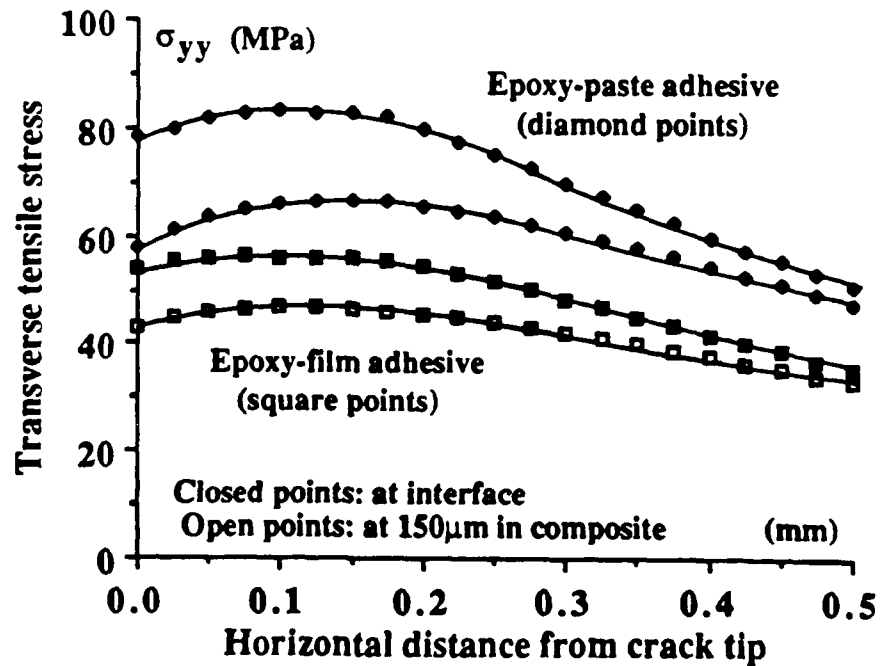
Fig. 5.17. Transverse tensile stress distribution in the crack tip regions for the U/C-PI composite joint.
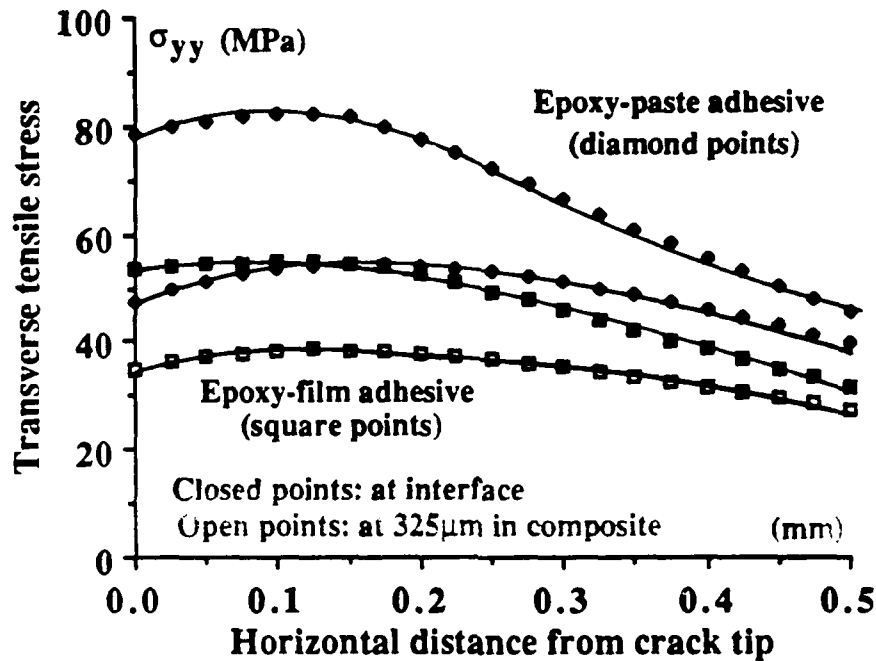
Fig. 5.18. Transverse tensile stress distribution in the
crack tip regions for the W/C-PI composite joint.

Now in Table 5.5 for those cases when the calculated values of σ_{yy}, at a distance of about a lamina in the composite, are lower than the measured out-of-plane transverse tensile fracture stress, σ_{yyc}, of the composite then it would be predicted that interlaminar fracture of the composite would not occur. Thus, provided the intrinsic strength of the interface is sufficient, the DCB joint would be expected to fail by a cohesive fracture through the adhesive layer. Conversely, when the calculated values of σ_{yy}, at a distance of a lamina in the composite, are higher than the measured out-of-plane transverse tensile fracture stress, σ_{yyc}, of the composite then it would be predicted that delamination of the composite substrate would now be the preferred mode of failure. As may be seen from the data presented in Table 5.5, the predictions based upon the above arguments are in excellent agreement with the experimental observations of the locus of failure. Thus, the locus of joint failure for DCB joints is governed by the relative values of the transverse tensile stress, σ_{yy}, in the composite in the region of the crack tip compared to the transverse fracture stress, σ_{yyc}, of the composite; assuming that a

sufficiently adequate surface pretreatment has been employed for the composite substrate prior to bonding.

Table 5.5. Values of the calculated out-of-plane transverse tensile stresses, σ_{yy}, (from FEA) when DCB tests are loaded to the equivalent of the maximum, plateau values of G_c for cohesive failures, the observed locus of joint failure (L o F) and values of the measured out-of-plane transverse tensile fracture stresses, σ_{yyc}, of the composites.

Composite	Data for DCB Joints - adhesive employed:						Composite
	Epoxy-paste adhesive			Epoxy-film adhesive			
	Maximum σ_{yy} at:			Maximum σ_{yy} at:			
	Interface	A lamina	L o F	Interface	A lamina	L o F	σ_{yyc}
U/C-PEEK	83.8	69.9	Coh	57.4	48.8	Coh	84.3
U/C-PA	82.9	69.3	Coh	55.6	48.5	Coh	83.7
W/C-PA	82.4	67.4	Coh	55.7	47.5	Coh	83.7
U/K-PA	81.2	61.8	Il	55.0	44.1	Il	21.5
W/K-PA	82.3	61.5	Il	54.2	42.9	Il	21.5
W/C-PEI	81.9	58.4	Il	54.2	41.9	Coh	42.8
U/C-PI	83.2	66.5	Il	56.4	48.5	Il	46.7
W/C-PI	82.4	55.6	Il	54.8	37.6	Coh	46.7
U/C-PPS	83.7	66.5	Il	55.5	48.2	Il	29.4
U/C-epoxy	83.7	69.1	Il	55.7	48.4	Coh	58.9

Notes: (i) G_c(plateau) is plateau value of the adhesive fracture energy which for, the thermoplastic composites, occurs after a given corona pretreatment level; obviously this is the uniform constant value for the carbon-fibre/epoxy composite since no corona treatment is needed for this composite to ensure high G_c values and cohesive fracture.

(ii) All stresses in MPa.

(iii) "Coh": cohesive in adhesive layer failure; "Il": interlaminar fracture in composite.

5.4.4.2. Effect of Initial Crack Length on the Mode of Failure

In the previous section it was shown that there was an excellent agreement between the experimental observations and the predictions from FEA. However, all the analyses presented so far have been based on DCB joint specimens with 20mm initial crack lengths. One interesting point to consider is whether the locus of failure is dependent on the initial crack length. This aspect will be discussed in this section.

If the bending moment M=Pa is substituted in Equation (5.7) then:

$$G_c = 12 \frac{M^2}{B^2 E h^3} \tag{5.9}$$

where B is the width, E is the modulus and h is the height of one arm of the composite beam.

From Equation (5.9) it can be seen that for a particular adhesive/composite DCB joint, the fracture energy and the material properties being constant, then the bending moment is also a constant and is therefore independent of the crack length. This observation suggests that the locus of failure should be independent of the initial crack length.

To confirm the above argument, experiments were conducted using the two epoxy adhesives bonded to two composites which exhibited different loci of failure: one cohesive using the U/C-PA as the substrate, and the other interlaminar using the W/C-PI as a substrate. The initial crack lengths were varied between 20 and 80mm. The locus of failure from such experiments confirmed the above argument i.e., the failure modes remained the same independent of the initial crack lengths.

In the FEA studies a new mesh was generated to predict the transverse tensile stress in the vicinity of the crack tip, now using an initial crack length of 40mm. It can be seen from Figure 5.19 that the transverse tensile stress distribution in the vicinity of the crack tip is very similar to the one presented previously in Figure 5.12, where the initial crack length was 20mm. Therefore, confirming the experimental observations discussed in the previous paragraph.
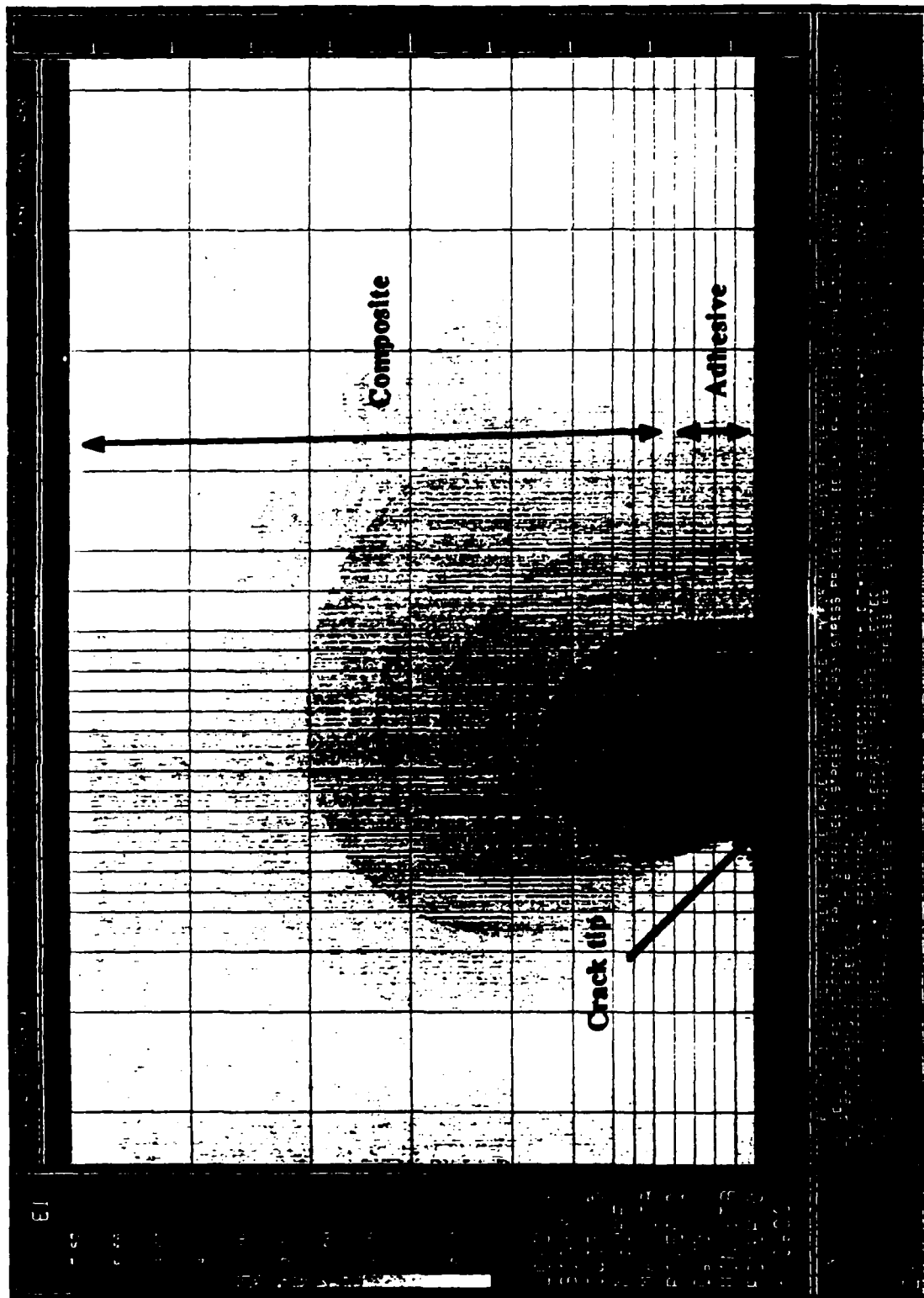
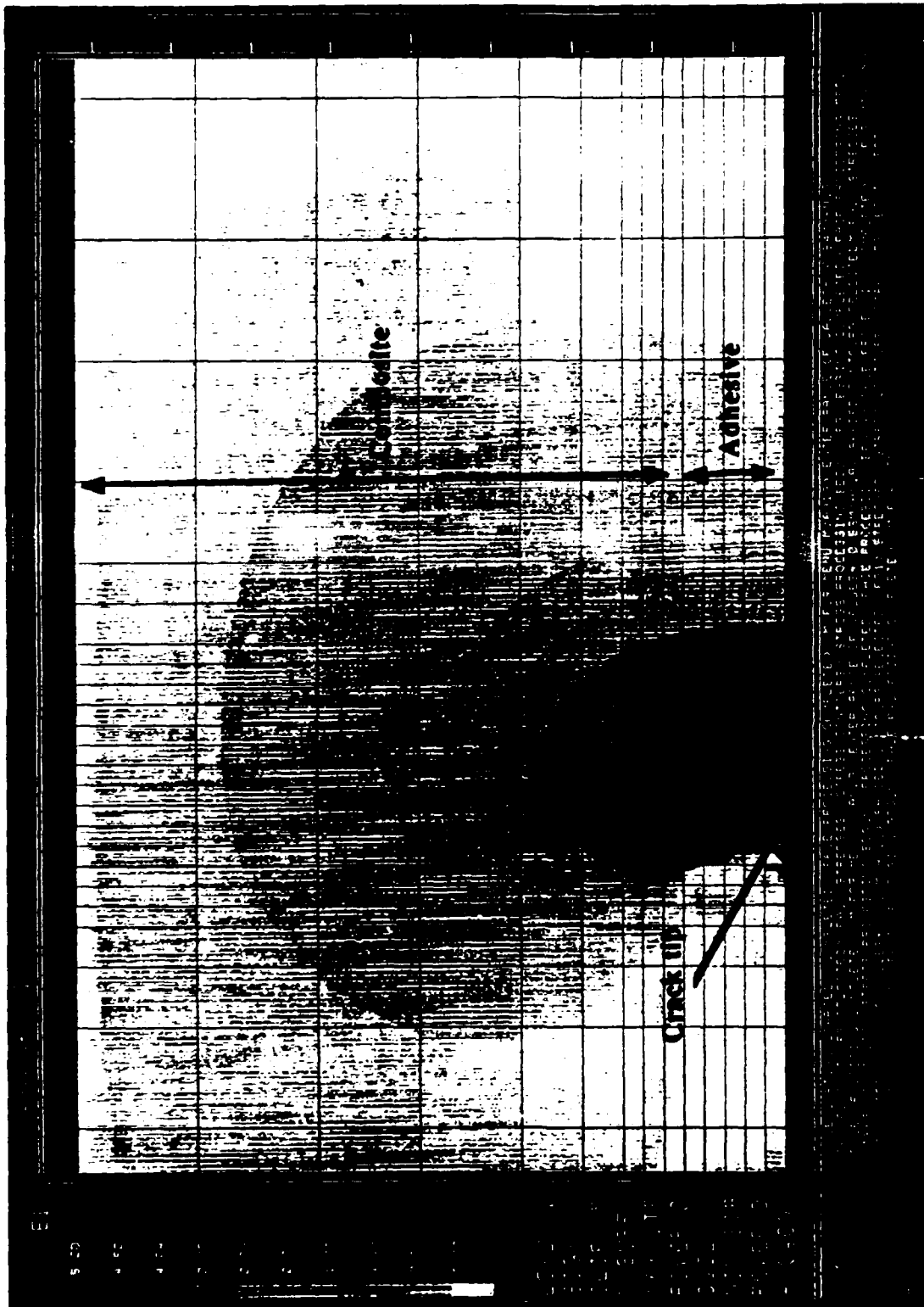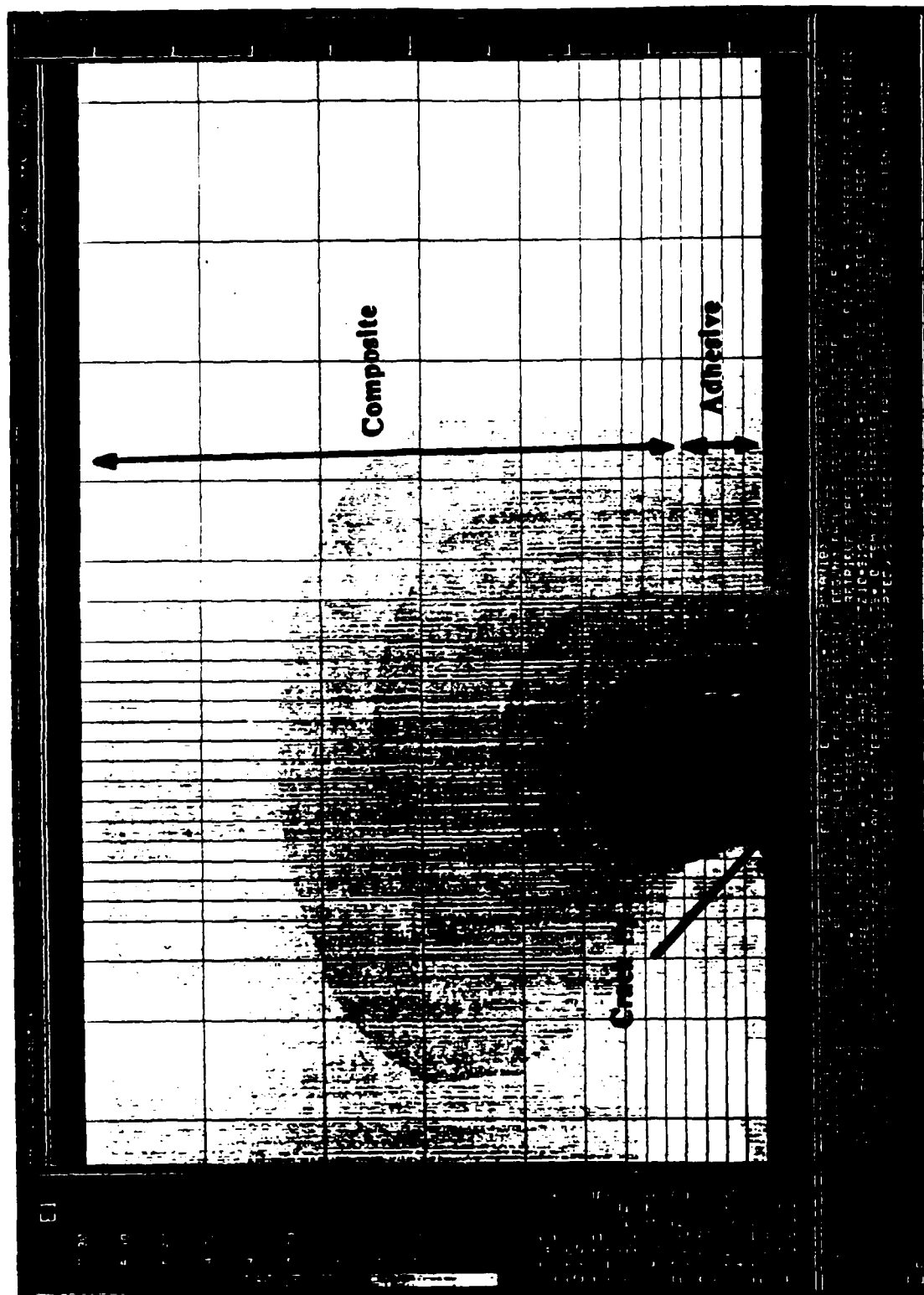Fig. 5.19. Transverse tensile stress distribution in the vicinity of the crack tip for the UC-PA composite bonded to the epoxy-paste adhesive; crack length is 40mm.

5.4.4.3. Effect of Adhesive and Composite Thickness on the Mode of Failure

In the previous chapter it was shown that the locus of failure and the fracture energy value were independent of the thickness of the composite materials employed. It was also shown that the locus of failure was independent of the thickness of the adhesive employed. However, the thickness of the adhesive layer did affect the measured fracture energy. To study the stresses in the vicinity of the crack tip from the above cases, new meshes had to be generated. The results from such analyses are summarized in Tables 5.6 and 5.7. It can be seen that the predicted modes of failure are in agreement with the experimental ones.

An interesting feature that emerges from the results in Table 5.6 is that, the adhesive thickness has vertually no effect on the predicted σ_{yy} stresses in the composite at the distances of interest in the current work. Although the adhesive fracture energy values from thicker adhesive layers are higher and therefore the applied deflections are higher (implying the predicted transverse tensile stresses will also be higher), but the distance from the crack tip to the interface is now longer which may neutralise the effect of the higher G_c values on the predicted σ_{yy} values in the substrate. In fact, Kodokian and Kinloch [111] showed that the transverse tensile stress in the adhesive in a DCB composite joint (along the y-axis passing through the crack tip) varies according to the relationship:

$$\sigma_{yy} = \frac{K_I}{\sqrt{2\pi r}} \cos\theta \left[1 + \sin\frac{\theta}{2} \sin\frac{3\theta}{2} \right] \qquad (5.10)$$

where r is the distance from the crack tip, θ in this case is 90^0 and K_I is given by:

$$K_I^2 = \frac{EG_c}{(1 - \upsilon^2)} \qquad (5.11)$$

where E is the Young's modulus of the adhesive, υ is its Poisson's ratio. Therefore, for longer distances, r, the σ_{yy} stress in the adhesive decreases which will, of course, decrease the transverse tensile stress in the composite substrate (i.e. neutralise the effect of a higher G_c).

An interesting feature also emerges from the results presented in Table 5.7. The transverse tensile stress at a lamina distance inside the composite increases. This can be readily

understood if it is considered that the substrate is now stiffer and therefore the stresses may be higher. The obvious question that arises is whether the mode of failure would switch into one of interlaminar if the thickness of the composite substrates are further increased. Although this point is beyond the scope of this study but the FEA predictions certainly indicate that interlaminar failure may occur, especially if a composite is employed which has a transverse tensile fracture stress close to the predicted σ_{yy} values at a distance of a lamina.

Table 5.6. Values of the predicted out-of-plane transverse tensile stresses, σ_{yy}, from FEA for DCB U/C-PEEK composite (h=1.5mm) joints bonded using the epoxy-paste adhesive.

| Total adhesive thickness | Experimental | | FEA predictions | |
| | Fracture energy | Locus of failure | Maximum σ_{yy} at: | |
t (mm)	G_c (kJ/m^2)		Interface	A lamina
0.2	2.52	Cohesive	83.4	70.1
0.3	3.41	Cohesive	82.9	70.6
0.4	3.82	Cohesive	83.8	69.9
0.5	5.12	Cohesive	83.1	68.5
0.6	5.85	Cohesive	83.1	69.8

Table 5.7. Values of the predicted out-of-plane transverse tensile stresses, σ_{yy}, from FEA for DCB U/C-PEEK composite joints bonded using the epoxy-paste adhesive, (thickness is 0.4mm) and loaded (deflection) to equivalent value of G_c=3.9kJ/m^2.

| Composite thickness | Maximum σ_{yy} at: | | |
t (mm)	Interface	A lamina	Locus of failure
1.0	83.9	65.0	Cohesive
1.5	83.8	69.9	Cohesive
2.0	83.5	71.1	Cohesive
3.0	82.8	72.9	Cohesive
4.0	82.0	73.4	Cohesive

(Recall that the transverse tensile fracture stress, σ_{yyc}, of the U/C-PEEK composite is 84.3MPa which is higher than the predicted values in the above tables).

5.4.4.4. Prediction of σ_{yy} Stresses at the Onset of Delamination

In Section 5.4.4.1 the crack was assumed to run in a cohesive manner for all the adhesive/composite combinations. Hence the transverse tensile stresses, σ_{yy}, were predicted to confirm if the crack would propagate in the adhesive in a cohesive manner. For this reason the σ_{yy} values were compared with the tensile fracture stress of the composites, σ_{yyc}. In this section the actual deflection (obtained from fracture experiments) at the onset of delamination will be employed to predict the transverse stresses in the vicinity of the crack tip.

The two cases studied were the U/K- and W/K-PA thermoplastic composites (1.5mm thick) bonded using the epoxy-paste adhesive (0.4mm thick). The bending moments for delamination were calculated from the experiments and they were found to be about 1750 and 1200Nmm respectively. Further, the actual deflections at the onset of delamination were employed in the FEA studies. The maximum transverse tensile stresses occurring at the interface and about a distance of about a lamina inside the composites were predicted to be 24.2 and 21.8MPa for the U/K-PA and 23.6 and 19.8MPa for the W/K-PA thermoplastic composites respectively, see also Figure 5.20. These stresses are in excellent agreement with the measured transverse tensile failure stress for this particular composite which is 21.5MPa. Therefore, these FEA studies confirm that once the transverse tensile stresses in the vicinity of the crack tip in the substrate reach the transverse tensile failure stress of the composite then the substrate delaminates, and subsequently the crack propagates in an interlaminar manner at a value of G_c equal to the interlaminar fracture energy.
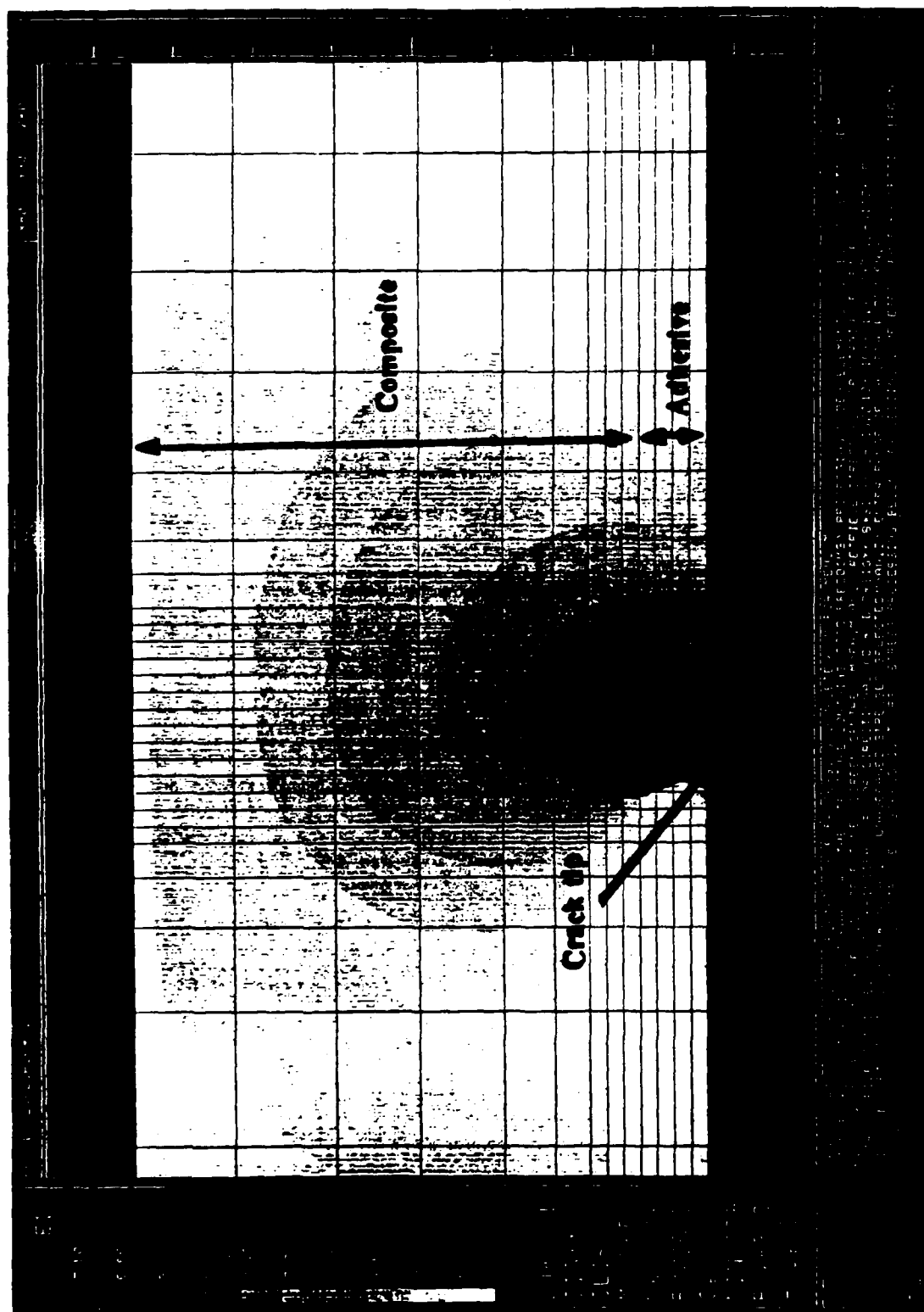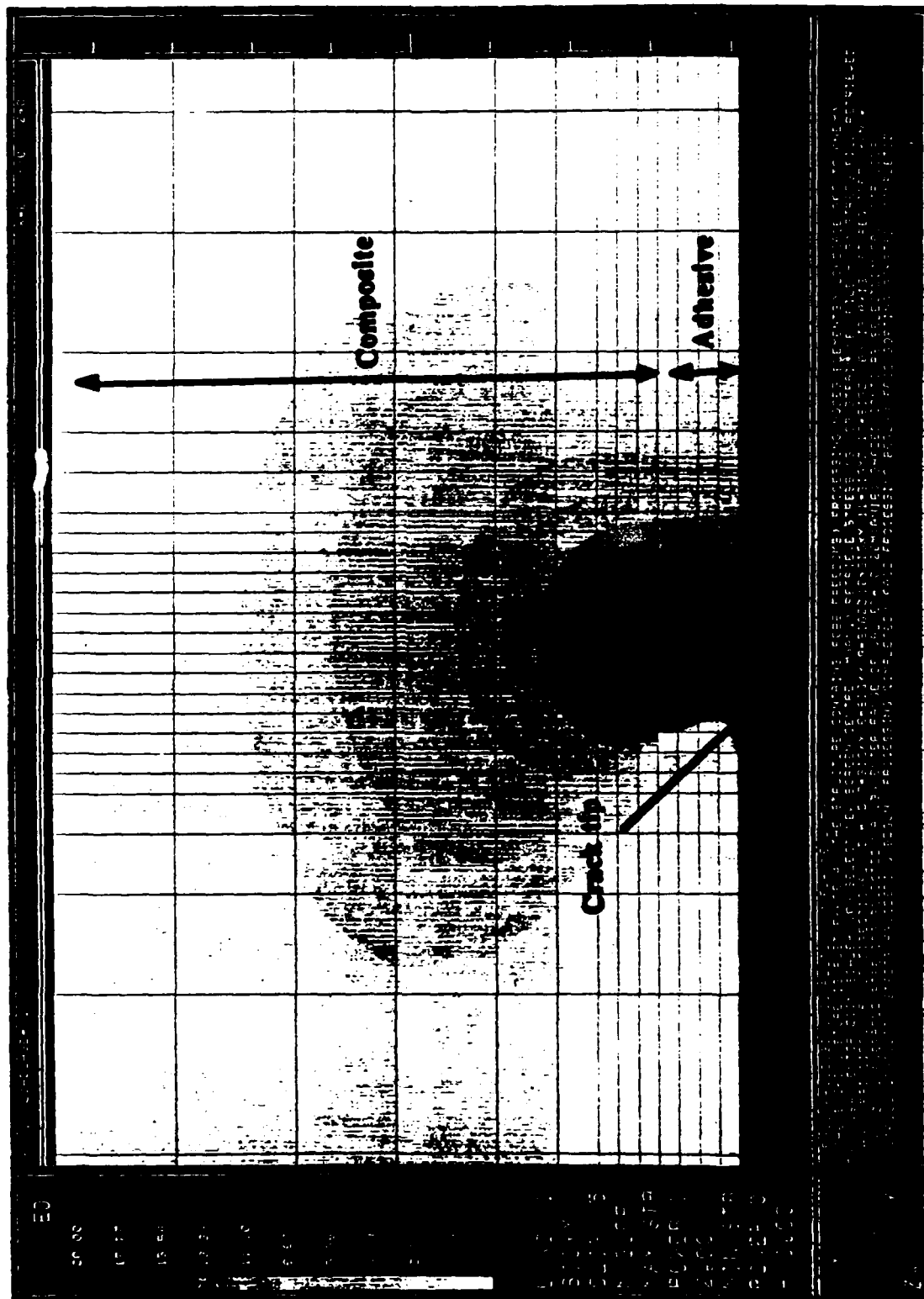
Fig. 5.20. Transverse tensile stress distribution in the vicinity of the crack tip for the W/K-PA thermoplastic composite bonded to the epoxy-paste adhesive; stresses from actual deflection.

5.5. CONCLUSIONS

The conclusions that may be drawn from this chapter are:

1. Scanning electron microscopy (SEM) was successfully employed to identify the regions of interfacial, interlaminar, cohesive and mixed loci of joint failure. It was shown that the interlaminar fracture studies can provide a good qualitative assessment of the fibre/resin bond strength. X-ray photoelectron spectroscopy (XPS) was successfully employed to confirm the loci of joint failure.

2. It was shown that the composite property which governs the mode of failure, provided the composites had been pretreated to an adequate corona energy level, was the out-of-plane transverse tensile fracture stress, σ_{yyc}. Composites possessing low values of σ_{yyc} resulted in crack propagation in the composite, whereas, composites possessing high values of σ_{yyc} resulted in the crack propagating now in the adhesive in a cohesive manner. It was also shown that there was a good correlation between the quality of the fibre/resin bond, assessed employing SEM, and the measured transverse tensile failure stresses of the fibre-composites.

3. Finite element analysis (FEA) was successfully employed to predict the transverse tensile stresses in the vicinity of the crack tip. It was shown that if the predicted transverse tensile stress was higher than the measured transverse tensile stress of the composite then the "weak" link was the composite, provided that the interfacial contact was strong due to corona treatment. Now, if the predicted transverse tensile stresses were lower than the measured transverse failure stress then failure occurred in the composite. If the predicted values were lower than the measured ones then failure occurred in the adhesive. The modes of failure from experimental observations and the FEA predictions were in excellent agreement.

4. It was shown that, conditions such as adhesive thickness and initial crack length do not determine the mode of failure. Further, it was shown that there was a tendency of the predicted σ_{yy} values to increase with increasing composite thickness. However, for the composite thicknesses employed in the current work the locus of failure was not influenced by the relatively small change in the predicted σ_{yy} values. Finally, it was shown that the locus of failure was governed by the transverse tensile failure stress of the composite, thickness of the lamina and the fracture energy of the adhesive employed.

CHAPTER SIX

THE MECHANISMS OF ADHESION

6.1. INTRODUCTION

In the previous chapters treatment techniques have been described, especially corona-discharge, which increase the intrinsic adhesion of the TPFC substrates to the structural adhesives employed. Surface characterisation was employed to understand the effects of these treatment techniques on the surfaces of the composites and a fracture mechanics approach was used to give a mechanical evaluation of the quality of the adhesive/composite bond. The aim of the present chapter is to identify the mechanisms of adhesion.

6.2. LITERATURE SURVEY

6.2.1. Introduction

The literature survey will present a critical review of the current philosophies in the field of adhesion science. The review will first consider surface and interfacial aspects of adhesion and, secondly, the theories of adhesion.

6.2.2. Interfacial Contact

The establishment of intimate molecular contact at the adhesive/substrate interface is a necessary but sometimes insufficient requirement for developing strong joints. This means that the adhesive needs to spread over the solid substrate and needs to displace air and contaminants that may be present on the surface. An adhesive which conforms ideally to these conditions should [112]:

(a) when liquid, exhibit zero or near zero contact angle,

(b) at some time during the bonding operation have a viscosity that should be relatively low,

(c) be brought together with the substrate at a rate and manner that should assist the displacement of any trapped air.

In order to assess the ability of a given adhesive/substrate combination to meet the above criteria it is necessary to consider wetting, to ascertain the surface free energies of the adhesive/substrate interface and to examine the kinetics of wetting. Some of the above topics

have already been reviewed in detail in Chapter Three (Section 3.2). Therefore, firstly, some aspects of the thermodynamics of wetting will be discussed further and, secondly, the kinetics of wetting will be reviewed.

6.2.2.1. Thermodynamics of Wetting

In Section 3.2.2.2, the wetting equilibria of a liquid on a solid was presented and it was shown, that (Equation (3.2)):

$$\gamma_s = \gamma_{SL} + \gamma_{LV} \cos\theta \qquad (6.1)$$

when $\theta > 0^0$ the liquid is nonspreading, see Figure 3.1 (page 39), but when $\theta = 0^0$ the liquid wets the substrate completely and spontaneously, and spreads over the surface at a rate depending on the liquid viscosity and solid surface roughness. Thus, for spontaneous wetting to occur the.

$$\gamma_s \geq \gamma_{SL} + \gamma_{LV} \qquad (6.2)$$

This criterion may also be expressed by defining a parameter termed the equilibrium spreading coefficient, S_c, where [113]:

$$S_c = \gamma_s - \gamma_{SL} - \gamma_{LV} \qquad (6.3)$$

Hence, a liquid will spread spontaneously and completely wet a solid surface when $S_c \geq 0$. It

is also possible of course, to make a liquid spread across a solid surface when $\theta \geq 0^0$, but this would require the application of pressure to the liquid to spread it forcibly over the substrate. By analogy to Equations (3.6) to (3.8) it is possible to rewrite Equation (3.8) as:

$$\gamma_{SL} = \gamma_s + \gamma_{LV} - 2(\gamma_s^d \gamma_{LV}^d)^{0.5} - 2(\gamma_s^P \gamma_{LV}^P)^{0.5} \qquad (6.4)$$

Substituting Equation (6.4) into Equation (6.3) and rearranging then:

$$S_c = 2(\gamma_s^d \gamma_a^d)^{0.5} + 2(\gamma_s^P \gamma_a^P)^{0.5} - 2\gamma_a \qquad (6.5)$$

Where the subscripts s and a stand for the substrate and adhesive respectively. Therefore, from a knowledge of the surface free energies of the adhesive and the composite it is possible to

evaluate the spreading coefficient, S_c.

6.2.2.2. Kinetics of Wetting

So far wetting has been considered from a thermodynamic point of view but the kinetics of wetting are also important.

(i) Surface Tension Gradients

Bascom et al. [112, 114] employed interference microscopy and ellipsometry to show that if the contact angle is zero, surface tension gradients may exist at the spreading front which may assist or hinder spreading depending on their direction. These surface tension gradients arise from thermal gradients or, in the case of liquids containing a more volatile component of different surface free energy, they may arise from a concentration gradient. This effect is shown in Figure 6.1. At the leading edge there is a thin (either 1 or 2 monomolecular layers) primary film which is followed by a transition region in which thermal or concentration gradients create a surface flow that drags the underlying liquid forward. Spreading rates resulting from this gradient effect are relatively low: typically about $0.1\mu m/s$ for a polysobutylene fluid on polished steel [115] and therefore, surface tension gradients will be ignored in the current research work.
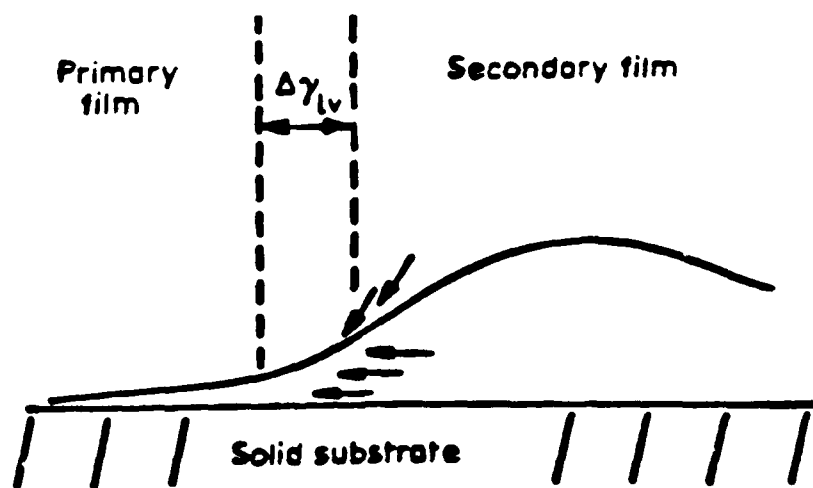
Fig. 6.1. Schematic diagram of the surface and bulk flow patterns
at the edge of a spontaneously spreading film [112].

(ii) The Influence of Surface Roughness

The topography of the substrate surface may assist the kinetics of wetting.

Firstly, Bascom et al. [114] have reported that random surface scratches increased the spreading rate of some liquids by as much as 50% and that open capillaries filled well ahead of the advance of the primary film. Similar observations have also been reported by Cottington et al. [116]. Cheever [117] has studied zinc phosphate conversion coatings and treated the situation theoretically as a capillary matrix in which the capillaries assume the particular shape of slits. He calculated the capillary pressure which was generated in the zinc phosphate coating to be about 0.7MPa. However, spreading rates from this effect and surface tension gradients are not high and may be overshadowed when a liquid is forcibly spread on a substrate. For example, the pressures required to cure the adhesives in the current project were much higher than the above capillary pressure. Nevertheless, Bascom and Patrick [112] have suggested that such effects may indeed play a role in the redistribution of the adhesive after its initial application.

Secondly, Wenzel [38] has shown that another effect of surface roughness is to change the apparent contact angle observed for a rough solid surface compared to the same angle observed for a smooth surface. This change in the apparent contact angle was considered in Section 3.2.2.5. On a smooth surface, if θ is less than 90^0, roughening the surface will result in the measured contact angle being even smaller, thus increasing the apparent surface free energy of the solid surface and consequently also the extent of wetting. However, if θ is greater than 90^0 on a smooth surface then roughening the surface will have the opposite effect i.e., the measured contact angle will increase and hence lead to a decrease in the apparent surface free energy.

Thirdly, de Bruyne [118] has modelled various types of substrate surface topography and obtained quantitative expressions for the relationship between the extent of wetting and the driving pressure. Figure 6.2 shows the capillary penetration to be expected under atmospheric pressure and against the back pressure of trapped air, as a function of the contact angle made on the solid by the penetrating liquid. The limited penetration of the "ink-bottle" pits is especially marked and this situation will further be aggravated if the liquid has a viscosity greater than a few centipoises and is forced rapidly across the substrate surface. Under these circumstances the liquid cannot keep up with the advancing front and so a higher dynamic contact angle develops [112, 119, 120]. The model developed by de Bruyne provides some interesting insights into the way liquids penetrate particular surface topographies. Unfortunately, surface pores developed from pretreatment techniques, especially from pretreatments employed in the current work, will very rarely possess idealised 90^0 corners or be "ink-bottle" pits but are more likely to be "crater" pores. Therefore, his work is of limited application in a practical situation.
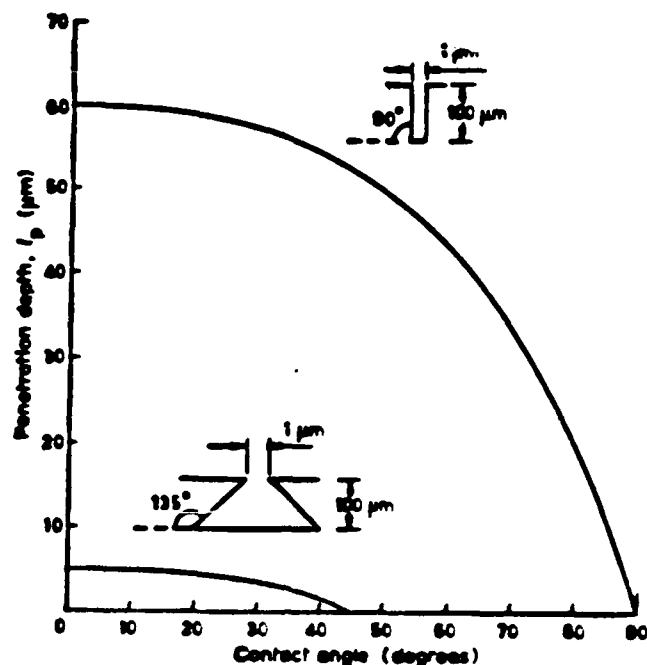
Fig. 6.2. Comparison of the penetration of a film into cylindrical and "ink-bottle" pits [118].

6.2.3. The Theories of Adhesion

In the literature, there is much controversy regarding the basic reason for the intrinsic adhesion that may exist between two different materials. However, there does appear to be agreement that intrinsic adhesion forces that may occur across an interface may be explained by one, or more, of the following theories:

a) the mechanical interlocking theory,

b) the diffusion theory,

c) the electrostatic theory and

d) the adsorption theory.

6.2.3.1. The Mechanical Interlocking Theory

According to this theory, mechanical interlocking occurs between an adhesive and the irregularities or pores of a substrate. In the literature, there is evidence to show that in few isolated cases mechanical interlocking can be of prime importance. A very good common example is mercury amalgam for filling tooth cavities. However, when adhesion to a rough surface is concerned, other factors must be considered. For example, a rough surface will have a larger potential bonding area than a smooth one and wetting will be improved as discussed above.

An area where mechanical interlocking may contribute significantly to the intrinsic adhesion is in the metal plating of plastics where a chemical pretreatment of the plastic substrate is employed prior to plating. Some workers [121-125] have argued that the adhesion of metal plating to polymeric substrates is a function of the surface topography of the substrate. However, others [126-128] have emphasized the role of increased oxidation of the plastic. The metal plating of acrylonitrile-butadiene-styrene (ABS) copolymer is probably a good example to demonstrate the above arguments. To obtain satisfactory adhesion it is necessary first to carry out a pretreatment with chromic-acid solution, which dissolves rubber particles near the polymer surface leaving a porous structure providing, as some workers suggest, a mechanical keying. Atkinson et al. [129] in 1967 produced scanning electron micrographs which supported this theory. However, micrographs alone can be misleading and unfortunately in 1967 XPS was not yet developed and any surface chemical changes that accompanied the chromic-acid treatment of the the polymers could not be detected.

Packham et al. [130, 131] have provided much evidence showing the importance of surface roughness in the adhesion between polyethylene and metals. Wake [132] has shown that stress concentrations due to voids may be important and Kinloch [133] has emphasized that the energy dissipated viscoelastically and plastically during fracture may be much larger with a rough surface. Further, Tabor et al. [134, 135] and Johnson et al. [136] have examined the adhesion between very smooth surfaces. Their work provided clear evidence that with smooth surfaces it is possible to attain good adhesion. Therefore, their work exposes the mechanical interlocking theory to be far from proven.

Therefore, from the arguments presented above it can be concluded that, if surface roughness is increased by a treatment technique, then before suggesting that mechanical interlocking is the adhesion mechanism:
(i) The effect of the pretreatment on the surface chemistry of the susbtrates should be investigated.
(ii) It should be noted that the increased surface roughness will give an increased surface area.
(iii) Further, surface roughness will undoubtedly assist in the kinetics of wetting as was discussed earlier in Section 6.2.2.2.
Therefore, the above effects should be assessed.

6.2.3.2. The Diffusion Theory

According to this theory chain segments of the adhesive macromolecules diffuse into the substrate, thereby essentially eliminating the interface. This theory can only apply to polymeric substrates since it requires macromolecules of the adhesive and the substrate to possess

sufficient chain mobility and be mutually soluble (i.e. have very similar solubility parameters). The solubility parameter, δ_s, may de defined by [137]:

$$\delta_s = \left[\frac{\Delta H_v - R_g T}{V_{mv}} \right] \tag{6.6}$$

where ΔH_v is the molar heat vaporization, R_g is the gas constant, T is the temperature (K) and V_{mv} is the molar volume.

Voyutskii [138] and Vasenin [139] have been strong advocates of the diffusion mechanism. Voyutskii's evidence is based on bonding experiments where the adhesive and the substrate are identical. In particular, he studied the bonding of rubbers at elevated temperatures and found that the joint strength increased with increasing period of contact, increasing temperature, increasing pressure, decreasing molecular weight, the addition of plasticisers and decreased with cross-linking.

There is little direct evidence of diffusion in adhesive joints although various workers, including Bueche et al. [140], have demonstrated self-diffusion in the bulk phase by employing radiometric studies. However, although diffusion undoubtedly occurs when two identical polymers are brought together at relatively high temperatures, the evidence of stronger adhesion is equally applicable to the adsorption theory. For example, Anand et al. [141-145] argue that the dependence of the measured joint strength on parameters such as time of contact, may be readily explained by their effect on the kinetics of wetting. Anand [145] believes that, whilst interdiffusion occurs in the case of autoadhesion of polymers (i.e. adhesion of a polymer to an identical polymer), its contribution to the intrinsic adhesion is minimal compared to that from the formation of interfacial secondary bonds.

In conclusion, this theory cannot be a broad-based one, since it cannot explain the development of joint strength in systems which contain ceramic or metallic substrates such as glass or metal, or the development of strong adhesion between a polymeric substrate and an epoxy adhesive. It is accepted that such materials do not possess the molecular mobility required for interdiffusion at the typical relatively low temperatures used for adhesive joint formation. Therefore, this argument sheds some doubt on the application of this theory alone in the adhesive bonding of polymeric substrates. Further, for identical adhesives and substrates whilst there must be interdiffusion especially at high temperatures, to quantitatively determine the separate contributions to the intrinsic adhesion from interdiffusion and physisorption is

obviously extremely difficult and the relative levels of the respective contributions have yet to be resolved.

6.2.3.3. The Electrostatic Theory

According to this theory, adhesion is due to electrostatic forces acting at the interface and the joint acts as a capacitor which becomes charged due to the contact of two different materials. The strength of the joint is derived from the electrical double layer acting at the interface.

The chief proponents of the electrostatic theory have been Derjaguin (in some scientific journals translated also as Deryagin) and his co-workers [146]. Derjaguin and Smilga [146] observed that the parts of a broken joint are sometimes charged and pointed out that peeling forces are often very much greater than can be accounted for by van der Waals forces or chemical bonds. They also pointed out that the strong dependence of peel strength on testing speed cannot be explained in terms of these forces. They claimed that these aspects could be explained by means of the electrostatic theory. However, Schonhorn [147] points out that most of the work done in a peeling experiment is due to deformation of the materials comprising the joint (which is often rate dependent) rather than overcoming the molecular forces across the interface. Nevertheless, there is some independent evidence for the electrostatic theory. For example, Weaver [148] found that the bond between copper and poly(methyl methacrylate) was so low that the joint fell apart after exposure to a glow discharge (i.e. due to bleeding the electrostatic charge at the interface of the joint) in a vacuum chamber for a few minutes.

However, it should be noted that there are important points which weaken the argument of the electrostatic theory to be solely responsible for adhesion. Firstly, the electrical phenomena, which are the basis of this theory, occur only when the joint is broken. Hence, a phenomenon of fracture is used to explain the phenomenon of joining. Secondly, it is difficult to see how failure phenomena bear a direct relationship to joining phenomena, since the chemical and rheological states of the adhesive are different for the two cases, except perhaps for pressure-sensitive adhesives. Thirdly, there is no evidence to support the belief that charged fracture surfaces are identically the same two initially uncharged surfaces which were put together to form the joint. Finally, conductive materials should not form joints and of course, they do.

6.2.3.4. The Adsorption Theory

(i) Introduction

The adsorption theory seems to be the most widely accepted theory hence, it will be discussed in some detail. According to this theory, the adhesive macromolecules are adsorbed onto the surface of the substrate and are held there by various forces of attraction. The adsorption is usually physical, i.e. due to van der Waals forces of attraction. However, in some cases, hydrogen bonding and primary bonding (ionic or covalent) may be involved. Also, more recently, it has been proposed that acid-base interactions may occur across an interface.

(ii) Secondary Force Interactions

Tabor [149] and others [150, 151] have shown that dispersion forces alone, which are one of the three types of van der Waals interactions, are more than sufficient to account for the highest joint strength. They showed that such attractive forces, between two planar bulk phases, even at a separation distance of one nanometer would result in a joint strength in tension of about 100MPa. It is argued that the discrepancy between the theoretical and practical values is due to defects such as voids, geometric features acting as stress raisers and weak boundary layers. The hypothesis that dispersion forces are sufficient in the case of joints which are to be highly loaded, is discussed later in the present chapter.

Much experimental work, example [37, 152-156], has been reported to support the concept that secondary forces of attraction, especially polar interactions are sufficient to account for the joint strengths. With the advent of surface chemical analyses techniques there is now some evidence for the formation of secondary bonds [16, 47, 157-161]. For example, Briggs and Brewis [47] employed XPS to assess the increase in the oxygen peak on polyethylene (PE) surfaces by using corona-discharge treatment. They correlated this increase in the oxygen peak with the strength of the joints. They found an increase in the joint strength as the level of oxygen peak was increased. Perhaps of major importance in their work is their comment about the increased level of oxygen-rich carbon species, which they observed under the high binding energy shoulder of the carbon peak.

The above evidence leads to the conclusion that the mechanism of adhesion in an adhesive joint may indeed involve only secondary forces. To account for these secondary forces of attraction several mathematical equations have been developed to provide a numerical comparative approach to the concept of adhesion and joint strengths.

The thermodynamic work required to seperate a unit area of a solid and a liquid forming an interface across which secondary forces act is termed the thermodynamic work of adhesion, W_A, which for the solid-solid case can be expressed by [153]:

$$W_A = W_A^d + W_A^p \qquad (6.7)$$

where d and p stand for the dispersion and polar components. Equation (6.7) can be expressed in terms of energy components as [153]:

$$W_A = 2(\gamma_a^d \gamma_s^d)^{0.5} + 2(\gamma_a^p \gamma_s^p)^{0.5} \qquad (6.8)$$

where a and s stand for adhesive and substrate respectively. It is of interest to note that to maximize the thermodynamic work of adhesion, W_A, the values of the surface free energy components of both the adhesive and the substrate should be maximized. However, this conflicts with the concept of the spreading phenomenon, by analogy to Equation (6.2), where:

$$\gamma_s \geq \gamma_{as} + \gamma_a \qquad (6.9)$$

where γ_{as} is the interfacial free energy between the adhesive and the substrate.

Several workers [162, 163] have attempted to correlate the measured strengths of adhesive joints with the thermodynamic work of adhesion, W_A. For example, Andrews and Kinloch [37, 152, 164] and Gent and Kinloch [154] defined a geometry-independent measure of joint strength, the adhesive fracture energy, G_c. They demonstrated that the adhesive fracture energy, G_c, for a crosslinked rubbery-adhesive/rigid-plastic interface could be divided into two major components:

(a) The energy required to propagate a crack through unit area of interface in the absence of viscoelastic energy losses.

(b) The energy dissipated viscoelastically per unit area of interface within the rubbery adhesive at the propagating crack.

The second component being the dominant term and is by definition, rate, c, and temperature, T, dependent. Kinloch showed that the total failure energy could be described by:

$$G_c = G_0 f(c, T) \qquad (6.10)$$

where f is viscoelastic loss function. G_0 was divided into weighted average components

depending on the proportion of failure which could be ascribed either interfacial, cohesive within the adhesive or cohesive within substrate modes (interlaminar for composites) and that for purely interfacial failure $G_0 = W_A$.

However, in many cases the thermodynamic work of adhesion does not correlate with the measured joint strengths because the failure path is not interfacial, but cohesive within one or other phase on either side of the interface. Furthermore, the very low fracture energy values associated with interfacial failures may be dominated by other more important factors such as weak boundary layers of releasing agents on the substrates.

Interfacial bonds which have been prepared in the dry state may weaken and eventually fail after a period of exposure to a number of liquid environments. The principal environmental threat for structural adhesives is from water ingress. The ability of water to displace an adhesive from a substrate has been discussed by Gledhill and Kinloch [153] in terms of the thermodynamic work of adhesion between two materials. The work of adhesion (separation) of the material in a liquid phase, L, Equation (6.8) becomes:

$$
W_{AL} = 2 \left[\begin{array}{l} \gamma_{LV} - (\gamma_s^d \gamma_{LV}^d)^{0.5} - (\gamma_s^p \gamma_{LV}^p)^{0.5} - (\gamma_a^d \gamma_{LV}^d)^{0.5} \\ - (\gamma_a^p \gamma_{LV}^p)^{0.5} + (\gamma_a^d \gamma_s^d)^{0.5} + (\gamma_a^p \gamma_s^p)^{0.5} \end{array} \right] \tag{6.11}
$$

For interfaces where the calculated value of W_{AL} from Equation (6.11) is negative, then there is a strong driving force for displacement of the adhesive from the substrate in the presence of the liquid. In some cases where the value of W_{AL} is not negative but $W_A > W_{AL} \geq 0$ then it has been shown [165] that the adhesive fracture energy is reduced by the presence of the liquid.

(iii) Acid-Base Interactions

Calculations of surface free energy in Chapter Three were simplified by assuming that all polar interactions at the interfaces would be taken into one term and treated in the same way as dispersion force interaction. However, Fowkes has suggested [166, 167] that hydrogen bonding and acid-base type interactions at the surfaces of solids are highly specific and hence should be treated seperately. The method which Fowkes developed is based upon the earlier work by Drago et al. [168, 169]. Drago measured the enthalpy of acid-base interactions ΔH^{ab} for different acids and bases, characterising each acid (A) and base (B) by two constants C and

E such that:

$$-\Delta H^{ab} = C_A C_B + E_A E_B \tag{6.12}$$

Liquids and polymeric surfaces can have one of three types of hydrogen bonding capabilities as suggested by Rance [170]:

1. Proton acceptor (electron donor or basic) such as esters, ketones, ethers or aromatics to include polymers such as ploy(methyl methacrylate), polystyrene, polycarbonate, etc.

2. Proton donor (electron acceptor or acidic) such as partially halogenated molecules, including polymers such as poly(vinyl chloride), polypropylene, etc.

3. Both proton acceptor and proton donor molecules such as amides, amines and alcohols, including polymers such as polyamides, polyimides and poly(vinyl alcohol).

Fowkes and Maruchi [171] measured the contact angles of various acidic and basic liquids on different acidic and basic surfaces. Fowkes calculated W_A and W_A^d for the liquid and solid and examined the difference between these two quantities:

$$W_A^{ab} + W_A^p = W_A - W_A^d = \gamma_{LV}(1 + \cos\theta) - 2(\gamma_s^d \gamma_{LV}^d)^{0.5} \tag{6.13}$$

where the work of adhesion due to acid-base interactions, W_A^{ab}, is a more general term which also includes hydrogen bonding interactions. Fowkes discovered that for either acidic liquids on acidic surfaces or for basic liquids on basic surfaces the left-hand side of Equation (6.13) was always zero. This implies that liquids and solids which may be polar, but have the same electron accepting or donating capability, interact by dispersion forces alone. For a basic surface, only acidic liquids were found to produce a positive contribution to W_A^{ab}. These observations led Fowkes to conclude that the contribution to interfacial interactions purely by polar forces W_A^p is very small and may be neglected. In a later work, Fowkes [172] came to the conclusion that polarity as measured by dipole moments played a negligible role. Fowkes and Mostafa [173] related W_A^{ab} to the enthalpy of acid-base interaction, ΔH^{ab}, from Equation (6.12) such that:

$$W_A^{ab} = -f(C_A C_B + E_A E_B)n^{AB} \tag{6.14}$$

where n^{AB} is the number of acid-base pairs per unit area of the surface and $f \approx 1$ converts the enthalpy per unit area to surface free energy.

Huntsberger [174] has compared the predictions of the interfacial forces between a basic polyimide and various liquids by using the two rival techniques of analysis, i.e. the geometric mean relation embodied by Equation (3.8) (and hence in Equation (6.8)) and the acid-base interaction contributions from Equation (6.12). He concluded that firstly, the polar force interaction was not negligible and that Equation (3.8) predicted the polar force interactions to a good approximation. Secondly, the acid-base interaction contributions from Equation (6.12) were not always consistent with the known acidity and basicity values of the liquids he used. Further, the constants in Equation (6.14) are not always available and if they are this equation may not correctly predict interfacial acid-base interactions. Finally, Kinloch [175] has suggested that polar contributions may be included in Equation (6.14) and that acid-base interactions may also be included in the polar force interactions deduced from Equation (6.8).

(iv) Primary-Force Interactions

Various types of primary bonds have been reported to be formed across an interface depending on the chemistry of the interface. For example, Andrews and Kinloch [37, 152, 164] and Gent and co-workers [176-179] report the formation of covalent bonds when bonding and crosslinking elastomers against reactive substrates, and interfacial covalent bonds resulted in the highest values of the measured fracture energies. Similarly, by employing infrared analysis, Klien et al. [180] reported the formation of covalent primary bonds between a polyurethane adhesive and epoxy-based primers. Further, they showed that such interfacial interactions gave the highest joint strengths. It should be noted that covalent bonds will usually have some degree of ionic character due to the different electronegativities involved in the bond.

6.2.3.5. Weak Boundary Layers

Weak boundary layers can be one or a combination of: (i) weak surface layers in the substrate or the adhesive and (ii) a weak layer of releasing agent present on the surfaces.

(i) Inherent Weak Boundary Layers

Inherent weak boundary layers may originate in the adhesive or the substrate. A literature review on this subject was presented in Section 5.2.2 where it was shown that inherent weak boundary layers may exist, but their importance, has probably been exaggerated.

(ii) Weak Boundary Layers from Releasing Agents

Many substrates may often be coated by protective oils, greases, waxes etc. If such layers are not removed prior to adhesive bonding then they may act as potential weak boundary layers in the joint [104]. Further, as mentioned in Chapter Two, the general literature [6-8] suggests employing a simple abrasion/solvent-wipe pretreatment prior to adhesive bonding of fibre-composites. This technique would ensure that any weak boundary layers, due to releasing agents, transferred to the surfaces whilst processing, are reduced substantially. Further, provided that the surfaces are not heavily contaminated with releasing agents, Hart-Smith et al. [9] have suggested that grit blasting with aluminium oxide is the best surface preparation technique known for thermosetting-based fibre-composites.

6.2.4. Conclusions

From the literature review in this chapter it is clear that in certain circumstances, provided that the surfaces are not heavily contaminated with releasing agents, any of the four main mechanisms of adhesion may be responsible for the intrinsic adhesion. Nevertheless, the adsorption theory seems to be the most widely applicable mechanism of adhesion. Although, it was shown that surface roughness may indeed assist in establishing intimate interfacial contact.

The adsorption theory states that, provided intimate molecular contact is established at the interface, then the materials will adhere if chemical species, such as oxygen-rich carbon species, are present on the surfaces which will ensure that interatomic and intermolecular secondary forces are established.

In this chapter no separate section for experiments will be given due to firstly, most experiments have been reported in earlier chapters notably in Chapter Three and secondly, the few experiments performed here relate only to specific problems in an attempt to further understand the mechanisms of adhesion. Hence, the results reported so far will be re-examined to provide (i) an understanding of the problem of why TPFC materials require pretreatment prior to bonding using structural adhesives, and (ii) an assessment of the mechanisms involved in the adhesive bonding of TPFC materials.

6.3. IMPORTANCE OF WEAK BOUNDARY LAYERS

6.3.1. Inherent Weak Boundary Layers

As discussed in Section 5.3.3, XPS analyses revealed that the atomic % concentrations of

chemical-elements from specimens which had failed interfacially and from "control" specimens, see Table 5.1 (page 146), were equal. Therefore, there is no inherent weak boundary layer present on the TPFC substrates employed.

6.3.2. Role of Releasing Agents

(i) Initial Studies

The primary purpose of employing an abrasion/solvent-wipe pretreatment is to remove any weak boundary layers due to releasing agents that may have been present on the surfaces of the fibre-composite materials. It is therefore interesting to consider the results from Tables 4.5, 4.6 and 4.7 (pages 117 and 118). The important conclusion that emerges from these results is that the U/C-epoxy composite bonds to the epoxy and acrylic adhesives employed, yielding in all cases (except one which failed in an interlaminar manner) cohesive failures with high adhesive fracture energy values. Therefore, contamination due to releasing agents on the U/C-epoxy thermosetting composite of the order of 1%, see Table 3.13 (page 76), does not prevent this material from attaining high interfacial strength. However, levels of contamination of the order of 4.4%, recorded when no abrasion/solvent-wipe was used, see Table 3.12 (page 75), for the same material leads to interfacial failure and low G_c values being recorded.

Now, in the case of the TPFC materials when an abrasion/solvent-wipe pretreatment was used all the subsequent joints failed interfacially, yielding low G_c values. Further, an aluminium foil/NaOH etching technique was employed to avoid any releasing agents from being transferred to the surfaces of the U/C-PEEK thermoplastic composite during moulding of the material. This was successfully achieved, as can be seen from the values in Table 3.14 (page 78), where XPS did not detect any elements from releasing agents. However, even with the absence of releasing agents, the adhesive fracture energy reported from such experiments was very low, typically less than $0.5kJ/m^2$ when the epoxy adhesives were employed.

The above experiments therefore provided direct and conclusive evidence that the poor adhesive bonding of TPFC materials cannot be due to weak boundary layers. Therefore, it may be concluded that provided the composite materials are not heavily contaminated with releasing agents then the essence of the problem is lack of intrinsic adhesion. However, it is important to identify a level of contamination where releasing agents will have little effect on the fibre-composites from attaining high interfacial strengths.

(ii) U/C-PPS Composite

Now, by employing various types of releasing agents, other than "Frekote 44", Phillips Petroleum supplied "accidently" heavily contaminated U/C-PPS composite sheets, with a releasing agent concentration level of just under 17% for the untreated surfaces. These materials were employed to study the effects of corona-discharge on the adhesive fracture energy. The material was abraded and then subjected to a corona-discharge pretreatment. The fracture results from such experiments are shown in Figure 6.3. It can be seen from this figure that joints prepared using such substrates do not attain, even at very high corona treatment energies of $100J/mm^2$, the value of G_c as from employing "clean" U/C-PPS substrates (i.e. $1.45kJ/mm^2$). This can be readily understood by considering the locus of failure which was interfacial for the joints using the heavily contaminated substrates.
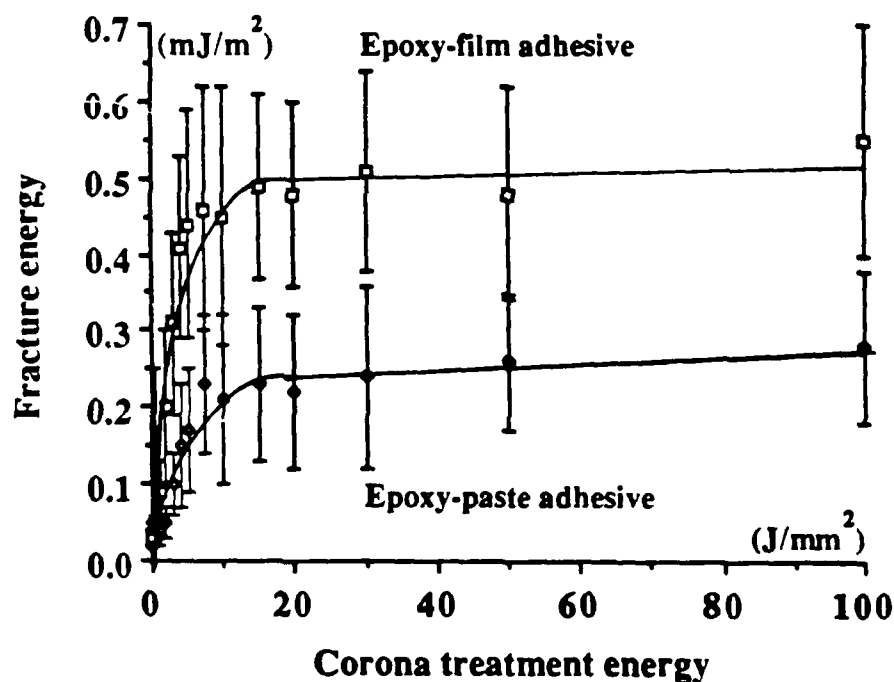
Fig. 6.3. Adhesive fracture energy from heavily contaminated U/C-PPS composite subjected to corona-discharge pretreatment.

Furthermore, XPS analysis was carried out on the contaminated U/C-PPS material and the results are shown in Table 6.1. Several interesting features emerge from these results. Firstly, abrasion/solvent-wipe pretreatment is effective in lowering the level of releasing agents from about 17% to about 4.4%. Secondly, the carbon, oxygen, sulphur and nitrogen levels follow the same pattern as described for the "clean" U/C-PPS material discussed in Chapter Three. Therefore, even at high levels of oxygen-rich species the U/C-PPS composite does not

attain high interfacial strength. Thirdly, however, the level of releasing agents does not drop below a level of 3%. This should be compared to the level of releasing agents on the "clean" U/C-PPS material subjected to corona treatment which was about 1.1%. It is noteworthy that this latter level of releasing agent did not interfere with the material's ability to attain high interfacial strength giving at a treatment level of 5J/mm^2 a far higher interlaminar fracture energy value of 1.45kJ/m^2.

Table 6.1. XPS results of contaminated U/C-PPS composite subjected to corona treatment.

Corona treatment energy (J/mm^2)	C1s	O1s	N1s	Si2p + F1s	S2p	(Si2p+F1s)/C1s
Untreated (control)	68.1±2.1	6.9±0.9	*	16.8±1.2	5.8±0.5	0.25
0.0	81.4±1.7	6.2±0.9	*	4.4±0.5	7.8±0.7	0.054
2.5	58.4±1.9	26.1±1.5	4.1±1.1	3.4±0.6	6.8±1.0	0.058
50.0	36.0±1.6	46.9±1.4	6.0±1.1	3.2±0.5	6.2±1.0	0.089
100.0	36.4±1.4	46.3±1.5	6.4±1.0	3.1±0.7	5.9±1.1	0.085

(iii) U/C-PEEK Composite

A most interesting experiment was also conducted on the U/C-PEEK thermoplastic composite. Unabraded specimens from this material were subjected to a corona treatment levels of 20J/mm^2. The locus of failure from employing the epoxy-paste adhesive was cohesive, giving a G$_c$ value of about 3.9kJ/m^2. Furthermore, XPS analysis on such specimens revealed that, at a corona treatment level of 20J/mm^2, the level of releasing agents was about 1.3%. This indicates that corona treatment indeed etches away some of the surface, hence decreasing the level of the contamination from releasing agents.

Finally, it is interesting to note that the level of releasing agents for all TPFC materials subjected to corona treatment was always under about 1.5%.

6.3.3. Conclusions

From the arguments presented above it can be concluded that:

1) Inherent weak boundary layers do not exist in the TPFC materials or the adhesives employed and fracture through such weak boundary layers does not occur. Therefore, the weak adhesion associated with these materials cannot be due to this effect.

2) Releasing agent concentration levels of the order of 3%, or greater, prevent either the TSFC or the TPFC joints attaining high interfacial strength. However, releasing agent levels of about the same concentration as that of the epoxy composite (i.e., 1 to 2%), do not lead to the TPFC materials attaining high interfacial strengths. Indeed, even in the absence of weak boundary layers, i.e. very low or undetectable levels of releasing agents, as from the aluminium/etch pretreatment, TPFC materials still failed interfacially leading to very low fracture energy values. Therefore, the weak adhesion of the TPFC materials cannot be due to weak boundary layers.

3) As well as oxidising the surfaces of the TPFC materials the corona treatment etches the surfaces and the concentration of releasing agents decreases. However, the corona treatment is ne····.lly effective in this respect and the surfaces must not be too heavily contaminated with releasing agents, as in the case of the contaminated U/C-PPS composite considered above.

6.4. IMPORTANCE OF MECHANICAL INTERLOCKING

6.4.1. Introduction

The SEM micrographs shown in Chapter Three revealed an increase in surface roughness as the intensity of corona-discharge treatment increased. Surface roughness may well have an effect on the degree of wetting and adhesion. Therefore, the effects of surface roughness and the possible extent of any mechanical interlocking will now be examined.

6.4.2. Substrate Surface Topography

Surface analysis using SEM gives a qualitative assessment of the surface roughness. To investigate in a quantitative technique the extent of surface roughness associated with the pretreatment techniques a "talysurf" was employed. The main components of the "talysurf" are its diamond head-needle which slides horizontally on the surfaces to be examined and the electrical resistance control-box which amplifies the movement of the diamond head-needle in the vertical direction. The specimens were 2X2cms in size and were mounted onto a small table under the "talysurf" diamond needle. Care was taken to align the small table with the horizontal direction to minimize the effects of misalignment of the specimen on the output from the "talysurf".

The traces from such investigations can be seen in Figure 6.4. The "talysurf" profilometer traces reveal several interesting features. Firstly, Figure 6.4(a) shows that the laboratory slide

coated with a thin layer of gold, employed for the surface roughness calculations in Chapter Three, has a very smooth surface. This, justifies the concept of employing a laboratory slide as a smooth reference surface. Secondly, Figures 6.4(b) and 6.4(c) reveal that gold coating of the composites after abrasion has little effect on the surface topography. This indicates that the amount of gold deposited on the surfaces, about 700Å, has little effect on the surface topography. Therefore, the calculations of the surface roughness factor of the composite materials employed, see Section 3.2.4.3, were a true reflection of the "real" surface roughness of these materials when subjected to treatment techniques. Thirdly, Figure 6.4(d) reveals that, as expected, the corona-treated U/C-PEEK thermoplastic composite has a very rough surface compared to the other traces mentioned above. Finally, the "talysurf" profilometer observations are in qualitative agreement with the scanning electron microscopy and contact angle analysis observations made earlier in Sections 3.3.3 and 3.2.4.3 respectively. However, these figures alone do not provide any deep insight into the degree of mechanical interlocking. Since they cannot detect, for example, the presence of "ink-bottle" shaped cavities.

(a)

(b)

(c)

(d)
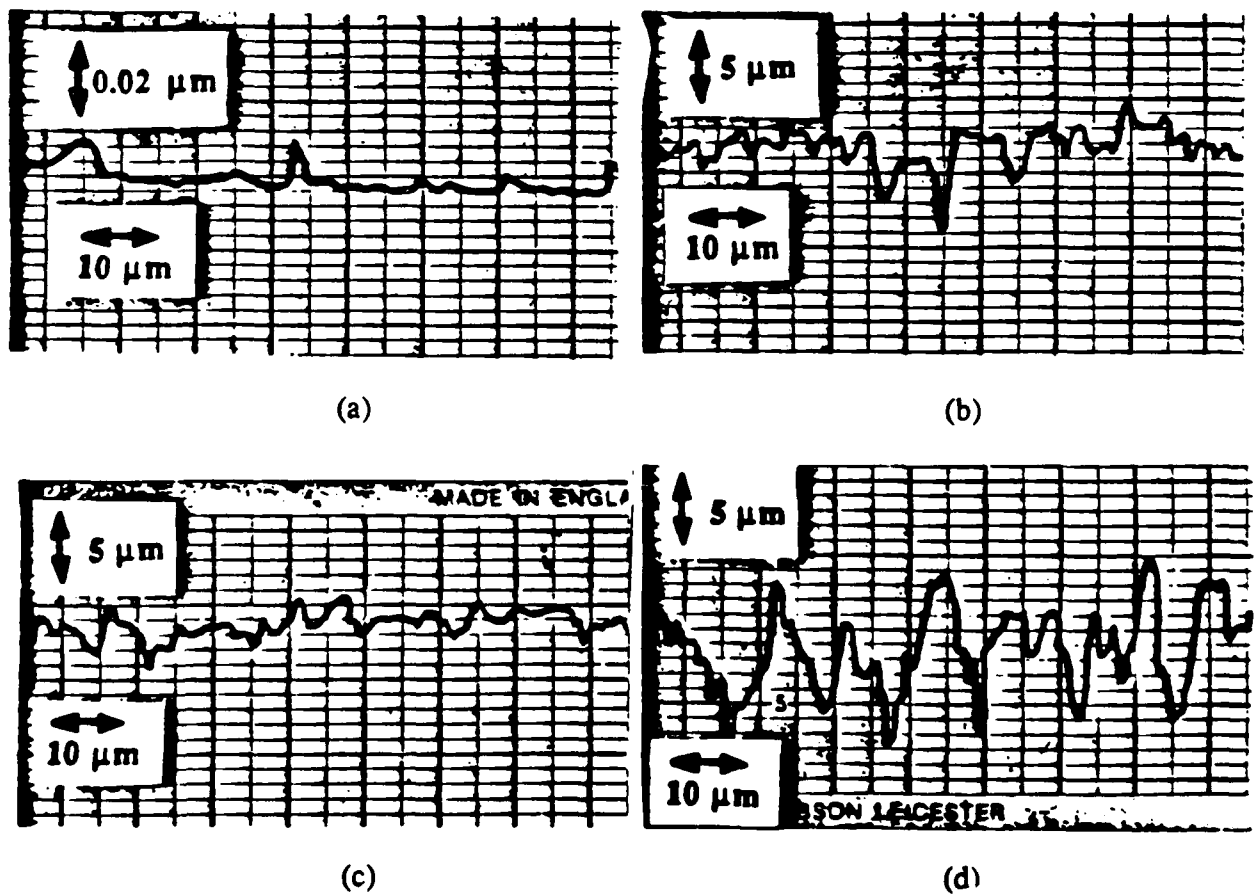
Fig. 6.4. "Talysurf" profilometer traces for (a) laboratory slide coated with gold; U/C-PEEK composite subjected to (b) abrasion; (c) abrasion and coated with a thin layer of gold; and (d) corona treatment level of $20J/mm^2$.

6.4.3. Scope for Mechanical Interlocking

The SEM micrographs presented in Section 3.3.3, of pretreated surfaces, reveal that the type of surface roughness associated with the treatment techniques can be associated more with "crater" type surface roughness, rather than with the "ink-bottle" surface roughness which is required for mechanical interlocking.

Indeed, other experiments also indicate that mechanical interlocking is not an important adhesion mechanism. As mentioned earlier, experiments were conducted employing the heavily contaminated U/C-PPS thermoplastic composite materials. The adhesive fracture energy results, employing either of the two epoxy adhesives, were never higher than $0.6kJ/m^2$, see Figure 6.3. This value was far below the G_c value (about $1.45kJ/m^2$) that was attained employing "clean" PPS composite surfaces. Since any degree of mechanical interlocking would not necessarily be affected by the presence of the very thin layer of the releasing agent, this is a strong indication that "ink-bottle" cavities cannot be present on the treated surfaces.

6.4.4. Effect of Surface Roughness

Thick films (500µm) of PEEK and PA resins were added on top of the pre-preg stacks of the U/C-PEEK and U/C-PA thermoplastic composites respectively. Afterwards, the composites were consolidated according to the manufacturers' recommendations. The main aim of these experiments was to investigate the effect of smoother surfaces on adhesion. The two thermoplastic composites with their corresponding thick layers of resin were then corona-treated. The purpose of employing this type of specimen for SEM, XPS, contact angle and fracture analyses was two fold. Firstly, to compare the XPS results from such specimens with the normally produced U/C-PEEK and PA composites to identify the extent of the effect of not exposing carbon-fibres. Secondly, to produce smoother surfaces after exposure to the corona treatment, since now the thicker resin film will prevent the sparks from etching away the top layer of the thermoplastic resin to expose the carbon-fibres.

XPS was performed on the specimens after having subjected them to corona treatment. The XPS results revealed that the concentrations of the various elements agreed well with the earlier reported data in Section 3.4.4.4 for the normally produced composites. Further, carbon-fibres were treated separately to different corona treatment levels. The results from XPS analysis revealed that at corona treatment energy of $10J/mm^2$ and beyond the concentrations of the oxygen and carbon elements were similar to the corona-treated ($10J/mm^2$ and beyond) U/C-PEEK surfaces. Therefore, from the XPS analysis, it can be concluded that the exposure of some fibres for the U/C-PEEK thermoplastic composite at a corona treatment level of

$20J/mm^2$, reported in Chapter Three, has little effect on the measured concentrations of the different elements.

The results from contact angle analysis revealed the following features. Firstly, the surface roughness correction factor for both types of composites, i.e. U/C-PEEK and U/C-PA with thick films, remained fairly constant at around a value of 1.1 for all corona treatment levels up to $20J/mm^2$. This surface roughness value was equal to the value obtained when these materials were subjected to only an abrasion/solvent-wipe pretreatment. Indicating that, for such specimens, surface roughness does not increase with the level of corona treatment. This observation is in agreement with the SEM observations, see Figure 6.5. Secondly, the surface energy components, after being corrected for the surface roughness, were similar to the ones reported in Section 3.2.4.5. For example, the dispersion and polar energy components from U/C-PA (with "thick layer" of resin) composite subjected to $5J/mm^2$ were 39.2 and $27.6mJ/m^2$ respectively.

(a)   (b)
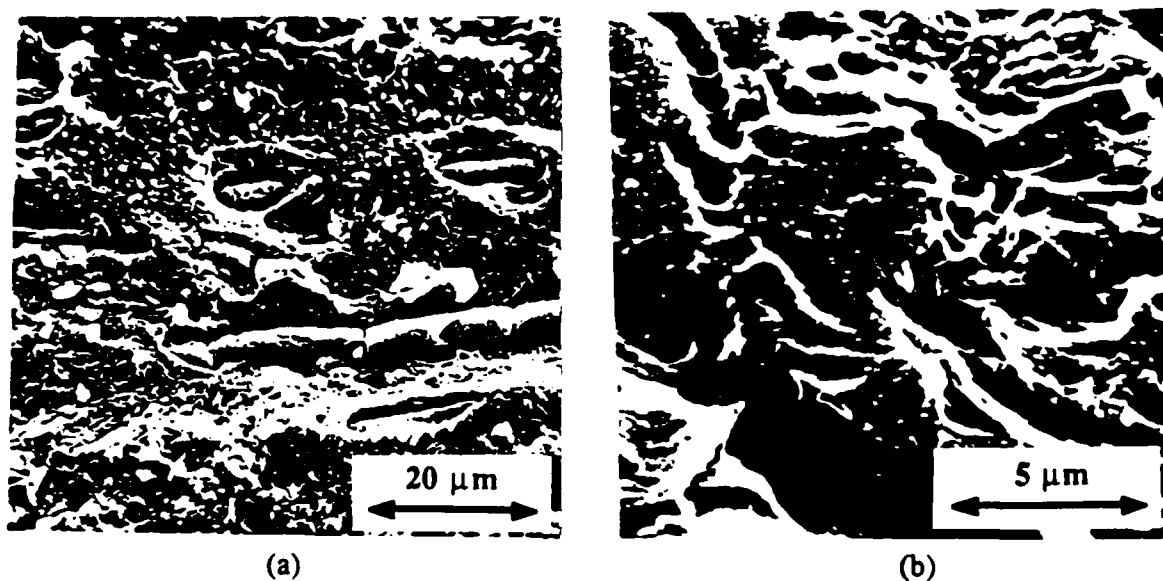
Fig. 6.5. U/C-PEEK thermoplastic composite (a) without and (b) with thick
layer of PEEK resin subjected to corona treatment level of $20J/mm^2$.

The fracture results from substrates with "thick layer" of resin showed clearly that surface roughness has little effect in changing the level at which cohesive failure can be attained when the epoxy-film adhesive is employed. However, "thick layer" of resin TPFC composites bonded using the tougher epoxy-paste adhesive attained G_c values of about $3.5kJ/m^2$ when corona-treated to the levels where cohesive fracture ($G_c=3.85kJ/m^2$) is observed from normally produced composite sheets. The obvious difference between the two types of substrates, i.e. normally produced and "thick layer" of resin, is the surface roughness (since the surface energy and surface chemical changes were shown above to be the same). For

example, the surface roughness correction factor, r_c, for the normally produced U/C-PEEK and U/C-PEEK with "thick layer" of resin treated to corona energy level of $20J/mm^2$ are 1.18 and 1.1 respectively. Therefore, although increased surface roughness may not be important for joints bonded using the epoxy-film adhesive but when the TPFC materials are bonded to the tougher epoxy-paste adhesive then the increased surface roughness has some effect in the bonding process. This can be explained since increased surface roughness (i) will undoubtedly provide an increased surface bonding area and (ii) will assist the kinetics of wetting especially that the tougher epoxy-paste adhesive solidifies in less than 20minutes (after being degassed).

6.4.5. Conclusions

The important conclusions from this section are:

1) It was shown that the "ink-bottle" type surface roughness required for mechanical interlocking is not produced by the treatment techniques employed. Indeed, SEM micrographs revealed that surface roughness associated with the treatment techniques was "crater" type. Therefore, the scope for mechanical interlocking in the adhesive bonding of the fibre-composites employed is indeed very small.

2) It was shown that surface roughness may assist in the spreading and wetting of the surfaces especially in the case of the room-temperature cured (viscous) epoxy-paste adhesive. However, this is not sufficient for the TPFC materials from attaining strong interfacial bonds. Strong interfacial intermolecular forces arise from the interaction of specific chemical groups which need to be present on the substrates.

6.5. INTERDIFFUSION ACROSS THE INTERFACE

6.5.1. Introduction

So far, the effects of weak boundary layers and the extent of mechanical interlocking have been presented Next, interdiffusion across the interface will be discussed.

6.5.2. Requirements

In Section 6.2.3.2 a critical review of the diffusion theory was presented and it was established that the criteria for interdiffusion to occur were:
a) The adhesive and the composite should have sufficient molecular chain mobility for part of the adhesive macromolecule to diffuse into the substrate.

b) Diffusion is more likely to occur between two identical polymers, or those which have very similar solubility parameters.

c) Diffusion will not occur when the substrate is an inorganic or metallic material.

If the above requirements are met then the diffusion of an adhesive into a substrate will increase as the period of contact, temperature, pressure are increased. Further, diffusion will decrease if molecular weight and crosslinking are increased.

6.5.3. Relevance to Present Work

6.5.3.1. Thermosetting Composite Bonded to the Epoxy and Acrylic Adhesives

To consider the possibility of diffusion when the epoxy and acrylic adhesives are employed to the U/C-epoxy composite then several facts have to be considered. Firstly, it was mentioned in Section 2.2.2 that thermosetting polymers have highly cross-linked three dimensional molecular chains. Secondly, the thermosetting composite employed had a T_g value (131^0C see Table 2.2) above the curing temperature of the hot-cured epoxy-film adhesive (120^0C see Section 2.3.2). All other adhesives were cured at room temperature. Thirdly, the U/C-epoxy composite and the adhesives employed are not identical polymers.

Therefore, firstly, the molecular chains of the adhesive at the temperatures considered, (i.e. below the T_g of the substrate) will not be able to diffuse across the interface into the substrate since the substrate will still be a relatively rigid material. Secondly, the crosslinked nature of the thermosetting polymers will not allow extensive interdiffusion across the interface. Hence, it is very unlikely that interdiffusion across the interface is responsible for the strong intrinsic adhesion when the U/C-epoxy composite is bonded to the epoxy adhesives.

6.5.3.2. Thermoplastic Composites Bonded to the Epoxy and Acrylic Adhesives

From the arguments mentioned above for the thermosetting composite, one can immediately arrive at the same conclusion for the thermoplastic composites. Most of the TPFC materials employed not only have higher T_g values but have completely different chemical

structures compared to the adhesives employed. Indeed, the solubility parameter, δ_s, is usually very different for different polymers, let alone between thermoplastic and thermosetting

polymers. For example, the solubility parameters for a typical polyamide and epoxy resin are $0.0182J^{0.5}m^{-1.5}$ and $0.0223J^{0.5}m^{-1.5}$ respectively [181]. Another aspect relevant to the discussion is that the untreated U/C-PPS composite, which has a T_g value lower than the curing temperature of the epoxy-film adhesive, still fails interfacially along the adhesive/composite interface. Therefore, diffusion cannot be of any relevance for the cases considered here.

6.5.3.3. Thermoplastic Composites Bonded to the Hot-Melt Adhesives

It was shown in Chapter Four that hot-melt thermoplastic adhesives could be successfully employed for the adhesive bonding of the parent TPFC materials. For example, the results presented in Table 4.10 (page 136) indicate that such hot-melt adhesives resulted in adhesive fracture energy values comparable with those from the interlaminar fracture experiments reported in Table 4.1 (page 110).

It can be argued that the process of employing the "self-similar" hot-melt thermoplastic adhesives involves the strict application of the diffusion theory. Especially now that the substrate and the hot-melt adhesive are not only identical polymers, and therefore have the same solubility parameter, but also the molecular chains of the adhesive and the substrate, at the melting temperatures, will have the mobility to interdiffuse across the interface at the high pressures employed. Some evidence for this suggestion comes from work on the heavily contaminated U/C-PPS material which was employed in hot-melt adhesive bonding using a layer of PPS resin. This composite material had a silicon plus fluorine level of just under 17%. The G_c value obtained was only $0.85kJ/m^2$ whereas, the value obtained from "clean" U/C-PPS material was about $1.45kJ/m^2$. These observations give some indirect evidence that diffusion does occur when the TPFC materials are bonded to their resins otherwise the heavily contaminated U/C-PPS material should have failed at a very low or even at an undetectable G_c value. Therefore, interdiffusion may occur for the cases considered here however, to quantitatively determine the contribution to the intrinsic adhesion from interdiffusion for "clean" TPFC materials is obviously extremely difficult, especially since most of the requirements for diffusion to occur can equally be important for physisorption.

6.5.3.4. Conclusions

Several conclusions can be reached from the discussions in this section:

1) Diffusion of segments of the molecules across the substrate/adhesive interface is

unlikely to be responsible for the U/C-epoxy composite attaining strong interfacial bonds when the epoxy and acrylic adhesives are employed. The U/C-epoxy not only remains a relatively rigid material at 120^0C but also is a three-dimensional cross-linked material.

2) When the abraded/solvent-wiped only thermoplastic composites are bonded to the epoxy- and acrylic-based adhesives then interdiffusion is most unlikely. This because (i) the thermoplastics composites and the adhesives employed are not only of different chemical structures but also have different solubility parameters and (ii) most TPFC materials have even higher T_g values than the hot-cured epoxy-film adhesive, let alone the room temperature curing adhesives. Finally, of course, there is the experimental observation that the locus of failure for such joints is interfacial, exactly along the adhesive/composite interface (see Section 5.3.3).

3) When the thermoplastic resins are bonded to their parent TPFC materials as hot-melt adhesives then interdiffusion across the adhesive/composite interface will undoubtedly occur. However, it is difficult to assess the extent of the diffusion in these cases, since the requirements for interdiffusion are equally valid for physisorption to occur.

6.6. THE ADSORPTION THEORY

6.6.1. Introduction

So far, the weak boundary, the mechanical interlocking and the diffusion theories have been shown to be of little importance in the current work when the epoxy adhesives were employed. The electrostatic theory will not be considered since a strong argument against this theory was presented in the literature survey.

Now, the XPS, contact angle and fracture results revealed that when, for example, the concentration of the oxygen element is increased then this was accompanied by an increase in the surface free energy and an increase in the adhesive fracture energy, G_c, values. Therefore, from such observations, one can suggest that the adsorption theory may play a crucial role. To investigate this aspect a detailed analysis of the adsorption theory will be presented. Firstly, the importance of interfacial contact will be discussed. This will be followed by establishing correlations between the XPS and contact angle analyses results, since both of these experimental methods attempt to assess the surface intermolecular forces. Secondly, the data from these surface characterisation studies will be correlated to the fracture results. Finally, the thermodynamic work of adhesion and the acid-base interaction theories will be discussed.

6.6.2. Interfacial Contact

A detailed review of the conditions for spreading was given in Section 6.2.2. A necessary but insufficient condition for strong adhesion is that the adhesive should spread completely on the surface. Spreading can be achieved by one or a combination of the following:

a) forcibly by applying pressure,

b) attaining a zero contact angle or a positive spreading coefficient to maximize the rate of wetting,

c) by increasing the surface roughness which will reduce the contact angles measured and therefore assist in the spreading,

d) by increasing the total surface free energy of the substrates thereby decreasing the contact angles measured, see Figure 6.6, hence increasing the likelihood of attaining a positive spreading coefficient and/or assisting the kinetics of wetting.

(a)   (b)
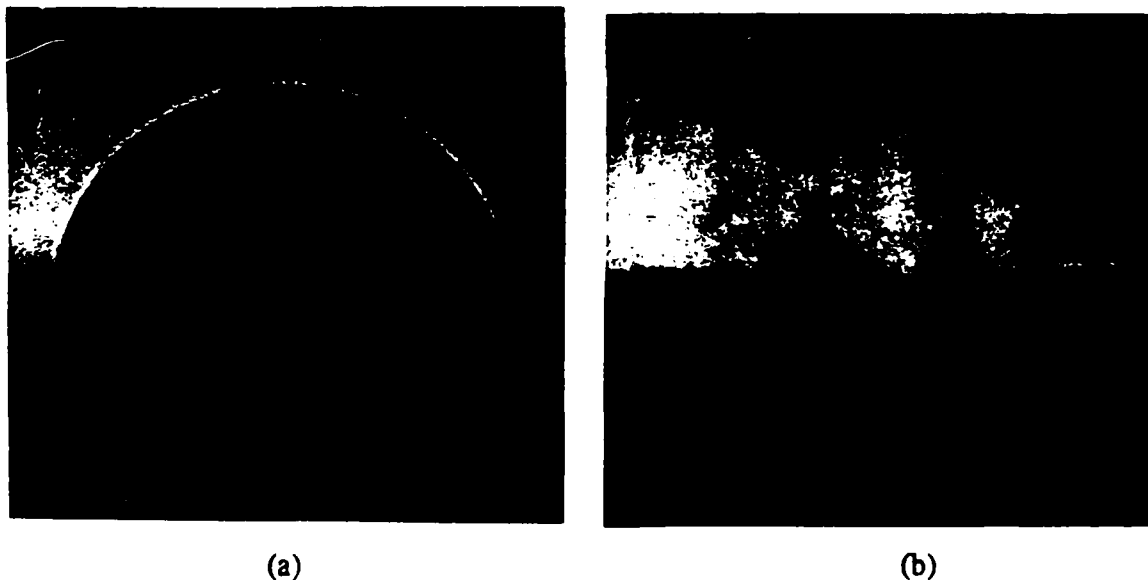
Fig. 6.6. Double-distilled water droplets on U/C-PEEK composite; (a) untreated; and (b) corona-treated to $20J/mm^2$. Note that in the latter the contact angle measured is due to increased surface roughness and increased surface free energy (due to surface chemical changes).

Equation (6.3) established the condition for complete wetting of surfaces i.e., $S_c \geq 0$. For the condition where the adhesive just spreads the surface then $S_c = 0$ and Equation (6.5) can be rewritten as:

$$\gamma_a = (\gamma_s{}^d\gamma_a{}^d)^{0.5} + (\gamma_s{}^p\gamma_a{}^p)^{0.5} \qquad (6.15)$$

Equation (6.15) requires the surface free energy components of the adhesives which were calculated, using contact angle analysis, and the results are given in Table 6.2. Therefore, from a knowledge of the adhesive surface energy components it is possible to plot an energy boundary line, using Equation (6.15), to predict if an adhesive will spread on a given substrate whose surface energy components are known.

Table 6.2. The surface energy components of the epoxy adhesives employed.

Adhesive	Dispersion energy γ_a^d (mJ/m^2)	Polar energy γ_a^p (mJ/m^2)	Total surface free energy γ_a (mJ/m^2)
Epoxy-paste	35.2±2.9	3.8±0.9	39.0±3.8
Epoxy-film	32.3±2.5	3.0±0.8	35.3±3.3

Figure 6.7 shows the plots of the spreading boundary lines for the two epoxy adhesives employed. Note that the points in this figures are from contact angle values which have not been corrected for surface roughness effects. (Since the wetting of the adhesive will obviously be influenced by both the surface roughness and chemsitry). Figure 6.7 reveals that adhesives which possess a combination of dispersion and polar surface energy components which are higher than those given by the spreading boundary lines will have spreading coefficients, S_c, which are positive, and therefore the adhesive will completely spread on the surface. Several interesting features emerge from Figure 6.7. Firstly, the epoxy-film and epoxy-paste adhesives are predicted to spread on all the fibre-composite materials employed. Secondly, note that even with a simple abrasion/solvent-wipe pretreatment all the fibre-composites attain positive-spreading coefficients. Therefore, further gains in this coefficient by corona treatment may only affect the rate of spreading, i.e. the kinetics of wetting. Finally, the important implication of the above discussion is that, the epoxy adhesives may achieve intimate molecular contact with the surfaces of the "clean" abraded TPFC materials. However, the DCB TPFC joints failed in an interfacial manner along the adhesive/composite interface, resulting in low G_c values being recorded. Again, this observation highlights the importance of the corona pretreatment in increasing the intrinsic adhesion at the TPFC/adhesive interface.
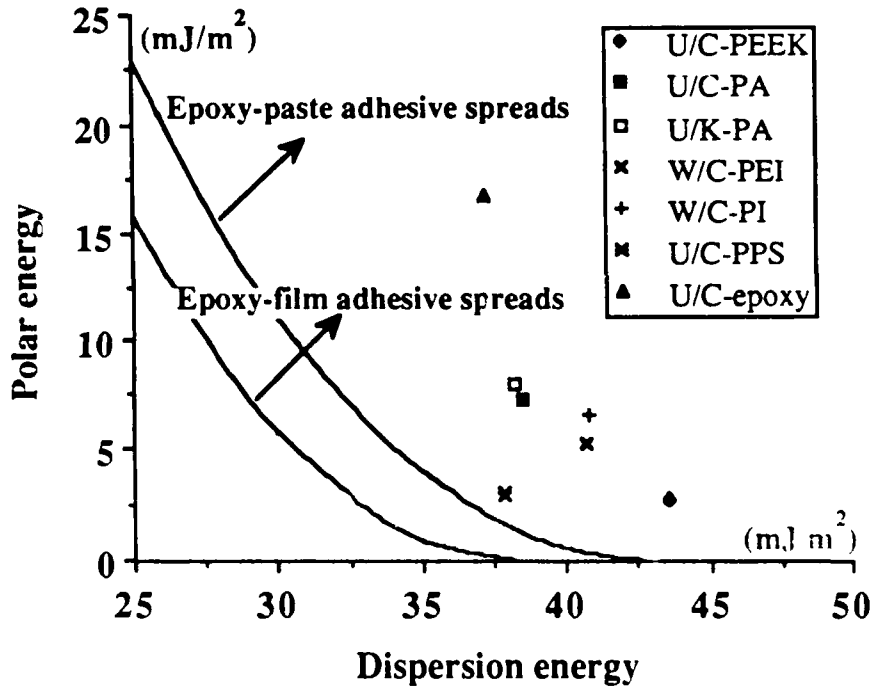
Fig. 6.7. Spreading boundary energy lines for the epoxy-paste and epoxy-film
adhesives; the experimental data are from abraded specimens.

6.6.3. Correlation Between XPS and Contact Angle Results

6.6.3.1. Introduction

It was shown in Chapter Three (Section 3.4.4.4) that as the level of corona treatment was
increased then the atomic percentage concentrations of the oxygen and oxygen-rich species
increased. This increase was also accompanied by a dramatic increase in the calculated polar
surface energy component. Accompanying these effects, the locus of joint failure, changed
from interfacial to one of cohesive or interlaminar and high G_c values were measured.
However, when the TPFC materials were treated with corona-discharge and allowed to age for
up to six months then, the oxygen level and the polar energy component decreased and the
locus of joint failure changed from cohesive back to interfacial.

The present aims are, therefore, firstly to re-examine the data presented in the earlier
chapters to assess the possibility of establishing relationships between the XPS and contact
angle data (since the initial measures the percent oxygen-rich species which will be reflected in
the latter as polar surface energy). Secondly, to examine correlations between these results and
the results from the fracture studies.

6.6.3.2. Dipole Moments

Polar forces arise from the orientation of the permanent electric dipoles and, therefore, by definition there should be a relationship between the calculated polar energy component and the dipole moment of the chemical species present on the surfaces of the substrates. However, such a relationship has not been explored in the literature and to investigate this aspect the definition of the dipole moment will first be presented together with some dipole moment values for relevant chemical linkages.

When a bond is formed between two identical atoms, example, A : A, the electron pair may be regarded as shared equally between the two atoms. Whereas, in bond formations between unlike atoms, example, A : B, then one atom is usually more electronegative than the other, that is the shared electrons are more likely to be found in the vicinity of one atom than the other. If for example, A is more electronegative than B, then A has a greater tendency to attract electrons than B. The important consequence of the different electron affinities of various elements is that most covalent bonds constitute electrical dipoles, so that the electrical centre of the electrons is not the same as that of the nuclei. In other words, a covalent bond between two different atoms will be associated with a dipole moment; its value is given by the product of the electronic charge and the relative displacement of the positive and negative electrical centres. The magnitude of the dipole moment depends primarily on the difference of the electronegativity of the two elements forming it. The dipole moments of bonds is represented as the additive vector quantities acting along in the direction of the chemical bond, and so the total dipole moment is the vector sum of the constituent moments given by:

$$\mu^2 = \mu_1^2 + \mu_2^2 + 2\mu_1\mu_2 \cos\theta \tag{6.16}$$

A perfectly symmetrical molecule will therefore be nonpolar, although it may contain polar linkages. Unsymmetrical compounds, however, are almost invariably polar and the presence of oxygen or nitrogen in a carbon compound makes this polarity very marked. Since the dipole moment arises because of the difference in the electronegativity of two atoms connected by a chemical bond, it is evident that it should be possible to associate a dipole moment with every chemical linkage, see Table 6.3.

Table 6.3. Dipole moments for some chemical linkages [182].

Chemical linkage	Dipole moment (debye)
C-N	0.2
C-O	0.7
C=O	2.3
O-C=O[a]	2.02
S=O[a]	2.3[b]
N-H	1.3

Notes: ([a]): Values calculated in the current work from employing Equation (6.16).

([b]): S=O was assumed to be 2.3 debye since O-S-O angle is similar to the O-C-O angle and the electronegativity of S is the same as C.

6.6.3.3. Calculation of the Weighted % Dipole Moments

The weighted % dipole moment (WDM), will be defined as the total dipole moment associated with a given surface. WDM is calculated from the % species present on a given surface, obtained by XPS analysis, and multiplied by their corresponding dipole moments from Table 6.3. The summation of the individual dipole moments of the different species is normalised by 1Debye and yields the total WDM value. To identify the species which will contribute to the dipole moment, extensive use was made of XPS and peak deconvolution techniques. The deconvolution was carried out using a dedicated computer connected to the analogue-digital converter of the XPS machine. The number of species that a particular peak was to be deconvoluted into, the binding energy (eV) of the centre of each species, the peak width at half the maximum height (PWHM) (eV) of the species had all to be defined (using standard guide values see Chapter Nine and the appendices of [183]) before deconvolution could be undertaken. Further, the error from the deconvoluted areas could be added and compared with the original peak area. This was necessary to ensure satisfactory deconvolution of the peaks.

The species of interest were: N-H, C-N, C-O, C=O, O-C=O and S=O. Note that the C-H species although present in substantial concentrations was not included in the WDM assessment since this species will contribute only to the dispersion surface energy. For example, polyethylene (PE) is composed of the monomer CH_2-CH_2 and has a near zero polar energy component. The dipole moments of the above groups are given in Table 6.3 and the details of calculating the WDM values are given below:

(a) It was assumed that the dipole moments of the species being calculated are from side-group species i.e., are not in the main molecular chain. This assumption will be justified at the end of the present section.

(b) C-N species: This species was assumed to be present in all the TPFC substrates under investigation except in the polyamide (PA) composites. This assumption is justified when the chemical structures of these thermoplastic matrices are considered, see Section 2.3.1. It was shown in Figure 3.37(b) (page 88) that the nitrogen, N1s, peak had a narrow electron binding energy region. Indicating the absence of oxygen type species from the nitrogen peak since, the presence N-O type species would broaden the nitrogen peak by about 5eV, see Table 3.11. Therefore, the atomic percentage of the N1s was assumed to be of C-N type and hence this value was multiplied by the corresponding dipole moment (0.2Debye), see Table 6.3.

(c) N-H species: This species was assumed to be present only in the polyamide (PA) composites, see Figure 2.5 (page 28). Therefore, the % concentration of this species was multiplied by 1.3Debye, see Table 6.3.

(d) C-O, C=O and O-C=O species: The concentration of these species can be obtained via:

(i) The oxygen, O1s, peak: most species in the O1s fall within a narrow range of 2eV. This renders the deconvolution of the O1s peak very difficult.

(ii) The carbon, C1s, peak: most species in the C1s peak are well defined at specific electron binding energies, see Table 3.11. Thus, the C1s peak was deconvoluted and the values of the oxygenated species were obtained, see for example Figure 6.8. The concentrations of oxygenated carbon species i.e., the C-O, C=O and O-C=O, are relative to the C1s peak and to assess these values relative to the total element atomic % concentration then, these values had to be multiplied by the atomic percentage concentration of the parent C1s element. However, a further complication is that the C-N species is also present in the carbon peak and has a binding energy which is close to that of the C-O species (especially in the presence of oxygen-rich species the electron binding energy of the C-N species increases by about 0.9eV [184]). Therefore, to avoid the duplication of the estimated C-N values the following route was adopted. It was assumed that the calculated values of the C-O species included those of the C-N species. For this reason the value of the C-N species, calculated from the nitrogen peak, was subtracted from that of the C-O species and the resultant was assumed to be now only due to the C-O species. The results from such calculations were then multiplied with their respective dipole moments from Table 6.3.

(e) S=O species: The sulphur S2p element was present in the U/C-PPS material. The sulphur peak was deconvoluted to assess the S=O species. This value was first multiplied by the atomic % concentration of the parent element, S2p, and then by 2.3Debye.

(f) Having obtained the individual % dipole moments from the different species, then these values were first added and then normalised by 1Debye to give the total weighted % dipole moment (WDM).

(a)
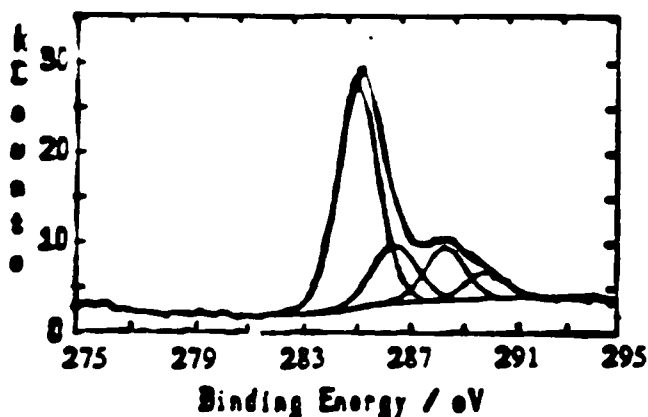
(b)

Fig. 6.8. Deconvolution of the C1s peak of the U/K-PA composite subjected to corona-discharge treatment levels of: (a) $0.25J/mm^2$ and (b) $5J/mm^2$. The detailed numerical results from the deconvolutions are given in Appendix A.8.

The values of WDM for the TPFC materials employed as a function of corona treatment level are shown in Figure 6.9. Several interesting features emerge from this figure. Firstly, with increasing corona treatment level, there is a dramatic increase in the WDM values for all the TPFC materials employed. Secondly, the increase in the WDM seems to follow a separate curve for each TPFC material. This indicates that each material attains a higher WDM value in a "unique manner" and that the increased value is also dependent on the untreated WDM value for a particular composite.

Finally, a check on the error of the calculated WDM values, from assuming that the species under consideration are side-group species reveals low values for all the TPFC materials, especially after corona treatment. For example, the C-O species is present in the main molecular chain of the untreated PEEK matrix, see Figure 2.4 (p. 28). Now, if it is assumed that the

dipole moment of this species is zero (a somewhat underestimate) since it is in the main molecular chain, then the error on the given WDM value, at a corona treatment level of $20J/mm^2$, is less than 20%. This error is an overestimate especially that the additional gains of the C-O species after corona treatment will be side-group species.
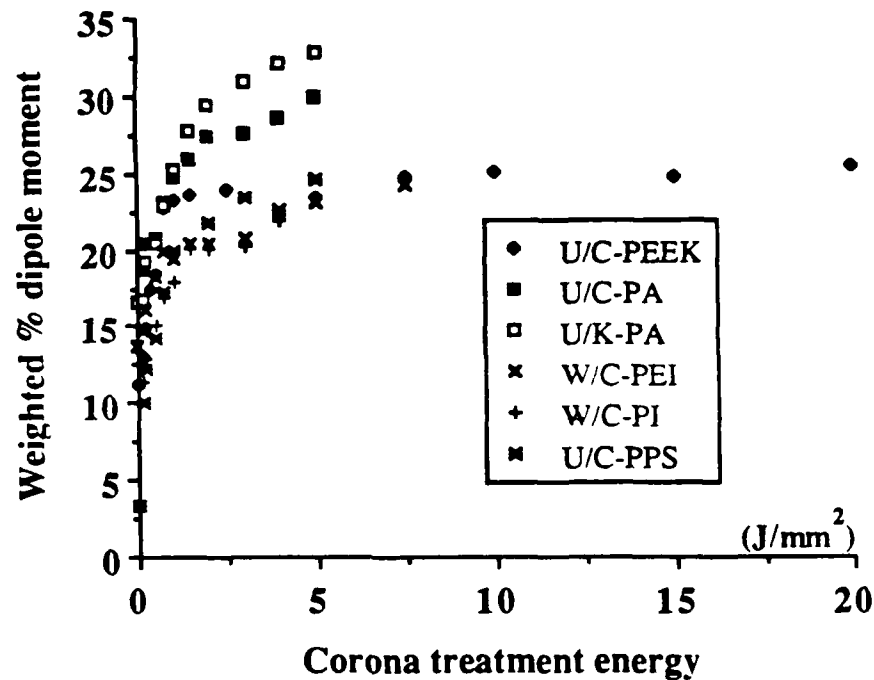
Fig. 6.9. WDM versus corona treatment for all the TPFC materials employed.

6.6.3.4. Calculation of the Percentage Polar Surface Energy

The dipole moments calculated in the previous section were percentage values and, therefore, to make a direct comparison between the calculated WDM values and the polar surface energy component then, the percentage polar energy component, $\%\gamma^P$, has to be calculated. The $\%\gamma^P$ value can be obtained by simply taking the ratio of the "corrected" polar energy with the total energy and multiplying the result with hundred. The reason for employing the "corrected" values was to eliminate any surface roughness effects and obtain the energy component due to change in only the surface chemistry brought about by the corona treatment. The results from such calculations are shown in Figure 6.10.

Several interesting features emerge from this figure. Firstly, there is a dramatic increase in the $\%\gamma^P$ for all the TPFC materials employed. Secondly, this increase seems to be a seperate

curve for each TPFC material. This indicates that each material attains a higher $\%\gamma^p$ value in a "unique manner".
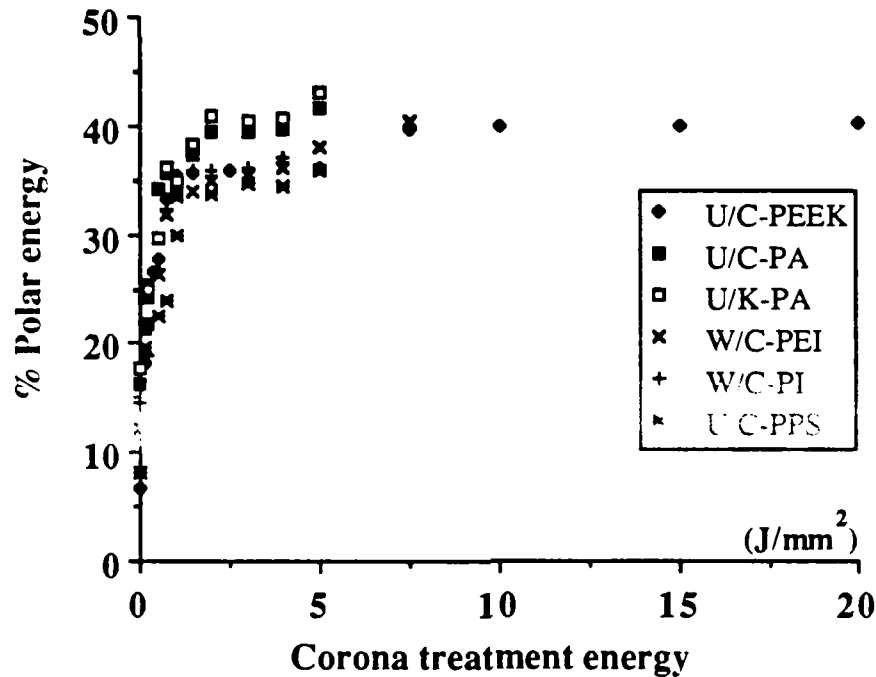
Fig. 6.10. Percent surface polar energy versus corona treatment energy for all the TPFC materials employed.

6.6.3.5. Relationship Between the Weighted % Dipole Moment and the % Polar Surface Energy

In the previous two sections the weighted % dipole moment and the % polar surface energy values were calculated and plotted against the corona treatment energy. In this section, these two parameters will be plotted against each other to examine the possibility of establishing a relationship.

Before embarking on such an investigation, it should be recalled that the polar energy is strictly a surface area parameter whereas the results from XPS are from a volumetric analysis. However, it was shown in Section 3.4.4.5 that depth profiling analyses, using XPS, had very little effect on the measured concentrations of the various elements. This indicates that the top surface, or at least the outermost 7nm of the surface, is uniform. This observation now enables a valid comparison of the two different sets of data.

Figures 6.11 to 6.13 show the plots of the WDM values versus the percent polar surface

energy for the TPFC materials employed. Several interesting features emerge from these figures. Firstly, for all the TPFC materials there is a direct relationship between the WDM values and the $\%\gamma^P$. However, sometimes one point does not fall close to the straight lines, see the circled points in Figures 6.11 and 6.12. The reasons for this kind of scatter can be one or a combination of the following reasons:

(1) There is certain to be experimental error in such plots where the results have been obtained via employing completely different techniques; namely, XPS and contact angle analyses. Typical estimates of these errors are ±12% and ±20% relative to the given WDM and $\%\gamma^P$ values respectively.

(2) The points which lie furthest from the straight lines, were always the first points i.e., from specimens which had not been treated with corona-discharge. It is interesting to note such points have an overestimated WDM value. Perhaps this behaviour can be understood if one considers that in the abraded materials some of the species which were assumed to contribute to the WDM may have far lower dipole moments. For example, the dipole moment of the C-O species is 0.7Debye. However, in an untreated U/C-PEEK composite this species is in the main molecular chain, see Figure 2.4, and therefore may have a lower effective dipole moment value than 0.7Debye.

Secondly, the relationship between the WDM and the $\%\gamma^P$ values from corona-treated and from aged substrates (corona-treated substrates which had been aged in controlled laboratory environment T=20±2^{0}C and R.H.=60%) is not only linear but seems to be also "universal", see Figure 6.13.

Thirdly, the result from the thermosetting composite, which does not require corona treatment, lies very close to the "universal" line.

Thus, the important implication of all the above observations is that all the fibre-composite materials employed have a direct "universal" relationship between the WDM and $\%\gamma^P$ values. This is in agreement with the definition of the polar energy and shows that it is possible to predict WDM from the $\%\gamma^P$ value and vice-versa.
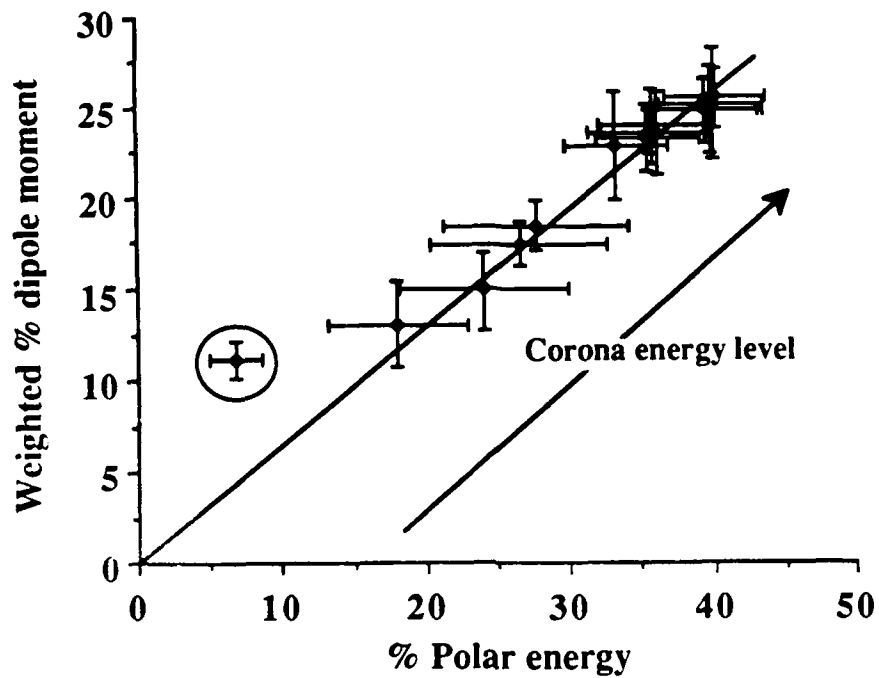
Fig. 6.11. Weighted % dipole moment versus % polar surface
energy for the U/C-PEEK composite.
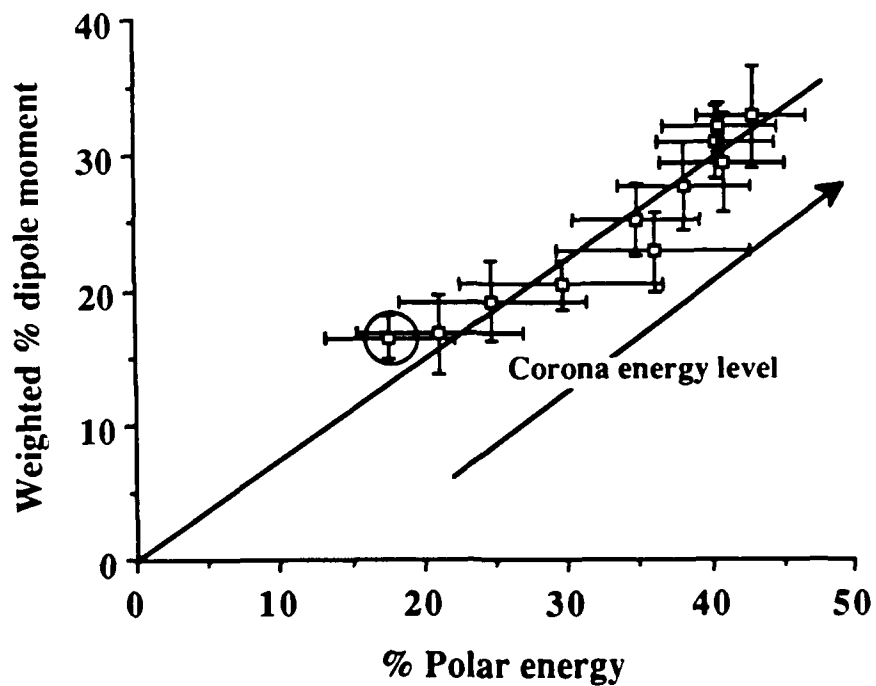
Fig.6.12. Weighted % dipole moment versus % polar
surface energy for the U/K-PA composite.
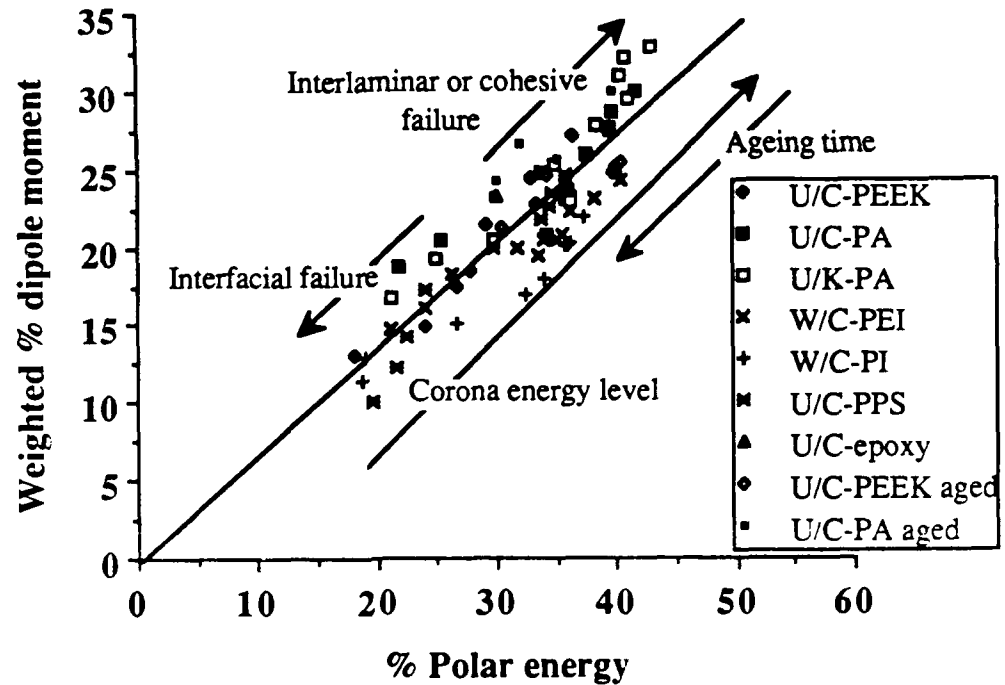
Fig. 6.13. Weighted % dipole moment versus % polar surface energy for all the fibre-composites employed from corona treatment and ageing.

6.6.3.6. Relationship Between Weighted % Dipole Moment, % Polar Surface Energy and Interfacial Strength

The interesting relationship between the WDM and the $\%\gamma^P$ values would have remained somewhat insignificant without establishing a further relationship between the results from Figure 6.13 and the interfacial adhesion in the fibre-composite joints. It appears that a WDM

value of 20 to 30%, or a $\%\gamma^P$ value of about 30 to 40% is required if a cohesive (or interlaminar failure) is to be expected when the epoxy adhesives are employed. However, the precise values will depend on: (i) the toughness of the adhesive used, (ii) the surface free energy of the adhesive, and (iii) the out-of-plane transverse stress of the composites employed. For example, if a composite which has a relatively low transverse tensile stress is employed then lower values of weighted % dipole moment and % polar surface energy would be required for interlaminar failure to be recorded.

To enable a more unambiguous comparison between interfacial strength, WDM and $\%\gamma^P$, then results corresponding to the critical corona treatment energies at which the locus of failure switched from interfacial to cohesive in the adhesive are shown in Figures 6.14 and 6.15.
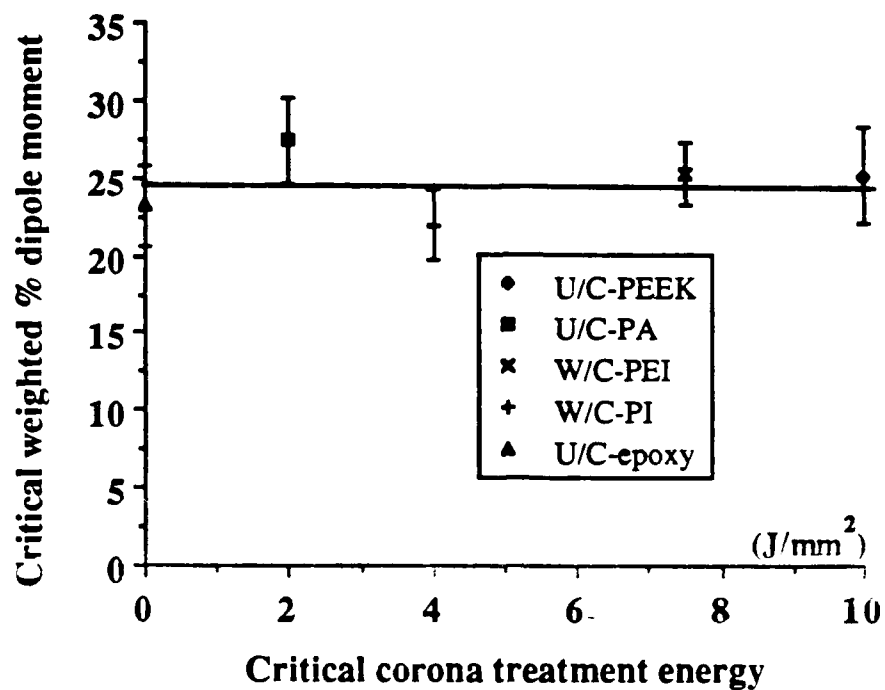
Fig. 6.14. Critical weighted % dipole moment versus the critical corona treatment energy for the composite materials which give cohesive failure when bonded using the epoxy-film adhesive.
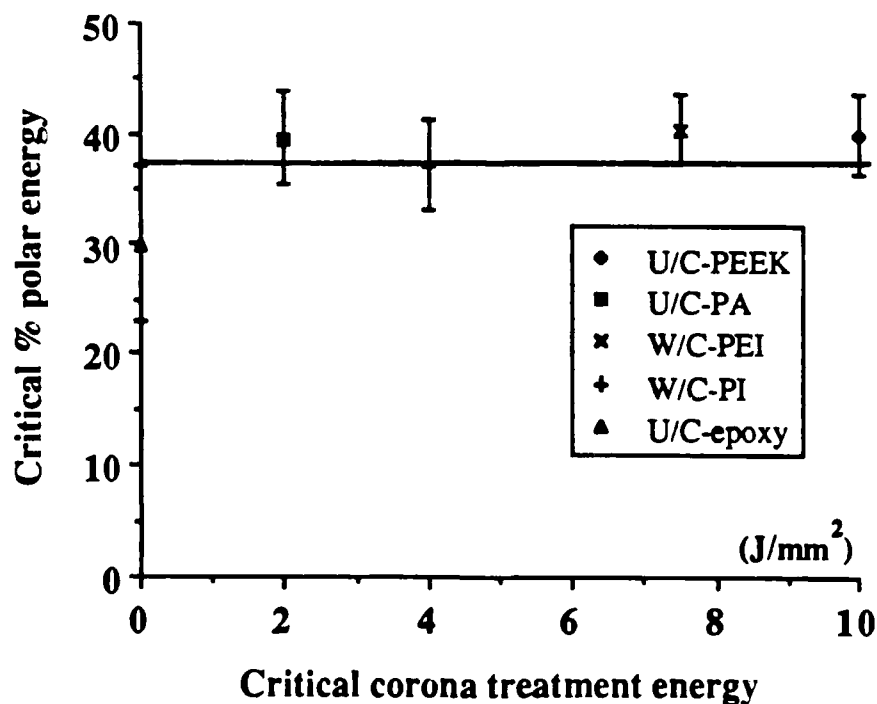
Fig. 6.15. Critical % polar surface energy versus the critical corona treatment energy for all the composite materials which give cohesive failure when bonded using the epoxy-film adhesive.

The most interesting feature in these figures is that all the fibre-composites employed, even the U/C-epoxy which does not require any corona treatment, have similar critical values of WDM and $\%\gamma^P$. (Note that the results are all from cohesive failure in the epoxy-film adhesive). WDM and $\%\gamma^P$ values from using the critical corona treatment where the locus of failure changed from interfacial to interlaminar in the composite are not shown in the above figures, since such values will depend on the transverse tensile failure stress of the composite. For example, the U/C-PPS composite, which has a rather low transverse tensile failure stress, fails in an interlaminar manner when bonded to the epoxy-film adhesive at a WDM value just under 23.0%. Obviously, this value is relatively lower than the values shown in Figure 6.14.

The results from employing the epoxy-paste adhesive are given in Table 6.4. The interesting feature again is that the respective values of critical $\%\gamma^P$ and WDM from the two different composites are again very similar. Note that the other composites have lower transverse tensile stress and therefore are not included in this table since they failed in an interlaminar manner.

Table 6.4. Critical weighted % dipole moments and critical % polar energy
values corresponding to critical corona treatment level which gives
cohesive failure through the epoxy-paste adhesive.

Composite	Corona treatment energy (J/mm^2)	WDM	$\%\gamma^P$
U/C-PEEK	20.0	25.5±1.6	40.3±3.5
U/C-PA	5.0	29.9±2.8	41.7±3.6

The WDM and $\%\gamma^P$ values from corona-treated aged specimens support the above proposed critical WDM and $\%\gamma^P$ values. When the WDM or the $\%\gamma^P$ values of aged thermoplastic substrates dropped below the critical values then the locus of failure changed from cohesive to interfacial.

The important implication of the above observations is that, dipole moments and/or the polar energy components should not be ignored, as suggested by some workers [166, 167, 171, 172], since there seems to be a relationship between these values and the locus of failure.

6.6.4. Thermodynamic Work of Adhesion

In the previous sections, it was shown that there is a relationship between the dipole moments and the polar energy. In this section the relationship presented for the thermodynamic work of adhesion, Equation (6.8), will be applied to the data obtained in Chapter Three.

Figure 6.16 shows a typical relationship between the thermodynamic work of adhesion, W_A, and corona energy. This figure shows that the thermodynamic work of adhesion, W_A, increases as the corona treatment energy is increased. The detailed numerical results from the other TPFC materials are given in Appendix A.9. Figure 6.17 shows a typical relationship between W_A and G_c. It is interesting to note that as the W_A values increased then the G_c values also increased. However, as expected, there is no direct simple relationship between the W_A and G_c values. (Since a direct relationship implies interfacial failure and of course, at relatively high corona treatment levels, plastic deformation was observed around the crack in the adhesive). Finally, Figures 6.16 and 6.17 show that W_A had to increase by less than 20% for the locus of failure to change from interfacial, with low values of G_c being recorded, to one of cohesive in the adhesive where high G_c (about 4kJ/m^2) values were recorded.
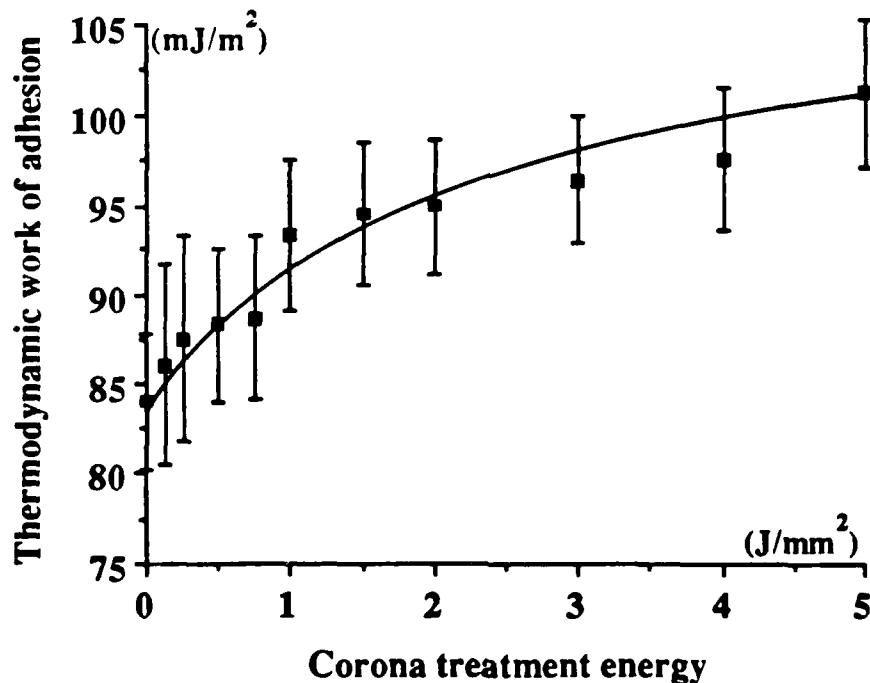
Fig. 6.16. Thermodynamic work of adhesion versus corona treatment the for U/C-PA composite.
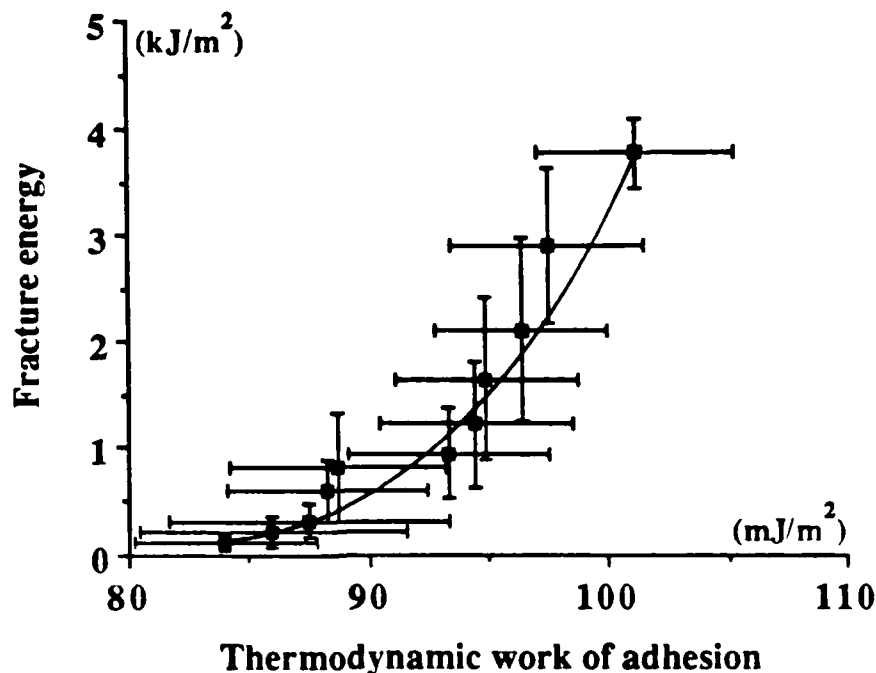
Fig. 6.17. Adhesive fracture energy versus thermodynamic
work of adhesion for the U/C-PA composite.

But, at first, it might be expected that there is a critical W_A value where the locus of failure might change from interfacial to cohesive in the adhesive. Figures 6.18 and 6.19 show the results from such analyses. The latter figure is similar to the former, but in Figure 6.19 the critical W_A values are calculated from surface chemical changes only (i.e. corrected for surface roughness effects). All the increases in the W_A values, from Figure 6.19, were due to the

increase in the γ_s^P of the composites, since γ_s^d remained constant in value. Therefore, although Equation (6.10) is valid, i.e. there is a relationship between G_c and W_A, see Figure 6.17, but for the above reasons and also due to some plastic deformation in the adhesive in the regions where some cohesive failures were observed, this relationship could not be clearly established, as seen from the scatter in Figures 6.18 and 6.19. Further, composites bonded using the epoxy-film adhesive, then the critical W_A value of the U/C-epoxy composite ($83.2 mJ/m^2$ see Figure 6.18) is even lower than a W_A value of the U/C-PEEK composite ($86.5 mJ/m^2$ see Appendix A.9) at a corona treatment level of $0.25 J/mm^2$. The initial material failed in a cohesive manner yielding a G_c value of about 1.9 kJ/m^2 whereas the latter failed in . an interfacial manner yielding a G_c value of only 0.12kJ/m^2.
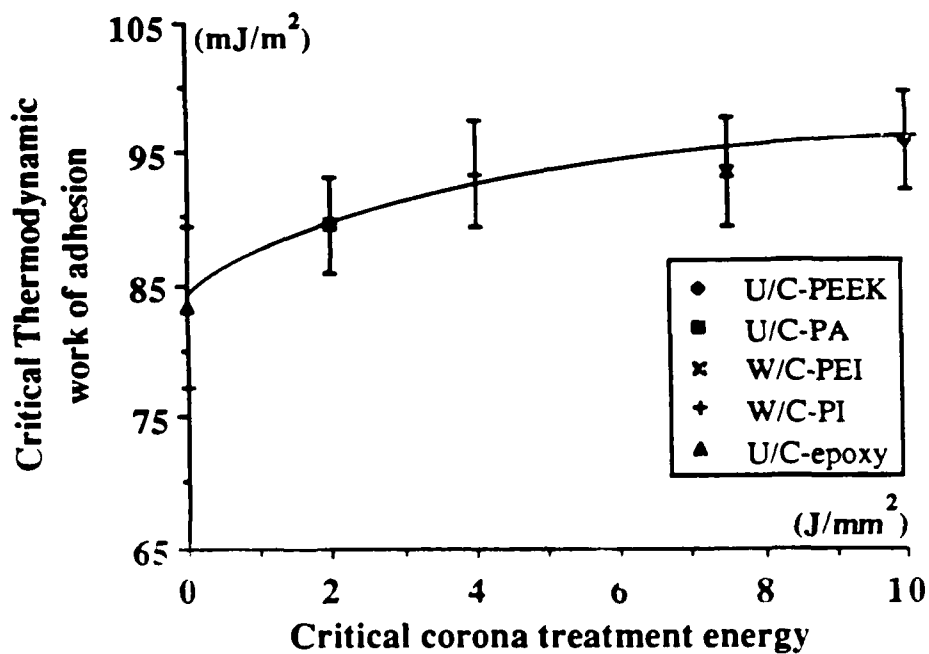
Fig. 6.18. Critical thermodynamic work of adhesion versus critical corona treatment energy for the composite materials yielding cohesive failures when bonded to the epoxy-film adhesive.
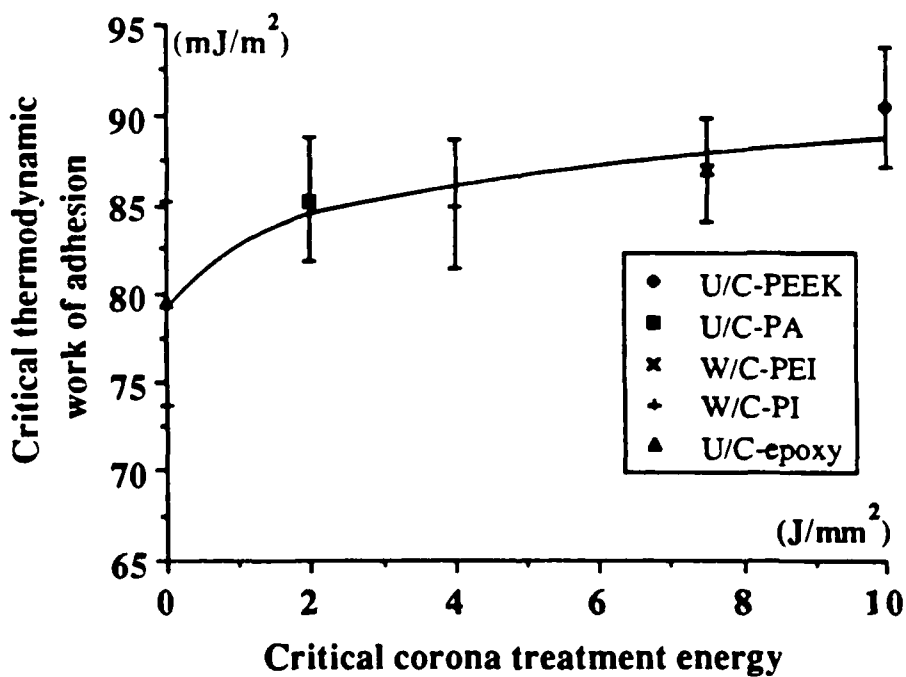
Fig. 6.19. "Corrected" critical thermodynamic work of adhesion versus critical corona treatment energy for the composite materials yielding cohesive failures when bonded to the epoxy-film adhesive.

From these observations it can be concluded that an analysis based on W_A to predict strong bonds may be somewhat difficult. Therefore, the thermodynamic work of adhesion in its current form, may yield useful information for weak bonds where strong intermolecular forces have not been establshed yet. However, its application to predict the critical W_A values for strong bonds is somewhat curtailed in this project perhaps due to specific chemical interactions at the interface and for this purpose the acid-base interaction will be considered next.

6.6.5. Acid-Base Interactions

So far correlations have been established between the weighted % dipole moment, % polar surface energy and the fracture results. Further, the thermodynamic work of adhesion was discussed above and it was shown that there is poor correlation between the critical W_A values and the critical adhesive fracture energy results. An alternative approach to predicting the intrinsic adhesion from interactions of the surface polar groups is the concept of specific interactions, such as acid-base interactions.

Now, two of the eight test-liquids employed in Chapter Three, were specifically employed for their basic and acidic characteristics namely, dimethylsulfoxide (DMSO) which is basic and, iodoethanol which is acidic. Equation (6.13) was employed to calculate the acid-base work of adhesion and the results are shown in Table 6.5.

Several interesting features emerge from this table. Firstly, the interpretation of the results is somewhat difficult. For example, the U/C-epoxy composite had the highest basicity and acidity when compared to the other composites employed. Therefore, i. was difficult to ascertain which one of these two characteristics should dominate the adhesion of the U/C-epoxy composite to the epoxy adhesives. Secondly, at moderate corona treatment levels the two test liquids completely wet the surfaces. Therefore, this technique will not provide values for the acidity or basicity of the more important stronger adhesive/composite interfaces. Thirdly, analysis of such results revealed that there was no relation between say a TPFC material attaining the same acidity and/or basicity characteristics as that of the U/C-epoxy composite and adhesion. For example, the U/C-PPS material attained equal basic and acidic characteristics as the U/C-epoxy material at a corona treatment level of $0.75 J/mm^2$. However, the U/C-PPS composite failed in an interfacial manner at this treatment level whereas the U/C-epoxy composite failed in a cohesive or interlaminar manner when the epoxy adhesives were employed.

Table 6.5. Examples of acid-base, $W_A{}^{ab}$, interactions of the composites employed.

Material	Corona treatment (J/mm^2)	Dimethylsulfoxide Acidity (mJ/m^2)	Iodoethanol Basicity (mJ/m^2)	Locus of joint failure
U/C-PEEK	0.0	12.8	5.0	Interfacial
U/C-PEEK	0.125	14.2	5.6	Interfacial
U/C-PA	0.0	15.1	5.6	Interfacial
U/C-PA	0.25	16.7	6.2	Interfacial
U/C-PPS	0.0	13.8	3.8	Interfacial
U/C-PPS	0.75	18.4	9.4	Interfacial
U/C-epoxy	0.0	18.9	9.9	Cohesive or interlaminar

Notes: (a) The acidity and basicity values of the epoxy-paste adhesive were 15.1 and $9.5 mJ/m^2$ respectively. Similarly, for the epoxy-film adhesive were 18.1 and $11.7 mJ/m^2$.

(b) The corona treatment energies are up to levels where complete spreading of the two test-liquids were obtained.

(c) The interfacial failures for the thermoplastic composites were observed from both epoxy adhesives.

6.6.6. Potential for Interfacial Covalent Bonding

So far, it was established that the critical thermodynamic work of adhesion does not correlate with the critical adhesive fracture energy, G_c, values due to specific interactions and for this purpose the acid-base interaction was considered. This technique also failed in giving any deep insight into the chemical interactions that may occur at the adhesive/composite interface. However, it was shown that there is a critical WDM or $\%\gamma^p$ value which correlate well with the critical G_c values.

The reason why a critical level of WDM or $\%\gamma^p$ may be needed is that this reflects the presence of polar groups on the TPFC substrates which might form interfacial primary covalent bonds to the epoxy adhesives. (Such bonding would not be accounted for in the calculation of the thermodynamic work of adhesion, W_A). Thus, a critical WDM or $\%\gamma^p$ value might reflect a

critical concentration of potential primary interfacial bonds.

Of the various groups detected using XPS the carboxylic acid group (O-C=O) is the only commonly detected group which would readily react with either the room-temperature cured epoxy-paste or hot-cured epoxy-film adhesives (note that amine groups, if present, will most definitely react with both epoxy adhesives). For both epoxy-adhesives, such a reaction would lead to the formation of the interfacial covalent bonds. Obviously, such relatively strong interfacial bonds would greatly increase the intrinsic adhesion.

6.6.7. Prediction of Environmental Ageing

The U/C-PEEK thermoplastic composites bonded to the epoxy-paste and the epoxy-film adhesives which had been immersed in a bath of warm water always yielded cohesive in adhesive failures, see Section 4.4.4.2. However, the G_c values from such specimens, decreased upon prolonged exposure to environmental attack.

Now, Equation (6.11) was employed to calculate the work of adhesion, W_{AL}, due to immersing the U/C-PEEK DCB joints in water. The W_{AL} results for the epoxy-paste and the epoxy-film adhesives were 17.5 and 16.5 mJ/m^2 respectively. Clearly, these values are far lower than the thermodynamic work of adhesion, W_A, which were calculated to be 103.3 and 95.9 mJ/m^2 for the cold-cured and the hot-cured epoxy adhesives respectively, (see Appendix A.9 Table A.10) but are still positive. Therefore, Equation (6.11) predicts that the interface should remain stable, and no interfacial failures were indeed observed.

The decrease in G_c for the environmentally aged joints is likely to be due to (i) plasticisation of the adhesive by water ingress and/or (ii) degradation of the adhesive.

6.7. CONCLUSIONS

The main conclusions from the discussions in this chapter are:

1) It was shown that the observed poor adhesion of the TPFC materials to the epoxy adhesives was not due to weak boundary layers. It was also shown that mechanical interlocking and surface roughness had a minimal effect on the adhesion of TPFC materials after they were treated with corona-discharge. Further, the epoxy adhesives employed spread on the untreated TPFC materials, and therefore lack of wetting could not be the reason for the weak adhesion either. Therefore, it was suggested that the lack of intrinsic adhesion was due to

the lack of active chemical groups which if present can establish strong interatomic and intermolecular forces across the adhesive/composite interface. Corona pretreatment introduces such chemical (polar) groups onto the surfaces of the TPFC substrates and so greatly enhances the intrinsic adhesion at the adhesive/substrate interface.

2) However, the available techniques for predicting "strong bonds" seem to be inadequate, and sometimes limited in their application; as for example is the acid-base interaction theory. For this reason attempts have been made to quantify the concentration of chemical (polar) groups needed to give "strong" intrinsic adhesion, and hence avoid interfacial failure of the joints which is associated with low G_c values. Namely:

A correlation between the XPS and CAA results was established by a new idea. The weighted % dipole moments (WDM) estimated from XPS were correlated with % polar surface energy values. These two estimated values followed a "universal" curve whereby, data from all TPFC materials, (including those which had been aged prior to bonding and the results from the thermosetting composite) fell upon the "universal" curve. There appeared to be a narrow range of critical WDM, or critical % polar energy, values at which the interfaces of the fibre-composite materials employed attained sufficiently high intrinsic adhesion to prevent interfacial failure occurring in the bonded joints.

Having successfully bonded the TPFC substrates, the final part of the present thesis is concerned with employing this type of technology in engineering lap joints in an attempt to make use of the higher toughness of TPFC materials to produce strong and efficient joints.

CHAPTER SEVEN

JOINT DESIGN

7.1. INTRODUCTION

The work described in the previous chapters has demonstrated how the adhesive bonding of thermoplastic fibre-composite (TPFC) materials may be successfully achieved, and work reported in the literature has shown that the failure loads of lap joints may be greatly increased by careful joint design, such as choosing an appropriate overlap length and considering overlap end effects. Therefore, for the first time, thermoplastic fibre-composite (TPFC) materials will be employed in an attempt to design highly-efficient lap joints. Further, the experimental results will be compared with the predicted joint strengths from using finite element analysis (FEA). It should be noted that only the unidirectional-carbon/poly(ether-ether ketone) (U/C-PEEK) and the unidirectional-carbon/polyamide (U/C-PA) composites bonded employing the epoxy-paste adhesive will be considered in the above studies, since these materials possess the best mechanical properties of the all-round materials examined. The thermosetting composite will also be employed, but only for comparative purposes.

7.2. LITERATURE SURVEY

7.2.1. Introduction

The literature survey will first review the current methods recommended for measuring the basic engineering properties of composites and adhesives needed to undertake the FEA studies of joints. This will be followed by a review of the design of double-lap joints.

7.2.2. Mechanical Properties of Substrates and Adhesives

The material properties required for the computer analyses were:
1) the tensile moduli and strengths of the composites,
2) the tensile modulus, the elastic stress and strain limit and the tensile failure stress and strain of the adhesive, and
3) the shear elastic stress and strain limit, the shear failure stress and strain and the shear modulus of the adhesive.

Before discussing the test methods for the adhesives it should be noted that some

controversy exists whether adhesive properties in the "thin film form" are the same as when bulk specimens are tested. For instance, Volkersen [185] quoted experimental work by Muller [186] which showed that the Young's modulus of an adhesive decreased as the adhesive layer thickness was increased, whereas the shear modulus of the adhesive was independent of the adhesive thickness. Franzblau and Rutherford [187] have reported similar observations. However, the popular belief that the adhesive has different properties in these two cases i.e., "thin film form" and bulk, is essentially due to the fact that, in almost all bonded specimens, the adhesive layer is in a complex state of stress. Indeed, in more recent work, Dolev and Ishai [188] have reported that a good correlation exists between the "thin film form" and the bulk properties of structural adhesives. Hence, in the present work it will be assumed that the properties of adhesives in bulk and in "thin film form" are the same, and this assumption will indeed be shown to be valid in Section 7.4.1.2.

7.2.2.1. Tensile Properties

The tensile properties of the composites and the adhesive were obtained employing the ASTM recommended test methods.

(i) Composite Substrates

To determine the tensile modulus and the tensile failure stress of fibre-reinforced-plastics ASTM Standard D3039-74 recommends the use of rectangular-shaped specimens, as shown in Figure 7.1. For a thickness of 2mm then a width of 12.7mm can be employed to determine the desired mechanical properties. This Standard recommends the application of the load via cross-ply (woven) tabs bonded to the ends of the specimens. These tabs prevent the premature delamination of unidirectional-fibre-composites in the unreinforced direction.
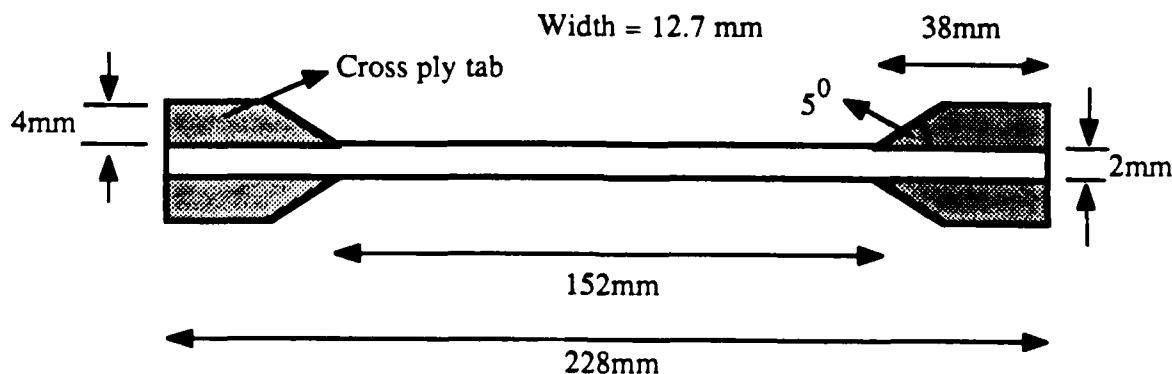
Fig. 7.1. The specimen dimensions recommended by ASTM Standard D3039-74.

(ii) Adhesives

To determine the various mechanical tensile properties of polymers the ASTM Standard D638-77 recommends the use of "dog-bone" type specimens, the dimensions of which are given in Figure 7.2. This Standard recommends different dimensions for different specimen thicknesses. The dimensions shown in Figure 7.2 can be used for a specimen which is 5 mm thick. This Standard also recommends the use of the 50mm section of the specimen, see Figure 7.2, to perform the strain measurements.
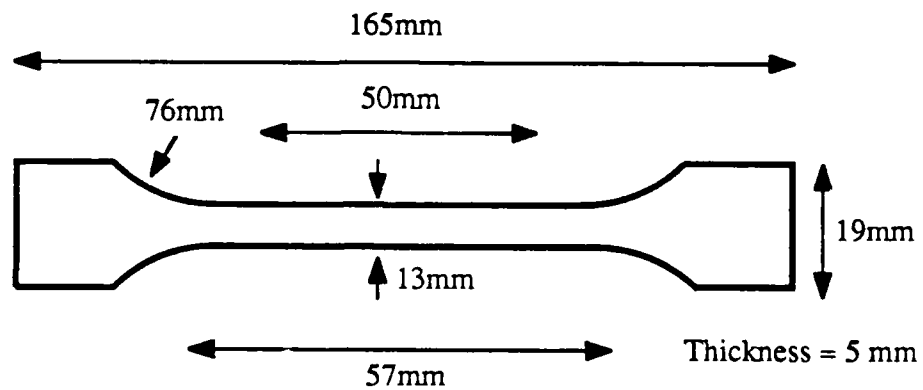
Fig. 7.2. The "dog-bone" type specimen recommended by ASTM Standard D638-77.

7.2.2.2. Shear Properties of Adhesives

There are two general types of specimen configuration, commonly employed to obtain the shear properties of adhesives: (i) the thick-adherend-test (TAT) specimen, see Figure 7.3 and (ii) a cylindrical butt-joint design loaded in torsion, see Figure 7.4.
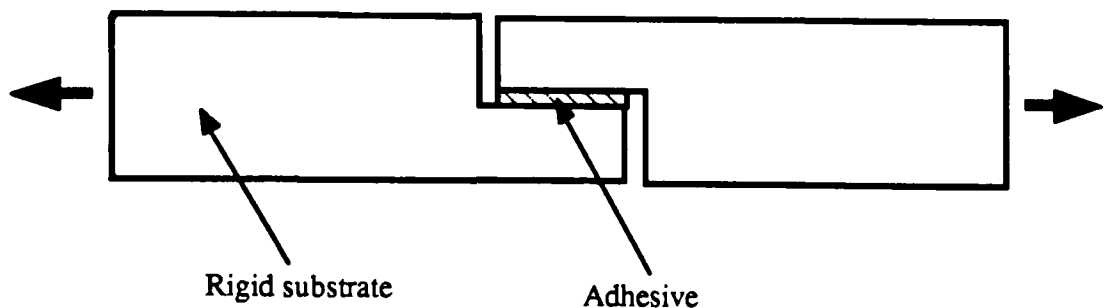
Fig. 7.3. Schematic presentation of a thick-adherend-test specimen which is loaded in tension to yield the shear properties of the adhesive.
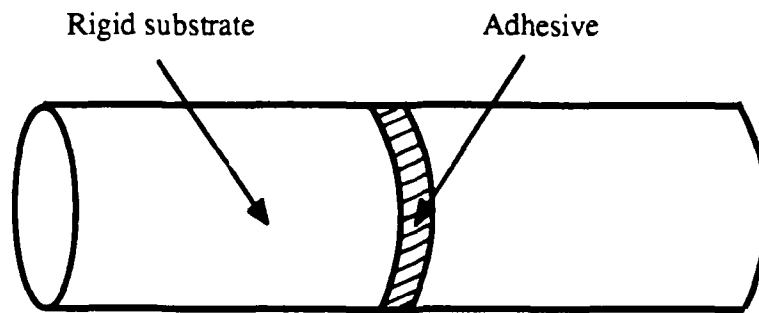
Fig. 7.4. A schematic presentation of a cylindrical-butt joint geometry.

However, papers published by several workers [189-193] suggest that problems do exist in measuring the shear properties of adhesives. Such problems include:

1) the difficulty in measuring the shear strain of the adhesive [194, 195], and

2) the effects due to the geometry of the specimen on the shear properties of an adhesive [189-191, 195].

(i) Thick-Adherend-Test (TAT) Specimen

A recently developed method is the TAT specimen which is recommended by ASTM Standard D3983-81 and is shown in Figure 7.3. In this specimen the effects of differential shearing in the adhesive layer are minimized by using rigid and thick metallic substrates. Further, in this form of joint there is considerable increase in the flexural stiffness of the substrates and the out-of-plane transverse tensile stress concentrations are therefore also minimal. There is, therefore, a popular belief [194, 196] that the adhesive is now in a state of uniform shear and that there are no significant transverse peeling loads. However, other workers [190, 191, 195] have shown that, experimentally it is difficult to measure accurately the shear properties of the adhesive. Nevertheless, they employed [190, 191, 195] "improved" designs of the TAT specimen by changing the overlap length and thickness of the substrate from those recommended by ASTM D3983-81. The aim of such geometrical changes was to obtain a more uniform shear stress distribution across the overlap length of the TAT specimen.

However, the results from TAT specimens should still be interpreted with caution since there are two main sources of error: (i) a non-uniform adhesive stress distribution and (ii) substrate deformation, the magnitudes of which are normally not quoted [190, 191, 194-196]. For example the ASTM D3983-81 is limited to the measurement of the shear modulus of "nonrigid" adhesives and the ratio of the tensile modulus, E, of the substrate to the shear modulus, G, of the adhesive should be greater than 300:1. Renton [197] using a closed-form analysis, has shown that bending deformation of the substrates can introduce significant errors,

and recommended that if a substrate-surface measuring device is to be used then a realistic limit of E to G ratio of 2000:1 should be employed. Hence, for aluminium substrates, as employed by the above workers, this limits the shear modulus that can be measured accurately to less than 0.035GPa (generally structural adhesives have higher moduli). In order to overcome the problem of errors due to substrate deformation, a very accurate linear-variable displacement-transducer (LVDT) extensometer was developed by Krieger [198]. This extensometer is attached to the TAT specimen at points only 1 to 2mm each side of the adhesive layer. However, even with this device, a correction may be required, to account for the substrate deformation between the extensometer and the adhesive layer. Again this value is never quoted, so that its significance is not known. For example, Krieger in a recent work [194] reported the shear moduli and the complete shear stress-strain curves up to failure for three adhesives, based upon the assumption that the adhesive layer is in uniform shear and ignoring the deformation between the extensometer and the adhesive.

Thus, although the TAT specimen may be cheaper and a more simple joint to produce, than say a cone-and-plate specimen (see Figure 7.6), a number of limitations apply to its applicability which are not generally recognized. For the above reasons the TAT specimen was not employed in this project.

(ii) Torsion Test Methods

a) Napkin-ring specimen: The ASTM Standard E229-70 suggests the use of a cylindrical joint design similar to the one shown in Figure 7.5. This type of specimen design will yield a pure shear stress distribution, which is never achieved with a TAT specimen. This Standard recommends the use of mirrors and a light source as a means of measuring the shear strain. To measure the shear strain of the adhesive by this technique requires manual recording. Further, this Standard recommends loading the specimen so as to produce failure in two to five minutes. Most tough adhesives have very low elastic shear strains, typically 3 to 5% , compared to shear failure strains which are typically 100 to 200% [192]. To achieve a failure in two to five minutes would require a loading speed which would exceed the elastic shear strain limit in a matter of seconds.

Therefore, the technique recommended by ASTM Standard E229-70 is somewhat outdated since it is inconceivable to obtain manually enough data points to determine the behaviour of the shear stress/strain curve in the elastic region. Further, the preparation of a cylindrical joint design is somewhat difficult; for example it is difficult to ensure a uniform adhesive thickness throughout the cylindrical bonded region.
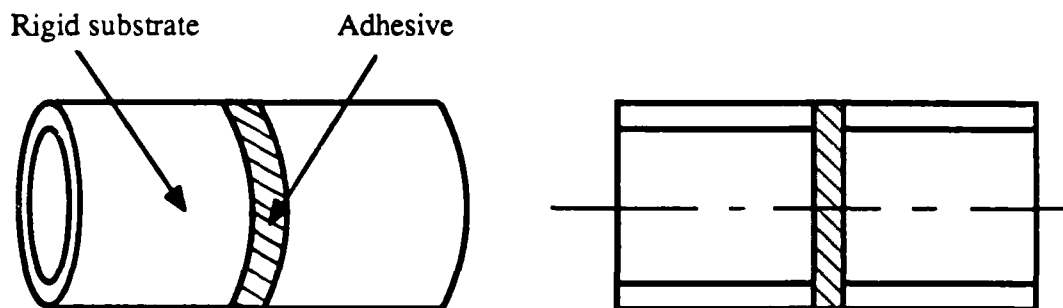
Fig 7.5. Schematic presentation of a napkin-ring test geometry.

(b) Cylindrical butt joints (Figure 7.4): Stringer [192] employed this joint design to determine the shear properties of structural adhesives but his technique suffers from several disadvantages. Firstly, the shear strain was measured at the twistometer arm, and hence there was a need to subtract the contribution of shear strain of the substrates from the total measured shear strain. Stringer indicated that this subtraction was indeed substantial, but he did not quote any values. Secondly, employing cylindrical butt substrates results in a pure shear stress distribution where the shear strain varies directly with the radius of the cylinder. Therefore, this type of specimen may introduce an element of error dependent on the geometry of the specimen. Thirdly, a calculation using the reported data reveals that the joints failed in less than two minutes, which is outside the time limit specified by the ASTM Standard. Finally, Stringer did not give the details of the adhesives which he employed, and hence no comparisons can be made with reported data from other specimens.

(c) Cone-and-plate: In order to achieve a more uniform state of shear stress distribution in torsion tests, Grant and Cooper [193] proposed employing a cone-and-plate specimen design, see Figure 7.6. They calculated the change in the shear stress distribution in the bonded region for different cone angles and concluded that the change was very small when cone angles less than 10^0 are employed. For example, the change is only 0.77% when a cone angle of 5^0 is employed. The advantages of employing such a specimen include: (i) a uniform pure shear stress distribution in the bonded region is obtained and (ii) the cone angle predetermines the adhesive thickness and, therefore no spacers are required to establish the adhesive thickness.

The theoretical analysis presented by Grant and Cooper [193] is correct, however, their experimental technique is somewhat weak. They do not give details of the procedure employed in calculating the shear strain and, unfortunately, their calculated SI units seem to be wrong by three orders of magnitude. For example, they quote a shear modulus of an adhesive of 2.11MPa which is even less than that of a rubber, and obviously this value cannot be correct. In the current work cone-and-plate test specimens will be employed and a new technique will be developed to determine the shear strain of the epoxy-paste adhesive.
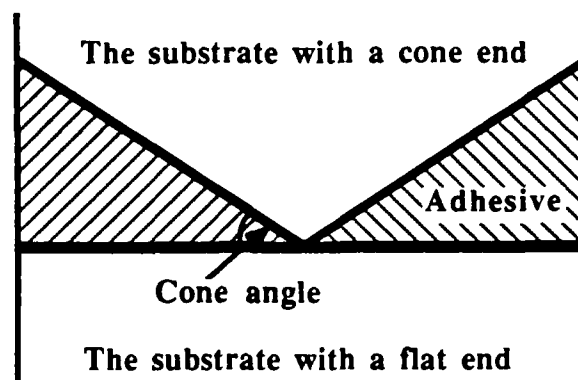
Fig. 7.6. A schematic presentation of a cone-and-plate joint geometry.

Finally, it should be noted of course that the shear modulus of an isotropic material is related to the Young's modulus by the following equation:

$$G = \frac{E}{2(1 + \upsilon)} \qquad (7.1)$$

where G is the shear modulus, E is Young's modulus and υ is the Poisson's ratio.

7.2.3. Designing Efficient Lap Joints

7.2.3.1. Introduction

The structural engineer is interested in obtaining high failure loads, and hence a higher "efficiency" from a given engineering joint, where:

Efficiency = Strength of the joint/Strength of the weaker substrate (7.2)

The structural engineer is also concerned with the ability to predict the loads and stresses which are likely to be encountered in practice. The basic theoretical treatment of the stress distribution in adhesively bonded joints, based on the classical analytical methods of continuum mechanics was developed some 50-60 years ago. Recently, these methods have been modified for composite materials to take into account their anisotropic properties. Although many other joint designs exist, the literature survey will consider mainly the double-lap joint (DLJ) design. This specimen was chosen since (i) it requires only relatively simple preparation methods compared to, for example, the stepped-lap joint, see Figure 7.7, and (ii) the DLJ design is superior to the single-lap joint (SLJ) design, as will be shown in the following section.
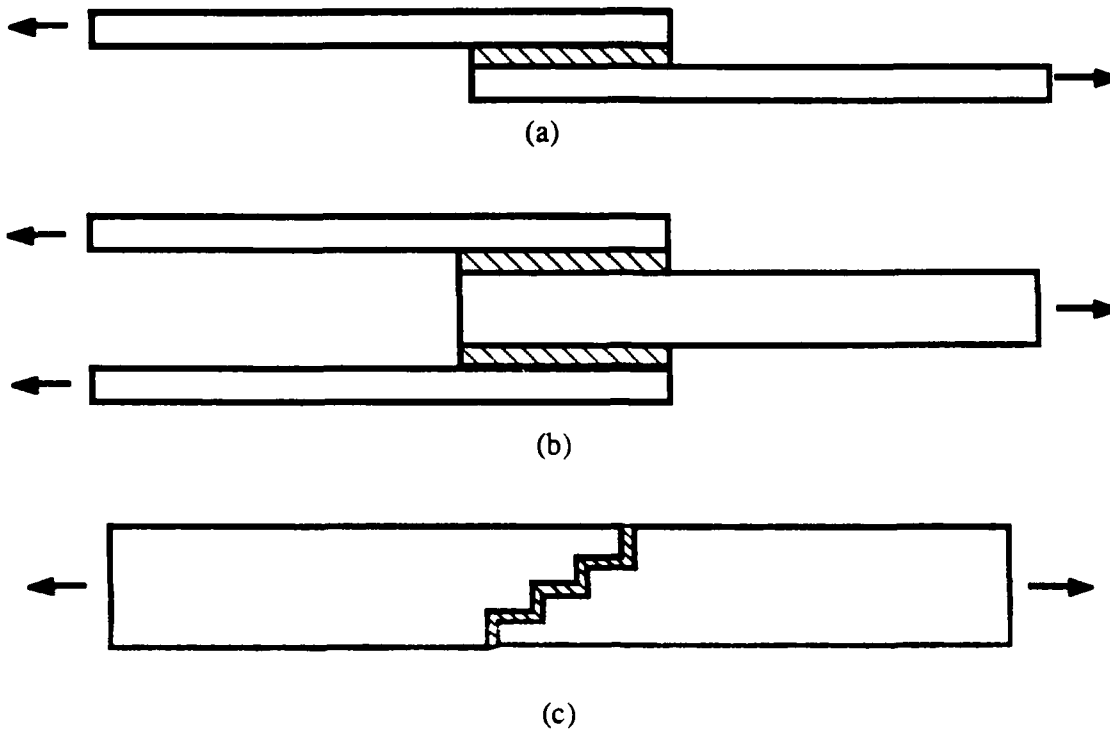
Fig. 7.7. (a) Single-lap joint, (b) double-lap joint and (c) stepped-lap joint.

7.2.3.2. Early Work

Early work on the stress analysis of lap joints was concentrated on the single-lap joint, see Figure 7.7(a). The simplest analysis considered the substrates to be relatively rigid and the adhesive to deform only in shear. This is shown in Figure 7.8(a). If the width of the joint is B, the length l, and the load P, then the uniform value of the shear stress τ is given by:

$$\tau = P/(Bl) \tag{7.3}$$

and the substrate tensile stress will decrease linearly to zero over the joint length from point A to B. In Figure 7.8(b) a similar joint is shown but in which the substrates are elastic. For the upper substrate, the tensile stress is a maximum at A and falls to zero at B. Thus, the tensile strain at A is larger than that at B and this strain must progressively reduce over the length l. The converse is true for the lower substrate. Thus, assuming continuity of the adhesive/substrate interface, the uniformly sheared parallelograms of the adhesive shown in Figure 7.8(a) become distorted to the shapes given in Figure 7.8(b) giving relatively high shear stresses at the ends of the overlap. This phenomenon is called differential shear and this is essentially what Volkersen analysed [199] in 1938.

Volkersen's analysis did not take into account the tensile stresses generated in the

adhesive as a result of the eccentricity of the loading of the joint. This is shown schematically in Figure 7.8(c) and this feature was first analysed by Goland and Reissner [200] in 1944. They assumed that the adhesive and the substrates behaved as linear elastic (Hookean) materials and expressed a bending moment factor, k, which relates the bending moment, M, on the substrates at the end of the overlap to the in-plane load, P, and the substrate thickness, t, by the relationship:

$$M = kPt/2 \tag{7.4}$$

This is true if the applied load on the joint is small. As the load is increased then the overlap rotates bringing the line of action of the load closer to the centre-line of the substrates.
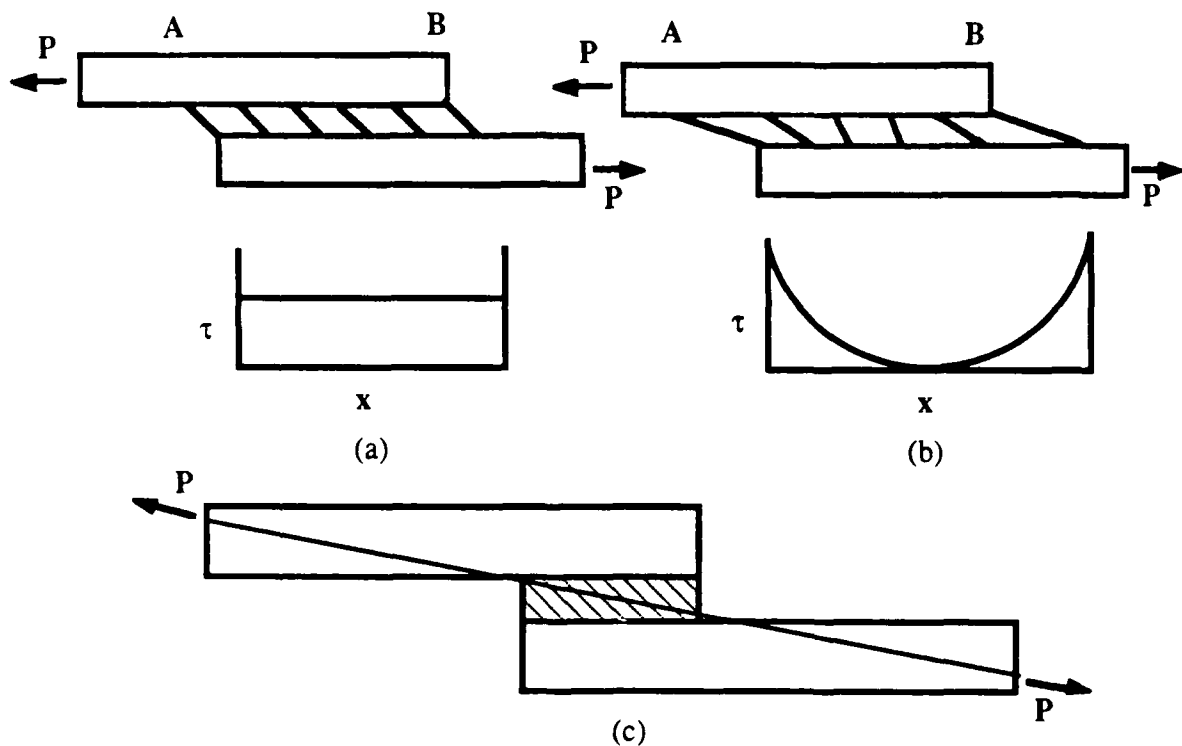
Fig. 7.8. Schematic presentations of SLJ specimens: (a) deformed with rigid substrates, (b) deformed with elastic substrates, and (c) undeformed but under eccentric loading.

Although there is no net bending moment in the DLJ specimen, as there is with the SLJ, because the load is applied through the adhesive to the substrates away from their neutral axes, the DLJ specimen experiences internal bending as shown schematically in Figure 7.9. This effect was first considered by Volkersen [185], and subsequently by Adams and Peppiatt [201]. In a DLJ specimen, the centre substrate experiences no net bending moment, but the outer substrates bend, giving rise to tensile stresses across the adhesive layer at the end of the overlap where they are loaded, and compressive stresses at the end where they are not loaded,

as shown in Figure 7.9.
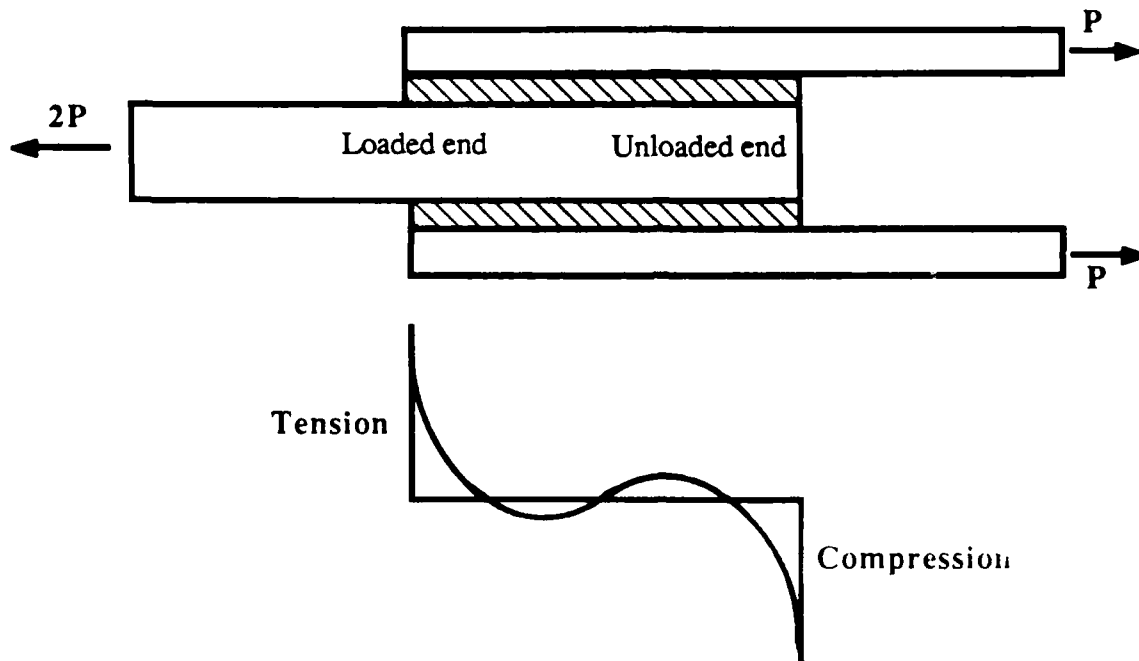
Fig. 7.9. Bending moments induced in the outer substrates of a DLJ
specimen and adhesive transverse normal stress distribution.

Published work [202-206] and commercial computer programs (for example the ESDU
program [207]), use the differential shear theory to predict failure loads versus overlap lengths,
see Figure 7.10.
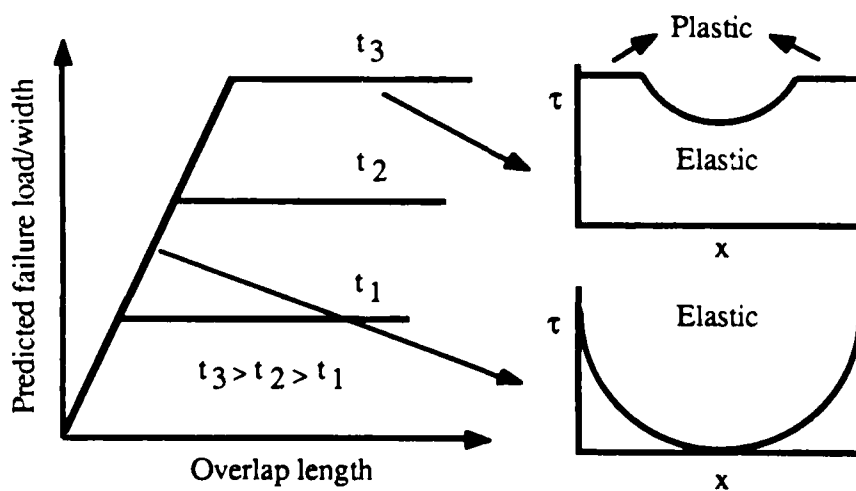
Fig. 7.10. A typical schematic presentation of failure load versus
overlap length curves based on differential shear theory.

Two interesting features emerge from this type of analysis. Firstly, as the overlap length
is increased then the failure load increases until a plateau value is reached where plastic

deformation at the ends of the overlap govern the failure (since the shear stress and strain at the ends of the overlap are maximum from differential shear analysis). Secondly, as the thickness of the adhesive is increased then the failure load may be increased. But, of course, the maximum failure load that can be attained is limited by the failure load of the substrate, see Equation (7.2).

7.2.3.3. Application of FEA to Joint Design

The idealised DLJ shown in Figure 7.9 can be analysed employing closed-form continuum mechanics equations. The solutions from these equations, based upon differential shear, predict that the highest stresses should occur near the ends of the joint. However, this type of an idealised joint with 90^0 corners is rarely observed in practice. In fact, most adhesives leave behind a fillet during spreading and consolidation which influences the stresses in the corners where joint failure usually initiates. Therefore, analysis of the stresses in different adhesive and substrate geometries is best carried out employing finite element analysis (FEA). The important advantage of employing FEA lies in the fact that the location and magnitude of all stresses in a body of almost any geometrical shape under load can be predicted. However, FEA packages may also have limitations in predicting stresses especially in an elastic-plastic analysis, as will be demonstrated.

7.2.3.4. Adhesive End Effects

In 1954 Mylonas [208] investigated the stresses induced at the end of an adhesive layer for a number of adhesive edge-shapes using photoelastic techniques and showed that the position of the maximum stress is dependent on the edge-shape and that this influenced the failure loads. This observation led to more detailed analyses by many workers and it was demonstrated that adhesive fillets not only portray a more realistic joint, but may indeed be beneficial. More recently, Adams and Peppiatt [201] employed FEA to analyse the principal stress pattern at the end of a square-edged (i.e. 90^0) adhesive layer with that of an adhesive layer with 0.5mm fillet length, see for example Figure 7.11. They assumed [201] that the adhesive behaves in an elastic manner and therefore failure occurs due to principal stress failure criterion. Further, Adams and Peppiatt showed that adhesive fillets have significant effect on the stress distribution, compare Figures 7.12(a) and (b) (the length and direction of the lines represent the magnitude and direction of the principal stresses and a bar at the end of the lines indicates a compressive principal stress). It can be seen that the inclusion of an adhesive fillet has indeed lowered the magnitude of the principal stress in the adhesive adjacent to the middle substrate, see Figure 7.12(a) and (b). Thus indicating that such end effects may increase the failure load.

Adhesive fillet length
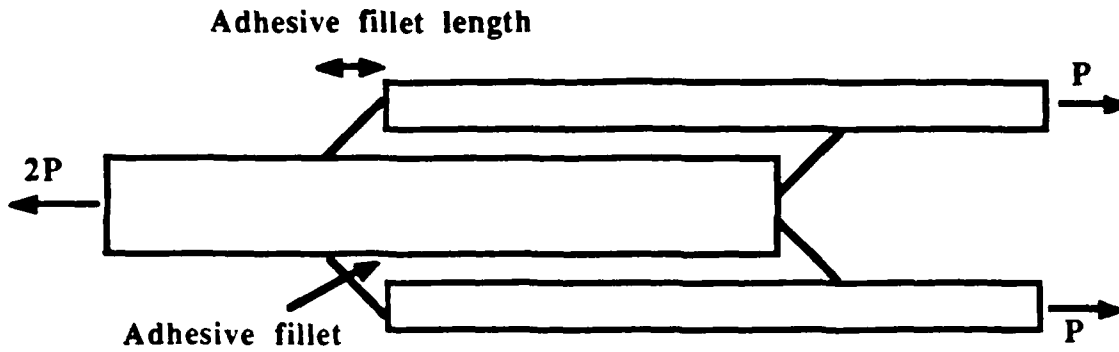
Adhesive fillet

Fig. 7.11. A schematic presentation of a DLJ specimen with adhesive fillets.

(a)   (b)
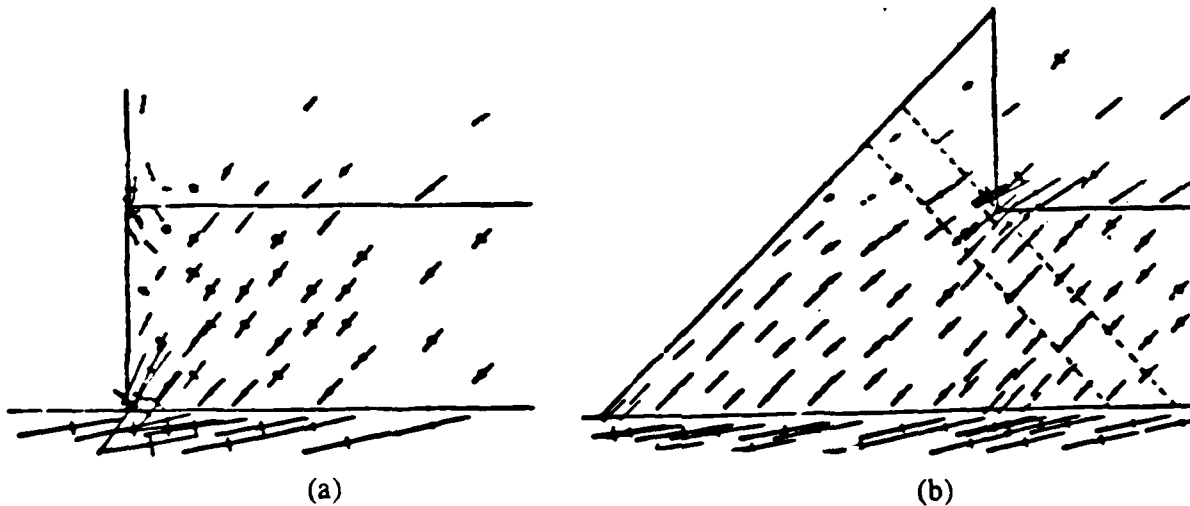
Fig. 7.12. Finite element prediction of the principal stress pattern at the end of
(a) a square-edged adhesive layer and (b) an adhesive layer with a fillet [201].

Crocombe and Adams [209] studied the effect of the adhesive fillet on the adhesive stress distribution over a range of material and geometric properties. They concluded that the position of the maximum stress occurs in the overlap under the outer substrate. The maximum principal stress being at the loaded substrate corner, acting at about 45^0 to the longitudinal axis of the joint, the maximum peel stress being at the overlap end just within the adhesive layer and the maximum shear stress being at the adhesive/substrate interface at a small distance from the overlap end.

They used a DLJ specimen to examine crack initiation in the adhesive joint. By inserting a metal shim to act as a crack stopper, they showed that the crack starts near the corner and propagates to the free surface as shown in Figure 7.13(a). Further, Crocombe and Adams concluded, from experimental observations, that when a crack is allowed to run completely in the joint then it runs along the adhesive/substrate interface. It then meets a similar crack running in the opposite direction and this results in complete failure of the joint as shown schematically in Figure 7.13(b).
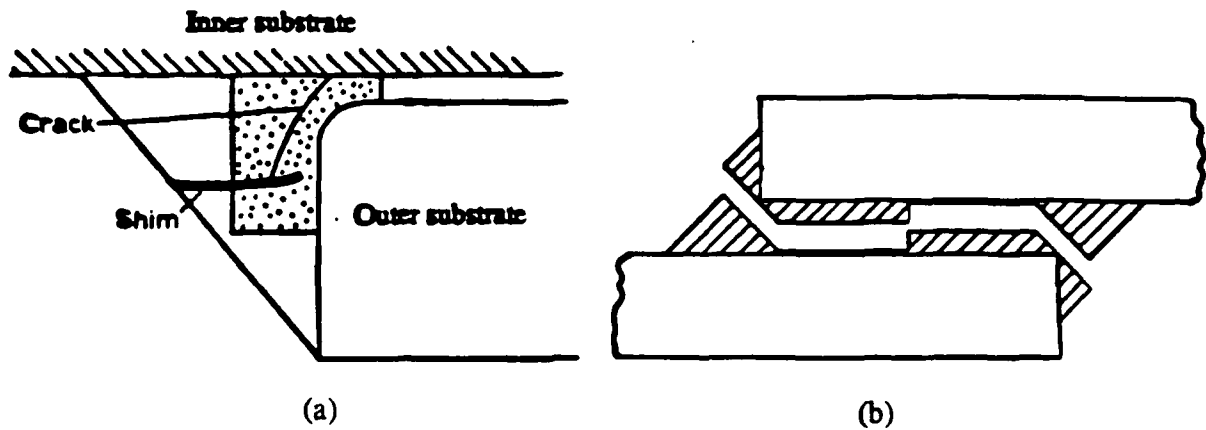
Fig. 7.13. A shematic presentation of the position of (a) crack initiation and (b) crack propagation in a DLJ specimen [209].

7.2.3.5. Nonlinear Analysis

(i) Early Work

Nonlinear FEA studies are extremely expensive because of the large amount of computer time required. All reported FEA work is based on employing elements with linear strain fields. Cooper and Sawyer [210] are the only authors who have used elements with linear stress fields, thus being able to satisfy equilibrium on a stress-free boundary.

The SLJ test piece geometry was analysed by Harris and Adams [211] with aluminium substrates and they included various nonlinearities, such as the nonlinear effects of joint rotation. They maintained the material properties as linear elastic. They showed the effect of the large displacement joint rotations on the maximum principal stress in the adhesive layer, see Figure 7.14. Note that as the load is increased joint rotation may occur which deforms the substrates resulting in a reduction in the peak stress concentration at the edge of the overlap.

In 1976 Thamm [212] argued, based on a closed-form theoretical analysis, that sharpening the substrates at the edges of the overlap leads to a reduction of the maximum shear stress at these edges. Unfortunately, he did not perform experiments to show that employing such geometries may indeed increase the failure load.
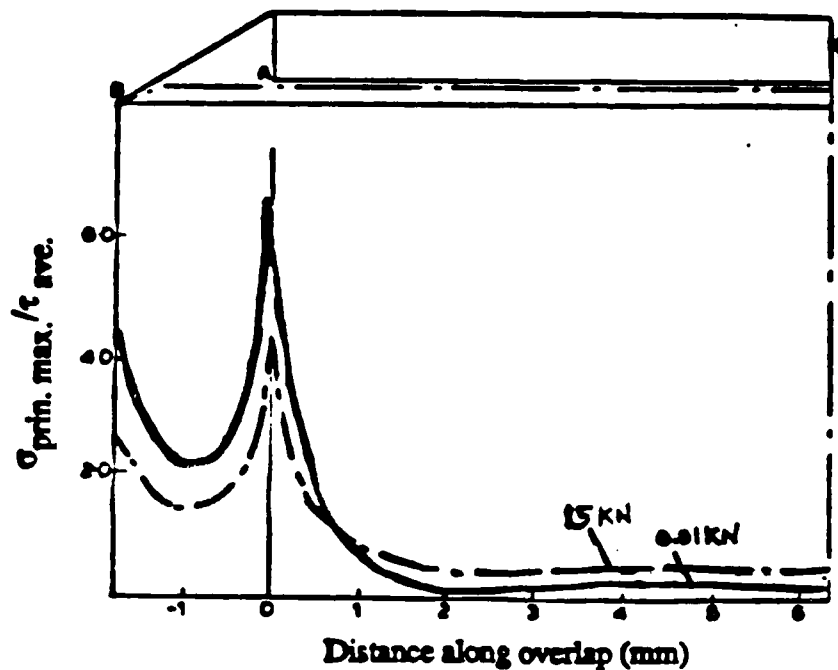
Fig. 7.14. Variation of the maximum principal stress distribution (normalised) along the adhesive layer of a SLJ specimen with applied load [211].

(ii) Work of Adams, Atkins, Harris and Kinloch [213]

More recently, Adams et al. [213] conducted experimental and theoretical analyses of DLJ specimens of various geometries. They employed FEA to various joint designs, including sharpening of the edges as suggested by Thamm, as shown in Figure 7.15. The DLJ specimens were made of steel outer-substrates which were bonded with a hot-cured epoxy adhesive to the inner substrate, which was a unidirectional thermoset fibre-composite (TSFC) material. The FEA studies were carried out in two dimensions, where a state of plane-strain was assumed across the width of the joint. In the model both the steel and the TSFC material were assumed to behave in a linear elastic manner. In contrast, the adhesive was modelled as an elastic fully-plastic material and they employed a failure criterion of the adhesive which was developed by Raghava et al. [214] and takes into account both the hydrostatic and deviatoric stresses. Finally, the overlap length employed was 80mm long with an adhesive thickness of 1mm, which they chose from a differential shear analysis [207] and suggested that this joint would yield 100% efficiency if no tensile stress concentrations were present at the loaded end of the overlap.
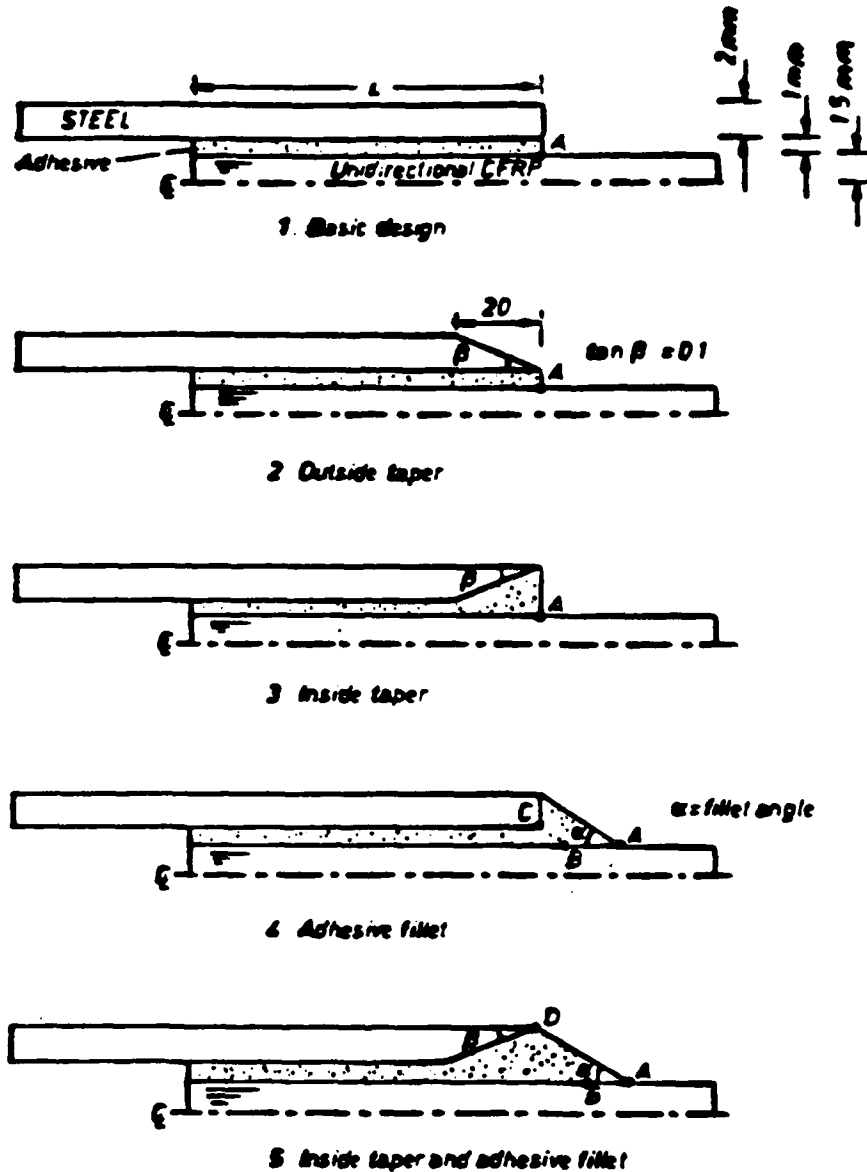
Fig. 7.15. The designs employed by Adams et al. [213] to analyse TSFC/steel DLJ specimens.

The results that they obtained are reproduced here in Tables 7.1 and 7.2. From Table 7.1 it can be seen that design number 5 (with an adhesive fillet of 17^0) gives the minimum transverse tensile stress. The failure loads that they obtained from the experiments are compared with the FEA predictions in Table 7.2. In all cases, the mode of joint failure was reported to be interlaminar through the TSFC inner substrate. They observed that failure initiated in the region of the overlap where the steel outer substrates ended. They argued that there were two possible failure mechanisms for this phenomenon: either excessive transverse tensile stresses at the edge of the joint close to the interface would result in the interlaminar failure of the TSFC material or that the principal stresses in the adhesive would result in a crack initiating in the adhesive, which would then propagate through the composite substrate. It should be noted that for interlaminar failure of the composite they used a maximum transverse

tensile stress of 40MPa and for cohesive failure of the adhesive they employed the principal tensile failure criterion.

Table 7.1. FEA predictions of the maximum transverse tensile stresses in the TSFC inner substrate when a load per unit width of 1MN/m is applied [213].

Specimen design number (From Figure 7.15)	Description	Fillet angie (Degrees)	Transverse stress (MPa)
1	Basic	≈90	38
2	Outer taper	≈90	37
3	Inside taper	≈90	36.5
4	Adhesive fillet	45	16
4	Adhesive fillet	30	10
4	Adhesive fillet	17	10
5	Inside taper and adhesive fillet	45	13
5	Inside taper and adhesive taper	30	6.5
5	Inside taper and adhesive fillet	17	5

A comparison of the theoretical predictions and the experimental results is shown in Table 7.2. For design number 1, which has a 90^0 edge, they predicted that transverse tensile failure in the composite occurred before failure in the adhesive. They showed that, because elastic analyses indicated that tapering design numbers 2 and 3 had little effect in the predicted strength based on the cohesive failure of the adhesive in design number 1, then interlaminar failure of the TSFC material was also expected for these designs. Thus they concluded that, based on the TSFC transverse tensile failure stress, the strength to failure of the first three designs should indeed be expected to be similar.

For the fillet joint, design number 4, the failure load increased as the fillet size increased. For a 30^0 fillet angle the elastic-plastic analysis predicted that the failure load, based upon transverse tensile TSFC failure rather than tensile failure, in the adhesive, was higher. Thus, failure should have initiated in the adhesive and once a crack was formed the geometry of the joint became that of design number 1. Therefore, they argued that failure of the TSFC material should follow because the failure load of that joint had been exceeded.

Table 7.2. Comparison of the experimental joint strenghts
with theoretical predictions from FEA [213].

| | | | | Theoretical predictions | |
Joint design number	Discription	Fillet angle (Degrees)	Observed failure load (MN/m)	Interlaminar TSFC failure[a] (MN/m)	Tensile adhesive failure[b] (MN/m)
1	Basic	90	0.93	1.05^c	1.6
2	Outside taper	90	0.89	1.08^c	*
3	Inside taper	90	0.94	1.10^c	*
4	Adhesive fillet	45	*	2.70^c	*
4	Adhesive fillet	30	*	4.24^c	2.0
4	Adhesive fillet	17	*	4.24^c	*
5	Inside taper and adhesive fillet	45	2.72	3.53	4.0
5	Inside taper and adhesive fillet	30	3.05	7.44	3.3
5	Inside taper and adhesive fillet	17	2.80	9.08	2.4

Notes: (*): Not determined.

(a): Based upon a maximum transverse tensile stress of 40MPa.

(b): Based upon a maximum principal tensile strain of 0.0475mm/mm.

(c): From elastic analysis (if without any mark then from elastic-plastic analysis).

Considering increasing the size of the fillet for design number 5, then they found that the joint strength increased based on TSFC transverse tensile failure and that the joint strength decreased based on the initial failure in the adhesive. Adams et al. [213] suggested that there was a fillet angle above which TSFC fracture was responsible for joint failure and below which adhesive failure was responsible. They suggested that this angle was between 30^0 and 45^0. For the 45^0 fillet case, the predicted strength based on TSFC failure was high. As they increased the fillet size such that the fillet angle became less than 30^0, the joint strength reduced as the tensile strength in the adhesive occurred at lower loads. They argued that this may be due to the stress concentration in the critical region, indicated in Figure 7.16, increased as more load was transferred through the fillet to this point.

Finally, they concluded that design number 5 gave a three-fold increase in the joint strength giving a high joint efficiency (73%). This high efficiency was achieved because the concentration in the transverse tensile stress in the TSFC material was reduced. Premature

transverse tensile failure in the TSFC was thus avoided and the failure initiated in the adhesive.
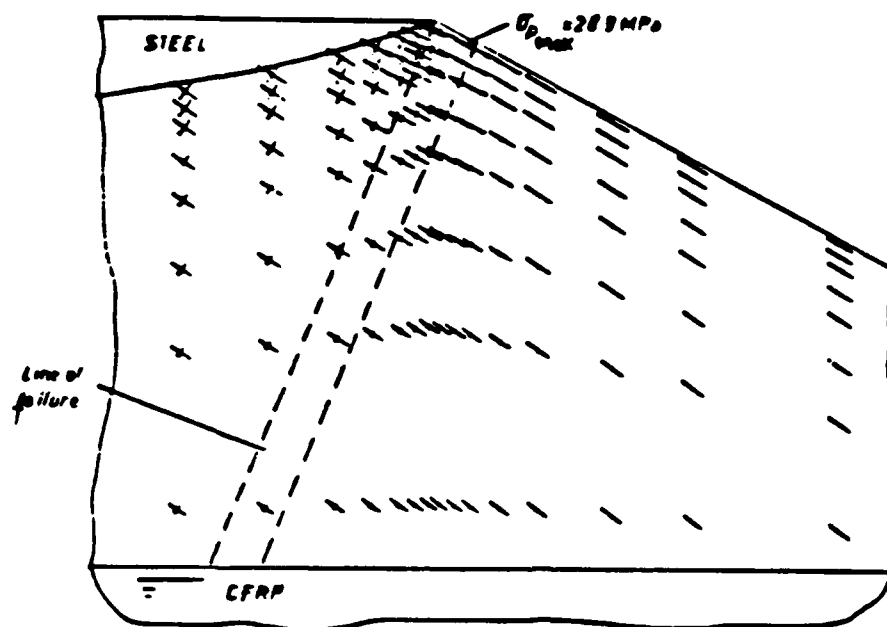
Fig. 7.16. Joint design number 5 with an adhesive fillet of 30^0; principal stress distribution in the adhesive end of the overlap for an applied load of 1MN/m [213].

(iii) Criticism of Adams et al.'s [213] Work

Adams et al.'s [213] experimental results are important, especially since they were able to increase the failure load three-fold. However, the theoretical work has a few weaknesses. Firstly, for joint design number 5 the FEA predictions do not agree with the experimental results. This suggests that either the material properties employed in the elastic-plastic analysis may not have been correct or that the theories employed to predict the stresses in their computer program could not handle elastic-plastic computations accurately. Secondly, they employed a differential shear analysis [207], based upon shear failure of the adhesive, to determine the dimensions of the specimen. However, when they employed FEA they assumed that the adhesive does not fail in shear but fails due to principal tensile stresses, as in the case of joint design number 5. The better alternative would have been to base the specimen dimensions on experimental analyses. By varying the overlap length, for a particular adhesive thickness, then the plateau value of the failure load could have been determined. Hence, all subsequent end effects would have given a clear indication of their effect on the failure load. In this thesis similar joint designs presented above will be examined and FEA will be employed to predict the failure loads.

Next, a brief review of the failure criteria employed in the analyses will be presented.

7.2.3.6. Failure Criteria

In this section the failure criteria used in the following analyses will be presented, more details of these criteria can be found elsewhere [215-217]. Three types of failure may occur in a composite joint.

(i) Interfacial Failure

Interfacial failure is indeed a common type of failure observed if the substrates are not adequately prepared for adhesive bonding. This type of failure would certainly yield low failure loads. Corona-discharge was employed to ensure that interfacial failure would not occur when DLJ specimens, prepared using the TPFC materials, are employed.

(ii) Composite Failure

(a) Transverse tensile stress failure criterion: This failure criterion was explained in some detail in Chapter Five. The composite will fail in the direction normal to the fibre axis if the transverse tensile stress exceeds that of the transverse tensile failure stress of the composite.

(b) Axial tensile-stress (longitudinal) failure criterion: This failure criterion states that when the tensile principal stress in the composite is higher than the measured uniaxial tensile failure stress then the substrate fails. This type of failure is desirable, since the fibre-reinforced composite substrate would certainly have a high tensile failure stress and consequently the joint would possess a very high failure load. Indeed, under such circumstances then 100% joint efficiency is attained.

(iii) Failure in the Adhesive layer

(a) Principal tensile-stress failure criterion: According to this theory, failure will occur when the maximum principal stress in a complex stress state reaches the value of the maximum stress at the elastic limit from a tension test. This failure criterion may be applied to materials which behave in a brittle manner.

(b) Maximum shear stress failure criterion: The assumption in this theory is that failure is dependent on the maximum shear stress in the material if it exceeds a critical value which is given by:

$$\tau = (\sigma_1 - \sigma_3)/2 \tag{7.5}$$

where τ is the principal maximum shear stress and σ_1 and σ_3 are the maximum and minimum principal stresses respectively.

(c) Modified Von Mises failure criterion: The original form of the Von Mises failure criterion has been modified for materials which are sensitive to hydrostatic stress. Such materials, for example toughened adhesives, can attain a higher compressive failure stress than their corresponding tensile failure stress [218]. The ratio of the compressive stress to the tensile stress is usually considered to be about 1.3. The modified Von Mises failure criterion for materials sensitive to hydrostatic stress may then be presented by:

$$2(\sigma_c - \sigma_t)(\sigma_1 + \sigma_2 + \sigma_3) + (\sigma_1 - \sigma_2)^2 + (\sigma_1 - \sigma_3)^2$$

$$+ (\sigma_2 - \sigma_3)^2 = 2\sigma_t\sigma_c \qquad (7.6)$$

Where σ_1, σ_2 and σ_3 are the principal stresses and σ_c and σ_t are the compression and tension stresses of the material respectively. This criterion assumes that failure of the material will occur when the left-hand side of the equation is greater than the right-hand side. The implication of the above equation is that failure in a complex stress state occurs more readily when the principal stresses are in tension rather than in compression.

7.3. EXPERIMENTAL METHODS

7.3.1. Mechanical Properties of Substrates and Adhesives

7.3.1.1. Tensile Tests

The tensile test specimen dimensions were given in Section 7.2.2.1 (page 223) and in the present section the methods employed for preparation and testing of specimens will be given.

(i) Composites

The U/C-PEEK, U/C-PA and U/C-epoxy tensile specimens were prepared by cutting composite sheets to the dimensions given in Figure 7.1. Both sides of the two ends of the thermoplastic composites were treated with corona-discharge to enable the adhesive bonding of the woven-carbon-fibre thermosetting-based composite tabs. The bonding was carried out using a room-temperature curing "Permabond E38" epoxy-paste adhesive. The strain was recorded via employing rosette strain gauges ("RS 632-130" from Radio Spares Ltd.) bonded to the middle section of the composite specimens. Each rosette strain gauge consisted of two 2mm steel identical strain gauges; one in the vertical direction and the second in the horizontal direction. Employing two identical strain gauges yields not only the strains required but also, from the difference in the strains, the Poisson's ratio can be obtained. The outputs from the

strain gauges were first amplified and then connected to an oscilloscope. The output from the oscilloscope and from the load cell of the tensile testing machine were connected to a chart recorder to plot load versus strain. The cross-head speed employed was 1mm/min.

(ii) Adhesive

Only the cold-cured epoxy-paste adhesive was employed in the DLJ specimens and therefore, only the properties of this adhesive were determined. The main problem that had to be overcome was making "bubble-free" "dog-bone" specimens. High viscosity and short handling times (less than 60minutes) limited the time that the adhesive could be degassed (40minutes) before pouring it into rubber moulds to give a sheet of epoxy-paste adhesive of 7mm thick. The sheet was cut to the dimensions given in Figure 7.2 (page 224). Afterwards, the edges of the central portion of the specimen were polished and the specimens were tested in tension at a cross-head speed of 1mm/min. The same load versus strain recording technique employed for testing the composites was adopted.

7.3.1.2. Shear Tests

The shear specimen employed in the current research work is similar to the one proposed by Grant and Cooper [193] i.e., cone-and-plate as shown in Figure 7.6 (page 228). Extreme care was taken in preparing the specimens and the various components. These components were machined using a computer controlled milling machine, which required that the equations of the various sides be written into a computer file. The accuracy of the dimensions was within $\pm 3\mu$m. Figure 7.17 shows the various components employed to make the joints and the details of specimen preparation and the techniques employed are:

a) The cone end of the aluminium substrates were made of two different angles, 3^0 and 5^0, see Figure 7.17(a). These angles were employed to investigate any effect the adhesive thickness might have on the measured shear properties.

b) The mould to hold the substrates aligned, see Figure 7.17(b) was made of two halves of cylindrical semicircles to fit tightly around the substrates. The aluminium moulds had two 45^0 holes to allow excess adhesive to flow out of the bonded region. To ensure the easy removal of the mould after the bonding opertation, these were sprayed with a releasing agent ("Frekote 44" from Hysol Dexter).

c) Prior to the adhesive bonding, the aluminium substrates were dipped into a bath of chromic acid solution. Afterwards, the degassed epoxy-paste adhesive was poured onto the plate surface of the substrate and the cone surface was brought into contact. Finally, the mould was tightly fixed around the specimen. After curing the adhesive for five days at room temperature, the mould was carefully removed, the bonded regions were lightly polished and

the steel cams were added to the very ends of the substrates, see Figure 7.18. A ten-second room-temperature curing brittle adhesive (Loctite "Super Glue-3") was employed for this purpose.
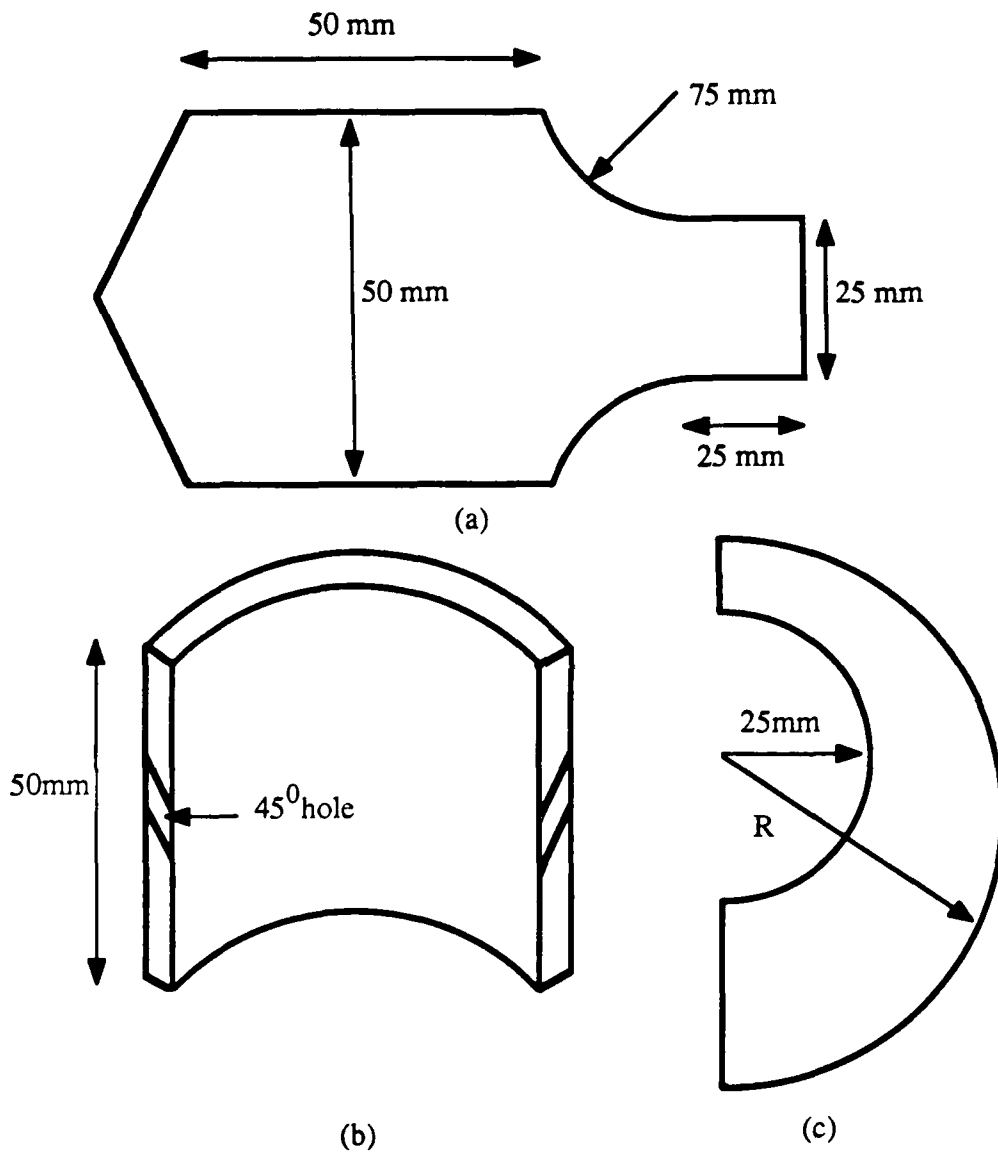
Fig. 7.17. (a) The dimensions of the cone side of the substrate, (b) one half of the cylindrical mould employed to make the joint, and (c) the steel cam employed for measuring shear strain.

d) The cams, see Figure7.17(c), were employed to measure the shear strains. The cams had several noteworthy features. Firstly, the thickness of the cams was only 2mm. This ensured minimizing the effect of the shear strain contribution of the aluminium substrates. Secondly, the inner circle was made up of two stepped-up circles. One with a radius of 25mm and the other with a radius of 25.05mm and each with a thickness of 1mm. The former circle ensured that the cam fitted tightly onto the aluminium substrates. The latter was employed to bond the cams onto the substrates to ensure that they did not slip whilst recording the data.

Thirdly, the steel cams were designed such that as the substrates rotated the cams gave a linear stroke to the two linear-variable displacement-transducers (LVDTs), see Figure 7.18. The equation of the outer cam radius, R, in terms of the angle of rotation θ is given by:

$$R = 37.5 + \frac{37.5\theta}{180} \qquad (7.7)$$

e) The LVDTs were supplied by Sangamo Ltd. The linearity of the LVDTs was within 0.1%, resulting in an output which was extremely accurate. The LVDTs were first calibrated and then connected to a digital/analogue converter which in turn was connected to an Apple "512" computer.
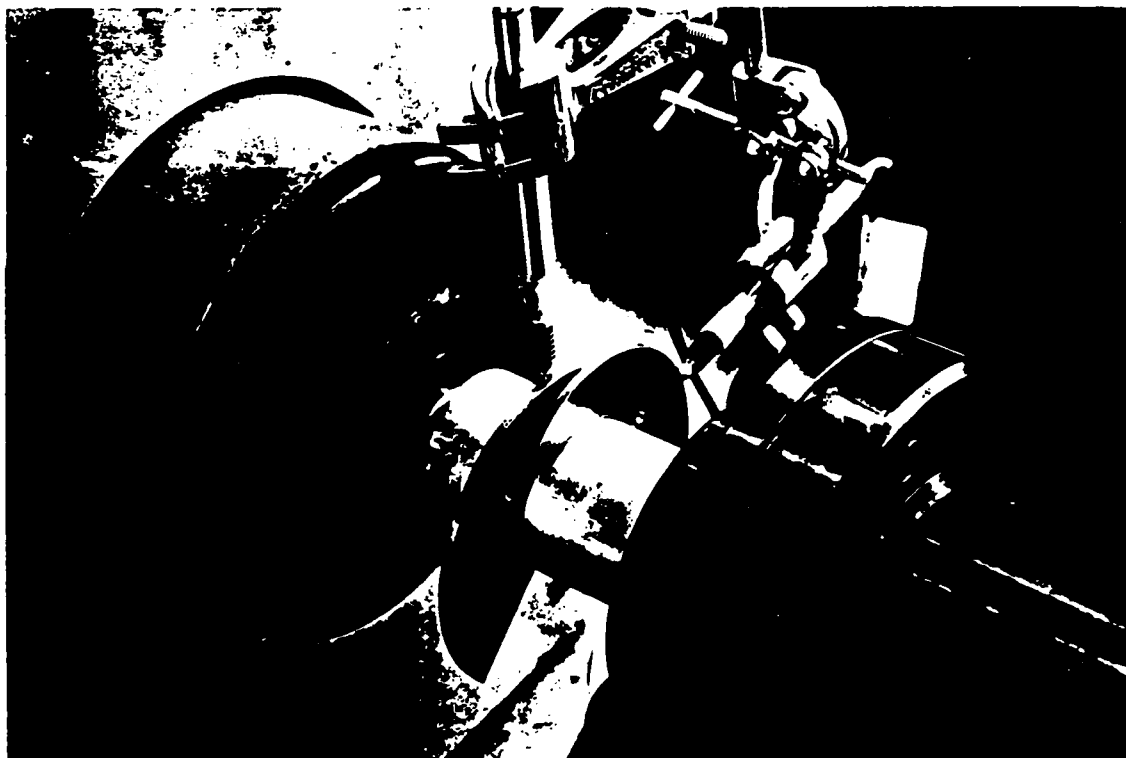
Fig. 7.18. The experimental setup for the cone-and-plate shear experiment.

f) The specimens were mounted onto the torsion testing machine. Prior to the actual experiment, a test was carried out to ensure the alignment of the specimen and the LVDTs with the specimen. One end of the specimen was first clamped to the rotating end of the torsion machine and allowed to rotate. Once agreement was established between the outputs from the two LVDTs and the rotation of the specimen (calculated from Equation (7.7)), then the free end of the specimen was clamped to the stationary part of the torsion machine i.e., to the load cell.

g) The speed of the angular rotation employed was 3 $1/3^0$ per minute which resulted in failure times between two to three minutes. This is within the time limits recommended by ASTM Standard E229-70.

h) From the recorded torsional moment then the shear stress, τ, was calculated from:

$$\tau = \frac{3T_{tm}}{2\pi R^3}$$ (7.8)

where T_{tm} is the measured torque and R is the radius of the specimen. Note that the torsional machine employed could not be connected directly to a digital/analogue converter (mechanically controlled load cell) and hence the torque had to be recorded separately on a load/time chart.

From the difference of the measured linear displacements then the angular rotation θ was calculated from Equation (7.7). Then the shear strain, γ_{ss}, was obtained from:

$$\gamma_{ss} = \frac{\pi R \theta}{180t}$$ (7.9)

where t is the thickness of the adhesive at radius R=25mm. It should be noted that the outputs were recorded into the computer at one second intervals. Finally, the results from the shear stress were superimposed onto the results obtained from the shear strain, and a shear stress/strain curve was obtained.

7.3.2. Preparation and Testing of Double-Lap Joints (DLJs)

7.3.2.1. Substrate Preparation

(i) Cutting of the Composites

To obtain symmetrical DLJ specimens, then 3mm thick inner substrates were bonded to 1.5mm thick outer composites. A diamond-tipped wheel was employed in cutting the composites to a width of 25mm. To obtain different overlap lengths, then the composites were cut to different lengths such that the overall length of the DLJ specimens remained constant at 190mm, see Figure 7.19. The desired taper angle, β, of the composite was obtained by cutting the composites at different angles. By a knowledge of the composite thickness and measuring

the length of the tapered regions then the accuracy of the angles, β could be checked. Only specimens within $\pm 1^0$ of the desired β angles were accepted and about 20% of the cut specimens had to be discarded.
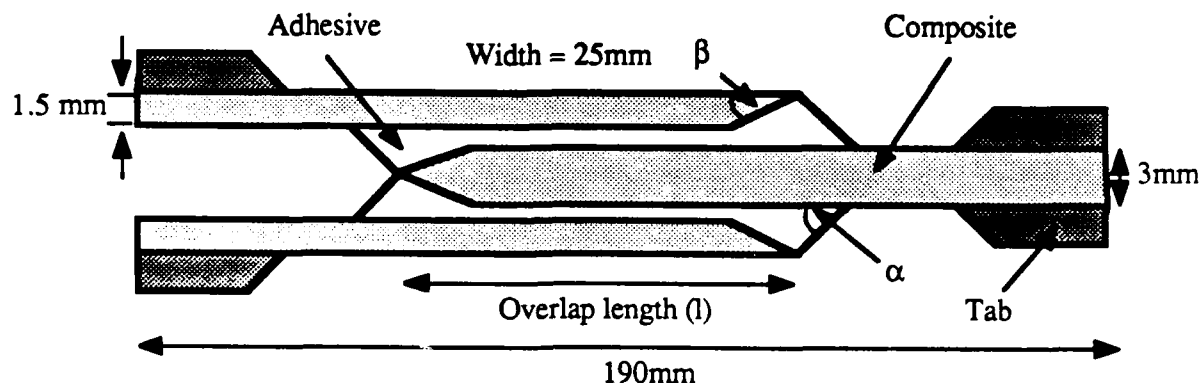
Fig. 7.19. Schematic presentation of the DLJ specimen employed.

(ii) Surface Treatment

For the thermoplastic composites i.e., the U/C-PEEK and U/C-PA, the two sides of the inner substrates and inner surface of the outer substrates were treated with corona-discharge to levels of 20J/mm^2 and 5J/mm^2 respectively. In section 4.4.3.7 it was shown that at these corona treatment levels no interfacial failure was observed. The U/C-epoxy thermosetting composite was subjected to an abrasion/solvent-wipe pretreatment.

7.3.2.2. Joint Preparation and Testing

(i) The Mould

To make high quality DLJs a special steel mould was designed as shown in Figure 7.20 and it included the following features:

a) The end pins ensured that the overall length of the specimens was kept constant at 190mm.
b) The middle holes ensured easy removal of the DLJ specimens once the adhesive had cured. (Note that the mould was sprayed with the releasing agent "Frekote 44".)
c) Most importantly, the side pins ensured that the substrates were aligned.
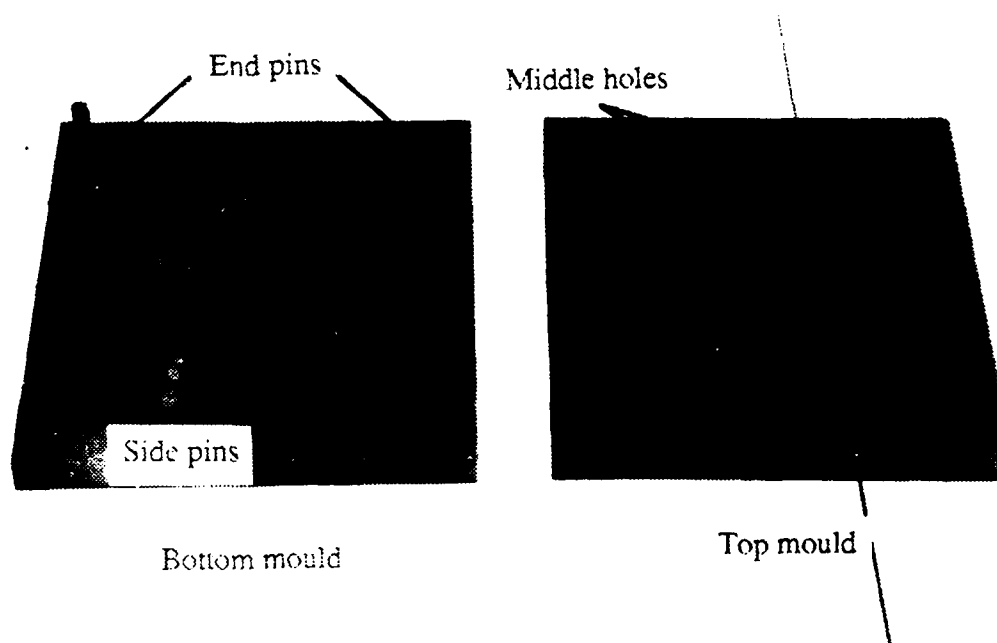
Fig. 7.20. The mould employed for the DLJ specimens.

(ii. The Shims

Special steel shims of different angles and lengths were designed and were employed with the composite substrates in the above mould. Four identical shims were used for each specimen in a sandwich assembly as shown in Figure 7.21. These shims were employed:

1) To ensure that the substrates did not slip inwards whilst the adhesive was still viscous.

2 To give the desired adhesive fillet angle, α. The fillet angles were confirmed using the same

technique employed for measuring the composite taper angle β (see page 245), and were found to be within $\pm 1^0$ of the desired angle.

(iii. Preparation of the DLJ specimens and Testing

(a) Preparation of DLJs: The composite substrates were put into the mould shown in Figure 7.20 and the sequence of preparation is shown in Figure 7.21. The epoxy-paste adhesive was first degassed for 40 minutes and then poured onto the surfaces of the composites. To obtain uniform adhesive thickness a small amount (i.e. less than 1% by weight) of glass beads whose nominal diameter was 350μm were sprinkled onto the surfaces of the composites. The adhesive layer was measured using a travelling microscope and a thickness of 350($\pm$40μm) was recorded. The adhesive was allowed to cure for five days and the

specimens were then removed from the mould. The shims were also removed from the specimens. The edges of the specimens were then first abraded to remove the excess adhesive and, second, were polished to remove any defects.

(b) Bonding of tabs: The ends of the thermoplastic DLJs were again treated with corona-discharge. Woven-carbon-fibre tabs were then bonded to the DLJs using the room-temperature curing "Permabond E38" adhesive. For the final shape of the DLJs see Figure 7.19.

(c) Testing: The DLJs were mounted onto a tensile testing machine and loaded at a constant cross-head speed of 1mm/min.
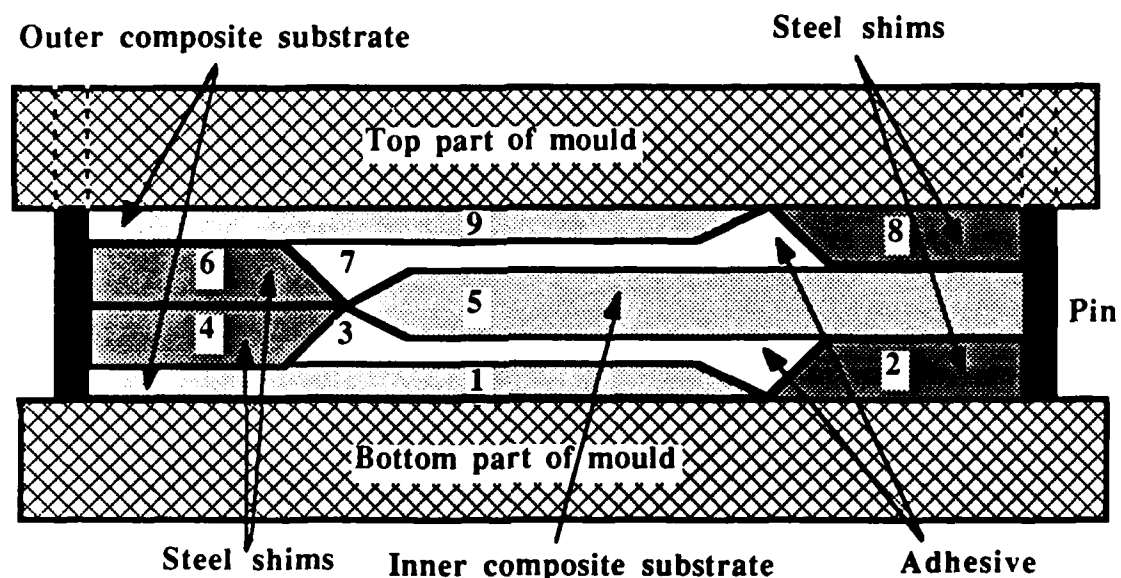
Fig. 7.21. A schematic presentation of the sandwich assembly of the DLJ
and the shims; numbers indicate the sequence of preparation.

7.4. EXPERIMENTAL RESULTS AND DISCUSSION

7.4.1. Mechanical Properties

7.4.1.1. Tensile Tests

The experiments from tensile tests on the composites and adhesive materials were not always successful. For the epoxy-paste adhesive about 25% of the specimens failed due to stress concentration from "air-bubbles". For the composites 10% of the failures occurred in the composite under the tabs in the unreinforced direction. Results from the above experiments were ignored. Results from successful tensile tests are summarized in Tables 7.3 and 7.4. As mentioned earlier in this chapter, only those tensile properties required for computer analyses were obtained. Finally, it should be noted that the results represent the mean and standard

deviation from eight replicate specimens.

Table 7.3. The mechanical properties of the epoxy-paste adhesive in tension.

Elastic stress limit (MPa)	Elastic strain limit (mm/mm)	Young's modulus (GPa)	Failure stress (MPa)	Failure strain (mm/mm)	Poisson's ratio
37.0±3.5	0.02±0.002	1.85±0.12	44.0±3.2	0.16±0.02	0.36±0.01

Table 7.4. The mechanical properties of the composites in tension.

Material	Young's modulus (GPa)	Failure stress (MPa)	Transverse tensile stress (MPa)	Major Poisson's ratio
U/C-PEEK	133±11	1380±85	84.1±4.1	0.28±0.01
U/C-PA	122±11	1330±65	83.7±4.2	0.29±0.01
U/C-epoxy	128±10	1140±70	58.9±3.3	0.26±0.01

Note: Transverse tensile stress from Table 5.3.

7.4.1.2. Shear Tests

The shear properties obtained from cone-and-plate specimens are summarized in Table 7.5. The results reported in Table 7.5 are from testing three replicate specimens for each cone angle. Figure 7.22 shows a typical shear stress/strain curve obtained.

Table 7.5. The mechanical properties of the epoxy-paste adhesive in shear.

Cone angle (^{0})	Elastic stress limit (MPa)	Elastic strain limit (mm/mm)	Shear modulus (GPa)	Failure stress (MPa)	Failure strain (mm/mm)
3	23.1±3.4	0.035±0.004	0.66±0.09	37.3±3.7	1.68±0.22
5	25.9±2.9	0.039±0.004	0.65±0.08	35.6±3.3	1.58±0.18
From [219]	*	*	0.51	35.6	1.60

Note: McCarthy and Gudge [219] state their data without indicating how they obtained these values.
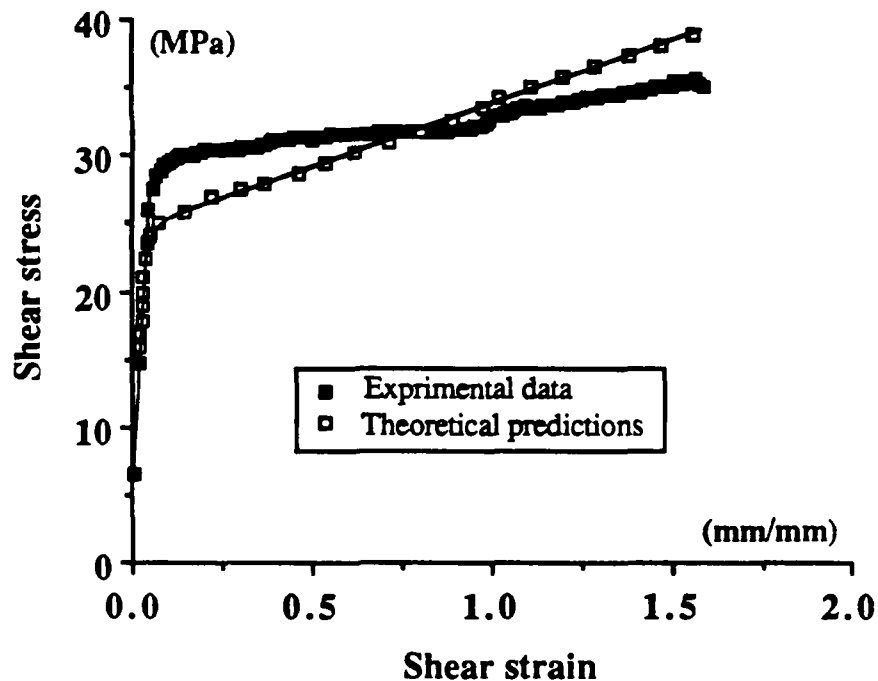
Fig. 7.22. A typical shear stress/strain curve obtained from employing the cone-and-plate specimen for the epoxy-paste adhesive (the theoretical curve will be explained in Section 7.4.4.2).

The noteworthy features of the techniques employed are the following. Firstly, the shear strain due to the aluminium substrates can be calculated and the error in the measured strains and thus the modulus estimated. This error will have the greatest effect in the elastic region. The shear stress at the elastic limit is less than 26MPa. The shear modulus of the aluminium is about 26GPa, hence the shear strain of the substrates is 1.0×10^{-3}mm/mm. Assuming that the distance, t, of the aluminium substrates between the cams is 4mm (a somewhat overestimate) then the angular rotation, θ, calculated from Equation 7.9 is 0.009^0. This error is less than 10% of the angle calculated for the 3^0 cone specimen and is about 5% of the calculated angle for the 5^0 cone specimen. Therefore, the error in the shear modulus should be less than 10%. Secondly, the results could only be compared with data reported by McCarthy and Gudge [219]. Although there seems to be a good agreement between the two sets of data they do not, unfortunately, indicate how they obtained their values. Thirdly, the results in Table 7.5 show that the adhesive thickness has very little effect on the measured shear properties. This confirms the observations made by Dolev and Ishai [188]. Fourthly, if the Young's modulus and Poisson's ratio, from Table 7.3, are employed in Equation (7.1) then a shear modulus of 0.68GPa is obtained. This calculated value is in excellent agreement with the experimental results reported in Table 7.5. The above observations and analyses obviously illustrate the accuracy of the techniques employed.

7.4.2. Double-Lap Joints (DLJs)

7.4.2.1. Introduction

The results from DLJs will be presented in this section. Comparisons will be made with reported data from previous research work especially those from Adams et al. [213] and Kinloch and Taig [10]. Scanning electron spectroscopy (SEM) will be employed to record the locus of joint failure. It should be noted that, as in the literature survey, all failure loads reported are divided by the width of the specimens and the results reported are the mean and maximum/miniumum obtained from three replicate specimens.

7.4.2.2. Failure Load Versus Overlap Length

The presentation of the results will start by examining the variation of the overlap length of basic (adhesive corners≈90^0 obtained using the shims and no composite taper) DLJ specimens. The failure loads from basic DLJ specimens are presented in Figures 7.23 and 7.24 for the U/C-PEEK, U/C-PA and U/C-epoxy composites bonded using the epoxy-paste adhesive, and Table 7.6 summarizes the important results.
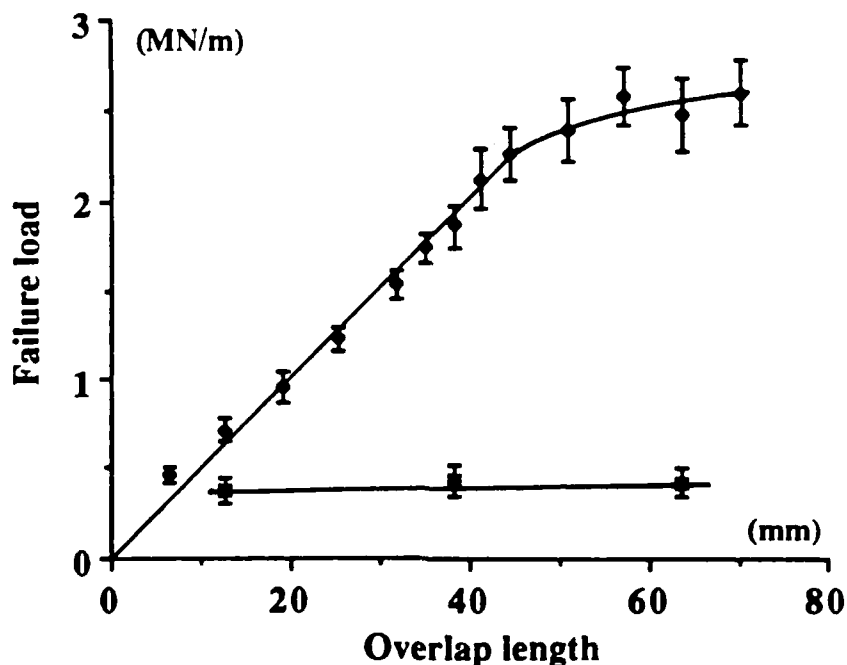
Fig. 7.23. Failure load versus overlap length for the U/C-PEEK composite bonded to the epoxy-paste adhesive from DLJ specimens with ≈90^0 adhesive corners and no composite taper. "Diamond" points from current work employing corona-discharge pretreatment; "star" points are from work by Kinloch and Taig [10] who simply employed an abrasion/solvent-wipe pretreatment.
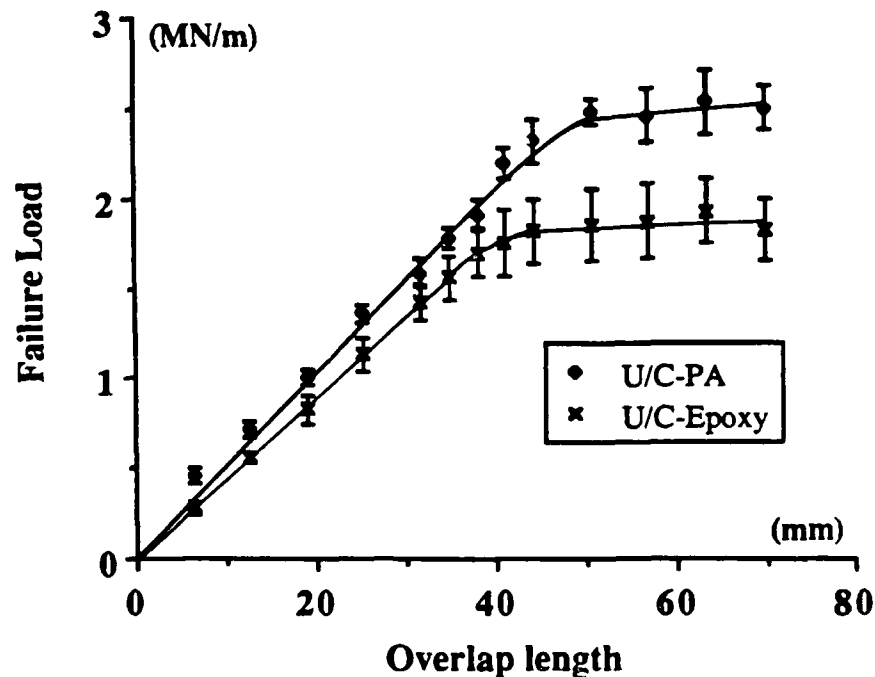
Fig. 7.24. Failure load versus overlap length for the U/C-PA and U/C-epoxy composites bonded to the epoxy-paste adhesive for $\approx 90^0$ adhesive and composite corners.

It is important to note that the adhesive and composites corners will never be exactly 90^0, since the adhesive corners obtained using the shims or cutting the composites will always leave rounded corners at the edges. For this reason the "$\approx 90^0$" notation has been adopted in the current work. Further, in Section 7.5.3.2, such rounded corners will be first assessed using optical microscopy and then modelled using finite element analysis.

Table 7.6. Summary of the results from DLJ specimens for 60mm overlap length for $\approx 90^0$ adhesive and composite corners.

| | Composite substrate | | Joint | | |
Composite	Transverse tensile stress (MPa)	Longitudinal failure stress (MPa)	Maximum failure load (MN/m)	Locus of failure	Efficiency (%)
U/C-PEEK	84.3	1380	2.58±0.20	Interlaminar/inner	62
U/C-PA	83.7	1330	2.54±0.18	Interlmainar/inner	64
U/C-epoxy	58.9	1140	1.85±0.20	Interlaminar/inner	54

Note: Interlaminar/inner: Interlaminar in the inner substrate in the region of the overlap where the outer substrates end, see Figure 7.25.

Failure in the inner substrate
where outer substrates end.
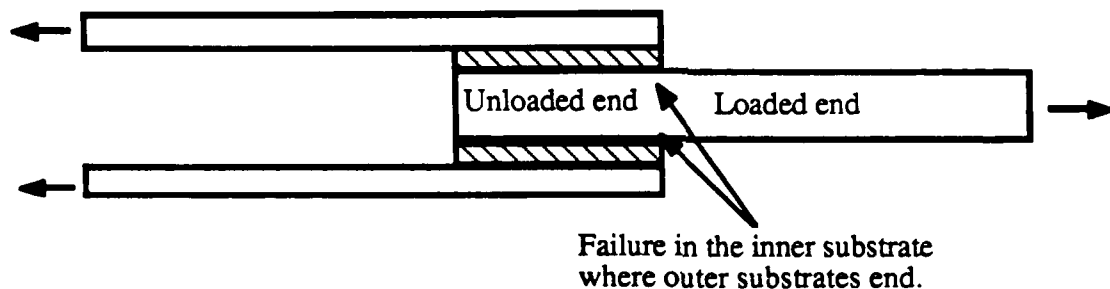
Fig. 7.25. Failure initiation in the basic DLJ specimens in the inner substrate
(loaded end) in the region of the overlap where the outer substrates end.

Several interesting features emerge from the above results.

Firstly, for both thermoplastic composites (U/C-PEEK and U/C-PA) the failure load increases as the overlap length is increased. At about 50mm overlap length a plateau value is reached. Further, the failure loads from these two composites joints are the same for all overlaps lengths.

Secondly, the values of the U/C-PEEK composite obtained in the current work are plotted together with the results reported by Kinloch and Taig [10]. It should be noted that they employed the same materials but the composite in their case was subjected to an abrasion/solvent-wipe pretreatment and the ply direction was $[0^0, 90^0, 90^0, 0^0, 0^0, 90^0]_n$. The benefits of employing corona treatment are evident. The substantial increase in the failure load can be understood when it is noted that Kinloch and Taig [10] observed interfacial failure, whereas the locus of failure in the present studies was interlaminar in the inner composite, as shown in Figure 7.25.

Thirdly, the failure load of the U/C-epoxy composite joint is lower than the failure loads from the two thermoplastic composites. This feature can be understood by considering the locus of failure. The inner susbtrate, for all DLJ composites, failed in an interlaminar manner in its transverse direction. Thus the thermoplastic composites, which have higher transverse failure stresses than the epoxy composite, will obviously fail at higher loads. Indeed, Adams et al. [213] employed a different U/C-epoxy composite whose transverse tensile failure stress was 40MPa. They also observed interlaminar failure in the inner composite however, the joint failure load in their case was about 1MN/m. This observation confirms the above conclu. on that the magnitude of the transverse tensile failure stress of the composites influences the failure load, provided a strong adhesive/composite interface has been established.

The effects of adhesive fillet and composite tapering can now be compared with the plateau failure loads obtained above. Therefore, all subsequent experimental work will be

based on a 60mm overlap length unless stated otherwise. The reasons for employing this overlap length instead of 50mm (which is the first point on the plateau curve) will be obvious from the discussions in Section 7.4.2.5.

7.4.2.3. Failure Loads from Using Tapered Composite Substrates

Two types of composite tapering were employed, "inside taper" Figure 7.26(a) and "outside taper" Figure 7.26(b). The failure loads from such specimens are summarized in Table 7.7. Comparing the results from this table with the results from basic DLJ specimens (Table 7.6), it is evident that composite tapering does not change the failure load for any of the composite DLJ design specimens considered so far. Also, the locus of failure remained interlaminar through the inner substrate. Since the inner substrate fails in an interlaminar manner in its transverse direction then this may explain the reason for obtaining the same failure loads as from the basic DLJ specimens.

The three DLJ specimen designs investigated so far give a clear indication that, for $\approx 90^0$ adhesive corners, the transverse tensile stress in the inner substrate governs the failure load. Therefore, employing adhesive fillets may seem at first to be a logical development and this will be the subject of the following section.
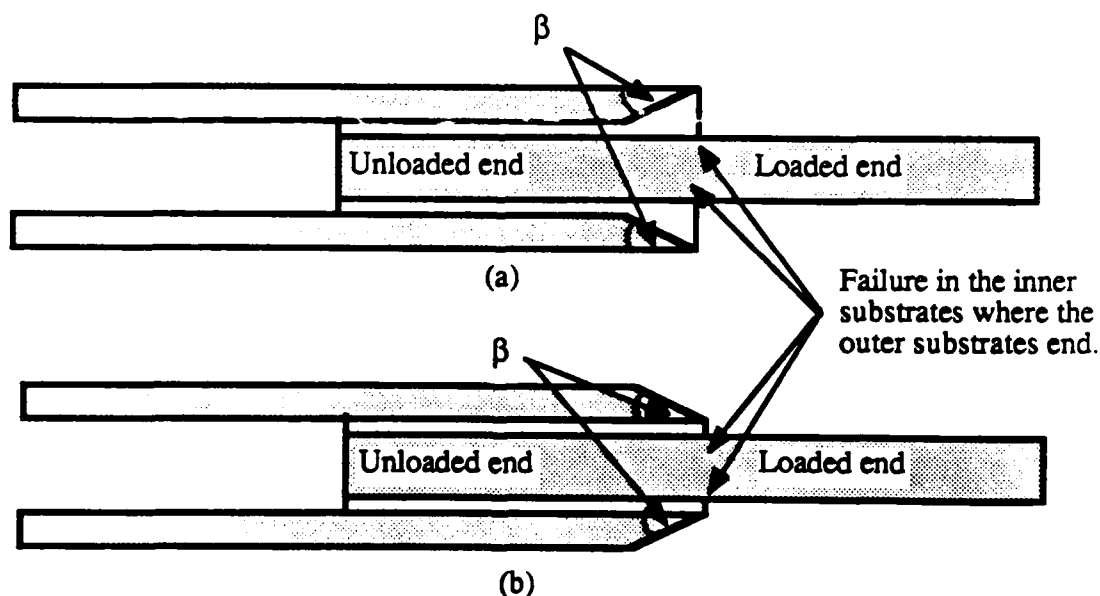
Figure 7.26. DLJ specimens with (a) inside composite taper and (b) outside composite taper. (In both joint designs failure initiated in the inner substrate at the region of the overlap where the outer substrates ended).

Table 7.7. Effects of inside and outside composite taper on the failure loads; adhesive corners ≈90°; overlap length is 60mm.

Composite	Design type	Composite taper angle β (°)	Maximum failure load (MN/m)	Locus of failure
U/C-PEEK	Inside	50	2.45±0.28	Interlaminar/inner
U/C-PEEK	Inside	30	2.58±0.23	Interlaminar/inner
U/C-PEEK	Inside	10	2.55±0.25	Interlaminar/inner
U/C-PEEK	Outside	50	2.52±0.19	Interlaminar/inner
U/C-PEEK	Outside	30	2.49±0.22	Interlaminar/inner
U/C-PEEK	Outside	10	2.61±0.23	Interlaminar/inner
U/C-PA	Inside	30	2.51±0.27	Interlaminar/inner
U/C-PA	Outside	30	2.48±0.24	Interlaminar/inner
U/C-epoxy	Inside	30	1.84±0.19	Interlaminar/inner
U/C-epoxy	Outside	30	1.91±0.17	Interlaminar/inner

Note: Interlaminar/inner: Interlaminar in the inner substrate in the region of the overlap where the outer substrates end, see Figure 7.26.

7.4.2.4. Failure Loads from Using Adhesive Fillets

The adhesive fillet angle, α, was varied, keeping the composite corners at β≈90°, i.e. using non-tapered composite substrates, see Figure 7.11 (page 233). The results from such specimens are presented in Figures 7.27 and 7.28. Several noteworthy features emerge from these figures. Firstly, there is no change in the failure load from varying the adhesive fillet angle even when the total adhesive length has increased by about 7mm, when the 10° adhesive fillet is employed. Secondly, the locus of failure for the adhesive fillet angles considered was interlaminar, as observed in the previous designs. This suggests that adhesive fillets do not alter the transverse tensile stress concentrations in the inner composite where the outer substrates end (loading side). Therefore, this leads to failure of the joints at the same failure loads as those from the previous designs.
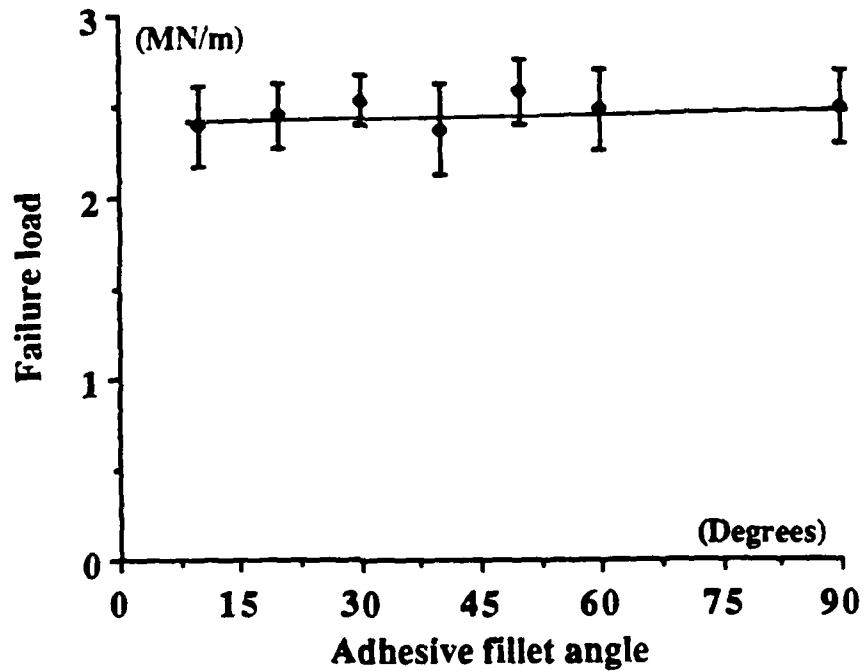
Fig. 7.27. Failure load versus adhesive fillet angle for the U/C-PEEK composite *bonded to the* epoxy-paste adhesive; overlap length of the composite is 60mm.
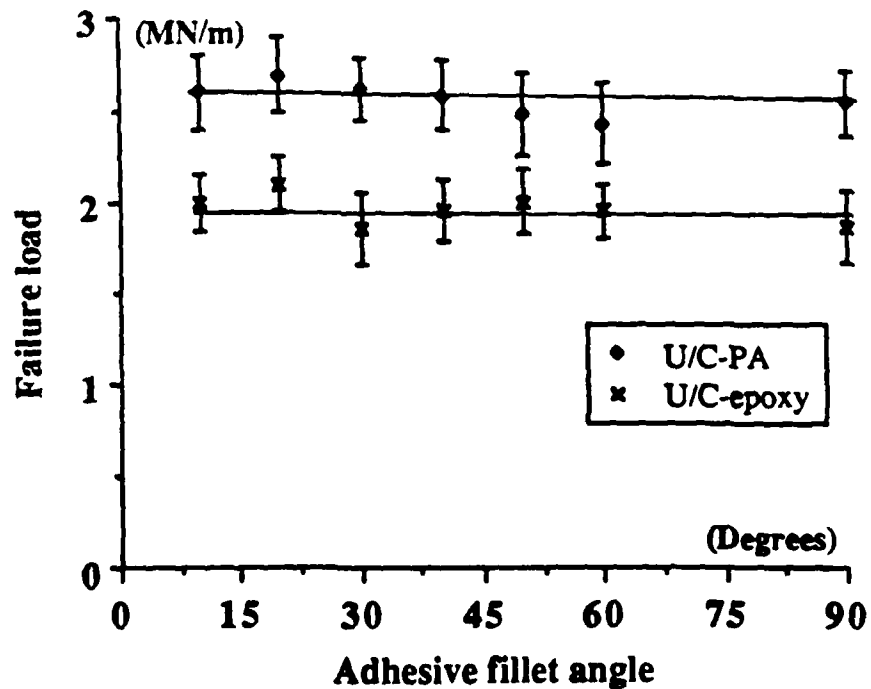
Fig. 7.28. Failure load versus adhesive fillet angle for the U/C-PA and U/C-epoxy composites bonded to the epoxy-paste adhesive; overlap length of the composites is 60mm.

7.4.2.5. Failure Loads from Using Both Composite Tapered Substrates and Adhesive Fillets

Since the properties of U/C-PEEK and U/C-PA composites were similar (see Table 7.4 page 249) and since the failure loads presented from DLJ specimens were also similar then subsequent analyses were concentrated on the U/C-PA composite. Two types of DLJ designs were employed. (i) "Unsymmetrical" DLJs see Figure 7.29(a) and (ii) "symmetrical" DLJs see Figure 7.29(b). The obvious differences between the latter and the former are the presence of adhesive fillets and composite tapering at the unloaded end of the inner substrate. The results from such specimens are summarized in Tables 7.8 to 7.10.
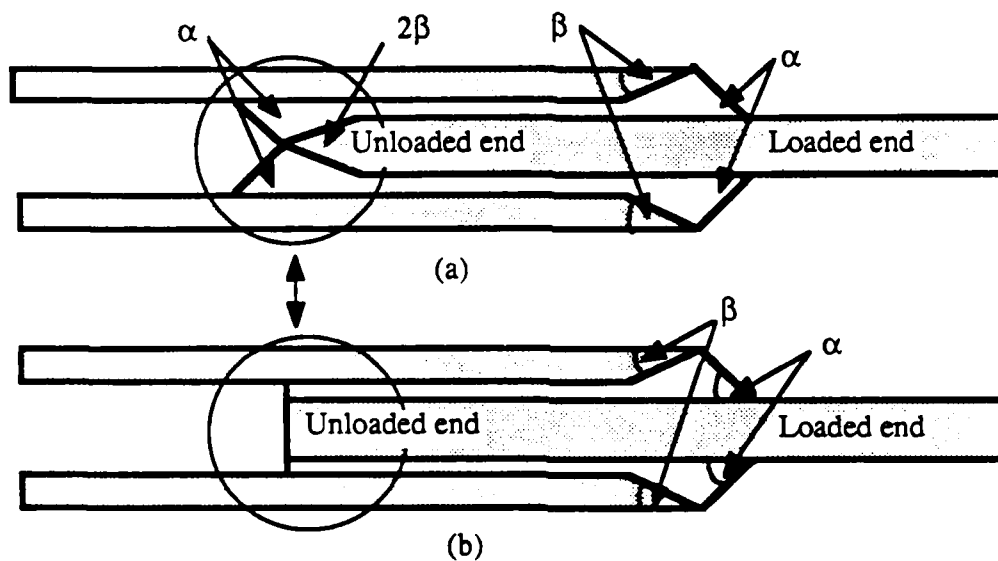
Figure 7.29. DLJ specimens (a) symmetrical, i.e. composite taper and adhesive fillet at both the loaded and unloaded overlap ends, and (b) unsymmetrical, i.e. composite taper and adhesive fillets only at the loaded end of the overlap.

(i) Symmetrical Versus Unsymmetrical Specimens

The results in Table 7.8 reveal that the failure load increases as the composite taper angle, β, is reduced. However, the unsymmetrical joints reach a maximum plateau value of about 3.25MN/m, see Table 7.8, which is lower than the failure load of about 3.9MN/m achieved for the symmetrical specimens where nearly 100% joint efficiency is attained (for $\alpha=10^0$ and $\beta=10^0$), see Table 7.8. The reasons for the differences in the failure loads from the two joint designs can be best understood by considering the following observations:

(i) Figure 7.30 shows typical SEM micrographs of the fracture surfaces for both

symmetrical and unsymmetrical joints. Based on the SEM observations the locus of failure has been identified and is schematically presented in Figure 7.31. This shows cohesive failure occurs at the edges of the overlap where failure initiated, followed by mixed cohesive/interlaminar regions and this is followed by a region of interlaminar failure through the composite.

(ii) Figure 7.9 (page 231) showed that the loaded end, next to the inner substrate, of the adhesive will be in tension and the unloaded end in compression.

(iii) It was shown in Section 7.2.3.6 (page 240) that materials sensitive to hydrostatic stress can lead to higher loads to failure under a compressive stress than under a tensile stress.

These observations indicate that firstly, the unsymmetrical joints may have failed in the adhesive at the edges of the unloaded end of the inner substrate. Thus, indicating that adhesive failure is beneficial in increasing the failure load. (Note that for joints with no adhesive fillets and composite taper, failure initiated at the loaded end of the overlap in the inner composite). Therefore, to obtain higher failure loads it is beneficial to taper the composites and have adhesive fillets which may reduce the transverse tensile stresses in the composite and for failure to initiate in the adhesive. However, the failure load for unsymmetrical joints (maximum about 3.25MN/m) is lower than for symmetrical joints (maximum about 3.9MN/m). This may be explained by considering that the composite taper and the adhesive fillets, which are now also present at the unloaded end, may reduce the critical stresses (responsibe for the adhesive failure) in the adhesive at the unloaded end which had caused the failure of the unsymmetrical joints. Therefore, to attain a very high joint efficiency it is necessary to use symmetrical specimens with the appropriate composite taper and adhesive fillets.

(ii) Effect of β and α Values on the Failure Loads

1) For the TPFC symmetrical joints then tapered composite ends with adhesive fillets lead to an increase in the failure load from about 2.5MN/m (from the previous joint designs) to about 3.9MN/m (e.g. $\alpha=10^0$ and $\beta=10^0$ see Tables 7.8 and 7.9). The failure load for the symmetrical U/C-epoxy joints also increases but only from 1.85MN/m (for the basic joint design) to about 3.25MN/m (for $\alpha=10^0$ and $\beta=10^0$ see Table 7.10). These observations indicate that the transverse tensile stresses at the edges of the overlap where failure initiated may well be lower than in the previous joint designs.

2) The results for the U/C-epoxy composite joints show that the maximum failure load is attained for symmetrical specimens at angles below $\beta=30^0$ and $\alpha=30^0$ which yield a joint

efficiency of about 95%. Further, for higher β and α angles the failure loads are in good agreement with the results from the thermoplastic composite joints. This observation further confirms the earlier conclusion that, for DLJ specimens with composite taper and adhesive fillets, the adhesive governs the mode of failure until a very high efficiency is attained.

(iii) Effect of Substrate Tensile Properties on the Failure Loads

The results for the U/C-PEEK and U/C-PA composite joints confirm the earlier conclusion that provided the material properties are similar (especially the transverse tensile fracture stress and axial failure stress) then the locus of failure and indeed the failure loads are also similar, see Tables 7.8 and 7.9. Further, the U/C-epoxy composite has a lower axial failure stress than the thermoplastic composites and obviously, the failure loads for the thermoset composite joints are also lower, compare the failure loads in Tables 7.8 and 7.10.

(iv) Very High Joint Efficiency

At the very high joint efficiencies, about 95%, it was not possible to ascertain where joint failure had initiated. This was due to the shattering of the DLJs at very high loads (about 100kN for the thermoplastic composite joints and about 80kN for the U/C-epoxy composite joints). However, the shattering was most severe at the centre of the joints in the regions of the overlap away from the loading grips. Which may indicate that adhesive failure at the regions of the overlap where the outer composites ended may have been responsible. However, the lower maximum loads attained for the U/C-epoxy DLJ specimens indicate that longitudinal failure may have been responsible rather than failure of the adhesive.

Finally, Table 7.11 shows very important results when composite overlap lengths of 50mm are employed with composite and adhesive taper. For $\beta=30^0$ and $\alpha=30^0$ the failure load is equal to that from the 60mm overlap joints i.e. about 3.45MN/m, see Table 3.8. However, when $\beta=10^0$ and $\alpha=10^0$ the failure load from the 50mm overlap joints does not increase, unlike the 60mm overlap, and is still equal to the above value, i.e. 3.45MN/m. This may suggest that if the transverse tensile failure stress of the composite from the basic specimens could have been avoided, then the adhesive could have failed and that the 50mm overlap length would have yielded a failure load before a plateau value is attained in a differential shear analysis. Further, the above comparisons may suggest that the 60mm overlap length specimens ($\beta=10^0$ and $\alpha=10^0$) are in the plateau region, as will be shown later from differential shear analysis.

Table 7.8. Failure loads for the U/C-PA composite bonded to the epoxy-paste
adhesive; composite overlap length (including taper) is 60mm.

Composite taper β, (degrees)	Adhesive fillet α, (degrees)	Unsymmetrical specimens		Symmetrical specimens	
		Maximum failure load (MN/m)	Efficiency* %	Maximum failure load (MN/m)	Efficiency* %
50	50	2.76±0.22	69	2.87±0.17	72
50	40	2.78±0.19	70	2.78±0.21	70
50	30	2.82±0.23	71	2.96±0.14	74
50	20	2.87±0.25	72	2.92±0.18	73
50	10	2.95±0.23	74	3.02±0.15	76
40	50	3.05±0.12	76	3.10±0.14	78
40	40	3.22±0.19	81	3.24±0.15	81
40	30	3.29±0.16	82	3.27±0.16	82
40	20	3.22±0.23	81	3.15±0.16	79
40	10	3.14±0.11	79	3.25±0.17	81
30	50	3.20±0.09	80	3.45±0.20	86
30	40	3.22±0.17	81	3.47±0.17	87
30	30	3.33±0.22	83	3.55±0.10	89
30	20	3.29±0.10	82	3.38±0.16	85
30	10	3.16±0.14	79	3.51±0.12	88
20	50	3.21±0.15	80	3.65±0.11	91
20	40	3.18±0.17	80	3.58±0.12	90
20	30	3.28±0.24	82	3.67±0.14	92
20	20	3.32±0.18	83	3.78±0.19	95
20	10	3.25±0.14	81	3.69±0.18	92
10	50	3.18±0.18	80	3.75±0.19	94
10	40	3.33±0.08	83	3.82±0.25	96
10	30	3.24±0.10	81	3.72±0.19	93
10	20	3.23±0.13	81	3.84±0.21	96
10	10	3.16±0.26	79	3.88±0.20	97

Note: (*): Efficiency = Strength of the joint divided by the strength of the weaker substrate.

Table 7.9. Failure loads for symmetrical U/C-PEEK DLJs bonded to the epoxy-paste adhesive; composite overlap length (including taper) is 60mm.

Composite taper β, (degrees)	Adhesive fillet α, (degrees)	Failure load (MN/m)	Efficiency %
50	50	3.05±0.17	74
40	40	3.31±0.14	80
30	30	3.60±0.19	87
20	20	3.92±0.14	95
10	10	3.96±0.16	96

Table 7.10. Failure loads for symmetrical U/C-epoxy DLJs bonded to the epoxy-paste adhesive; composite overlap length (including taper) is 60mm.

Composite taper β, (degrees)	Adhesive fillet α, (degrees)	Failure load (MN/m)	Efficiency %
50	50	2.95±0.23	86
40	40	3.12±0.21	91
30	30	3.21±0.13	94
20	20	3.15±0.16	92
10	10	3.24±0.19	95

Table 7.11. Failure loads for symmetrical U/C-PA DLJs bonded to the epoxy-paste adhesive; composite overlap length (including taper) is 50mm.

Composite taper β, (degrees)	Adhesive fillet α, (degrees)	Failure load (MN/m)	Efficiency %
30	30	3.42	86
10	10	3.48	87

(a)

(b)

(c)
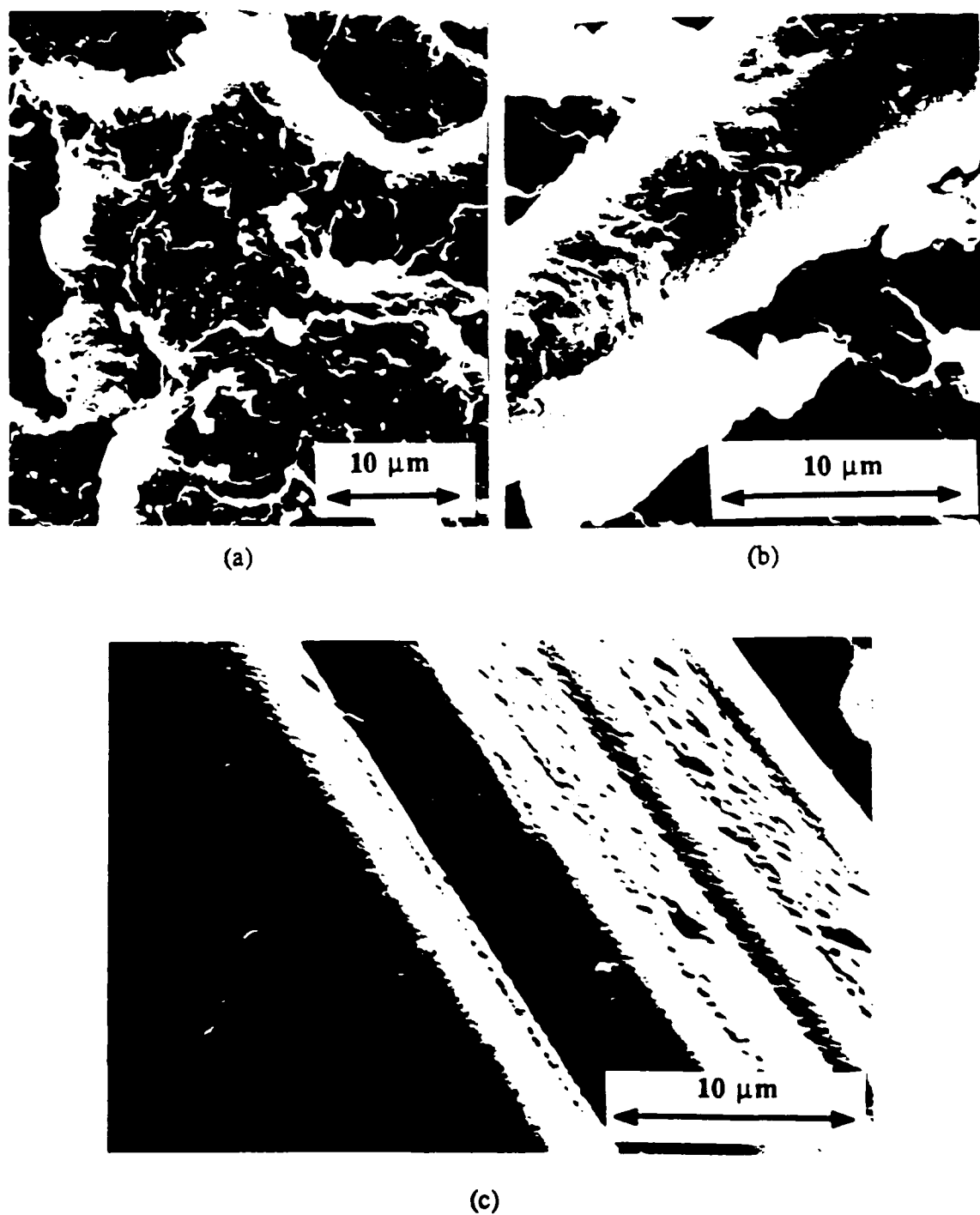
Fig. 7.30. SEM micrographs of the failure surfaces from DLJ specimen for adhesive taper

$\alpha=30^0$ and composite taper $\beta=10^0$; (a) failure in the adhesive in a cohesive manner

followed by (b) failure which is mixed interlaminar and cohesive

and followed by (c) interlaminar failure in the composite.
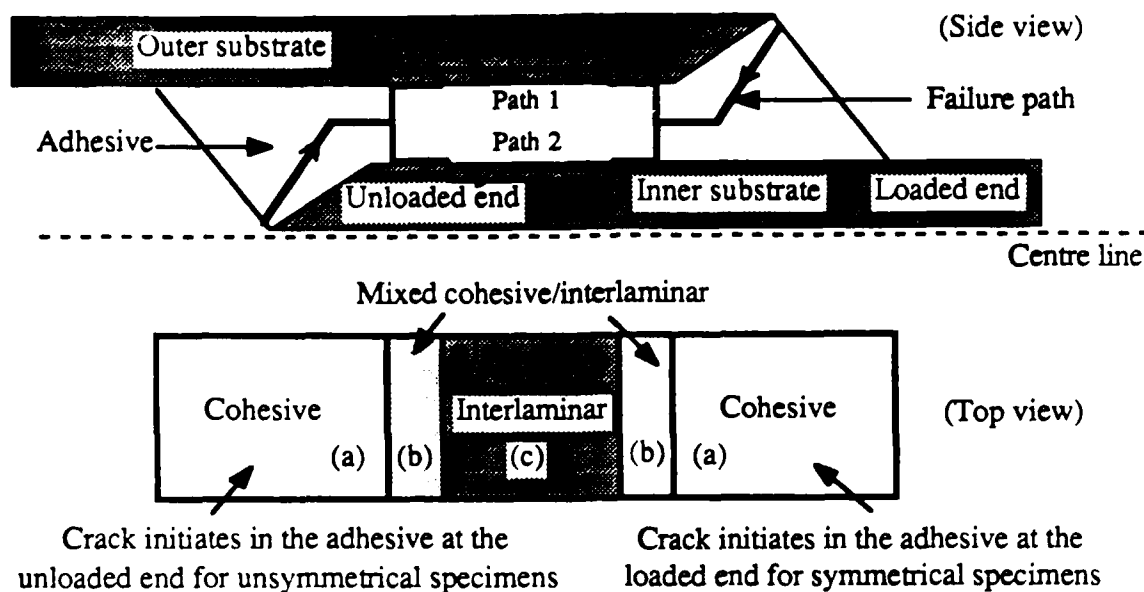
Fig. 7.31. Schematic presentation of the locus of failure, for symmetrical and unsymmetrical specimens in the overlap region of DLJ specimens with tapered composites and adhesive fillets; crack propagates through path 1 or path 2; crack initiates in the adhesive in the corners of the overlap. Letters (a), (b) and (c) in the "top view" figure correspond to the micrographs in Figure 7.30(a) (b) and (c) respectively.

7.5. THEORETICAL STUDIES

7.5.1. Introduction

So far only the experimental results from DLJ specimens have been reported. In this section, the stress predictions from computer analyses employing a differential shear computer program [219] and FEA will be presented.

7.5.2. Differential Shear Analysis

The computer program employed [219] in the current work is superior to the ESDU [207] program employed by Adams et al. [213]. The difference between this program [219] and the ESDU [207] being the fact that the current program takes into account the peel stresses near the edges of the overlap as well as the shear stresses in the adhesive, whereas ESDU is based only on a shear failure. The current computer program requires the tensile moduli of the adhesive and the composite as well as the shear modulus, shear failure stress and shear failure strain of the adhesive. These data were supplied to the computer program and an elastic fully-plastic analysis was carried out on an IBM "920" computer to determine the failure loads.

Figure 7.32 shows the shear stress predictions in the adhesive along the overlap of a DLJ specimen. This figure shows two interesting features. Firstly, the mean of the predicted shear stress values is in excellent agreement with the applied shear stress calculated from the failure load. Secondly, this figure shows that failure should initiate in the adhesive at some distance inside the edges in the overlap where the predicted shear stress reaches the shear failure stress.
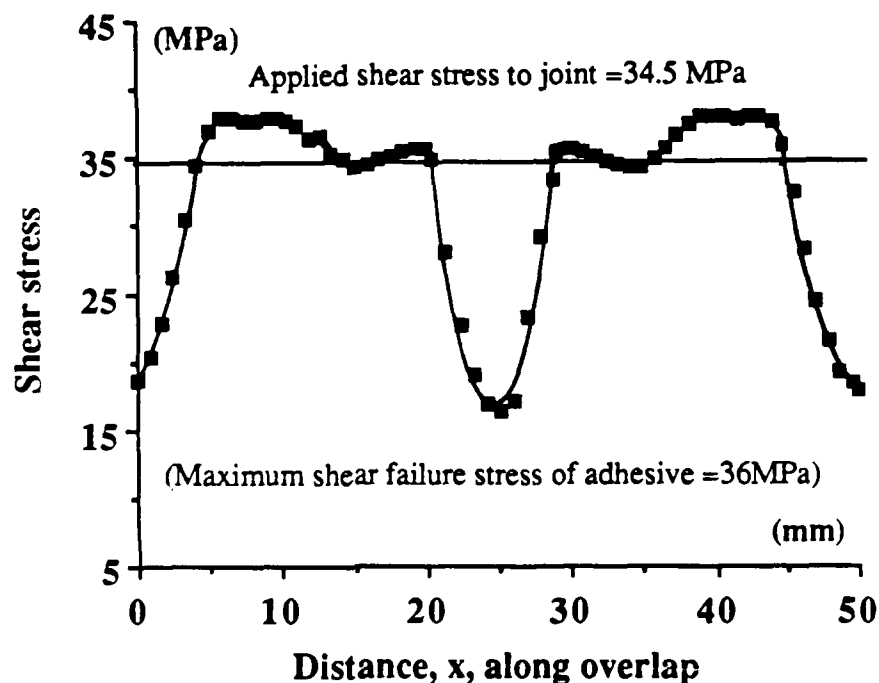
Fig. 7.32. Predicted shear stress variation along the overlap of a U/C-PA DLJ specimen from employing a differential shear analysis.

Figure 7.33 shows the predicted failure loads from differential shear analysis which are compared with the experimental results employing the basic U/C-PA DLJ specimens. It is interesting to note that the theoretical analysis overestimates the failure loads. This may be due to the fact that such an analysis does not consider other modes of failure, such as the transverse tensile failure of the composite. However, it is most interesting to note that if it were possible to obtain failure in the adhesive, then the failure load may be increased to about 4MN/m at an overlap length of 60mm. Which is indeed what was attained in later experiments from tapering the composite and the addition of adhesive fillets. Further, for a composite overlap length of 50mm, with composite and adhesive tapers, it can be seen that the predicted failure load is just under 3.5MN/m. This is again in excellent agreement with the results reported in Table 7.11.

The important implication of these observations is that, if tapering of the composite and

the addition of adhesive fillets can lower the transverse tensile stress in the composite, then shear failure of the adhesive may be responsible for joint failure and relatively high joint failure loads may be achieved. However, the differential shear analysis cannot consider tapered composite ends or adhesive fillets. Therefore, these limitations lead to the use of finite element analysis to predict the stress distributions.
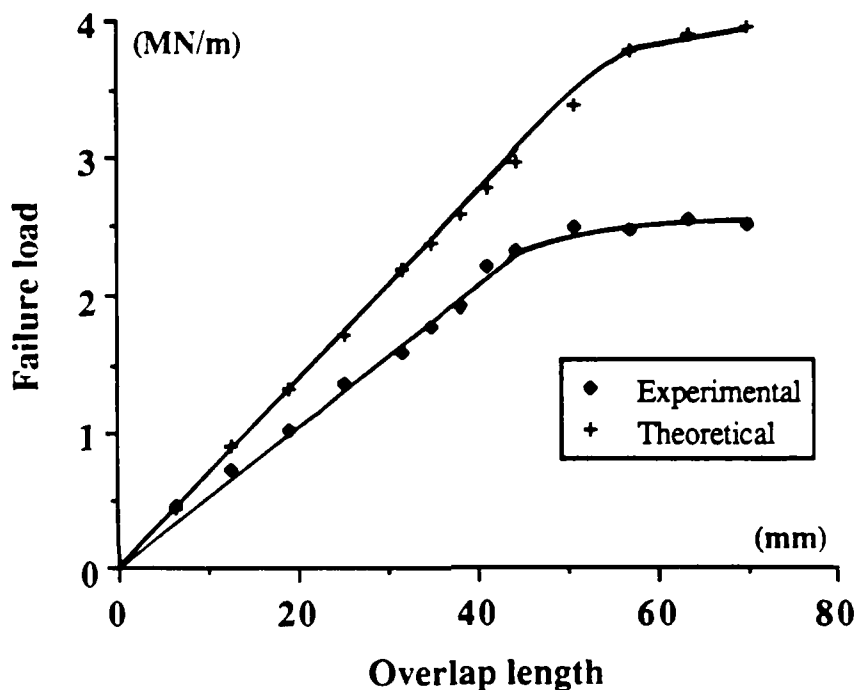
Fig. 7.33. Failure load versus overlap length for the U/C-PA composite bonded to the epox.'-paste adhesive. (Theoretical predictions based upon maximum shear stress in adhesive failure criterion).

7.5.3. Finite Element Analysis (FEA) Studies

7.5.3.1. Introduction

The PAFEC finite element package was employed to predict the stresses in the composite and the adhesive. The assumptions in employing the FEA were:

(i) the composite substrates behave in an elastic manner,

(ii) the adhesive behaves in an elastic-plastic manner with a constant strain-hardening slope, and

(iii) the specimens are in plane-strain.

The details of employing PAFEC and the type of elements employed were given in

Section 5.4.3. However, subroutines had to be written to enable the calculation of the principal stresses and the modified Von Mises stress in the adhesive; PAFEC Level 6.1, does not permit calculation of these stresses using a plastic analysis. It should noted that the computer time, known as CPU hours, on the Vax "8600" computer for a particular elastic-plastic analysis was more than twenty hours and a typical interactive time used was about five days. Finally, as will be discussed, to enable the accurate prediction of stresses in an elastic-plastic analysis, additional FEA work was undertaken to model the tensile stress/strain curve.

7.5.3.2. Mesh Generation

(i) Modelling of Corners

In the FEA studies the adhesive/composite corners were rounded for the following reasons:

(a) Observations, employing a Nikon "Optiphot" optical microscope, revealed that the adhesive/composite corners are indeed "naturally" rounded. Figure 7.34(a) shows a typical small adhesive fillet whereas Figure 7.34(b) shows that cutting composites, by machining, leaves behind rounded corners.
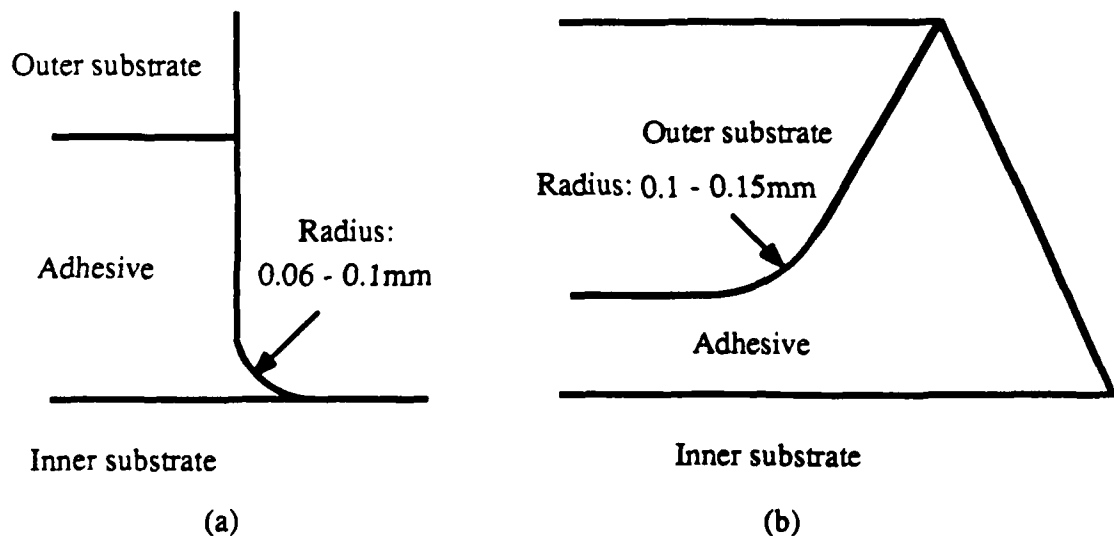
Fig. 7.34. Idealised schematic presentations of the rounded corners for (a) the adhesive and (b) the composite; values measured using optical microscopy.

(b) Sharp corners in FEA lead to very high stress concentrations (singularities) and this may lead to errors when failure criteria are to be applied. Rounding of corners can lead to a substantial decrease in these stresses when a proper rounding technique is employed, as will be discussed next.

Recently, Adams and Harris [220] employed FEA to predict the dimensions of rounded corners and the location of stresses which were not affected by stress concentrations. They performed such analyses to round the corners of lap-joints and predicted the plastic-energy contours in an epoxy adhesive next to a rigid corner. Based on the results of their work, if the rounded corners shown in Figure 7.34 are employed (i.e adhesive radius $70\mu m$ and composite taper radius $125\mu m$) then indeed the plastic-energy contours should depart from singularity dominated regions at distances greater than $10\mu m$ from the rounded corner. In the current work corners were rounded, see Figure 7.35, and the stresses were analysed at least $35\mu m$ away from these corners.

(ii) Models Analysed

Due to the symmetry of the DLJ specimen around the x-axis, only one half of the specimen was modelled for the FEA studies. The boundary condition details are given in Figure 7.35. To compare the predicted stresses from FEA with the experimental results three different models were analysed:

(a) $\approx 90^0$ corners specimen with 50mm overlap. This geometry was employed since the 50mm overlap represents the start of the plateau curve of the failure load. The mesh contained 1448 elements.

(b) $\approx 90^0$ corners specimen with 20mm overlap and the mesh contained 848 elements.

(c) Unsymmetrical joint with composite taper angle, $\beta=30^0$, and adhesive fillet angle, $\alpha=30^0$, see Figure 7.29(b) (page 257). The overlap length of this model was 50mm and the mesh contained 1500 elements. The reason for employing the unsymmetrical DLJ specimen instead of the symmetrical joint design was to enable a direct comparison of the stresses from the two different overlap-edges and therefore to reduce the number of computer runs. It is important to note that 60mm overlap lengths could be modelled. However, a satisfactory refinement of the elements and hence convergence could not be obtained due to the limit in the size of the stiffness matrix which could not be changed without altering some of the original subroutines of the PAFEC FEA package.
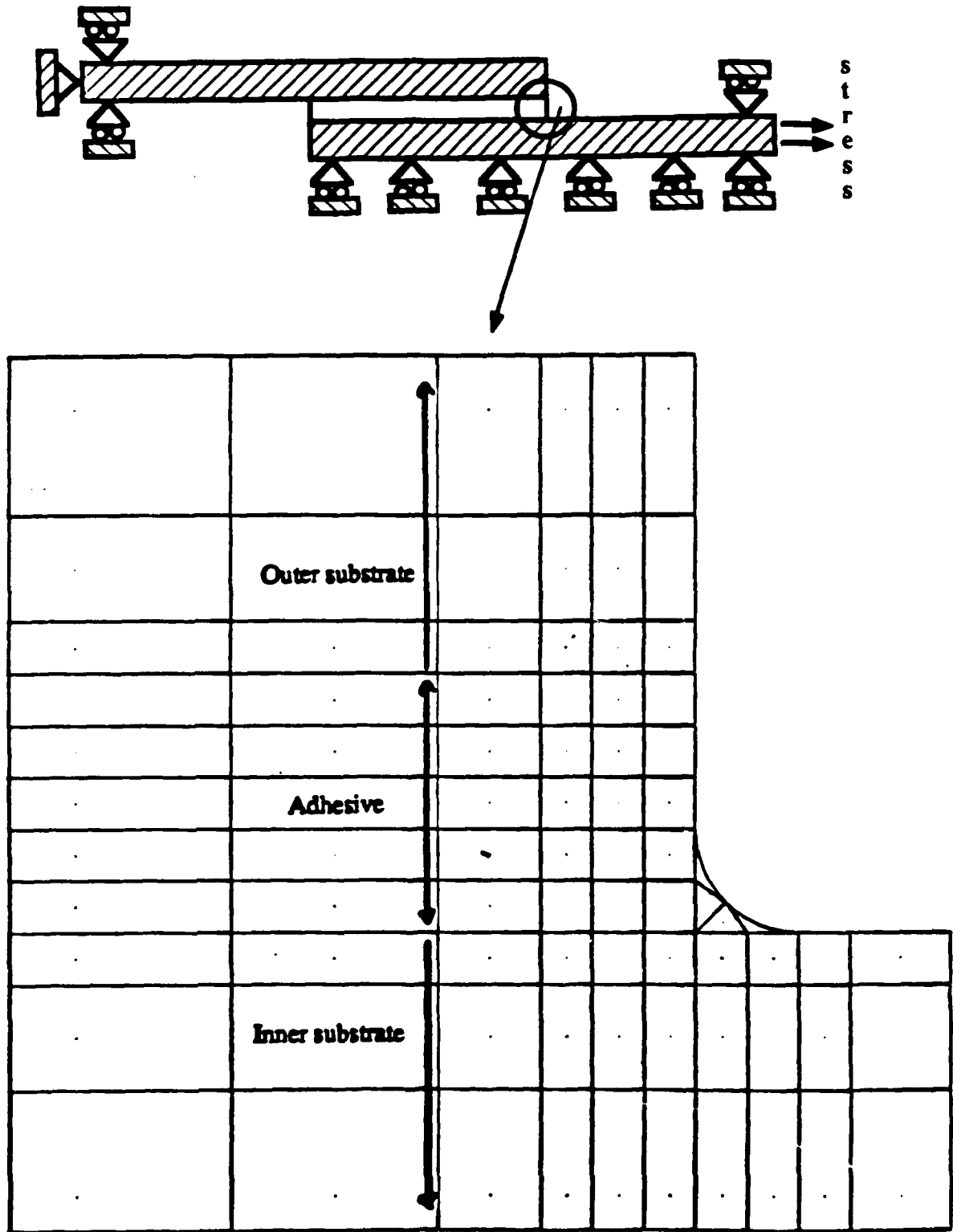
Fig. 7.35. The boundary conditions employed for the FEA and the refinement of
elements employed; note the rounding of the corner employed
(radius=70μm) for the ≈90⁰ corner DLJ specimens.

7.5.3.3. Convergence

(i) Stress/Strain Curve

To obtain a satisfactory convergence in the FEA studies required the prediction of a theoretical tensile elastic-plastic stress/strain curve. To calculate the shear stresses, FEA packages such as PAFEC, COSMOS [221], LUSAS [222] and ABAQUS [223], require the tensile stress/stain curve. For example, PAFEC employs the Prandtl-Reuss equations to predict from the tensile stress/strain curve the shear strain:

$$d\gamma_{12} = \left[\frac{3d\bar{\varepsilon}^p}{2\bar{\sigma}}\right]\sigma_{12} + \frac{d\sigma_{12}}{2G} \qquad (7.10)$$

where γ is a shear strain, $\bar{\sigma}$ is equivalent stress, $\bar{\varepsilon}^p$ is equivalent plastic strain, G is shear modulus and 1 and 2 represent orthogonal axes. It can be seen from the above equation that the prediction of the plastic shear strain and shear stress will depend on the slope of the strain-hardening curve of the tensile stress/strain curve. This dependency will be shown to be indeed a very important aspect which has been previously ignored. Therefore, FEA studies were undertaken to predict the best strain-hardening slope which would give ideally:

1) equal areas under the theoretical and experimental tensile stress/strain curves,

2) equal areas under the predicted and experimental shear stress/strain curves, and

3) predict average shear stress values in the joint equal to the applied shear stress.

The boundary conditions of the model employed are shown in Figure 7.36. The analysis was undertaken in an elastic-plastic (isotropic), plane-strain condition. Special elements were used in the adhesive to account for large displacements and a special subroutine was employed to permit large displacements [109]. Figure 7.37 shows that as the strain-hardening slope is increased then the error in the predicted average shear stress (in the adhesive) decreases. However, for the very high and the very low strain-hardening slopes the predicted value of the shear strain distribution in the adhesive was in considerable error. From about fifty cases considered, it was found that a tensile stress/strain curve with an elastic stress limit of 38MPa and a strain-hardening slope of 0.050GPa was the best in satisfying the above three conditions, see Figures 7.37, 7.38 and 7.22 (the latter figure can be found on page 250). The predictions in Figure 7.37 may indicate the reason why Adams et al. [213] found difficulty in accurately predicting failure loads which agreed with their experimental results. In their case they modelled the adhesive as an elastic fully-plastic material and for small strain-hardening slopes, as shown in Figure 7.37, the predicted average shear stress value in the adhesive is only 60% of the applied shear stress.
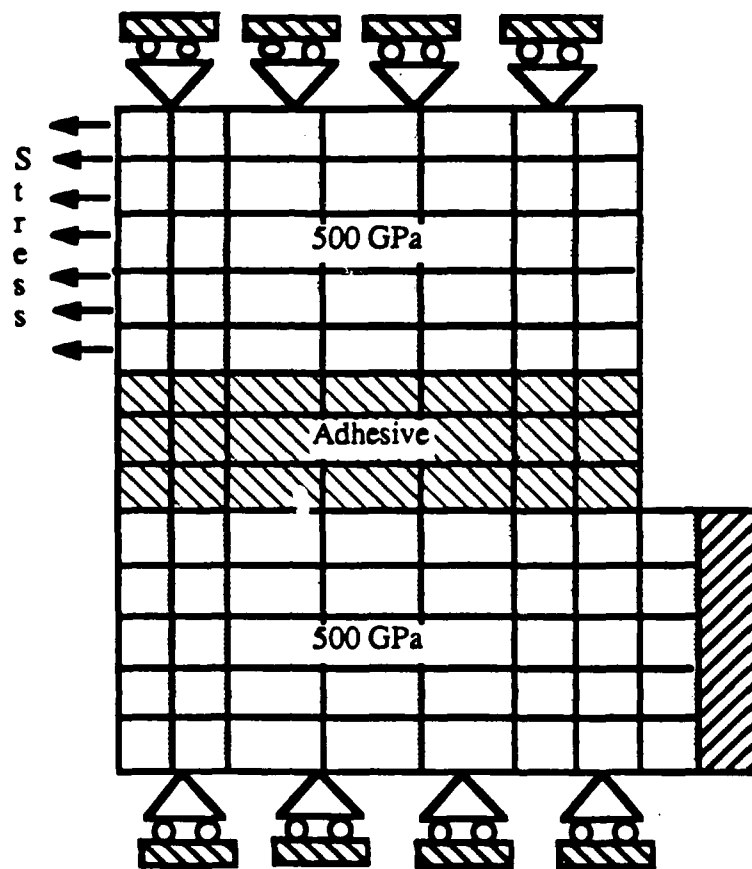
Fig. 7.36. The model employed for FEA analysis to predict the strain-hardening slope.
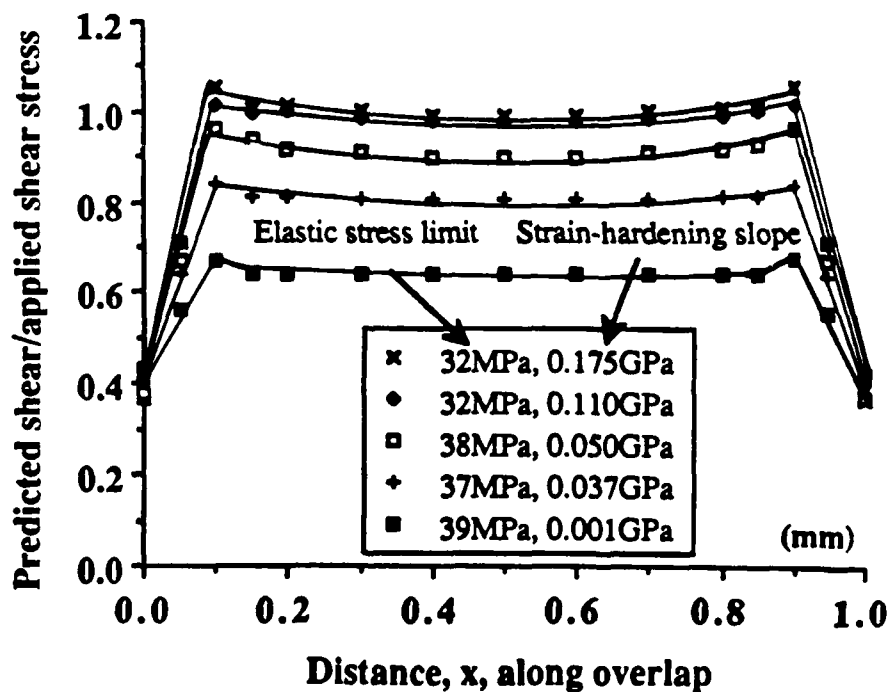
Fig. 7.37. Predicted shear stress (normalised by the applied shear stress to the joint presented in Figure 7.36) obtained from different tensile elastic stress limits and strain-hardening slopes.

It should be noted that in Figure 7.37 the free surfaces have shear stress values and obviously this cannot be true. However, the FEA package employed calculates the stresses first at the "Gaussian" integration points which are some distance inside the elements and then extrapolates these stresses to the corner nodes. Further, the elements employed in the current work were strain elements and only stress elements satisfy the stress-free boundary condition.
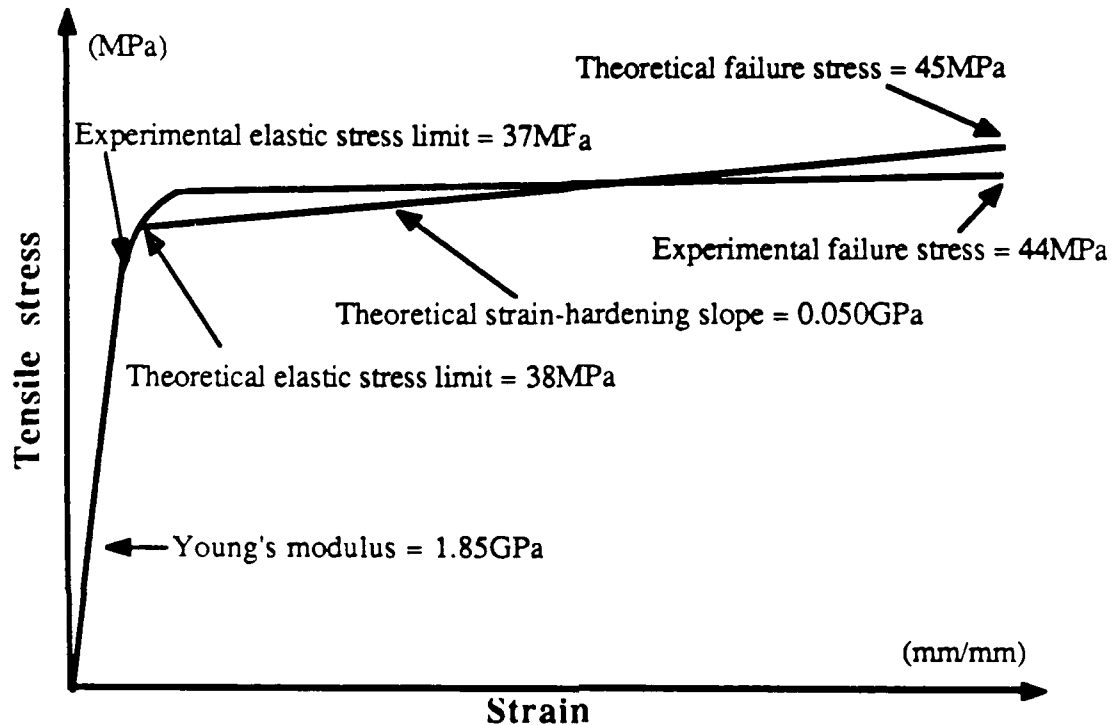
Fig. 7.38. Schematic presentation of the tensile stress/strain curves. Note that to obtain equal strain energies from the theoretical and experimental results the areas under the curves were kept equal.

(ii) Convergence

The predicted tensile stress/strain curve was employed in the FEA studies. The adhesive was therefore considered to be an elastic-plastic isotropic material and the composite (U/C-PA) was considered as an elastic orthotropic material (for the U/C-PA composite properties employed see Table 5.4 (page 160)). The convergence of the DLJ model in the FEA studies was satisfied by firstly, comparing the applied stress with the reactions from the left-end elements of the model, see Figure 7.35. The ratio was found to be more than 99.5%. Secondly, the error in the convergence value of the FEA stress predictions compared to the supplied elastic-plastic curve was less than 0.72%. To achieve these stringent conditions more than twenty incremental loading steps and more than three hundred iterations had to be performed in the plastic regions, which explains the amount of CPU hours used.

7.5.3.4. Failure Conditions

Joint failure was assumed to occur if one or more of the following conditions were satisfied:

(a) Adhesive

(i) If the maximum principal stress in the joint exceeded the failure stress from a simple tensile test, i.e. 44MPa.

(ii) If the maximum shear stress exceeded the the shear stress to failure, i.e. 36MPa.

(iii) If the modified Von Mises stress exceeded a stress value of 50.2MPa. This value was

calculated from the square root of $2\sigma_c\sigma_t$, where $\sigma_c = 1.3\sigma_t$, see also Equation 7.6 (page 241).

(b) Composite:

(i) If the transverse tensile stress exceeded the transverse tensile failure stress, i.e. 83.7MPa.

(ii) If the longitudinal tensile stress exceeded the longitudinal failure stress, i.e. 1330MPa.

7.5.3.5. Prediction of Stresses

(i) All Corners $\approx 90^0$, Overlap Length 50mm and Applied Load 2.45MN/m

The stresses from this model are presented in Figures 7.39 to 7.42. An applied load of 2.45MN/m has been used in these analyses, since this load is equivalent to the average measured failure load for this design of a basic U/C-PA DLJ specimen. It should be noted that firstly, the stresses are plotted along the overlap. Secondly, the plots are along an axis where the stresses are highest and this corresponds to the first node next to the adhesive/composite interface, i.e. at 35μm. Thirdly, the change in the stresses from the interface to a distance of 70μm was small, hence, plotting the stresses at 35μm, instead of a smaller distance from a more refined mesh, is valid.

Several interesting features emerge from Figures 7.39 to 7.42. Firstly, the principal tensile, the maximum shear and the modified Von Mises stresses in the adhesive are all below the critical failure stresses and therefore the adhesive does not fail. Secondly however, the transverse tensile stress, Figure 7.42, in the inner composite reaches 90.2MPa in the region of the overlap where the outer substrates end (transverse tensile fracture stress of U/C-PA composite is 83.7MPa). Thus indicating that the composite fails in the transverse mode and this prediction is in excellent agreement with the experimental observations. Thirdly, the transverse stress in the composite decreases rapidly beyond the overlap, i.e. for distances greater than 50mm, see Figure 7.42. This indicates that tapering the composite and the addition of adhesive fillets may indeed reduce the magnitude of the transverse tensile stress.
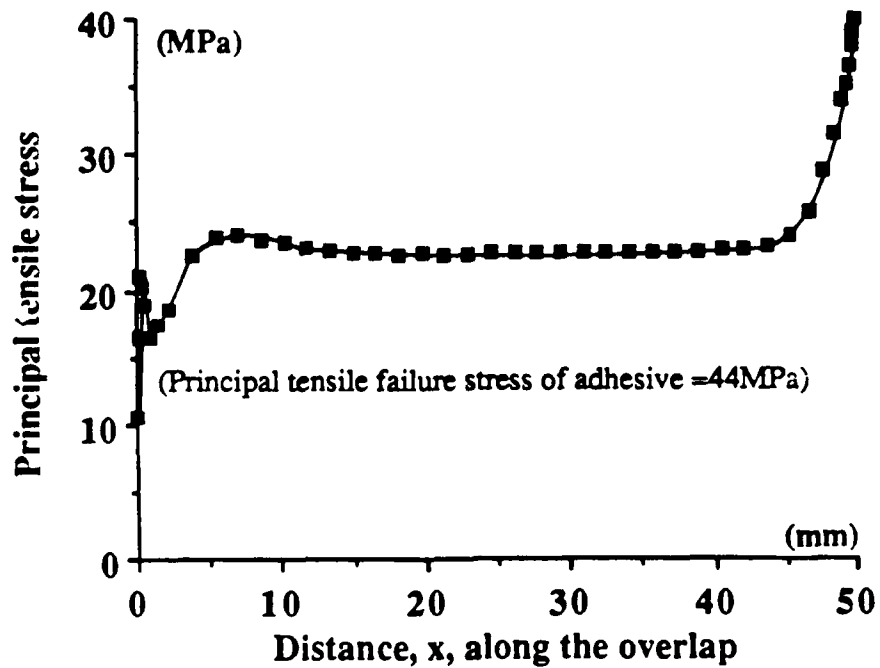
Fig. 7.39. Principal tensile stress in the adhesive adjacent to the inner substrate at a distance of 35μm; applied load is 2.45MN/m and composite overlap length is 50mm.

Fig. 7.40. Modified Von Mises stress in the adhesive adjacent to the inner substrate at a distance of 35μm; applied load is 2.45MN/m and composite overlap length is 50mm.

Fig. 7.41. Maximum shear stress in the adhesive adjacent to the inner substrate at a distance of 35μm; applied load is 2.45MN/m and composite overlap length is 50mm.

Fig. 7.42. Transverse tensile stress in the inner composite adjacent to the adhesive at a distance of 35μm; applied load is 2.45MN/m and composite overlap length is 50mm.

(ii) All Corners ≈90⁰, Overlap Length 20mm and Applied Load 1MN/m

It is of interest to analyse a specimen with a different overlap length than the one from the plateau value. The applied load of 1MN/m corresponds to the average failure load for this design of a U/C-PA DLJ specimen. The results from such a model showed that the inner composite fails by transverse fracture at the region of the overlap where the outer substrates end, see Figure 7.43. It is interesting to note that the transverse tensile stress follows the same pattern as for the 50mm overlap and that this stress at the end of the overlaps, from both the 20 and 50mm overlap lengths, are indeed equal. These theoretical analyses show that for all overlap lengths, with adhesive and composite corners ≈90⁰, the transverse tensile failure stress of the composite governs the failure load. This observation also explains why the differential shear analysis, which ignores such composite substrate failure, overestimated the failure load, see Figure 7.33. Finally, it is interesting to note that the predicted transverse tensile stress is a function of the overlap length. This observation is in agreement with Goland and Reissner's theoretical calculations [200]. They showed that the bending moment factor, k, (see Equation 7.4) decreases with overlap length thus they predicted that the joints should fail at higher loads.

Fig. 7.43. Transverse tensile stress in the inner composite adjacent to the adhesive at a distance of 35μm; applied load is 1MN/m and composite overlap length is 20mm.

(iii) Unsymmetrical DLJ Specimens: Composite Taper β=30⁰, Adhesive Fillet α=30⁰,
Overlap Length 50mm and Applied Load 3.45MN/m

The stresses from such a joint are shown in Figures 7.44 to 7.47. The applied load of 3.45MN/m has been used in these analyses, since this is equivalent to the average measured failure load for the symmetrical U/C-PA DLJ specimen. The reason in applying the failure load of the symmetrical joint to the unsymmetrical FEA model was to make a direct comparison of the stresses at both ends of the overlap and to minimize the number of computer runs. The positions of points a, b and c in these Figures are shown in Figure 7.48. Note that the stresses in these figures have been plotted at a distance of 43.75µm from the adhesive/composite interface and it was mentioned earlier that this was a valid method sin~ the change in stresses to a distance of 70µm was small. The noteworthy features from Figures 7.44 to 7.47 are:

Firstly, it is evident that tapering the composite and the addition of adhesive fillets leads to a reduction in the transverse tensile stress in the inner composite, at the region of the overlap where the outer substrates end. This reduction, from 90.2MPa to 49.8MPa (compare Figure 7.44 "point b" with the stresses in Figures 7.42 or 7.43) is significant, especially when it is recalled that the stresses quoted here are from the application of a higher failure load. However, at the unloaded end of the inner substrate the transverse stress increases from 88.9MPa to 176MPa. This increase in the compressive transverse stress is expected since at this end of the overlap the corners were modelled to be ≈90⁰, see Figure 7.48. Further, even at those high levels of compressive transverse stress the composite should not fail. In fact, Hull [224] has indicated that in unidirectional composites the transverse failure stress in compression can be four times higher than in tension (i.e. 4X83.7 = 335MPa). Therefore, these observations show that the transverse stresses are not responsible for joint failure for either the symmetrical or the unsymmetrical U/C-PA DLJ specimens.

Secondly, it is evident again that tapering the composite and the addition of adhesive fillets lead to a reduction in the maximum shear stress from 38.7MPa to 35.8MPa, see Figure 7.45. The shear stress of 38.7MPa, in the adhesive at the region of the overlap where the inner substrate ended with ≈90⁰ corners, is higher than the maximum shear stress measured for the epoxy adhesive. This shows that unsymmetrical specimens should fail at lower loads, which is in agreement with the experimental results. Further, the shear stress of 35.8MPa in the adhesive at the position of the overlap where the outer composites start the taper (point a), may indicate that the shear stress of the adhesive is responsible for the failure of the symmetrical DLJ specimens. However, the above observations are also true when the principal tensile or the modified Von Mises stresses are considered. Therefore, it is not possible to ascertain which one of these stresses is responsible for the adhesive failure.
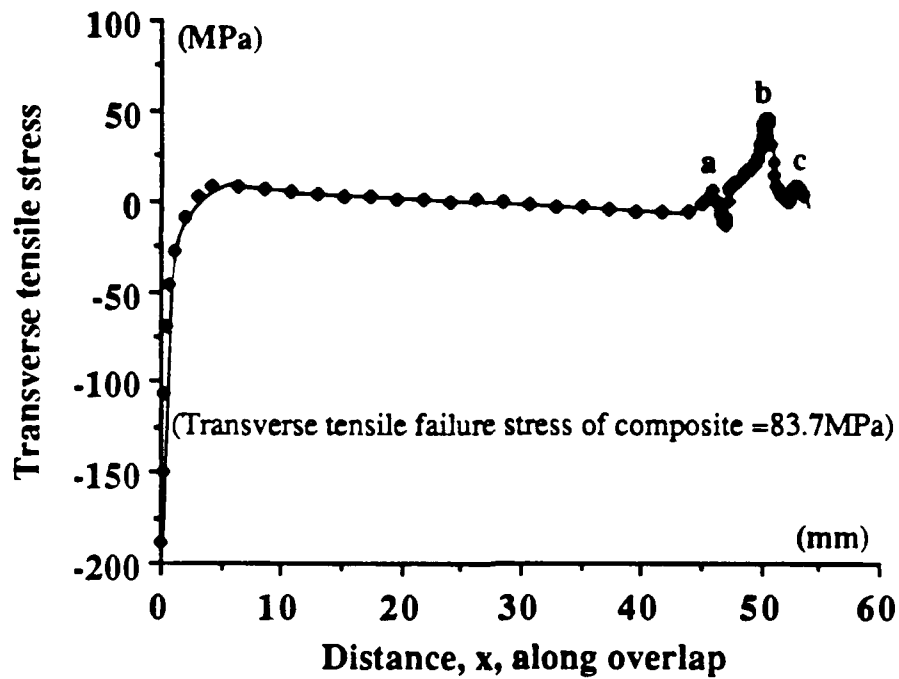
Fig. 7.44. Transverse tensile stress in the inner composite adjacent to the adhesive at a distance of 43.75μm; applied load is 3.45MN/m and composite overlap length is 50mm.
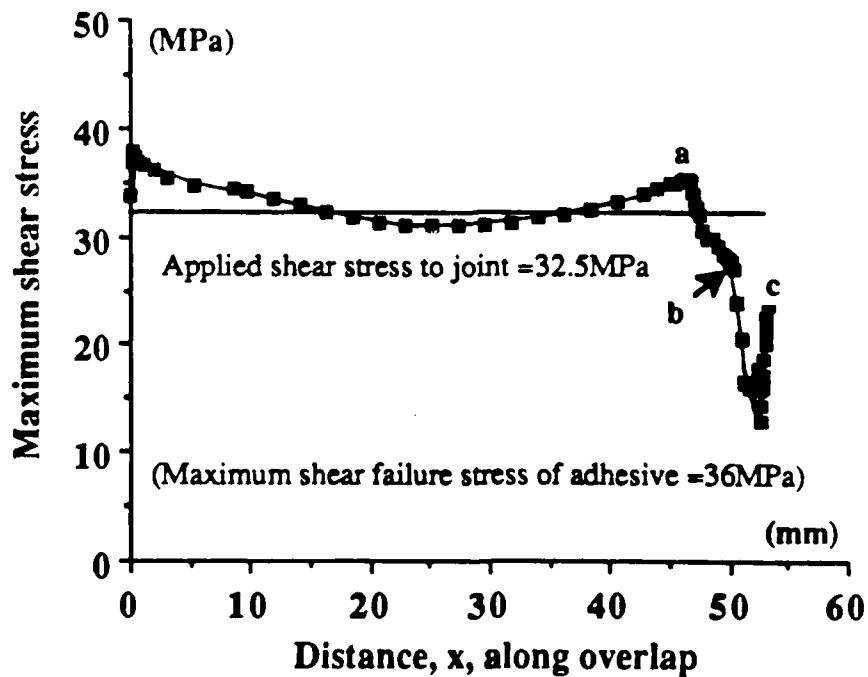
Fig. 7.45. Maximum shear stress in the adhesive adjacent to the inner substrate at a distance of 43.75μm; applied load is 3.45MN/m and composite overlap length is 50mm.
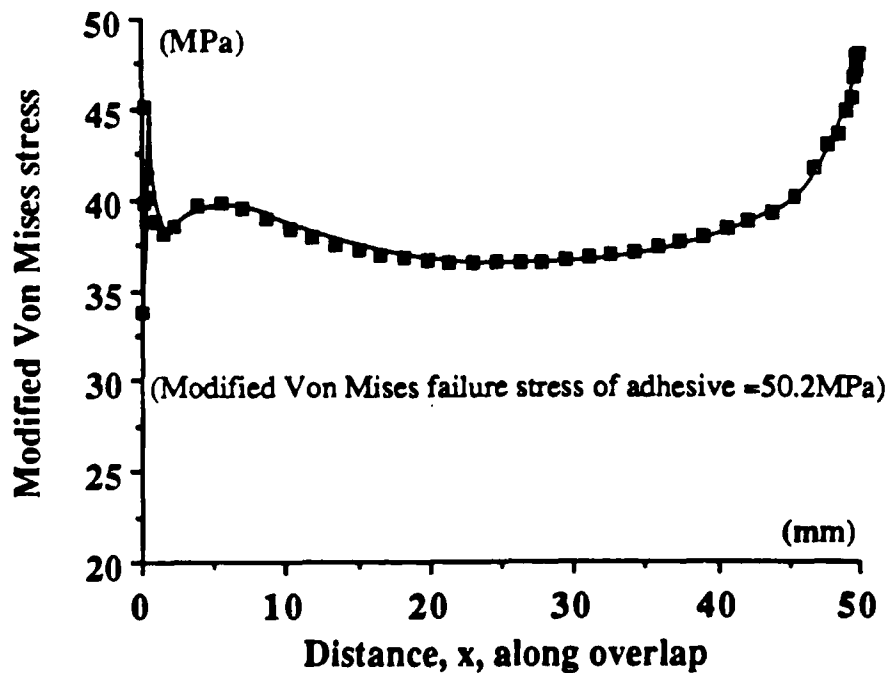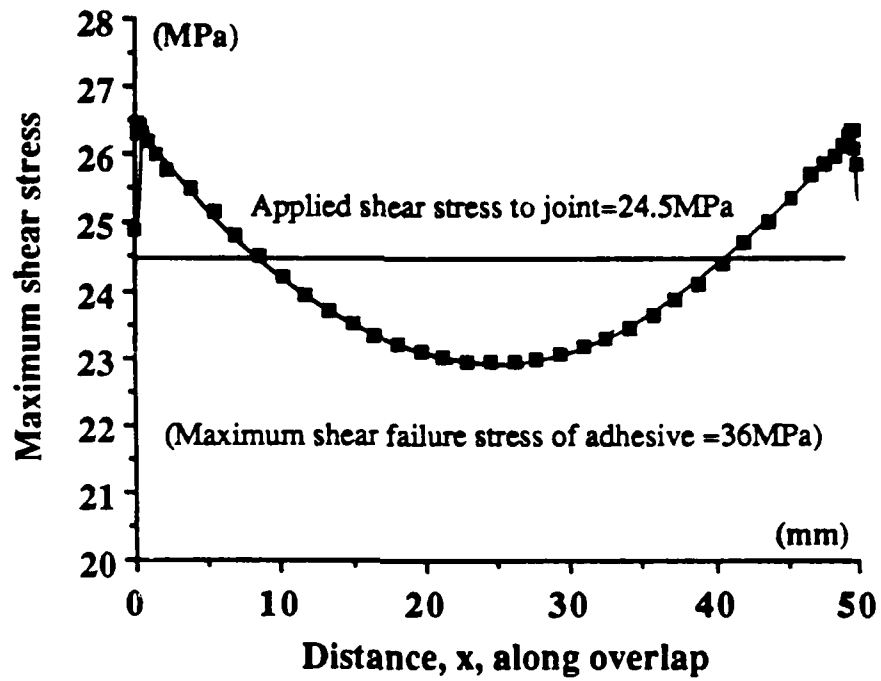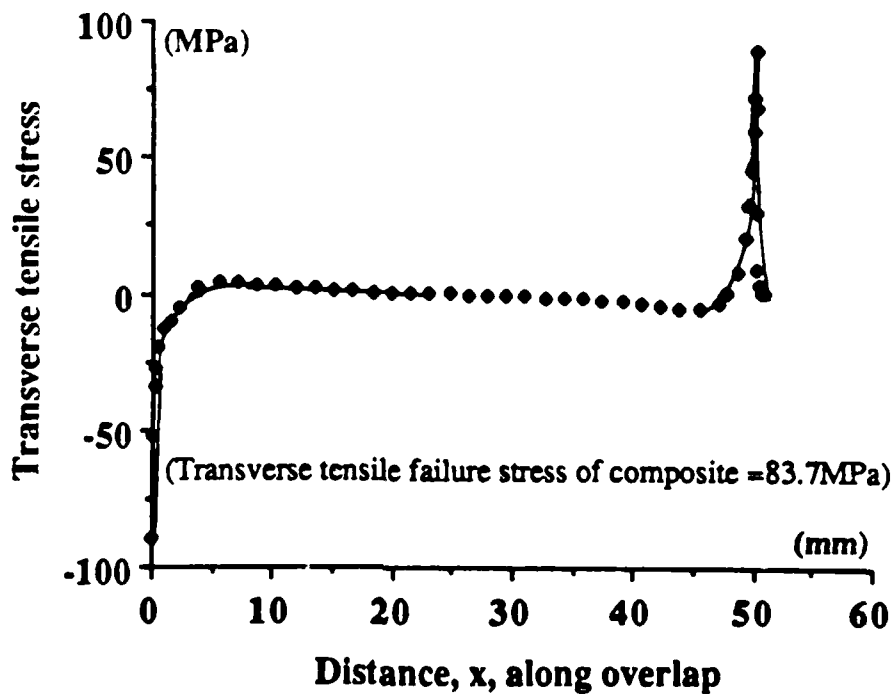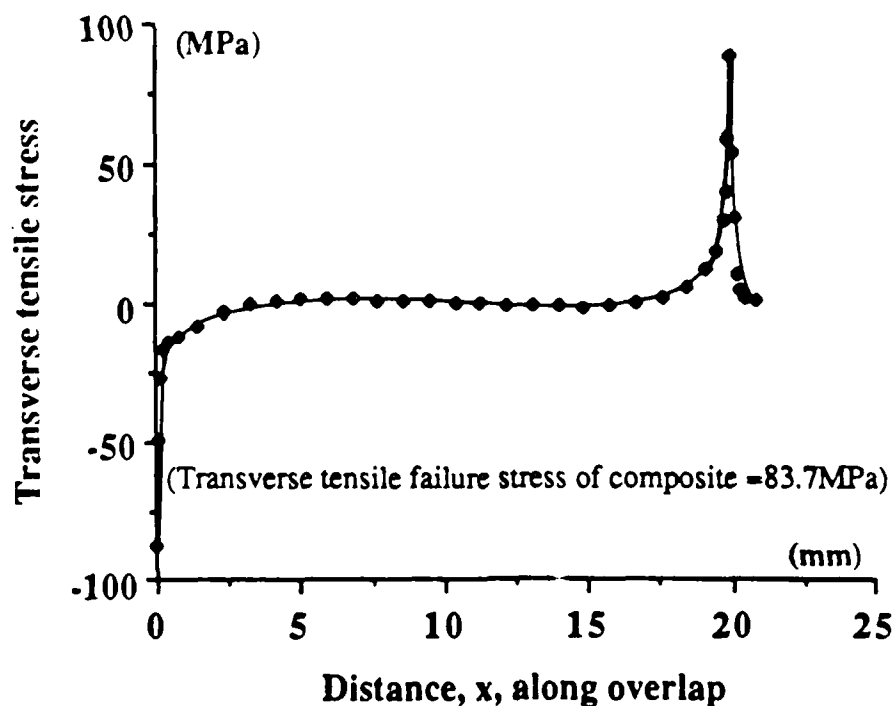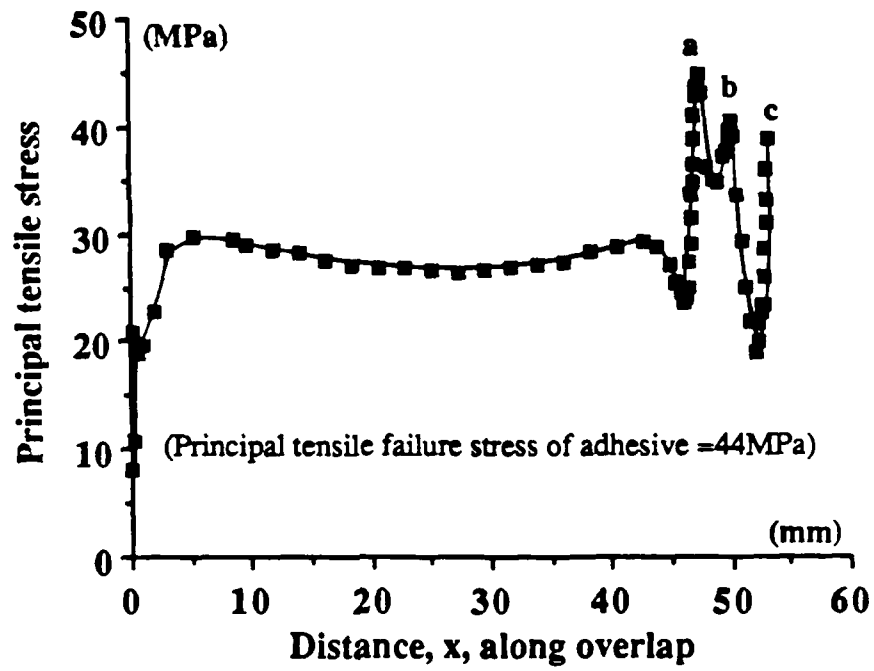
Fig. 7.46. Principal tensile stress in the adhesive adjacent to the inner substrate at a distance of 43.75µm; applied load is 3.45MN/m and composite overlap length is 50mm.
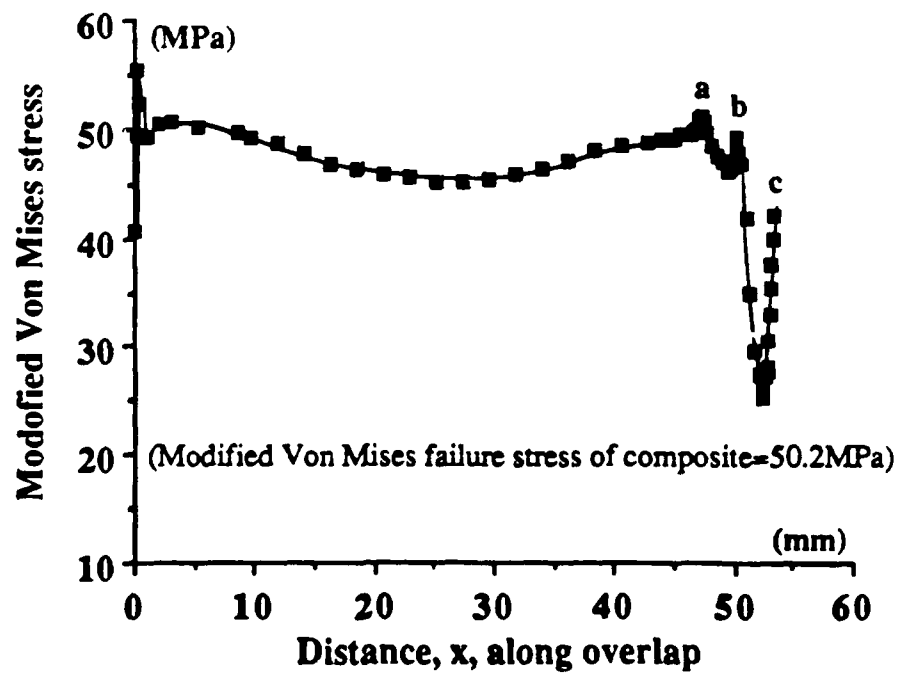
Fig. 7.47. Modified Von Mises stress in the adhesive adjacent to the inner substrate at a distance of 43.75 µm; applied load is 3.45 MN/m and composite overlap length is 50mm.

(0) Distance, x, along overlap   **a (47mm)** **b (50mm)** **c (53.025mm)**

Outer substrate

(53.1mm)

Adhesive

Inner substrate   Loaded end

Unloaded end

Centre line

Position where failure initiates for unsymmetrical specimens
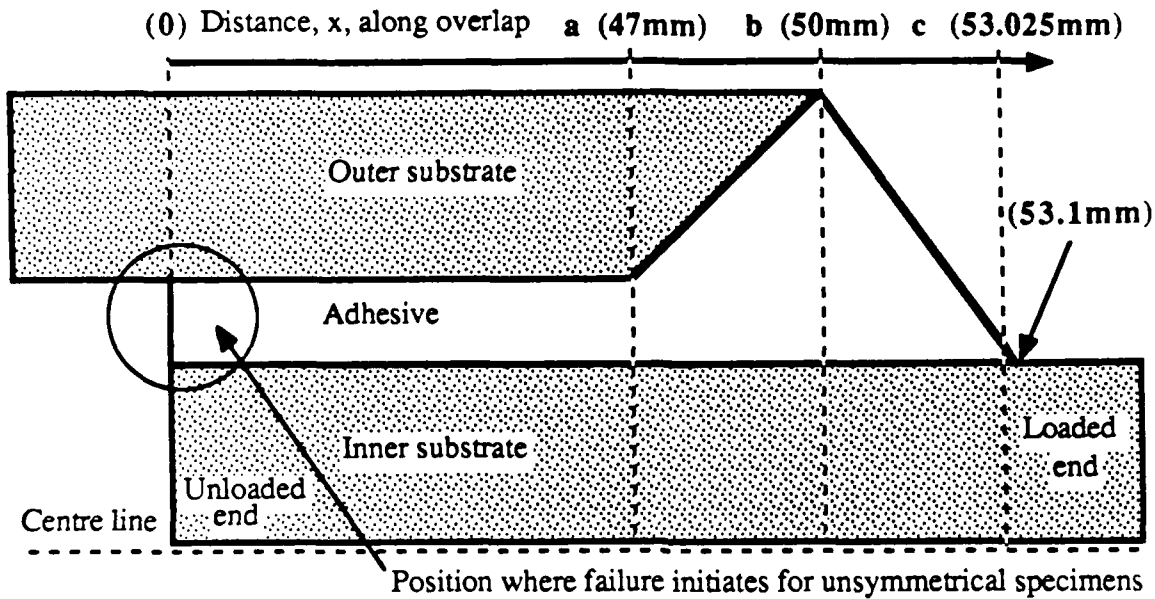
Fig. 7.48. Position of the points a, b and c in Figures 7.44 to 7.47.

The important implication of the above observations is that FEA predicts that tapering the composite and the addition of the adhesive fillets changes the locus of failure from interlaminar through the composite to one of initiating in the adhesive. This leads to an increase in the failure loads and therefore to higher joint efficiencies.

7.6. COMPARISON OF EXPERIMENTAL AND THEORETICAL RESULTS

The experimental results are compared with the theoretical predictions from employing FEA and the differential shear analyses in Table 7.12. Several noteworthy features emerge. Firstly, for the 20mm overlap joint with $\approx 90^0$ corners FEA predicts that the stresses in the adh' .ve are lower than the failure stresses measured. However, the transverse tensile stress of the inner composite in the region where the outer substrates ended was shown to be 89.5MPa. This stress is close to the measured failure stress of the U/C-PA composite of 83.7MPa, indicating that the composite should fail. Further, FEA predicts joint failure by transverse tensile interlaminar fracture at applied load of 1MN/m as "lowest" mode whereas, differential shear does not consider the aspect of substrate failure and hence predicts that the failure load should be about 30% higher. The above observations also apply to the 50mm overlap joint with $\approx 90^0$ corners. The experimental results and the analyses of the locus of failure are therefore in excellent agreement with the FEA predictions.

Secondly, for the 50mm symmetrical overlap joint with a composite taper ($\beta=30^0$) and

adhesive fillet ($\alpha=30^0$) the FEA predictions show, however, that the transverse tensile stress is lower than the transverse tensile failure stress of the composite. Therefore, the composite does not fail which is in agreemnt with the experimental observations of the locus of joint failure (Section 7.4.2.5 page 257). Further, FEA predicts that the maximum shear, principal tensile and modified Von Mises stresses all reach the measured failure stresses at the applied failure load. Even the differential shear analysis indicates that the shear stress in the adhesive should lead to the failure of the joint.

Therefore, although it cannot be ascertained which one of these stresses in the adhesive is responsible for the joint failure, the analyses agree that the adhesive fails giving a theoretical joint failure load close to the failure load observed. The SEM observations showed that the crack initiates in the adhesive at the edges of the overlap, see Figures 7.30 and 7.31. Therefore the theoretical and experimental results are again in agreement.

Thirdly, for the unsymmetrical 50mm overlap length, the FEA predicts that the unloaded end of the inner substrate should fail due to failure initiation in the adhesive. Therefore, this again is in excellent agreement with the experimental observations, see Figures 7.30 and 7.31.

Fourthly, for the symmetrical 60mm over ip length with $\beta=10^0$ and $\alpha=10^0$ the overlap regions shattered away from the grips but it was not possible to predict the stresses from FEA due to the limits imposed by the size of the stiffness matrix. However, the theoretical prediction from differential shear analysis are again in excellent agreement with the experimental results.

Finally, it was shown in the above discussions that there is good agreement between the theoretical predictions and the experimental observations. However, recall that the applied loads in the FEA studies correspond to the failure loads from the experiments. One aspect which was not considered in the FEA studies so far was the variation of the predicted critical stresses with applied load. For this reason, the applied load for the basic ($\approx90^0$ corners and 20mm overlap length) DLJ FEA model was varied and the transverse tensile stresses at the edges where this joint failed were noted. From such analyses, it was found that when the applied load (1MN/m) was varied by $\pm10\%$ then the critical transverse tensile stress at the corners where failure initiated varied accordingly, i.e. by about $\pm11.5\%$. This variation in the predicted stress gives values lower and much higher than the transverse fracture stress of the U/C-PA composite. (Note that the predicted maximum transverse tensile stress in the composite from the application of 1MN/m was 89.5MPa and the fracture transverse tensile stress of the U/C-PA composite is 83.7MPa). These observations confirm the accuracy of the techniques employed in the FEA analyses.

Table 7.12. Comparison of experimental and theoretical studies on double-lap joints
of various designs of the U/C-PA composite bonded to the epoxy-paste adhesive.

Desciption of joints			Experimental	Theoretical predictions for possible failure modes (MN/m)				
				In composite		In adhesive		
Overlap (mm)	β	α	Maximum failure load (MN/m)	Transverse tensile	Maximum shear	Modified Von Mises	Principal tensile	Differential shear
20	90	90	0.98	1.0	>1.0	>1.0	>1.0	1.30
50	90	90	2.45	2.45	>2.45	>2.45	>2.45	3.45
50	30	30	3.45	>3.45	3.45	3.45	3.45	3.45
50[a]	30	30	3.25	>3.45	<3.45	<3.45	<3.45	3.45
60	10	10	3.85	*	*	*	*	3.95

Notes: ([a]): Unsymmetrical joint, rest all symmetrical.

$\quad$ (*): Could not be calculated due to the restriction on the size of the stiffness matrix.

$\quad$ β: Composite taper angle.

$\quad$ α: Adhesive fillet angle.

7.7. CONCLUSIONS

The conclusions from this chapter are:

1. Most of the mechanical properties of the composites and the adhesive were obtained employing the recommendations of the ASTM Standard. However, the current available techniques for measuring the shear properties are not satisfactory. For this purpose a cone-and-plate shear specimen was designed and a novel technique was developed to measure the shear strain.

2. For the first time an experimental double-lap joint (DLJ) design analysis was conducted using thermoplastic fibre-composite substrates. This being made possible by the development of the corona pretreatment method for ensuring that premature interfacial failure of the joints did not occur. The results showed that a joint efficiency of nearly 100% is attainable. This being achieved by reducing (i) the transverse tensile stresses in the inner composite substrate, and, (ii) the stresses in the adhesive at both edges of the overlap. These stresses were successfully reduced by tapering both the adhesive and the composite at both ends of the

overlap. Further, for the first time an efficiency of nearly 100% was also attained for the thermosetting fibre-composite joints using a double-lap joint design.

3. It was demonstrated, by using FEA elastic-plastic studies, that the shear stress and strain distributions in the joint are highly dependent on the slope of the strain-hardening curve of the adhesive. FEA was used to predict the tensile stress/strain curve which would, in turn, accurately predict the stresses in the DLJ specimens.

4. FEA studies showed that for the $\approx 90^0$ corner specimens (i.e. neither tapered substrates nor angled adhesive fillets) the transverse tensile stress in the inner composite in the regions of the overlap (where the outer substrates ended) was responsible for the failure of the basic DLJ specimens. Neither tapering the composite, whilst keeping the adhesive corners $\approx 90^0$, nor having adhesive fillets, with composite corners at $\approx 90^0$, changed the locus of failure or the measured failure loads.

5. For specimens with tapered composites and adhesive fillets, the results from the FEA studies showed that the transverse tensile stresses decrease and that failure of the adhesive is now responsible for the failure of the DLJ specimens. It could not be ascertained which one of the stresses was responsible for failure. However, the failure loads from differential shear analysis were in excellent agreement with the theoretical results. This may indicate that the maximum shear stress in the adhesive is responsible for the failure of the DLJ specimens. In any case the failure loads were relatively high giving joint efficiencies of approximately 100%.

6. A comparison of the experimental results with the theoretical predictions showed that the FEA predictions of the failure loads and the mode of failure were in excellent agreement with the experimental failure loads and the SEM observations. However, it was not possible to ascertain whether the composite or the adhesive was responsible for the failure of the very high efficiency DLJ specimens.

CHAPTER EIGHT

THE MAIN CONCLUSIONS AND RECOMMENDATIONS
FOR FUTURE WORK

8.1. INTRODUCTION

In this chapter the main conclusions will be drawn together from the previous chapters. This will be followed by presenting the recommendations for future work.

8.2. THE MAIN CONCLUSIONS

The main conclusions are:

1. When the unidirectional-carbon-fibre/epoxy composite was subjected to an abrasion/solvent-wipe pretreatment and bonded to the epoxy and acrylic adhesives the resulting double-cantilever beam joints failed either cohesively through the adhesive, or in one case in an interlaminar manner through the composite. Such loci of failure indicated that this thermosetting material indeed attains strong intrinsic adhesion to the engineering adhesives and the resulting adhesive joint fracture energy, G_c, values are relatively high.

2. When this simple pretreatment techni.. .: i.e., abrasion/solvent-wipe, is applied to the thermoplastic fibre-composite (TPFC) materials the resulting joints were very weak and the locus of joint failure was at the composite/adhesive interface, resulting in very low fracture energy, G_c, values. An aluminium/NaOH pretreatment technique (composite sheets were moulded against "clean" aluminium foil and after consolidation of the composites, the aluminium foil was dissolved away in a two molar sodium hydroxide solution) ensured "releasing agent free" TPFC surfaces. However, the resulting joints were still weak indicating that the problem is due to the lack of intrinsic adhesion associated generally with thermoplastic polymers, rather than a "weak boundary layer" of releasing agent being present on the TPFC surfaces.

3. An acid-etch pretreament technique was employed in an attempt to improve the adhesive bonding of TPFC materials. Fracture results showed a relatively small increase in the measured G_c values, indicating that a controlled oxidation technique of the surfaces of the TPFC materials might be beneficial. For this purpose a corona-discharge equipment was

designed and employed for pretreating the TPFC materials prior to adhesive bonding. Special features were included in this equipment to treat carbon-fibre reinforced thermoplastic composite materials which are electrically-conductive materials.

4. Corona-treated TPFC materials bonded using the epoxy and acrylic structural adhesives showed a major increase in the measured fracture energy, G_c, values. The locus of failure changed from that of interfacial failure at the adhesive/composite interface to one of either cohesive through the adhesive or one of interlaminar through the composite. The cohesive failures resulted in the higher fracture energy values. Therefore, by employing corona treatment it was possible to attain strong adhesion to the TPFC substrates.

5. As mentioned above in (4), provided the TPFC materials had been adequately treated with corona-discharge then the locus of failure was either cohesive in the adhesive or interlaminar through the composite. A finite element analysis (FEA) approach was adopted to explain the locus of failure in the DCB joints. It was shown that the locus of failure can be predicted from a knowledge of the transverse tensile failure stress, σ_{yyc}, of the composites. It was demostrated that once the transverse stress in the composite in the vicinity of the crack tip reaches σ_{yyc} of the composite then the composite is predicted to fail in an interlaminar manner. For composites which have relatively high transverse tensile failure stress then it was successfully demonstrated that the locus of failure should be one of cohesive through the adhesive.

6. Surface analysis, by scanning electron microscopy (SEM), contact angle analysis (CAA) and X-ray photoelectron spectroscopy (XPS) of corona-treated TPFC surfaces indicated that:
(a) The surface roughness of the composites increased as the level of treatment level was increased.
(b) The surface free energy of the composites increased substantially (calculated based upon a new mathematical technique). This increase was due to a dramatic increase in the polar energy component, whilst the dispersion component remained at a virtually constant value.
(c) The level of oxygen-rich species increased as the level of treatment was increased whereas, the relative level of carbon and silicon elements decreased. Deconvolution of the carbon and sulphur peaks gave additional information on the type of oxygen-rich species.

7. In the current work, mechanical interlocking, surface roughness, electrostatic theory and diffusion do not contribute greatly to the mechanisms of adhesion. It was demonstrated

that the adsorption theory is the most credible mechanism to adhesion. However, the currently available detailed theories of adhesion, such as work of adhesion and acid-base interactions, remain limited in their prediction of strong interfaces for the fibre-composite materials bonded using the epoxy adhesives. Analyses of the dipole moments calculated via deconvolution of the elements from XPS (hence termed weighted percent dipole moment (WDM)) indicated that there is a direct relationship between the level of the surface WDM and the percent polar surface energy (i.e. percentage of polar surface energy relative to the total surface free energy) of the fibre-composite materials. Furthermore, it was demonstrated that by superimposing the results of WDM and percent polar surface energy for all the composites it was possible to attain one universal curve. Finally, it was shown that there seems to be a critical level of WDM or percent polar surface energy at which strong adhesion can be attained, provided the surfaces are not heavily contaminated with releasing agents.

8. Ageing of corona-treated TPFC materials, in a controlled laboratory environment (T=20±2^{0}C and R.H.=60%) showed that the measured fracture energy, G_c, decreases as the ageing time was increased beyond about thirty days and the locus of failure reverted back to one of interfacial. This was associated with a drop in the oxygen-rich species as indicated by XPS and a decrease in the surface free energy of the TPFC materials. Therefore, this is also in agreement with the predictions from the adsorption theory that for strong interfacial adhesion specific chemicals species are required.

9. Environmental attack (in a heated water at 50^{0}C) of adhesively-bonded TPFC joints showed that the locus of joint failure remains cohesive although, the value of G_c, drops due to water absorption of the adhesive.

10. To conduct theoretical analyses of engineering double-lap joints (DLJs) using finite element analysis (FEA), the mechanical properties of the composites and the epoxy-paste adhesive were obtained. The shear properties of the adhesive were obtained using a cone-and-plate specimen and a novel technique was employed for measuring the shear strain of the adhesive. Further, to enable the accurate prediction of stresses and in particular the maximum shear stresses from FEA required the modelling of the tensile stress/strain curve of the adhesive.

11. It was demonstrated that the efficiency of a DLJ specimen can be increased by tapering the ends of the composite and by the addition of adhesive fillets at the ends of the overlap. (The TPFC substrates needed, of course, to be subjected to the corona pretreatment prior to bonding to avoid interfacial failure). Such techniques increased the failure load from about 2.5 MN/m to about 4 MN/m for the unidirectional-carbon-fibre/poly(ether-ether ketone)

(U/C-PEEK) and the unidirectional-carbon-fibre/polyamide (U/C-PA) joints and from 1.85MN/m to about 3.2MN/m for the thermosetting composite joints. The joint efficiency for all the composite materials increased to levels close to 100%. This increase was due to the modifications in joint design causing the locus of failure to change ᵢrom one of interlaminar in the composite to one of fracture initiating in the adhesive. This was successfully predicted from the FEA analyses.

12. Finally, it was demonstrated that, after using corona-discharge treatment, employing the TPFC materials does yield higher failure loads (about 100kN and/or about 1350MPa) when compared to the thermoset fibre-composite (TSFC) material employed (about 80KN and/or 1050MPa). This was due to the higher longitudinal and transverse tensile failure stresses of the two TPFC materials employed.

8.3. RECOMMENDATIONS FOR FUTURE WORK

The present research work has established the techniques required for successful bonding of thermoplastic-fibre-composite materials.To give a further understanding of the mechanisms of adhesion and establish critical engineering design data the following suggestions are recommended for future work:

1) It was shown in Chapter Six that the percent polar surface energy or the weighted percent dipole moment may predict the level of surface polarity required for adhesive bonding. However, it was also shown that the qualitative expressions for predicting the extent of secondary force and/or acid-base interactions were inadequate. To explore this aspect further it is recommended that the type of interfacial interactions be investigated to ascertain whether covalent bonding is established at the corona-treated composite/adhesive interface. The type of interfacial interactions can be investigated using static secondary ion mass spectroscopy (SIMS) where the ionized particles ejected by the action of the argon beam can be mass analysed and, therefore, the first one or two monolayers can be investigated.

2) That the fatigue performance on double-cantilever beam and lap-joint specimens from corona-treated thermoplastic composites be assessed under different environmental and loading conditions to predict the life-time of an engineering structure. This type of information would enable the design engineer to employ such performance data in engineering applications, such as in the aircraft industry. Problems may be encountered studying the fatigue behaviour of joints, possibly due to the rate-sensitivity of the corona-treated adhesive/composite interface. This rate-sensitivity may arise from testing in an aggressive environment such as at relatively high temperatures and/or relatively high humidity levels, either of which may result in

interfacial failure. Therefore, higher corona treatment levels may be required to avoid such interfacial failure.

3) It was demonstrated in the current work that thermoplastic composites are generally tougher than thermosetting-based composites. Therefore, a study of the impact behaviour of adhesively-bonded thermoplastic composite joints under different impact speeds and environmental conditions may demonstrate the benefits of employing such materials, especially in the aerospace industry. A particular problem that might be encountered in the impact tests is accurately measuring the shear stress/strain curve of adhesives, since it may be difficult to employ the cone-and-plate specimen described in this thesis. Therefore, it is recommended that thick-adherend-test (TAT) joints be used with the impact load being applied to one end of the joint so as to assess under different impact loading conditions the shear stress/strain curve. If the TAT joint is employed then the possibility of reducing the peel stresses at the ends of the overlap should be explored. This may be achieved by increasing the thickness of the substrates. Another possible problem that might be encountered is the rate-sensitivity of the corona-treated adhesive/composite interface which may result in interfacial failure, and hence low failure loads being recorded. If this occurs, it is recommended that higher corona treatment levels be used to investigate the possibility of avoiding interfacial failure, especially at high impact speeds.

THE END

APPENDIX I

CHAPTER THREE

A.1. CAA of Corona Treated TPFC Materials
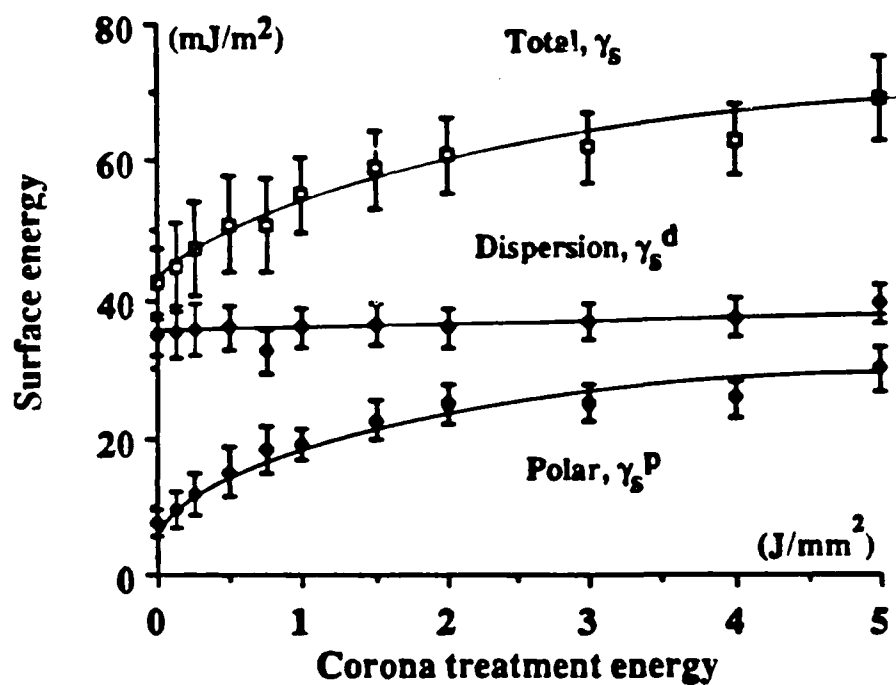
Fig. A.1 Surface energy versus corona pretreatment energy of U/K-PA composite.
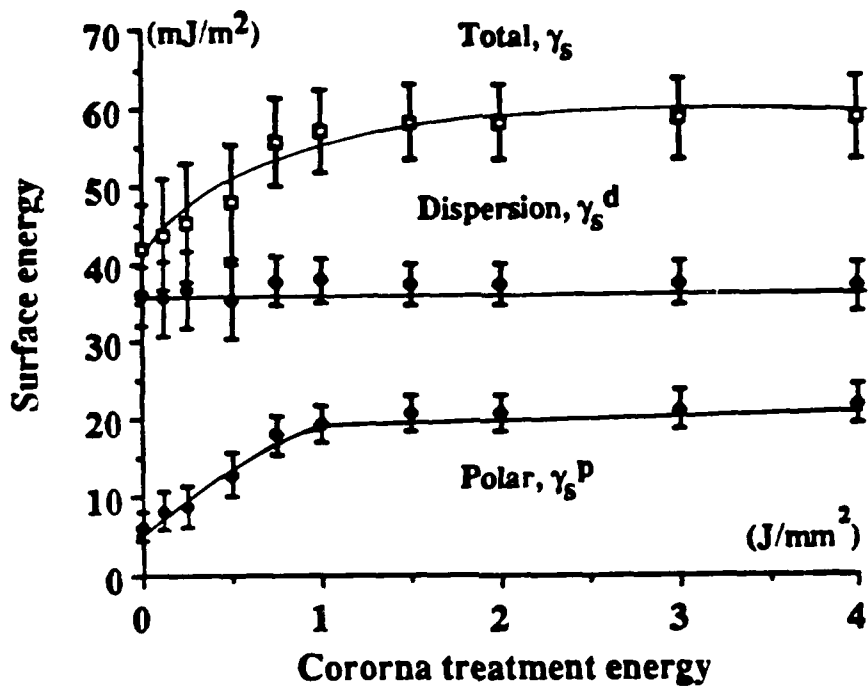
Fig. A.2. Surface energy versus corona pretreatment energy of W/C-PI composite.
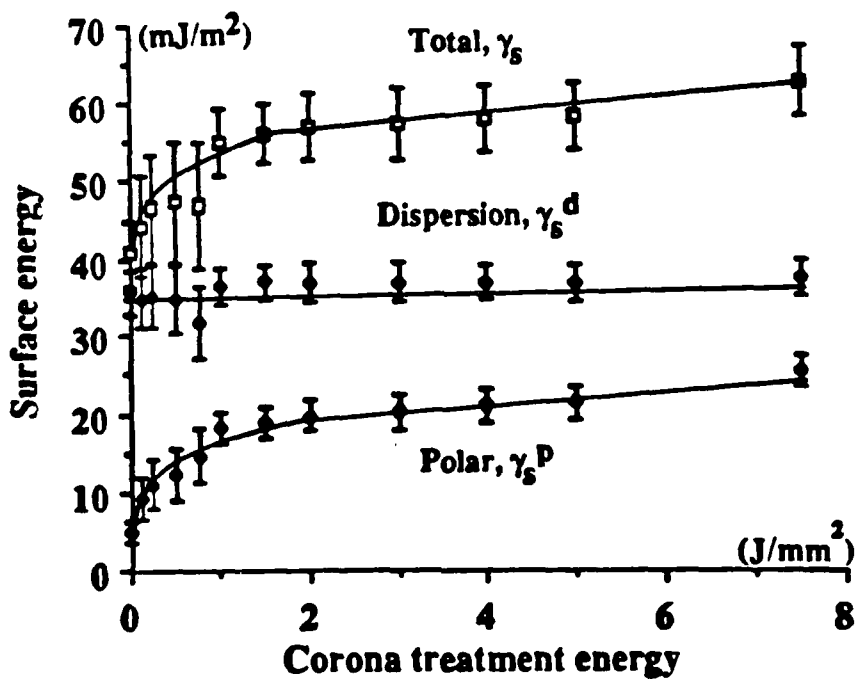
Fig. A.3. Surface energy versus corona pretreatment energy of W/C-PEI composite.
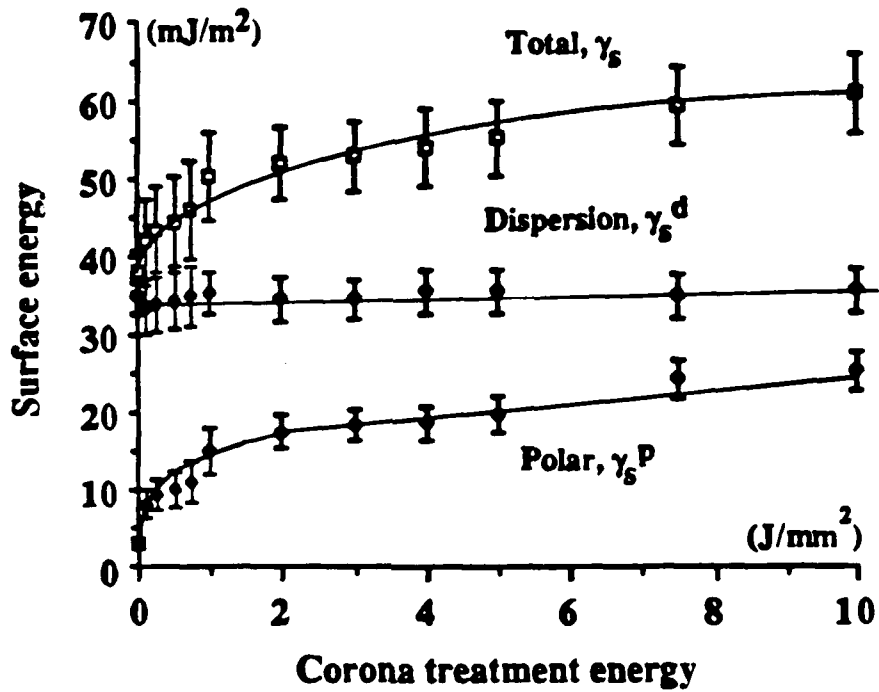
Fig. A.4. Surface energy versus corona pretreatment energy of the U/C-PPS composite.

A.2. XPS Results from Corona-Treated TPFC Materials
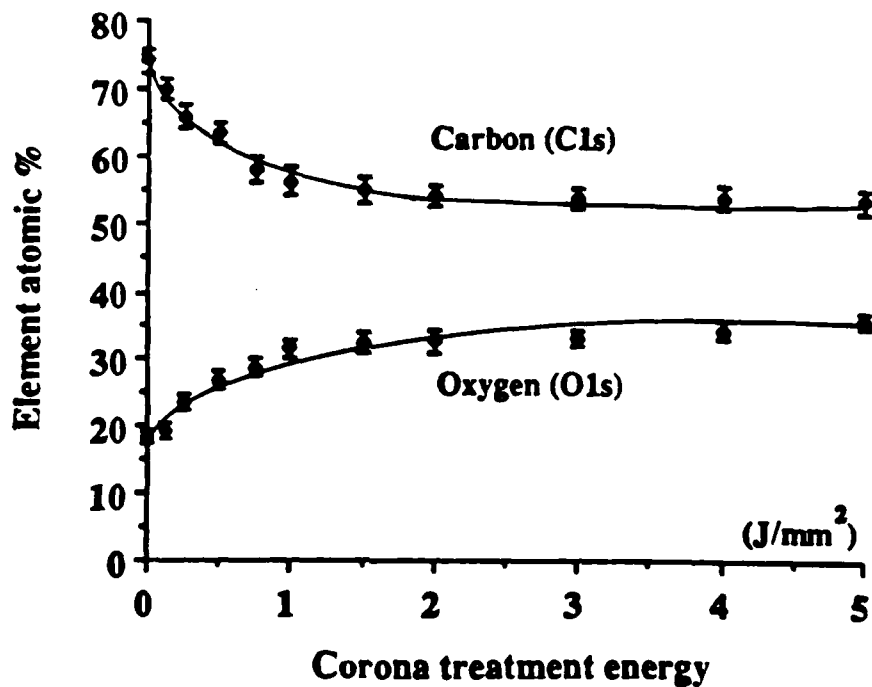
Fig. A.5. Concentrations of the carbon and oxygen elements for the U/K-PA composite subjected to corona treatment.
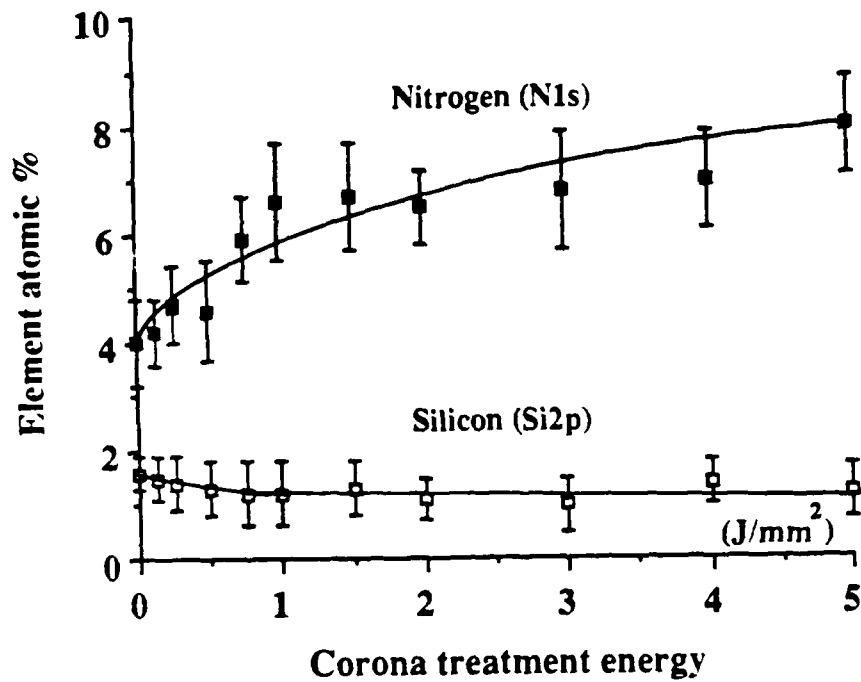
Fig. A.6. Concentrations of the nitrogen and silicon elements for the U/K-PA composite subjected to corona treatment.
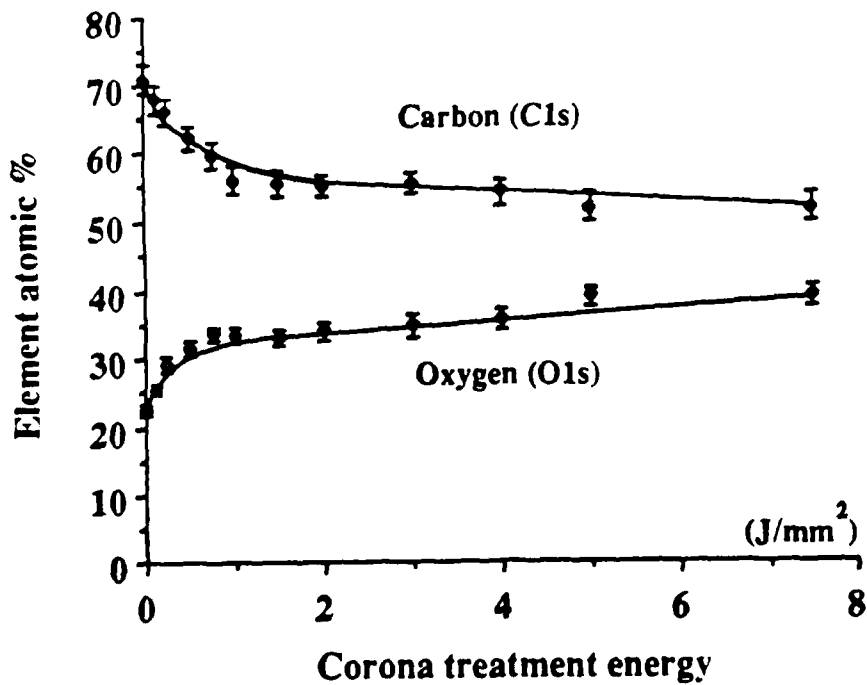
Fig. A.7. Concentrations of the carbon and oxygen elements for the W/C-PEI composite subjected to corona treatment.
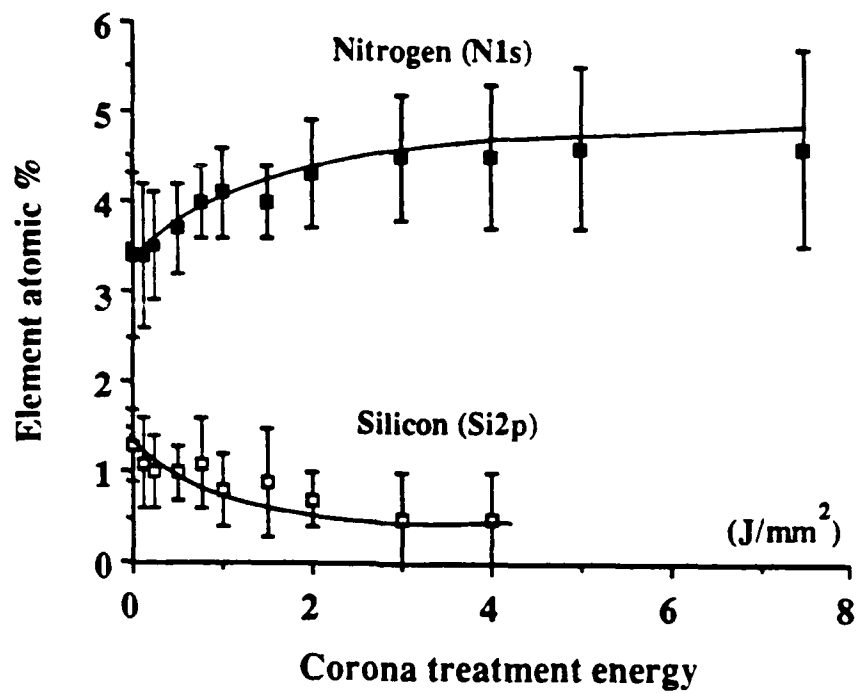
Fig. A.8. Concentrations of the nitrogen and silicon elements for the W/C-PEI composite subjected to corona treatment.
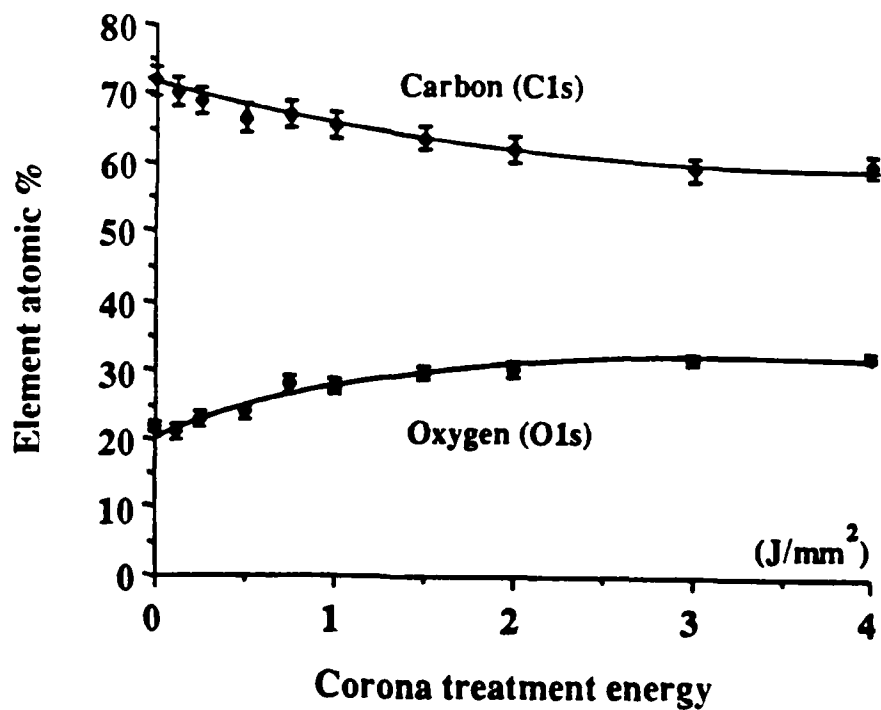
Fig. A.9. Concentrations of the carbon and oxygen elements for the W/C-PI composite subjected to corona treatment.
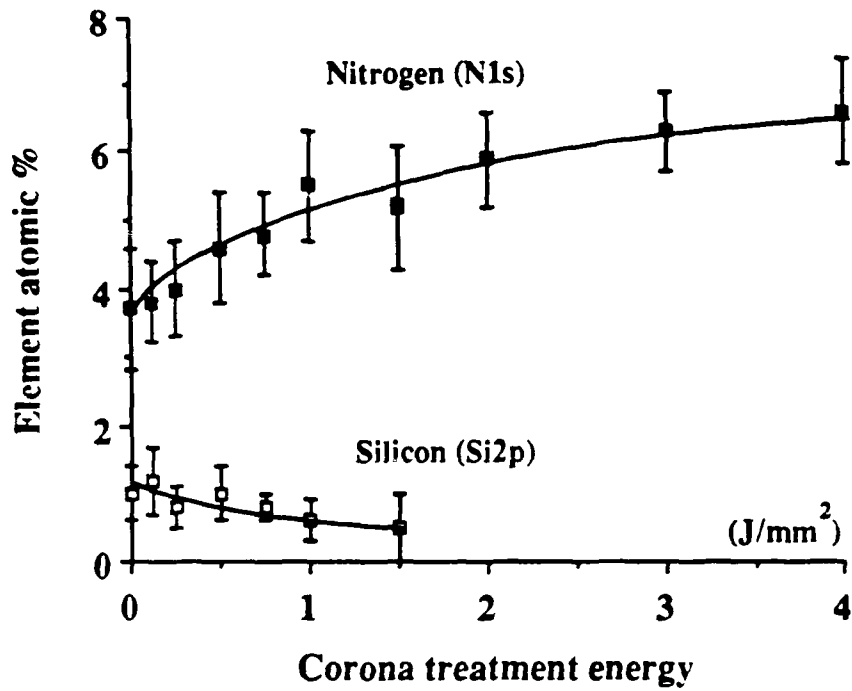
Fig. A.10. Concentrations of the nitrogen and silicon elements for the W/C-PI composite subjected to corona treatment.
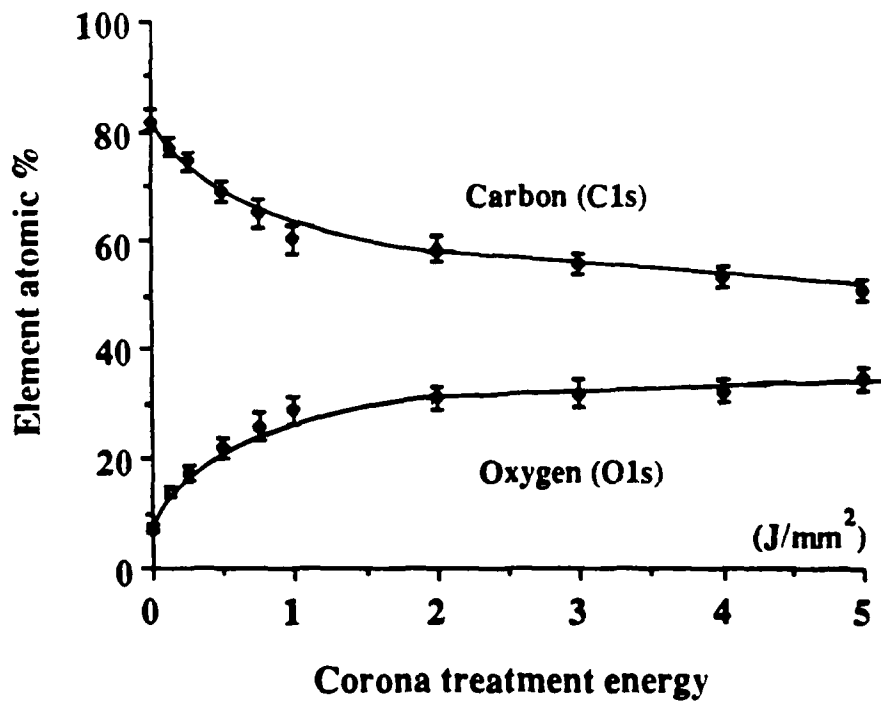
Fig. A.11. Concentrations of the carbon and oxygen elements for the U/C-PPS composite subjected to corona treatment.

CHAPTER FOUR

A.3. The J-Integral Approach

The J-integral approach provides a means to determine the energy release rate for cases where plasticity effects are not negligible. Measurement procedures to determine J are based on the interpretation of J as an energy release rate. One such procedure was demonstrated by Rice et al. [225] and Ernst and Paris [226]:

$$J = \frac{2}{b} \int_0^P P \, du \qquad (A.1)$$

Where, b is the ligament size, P is the load and u is the displacement. Clearly, the integral in Equation (A.1) is the area under the load-deflection diagram, so that:

$$J = \frac{2A}{B(W_J - a)} \qquad (A.2)$$

where A is the area under the curve, see Figure A.12(b).

Landes and Begley [227, 228] have proposed an experimental procedure to measure J using a series of specimens with the same initial crack size, such that $a/W_J > 0.5$, see Figure A.12(a). Each specimen is loaded to a different point on the load-deflection curve and then unloaded, see Figure A.12(b). After unloading, the crack is marked to enable the measurement of the stable crack growth Δa. For polymers, an accurate measurement of the crack growth can be achieved by dipping the specimens in liquid nitrogen and breaking the rest of the ligament in a brittle manner. Hence, Δa can be assessed through a travelling microscope. The J values are then calculated from Equation (A.2) and these J values are plotted against crack extension Δa. The intersection of the variation of J due to crack blunting with the experimental points is taken to be the J_{Ic} value of the material, see Figure A.13. The crack blunting line is given by:

$$J = 2\sigma_{ys} \, \Delta a \qquad (A.3)$$

where σ_{ys} is the yield stress.

The bulk fracture energy value of the epoxy-paste adhesive was obtained using bulk single-edged-notched three-point-bend specimens of 14X14X90mm with cracks of 7mm deep,

see Figure A.12(a). These specimens were tested, in three-point-bend with a span of 56mm and the procedure to calculate J was outlined above. The blunting line was drawn and the intersection with the line from the experimental results gave a J_{Ic} value of about $3.9kJ/m^2$, see Figure A.13.
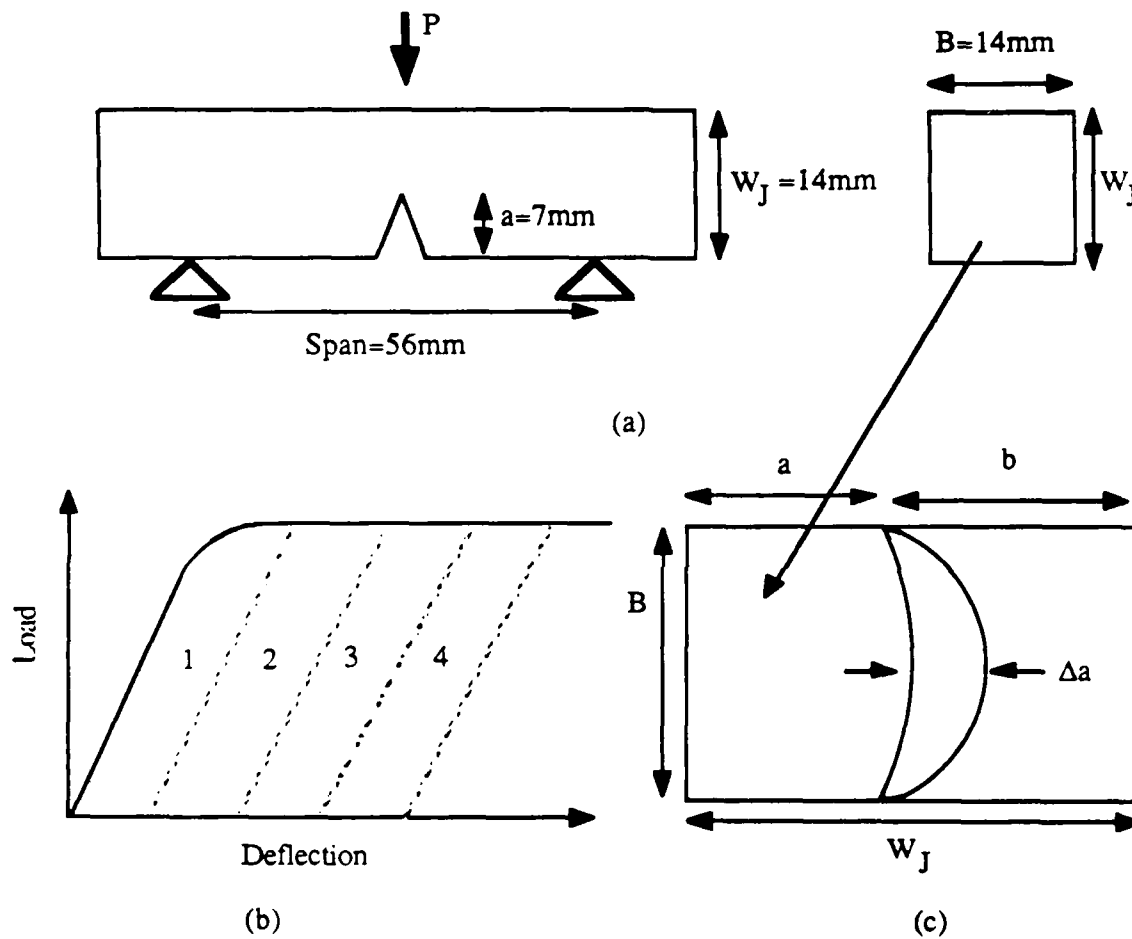
Fig. A.12. (a) Single-edged-notched three-point-bend-specimen,
(b) Load-deflection diagram, and (c) plastic crack growth Δa.
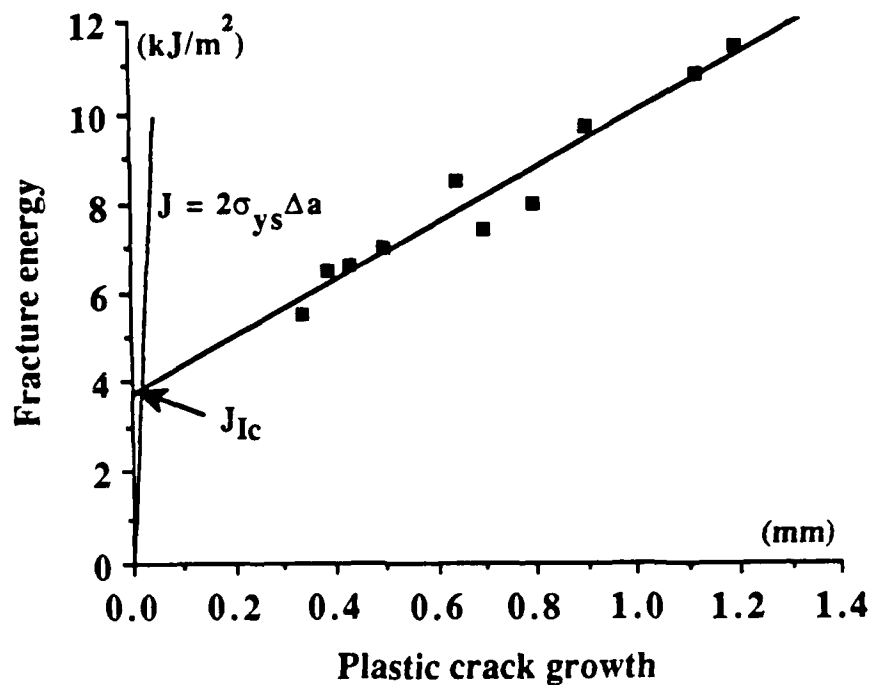
Fig. A.13. The J-integral test results for the bulk epoxy-paste adhesive.

A.4. Listing of Computer Program to Curve Fit Compliance and Crack Length

```
      PROGRAM FITTING(INPUT,OUTPUT,DADA,TAPE5=INPUT,TAPE6=
     +OUTPUT,TAPE7=DADA)
      DIMENSION XX(50),YY(50),SUMX(20),B(20),A(20,20)
     +,YYC(50),ZY(50),XXX(50),X(20)
C

      WRITE(6,60)
60    FORMAT('ENTER NUMBER OF POINTS AND ORDER OF FITTING')
      READ(5,*) NPT,NORD
C

      B(1)=0.0
      DO 1 I=1,NPT
      READ(7,*) XX(I),YY(I)
      XXX(I)=1.0
      B(1)=B(1)+YY(I)
1     CONTINUE
      WRITE(6,61)
```

```
    61    FORMAT('VALUES OF XX AND YY HAVE BEEN READ FROM DADA')
          WRITE(6,63)
    63    FORMAT('FIRST POWER TERM=0? (1), CONSTANT=0? (2), ELSE (3)')
          READ(5,*) NCHOICE
C

          NEQN=NORD+1
          SUMX(1)=FLOAT(NPT)
          DO 2 K=2,NORD*2+1
          SUMX(K)=0.0
          IF(K.GT.NEQN) GOTO 4
          B(K)=0.0
    4     DO 3 I=1,NPT
          XXX(I)=XX(I)*XXX(I)
          SUMX(K)=SUMX(K)+XXX(I)
          IF(K.GT.NEQN) GOTO 3
          B(K)=B(K)+YY(I)*XXX(I)
    3     CONTINUE
    2     CONTINUE
          WRITE(6,66)
    66    FORMAT('ARRAY A-(SUMX) IS COMPLETED')
C

          WRITE(6,67)
    67    FORMAT('ARRAY B IS COMPLETED')
C

          DO 10 I=1,NEQN
          DO 10 J=1,NEQN
          K=I-1
    10    A(I,J)=SUMX(J+K)
C

          IF(NCHOICE.EQ.1) THEN
          NEQN=NEQN-1
          DO 22 J=1,NEQN+1
          DO 16 I=2,NEQN
    16    A(I,J)=A(I+1,J)
    22    CONTINUE
          DO 20 I=1,NEQN
          DO 18 J=2,NEQN
    18    A(I,J)=A(I,J+1)
```

```
   20   B(I+1)=B(I+2)
C

      ELSE IF(NCHOICE.EQ.2) THEN
      NEQN=NEQN-1
      DO 24 J=1,NEQN+1
      DO 26 I=1,NEQN
   26   A(I,J)=A(I+1,J)
   24   CONTINUE
      DO 28 I=1,NEQN
      DO 30 J=1,NEQN
   30   A(I,J)=A(I,J+1)
   28   B(I)=B(I+1)
C

      ENDIF
      WRITE(6,65)
   65   FORMAT('SOLVING SIMUL. EQUATIONS IN PROCESS')
C
C     CALL SUBROUTINE TO SOLVE SIMULTANEOUS EQUATIONS
      CALL SOLVE(A,B,X,NEQN,20)
C
C     CALL SUBROUTINE TO CALCULATE THE RMS ERROR OF FITTING
      CALL ERROR(XX,YY,NPT,X,YYC,NEQN,50,20,CORR,ZY,NCHOICE)
C
C     CALL SUROUTINE TO WRITE OUTPUT
      CALL OUTPUT(X,CORR,NEQN,20)
C
      STOP
      END
C
C*********************************************************************
C
      SUBROUTINE SOLVE(A,B,X,NEQN,NDIM)
      DIMENSION A(NDIM,NDIM),B(NDIM),X(NDIM)
C
C     SOLUTION OF SIMULTANEOUS LINEAR EQUATIONS BY GAUSS-SEIDEL
C     ITERATION
C
      RELAX=1.75
```

```
        TOLER=1.0E-09
        IFREQ=0
        NCYCLE=50000
C
C       TEST FOR VALIDITY OF THE NUMBER OF EQUATIONS
        IF(NEQN.LT.1.OR.NEQN.GT.20) STOP
C
C       SET INITIAL VALUES OF THE UNKNOWNS AS ZERO
        DO 3 I=1,NEQN
  3     X(I)=0.
C
C       APPLY THE GAUSS-SEIDEL METHOD
C       SET UP ITERATION LOOP
        DO 7 ITER=1,NCYCLE
        SUMX=0.
        SUMDX=0.
C
C       OBTAIN NEW ESTIMATE FOR EACH UNKNOWN IN TURN
        DO 5 I=1,NEQN
        DELTAX=B(I)
        DO 4 J=1,NEQN
  4     DELTAX=DELTAX-A(I,J)*X(J)
        DELTAX=DELTAX/A(I,I)
        SUMDX=SUMDX+ABS(DELTAX)
        X(I)=X(I)-DELTAX*RELAX
  5     SUMX=SUMX+ABS(X(I))
C
C       DEFINE THE RELATIVE ERROR
        ERROR=SUMDX/SUMX
C
C       TEST FOR SEVERE DIVERGENCE
        IF(ERROR.LT.1..OR.ITER.LE.5) GO TO 6
        WRITE(6,65) ITER
  65    FORMAT(27H DIVERGENCE IN GSITER AFTER,I5,7H CYCLES)
        RETURN
C
C       TEST FOR CONVERGENCE
  6     IF(ERROR.LT.TOLER) GO TO 8
```

```
C
C      OUTPUT PROGRESS INFORMATION EVERY IFREQ CYCLE, UNLESS
C      IFREQ=0
       IF(IFREQ.EQ.0) GO TO 7
       IF(MOD(ITER,IFREQ).EQ.0) WRITE(6,66) ITER,ERROR,(X(I),I=1,NEQN)
   66  FORMAT(1X,I5,E12.4,7E17.10/18X,7E17.10)
    7  CONTINUE
C
C      NORMAL EXIT FROM ITERATION LOOP INDICATES FAILURE TO
C      CONVERGE
       WRITE(6,67) NCYCLE
   67  FORMAT(31H NO CONVERGENCE IN GSITER AFTER,I10,7H CYCLES)
       RETURN
C
C      OUTPUT NUMBER OF ITERATIONS AND TOLERENCE FOR CONVERGED
      +ITERTION
    8  WRITE(6,68) TOLER,ITER
   68  FORMAT(38H ITERATION CONVERGED TO A TOLERANCE OF,E12.4,
      +6H AFTER,I7,7H CYCLES)
       RETURN
       END
C
C***********************************************************************
C
       SUBROUTINE
      +ERROR(XX,YY,NPT,X,YYC,NEQN,MDIM,NDIM,CORR,ZY,NCHOICE)
       DIMENSION XX(MDIM),YY(MDIM),X(NDIM),YYC(MDIM),ZY(MDIM)
C
       WRITE(6,60)
   60  FORMAT(13X,'ERROR',9X,'SMOOTH Y',12X,'OLD Y')
       SUMYY2=0.0
       SUMZY2=0.0
       ZYMEAN=0.0
       YMEAN=0.0
       DO 2 I=1,NPT
       YYC(I)=X(NEQN)
C
       IF(NCHOICE.EQ.1) THEN
```

```
          DO 5 K=NEQN,3,-1
    5     YYC(I)=YYC(I)*XX(I)+X(K-1)
          YYC(I)=X(1)+YYC(I)*XX(I)**2.0
C
          ELSE IF(NCHOICE.EQ.2) THEN
          DO 7 K=NEQN,2,-1
    7     YYC(I)=YYC(I)*XX(I)+X(K-1)
          YYC(I)=YYC(I)*XX(I)
C
          ELSE
          DO 3 K=NEQN,2,-1
    3     YYC(I)=YYC(I)*XX(I)+X(K-1)
          ENDIF
C
          ZY(I)=YY(I)-YYC(I)
          SUMYY2=SUMYY2+YY(I)**2.0
          SUMZY2=SUMZY2+ZY(I)**2.0
          ZYMEAN=ZYMEAN+ZY(I)
          YMEAN=YMEAN+YY(I)
          WRITE(6,61) ZY(I),YYC(I),YY(I)
   61     FORMAT(1X,3E17.10)
    2     CONTINUE
C
          ZYMEAN=ZYMEAN/FLOAT(NPT)
          YMEAN=YMEAN/FLOAT(NPT)
C
          VARZY=(SUMZY2-FLOAT(NPT)*ZYMEAN**2.0)/FLOAT(NPT)
          VARYY=(SUMYY2-FLOAT(NPT)*YMEAN**2.0)/FLOAT(NPT)
          CORR=1.0-(VARZY/VARYY)*((FLOAT(NPT)-1.0)/(FLOAT(NPT)-
         +FLOAT(NEQN)))
C
          RETURN
          END
C
C***********************************************************************
C
          SUBROUTINE OUTPUT(X,CORR,NEQN,NDIM)
          DIMENSION X(NDIM)
```

```
C
      WRITE(6,61)
61    FORMAT('THE COEFFICIENTS OF REQUIRED POLYNOMIAL ARE AS
      +FOLLOWS')
      WRITE(6,62) (X(I),I=1,NEQN)
62    FORMAT(1X,7E17.10)
      WRITE(6,63) CORR
63    FORMAT('THE COEFFICIENT OF DETERMINATION IS ',F12.8)
      RETURN
      END
```

CHAPTER FIVE

A.5. Stress-Strain Relationships for Anisotropic Materials

An isotropic body is a body in which the elastic properties are the same for all directions drawn through a point, example is aluminium. An anisotropic body has, in general, different elastic properties for different directions drawn through a given point, example is a fibre composite.

In the general case of anisotropy each strain component is a linear function of all six stre·components. The generalized Hooke's law for such a system can be given in matrix notation by:

$$
\begin{bmatrix} \varepsilon_x \\ \varepsilon_y \\ \varepsilon_z \\ \gamma_{yz} \\ \gamma_{xz} \\ \gamma_{xy} \end{bmatrix} =
\begin{bmatrix}
S_{11} & S_{12} & S_{13} & S_{14} & S_{15} & S_{16} \\
S_{21} & S_{22} & S_{23} & S_{24} & S_{25} & S_{26} \\
S_{31} & S_{32} & S_{33} & S_{34} & S_{35} & S_{36} \\
S_{41} & S_{42} & S_{43} & S_{44} & S_{45} & S_{46} \\
S_{51} & S_{52} & S_{53} & S_{54} & S_{55} & S_{56} \\
S_{61} & S_{62} & S_{63} & S_{64} & S_{65} & S_{66}
\end{bmatrix}
\begin{bmatrix} \sigma_x \\ \sigma_y \\ \sigma_z \\ \tau_{yz} \\ \tau_{xz} \\ \tau_{xy} \end{bmatrix}
\tag{A.4}
$$

where S_{ij} are the compliances of the anisotropic material. The strains can be defined by:

$$\varepsilon_x = \partial u/\partial x \qquad \varepsilon_y = \partial v/\partial y \qquad \varepsilon_z = \partial w/\partial z$$

$$\gamma_{yz} = \partial v/\partial z + \partial w/\partial y \quad \gamma_{zx} = \partial w/\partial x + \partial u/\partial z \quad \gamma_{xy} = \partial u/\partial y + \partial v/\partial x \tag{A.5}$$

where u, v and w are the displacements in the x, y and z directions respectively. In an alternative form, Hooke's law equations for the general case can be given by:

$$
\begin{bmatrix} \sigma_x \\ \sigma_y \\ \sigma_z \\ \tau_{yz} \\ \tau_{xz} \\ \tau_{xy} \end{bmatrix}
=
\begin{bmatrix}
C_{11} & C_{12} & C_{13} & C_{14} & C_{15} & C_{16} \\
C_{21} & C_{22} & C_{23} & C_{24} & C_{25} & C_{26} \\
C_{31} & C_{32} & C_{33} & C_{34} & C_{35} & C_{36} \\
C_{41} & C_{42} & C_{43} & C_{44} & C_{45} & C_{46} \\
C_{51} & C_{52} & C_{53} & C_{54} & C_{55} & C_{56} \\
C_{61} & C_{62} & C_{63} & C_{64} & C_{65} & C_{66}
\end{bmatrix}
\begin{bmatrix} \varepsilon_x \\ \varepsilon_y \\ \varepsilon_z \\ \gamma_{yz} \\ \gamma_{xz} \\ \gamma_{xy} \end{bmatrix}
\qquad (A.6)
$$

The stiffness matrix C_{ij} has thirthy six constants. However, it can be shown that less than thirthy six of these constants are actually independent for elastic materials. Elastic materials for which an elastic potential or strain energy density function exists have incremental work per unit volume of [229]:

$$ dW = \sigma_j d\varepsilon_i \qquad (A.7) $$

where the stresses σ_j act through the strains $d\varepsilon_i$. However, because of the stress-strain relations in Equation (A.6) then the incremental work becomes:

$$ dW = C_{ij}\varepsilon_j d\varepsilon_i \qquad (A.8) $$

Upon integrating for all the strains, the work per unit volume can be given by:

$$ W = 1/2\, C_{ij}\varepsilon_i\varepsilon_j \qquad (A.9) $$

Hooke's law can now be derived as:

$$ \partial W/\partial\varepsilon_i = C_{ij}\varepsilon_j \qquad (A.10) $$

whereupon $C_{ij} = \partial^2 W/(\partial\varepsilon_i\partial\varepsilon_j)$ \qquad (A.11)

also $C_{ji} = \partial^2 W/(\partial\varepsilon_j\partial\varepsilon_i)$. But the order of differentiation of W is immaterial, so:

$$C_{ij} = C_{ji} \tag{A.12}$$

with an analogous argument it can be shown that:

$$S_{ij} = S_{ji} \tag{A.13}$$

Therefore, in matrices [S] and [C] there are now only twenty one independent constants. Where the matrix [S] is now given by:

$$[S] = \begin{bmatrix} S_{11} & S_{12} & S_{13} & S_{14} & S_{15} & S_{16} \\ S_{12} & S_{22} & S_{23} & S_{24} & S_{25} & S_{26} \\ S_{13} & S_{23} & S_{33} & S_{34} & S_{35} & S_{36} \\ S_{14} & S_{24} & S_{34} & S_{44} & S_{45} & S_{46} \\ S_{15} & S_{25} & S_{35} & S_{45} & S_{55} & S_{56} \\ S_{16} & S_{26} & S_{36} & S_{46} & S_{56} & S_{66} \end{bmatrix} \tag{A.14}$$

Completely anisotropic materials are of little importance to the engineer and the following sections relate to materials encountered in the field of fibre-reinforced plastics. Such materials are often referred to as anisotropic materials. In practice, materials usually exhibit planes of symmetry with principal constants not varying with position: these materials are more correctly termed [230] monoclinic.

If there is one plane of material property symmetry then the compliance matrix reduces. Now if this plane of symmetry is the z-axis, see Figure 5.9 (page 155), then the compliance matrix can be given by:

$$[S] = \begin{bmatrix} S_{11} & S_{12} & S_{13} & 0 & 0 & S_{16} \\ S_{12} & S_{22} & S_{23} & 0 & 0 & S_{26} \\ S_{13} & S_{23} & S_{33} & 0 & 0 & S_{36} \\ 0 & 0 & 0 & S_{44} & S_{45} & 0 \\ 0 & 0 & 0 & S_{45} & S_{55} & 0 \\ S_{16} & S_{26} & S_{36} & 0 & 0 & S_{66} \end{bmatrix} \tag{A.15}$$

with only thirteen independent constants. Now if there are two orthogonal planes of mechanical-property-symmetry for a material, symmetry will exist relative to a third mutually orthogonal plane. Therefore, the compliance matrix is further reduced [107], and now has nine independent constants and this type of material is defined as a generally orthotropic material.

$$[S] = \begin{bmatrix} S_{11} & S_{12} & S_{13} & 0 & 0 & 0 \\ S_{12} & S_{22} & S_{23} & 0 & 0 & 0 \\ S_{13} & S_{23} & S_{33} & 0 & 0 & 0 \\ 0 & 0 & 0 & S_{44} & 0 & 0 \\ 0 & 0 & 0 & 0 & S_{55} & 0 \\ 0 & 0 & 0 & 0 & 0 & S_{66} \end{bmatrix} \tag{A.16}$$

where $\quad S_{11}=S_{xx}=1/E_{11} \qquad S_{22}=S_{yy}=1/E_{22} \qquad S_{33}=S_{zz}=1/E_{33}$

$$S_{12}=S_{xy}=-\upsilon_{12}/E_{11} \quad S_{23}=S_{yz}=-\upsilon_{23}/E_{22} \quad S_{31}=S_{zx}=-\upsilon_{31}/E_{33} \tag{A.17}$$

$$S_{44}=SH_{yz}=1/G_{23} \quad S_{55}=SH_{xz}=1/G_{13} \quad S_{66}=SH_{xy}=1/G_{12}$$

and where E is the Young's modulus, G is the shear modulus, SH is shear compliance and υ is Poisson's ratio.

A.6. Derivation of Equations (5.7) and (5.8)

Analysis assuming linear isotropic cantilever beam bending has been applied to obtain an expression in the form of Equation (4.10) (page 102) for a DCB specimen [231, 232]. For specimens with rectangular cross sections and negligible shear contribution the equation for the compliance, S, is given by:

$$S = \frac{8a^3}{BEh^3} \tag{A.18}$$

where E is the Young's modulus, h is the height of one arm of the specimen, B is the width of the substrate and a is the crack length. Substituting Equation (A.18) into Equation (4.10) the load, P, approach expression is obtained:

$$G_c = 12\frac{P^2a^2}{B^2Eh^3} \tag{A.19}$$

Instead of the compliance S in Equation (A.18) if deflection over load is substituted and the equation rearranged then the following expression can be obtained:

$$E = \frac{8a^3 P}{Bh^3 \Delta} \qquad \text{(A.20)}$$

Substituting Equation (A.20) into Equation (A.19) and simplifying then the displacement approach equation can be obtained:

$$G_c = \frac{3P\Delta}{2Ba} \qquad \text{(A.21)}$$

Note that in the above equations no crack tip rotation correction factors were used as suggested by Hashemi et al. [93]. This was justified in the current work due to the accurate prediction of the load from the applied deflection (see Section 5.4.3.3).

A.7. Transverse Tensile Stress Predicted from FEA for DCB Composite Joints
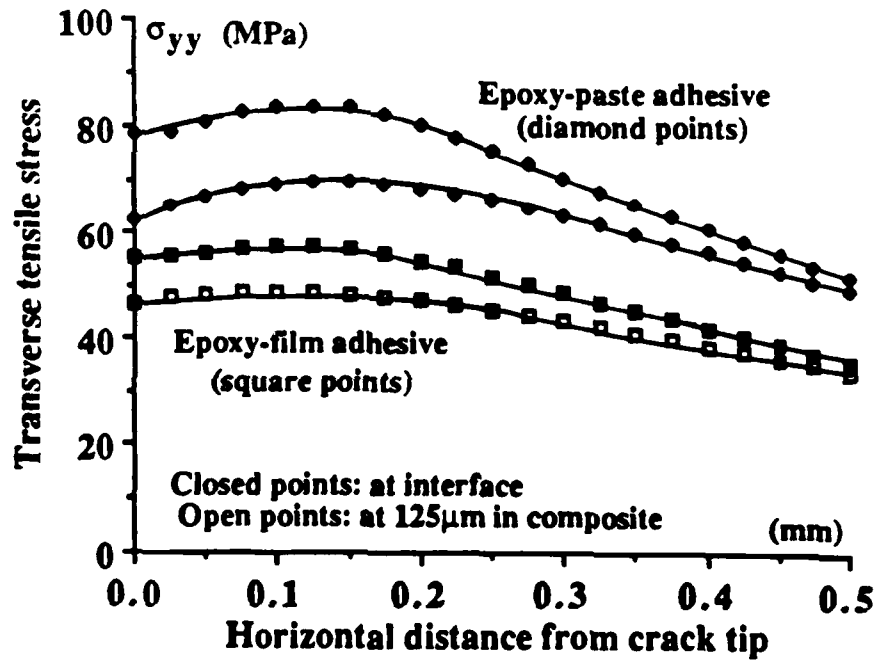
Fig. A.14. Transverse tensile stress distribution in the crack tip regions for the U/C-PEEK composite joint.
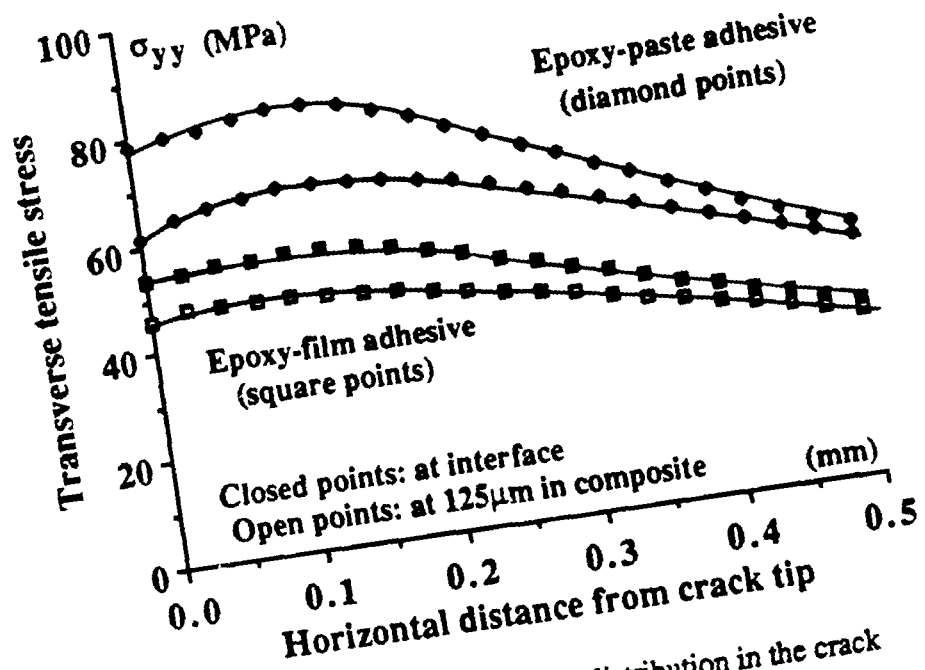
Fig. A.15. Transverse tensile stress distribution in the crack tip regions for the W/C-PA composite joint.
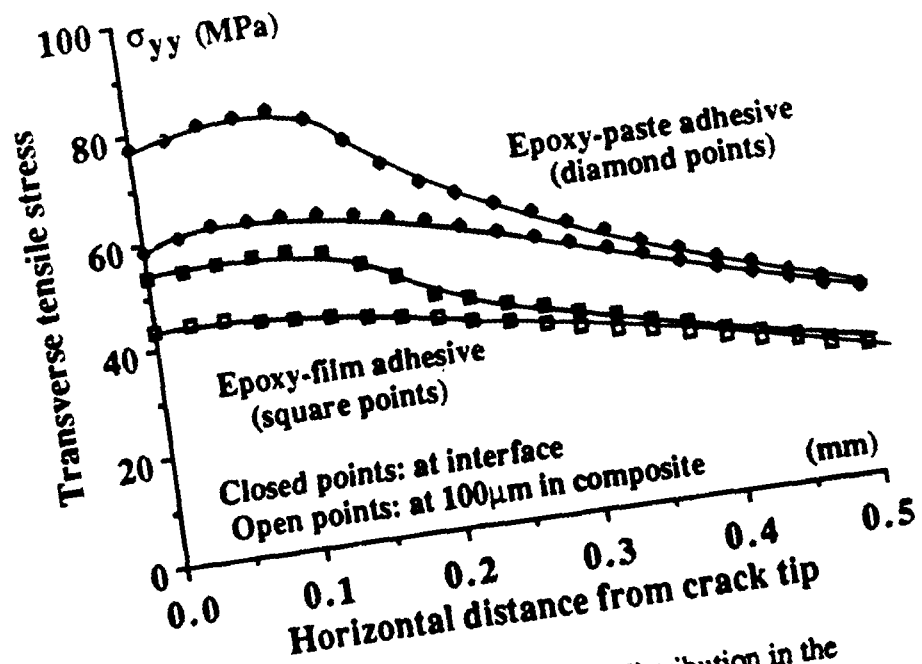
Fig. A.16. Transverse tensile stress distribution in the crack tip regions for the U/K-PA composite joint.
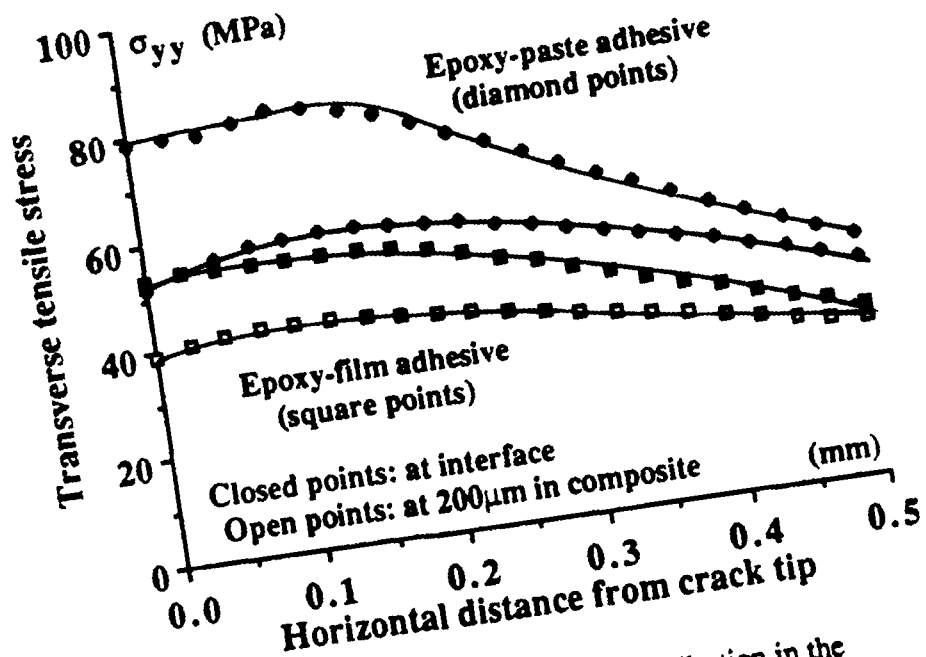
Fig. A.17. Transverse tensile stress distribution in the crack tip regions for the W/C-PEI composite joint.
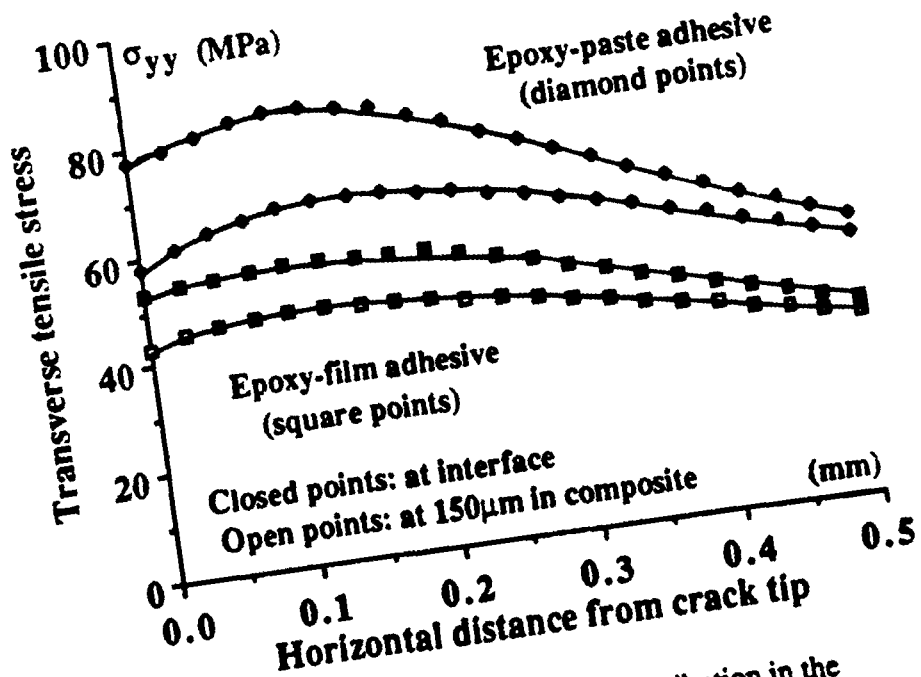
Fig. A.18. Transverse tensile stress distribution in the crack tip regions for the U/C-PPS composite joint.
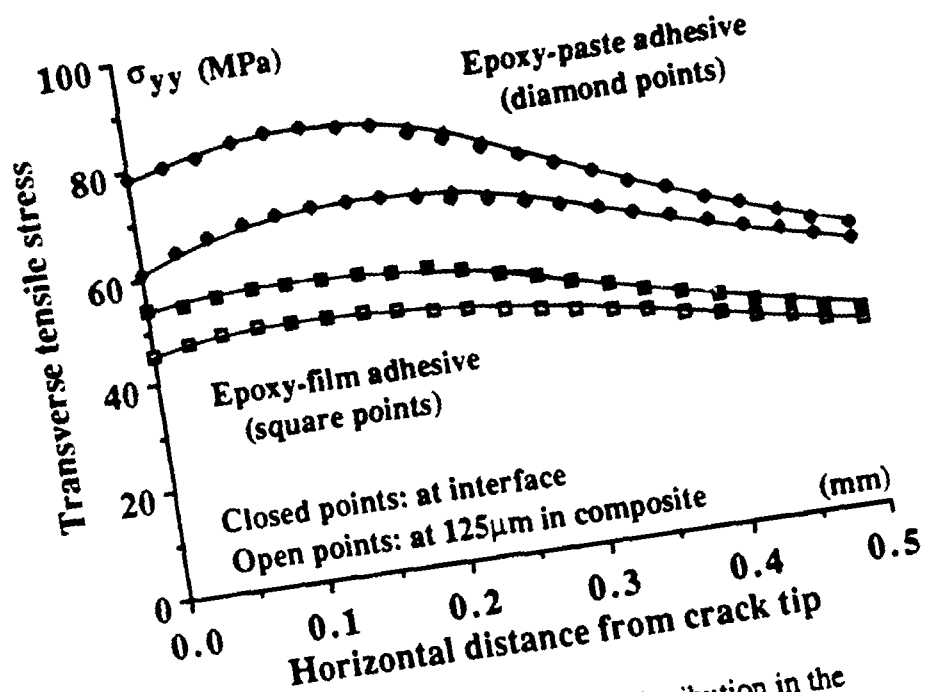
Fig. A.19. Transverse tensile stress distribution in the crack tip regions for the U/C-epoxy composite joint.

CHAPTER SIX

A.8. Deconvolution Results of XPS Data

Table A.1. Deconvolution of the C1s element from the U/C-PEEK
composite subjected to corona-discharge pretreatment.

Corona treatment energy (J/mm^2)	C-H	C-O	C=O	O-C=O
0.0	82.5±0.5	16.0±0.0	1.5±0.5	*
0.125	81.0±2.0	16.0±1.0	3.0±1.0	*
0.25	78.5±1.5	17.5±0.5	4.0±1.0	*
0.375	76.0±1.0	18.5±0.5	5.5±0.5	*
0.50	74.5±1.5	19.0±1.0	6.5±0.5	*
0.75	72.0±2.0	19.0±0.0	7.0±1.0	3.0±1.0
1.0	71.5±1.5	18.5±0.5	8.0±1.0	3.0±0.0
1.5	71.5±0.5	18.0±1.0	8.0±1.0	3.5±0.5
2.5	71.0±2.0	18.0±1.0	8.0±1.0	4.0±0.0
5.0	69.0±1.0	18.5±0.5	8.5±0.5	4.0±1.0
7.5	68.0±2.0	18.0±1.0	9.0±0.0	5.0±1.0
10.0	67.0±3.0	19.0±1.0	9.0±1.0	6.0±1.0
15.0	65.5±2.5	18.0±1.0	9.0±1.0	6.5±0.5
20.0	64.0±2.0	20.0±1.0	9.0±0.0	7.0±1.0

Note: (*): Trace.

Table A.2. Deconvolution of the C1s element from the U/C-PA
composite subjected to corona-discharge pretreatment.

Corona treatment energy (J/mm^2)	C-H	C-O	C=O	O-C=O
0.0	81.0±1.0	15.0±0.0	4.0±1.0	*
0.125	79.0±0.0	16.0±1.0	5.0±1.0	*
0.25	78.5±0.5	14.5±0.5	7.0±0.0	*
0.5	77.0±1.0	15.0±0.0	8.0±1.0	*
0.75	76.0±1.0	13.0±0.0	10.0±1.0	1.0±0.0
1.0	75.0±1.0	11.5±0.5	11.5±0.5	2.0±0.0
1.5	73.0±1.0	14.0±0.0	11.0±0.0	2.0±1.0
2.0	71.0±2.0	15.0±1.0	11.5±0.5	2.5±0.5
3.0	70.0±2.0	15.0±1.0	12.0±0.0	3.0±1.0
4.0	69.5±2.5	15.0±1.0	12.0±1.0	3.5±0.5
5.0	68.0±1.0	15.0±0.0	13.0±1.0	4.0±0.0

Table A.3. Deconvolution of the C1s element from the U/K-PA
composite subjected to corona-discharge pretreatment.

Corona treatment energy (J/mm^2)	C-H	C-O	C=O	O-C=O
0.0	80.5±0.5	16.0±0.0	3.5±0.5	*
0.125	80.0±0.0	16.0±1.0	4.0±1.0	*
0.25	78.0±2.0	16.0±1.0	6.0±1.0	*
0.5	77.0±1.0	15.5±0.5	6.5±0.5	1.0±0.0
0.75	75.0±0.0	15.0±1.0	8.0±1.0	2.0±0.0
1.0	72.5±0.5	15.5±0.5	9.5±0.5	2.5±0.5
1.5	70.0±2.0	15.5±0.5	11.5±0.5	3.0±1.0
2.0	68.0±2.0	16.0±0.0	12.0±1.0	4.0±1.0
3.0	66.0±1.0	17.0±0.0	13.0±1.0	4.0±0.0
4.0	65.0±1.0	17.0±1.0	13.0±0.0	5.0±0.0
5.0	64.5±2.5	17.0±1.0	13.0±1.0	5.5±0.5

Table A.4. Deconvolution of the C1s element from the W/C-PEI
composite subjected to corona-discharge pretreatment.

Corona treatment energy (J/mm^2)	C-H	C-O	C=O	O-C=O
0.0	76.0±1.0	19.0±1.0	4.0±0.0	*
0.125	76.0±0.0	19.0±1.0	5.0±1.0	*
0.25	75.0±2.0	17.0±1.0	6.0±1.0	1.0±0.0
0.50	72.5±1.5	17.0±0.0	7.0±1.0	2.5±0.5
0.75	72.0±1.0	16.0±1.0	8.0±1.0	4.0±1.0
1.0	71.5±0.5	15.5±0.5	8.5±0.5	4.5±0.5
1.5	71.0±2.0	15.0±1.0	9.0±1.0	5.0±0.0
2.0	70.0±0.0	16.0±1.0	9.0±0.0	5.0±1.0
3.0	69.0±1.0	17.0±1.0	9.0±0.0	5.0±0.0
4.0	67.0±0.0	17.5±0.5	10.0±1.0	5.5±0.5
5.0	66.0±2.0	18.0±1.0	11.0±1.0	6.0±0.0
7.5	64.0±1.0	18.0±0.0	11.0±1.0	7.0±0.0

Table A.5. Deconvolution of the C1s element from the W/C-PI
composite subjected to corona-discharge pretreatment.

Corona treatment energy (J/mm^2)	C-H	C-O	C=O	O-C=O
0.0	82.0±1.0	14.0±1.0	4.0±0.0	*
0.125	81.0±1.0	15.0±0.0	4.0±1.0	*
0.25	79.5±1.5	15.5±0.5	5.0±1.0	*
0.50	77.0±1.0	16.0±1.0	6.0±0.0	1.0±0.0
0.75	75.5±1.5	16.5±0.5	7.0±1.0	1.0±0.0
1.0	75.0±0.0	16.0±1.0	8.0±1.0	1.5±0.0
1.5	74.5±1.5	15.0±1.0	9.5±0.5	2.0±0.0
2.0	72.0±1.0	16.0±1.0	10.0±0.0	2.0±0.0
3.0	70.5±0.5	16.5±0.5	10.5±0.5	2.5±0.5
4.0	71.0±1.5	14.0±0.0	12.0±1.0	3.0±0.5

Table A.6. Deconvolution of the C1s and S2p elements from the U/C-PPS
composite subjected to corona-discharge pretreatment.

Corona treatment energy (J/mm^2)	C1s element:				S2p element
	C-H	C-O	C=O	O-C=O	S=O
0.0	93.0±0.0	7.0±0.0	*	*	*
0.125	89.0±1.0	9.0±1.0	2.0±0.0	*	14.0
0.25	87.0±1.0	10.0±1.0	3.0±0.0	*	17.0
0.5	84.0±0.0	11.5±0.5	3.5±0.5	1.0±0.0	17.0
0.75	81.0±1.0	12.0±0.0	5.0±1.0	2.0±0.0	20.0
1.0	80.0±2.0	10.5±0.5	8.0±1.0	2.5±0.5	19.0
2.0	76.0±0.0	12.5±0.5	8.5±0.5	3.0±1.0	23.0
3.0	73.0±1.0	14.0±1.0	9.0±0.0	4.0±1.0	29.0
4.0	73.5±1.5	13.5±0.5	9.0±1.0	4.0±0.0	35.0
5.0	72.0±2.0	13.0±0.0	10.0±1.0	5.0±1.0	46.0

Table A.7. Deconvolution of the C1s element from the U/C-epoxy thermosetting
composite subjected to abrasion/solvent-wipe pretreatment.

C-H	C-O	C=O	O-C=O
69.0±0.0	26.0±1.0	5.0±1.0	*

Table A.8. Deconvolution of the C1s element from corona-treated
$(20J/mm^2)$ and aged U/C-PEEK composite.

Ageing time (weeks)	C-H	C-O	C=O	O-C=O
0	64.0±2.0	20.0±1.0	9.0±0.0	7.0±1.0
1	64.0±2.0	22.0±0.0	8.0±1.0	6.0±1.0
4	69.0±3.0	20.0±1.0	6.0±1.0	5.0±1.0
9	72.0±1.0	18.0±1.0	5.0±0.0	5.0±0.0
13	73.5±1.5	17.0±0.0	5.0±1.0	4.5±0.5
26	74.0±1.0	17.0±1.0	5.0±1.0	4.0±1.0

Table A.9. Deconvolution of the C1s element from corona-treated
$(5J/mm^2)$ and aged U/C-PA composite.

Ageing time (weeks)	C-H	C-O	C=O	O-C=O
0	68.0±1.0	15.0±0.0	13.0±1.0	4.0±0.0
1	71.0±1.0	14.0±0.0	11.0±1.0	4.0±0.0
4	77.0±1.0	12.0±1.0	7.0±0.0	4.0±0.0
9	76.0±0.0	13.0±0.0	7.0±1.0	4.0±1.0
13	78.0±1.0	12.0±1.0	6.0±0.0	4.0±0.0
26	79.0±1.0	12.0±1.0	6.0±0.0	3.0±0.0

A.9. "Uncorrected" Thermodynamic Work of Adhesion

Table A.10. Thermodynamic work of adhesion for the U/C-PEEK composite.

Corona treatment energy (J/mm^2)	Epoxy-paste adhesive W_A (mJ/m^2)	Epoxy-film adhesive W_A (mJ/m^2)
0.0	84.8±3.3	80.7±3.1
0.25	91.3±6.3	86.5±5.9
0.5	91.0±6.9	86.1±6.5
0.75	96.4±3.4	91.1±3.2
1.0	97.4±3.6	91.9±3.3
1.5	97.7±3.7	92.2±3.5
2.5	98.0±3.8	92.5±3.6
5.0	98.5±3.9	93.0±3.7
7.5	101.2±4.1	95.5±3.8
10.0	101.7±4.0	95.9±3.8
15.0	102.5±4.0	96.7±3.8
20.0	103.3±4.1	97.4±3.8

Table A.11. Thermodynamic work of adhesion for the U/C-PA composite.

Corona treatment energy (J/mm^2)	Epoxy-paste adhesive W_A (mJ/m^2)	Epoxy-film adhesive W_A (mJ/m^2)
0.0	84.0±3.8	79.8±3.5
0.125	86.0±5.6	81.5±5.2
0.25	87.5±5.8	82.8±5.5
0.5	88.3±4.2	83.4±3.9
0.75	88.7±4.5	83.7±4.2
1.0	93.3±4.2	88.2±3.9
1.5	94.5±4.0	89.2±3.7
2.0	94.9±3.8	89.5±3.6
3.0	96.4±3.6	90.9±3.3
4.0	97.5±4.0	92.0±3.8
5.0	101.2±4.1	95.4±3.8

Table A.12. Thermodynamic work of adhesion for the U/K-PA composite.

Corona treatment energy (J/mm^2)	Epoxy-paste adhesive W_A (mJ/m^2)	Epoxy-film adhesive W_A (mJ/m^2)
0.0	84.2±4.5	79.9±4.2
0.125	85.9±5.7	81.5±5.4
0.25	87.6±5.5	83.0±5.1
0.5	89.8±5.4	84.9±5.1
0.75	87.8±5.0	83.0±4.7
1.0	91.8±4.2	86.7±3.9
1.5	93.8±4.2	88.6±3.9
2.0	94.6±3.9	89.2±3.7
3.0	95.9±3.7	90.5±3.5
4.0	96.8±3.8	91.2±3.6
5.0	97.7±4.2	92.1±4.0

Table A.13. Thermodynamic work of adhesion for the W/C-PEI composite.

Corona treatment energy (J/mm^2)	Epoxy-paste adhesive W_A (mJ/m^2)	Epoxy-film adhesive W_A (mJ/m^2)
0.0	84.5±4.1	80.3±3.8
0.125	87.2±5.7	82.7±5.4
0.25	88.8±5.7	84.1±5.4
0.5	89.3±6.6	84.5±6.2
0.75	87.2±6.7	82.4±6.3
1.0	94.1±3.5	89.0±3.3
1.5	95.1±3.1	89.8±2.9
2.0	95.9±3.2	90.6±3.0
3.0	96.2±3.5	90.9±3.3
4.0	97.0±3.2	91.6±3.0
5.0	97.9±3.6	92.4±3.4
7.5	99.2±4.5	93.6±4.2

Table A.14. Thermodynamic work of adhesion for the W/C-PI composite.

Corona treatment energy (J/mm^2)	Epoxy-paste adhesive W_A (mJ/m^2)	Epoxy-film adhesive W_A (mJ/m^2)
0.0	85.6±5.5	81.3±5.2
0.125	87.1±6.6	82.6±6.2
0.25	88.5±7.2	83.9±6.7
0.5	89.5±6.6	84.7±6.2
0.75	95.2±4.4	89.9±4.2
1.0	96.2±4.2	90.9±3.9
1.5	96.6±3.9	91.2±3.6
2.0	97.4±4.0	92.0±3.7
3.0	98.2±3.9	92.7±3.7
4.0	99.0±4.4	93.4±4.1

Table A.15. Thermodynamic work of adhesion for the U/C-PPS composite.

Corona treatment energy (J/mm^2)	Epoxy-paste adhesive W_A (mJ/m^2)	Epoxy-film adhesive W_A (mJ/m^2)
0.0	79.7±2.7	75.9±2.5
0.125	83.2±5.0	78.9±4.7
0.25	84.5±4.8	80.1±4.5
0.5	85.3±5.1	80.8±4.8
0.75	86.6±5.4	82.0±5.1
1.0	89.6±4.1	84.7±3.8
2.0	89.8±3.7	84.5±3.5
3.0	90.3±3.7	85.3±3.5
4.0	91.4±3.8	86.3±3.6
5.0	92.3±3.8	87.1±3.5
7.5	94.4±3.9	89.0±3.7
10.0	96.1±3.9	90.6±3.6

Table A.16. Thermodynamic work of adhesion for the U/C-epoxy composite subjected to abrasion/solvent-wipe pretreatment.

Epoxy-paste adhesive W_A (mJ/m^2)	Epoxy-film adhesive W_A (mJ/m^2)
88.0±6.6	83.2±6.2

REFERENCES

[1] Cabinet Office, "Joining and Assembly", Advisory Council for Applied Research and Development, (Oct. 1979).

[2] A. J. Kinloch, "Adhesion and Adhesives: Science and Technology", Chapman and Hall, London, p. 2, (1987).

[3] A. Benatar and T. G. Gutowski, SAMPE Quarterly, p. 35, (Oct. 1986).

[4] M. G. Murch and M. N. Watson, "Welding of Aromatic Polymer Composites", The Welding Institute Progress Report, (Aug. 1986).

[5] B. M. Parker and R. M. Waghorne, J. of Composites, **13**, p. 280, (1982).

[6] A. V. Pocius and R. P. Wenz, 30th. National SAMPE Symposium, p. 1073, (March 1985).

[7] L. J. Matienzo, J. D. Venable, J. D. Fudge and J. J. Vewlten, 30th. National SAMPE Symposium, p. 302, (March 1985).

[8] L. W. Crane, C. H. Hamermesh and L. Maus, SAMPE Journal, p. 6, (March/April 1976).

[9] L. J. Hart-Smith, R. W. Oschner and R. L. Radecky, "Surface Preparation of Fibrous Composites for Adhesive Bonding or Painting", Chapter 51, Douglas Service First Quarter, (1984).

[10] A. J. Kinloch and C. M. Taig, J. of Adhesion, **21**, p. 291, (1987).

[11] J. R. Krone, T. P. Murtha and J. A. Stirling, 33rd International SAMPE Symposium, p. 829, (March 1988).

[12] S. Y. Wu , A. M. Schuler and D. V. Keane, 19th. International SAMPE Technical Conference, p. 277, (Oct. 1987).

[13] D. J. D. Moyer and J. P. Wightman, "Characterization of Surface Pretreatments of Carbon Fibre/Polyimide Matrix Composites", to be published in Surface and Interface Analysis, (1990).

[14] G. K. A. Kodokian and A. J. Kinloch, J. of Materials Science, 7, p. 625, (1988).

[15] J. A. Peacock, B. Fife, E. Neild and C. Y. Barlow, in "Composite Interfaces", Edited by H. Ishida and J. L. Koening, North-Holland, New-York, p. 143, (1986).

[16] D. Briggs, D. G. Rance, C. R. Kendell and A. R. Blythe, Polymer, 21, p. 895, (1980).

[17] A. J. Kinloch, "Adhesion and Adhesives: Science and Technology", Chapman and Hall, London, p. 19, (1987).

[18] T. Young, Trans. Roy. Soc., 95, p. 65, (1805).

[19] R. J. Good, in "Aspects of Adhesion-7", Editors ⌐. J. Alner and K. W. Allen, Transcripta Books, London, p. 182, (1973).

[20] W. A. Zisman, Ind. Eng. Chem., 55, p. 18, (1963).

[21] H. W. Fox and W. A. Zisman, J. of Colloid Sci., 5, p. 514, (1950).

[22] H. W. Fox and W. A. Zisman, J. of Colloid Sci., 7, p. 109, (1952).

[23] H. W. Fox and W. A. Zisman, J. of Colloid Sci., 7, p. 428, (1952).

[24] E. G. Shafrin and W. A. Zisman, J. of Phys. Chem., 64, p. 519, (1960).

[25] W. A. Zisman, in "Advances in Chemistry Series", 43, Edited by R. F. Gould, American Chemical Soc., Washington, p. 1, (1964).

[26] J. R. Dann, J. of Colloid Interf. Sci, 32, p. 302, (1970).

[27] L. A. Girifalco and R. J. Good, J. of Phys. Chem., 61, p. 904, (1957).

[28] R. J. Good and L. A. Girifalco, J. of Phys. Chem., 64, p. 561, (1960).

[29] F. M. Fowkes, Ind. Eng. Chem., **56** (12), p. 40, (1964).

[30] J. Schultz, K. Tsutsumi and J. B. Donnet, J. of Colloid Interf. Sci., **59**, p. 277, (1977).

[31] F. M. Fowkes, in "Treatise on Adhesion and Adhesives", **1**, Edited by R. L. Patrick, Marcel Dekker, New-York, p. 352, (1967).

[32] J. R. Dann, J. of Colloid Interf. Sci, **32**, p. 321, (1970).

[33] Y. Tamai, K. Makuuchi and M. Suzuki, J. of Phys. Chem., **71**, p. 4167, (1967).

[34] D. H. Kaelble and K. C. Uy, J. of Adhesion, **2**, p. 50, (1970).

[35] D. K. Owens and R. C. Wendt, J. of Appl. Polymer Sci., **13**, p. 1740, (1969).

[36] D. R. Williams and F. M. Fowkes, "The Acid-Base and Wettability Behaviour of Some Polymer Surfaces", to be published in J. of Colloid and Interf. Sci., (1989).

[37] E. H. Andrews and A. J. Kinloch, Proc. Roy. Soc., London, **A332**, p. 385, (1973).

[38] R. N. Wenzel, Ind. Eng. Chem., **28**, p. 988, (1936).

[39] A. Carre and J. Schultz, J. of Adhesion, **15**, p. 151, (1983).

[40] W. A. Zisman, J. of Paint Technol., **44**, p. 42, (1972).

[41] R. Rosty, D. Martinelli, A. Devine, M. J. Bodnar and J. Beetle, 32nd International SAMPE Symposium, p. 456, (1987).

[42] D. L. Messick, D. J. Progar and J. P. Wightman, "Surface Analysis of Graphite Reinforced Polyimide Composites", NASA Technical Momerandum 85700, (1983).

[43] K. Siegbahn, C. Nordling, A. Fahlman, R. Nordberg, K. Hamrin, J. Hedman, G. Johansson, T. Bergmark, S. Karlsson, I. Lindgren and B. Linberg, "ESCA, Atomic, Molecular, and Solid State Structure Studies by Means of Electron Spectroscopy", Almquist and Wiksells, Uppsala, (1967).

[44] J. E. Castle, Surf. Sci., **68**, p. 583, (1977).

[45] M. Stradal and D. A. I. Goring, Canadian J. of Chem. Eng., **53**, p. 427, (1975).

[46] D. K. Owens, J. of Appl. Polym. Sci., **19**, p. 265, (1975).

[47] D. M. Brewis and D. Briggs, Polymer, **22**, p. 7, (1981).

[48] D. Briggs, D. M. Brewis and M. B. Konieczko, J. of Materials Science, **12**, p. 429, (1977).

[49] D. Briggs, D. M. Brewis and M. B. Konieczko, J. of Materials Science, **11**, p. 1279, (1976).

[50] D. W. Fakes, J. M. Newton, J. F. Watts and M. J. Edgell, Surf. Interf. Anal., **10**, p. 416, (1987).

[51] J. F. Watts, Surf. Interf. Anal., **12**, p. 497, (1988).

[52] N. Cave, Ph.D. Thesis , Mech. Eng. Dept., Imperial College, London, (1989).

[53] G. R. Irwin, Appl. Mats. Res., **3**, p. 65, (1964).

[54] J. F. Knott, Materials Science and Eng., **7**, p. 1, (1971).

[55] J. G. Williams, Adv. Polym. Science, **27**, p. 68, (1978).

[56] H. Liebowitz, Editor, "Fracture- An Advance Treatise", **2**, Academic Press, New-York, (1968).

[57] J. F. Knott, "Fundamentals of Fracture Mechanics", Butterworths, London, (1973).

[58] D. G. H. Latzko, Editor, "Post-Yield Fracture Mechanics", Applied Science Publishers, London, (1979).

[59] D. Broek, "Elementary Engineering Fracture Mechanics", Fourth Revised Edition, Martinus Nijhoff Publishers, Dordrecht, The Netherlands, (1986).

[60] A. A. Griffith, Phil. Trans. Roy. Soc., **A221**, p. 163, (1920).

[61] E. Orowan, Reports on Propre. Phys., **12**, p. 185, (1948).

[62] H. M. Westergaard, J. of Appl. Mech., **A6**, p. 46, (1939).

[63] J. R. Rice, "Fracture - An Advance Treatise", **2**, Edited by Liebowitz, Academic Press, New-York, p. 191, (1968).

[64] A. J. Kinloch and S. J. Shaw, "Developements In Adhesives-2", Edited by A. J. Kinloch, Applied Science Publishers Ltd., London, Chapter 3, (1981).

[65] R. S. Rivlin and A. G. Thomas., J. of Polym. Science, **10**, p. 291, (1953).

[66] E. J. Ripling, S. Mostovoy and R. L. Patrick, Materials Research and Standards, **4** (3), p. 129, (1964).

[67] P. P. Gillis and J. J. Gilman, J. of Applied Physics, **35**, p. 647, (1964).

[68] J. G. Williams, "Large Displacement and End Effects in the DCB Interlaminar Test in Modes I and II", ICCM6 meeting in Imperial College, Edited by F. L. Matthews, N. C. R. Buskell, J. M. Hodgkinson and J. Morton, Elsevier Applied Science, London and New-York, **3**, p. 233, (1987).

[69] S. Hashemi, A. J. Kinloch and J. G. Williams, J. of Materials Science, **8**, p. 125, (1989).

[70] S. Hashemi, A. J. Kinloch and J. G. Williams, "Interlaminar Fracture of Composite Materials", ICCM6 meeting in Imperial College, Edited by F. L. Matthews, N. C. R. Buskell, J. M. Hodgkinson and J. Morton, Elsevier Applied Science, London and New-York, **3**, p. 254, (1987).

[71] D. J. Nicholls and J. P. Gallagher, J. of Reinforced Plastics and Composites, **2**, p. 2, (1983).

[72] J. G. Williams, Int. J. of Fracture, **36**, p. 101, (1988).

[73] S. M. Lee, J. of Composite Materials, **20**, p. 185, (1986).

[74] P. E. Keary, L. B. Ilcewicz, C. Shaar and J. Trostle, J. of Composite Materials, 19, p. 154, (1985).

[75] E. F. Rybicki, T. D. Hernandez, J. E. Deibler, R. C. Knight and S. S. Vinson, J. of Composite Materials, 21, p. 105, (1987).

[76] F. X. de Charentenay and M. Benzagegh, "Fracture Mechanics of Mode I Delamination Composite Materials", Proceedings of ICCM3, Paris, p. 241, (Aug. 1980).

[77] K. S. Han and J. Koutsky, J. of Composite Materials, 15, p. 371, (1981).

[78] W. M. Jordan and W. L. Bradley, Proceedings of the 29th National SAMPE Symposium, p. 1422, (1984).

[79] D. J. Wilkins, J. R. Eisenmann, R. A. Camin, W. S. Margolis and R. A. Benson, "Characterizing Delamination Growth in Graphite-Epoxy", in "Damage in Composite Materials", ASTM STP 775, p. 168, (1982).

[80] W. Jemian and M. Ventrice, J. of Adhesion, 1, p. 190, (1969).

[81] K. Loss, S. Ehlers and K. Kedward, "An Evaluation Cracked Lap Shear Testing for Bonded joint Applications", Report No. 85-0792, American Institute of Aeronotics and Astronomics, (1985).

[82] T. R. Brusat, S. T. Chiu, S. Mostovoy, "Fracture Mechanics for Structural Adhesive Bonds", Report No. AFWL-TR-77-163, (1977).

[83] P. D. Mangalgiri, W. S. Johnson and R. A. Everett Jr., J. of Adhesion, 23, p. 263, (1987).

[84] S. Mall and W. S. Johnson, "Characterization of Mode I and Mixed-Mode Failure of Adhesive Bonds Between Composite Adherends", ASTM STP 893, p. 322, (1986).

[85] D. L. Hunston, A. J. Kinloch and S. S. Wang, J. of Adhesion, 28, p. 103, (1989).

[86] A. J. Kinloch and S. J. Shaw, "The Fracture Resistance of Toughened Epoxy Adhesives", Presented at the Int. Conference on Adhesion and Adhesives of the Plastics and Rubber Institute, Durham University, England, (Sep. 1980).

[87] H. Chai, "Bond Thickness Effects in Adhesive Joints its Significance for Mode I Interlaminar Fracture of Composites", Composite Materials: Testing and Design (7th. Conference) ASTM STP 893, Editor J. M. Whitney, ASTM Philadelphia, p. 209, (1986).

[88] W. D. Bascom, R. L. Cottington, R. L. Jones and P. Peyser, J. of Applied Polymer Science, 19, p. 2545, (1975).

[89] H. Chai, J. of Materials Science, 7, p. 399, (1988).

[90] S. S. Wang, J. F. Mandell and F. J. Mcgarry, J. of Fracture, 14, p. 39, (1978).

[91] J. H. Crews, K. N. Shivakumar and I. S. Raju, "Factors Influencing Elastic Stresses in Double Cantilever Beam Specimens", ASTM Special Technical Publication 981 (1988).

[92] D. F. Devitt, R. A. Schapery and W. L. Bradley, J. of Composite Materials, 14, p. 270, (1980).

[93] S. Hashemi, A. J. Kinloch and J. G. Williams, "The Analysis of Interlaminar Fracture in Uniaxial Fibre-Polymer Composites", to be published in Proc. Roy. Soc., (1990).

[94] A. R. Wedgewood, K. B. Su, 19th International SAMPE Technical Conference, p. 454, (Oct. 1987).

[95] G. G. Trantina , J. of Composite Materials, 6, p. 192, (1972).

[96] M. L. Williams, Bulletin of Seismological Society of America, 2, p. 199, (1959).

[97] F. Erdogan, J. of Applied Mech., 30, Trans. ASME, 85, Series E, p. 232, (1963).

[98] G. C. Sih and J. C. Rice, J. of Applied Mech., 31, Trans. ASME 89, Series E, p. 477, (1964).

[99] A. H. England, J. of Appl. Mech., 32, p. 400, (1965).

[100] R. E. Smelser and M. E. Gurtin, Int. J. of Fract., 13, p. 382, (1977).

[101] J. F. Yau and S. S. Wang, Engng. Fract. Mech., 20, p. 423, (1984).

[102] A. J. Kinloch, "Adhesion and Adhesives: Science and Technology", Chapman and Hall, London, p. 123, (1987).

[103] J. J. Bikerman, Ind. Eng. Chem., **59** (9), p. 40, (1967).

[104] T. R. Bullett and J. L. Prosser, in "Adhesion, Fundamentals and Practice", Maclaren and Sons Ltd., London, p. 37, (1969).

[105] A. J. Kinloch and M. L. Yuen, J. of Materials Science, **24**, p. 2183, (1989).

[106] J. J. Bikerman, Adhesives Age, **2** (2), p. 23, (1981).

[107] S. G. Lekhnitski, "Theory of Elasticity of an Anisotropic Body", Mir Publishers, Moscow, p. 34, (1981).

[108] PAFEC Theory, PAFEC Ltd., Strelly Hall, Strelly Nottingham, NG8 6PE, p. 2.173, (1984).

[109] PAFEC Data Preparation User Manual Level 6.1 Strelly Hall, Strelly Nottingham, NG8 6PE, (1984).

[110] PIGS User Manual Level 4.1, Strelly Hall, Strelly Nottingham, NG8 6PE, (1984).

[111] G. K. A. Kodokian and A. J. Kinloch, "The Adhesive Fracture Energy of Bonded Thermoplastic Fibre-Composites", to be published in the J. of Adhesion, (1989).

[112] W. D. Bascom and R. T. Patrick, Adhesives Age, **17** (10), p. 25, (1974).

[113] A. J. Kinloch, "Adhesion and Adhesives: Science and Technology", Chapman and Hall, London, p. 20, (1987).

[114] W. D. Bascom, R. L. Cottington and C. R. Singleterry, "Advances in Chemistry Series, 43", Edited by R. F. Gould, Amer. Chem. Soc., Washington, p. 355, (1964).

[115] A. J. Kinloch, "Adhesion and Adhesives: Science and Technology", Chapman and Hall, London, p. 40, (1987).

[116] R. L. Cottington, C. M. Murphy and C. R. Singleterry, "Advances in Chemistry Series, 43", Edited by R. F. Gould, Amer. Chem. Soc., Washington, p. 341, (1964).

[117] G. D. Cheever, "Interface Conversions for Polymer Coatings", Edited by Weiss and G. D. Cheever, Elsevier, New-York, p. 150, (1968).

[118] N. A. de Bruyne, Aero Research Technical Notes, No. 168, p. 1, (1956).

[119] G. Z. Friz, Z. fur Angew Physik, 19, p. 374, (1965).

[120] A. M. Schwartz and S. B. Tegada, J. of Colloid Interf. Sci., 38, p. 359, (1972).

[121] K. Kato, Polymer, 8, p. 33, (1967).

[122] K. Kato, Polymer, 9, p. 419, (1968).

[123] K. Heynmann, Production Finish, 19, p. 38, (1966).

[124] M. Matsunaga, Y. Haywida and K. Ito, Metal Finish, 66 (11), p. 80, (1968).

[125] A Rantell, Trans. Inst. Metal Finish, 47, p. 197, (1969).

[126] J. M. Sykes and T. P. Hoar, J. of Polym. Sci., A1, p. 1385, (1969).

[127] I. A. Abu Isa, J. of Appl. Polymer Sci., 15, p. 2865, (1971).

[128] R. Roberts, F. W. Ryan, H. Schonhom, G. M. Sessler and J. E. West, J. of Appl. Polymer Sci., 20, p. 225, (1976).

[129] E. B. Atkinson, P. R. Brooks, T. D. Lewis, R. R. Smith and K. A. White, Plast. Inst. Trans. J., 35, p. 549, (1967).

[130] B. W. Malpass, D. E. Packham and K. Bright, J. of Appl. Polym. Sci., 18, p. 3249, (1974).

[131] J. R. G. Evans and D. E. Packham, J. of Adhesion, 10, p. 177, (1979).

[132] W. C. Wake, "Adhesion", Edited by D. D. Eley, Oxford Univ. Press, London, p. 191, (1961).

[133] A. J. Kinloch, J. of Mater. Sci., **15**, p. 2141, (1980).

[134] D. Tabor and R. H. S. Winterton, Proc. Roy. Soc., **A312**, p. 435, (1969).

[135] J. N. Israelachvili and D. Tabor, Proc. Roy. Soc., **A331**, p 19, (1972).

[136] K. L. Johnson, K. Kendall and A. D. Roberts. Proc. Roy. Soc., **A324**, p. 301, (1971).

[137] A. J. Kinloch, "Adhesion and Adhesives: Science and Technology", Chapman and Hall. London, p. 67, (1987).

[138] S. S. Voyutskii, "Autoadhesion and Adhesion of High Polymers", Wiley Interscience, New-York, (1963).

[139] R. M. Vasenin, "Adhesion Fundamentals and Practice", Edited by U. K. Min. of Tech., Elsevier, London, p. 29, (1969).

[140] F. J. Bueche, W. M. Cashin and P. J. Debye, J. of Chem. Phys., **20**, p. 1956, (1952).

[141] J. N. Amand and R. Z. Balwinski, J. of Adhesion, **1**, p. 24, (1969).

[142] J. N. Amand, J. of Adhesion, **1**, p. 31, (1969).

[143] J. N. Amand and L. Dipzinski, J. of Adhesion, **2**, p. 16, (1970).

[144] J. N. Amand, J. of Adhesion, **2**, p. 23, (1970).

[145] J. N. Amand, J. of Adhesion, **5**, p. 265, (1973).

[146] B. V. Derjaguin and V. P. Smilga, Proc. 3rd International Congress of Surface Activity, **11**, p. 349, (1960).

[147] H. Schonhorn, "Adhesion Fundamentals and Practice", Edited by the U. K. Min. of Tech., Elsevier, London, p. 12, (1969).

[148] C. Weaver, "Adhesion Fundamentals and Practice", Edited by the U. K. Min. of Tech., Elsevier, London, p. 46, (1969).

[149] D. Tabor, Rep. Prog. Appl. Chem., 36, p. 621, (1951).

[150] J. R. Huntsberger, "Treatise on Adhesion and Adhesives", 1, Edited by R. L. Patrick, Marcel Dekker, New-York, p. 119, (1967).

[151] E. Orowan, J. of Franklin Inst., 290, p. 493, (1970).

[152] E. H. Andrews and A. J. Kinloch, Proc. Roy. Soc., A332, p. 401, (1973).

[153] R. A. Gledhill and A. J. Kinloch, J. of Adhesion, 6, p. 315, (1974).

[154] A. N. Gent and A. J. Kinloch, J. of Polymer Sci., A2, p. 659, (1971).

[155] A. J. Kinloch, J. of Adhesion, 10, p. 193, (1979).

[156] D. K. Owens, J. of Appl. Polym. Sci., 19, p. 3315, (1979).

[157] A. R. Blythe, D. Briggs, C. R. Kendall, D. G. Rance and V. J. I. Zichy, Polymer, 19, p. 1273, (1978).

[158] D. Briggs, V. J. I. Zichy, D. M. Brewis, J. Comyn, R. H. Dahm, M. A. Green and M. B. Konieczko, Surf. Interf. Anal., 2, p. 107, (1980).

[159] D. Briggs, C. R. Kendall, A. R. Blythe and A. B. Wootton, Polymer, 24, p. 47, (1983).

[160] D. Briggs and C. R. Kendall, Int. J. of Adhesion and Adhesives, 2, p. 13, (1982).

[161] D. Briggs and C. R. Kendall, Polymer, 20, p. 1053, (1979).

[162] K. L. Mittal, Polym. Eng. Sci., 17, p. 467, (1977).

[163] D. H. Kaelble, J. of Adhesion, **1**, p. 102, (1969).

[164] E. H. Andrews and A. J. Kinloch, J. of Polym. Sci. Symp., **46**, p. 1, (1974).

[165] A. N. Gent and J. Schultz, J. of Adhesion, **3**, p. 281, (1972).

[166] F. M. Fowkes, J. of Adhesion, **4**, p. 155, (1972).

[167] F. M. Fowkes, in "Polymer Science and Technology", **12A**, "Adhesion and Adsorption of Polymers", Edited by L. H. Lee, Plenum, New-York, p. 43, (1980).

[168] R. S. Drago, G. C. Vogel and T. E. Needham, J. of Amer. Chem. Soc., **93**, p. 6014, (1971).

[169] R. S. Drago, L. B. Parr and C. S. Chamberlain, J. Amer. Chem. Soc., **99**, p. 3203, (1977).

[170] D. G. Rance, "Thermodynamic Approach to Adhesion Problems", in "Industrial Adhesion Problems", Edited by D. M. Brewis and D. Briggs, p. 66, Oxford, (1985).

[171] F. M. Fowkes and S. Maruchi, Coatings and Plastics Preprints, **37**, p. 605, (1977).

[172] F. M. Fowkes, "Physicochemical Aspects of Polymer Surfaces", **2**, Edited by K. L. Mittal, Plenum, New-York, p. 583, (1983).

[173] F. M. Fowkes and M. A. Mostafa, Ind. Eng. Chem. Prod. Res. Dev., **17**, p. 3, (1978).

[174] J. R. Huntsberger, J. of Adhesion, **12**, p. 3, (1981).

[175] A. J. Kinloch, "Adhesion and Adhesives: Science and Technology", Chapman and Hall, London, p. 32, (1987).

[176] A. N. Gent and A. Ahagon, J. of Polymer Sci., Polymer Phys. Ed., **13**, p. 1285, (1975).

[177] R. J. Chang, A. N. Gent, C. C. Hsu and K. C. Sehgal, J. of Appl Ploymer Sci., **25**, p. 163, (1980).

[178] R. J. Chang and A. N. Gent, J. of Ploymer Sci., Polymer Phys. Ed., **19**, p. 1619, (1981).

[179] A. N. Gent, Int. J. of Adhesion and Adhesives, **3**, p. 159, (1981).

[180] I. E. Klein, J. Sharon, A. E. Doduik and D. Katz, Int. J. Adhesion Adhesives, **3**, p. 159, (1983).

[181] "Polymer Handbook", Second Edition, Editors J. Brandrup and E. H. Immergut with the Collaboration of W. McDowell, John Wiley and Sons, New-York, pages IV-351 and IV-358, (1975).

[182] G. M. Barrow, "Physical Chemistry", McGraw-Hill, New-York, p. 302, (1961).

[183] D. Briggs and M. P. Seah, "Practical Surface Analysis: by Auger and X-ray Photoelectron Spectroscopy", John Wiley and Sons, New-York, (1987).

[184] Private communication with Dr. J. F. Watts, University of Surrey, Guildford, Surrey GU2 5XH, U.K. (Based on his assessment of the work reported by A. P. Pijpers and R. J. Meier, J. of Electron Spectroscopy and Related Phenomena, **43**, p. 131, (1987)).

[185] O. Volkersen, Construction Metallique, **4**, p. 3, (1965).

[186] G. Muller, "Der Verformungs und Bruchvorgang an Metallklebever-bindungen verschiedener Werskstoffe bei ein-und mehrachsiger statischer Belastung", Dissertation, Technical University, Berlin, (1959).

[187] M. C. Fransblau and J. L. Rutherford, "Study of Micromechanical Properties of Adhesive Bonded Joints", 1st Quarterly Progress Report, Contract No. DAAA 21-67-C-0500, Picatinny Arsenal, Picatinny, U. S. A., (1967).

[188] G. Dolev and O. Ishai, J. of Adhesion, **12**, p. 289, (1981).

[189] R. D. Adams and W. C. Wake, "Structural Adhesive Joints in Engineering", Elsevier Appl. Science Publishers, London, p. 121, (1984).

[190] R. A. Jurf and J. R. Vinson, J. of Material Science, **20**, p. 2979, (1985).

[191] J. K. Strozier, K. J. Ninow, K. L. DeVries and G. P. Anderson, J. of Adhesion Sci. Tech., **1** (3), p. 209, (1987).

[192] L. G. Stringer, J. of Adhesion, **18**, p. 185, (1985).

[193] J. W. Grant and J. N. Cooper, J. of Adhesion, **21**, p. 155, (1987).

[194] R. B. Krieger Jr., Adhesives Age, p. 27, Oct. (1985).

[195] D. Post, R. Czarnek, J. D. Wood and D. Joh, "Deformations and Strains in a Thick Adherend Lap Joint, Adhesively Bonded Joints: Testing, Analysis and Design", ASTM STP 981, Editor W. S. Johnson, ASTM, Philadelphia, P. 107, (1988).

[196] D. L. Flaggs and J. R. Vinson, J. of Aircraft, **16** (1), p. 51, (Jan. 1979).

[197] W. J. Renton, Experimental Mechanics, **33**, p. 409, (1976).

[198] R. B. Krieger, "Fatigue Testing of Structural Adhesives, Adhesion 4", Editor K. W. Allen, Applied Science Publishers, London, p. 55, (1980).

[199] O. Volkersen, Luftfahtforsch, **15**, p. 41, (1938).

[200] M. Goland and E. Reissner, J. of Appl. Mech., **2**, p. A-17, (1944).

[201] R. D. Adams and N. A. Peppiatt, J. of Strain Analysis, **9**, p. 186, (1974).

[202] L. J. Hart-Smith, "Induced Peel Stresses in Adhesive-Bonded Joints", Douglas Aircraft Company, McDonnel Douglas Corporation, Report MDC-J9422A, USAF Contract Report Number AFWAL-TR-82-4172, (Aug. 1982).

[203] L. J. Hart-Smith, "Analysis and Design of Advanced Composite Bonded Joints", Douglas Aircraft Company, NASA CR-2218, (Jan. 1973).

[204] L. J. Hart-Smith, "Adhesive-Bonded Joints for Composites-Phenomenological Considerations", Douglas Aircraft Technology Conference Associates, Conference on Advanced Composites Technology, El Segundo, California, (March 1978).

[205] L. J. Hart-Smith, "Adhesive-Bonded Single-Lap Joints", Douglas Aircraft Company, NASA CR-112236, (Jan. 1973).

[206] L. J. Hart-Smith, "Adhesively Bonded Joints for Fibrous Composite Structures", Douglas Paper 7740, Int. Symposium on Joining and Repair of Fibre-Reinforced Plastics, Imperial College, London, (Sep. 1986).

[207] Engineering Services Data Unit (U. K.) Report, "Inelastic Shear Stresses and Strains in the Adhesives Bonding Lap Joints Loaded in Tension or Shear", No. 79016, London, (1979).

[208] C. Mylonas, Proc. Soc. Experimental Stress Analysis, 12, p. 129, (1954).

[209] A. D. Crocombe and R. D. Adams, J. of Adhesion, 13 (2), p. 141, (1981).

[210] P. A. Cooper and J. W. Sawyer, "A Critical Examination of Stresses in an Elastic Single Lap Joints", NASA TP-1507, (Sep. 1979).

[211] J. A. Harris and R. D. Adams, "Adhesion 8", Edited by K. W. Allen, Appl. Sci. Publ., London, (1983).

[212] F. Thamm, J. of Adhesion, 7, p. 301, (1976).

[213] R. D. Adams, R. W. Atkins, J. A. Harris and A. J. Kinloch, J. of Adhesion, 20, p. 29, (1986).

[214] R. Raghava, R. M. Caddell and G. S. Y. Yeh, J. of Materials Science, 8, p. 225, (1973).

[215] G. H. Ryder, "Strength of Materials", MacMillan Publishers, London, p. 56, (1985).

[216] P. P. Benham and F. V. Warnock, "Mechanics of Solids and Structures", Pitman Publishers Ltd., London, p. 357, (1978).

[217] J. G. Williams, "Stress Analysis of Polymers", Ellis Harwood Ltd., Chichester, England, p. 83, (1980).

[218] A. J. Kinloch and R. J. Young, "Fracture Behaviour of Polymers", Elsevier Applied Science, London, p. 164, (1988).

[219] J. M. McCarthy and M. J. Gudge, Unpubished work, Engineering Projects Division, Harwell Laboratory, Oxfordshire OX11-ORA, (Dec. 1986).

[220] R. D. Adams and J. A. Harris, Int. J. of Adhesion and Adhesives, 7 (2), p. 69 (1987).

[221] COSMOS/M, User Manual Release 1.52, Structural Research and Analysis Corporation, 1661 Lincoln Boulevard, Suite 100, Santa Monica, CA. 90404, U.S.A., (1988).

[222] LUSAS, User Manual, Version 86.07, FEA Ltd., Forge House, 66 High Street, Kingston Upon Thames, Surrey KT1-1HN, U.K., (1986).

[223] ABAQUS, Introduction Workbook Manual Version 4.7, Hibbit Karlsson and Sorensen Inc., 100 Medway Street, Providence, Rhode Island 02906, U.S.A., (1988).

[224] D. Hull, "An Introduction to Composite Materials", Cambridge Solid State Science Series, p. 126, (1987).

[225] J. R. Rice, P. C. Rice and J. G. Merkle, "Some Further Results of J Integral Analysis and Estimates", ASTM STP 536, p. 231, (1973).

[226] H. A. Ernst and P. C. Paris, "Techniques of Analysis of Load-Displacement Records by J Integral Methods", Nuclear Regulatory Comm., Report NUREG/CR-122, (1980).

[227] J. D. Landes and J. A. Begley, "Test Results from J Integral Studies: An Attempt to Establsih a J_{Ic} Testing Procedure", ASTM STP 560, p. 170, (1974).

[228] J. D. Landes and J. A. Begley, "Recent Developments in J_{Ic} Testing", Westinghouse Scientific Paper 76-1E7-JINTF-P3, (1976).

[229] R. M. Jones, "Mechanics of Composite Materials", McGraw Hill, p. 32, (1975).

[230] R. M. Jones, "Mechanics of Composite Materials", McGraw Hill, p. 34, (1975).

[231] E. J. Ripling, S. Mostovoy and R. L. Patrick, Materials Research and Standards, 4 (3). p. 129, (1964).

[232] P. P. Gillis and J. J. Gilman, J. of Applied Physics, 35, p. 647, (1964).